MICROSCALE PHYSICAL AND NUMERICAL INVESTIGATIONS OF SHEAR BANDING IN GRANULAR SOILS

A Dissertation
Presented to
The Academic Faculty

By

T. Matthew Evans

In Partial Fulfillment
Of the Requirements for the Degree
Doctor of Philosophy in Civil Engineering

Georgia Institute of Technology

December, 2005

MICROSCALE PHYSICAL AND NUMERICAL INVESTIGATIONS OF SHEAR BANDING IN GRANULAR SOILS

Dr. J. David Frost, Chairman
School of Civil and Environmental Engineering
Georgia Institute of Technology

Dr. Susan Burns
School of Civil and Environmental Engineering
Georgia Institute of Technology

Dr. Arun Gokhale
School of Materials Science and Engineering
Georgia Institute of Technology

Dr. Paul Mayne
School of Civil and Environmental Engineering
Georgia Institute of Technology

Dr. J. Carlos Santamarina
School of Civil and Environmental Engineering
Georgia Institute of Technology

Date Approved: November 17, 2005

TO MY FAMILY

ACKNOWLEDGMENTS

The work presented in this thesis would not have been possible without the support and assistance of my family, friends, colleagues, and professors. I would first like to thank Dr. J. David Frost for his untiring and unwavering support, guidance, and assistance with this work. He consistently asked questions, provided ideas, and encouraged me to look deeper throughout my time at Georgia Tech. Thank you for providing me with the opportunity to pursue the research presented herein. Perhaps most of all, thank you for your friendship. I look forward to our future collaborations.

I would also like to thank my committee members, Dr. Susan Burns, Dr. Arun Gokhale, Dr. Paul Mayne, and Dr. J. Carlos Santamarina. You have all provided guidance, education, and support throughout this process, making it all possible.

The experimental work presented in this dissertation would not have been possible without Mr. Ken Thomas, who seems to know a little bit about everything. His help in troubleshooting the many problems that tend to arise in the laboratory was invaluable.

Before I came to graduate school, someone told me that I would learn more from my fellow graduate students than from just about anyplace else. The assistance of Greg Hebeler, Alec McGillivray, and Guillermo Zavala is gratefully acknowledged. Any time I found myself "stuck" on a particular problem, I could always count on their assistance. If they didn't know the answer to my questions, they would happily spend hours trying to help me find one – much to their advisors' chagrin, I imagine. I hope that they learned at least a fraction as much from me as I from them.

In addition to those mentioned above, I would like to thank the other members of my research group for always being willing to help and for their friendship – Andrew Fuggle and Catherine McGillivray – and for holding my hand and guiding me through the basics of surface preparation and image analysis – Xuan Yang and DuHwan Kim. To all of the other members of the Georgia Tech geotech group, past and present – thanks for the friendship, great times, and memories.

The biaxial device used in the experimental work was fabricated by Geotest Instrument Corporation. I was not always the easiest customer to work with, but Michael Granovsky was always willing to answer questions and worked extremely hard to ensure that we received a device in which everyone could be proud. The biaxial device itself is a superior piece of equipment and I am fortunate to have been able to use it (thanks again, Dr. Frost).

The National Science Foundation provided funding for this research through the Graduate Research Fellowship program and a major equipment grant. Their support is gratefully acknowledged.

I would like to thank my family: my mother, Lynne, father, Tim, and brother, Pete, have never been anything but loving and supportive, regardless of my pursuits – whether it be moving to New Mexico to eat chile or back east to Atlanta to pursue a Ph.D. They laid the foundation for everything I have done and helped make me the man I am today.

Michelle. Words could not ever adequately express the unending gratitude that I have for all that you do. This work is as much yours as it is mine. You have consistently done everything in your power to help me achieve my goals. Your generosity, kindness

and love know no bounds and I am lucky to have you put up with me, wearoutfullness and all. You are a wonderful wife and, more importantly, mother. I love you and Nova with everything inside me. Everything I do is with the two of you in my heart and mind.

TABLE OF CONTENTS

ACKNOWLEDGMENTS iv

LIST OF TABLES x

LIST OF FIGURES xi

SUMMARY xx

1. INTRODUCTION 1

2. LITERATURE REVIEW 5

2.1. Plane Strain Testing of Granular Soils 5
2.2. Membrane Effects in Strength Testing of Soils 17
2.3. Microstructure Evolution Studies: Experimental 28
2.3.1. Introduction 28
2.3.2. Homogenous Deformation 28
2.3.3. Localized Deformation 32
2.3.4. Deformation Adjacent to Continua 38
2.4. Microstructure Evolution Studies: Numerical 40

3. BIAXIAL SHEAR DEVICE AND TEST PROCEDURES 46

3.1. Biaxial Shear Device and Data Acquisition System 46
3.1.1. Biaxial Shear Device 46
3.1.2. Data Acquisition System 49
3.1.2.1. Instrumentation 49
3.1.2.2. Power Supply Unit 49
3.1.2.3. Data Acquisition 52
3.2. Specimen Preparation 57
3.3. Monitoring of Membrane Deformations 60
3.4. Two-Stage Resin Impregnation Procedure 62
3.5. Coupon Surface Preparation and Mosaic Generation 69

4. MATERIAL AND MODEL PROPERTIES 78

4.1. Material Properties 78
4.2. Model Properties 80
4.2.1. Introduction 80
4.2.2. Mathematical Formulation of the Discrete Element Method 80
4.2.3. DEM Modeling of Biaxial Compression Tests 84
4.2.4. Model Characteristics 87

5. EXPERIMENTAL PROGRAM 90

5.1. Introduction 90
5.2. Biaxial Compression Tests 91
5.2.1. Stress-Strain Response of Ottawa 20-30 Sand Specimens 91
5.2.2. Detailed Analysis of Global Response in Impregnated Specimens 97
5.3. Membrane Deformation Analyses 110
5.3.1. Introduction 110
5.3.2. Collection of Membrane Deformation Data 111
5.3.3. Analysis of Membrane Deformation Data 112
5.3.4. Correction of In-Plane Shear Stress after Localization 118
5.3.5. Analysis of Membrane Data for a Kaolinite Specimen 121
5.4. Microstructure Analyses 125
5.4.1. Introduction 125
5.4.2. Local Void Ratio Distributions 126
5.4.3. Subregional Analyses 137
5.4.4. Spatial Averaging Along Pre-Determined Inclined Strips 148
5.4.5. Histograms from Pre-Determined Inclined Strips 150
5.4.6. Virtual Surface Analysis 156

6. NUMERICAL MODELING PROGRAM 167

6.1. Discrete Element Method Modeling of Biaxial Compression 167
6.1.1. Introduction 167
6.1.2. Membrane Confinement Algorithm 168
6.1.3. Parametric Analysis of Constitutive Parameters 171
6.1.4. Comparison with Macroscale Laboratory Results 173
6.2. Microstructure Analyses 181
6.2.1. Introduction 181
6.2.2. Subregional Void Ratio and Mean Free Path Analyses 184
6.2.3. Local Void Ratio Distributions and Inclined Spatial Averaging 191
6.3. Virtual Surface Analyses 208

7. DISCUSSION AND ANALYSIS OF RESULTS 217

7.1. Introduction 217
7.2. Analysis of Experimental Results 217
7.2.1. Local Void Ratio Distributions 217
7.2.2. Terminal Density Inside the Shear Band 224
7.2.3. Void Ratios Above and Below Shear Bands 227
7.2.4. Shear Band Thickness 231
7.3. Analysis of Numerical Results 237
7.3.1. Local Void Ratio Distributions 237
7.3.2. Shear Band Thickness 239
7.3.3. Additional Notes on Numerical Simulations 248

8. CONCLUSIONS AND RECOMMENDATIONS 250

8.1. Conclusions 250
8.2. Recommendations 258

APPENDIX A.1 262

APPENDIX A.2 274

APPENDIX A.3 281

APPENDIX A.4 292

APPENDIX A.5 297

APPENDIX B 307

APPENDIX C 316

REFERENCES 333

LIST OF TABLES

Table 3.1: Excitation voltages and calibration factors for sensors in the biaxial device . 50

Table 3.2: Properties of Epo-Tek 301 67

Table 3.3: Parameters used for polishing and grinding 74

Table 3.4: Parameters used for mosaic stitching operation 77

Table 4.1: Physical characteristics of Ottawa 20-30 sand 79

Table 4.2: Examples of typical model properties under different unit systems..... 88

Table 4.3: Specimen-to-particle size ratios..... 89

Table 5.1: Test parameters for four impregnated specimens 91

Table 5.2: Test parameters for Ottawa 20-30 sand specimens 91

Table 5.3: Summary of friction, dilation, and shear band inclination angles 110

Table 5.4: Void ratios and standard deviations for each surface 137

Table 5.5: Calculated mean grain sizes..... 148

Table 6.1: Material properties for PFC-2D simulations 178

Table 6.2: Summary of friction, dilation, and shear band inclination angles for slightly dilatant and highly dilatant experimental (E) and numerical (N) specimens..... 181

Table 6.3: Void ratios for specimens by different measures 192

Table 7.1: Estimated means and standard deviations of local void ratios (numbers in parenthesis are percent change from as-prepared void ratio) 219

Table 7.2: Summary of shear band thickness measurements (experimental)..... 233

Table 7.3: Summary of shear band thickness measurements (numerical)..... 248

LIST OF FIGURES

Figure 2.1: Theoretical ratio of PS elastic modulus to CTC elastic modulus 10

Figure 2.2: Theoretical relationship between CTC and PS Poisson's ratios 11

Figure 2.3: Comparison of corrected and uncorrected stress paths for CU triaxial tests on a soil-bentonite mixture (after Baxter (2000)) 22

Figure 2.4: Experimental setup for assessment of membrane effects in triaxial specimens that fail along a single well-defined plane (after La Rochelle (1967)) 23

Figure 2.5: Comparison of measured and predicted load-deformation curves for latex membranes (after La Rochelle (1967)) 26

Figure 2.6: Horizontal and vertical displacement contours for wedge penetration into a sand mass under plane strain conditions (Butterfield et al., 1970) 34

Figure 2.7: Shear zone thickness as a function of counterface roughness (after Hebeler, 2005) 39

Figure 3.1: Photograph of the biaxial shear device with a sample in place and the confining cell removed 47

Figure 3.2: Schematic of instrumentation in the biaxial device (note three pancake load cells on the σ_2 plane are not shown) 48

Figure 3.3: External front view of the power supply unit 51

Figure 3.4: External rear view of the power supply unit 53

Figure 3.5: Data acquisition unit 54

Figure 3.6: Maximum measurement errors due to the accuracy of the DMM 56

Figure 3.7: Sample forming mold 57

Figure 3.8: Manual air pluviator 58

Figure 3.9: Aluminum insert for specimen former 59

Figure 3.10: Top loading platen 59

Figure 3.11: Sample image of deformed grid on the side of a membrane 61

Figure 3.12: Schematic of glue impregnation processes 64

Figure 3.13: Schematic of desiccation processes..... 65

Figure 3.14: Portion of the sample extracted after testing for resin impregnation and sectioning 66

Figure 3.15: Sample that fractured along the shear band during extraction from the biaxial device 69

Figure 3.16: Buehler Lapro slab saw 70

Figure 3.17: Specimen dimensions after trimming with the slab saw 70

Figure 3.18: Isomet 1000 precision saw 71

Figure 3.19: Specimen sectioned for planing, grinding, and polishing 71

Figure 3.20: SBEL surface planer..... 72

Figure 3.21: Buehler Metaserv polishing table with Autopol II attachment 74

Figure 3.22: Mosaic stitched with 20% overlap (note shadow effects)..... 76

Figure 4.1: Microscopic image of Ottawa 20-30 sand..... 78

Figure 4.2: Grain size distribution for Ottawa 20-30 sand 79

Figure 5.1: Stress-strain and volume change plots for specimens with $e_0 > 0.58$ (the numbers in parentheses in the legend indicate initial void ratio and confining stress) 94

Figure 5.2: Stress-strain and volume change plots for specimens with $e_0 < 0.58$ (the numbers in parentheses in the legend indicate initial void ratio and confining stress) 95

Figure 5.3: p-q plots for biaxial specimens (e_0, σ_3) 96

Figure 5.4: Stress-strain plot for slightly dilatant specimen 99

Figure 5.5: Specimen thickness plot for slightly dilatant specimen 99

Figure 5.6: Stress-strain plot for highly dilatant specimen 100

Figure 5.7: Specimen thickness plot for highly dilatant specimen 100

Figure 5.8: Total sled movement for slightly dilatant specimen 101

Figure 5.9: Incremental sled movement for slightly dilatant specimen..... 101

Figure 5.10: Total sled movement for highly dilatant specimen 101

Figure 5.11: Incremental sled movement for highly dilatant specimen..... 102

Figure 5.12: Shear band inclination for slightly dilatant specimen 103

Figure 5.13: Shear band inclination for highly dilatant specimen 104

Figure 5.14: Calculated and averaged dilation angles 105

Figure 5.15: Averaged dilation angle for slightly dilatant specimen..... 105

Figure 5.16: Averaged dilation angle for highly dilatant specimen..... 105

Figure 5.17: Friction angles for slightly dilatant specimen 108

Figure 5.18: Friction angles for highly dilatant specimen 108

Figure 5.19: Normal and shear stresses on the failure plane for slightly dilatant specimen 109

Figure 5.20: Normal and shear stresses on the failure plane for highly dilatant specimen 109

Figure 5.21: Membrane deformation contours for a biaxial specimen..... 112

Figure 5.22: Membrane grid point locations before localization and at the end of the highly dilatant test. Squares (□) indicate control points, triangles (△) indicate moving points before localization, and diamonds (◇) indicate moving points after localization. 115

Figure 5.23: Geometry used for the rigid block model..... 116

Figure 5.24: Membrane correction for slightly dilatant specimen..... 117

Figure 5.25: Membrane correction for highly dilatant specimen 118

Figure 5.26: Membrane normal stress correction for slightly dilatant specimen 119

Figure 5.27: Membrane normal stress correction for highly dilatant specimen 119

Figure 5.28: Corrected shear stress on the failure plane for slightly dilatant specimen 120

Figure 5.29: Corrected shear stress on the failure plane for highly dilatant specimen.. 120

Figure 5.30: Sample images for biaxial test on kaolinite (Peric, 2003)..... 122

Figure 5.31: Membrane shear stress (upper plot) and normal stress (lower plot) corrections for kaolinite specimen 123

Figure 5.32: Transect plots of membrane displacement contours for kaolinite specimen 124

Figure 5.33: Sample image before and after binarization..... 125

Figure 5.34: Polygon network for local void ratio calculations (after Jang, 1997) 126

Figure 5.35: Solid area weighted histogram for surface HDS-80..... 128

Figure 5.36: Total histograms for slightly dilatant specimens (e_{un} and e_{sh} indicate global image void ratios before and after shearing, respectively) 129

Figure 5.37: Total histograms for highly dilatant specimens (e_{un} and e_{sh} indicate global image void ratios before and after shearing, respectively) 130

Figure 5.38: Pearson probability space..... 132

Figure 5.39: Maximum likelihood fitting to the histogram from surface HDS-80..... 133

Figure 5.40: Probability distribution fitting to the histogram from surface HDS-80 134

Figure 5.41: Cumulative distribution fitting to the histogram from surface HDS-80 ... 134

Figure 5.42: Gamma distributions for slightly dilatant specimens (solid lines correspond to unsheared surfaces and dotted lines correspond to sheared surfaces). 136

Figure 5.43: Gamma distributions for highly dilatant specimens (solid lines correspond to unsheared surfaces and dotted lines correspond to sheared surfaces). 136

Figure 5.44: Schematic of 22 × 22 grid for subregional calculations..... 138

Figure 5.45: Void ratio contours for slightly dilatant unsheared specimen..... 140

Figure 5.46: Void ratio contours for slightly dilatant sheared specimen..... 141

Figure 5.47: Void ratio contours for highly dilatant unsheared specimen..... 142

Figure 5.48: Void ratio contours for highly dilatant sheared specimen..... 143

Figure 5.49: Mean free path contours for slightly dilatant unsheared specimen..... 144

Figure 5.50: Mean free path contours for slightly dilatant sheared specimen..... 145

Figure 5.51: Mean free path contours for highly dilatant unsheared specimen..... 146

Figure 5.52: Mean free path contours for highly dilatant sheared specimen..... 147

Figure 5.53: Schematic of oriented strips for calculation of void ratios..... 148

Figure 5.54: Incremental and accumulated void ratios for surface SDS-20 151

Figure 5.55: Incremental and ultimate void ratios for surface SDS-20 151

Figure 5.56: Incremental (top) and accumulated (bottom) void ratio transects for surface SDU-80 (LHS and RHS indicated inferred shear band extents; horizontal lines in accumulated void ratio plots indicate asymptotic values for each region) 152

Figure 5.57: Incremental (top) and accumulated (bottom) void ratio transects for surface SDS-20 (LHS and RHS indicated inferred shear band extents; horizontal lines in accumulated void ratio plots indicate asymptotic values for each region) 153

Figure 5.58: Incremental (top) and accumulated (bottom) void ratio transects for surface HDU-20 (LHS and RHS indicated inferred shear band extents; horizontal lines in accumulated void ratio plots indicate asymptotic values for each region) 154

Figure 5.59: Incremental (top) and accumulated (bottom) void ratio transects for surface HDS-60 (LHS and RHS are inferred approximations from sheared specimens; horizontal lines in accumulated void ratio plots indicate asymptotic values for each region) 155

Figure 5.60: Internal and external void ratio histograms for the slightly dilatant specimen 157

Figure 5.61: Internal and external void ratio histograms for the highly dilatant specimen 159

Figure 5.62: Initial particles and horizontal line used to form a virtual surface 162

Figure 5.63: After the rubber sheeting algorithm is applied to the segment of the surface in Figure 5.62 162

Figure 5.64: The minimum energy surface developed from the rubber sheets shown in Figure 5.63 163

Figure 5.65: Roughness parameters for slightly dilatant specimens 165

Figure 5.66: Roughness parameters for highly dilatant specimens 166

Figure 6.1: Assembled DEM specimen prior to consolidation 169

Figure 6.2: Magnified view of particle membrane conforming to particle assembly 170

Figure 6.3: Normalized axial and confining force (upper plot) and normalized volume change (lower plot) for parametric analyses on the effects of contact normal stiffness 174

Figure 6.4: Normalized axial and confining force (upper plot) and normalized volume change (lower plot) for parametric analyses on the effects of contact friction coefficient 175

Figure 6.5: Normalized axial and confining force (upper plot) and normalized volume change (lower plot) for parametric analyses on the effects of contact shear stiffness 176

Figure 6.6: Normalized axial and confining force (upper plot) and normalized volume change (lower plot) for parametric analyses on the effects of seed values in the random number generator 177

Figure 6.7: Normalized axial and confining force (upper plot) and normalized volume change (lower plot) for slightly dilatant specimen and corresponding numerical simulation..... 182

Figure 6.8: Normalized axial and confining force (upper plot) and normalized volume change (lower plot) for highly dilatant specimen and corresponding numerical simulation..... 183

Figure 6.9: Slightly dilatant specimen images at various levels of global axial strain.. 185

Figure 6.10: Highly dilatant specimen images at various levels of global axial strain . 186

Figure 6.11: Subregional void ratio contours for the slightly dilatant specimen..... 187

Figure 6.12: Subregional mean free path contours for the slightly dilatant specimen .. 188

Figure 6.13: Subregional void ratio contours for the highly dilatant specimen..... 189

Figure 6.14: Subregional mean free path contours for the highly dilatant specimen 190

Figure 6.15: Gamma distributions for local void ratios in the slightly dilatant specimen 193

Figure 6.16: Gamma distributions for local void ratios in the highly dilatant specimen193

Figure 6.17: Incremental and accumulated void ratios for the HD specimen at 8% strain 194

Figure 6.18: Incremental and asymptotic void ratios inside and outside of the shear band for the HD specimen at 8% strain 194

Figure 6.19: Incremental (upper) and accumulated (middle) void ratios of strips parallel to the shear band and a histogram (lower) of local void ratio distributions for regions inside and outside of the shear band, slightly dilatant specimen at 0% global axial strain..... 195

Figure 6.20: Incremental (upper) and accumulated (middle) void ratios of strips parallel to the shear band and a histogram (lower) of local void ratio distributions for regions inside and outside of the shear band, slightly dilatant specimen at 2% global axial strain..... 196

Figure 6.21: Incremental (upper) and accumulated (middle) void ratios of strips parallel to the shear band and a histogram (lower) of local void ratio distributions for regions inside and outside of the shear band, slightly dilatant specimen at 4% global axial strain..... 197

Figure 6.22: Incremental (upper) and accumulated (middle) void ratios of strips parallel to the shear band and a histogram (lower) of local void ratio distributions for regions inside and outside of the shear band, slightly dilatant specimen at 6% global axial strain..... 198

Figure 6.23: Incremental (upper) and accumulated (middle) void ratios of strips parallel to the shear band and a histogram (lower) of local void ratio distributions for regions inside and outside of the shear band, slightly dilatant specimen at 8% global axial strain..... 199

Figure 6.24: Incremental (upper) and accumulated (middle) void ratios of strips parallel to the shear band and a histogram (lower) of local void ratio distributions for regions inside and outside of the shear band, slightly dilatant specimen at 10% global axial strain..... 200

Figure 6.25: Incremental (upper) and accumulated (middle) void ratios of strips parallel to the shear band and a histogram (lower) of local void ratio distributions for regions inside and outside of the shear band, highly dilatant specimen at 0% global axial strain..... 201

Figure 6.26: Incremental (upper) and accumulated (middle) void ratios of strips parallel to the shear band and a histogram (lower) of local void ratio distributions for regions inside and outside of the shear band, highly dilatant specimen at 2% global axial strain..... 202

Figure 6.27: Incremental (upper) and accumulated (middle) void ratios of strips parallel to the shear band and a histogram (lower) of local void ratio distributions for regions inside and outside of the shear band, highly dilatant specimen at 4% global axial strain..... 203

Figure 6.28: Incremental (upper) and accumulated (middle) void ratios of strips parallel to the shear band and a histogram (lower) of local void ratio distributions for regions inside and outside of the shear band, highly dilatant specimen at 6% global axial strain..... 204

Figure 6.29: Incremental (upper) and accumulated (middle) void ratios of strips parallel to the shear band and a histogram (lower) of local void ratio distributions for regions

inside and outside of the shear band, highly dilatant specimen at 8% global axial strain..... 205

Figure 6.30: Incremental (upper) and accumulated (middle) void ratios of strips parallel to the shear band and a histogram (lower) of local void ratio distributions for regions inside and outside of the shear band, highly dilatant specimen at 10% global axial strain..... 206

Figure 6.31: Evolving void ratios in the slightly dilatant specimen 207

Figure 6.32: Evolving void ratios in the highly dilatant specimen 207

Figure 6.33: Roughness of virtual surfaces in the slightly dilatant specimen 209

Figure 6.34: Roughness of virtual surfaces in the highly dilatant specimen 211

Figure 6.35: Roughness of virtual surfaces inside and outside of the shear band as a function of global axial strain in the slightly dilatant specimen 213

Figure 6.36: Roughness of virtual surfaces inside and outside of the shear band as a function of global axial strain in the highly dilatant specimen 215

Figure 7.1: Standard deviation of local void ratio distributions as a function of the mean 220

Figure 7.2: Entropy of local void ratio distributions as a function of the mean 221

Figure 7.3: Comparison of void ratio distributions inside and outside the shear band for slightly dilatant and highly dilatant specimens..... 222

Figure 7.4: Comparison of void ratio distributions inside and outside the shear band for slightly dilatant specimens in the sheared and unsheared states..... 222

Figure 7.5: Comparison of void ratio distributions inside and outside the shear band for highly dilatant specimens in the sheared and unsheared states..... 223

Figure 7.6: e-log(p′) plot for slightly dilatant and highly dilatant specimens..... 225

Figure 7.7: Conceptual model of shear banding with transition zones..... 226

Figure 7.8: Standard deviations of void ratio distributions inside, above, and below the shear band 228

Figure 7.9: Entropies of void ratio distributions inside, above, and below the shear band 229

Figure 7.10: Measurement of shear band thickness from an image (HDS-60) captured in a laboratory specimen (measurement shown is in millimeters)..... 232

Figure 7.11: Measurement of shear band thickness from membrane deformations on the highly dilatant specimen (measurement shown is in millimeters) 232

Figure 7.12: Schematic of shear band extents for image HDS-60 234

Figure 7.13: Transition zone in interface shear 235

Figure 7.14: Shear band thickness as a function of void ratio 237

Figure 7.15: Standard deviation of local void ratio distributions as a function of global axial strain 238

Figure 7.16: Local void ratio distribution entropy as a function of global axial strain . 239

Figure 7.17: Standard deviation of local void ratio distribution as a function of estimated mean void ratios 240

Figure 7.18: Local void ratio distribution entropies as a function of estimated mean void ratios 240

Figure 7.19: Normal contact force chains for slightly dilatant specimen at ε_{ax} = 0% ... 242

Figure 7.20: Normal contact force chains for slightly dilatant specimen at ε_{ax} = 2% ... 242

Figure 7.21: Normal contact force chains for slightly dilatant specimen at ε_{ax} = 4% ... 243

Figure 7.22: Normal contact force chains for slightly dilatant specimen at ε_{ax} = 6% ... 243

Figure 7.23: Normal contact force chains for slightly dilatant specimen at ε_{ax} = 8% ... 244

Figure 7.24: Normal contact force chains for slightly dilatant specimen at ε_{ax} = 10% . 244

Figure 7.25: Normal contact force chains for highly dilatant specimen at ε_{ax} = 0% 245

Figure 7.26: Normal contact force chains for highly dilatant specimen at ε_{ax} = 2% 245

Figure 7.27: Normal contact force chains for highly dilatant specimen at ε_{ax} = 4% 246

Figure 7.28: Normal contact force chains for highly dilatant specimen at ε_{ax} = 6% 246

Figure 7.29: Normal contact force chains for highly dilatant specimen at ε_{ax} = 8% 247

Figure 7.30: Normal contact force chains for highly dilatant specimen at ε_{ax} = 10% ... 247

SUMMARY

Under loading conditions found in many geotechnical structures, it is common to observe failure in zones of high localized strain called shear bands. Existing models predict these localizations, but provide little insight into the micromechanics within the shear bands. This research captures the variation in microstructure inside and outside of shear bands that were formed in laboratory plane strain and two-dimensional discrete element method (DEM) biaxial compression experiments.

Plane strain compression tests were conducted on dry specimens of Ottawa 20-30 sand to calibrate the device, assess global response repeatability, and develop a procedure to quantitatively define the onset of localization. A new methodology was employed to quantify and correct for the additional stresses imparted by the confining membrane in the vicinity of the shear band. Unsheared and sheared specimens of varying dilatancy were solidified using a two-stage resin impregnation procedure. DEM tests were performed using an innovative servo-controlled flexible lateral confinement algorithm to provide additional insights into laboratory results.

The solidified specimens were sectioned and the resulting surfaces prepared for microstructure observation using bright field microscopy and morphological analysis. Local void ratio distributions and their statistical properties were determined and compared. Microstructural parameters for subregions in a grid pattern and along predefined inclined zones were also calculated. Virtual surfaces parallel to the shear band were identified and their roughnesses assessed. Similar calculations were performed on the DEM simulations at varying strain levels to characterize the evolution of microstructure with increasing strain.

The various observations showed that the mean, standard deviation, and entropy of the local void ratio distributions all increased with increasing strain levels, particularly within regions of high local strains. These results indicate that disorder increases within a shear band and that the soil within the shear band does not adhere to the classical concept of critical state, but reaches a terminal void ratio that is largely a function of initial void ratio. Furthermore, there appears to be a transition zone between the far field and the fully formed shear block, as opposed to an abrupt delineation as traditionally inferred.

1. INTRODUCTION

In soil mechanics and geotechnical engineering, strain localization (or, so-called "shear banding") consists of the failure of a soil specimen along a well-defined plane of very high shear strain. This plane is of some finite thickness and is typically characterized by high void ratios relative to the surrounding soil. Shear banding is evidenced in many field-scale failures of geotechnical systems, including shallow foundations and earth retaining structures. In fact, the presence of shear bands is implicitly suggested by both Coulomb and Rankine earth pressure theories, which are the most common bases for strength design of geotechnical structures.

Over the past three decades, there has been increased interest in understanding the mechanics of these shear bands. The problem is of interest to engineers and scientists in a wide range of disciplines: geotechnical engineering, physics, mathematics, structural geology, chemical engineering, and agricultural engineering. Across all of these disciplines, the driving force behind the research is broadly defined as the desire to minimize the adverse effects of localization, whether it be behind a retaining wall or when considering hopper flow (wherein localization can lead to material segregation). Often, however, this research can be divided into two distinct camps: theoretical and applied. Mathematicians and physicists come down on the theoretical side, often studying the solution of the constitutive equations used to describe material behavior once they lose their ellipticity or performing simple yet insightful experiments on idealized particles under idealized conditions. The applied research is often focused on

forensic investigations of failures or on developing better constitutive models to adequately describe material response (and, thus, solve boundary value problems) at points where solution of classical constitutive equations becomes troublesome. In many cases, there is relatively little opportunity for the sharing of ideas across such divergent fields.

In geotechnical engineering, the onset of localization is often considered either as a bifurcation problem or as a problem when second order work becomes negative (i.e., in the strain softening regime) and the constitutive equations no longer have a single unique solution. Several researchers (e.g., Jang and Frost, 2000) in the field of geotechnical engineering have noted that a better understanding of shear banding will come from a better understanding of the micromechanics of the shear band – but, from a conceptual standpoint. It is in this gray region that the current work falls. It is neither purely theoretical nor purely applied, but attempts to bridge the gap between the two.

Many studies of shear bands have concluded that shear band thickness is purely a function of mean particle diameter (e.g., Muehlhaus and Vardoulakis, 1987) and that shear band (i.e., failure plane) inclination is defined purely by plasticity considerations (Coulomb, 1773). These studies tend to overlook the underlying mechanics that may govern shear band behavior. While studies like those described above typically provide good general agreement with experimental results, comparisons are typically made with either global measurements of laboratory specimen response (Vardoulakis and Graf, 1985), with measurements on the boundaries of the specimen (Harris et al., 1995), or using wave-based analysis (Desrues et al., 1996). Each of these methods provides valuable insight into material response, but each also has its drawbacks. In using global

response, even the most highly instrumented laboratory equipment is capable only of measuring material response at scales many times greater than the particle diameter. Measurements made on specimen boundaries are, by definition, subject to significant boundary effects. Wave-based characterization is subject to tradeoffs between energy, wavelength, and depth of penetration, so the results are often on the scale of the shear band (say, 10 to 15 particle diameters) as opposed to on the 'true" particle scale.

The current study attempts to address some of the shortcomings of the above approaches by studying solidified sand specimens that failed via a single, localized shear plane. By solidifying, sectioning, and imaging failed specimens, it is possible to achieve study resolutions on the subparticle level, allowing for the detailed study of microstructure inside and outside of the shear band. The experimental work, which provides images of specimen microstructure only at the beginning and end of a test, is supplemented with numerical studies using the discrete element method. In this manner, it may be possible to interpolate between the beginning and ending states of the soil microstructure. This thesis is organized in the following manner:

- Chapter 2 provides an overview of previous work on plane strain testing of granular soils, membrane effects in laboratory strength testing of soils, and microstructure quantification of soil specimens;
- Chapter 3 describes the experimental work that was conducted as part of the current study, including plane strain testing and surface preparation for imaging;

- Chapter 4 addresses material and model properties for the current study and provides an overview of the mathematical formulation of the discrete element method;
- Chapter 5 presents macroscale results of a series of biaxial compression tests, results of microscale analyses on a number of tests, and proposes a new membrane correction for plane strain tests on soils that fail along a single well-defined plane;
- Chapter 6 describes the membrane confinement algorithm used for the current discrete element method studies and presents the results from a series of discrete element method tests;
- Chapter 7 provides an in-depth analysis of microscale results from the experimental and numerical test programs; and
- Chapter 8 presents conclusions and recommendations for future work.

References and appendices are presented at the end of this thesis.

2. LITERATURE REVIEW

2.1. Plane Strain Testing of Granular Soils

The most common laboratory tests for determining the stress-strain-strength response of granular materials are the conventional triaxial compression (CTC) test and the direct shear (DS) test. However, each of these tests has drawbacks, particularly with respect to the study of strain localizations. In the CTC test, applied stresses by definition are axisymmetric, providing no control over the intermediate principal stress. The CTC test is designed to induce homogenous deformation for the study of the constitutive behavior of soils and if shear banding does occur, localization geometries are typically complex fan-shaped patterns (Desrues et al., 1996; Alshibli et al., 2000). The DS test, by contrast, forces failure via a localized region of high strains, but this region is predetermined by the test device geometry and is not allowed to occur along its natural plane within the specimen.

The use of plane strain (PS) and true triaxial (TT) tests is becoming increasingly more widespread for the characterization of the stress-strain-strength response of granular soils, particularly when strain localization is being studied (e.g., Drescher et al., 1990; Lade and Wang, 2001). The TT test has the advantage that all three principal stresses are controlled during testing, allowing for the attainment of a wide variety of loading conditions. The PS test is essentially a specific implementation of the more complex TT test, wherein the major and minor principal stresses are controlled and the intermediate principal stress is measured on the plane of zero deformation. The primary advantage of

PS testing (as opposed to TT) with respect to studying strain localization is that it has been shown both experimentally (Lee, 1970) and theoretically (Peric et al., 1992) that soils subjected to plane strain compression are likely to fail along a well-defined plane of high local strains (i.e., a shear band). It is for this reason that a modified plane strain apparatus was selected for the present study. The remainder of this section focuses on previous experimental work related to soils subjected to plane strain compression.

The PS (or biaxial) compression test has been used since the 1930's as a tool for evaluating the stress-strain-strength response of soils (Kjellman, 1936) and has been gaining popularity over the last 25 years. Here, the so-called Kjellman soil testing machine was used to subject specimens of German standard sand to constrained uniaxial, PS, and TT compression. Results from PS and TT compression tests were compared to those obtained using a type of direct shear (DS) device known as the Krey shearing apparatus. A friction angle of 43° was measured for the sand in PS compression, versus 35° in TT ($\sigma_2 = \sigma_3$) compression and 34° in DS. Kjellman (1936) attributes the differences between PS and TT to the effect of the intermediate effective stress. Differences between DS and PS were ascribed to stress inhomogeneities within the DS device. Kjellman further mentioned that deformation in the DS device was 10 times greater at the end of the test than in the PS test. This would seem to indicate that the measurement in the Kjellman soil testing machine corresponded to the peak friction angle while the DS test was measuring the critical state friction angle.

Perhaps the largest body of work concerning PS compression tests on soils is focused on identifying the role of intermediate principal stress on soil strength or the effects of loading conditions on macroscopic material response (Cornforth, 1964; Henkel

and Wade, 1966; Rowe, 1969; Lee, 1970). The Cornforth paper focuses on the effects of strain influence on the strength of sand, rooted in the argument that the loading conditions for many geotechnical applications (e.g., retaining walls and embankment dams) are more closely approximated by the plane strain condition than the axisymmetric triaxial case. The study involved the repeated testing of "Brasted sand" under both CTC and plane strain compression. Based on "before" and "after" gradation curves, Cornforth concedes that "some breakdown in particle sizes occurred", but argues that there was no noticeable impact on soil behavior. Specimens for both PS and CTC tests were constructed using a complex combination of water pluviation and vibration.

In PS specimens, Cornforth generally found that the inclination of the shear band was consistent with that proposed by the Mohr-Coulomb failure criterion ($45° + \phi/2$) and that the width of the failure zone varied from 1.5 to 5 mm ($\cong 6d_{50}$ to $18d_{50}$), with thicker shear bands occurring in looser specimens. Furthermore, he noted that in PS tests the Brasted sand exhibited relatively low axial strain to peak and critical state strength, that major and intermediate principal stress curves as a function of axial strain were of the same shape, and that the ratio of major to intermediate principal stress was approximately constant. Critical state was achieved in PS specimens at axial strain values of 3% to 6% and was independent of initial void ratio.

In comparing results from PS and CTC tests with the same initial void ratio, Cornforth found that the peak friction angle for PS specimens was consistently 0.5° to 4° greater than for CTC specimens and that axial strains at failure were nearly three times greater in CTC specimens than in PS specimens. Cornforth postulates that peak strength was greater in PS tests but that critical state strengths are the same because soil grains are

free to move along the path of least resistance in a plane when the minor and intermediate principal stresses were equal but are constrained to move along a path contained in the intermediate stress plane when $\sigma_2 > \sigma_3$. By measuring water contents at different locations within failed specimens, it was found that the void ratio within the failure zone was considerably higher than in other areas of the specimens for both CTC and PS compression tests. Global dilatancy was less in PS tests (1%) than in CTC tests (4% to 5%). The critical state friction angle was similar in both types of tests (PS: 32.3°, CTC: 33.0°) although the major principal stress at critical state was, on average, 8% greater in PS compared to CTC, leading Cornforth to conclude that the critical state friction angle is independent of the intermediate principal stress. Of significant practical importance in this work, Cornforth determined that removal of the end caps which enforce the plane strain condition have little bearing on the test results and that when the end caps were omitted, longitudinal strain was approximately 20% of lateral strain. This appears to indicate that results of PS compression tests are highly relevant to field applications that approximate PS conditions.

Henkel and Wade (1966) used the same PS apparatus as Cornforth to study the effect of the intermediate effective stress on Weald clay. Both PS and CTC tests were performed on K_0-consolidated specimens and CTC tests were also performed on hydrostatically consolidated specimens. Undrained shear strength of Weald clay was found to be greatest in the hydrostatically consolidated CTC specimens, followed by the K_0-consolidated PS specimens. Among the K_0-consolidated specimens, pore pressure generation was greater in PS than in CTC tests. The effective angle of internal friction was only reported for K_0-consolidated tests, with an average value of 27.1° for PS and

25.9° for CTC. Similarly to Cornforth's (1964) results for sand, Henkel and Wade found that the principal effective stress ratio (σ'_2/σ'_1) did not vary appreciably during the course of the test. In octahedral stress space, the PS and CTC tests followed the same stress paths, but the termination points were different for the two tests.

Rowe (1969) compared the results of PS, CTC, and DS tests on quartz sand, feldspar, crushed glass, and glass ballotini. In all cases, he found that the maximum angle of internal friction (ϕ_{max}) was greater in plane strain than in CTC or DS, in spite of the fact that for a given material the angle of friction between particles (ϕ_μ) and the constant volume friction angle (ϕ_{cv}) are constant. Rowe also derives the expression

$$\tan\left(\phi_{ds}\right) = \tan\left(\phi_{ps}\right)\cdot\cos\left(\phi_{cv}\right) \tag{2.1}$$

where ϕ_{ds} and ϕ_{ps} are friction angles for direct shear and plane strain tests, respectively. Thus, the strength measured in DS will always be less than that measured in PS.

In addition to his own work, Lee (1970) provided an overview of previous work on the comparison of results from PS and CTC tests. In the overview, Lee considered both "typical" PS testing (i.e., tests on orthorhombic specimens) and torsional/hollow cylinder tests. The overall conclusion from analyzing these previous data indicated that the plane strain friction angle was consistently greater than the triaxial friction angle (by as much as eight degrees), but there was some scatter in the data. Lee further considered the effects of test type on elastic parameters, noting that for a linear elastic material:

$$E_p = \frac{E_t}{1 - \nu_t^2} \tag{2.2}$$

$$\nu_p = \frac{\nu_t}{1 - \nu_t} \tag{2.3}$$

where E_t and E_p are the elastic moduli for CTC and PS tests, respectively, and ν_t and ν_p are the Poisson's ratios for CTC and PS tests, respectively. Note that equations (2.2) and (2.3) were derived from the constitutive relationships for a linear elastic material given known test conditions for both CTC and PS tests. Figures 2.1 and 2.2 illustrate the theoretical relationships between elastic parameters from CTC and PS tests described by equations (2.2) and (2.3).

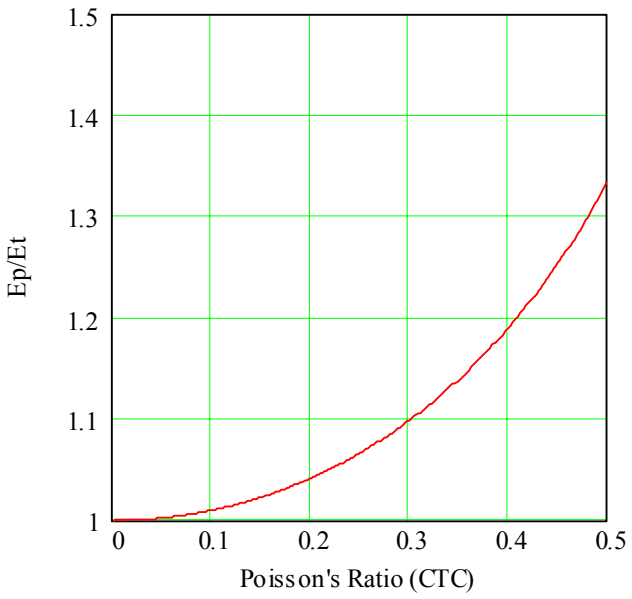

Figure 2.1: Theoretical ratio of PS elastic modulus to CTC elastic modulus

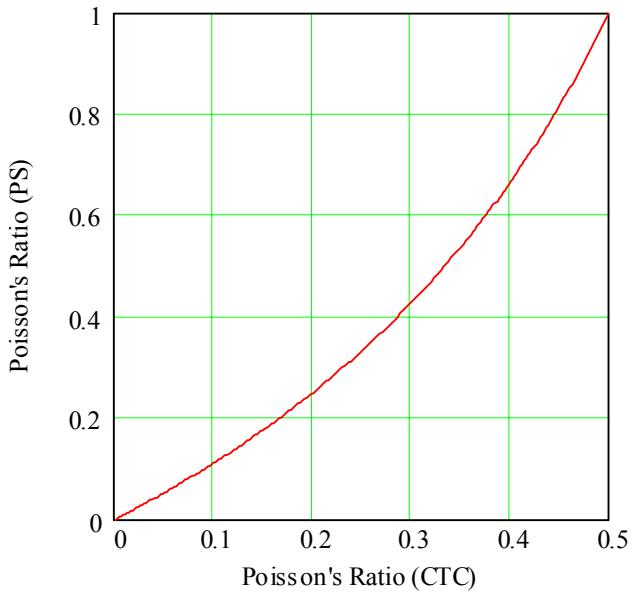

Figure 2.2: Theoretical relationship between CTC and PS Poisson's ratios

In addition to the review of previous studies and theoretical analysis of the elastic response of linearly elastic test specimens, Lee (1970) performed PS and CTC tests on specimens of Antioch sand and compared the results of tests performed under different loading conditions but with identical starting points in critical state space. Similarly to previous studies, Lee determined that initial tangent modulus and peak friction angle were greater in PS tests while strain to peak was greater in CTC tests. Additionally, the Poisson's ratios were higher in PS than in CTC and agreed well with linear elastic theory as outlined in equation (2.3) above. The measured elastic moduli were typically greater in PS (relative to CTC) than what is predicted from linear elasticity. Lee also performed undrained tests under both loading conditions, but results were non-unique and he recommended additional studies.

Bolton (1986) analyzed previously published data for 17 different sands in CTC and PS compression to study the effects of dilatancy on sand behavior. This work firstly provided an overview of the effects of dilation on the strength of sand and demonstrated mathematically why a free-forming failure surface is required (through the angle of dilatancy) to be of log spiral form. The so-called "dilatancy index" was empirically developed by Bolton as a means of calculating the maximum angle of internal friction and quantifying rates of strain based on limited laboratory data. The work by Bolton allows for the incorporation of dilatancy effects into practical design problems, although Bolton noted that this is often not done in practice, leading to overly conservative designs.

While the work discussed above typically focused on the differences in measurements between PS and CTC testing, an additional body of work (e.g., Vardoulakis, 1980) tends to focus more on the understanding of strain localization (specifically, shear banding) during PS compression and on the calibration of constitutive models to describe shear banding. The two most historically significant theoretical solutions for shear band (i.e., failure plane) inclination were given by Coulomb (1773) and Roscoe (1970) and may be expressed as follows:

$$\theta_C = \frac{\pi}{4} + \frac{\phi_p}{2} \tag{2.4}$$

$$\theta_R = \frac{\pi}{4} + \frac{\psi_p}{2} \tag{2.5}$$

where θ_C and θ_R are the shear band inclinations predicted by Coulomb and Roscoe, respectively; ϕ_p is the peak friction angle; and ψ_p is the angle of dilatancy at peak. In the work by Vardoulakis (1980), shear band formation in PS tests on dry sand was

considered as a bifurcation problem, yielding the Roscoe and Coulomb angles as the two real solutions for the inclination of the shear band.

Theoretically, Vardoulakis (1980) concluded that because there is a lack of normality (i.e., the incremental plastic strain tensor is not orthogonal to the yield locus) during localization of sands subjected to PS loading, localization must always occur in the strain hardening regime (see Nova (2004) for a thermodynamic explanation of why the associated flow rule does not apply to the localization of purely frictional materials) and that the Coulomb angle of inclination from equation (2.4) above is possible only at peak. The Roscoe solution from equation (2.5) above was shown to be the lower bound for the inclination of the shear band. Using trigonometric approximations and assuming that localization occurs near peak, an approximate solution to the bifurcation problem is the same as the solution first proposed by Arthur, et al. (1977):

$$\theta_A = \frac{\pi}{4} + \frac{1}{4}\left(\phi_p + \psi_p\right) \tag{2.6}$$

where θ_A is the Arthur, et al. prediction for shear band inclination.

For comparison with theory, Vardoulakis (1980) presented results from a series of 20 PS tests on Karlsruhe sand prepared at varying initial void ratios. The measured shear band inclinations from these tests fell approximately halfway between those calculated from Coulomb or Roscoe theory, but agreed very well with both the exact and approximate bifurcation solutions.

The design of a "biaxial device" for PS testing of soils is described in the work of (Drescher et al., 1990). The design of this biaxial device was significant in that the bottom platen on which the soil specimen rests is affixed to a frictionless linear sled that translates in a direction orthogonal to the plane defined by the minor principal stress

during testing. Thus, once the shear band was fully formed, the two theoretical rigid blocks defined by the specimen boundaries and the shear band translated freely with respect to one another. This ensured that post failure deformation is due solely to rigid block displacement, allowing for the constitutive study of soil behavior both before and after the onset of localization.

Drescher, et al. (1990) performed a series of PS tests on specimens of ASTM C-190 quartz sand to demonstrate the use of the biaxial device and the proper data reduction and evaluation procedures. The test results showed that the onset of localization was clearly indicated by monitoring sled displacement (i.e., there is very little sled movement prior to localization). Drescher, et al. noted two difficulties associated with the biaxial compression test: (i) there was some small amount of sled movement at the very beginning of the test, prior to the onset of localization; and (ii) the shear band tended to daylight very near the upper loading platen. Both difficulties can most likely be attributed to a slight misalignment of the specimen within the device. The small amount of sled movement at the beginning of the test corresponded to a self-alignment of the specimen to some equilibrium configuration and, according to Drescher, et al., (1990) was not preventable. However, stress concentrations may still be present at the upper corners of the specimen, leading to the daylight of the shear band near the top platen. To overcome this problem, they constructed inhomogeneous specimens with a zone of loose sand near the center of the specimen. This forced the localization to occur closer to the center of the specimen and did not appreciably affect the macroscopic response of the specimen.

Using the same device outlined by Drescher, et al. (1990), Han and Vardoulakis (1991) investigated the behavior of water-saturated fine-grained sand subjected to plane strain compression. Specimens of St. Peter Sandstone sand were prepared using moist tamping and tested under drained and undrained conditions. They noted that shear banding occurred in undrained tests only when the induced pore water pressures were negative (i.e., the specimen was dilatant) and that shear bands formed during strain softening. In drained tests, however, shear bands formed during strain hardening, which is consistent with bifurcation theory (Vardoulakis, 1980). The data from these tests were further analyzed in later work (Vardoulakis, 1996a, 1996b) to assess the applicability of elastoplastic continuum theory for describing the undrained and drained behavior of sands in plane strain compression using effective stress principles (Terzaghi, 1936). Vardoulakis concluded that for undrained tests a continuum approach was sufficient but that for drained tests the problem was mathematically ill-posed if the soil grains and water were allowed to move with different velocities.

The same biaxial device was next used by Han and Drescher (1993) to study the behavior of poorly graded dry sand under PS compression. Tests were performed on Ottawa sand (ASTM C-190, d_{50} = 0.72 mm) at various confining stresses (σ_c = 50, 100, 200, 400 kPa). They found that shear band inclination was less than the Coulomb prediction (eq. 2.4) for all confining stresses and that it approached the Roscoe prediction (eq. 2.5) from above at higher confining stresses. This is consistent with theoretical results (Vermeer, 1990) which indicated that for coarse sands, shear bands with stress discontinuities were unlikely to develop and, thus, Roscoe-type shear bands should form. Vermeer's analysis followed from the fact that the membrane will not be able to support

large out-of-balance forces at the ends of the shear band and was based on the assumption that the shear band thickness is proportional to the mean particle size of the soil (i.e., a larger particle size will generate a larger out-of-balance force).

Because soils are often treated as continua, shear bands in plane strain compression are often studied and described using continuum constitutive models of varying complexity, as discussed above. In these studies, shear bands are considered in terms of energy considerations and an empirically derived internal length scale. However, there has also been work on the effects of particle characteristics on shear bands (Yoshida et al., 1994; Yoshida and Tatsuoka, 1997; Alshibli and Sture, 2000; Cho, 2001; Dodds, 2003). The role of the mean particle diameter (d_{50}) in shear banding is considered to be well understood and is largely considered to affect shear band thickness, as noted previously. Yoshida and Tatsuoka (1997) found that particle shape had little influence on shear band deformation in plane strain compression tests, but Dodds (2003) noted that angular particles are less likely to form strain localizations due to rotational frustration. Based on plane strain tests of fine (subrounded), medium (subangular), and coarse (angular) sands, Alshibli and Sture (2000) found that increasing particle angularity resulted in greater axial strain prior to localization and a less dramatic softening after localization. They noted also that increasing particle angularity resulted in a decrease in the shear band inclination at low (15 kPa) and high(100 kPa) confining stresses. It should be noted, however, that in this study both particle size and shape were changing simultaneously and, thus, it is difficult to separate the effects of one parameter from the other.

The majority of previous studies of soils in plane strain compression have focused on evaluating specimen response through measurement of boundary loads and displacements (i.e., macroscale properties). There has been significantly less work performed on evaluating the microscale response of plane strain compression tests (see below for a discussion of these previous studies).

2.2. Membrane Effects in Strength Testing of Soils

When measuring the shear strength of soils in the laboratory using either the triaxial or biaxial compression method, it is necessary to use a membrane to enclose the soil specimen during the test. Most commonly, the membrane is made of latex rubber and may be from 0.2 mm to 0.5 mm thick. The membrane is pre-formed to the desired specimen shape (e.g., cylindrical for a CTC test or orthorhombic for a PS test) as part of the manufacturing process. As early as the 1950's (Henkel and Gilbert, 1952) researchers began to study the effects of the membrane on test results. Much of this research has focused on the conventional triaxial testing of soft clays at relatively low confining stresses (e.g., Henkel and Gilbert, 1952; e.g., Duncan and Seed, 1967; La Rochelle, 1967) when the membrane effects may be substantial relative to the strength of the soils being tested.

In their original work, Henkel and Gilbert (1952) examined the effects of both a confining membrane and filter paper drains (used to shorten consolidation time) on the measured strength of remolded specimens of London clay by comparing the results of triaxial tests to those from unconfined compression tests. The triaxial tests were conducted at varying confining stresses with membranes of three thicknesses: "thin"

(0.10 mm), "standard" (0.20 mm), and "thick" (0.50 mm). They found that the rubber membrane increased the ultimate compressive strength of the London clay by 0.3-1.4 psi (2.1-9.7 kPa) for all nonzero confining stresses in undrained triaxial compression when compared to the unconfined compression tests performed without membranes. Unconfined compression tests were also performed with the specimen surrounded by a rubber membrane. In these tests, strength increases were approximately half of that observed in the case of triaxial tests. In both sets of tests, thicker membranes tended to increase strength more than thinner membranes. Using compression shell theory and hoop stress theory and assuming that the soil specimens deformed as right cylinders, Henkel and Gilbert were able to compare measured results to theoretical predictions. Compression shell theory was assumed to apply during the triaxial tests when the membrane was forced against the specimen by confining stress. By this method, the rubber correction, σ_r, is given by:

$$\sigma_r = \frac{\pi \cdot D \cdot M \cdot \varepsilon \cdot (1 - \varepsilon)}{A_0} \tag{2.7}$$

where ε is the axial strain, A_0 is the initial area of the specimen, D is the initial diameter of the specimen, and M is the compression modulus of the membrane (assumed equal to the extension modulus, which is more readily measurable)..

In the second case, hoop stress theory was assumed to describe the behavior of the membrane in unconfined tests wherein the membrane could conceivably buckle over the course of the test. The rubber correction from hoop stress is:

$$\sigma_r = \frac{2 \cdot M}{D} \cdot \frac{1 - \sqrt{1 - \varepsilon}}{1 - \varepsilon} \tag{2.8}$$

They acknowledged that, in reality, membrane behavior in both cases was better described by some complex combination of both theories. In general, however, the theoretical predictions provided approximate agreement with the measured results. It should be noted that Henkel and Gilbert do not consider the fact that in an unconfined compression test the drainage conditions are unknown, but justify their comparisons by the observation that shear strength did not vary with confining stress (i.e., the so-called "$\phi_u = 0$" assumption).

Duncan and Seed (1967) considered the combined effects of membrane confinement, filter paper drains, and piston friction on the measured shear strength of San Francisco Bay Mud in CTC and PS, again assuming that specimens deform homogenously. They presented closed-form expressions for lateral and axial stress corrections in triaxial and plane strain tests that were derived using linear elasticity and by considering both volumetric and axial strain. For triaxial tests, the axial ($\Delta\sigma_{am}$) and lateral ($\Delta\sigma_{lm}$) corrections are, respectively:

$$\Delta\sigma_{am} = \frac{2\cdot E_m}{3}\cdot\left(1 + 2\cdot\varepsilon_{at} - \sqrt{\frac{1-\varepsilon_v}{1-\varepsilon_{at}}}\right)\cdot\frac{A_{0m}}{A_{0s}\cdot\left(1-\varepsilon_v\right)} \tag{2.9}$$

$$\Delta\sigma_{lm} = \frac{2\cdot E_m}{3}\cdot\left(2 + \varepsilon_{at} - 2\cdot\sqrt{\frac{1-\varepsilon_v}{1-\varepsilon_{at}}}\right)\cdot\frac{t_{0m}}{r_{0s}\cdot\left(1-\varepsilon_v\right)} \tag{2.10}$$

where E_m = Young's modulus of the membrane, A_{0m} = initial cross-sectional area of the membrane, A_{0s} = initial cross-sectional area of the specimen, t_{0m} = initial thickness of the membrane, r_{0s} = initial specimen radius, ε_{at} = axial strain due to consolidation and/or undrained deformation, and ε_v = volumetric strain.

In plane strain testing, the Duncan and Seed corrections are:

$$\Delta\sigma_{am} = -\frac{A_{0em}\cdot\left[\frac{4}{3}\cdot E_m\cdot\left(\varepsilon_{at}+\frac{1}{2}\cdot\varepsilon_{lt}\right)+\left(\sigma_e-\sigma_c\right)\right]+A_{0sm}\cdot\left[\frac{4}{3}\cdot E_m\cdot\varepsilon_{at}+\left(\sigma_s-\sigma_c\right)\right]}{\left(1-\varepsilon_v\right)\cdot A_{0s}} \quad (2.11)$$

$$\Delta\sigma_{lm} = \frac{2\cdot t_{0m}\cdot E_m\cdot\varepsilon_{0pm}}{\left(1-\varepsilon_{0pm}\right)\cdot L_s} - \frac{2\cdot t_{0m}\cdot\left[\frac{4}{3}\cdot E_m\cdot\left(\varepsilon_{lt}+\frac{1}{2}\cdot\varepsilon_{at}\right)+\left(\sigma_e-\sigma_c\right)\right]}{\left(1-\varepsilon_{0pm}\right)\cdot\left(1-\varepsilon_{at}\right)\cdot\left(1-\varepsilon_{lt}\right)\cdot L_s} \quad (2.12)$$

where A_{0sm} = initial cross-sectional area of the membrane on the sides of the specimen, A_{0em} = initial cross-sectional area of the membrane on the ends of the specimen, L_s = length of the specimen (distance between the ends), ε_{0pm} = initial perimetric strain in the membrane, ε_{lt} = lateral strain due to consolidation and/or undrained deformation, and σ_c, σ_s, and σ_e = cell pressure, stress on specimen sides, and stress on specimen ends, respectively.

The corrections at the end of consolidation and at failure were presented, with filter paper and membrane corrections typically being larger than the piston friction correction. Tests conducted at low confining stresses required larger (as a percentage of total deviator stress) corrections than tests conducted at relatively higher confining stresses. Duncan and Seed found that, for San Francisco Bay Mud, the uncorrected strength, elastic modulus, and consolidation stress were greater than their corrected values.

Baxter (2000) proposed the Baxter and Filz correction for combined area and membrane effects as derived from the testing of soil-bentonite mixtures. Again, the soil specimen was assumed to deform as a right circular cylinder, and she noted that all failures were of the bulging type. Baxter drew on the work of Henkel and Gilbert (1952), Duncan and Seed (1967), and La Rochelle, et al. (1988) in developing the membrane correction. Baxter noted that most previous studies had relied upon the use of a secant

modulus to describe membrane stiffness, which accounts for the changing cross-sectional area of the membrane during straining, and proposed to use the initial tangent modulus in the correction and to account for the changing membrane area separately. The Baxter and Filz corrections to the major and minor principal stresses after consolidation are, respectively:

$$\Delta\sigma_{1con} = \frac{4\cdot\sigma_a\cdot t}{D} \tag{2.13}$$

$$\Delta\sigma_{3con} = \frac{\sigma_t\cdot t}{r} \tag{2.14}$$

where t = thickness of the membrane, D = diameter of the membrane, r = radius of the specimen, σ_a = axial stress in the membrane, and σ_t = tangential stress in the membrane (note that all values are for the end of the consolidation phase). The correction to the major principal stress during shearing is given by:

$$\Delta\sigma_{1shear} = \frac{4\cdot\varepsilon_a\cdot t_0\cdot E}{D_0\cdot\left(1-\varepsilon_v\right)} \tag{2.15}$$

where ε_a = axial strain, ε_v = volumetric strain, t_0 = membrane thickness, and D_0 = specimen diameter (note that all quantities are measured from or at the beginning of shear). Baxter noted that for the soil-bentonite specimens that were tested, the failure envelope was linear and passed through the origin for the corrected data but not for the uncorrected data, as shown in Figure 2.3.

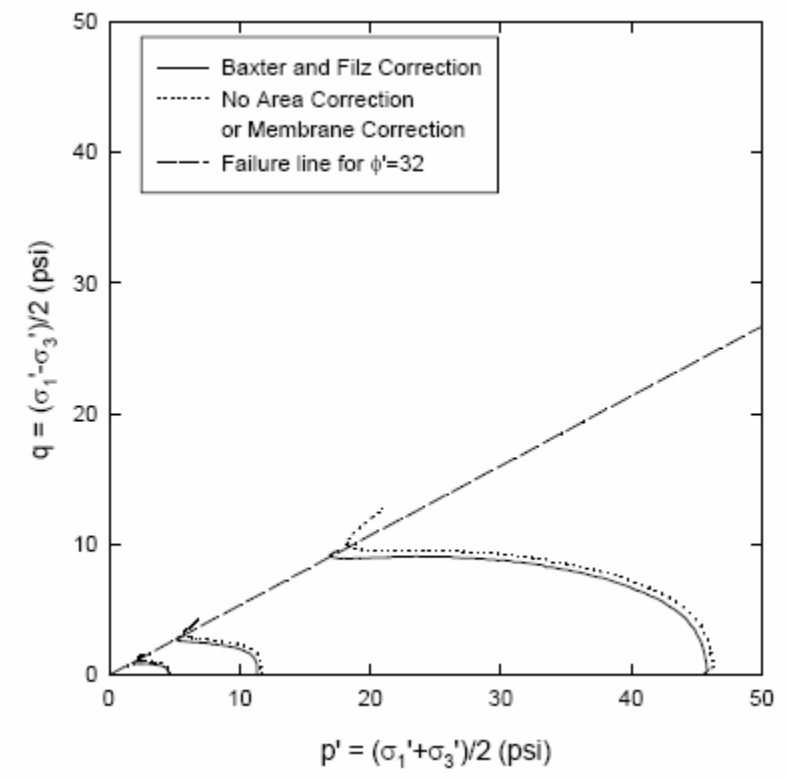

Figure 2.3: Comparison of corrected and uncorrected stress paths for CU triaxial tests on a soil-bentonite mixture (after Baxter (2000))

In addition to the corrections proposed by various researchers for membrane effects in homogenously deforming triaxial and plane strain tests, Frost (1989) has studied the effect of the confining membrane on the results of resonant column and torsional shear tests. Frost performed torsional shear tests on individual membranes to determine their resistance to applied rotations and used linear elastic theory to develop closed-form analytical expressions for stresses in the membrane as a function of shear strain. Hoop stress theory was also used to calculate the additional confinement effects due to membrane elongation during shear. While the absolute magnitude of these combined effects was relatively small (on the order of a few kilopascals at $\gamma = 20\%$), their

influence was notable in corrected test results, particularly if the confining stress was low.

In all of the studies of membrane confinement effects discussed previously, homogenous deformation has been assumed either explicitly or implicitly in the analyses. However, membrane effects for tests in which the soil specimen fails along a well-defined shear plane have also been studied (e.g., Chandler, 1966; e.g., Blight, 1967; La Rochelle, 1967; Symons, 1967; Pachakis, 1976; La Rochelle et al., 1988). The majority of these tests have considered a case of perfect sliding blocks, represented by Perspex cylinders with either lubrication or bearings at the interface of the two blocks, as shown in Figure 2.4. These studies have largely been experimental, due to the inherently

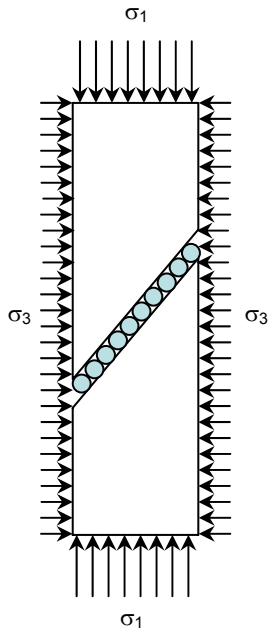

Figure 2.4: Experimental setup for assessment of membrane effects in triaxial specimens that fail along a single well-defined plane (after La Rochelle (1967))

complex nature of the membrane deformation during a triaxial test in which the specimen fails via shear banding, but the works of La Rochelle (1967), Pachakis (1976), and La Rochelle, et al. (1988) include theoretical considerations of the membrane effects.

The original work of La Rochelle (1967) considered the effects of both filter paper drains and membrane encapsulation through experimental and theoretical work. He suggested using the corrections of Bishop and Henkel (1962) prior to the onset of localization and used the experimental setup conceptualized in Figure 2.4 in conjunction with theoretical analysis to propose a new correction for membrane and filter paper effects after the onset of localization. La Rochelle stated that the membrane effect has two components: the rigidity component arising from the resistance of the membrane to deformation, and the friction component, which arises through the friction between the membrane and the soil. In an effort to separate these components, two sets of laboratory tests were performed. In the first set, four tests were performed at a constant confining stress ($0.35\ ^{kg}/_{cm^2}$) wherein the Perspex specimen was encased by one, two, three, or four rubber membranes. La Rochelle reasoned that the difference between any two adjacent stress-strain curves (e.g., the difference between the one membrane and two membrane tests) was due to the rigidity component of the membrane effect. He noted that the differences were similar between any two adjacent tests and calculated the average of these differences to be the overall rigidity component. The load carried by an individual membrane due to rigidity varied from zero at zero axial strain to 1.5 kg at 15% axial strain for the given confining stress.

To asses the friction component of the membrane effect, La Rochelle performed two tests on the Perspex specimen at different confining stresses ($0.35\ ^{kg}/_{cm^2}$ and 1.41

$^{kg}/_{cm^2}$) and a series of membrane-on-Perspex and membrane-on-London clay direct shear tests. He found that the friction coefficient increased semilogarithmically with increasing normal stress, in general agreement with Chandler (1966).

In developing the theoretical relationship between membrane load and axial strain, La Rochelle assumed (based on experimental observations) that membrane tension occurred only in the horizontal direction, that it was equally distributed around the perimeter of the shear plane, and that membrane deformation was intimately related to movement along the shear plane. The relationship proposed by La Rochelle is given as:

$$\Delta\left(\sigma_1 - \sigma_3\right) = \frac{p}{a_c} \cdot \sqrt{\frac{k \cdot f \cdot h \cdot \delta}{\cos(\alpha) \cdot \sin(\alpha)^2}} \tag{2.16}$$

where $\Delta(\sigma_1-\sigma_3)$ is the deviator stress carried by the membrane, p is the perimeter of the specimen, a_c is the corrected cross-sectional area of the specimen, f is the friction coefficient between the soil and the membrane, δ is the strain due to shearing along the plane, k is the modulus of elongation of the membrane, h is specimen height, and α is the inclination of the shear plane. As shown in Figure 2.5, the values predicted by Equation 2.16 are in good general agreement with the measured values.

A purely theoretical analysis using simple force balances and assuming rigid block sliding along the shear plane (Pachakis, 1976) has also been used to show that it is necessary to consider not only a correction to deviator stress, but also the stress in-plane on the shear band in triaxial specimens. The expressions derived by Pachakis for vertical (σ_1) and horizontal (σ_2) principal stress in the plane of movement are given by:

$$\sigma_1 = \sigma_D + \sigma_3 + \frac{P_a}{A}\left(\cos(\alpha)^2 - 1\right) \tag{2.17}$$

$$\sigma_2 = \sigma_3 + \frac{P_a}{A}\cos(\alpha)^2 \tag{2.18}$$

where σ_D is the deviator stress measured before correction, σ_3 is cell pressure, P_a is axial load, A is the horizontal projection of the effective contact area on the shear plane, and α is the inclination of the shear band. In deriving these expressions, Pachakis assumed that horizontal stress orthogonal to the direction of sliding was constant and equal to the confining stress (σ_3).

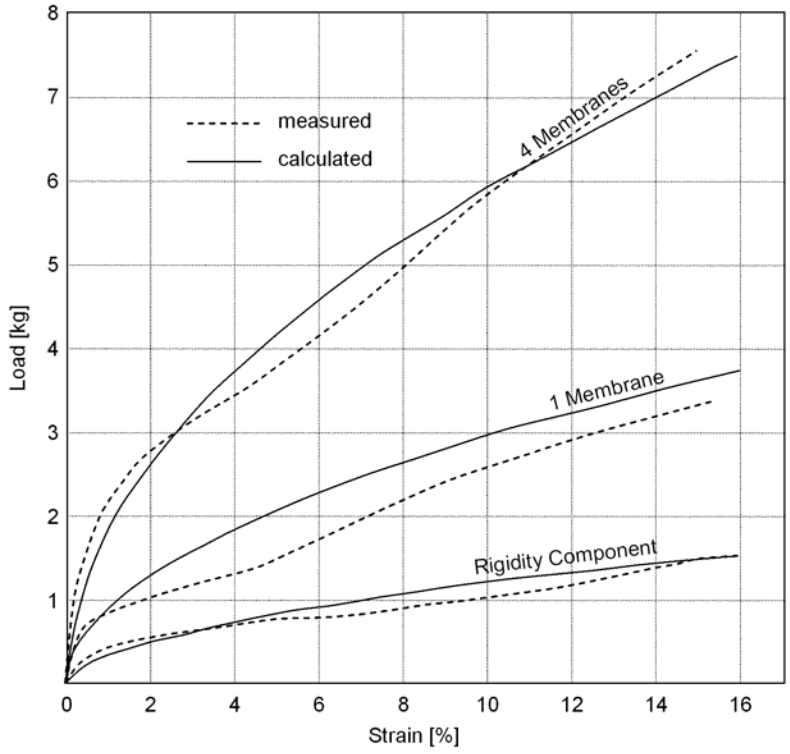

Figure 2.5: Comparison of measured and predicted load-deformation curves for latex membranes (after La Rochelle (1967))

La Rochelle, et al. (1988) considered membrane effects in triaxial tests from both a phenomenological and theoretical approach, allowing that different corrections are

required before and after the onset of localization. They recommended that an initial confining stress due to the membrane being stretched over the specimen be applied additively to the Henkel and Gilbert (1952) correction prior to the onset of localization and note that this additive correction results in a better fit to the experimental data presented by the original authors. For correction of membrane effects after the onset of localization, they provide a modified version of the La Rochelle (1967) equation without derivation:

$$\Delta\left(\sigma_1 - \sigma_3\right) = \frac{1.5 \cdot \pi \cdot d_0}{a_c} \cdot \sqrt{M \cdot f \cdot d_0 \cdot \delta} \tag{2.19}$$

where d_0 is the initial specimen diameter, a_c is the corrected area of contact on the shear plane, M is the extension modulus of the membrane, f is the unit friction between the membrane and the soil specimen, and δ is the strain due to movement along the shear plane. From the results of interface shear tests, La Rochelle, et al. noted that unit friction between the membrane and the soil is given by:

$$f = \sigma'_3 \cdot \tan(\phi') \tag{2.20}$$

where σ'_3 is effective confining stress and ϕ' is the effective angle of internal friction of the soil at high strains.

Most of the studies cited previously concern the correction of test data from specimens that fail homogenously. There are several studies that address the effects of the membrane on a triaxial specimen failing along a single shear plane, but none that assess these effects for plane strain specimens. Furthermore, many of the previously cited studies rely on simplifying assumptions that might not be valid for plane strain testing of orthorhombic specimens.

2.3. Microstructure Evolution Studies: Experimental

2.3.1. Introduction

There has been increasing interest in recent years in the effect that soil microstructure plays on soil macroscale response. To this end, several researchers have performed experimental studies to investigate soil microstructure both before and after subjecting soil specimens to shearing stresses. These studies may be broadly delineated into three categories: soil specimens that deform homogenously, soil specimens that have localized deformations, and soil specimens deforming adjacent to continua.

2.3.2. Homogenous Deformation

The microstructure of granular soil specimens has been previously investigated for both as-prepared and homogenously deformed triaxial specimens. The two predominant methods for microstructural analysis of granular soil specimens are X-ray tomography (e.g., Wang et al., 2004) and specimen solidification followed by slicing and microscopic imaging (e.g., Kuo and Frost, 1996). Both methods have strengths and weaknesses, but the X-ray tomography method is arguably more predominant. The primary advantage of the X-ray tomography method is that the soil specimen may be analyzed "as is" without additional preparations, which could potentially alter the internal soil structure. The drawback to this method, however, is that the resolution is not high enough to allow for the investigation on the scale of a single particle for most soil types, although this may be overcome by using large soil particles (see Wang et al., 2004) such as those found as aggregates in asphalt mixtures (the drawback here, though is that penetration distance is typically limited to a few particles). The digital image analysis

method, while more complex to implement, allows for resolution at the scale of the particle diameter for sands imaged using bright field microscopy (Frost and Kuo, 1996). While the digital image analysis technique operates only on two-dimensional surfaces, quantitative stereology allows for the unambiguous and rigorous determination of three-dimensional structural properties from measurements on two-dimensional surfaces (Underwood, 1970; Kuo et al., 1998). There has also been some recent work using the digital image analysis method in conjunction with serial sectioning and interpolative algorithms to reconstruct three-dimensional microstructure with particle-level resolution (Yang, 2005) which provides an abundance of high-quality data but is not yet widely used due to the labor intensiveness of the process.

The vast majority of work using the digital image analysis technique has been performed on triaxial specimens in both their sheared (e.g., Frost and Jang, 2000) and unsheared (Frost and Park, 2003) states. The focus has typically been on quantifying local void ratios, particle orientations, and/or higher-level fabric tensors (Kuo et al., 1998). Local void ratios are computed using the method first outlined described by Oda (1976). The Oda procedure consists of connecting the centers of gravity of particles surrounding a void space to define a polygon. The void ratio of the polygon is then calculated as the area of void space within the polygon divided by the area of solid space. In the limit, the average of these local void ratios will be the global void ratio of the specimen (Underwood, 1970). This method was implemented manually by Bhatia and Soliman (1990) and Ibrahim and Kagawa (1991) among others. Because the Oda method was implemented manually, the use of large images (i.e., images containing more than a few hundred particles) was precluded and the procedure was prone to operator error.

However, the process was ultimately automated, with specific details provided by Kuo and Frost (1995).

Perhaps the most complete studies on soil microstructure that employ the digital image analysis method are those performed by Kuo (1994), Jang (1997), Park (1999), Chen (2000), and Yang (2002). These researchers have studied the effects of specimen preparation method, axial strain, specimen size, specimen density, particle shape, particle size, and boundary conditions on the evolution of microstructure in sands subjected to CTC shearing. The general conclusions of the above experimental studies may be largely summarized as follows:

- Uniformity of local void ratios is highly dependent on the specimen preparation method. Water deposition creates the most uniform specimens, followed by air pluviation, and moist tamping creates the least uniform specimens.
- Localization is found to occur more readily on moist tamped specimens, whereas air and water pluviated specimens at the same initial state typically tend not to localize.
- In shearing, the middle portion of the specimen (from top to bottom) tends to evolve the most, compared to the specimen ends, due to end platen effects.
- In dilatant specimens, the mean of the local void ratios tends to increase and in contractive specimens, the mean tends to decrease. The standard deviation of the local void ratios tends to increase in both cases.

- A lognormal distribution may be used to adequately describe the frequency histogram of local void ratios in both sheared and unsheared specimens.
- Homogenously deforming specimens with a 2:1 height-to-diameter ratio and/or non-lubricated end platens tend to bulge during shear whereas specimens with a 1:1 height-to-diameter ratio and/or lubricated end platens tend to deform more like right cylinders.

Another significant result of the above work (e.g., Kuo, 1994) is the recognition of the importance of using "solid area weighted local void ratios" in analysis rather than local void ratios on their own. The motivation for the use of solid area weighted local void ratios can be seen from considering the mathematical formulation of the mean of local void ratios and the void ratio for an entire image. The mean of local void ratios (e_m) may be calculated as follows:

$$e_m = \frac{1}{N} \cdot \sum_{i=1}^{N} e_i = \frac{1}{N} \cdot \sum_{i=1}^{N} \frac{A_{V_i}}{A_{S_i}} \tag{2.20}$$

where N is the number of polygons, e_i is the void ratio of the i^{th} polygon and A_{vi} and A_{si} are the areas of voids and solids in the i^{th} polygon, respectively. Contrast this with the void ratio of the entire image (e_s):

$$e_S = \frac{\sum_{i=1}^{N} A_{V_i}}{\sum_{i=1}^{N} A_{S_i}} = \frac{A_V}{A_S} \tag{2.21}$$

From observation, the values calculated in Equations 2.20 and 2.21 will be equal only if $A_{si} = A_{s(i+1)}$ for all I, which will not be the case for a real soil specimen. Thus, it is difficult to compare the local void ratio measurements to measurements on the scale of the image (or, on the scale of the entire specimen). By weighting the local void ratios by their respective solid areas, Equation 2.20 becomes:

$$e_{ms} = \frac{\sum_{i=1}^{N} A_{S_i} \cdot e_i}{\sum_{i=1}^{N} A_{S_i}} = \frac{1}{A_S} \cdot \sum_{i=1}^{N} A_{S_i} \cdot \frac{A_{V_i}}{A_{S_i}} = \frac{A_V}{A_S} \tag{2.22}$$

where e_{ms} is the solid area weighted mean of the local void ratios. It is evident, then, that this value is equal to the void ratio of the entire image. Similar arguments lead to comparable expressions for other statistical parameters (e.g., standard deviation, skewness, and kurtosis).

2.3.3. Localized Deformation

Localized deformation (specifically, shear banding) has been studied on the microscale in granular materials using a variety of different methods, including stereophotogrammetry (Butterfield et al., 1970; Harris et al., 1995), computed tomography (Desrues et al., 1996), X-ray tomography (Oda and Kazama, 1998), observation of colored layer deformation through clear membranes (Towhata and Lin, 2003), specimen solidification followed by sectioning and bright-field microscopy (Alshibli and Sture, 1999; Jang and Frost, 2000), and digital image correlation (Finno and Rechenmacher, 2003). These methods can be broadly classified into three groups:

external analysis (stereophotogrammetry, digital image correlation), wave-based analysis (computed tomography, X-ray tomography), and internal analysis (specimen solidification and sectioning). As mentioned for the methods discussed in Section 2.3.1, each of these techniques has its own strengths and weaknesses, but external analysis methods are arguably the most predominant.

In external analysis methods, images of the specimen are captured during testing and particle movements adjacent to the confining membrane are analyzed. These methods have largely been applied to sand specimens tested in plane strain or torsional shear. In the stereophotogrammetric approach outlined by Butterfield, et al. (1970), a stationary analog camera was used to capture images of a sand model as it underwent displacement. Two subsequent images were then simultaneously projected (using stereoprojectors) to provide a single stereophotogrammetric image wherein displacements appeared as elevations above the plane. This is the exact inverse of the stereophotogrammetric procedures used in aerial land surveying, wherein a moving camera (typically in an airplane) is used to photograph a stationary target to determine its actual elevation. The Butterfield method was applied to the example of wedge penetration into a sand mass constrained by glass walls (i.e., plane strain loading) that results in a passive failure within the sand mass. Figure 2.6 illustrates the ability of this method to capture the failure surface associated with the passive wedge.

Stereophotogrammetry has been subsequently used by researchers (Harris et al., 1995; Finno et al., 1996; Finno et al., 1997; Mooney et al., 1998) to study displacements in sands that exhibit localized failures upon shearing in a biaxial compression device. The biaxial device described in Drescher, et al. (1990) was used for these studies. The

device had a clear side wall in the direction of the intermediate principal stress that allowed the sample to be photographed during shear.

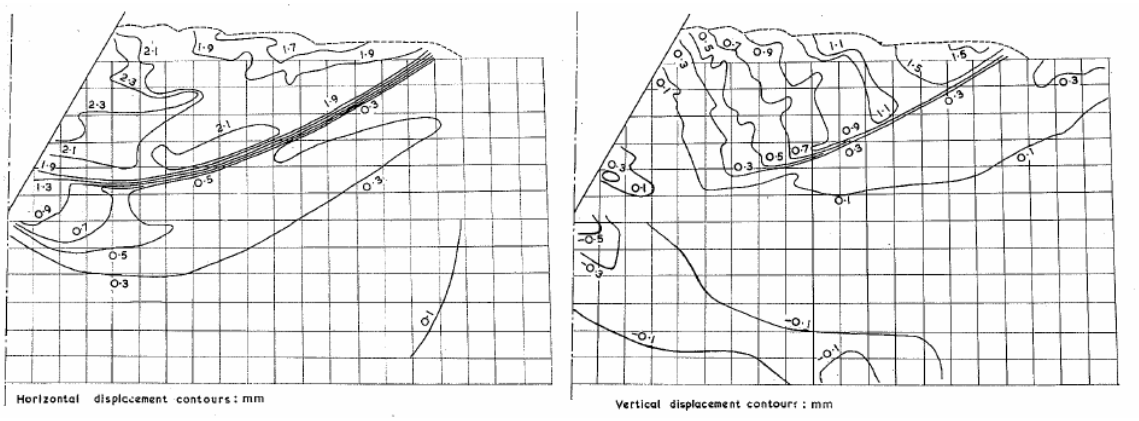

Figure 2.6: Horizontal and vertical displacement contours for wedge penetration into a sand mass under plane strain conditions (Butterfield et al., 1970)

Harris, et al. (1995) used stereophotogrammetry to observe deformations in specimens of masonry sand subjected to either drained or undrained compression. It was shown that stereophotogrammetry makes it possible to see zones of localized deformation when the soil specimen appears to be deforming homogenously, and some zones of localized failure were observed well before the peak deviator stress in these tests. The researchers also found that their technique allowed them to observe multiple shear bands in samples, even when only one major shear band was visible to the naked eye. In undrained tests, they noted that pore water pressure measured at the sample ends was related to the degree of dilation within the shear band, such that greater dilation within the shear band corresponded to a greater reduction in measured pore water pressure at the top and bottom of the specimen. They further found that the thickness of a given shear

band was not necessarily constant or uniform, but that its magnitude was typically 12 to 17 times the mean particle diameter. Shear band inclinations in this study ranged from 58° to 62°, which laid between the Roscoe and Coulomb predictions. The researchers noted that the inclinations of the shear bands decreased as global axial strain increased.

Finno, et al. (1996) described additional undrained biaxial compression tests on loose sands and divided specimen response into two categories: "Type A Behavior" (liquefaction) and "Type B Behavior" (limited liquefaction). Type A behavior was characterized by strain localizations that occur prior to the maximum effective stress ratio followed by a slight decrease in this ratio. In type B behavior, total deviator stress peaked shortly after the start of the test and then reached a minimum value prior to increasing again. Localization occurred at the peak effective stress ratio as total deviator stress continues to increase slightly. By observing the motion of particles within the shear bands, they found that the movement tangential to the shear band was consistent with global axial strain measurements, indicating that after the shear band is fully formed, the predominant (if not only) form of deformation was due to rigid block sliding. Particle movements normal to the shear band were largely irregular for both type A and type B behavior.

Using a combination of stereophotogrammetry and global measurements, Mooney, et al. (1998) found that in drained plane strain experiments on masonry sand shear bands formed spontaneously in dense air-pluviated specimens but more gradually in loose moist tamped specimens. They attributed this to the overall higher degree of uniformity in air pluviated specimens versus moist tamped specimens. In both cases, shear bands formed near the peak mobilized friction. Dilatancy angles within the shear

band were found to be slightly lower than the overall dilatancy angle for the specimen at peak strength due to the large shear strains associated with the formation of a shear band.

Oda and Kazama (1998) used a combination of X-rays and microscopic analysis on thin sections to analyze microstructural changes in shear bands formed in Toyoura and Ticino sands subjected to plane strain shearing. After shearing, the sand specimens were impregnated with a polyester resin that had been thinned with a solvent to allow for sectioning of the sample. They noted that in the upper one-third of the shear band only solvent was accumulated (they stated that the reason for this is not known) and, thus, only the lower portions of the shear band were analyzed. After the resin was cured, the specimens were sliced on the plane of minor principal stress (i.e., the unit normal was in the x_2-direction) to get plates for X-ray analysis and thin sections optical analysis. A thin section was also sliced from the plane of the shear band (i.e., the thin section shares a unit normal with the shear band). From X-ray analyses, Oda and Kazama found that the thickness of the shear band varied along the x_2-direction and that the shear band was not a straight line in the x_2-plane. The curvature of the shear band was assumed to be an artifact if the kinematically restrained end platens. On average, it was observed that the maximum void ratios within the shear bands was 13% higher (ranging from 4% to 19%) than the measured maximum void ratios of the materials. The presence of these large voids was attributed to the buckling of force chains that transect the shear band. Particle orientation inside the shear bands was significantly different than outside of the shear bands, indicating a high degree of particle rotation with the shear band. Based on results of both the X-ray and optical analyses, they concluded that shear band thickness is on the order of seven to eight times the mean particle diameter.

Alshibli and Sture (1999) also used optical techniques to investigate sand microstructure inside of shear bands formed in specimens subjected to plane strain compression. Results from images of membrane deformations and images taken from sections within a solidified sand sample were compared. A 5-mm by 5-mm grid was drawn on the membrane prior to straining. By analyzing images of the membrane before and after localization, it was determined that the shear band thickness was approximately 14 times the mean particle diameter and the angle of inclination was 54.5°. The specimen was solidified using an epoxy resin in the following manner:

- a 15-kPa vacuum was applied to the specimen after shearing (note that the test was conducted at a confining stress of 15-kPa);
- the confining stress was released and the test cell disassembled;
- a cylindrical split mold was placed around the specimen and the annulus was filled with plaster of Paris;
- once the plaster of Paris had set, the vacuum was released; and
- the sample was impregnated with a low viscosity resin.

Once the resin was cured, four thin sections were sliced from the plane of the intermediate principal stress. The void ratio outside of the shear band was found to be largely similar to the initial global void ratio of the specimen, with differences not exceeding 8%. Void ratios within the shear band were found to be as much as 30% greater than the initial global void ratio of the specimen and shear band thickness was measured as 14.5 and 15 times the mean particle diameter from two different images.

Recent studies using digital image correlation have shown the ability to achieve subpixel resolution when examining membrane displacement on plane strain specimens

by monitoring the movement of subsets of pixels within a given field of view (Finno and Rechenmacher, 2003). Because the digital image correlation procedure is largely automated, the number of points for which displacement can be monitored is an order of magnitude greater than that reported by Mooney, et al. (1998), which relied upon stereophotogrammetric analysis of manually digitized points.

Many of the previous microscale studies of localized deformation have involved the study of specimen behavior at the specimen boundary, where boundary effects may be significant. Furthermore, these procedures rely on measurements of membrane deformation rather than true observations of the soil microstructure. Studies on the internal structure of solidified specimens have typically relied on relatively few images that are small relative to the shear band extents. These studies have also tended to use thin sections that lie on the shear plane or normal to the propagation of the shear plane, which provide information about only a very small portion of the entire shear band.

2.3.4. Deformation Adjacent to Continua

Recent evidence (DeJong, 2001; Frost et al., 2004; Hebeler, 2005) has shown that the microstructural behavior of granular materials when sheared adjacent to a continuum counterface may be similar to the microstructural behavior of granular materials within a free-forming shear band. Hebeler (2005) found that the thicknesses of the shear zones for three different sands sheared axisymmetrically by a textured steel sleeve were a function of particle size and the roughness of the sleeve, as illustrated in Figure 2.7.

The structure of the sand specimens referenced in Figure 2.7 was “locked” after shearing using a powdered, heat-activated phenolic resin, allowing for the microscale

evaluation of the shear zones with high resolution. Additional details of the study as well as a thorough overview of interfacial shear zones may be found in Hebeler (2005).

In spite of the similarities that apparently exist between interfacial shear zones and free-forming shear bands in soil specimens, little effort has been put forth to integrate the knowledge gleaned from interfacial studies into the existing body of knowledge for free-forming shear bands.

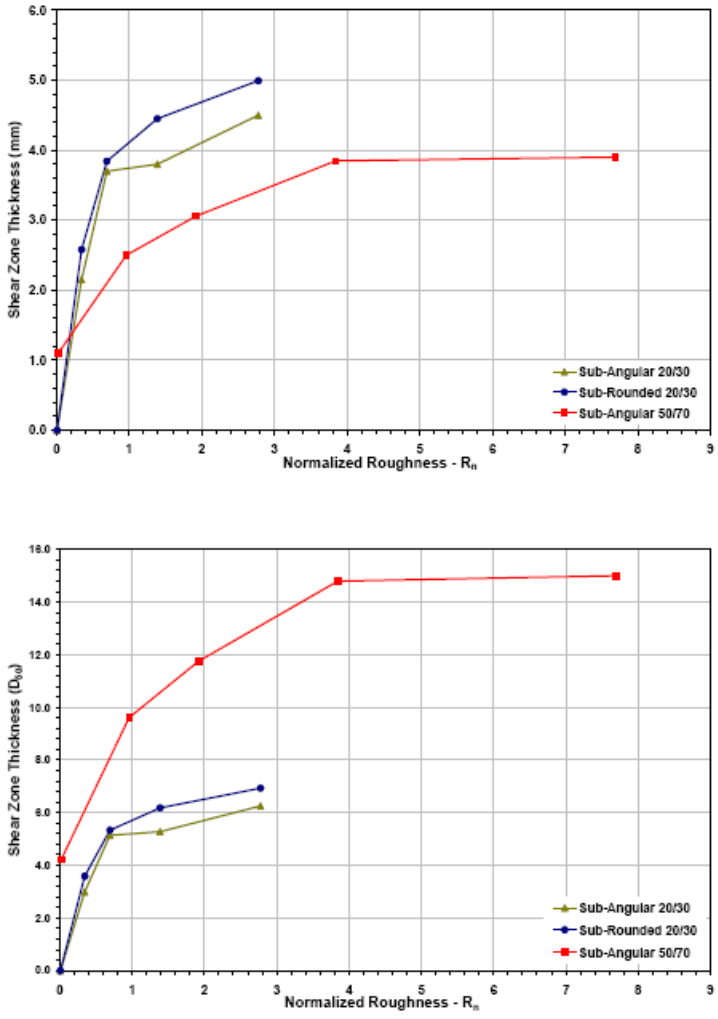

Figure 2.7: Shear zone thickness as a function of counterface roughness (after Hebeler, 2005)

2.4. Microstructure Evolution Studies: Numerical

Numerous numerical and analytical studies have been performed in an attempt to quantify the microstructure of granular soils subjected to shear. These studies may be broadly classified into three categories: theoretical, continuum, and discrete. Theoretical studies tend to focus on the fundamental physics of particle behavior at small scales (e.g., Radjai et al., 1995; e.g., Edwards and Grinev, 1999), continuum studies simulate soils by considering a soil mass as a continuous solid and applying various constitutive relationships that describe material response (e.g., Rudnicki and Rice, 1975; Voyiadjis and Song, 2005), and discrete approaches attempt to model the behavior of a soil mass by solving Newton's equations of motion for an assembly of densely packed spheres or disks (e.g., Cundall, 1989; Powrie et al., 2005). The use of continuum and discrete approaches to model strain localization in granular materials are described in this section.

In the continuum approach, two methods for simulating strain localization dominate the published work to date. In the first approach, material strength properties for a "standard" elastoplastic constitutive model (e.g., Mohr-Coulomb) are varied across the model grid to simulate material heterogeneity (e.g., Itasca, 1996; Kim, 2005). This method is commonly referred to as "smeared" modeling. The principle behind this approach is that model elements with weaker strength properties will tend to enter into failure first. Once a weak element fails, a portion of the load that it is carrying is transferred to its neighboring elements, thus forcing them towards failure (Santamarina and Cho, 2003), or localized failure may be due to the percolation of weak zones which coalesce into shear bands (Kim, 2005). In this manner, strains tend to localize with failure and shear bands will form. The significant advantage to this type of model is that

well-understood constitutive models with readily quantifiable parameters may be used in the modeling. However, assumptions regarding the spatial variability of the material properties are sometimes required (see Kim (2005) for a discussion of the parameters that describe variability and their selection) and shear band geometry is strongly influenced by grid geometry. It should be noted that for irregular meshes (i.e., grids with slopes or curved surfaces) shear bands will form even without spatial variation in strength properties, but these localizations will be entirely defined by grid geometry.

In the second approach, complex constitutive models (often thermomechanically derived) are used to describe strain localization in soils. Localization can be considered as a bifurcation problem (e.g., Rudnicki and Rice, 1975; Vardoulakis et al., 1978) wherein shear bands form when second-order work becomes negative (i.e., in the strain-softening regime) and the partial differential equations that govern stress and strain transition from elliptic to hyperbolic and have more than one real solution, even under homogenous deformation. Rudnicki and Rice (1975) refer to this as "an instability in the constitutive description of homogenous deformation". Thus, if the proper constitutive relationships are used and shear banding is treated as an *a priori* result of a given set of loading conditions (e.g., plane strain loading of dense sand) the formation of shear bands may be treated as a boundary value problem and successfully solved, even in homogenous materials. This method is often used to analyze laboratory tests on materials that fail through strain localization. It is also common to consider the problem in the framework of a Cosserat continuum (Muehlhaus and Vardoulakis, 1987) wherein particle rotations are considered in addition to particle displacements and the stress tensor becomes nonsymmetric. In this case, the problem remains elliptic even in the strain

softening regime (Vardoulakis, 1989). The persistent ellipticity of the problem allows for prediction of shear bands using various constitutive relationships, such as hypoplasticity (Gudehus and Nubel, 2004) or a single hardening model of plasticity (modified from the Lade (Kim and Lade, 1988; Lade and Kim, 1988) constitutive model) may be used (Voyiadjis et al., 2005). Other methods of preserving ellipticity, such as a gradient flow theory of plasticity (Vardoulakis and Aifantis, 1991) have also been used to model localization in soils. A common theme in each of these methods is the use of an internal length scale to minimize the dependence of shear band thickness on mesh size. This value is typically a constant and is often determined as a function of the mean particle diameter of the soil in question, but recent work (Voyiadjis et al., 2005) has attempted to address the effects of allowing the length scale to evolve over the course of a simulation. While these models are typically very good at predicting the onset and geometry of localization, they still require the input of a large number of constitutive parameters (including the internal length scale) and can only address the true microstructure of the material via empirical relationships (Voyiadjis and Song, 2005). Additionally, recent work (Borja and Aydin, 2004) on combined localization mode plasticity has successfully predicted three bounding cases of localizations (purely contractive, purely dilatant, and pure shear) based on geologic considerations. This represents a significant step towards true material property based modeling of localizations.

The discrete element method (DEM) is a powerful tool for simulating microstructures in granular materials and has gained increasing popularity over the last several years. DEM has been used to model the deformation of particle masses in two (e.g., Cundall, 1989) and three (e.g., Chantawarangul, 1993; Powrie et al., 2005)

dimensions, adjacent to continua (e.g., Jensen et al., 1999), and using spherical (e.g., Bardet, 1994), ellipsoidal (e.g., Rothenburg and Bathurst, 1991; Ng and Changming, 2001), and toroidal (Kuhn, 2002) particles. The DEM is computationally very expensive, particularly in scanning the assembly for particle contacts at every time step, but offers a significant advantage over continuum approaches when studying soil microstructure: macroscale behavior is governed entirely by particle mechanics which are described by Newton's equations of motion and simple constitutive relationships (e.g., linear, Hertz) that model contact mechanics. DEM models have been shown to successfully model strain localizations under certain conditions (e.g., Cundall, 1989), with localizations appearing as a function of particle stresses and strains as opposed to a global constitutive relationship.

Early DEM studies focused on the modeling of circular disks subjected either to biaxial compression or direct shear. The primary motivation for using circular particles is that contact detection algorithms for circles in a plane are very efficient and contact mechanics are well-defined. However, it has been shown (Bardet, 1994) that simulation of disks can tend to allow too much particle rotation, leading to a lower peak shear strength, variations in fabric tensors, less energy dissipation, and a collapse of inclined particle contacts. These effects are particularly pronounced in shear bands where local void ratios are higher. In an effort to prevent excessive particle rotation, some researchers (e.g., Ng and Dobry, 1992; e.g., Iwashita and Oda, 2000) have attempted to constrain individual particle rotations. Iwashita and Oda (2000) found that restricting particle motion in this manner tends to encourage the formation of bands of localized deformation. The more common approach is to simulate ellipses (2D) or ellipsoids (3D),

which will naturally tend to resist rotation better than circular or spherical particles. Ellipsoids (and ellipses) have the added advantage of being amenable to efficient contact algorithms similar to those used for spheres (or circles). Rothenburg and Bathurst (1992) determined that the primary difference between simulations of circular and elliptic particles was that elliptic particles underwent less rotation and that the macroscopic strength of assemblies of ellipses was greater than that simulated for circular disks due to the increase in the average number of contacts per particle. More recently, the advent of commercial software programs, specifically PFC (Itasca, 2004), has allowed for the simulation of complex particles that are formed by clumping together two or more elementary particles (i.e., circles or disks) (e.g., Thomas and Bray, 1999). The advantage to this approach is that complex particle shapes can be considered but the efficiencies of contact detection on elementary particles are still realized.

Because individual particle mechanics are modeled, DEM allows for direct observation of the simulated mechanics of granular materials on small scales. For example, in performing simulated biaxial compression tests on assemblies of disks, Kuhn (1999) found that vertically elongated voids are more likely to be dilatant whereas inclined voids typically undergo slip deformation and that significant zones of slip deformation exist on the mesoscale (i.e., on the order of several particle diameters). Furthermore, Powrie, et al. (2005) showed that 3D simulations of complex particles reasonably simulate published results for testing of real soils.

Most of the constitutive studies on shear banding are involved with the solution of boundary value problems and not a fundamental understanding of microstructure while most DEM studies have restricted the study of microstructure to the analysis procedures

specifically defined within the framework of the discrete element model (e.g., force chains or coordination numbers). There has not been an effort to use morphological processes developed to analyze sections sliced from laboratory specimens the results of numerical specimens. There has also been relatively little consideration of the effects of boundary conditions on localization in DEM simulations.

3. BIAXIAL SHEAR DEVICE AND TEST PROCEDURES

3.1. Biaxial Shear Device and Data Acquisition System

3.1.1. Biaxial Shear Device

The biaxial device used in the current study is manufactured by Geotest Instrument Corporation in Evanston, Illinois and is based on a similar device first conceived by Vardoulakis and Goldscheider (1981) and later refined and patented by Drescher, et al. (1990). The device allows for the plane strain compression of orthorhombic soil specimens under drained or undrained conditions. The device is internally instrumented with load cells and linear voltage displacement transducers (LVDT's). Additionally, the base platen on which the specimen is placed sits on a frictionless linear bearing (the "sled") allowing for the free translation of the lower portion of the specimen relative to the top portion after the onset of localization. This is significant because kinematically constrained end platens tend to curve the shear band unnaturally (Oda and Kazama, 1998) whereas a freely translating base platen will allow for the unrestricted formation of shear bands and subsequent deformation by rigid block sliding. A photograph of the biaxial shear device is presented in Figure 3.1.

The biaxial device is internally instrumented with seven load cells and seven LVDT's, allowing for the monitoring of boundary loads and displacements at several locations. A schematic of the instrumentation package is presented in Figure 3.2. Lateral displacements are measured in four locations, two on either side of the specimen, and axial displacements are measured at two locations to monitor any variations in axial

deformation due to load eccentricity. The final LVDT is used to monitor sled displacement, which is required for calculating the onset of localization and the dilation within the shear band, as discussed below. One large load cell monitors axial load at the

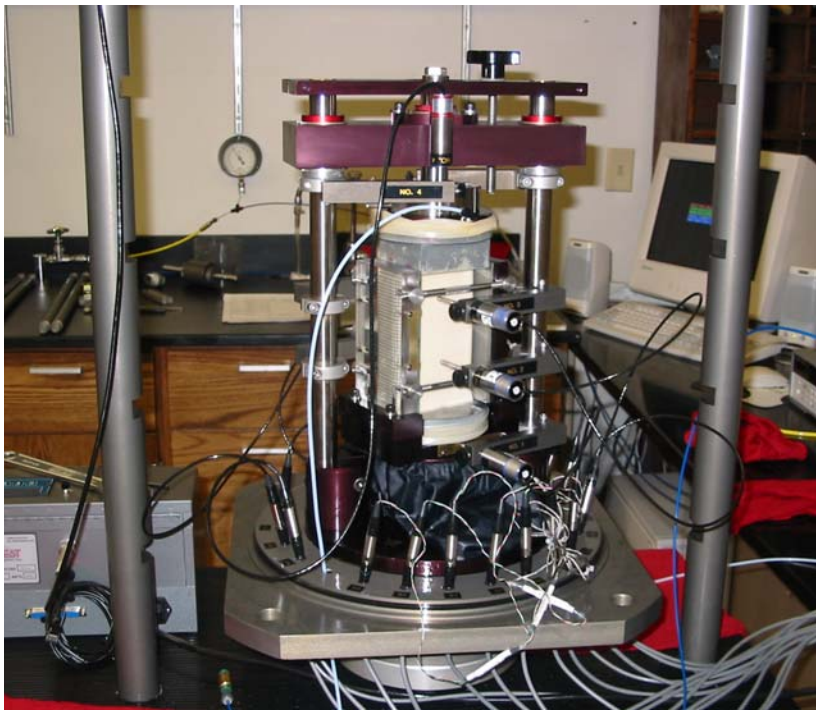

Figure 3.1: Photograph of the biaxial shear device with a sample in place and the confining cell removed

top of the specimen and the base platen rests on a plane defined by three "pancake" load cells, allowing for the assessment of friction in the system during the test. One side wall in the plane of zero strain (i.e., $\varepsilon_2 = 0$) rests on a plane defined by the other three "pancake" load cells, allowing for the measurement of intermediate principal stress.

Because the device is internally instrumented, confining pressure must be applied using a nonconducting fluid. In practice, either air or silicone oil is used as the confining

fluid. In early tests for this study, silicone oil was used, but it was found that over the long periods of time (~ 1 week) required to cure samples after testing, small amounts of

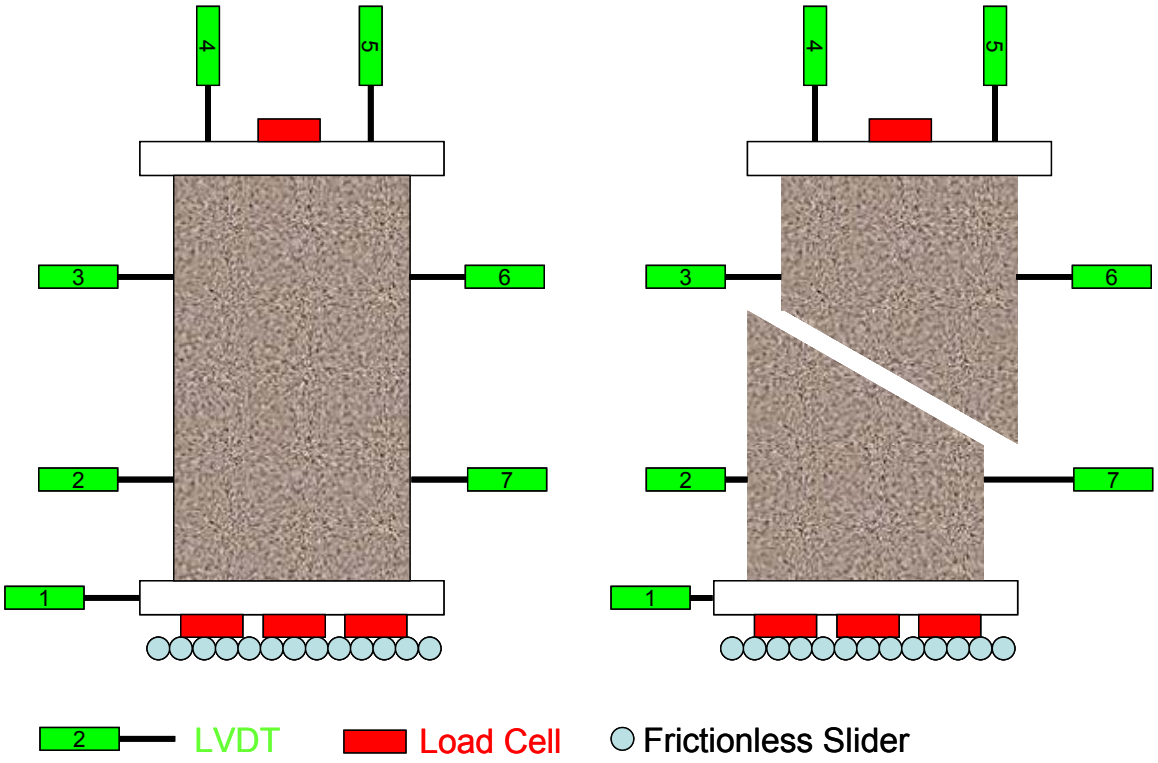

Figure 3.2: Schematic of instrumentation in the biaxial device (note three pancake load cells on the σ_2 plane are not shown)

silicone oil would leak into the sample, preventing proper curing of the glue (note that this is opposite to the findings of Leroueil, et al. (1988)). Thus, air was used as confining fluid for subsequent tests. The cell that surrounds the device is machined from a solid piece of Plexiglas and has a 32 mm (1.25 in.) thick wall. The maximum allowable confining stress is 690 kPa (100 psi). Instrumentation wiring accesses the interior of the cell through sealed Swagelok fittings in the base of the cell.

3.1.2. Data Acquisition System

3.1.2.1.Instrumentation

Each of the fourteen sensors (seven load cells and seven LVDT's) in the test cell require excitation voltage and provide output signals throughout the course of a test. There are two different types of load cells and two different types of LVDT's employed in the device, for a total of four distinct instrument types. The top load cell is an LGP 310 from Cooper Instruments and the remaining six load cells are pancake–type LPM 510 load cells also from Cooper Instruments. The two axial LVDT's are DCTH400AG devices from RDP Electrosense and the lateral and sled LVDT's are D2/200A models, also from RDP Electrosense. Axial LVDT's have an armature travel of ±10 mm and lateral LVDT's have an armature travel of ±5 mm. A summary of excitation power requirements and the current calibration factors for each device is presented in Table 3.1.

Note that the + 5 V excitation voltage indicated for the LGP 310 load cell in Table 3.1 is sufficient, but that the calibration factor had to be adjusted (Cooper, 2003) to reflect the lower excitation voltage. This value (+ 5 V) was selected so that excitation could be provided to all instruments with a single fixed output three channel power supply. These types of power supplies are typically less expensive and more stable than many-channeled variable supply power supplies.

3.1.2.2.Power Supply Unit

A single consolidated power supply unit was designed and fabricated for this study to provide excitation voltages for the instrumentation in the biaxial device (Figure 3.3). The core of the unit is a linear, three-output power supply from Sola/Hevi-

Table 3.1: Excitation voltages and calibration factors for sensors in the biaxial device

Channel Number	Instrument Type	Allowable Excitation Voltage	Actual Excitation Voltage	Calibration Factor
1	D2/200A LVDT	+ 6 V to + 12 V	+ 12 V	328.320 $^{mV}/_{mm}$
2	D2/200A LVDT	+ 6 V to + 12 V	+ 12 V	311.740 $^{mV}/_{mm}$
3	D2/200A LVDT	+ 6 V to + 12 V	+ 12 V	326.500 $^{mV}/_{mm}$
4	DCTH400AG LVDT	+/- 12 V or +/- 15 V	± 12 V	391.032 $^{mV}/_{mm}$
5	DCTH400AG LVDT	+/- 12 V or +/- 15 V	± 12 V	389.144 $^{mV}/_{mm}$
6	D2/200A LVDT	+ 6 V to + 12 V	+ 12 V	308.260 $^{mV}/_{mm}$
7	D2/200A LVDT	+ 6 V to + 12 V	+ 12 V	318.180 $^{mV}/_{mm}$
8	LPM 510 Load Cell	+ 5 V	+ 5 V	3.604 $^{\mu V}/_{N}$
9	LPM 510 Load Cell	+ 5 V	+ 5 V	3.860 $^{\mu V}/_{N}$
10	LPM 510 Load Cell	+ 5 V	+ 5 V	3.930 $^{\mu V}/_{N}$
11	LPM 510 Load Cell	+ 5 V	+ 5 V	3.880 $^{\mu V}/_{N}$
12	LPM 510 Load Cell	+ 5 V	+ 5 V	3.975 $^{\mu V}/_{N}$
13	LPM 510 Load Cell	+ 5 V	+ 5 V	4.087 $^{\mu V}/_{N}$
14	LGP 310 Load Cell	+ 10 V	+ 5 V	-0.676 $^{\mu V}/_{N}$

Duty, part number SLT12-31010-12T (Sola/Hevi-Duty, 1999). This power supply accepts 115 VAC input and provides + 5 VDC and ± 12 VDC outputs at low amperages. A linear power supply was selected instead of a switching power supply because its output is exceptionally stable (< 0.01% fluctuation) and the unit is essentially noise-free

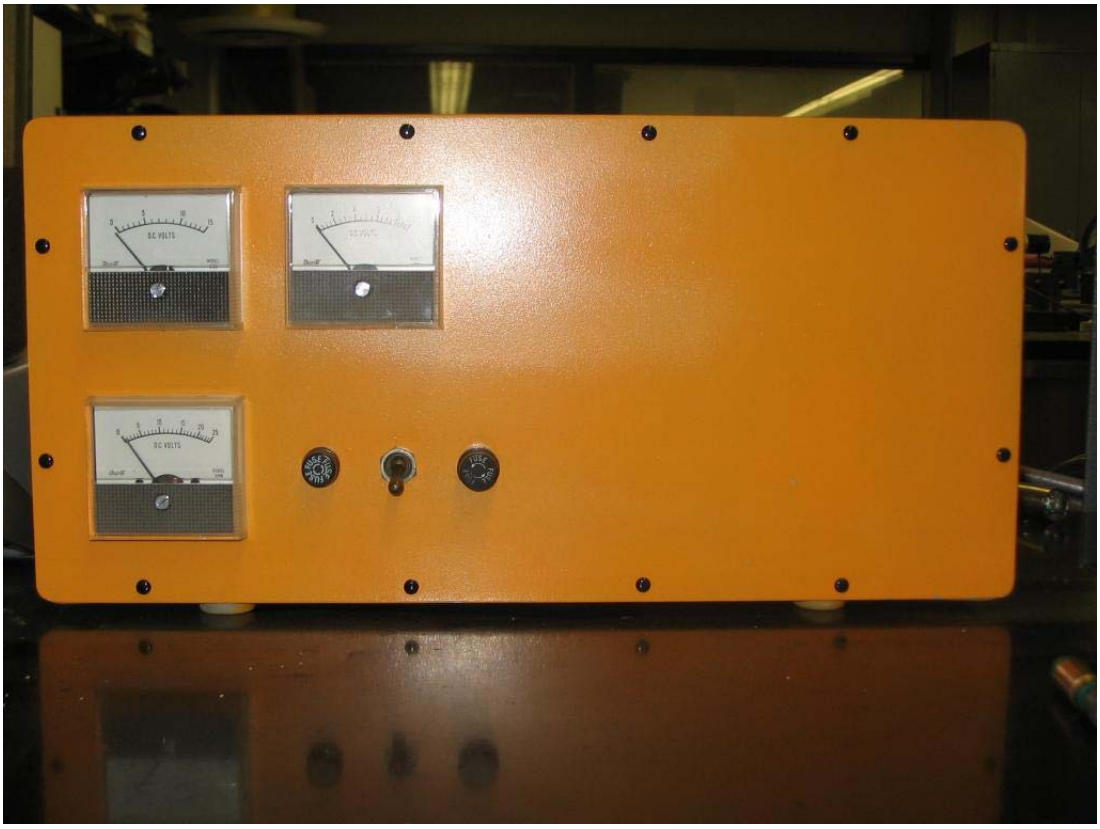

Figure 3.3: External front view of the power supply unit

compared to a switching unit. In a switching power supply, the rapid on-off load current cycling used to regulate output contains high frequency energy that can be propagated either as radio waves or though electromagnetic induction leading to interference with other devices. Linear power supplies are typically larger, heavier, hotter (by design, linear supplies dissipate excess energy as heat to regulate voltage), and less efficient (typically 50% efficient) than switching power supplies (typically 80% efficient). These issues were unimportant in the current work as the linear power supply was still small enough to fit in the manufactured enclosure used for electronics, was not rail-mounted

(i.e., weight was not an issue), could be cooled effectively, and provided plenty of power for the given instruments. When wiring the power supply, the – 5 VDC output was jumped to the 12 VDC common terminal to produce a common ground, which was tied to the case and then the building ground.

To protect the linear power supply from overheating and prevent a loss of efficiency, a fan was installed in the manufactured enclosure. An 80 mm diameter fan, 38 mm deep was used to provide 0.9 m^3/min (33 ft^3/min) of air flow through the manufactured enclosure. Power for the fan is supplied through the same 115 VAC that drives the power supply. Three gauges were installed in the enclosure to monitor the 5 VDC, 12 VDC, and 24 VDC (± 12 VDC) outputs. External fuses were used to protect the power supply and the instruments from power surges and/or short circuits.

Power leaves (and signals enter) the manufactured enclosure by means of fourteen microphone receptacles installed in the back of the device (Figure 3.4). The four-pin female receptacles matched four-pin male plugs that were installed on the ends of the wires that exit the biaxial device. Microphone connecters were selected for ease of use (their large size makes soldering easier), durability, and cost. The ground wire for the cables was tied to the sheath on the microphone plugs, which contacts the receptacle ground. Receptacle grounds were tied to the building ground.

3.1.2.3.Data Acquisition

Signals from the instrumentation are collected using an Agilent Technologies 34970A Data Acquisition Switch Unit (Figure 3.5). The 34970A is a three-bay digital

Figure 3.4: External rear view of the power supply unit

multimeter (DMM) that can scan up to 250 channels per second. The multimeter accepts up to three multiplexers for collecting data from multiple inputs. A 34902A 16 Channel Reed Multiplexer Module was used in this study. The 34902A is capable of accepting 2- or 4-wire leads in any combination across its sixteen channels. Two-wire leads were used in this study. Standard output from the device is through either RS-232 or GPIB interfaces. However, for increased throughput (compared to RS-232) and to avoid having to add a GPIB card to the computer controlling the device, an 82357A USB/GPIB Interface was employed to channel GPIB output from the DMM to the USB port on a

Figure 3.5: Data acquisition unit

personal computer (PC). The PC used to control the device is a Gateway Pentium-III 500 MHz desktop with 256 MB of RAM running Windows 2000. The interface was provided via Agilent Benchlink software. The Benchlink software is provided with the DMM and allows for setup and control of the device and also logs data to a text file and provides real-time plots during test execution.

The primary reason for the selection of the 34970A was that it is capable of measuring a wide range of voltages without external signal conditioning, which reduces the overall cost and increases the reliability of the data acquisition system. As can be seen from Table 3.1, LVDT outputs are on the order of millivolts to volts while load cell

outputs are on the order of microvolts to millivolts. The 34970A has the ability to measure voltages precisely (5½ digit precision) over a wide range and when coupled with the 34902A also provides a high degree of isolation between channels to prevent (e.g.) residual voltage from an LVDT measurement interfering with a subsequent load cell measurement. Channel-to-channel and channel-to-earth isolation is greater than 10 GΩ in the multiplexer.

When configuring the DMM, additional steps were also taken to ensure the highest quality measurements possible. First, the integration time for each measurement was selected as a multiple of the power line cycle for the AC voltage supplying the DMM. In this case, two power line cycles were used for integration, meaning that the integration time is:

$$\frac{1}{60\,\text{Hz}} \cdot 2 = 33.3\,\text{ms} \tag{3.1}$$

assuming that the frequency of the AC power coming from the wall is 60 Hz (the DMM measures this to be sure). By averaging over an integer number of power line cycles, the white noise associated with alternating current power is minimized. After taking a measurement, the multiplexer was configured to pause until the voltage reading in the DMM settles back to a constant value. Because this value may not be precisely zero, the DMM then integrates this value over two power line cycles and uses that measurement as its zero point. The multiplexer then moves to the next channel. Because of the forced zero, the time between measurements is actually something in the range of 67 to 70 ms (note that this will vary depending on the time required for the signal to settle between measurements). Thus, all fourteen channels are scanned every 0.94 to 0.98 s, which corresponds to a global axial displacement of 6.3 to 6.5 μm for a constant loading rate of

0.4 $^{mm}/_{min}$. The maximum absolute values for measurement errors for representative LVDT's and load cells are presented in Figure 3.6. Maximum errors as a percentage of peak load for the pancake load cells and axial load cell are 0.2% and 0.4%, respectively. Maximum errors as a percentage of maximum displacement are 0.03% for the lateral LVDT's and 0.01% for the axial LVDT's.

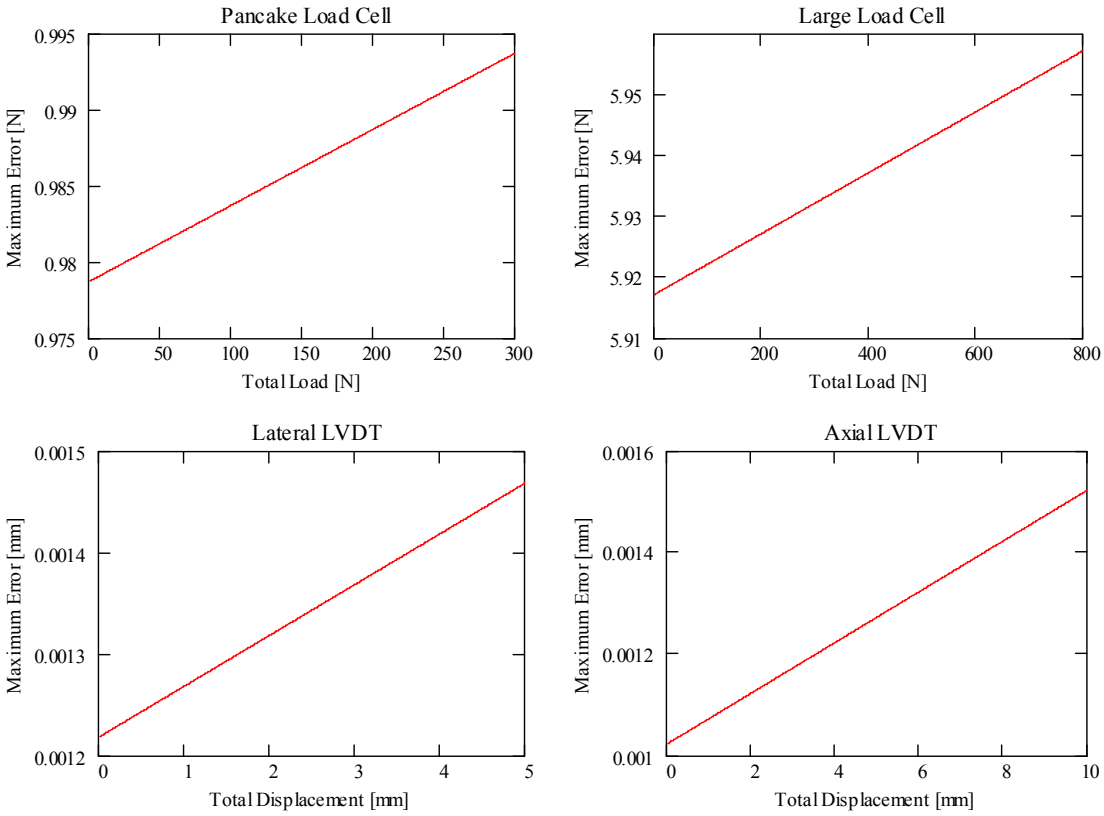

Figure 3.6: Maximum measurement errors due to the accuracy of the DMM

3.2. Specimen Preparation

Sand specimens for the current study were prepared using the air pluviation technique, as it has been shown (Park, 1999; Frost and Park, 2003) that air pluviation creates more uniform specimens relative to moist tamping, which tends to yield a layered soil profile (Han and Vardoulakis, 1991). Some researchers (Finno et al., 1997) have noted that moist tamping generates specimens with a high standard deviation referenced to global relative density (Gilbert and Marcuson, 1988) but have found it necessary to use this preparation technique to study very loose sands. Other researchers (Mooney et al., 1998; Finno and Rechenmacher, 2003) have used the moist tamping (loose specimens) and air pluviation (dense specimens) techniques in the same study, while many researchers (Han and Drescher, 1993; Alshibli and Sture, 2000) have relied solely on air pluviation.

Specimens were formed in a 0.45 mm (0.018 in.) rubber membrane placed inside of a split Lexan mold (Figure 3.7) using a manual air pluviator (Figure 3.8). Given nominal sample dimensions of 140 mm x 80 mm x 40 mm (5.5 in x 3.2 in x 1.6 in), the

Figure 3.7: Sample forming mold

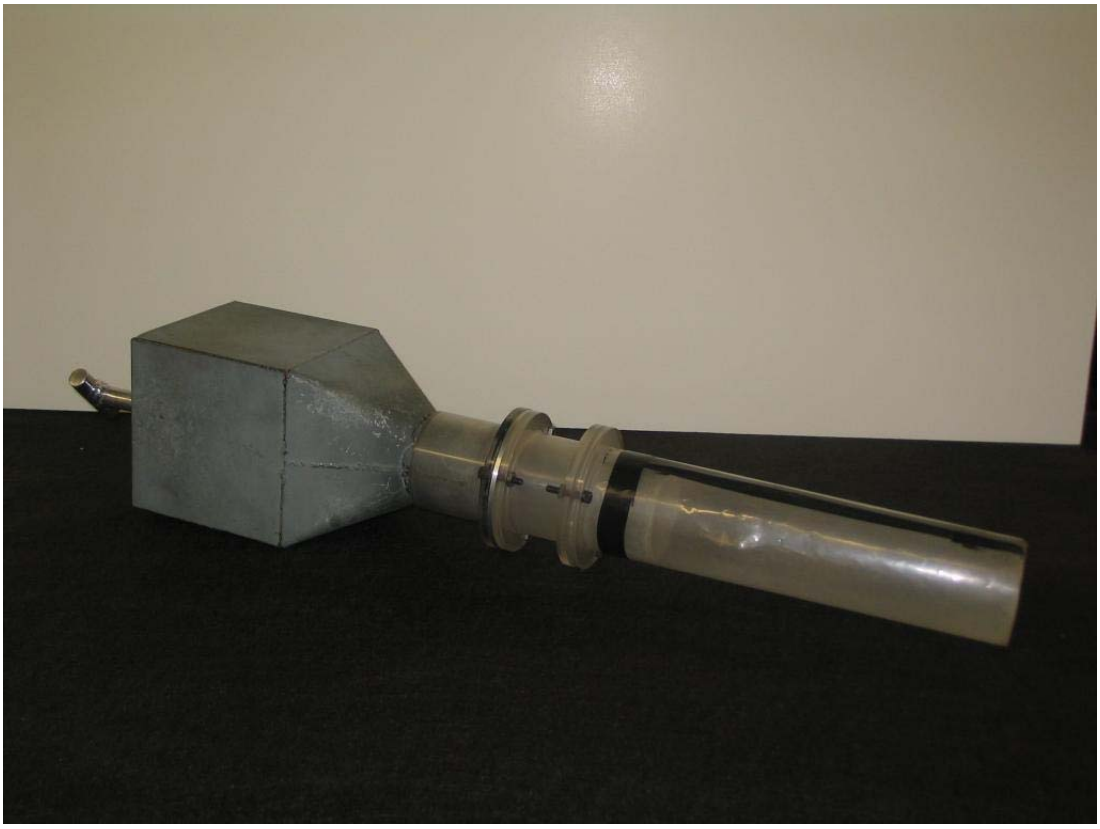

Figure 3.8: Manual air pluviator

mass of sand required to achieve the desired initial void ratio was calculated. An aluminum insert (Figure 3.9) was placed inside of the Lexan mold to prevent sand grains from accumulating on the ledge at the top of the mold and to catch overflow from the pluviation process. The overflow was subtracted from the total mass of sand used.

After filling the membrane with sand, the aluminum insert was removed and the top platen (Figure 3.10) was placed into the mold. The membrane was rolled up on the top platen and secured with three O-rings. The entire apparatus was then placed into the biaxial device, using the mounting bars on the base of the mold to align the specimen on

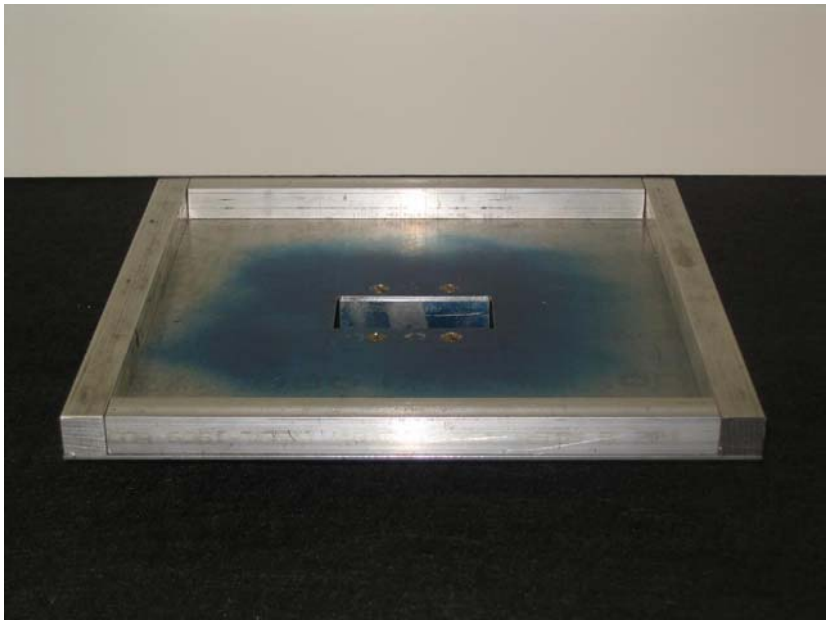

Figure 3.9: Aluminum insert for specimen former

Figure 3.10: Top loading platen

the sled. The piston was attached to the top platen and then vacuum was removed from the sample mold and applied to the specimen via the top and bottom platen. The specimen was allowed to equilibrate for five to ten minutes before the mold was removed. Specimen dimensions were then measured in each of the three orthogonal directions, taking averages of multiple measurements in each case. To minimize friction between the membrane and the side walls, silicone oil was applied to the membrane surface and silicone grease was applied to the glass side walls to create a situation involving two lubricants of different viscosities sliding against one another.

3.3. Monitoring of Membrane Deformations

Membrane deformation over the course of a test is monitored by means of a grid drawn onto one side of the sample membrane in the σ_2 plane. The grid point spacing is nominally 4 to 5 mm, but may vary due to stretching of the membrane over the sample and imperfections arising from manual creation of the grid. Small variations in grid spacing are not significant because only relative distances are being considered (i.e., the distance between two points as it varies over the course of a test is important, but the absolute positions of the two points are not).

The methodology described herein is similar to that used by Alshibli and Sture (1999) and Peric (2003). A 3.2-megapixel Canon PowerShot A75 digital camera is mounted to a tripod and pointed towards the sample in line with a unit normal vector from the σ_2 plane. Using no flash (to prevent glare) and a time-delayed capture option (to prevent camera vibrations from handling), images are captured approximately every two minutes over the course of a test, for a total of 15 to 20 images per test. The time

from the beginning of the test (to the nearest second) is recorded for each image so that images may be mapped back to global axial strain levels at the completion of the test. A sample image is presented as Figure 3.11. There will be some small amount of distortion associated with taking photos through the curved Plexiglas confining cell, but since neither the camera nor the cell is moved over the course of the test, these effects are offsetting from image to image as relative displacements are calculated.

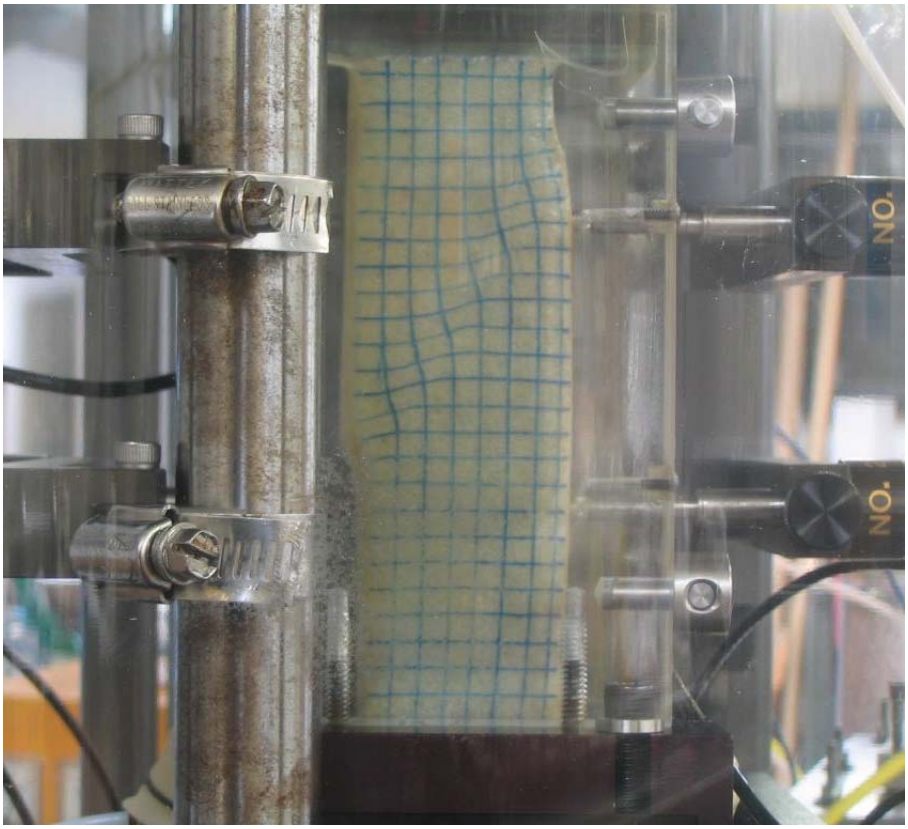

Figure 3.11: Sample image of deformed grid on the side of a membrane

The images of the deformed membrane are imported into AutoCAD 2004, where they are scaled up to actual size using reference measurements from the biaxial device itself (specifically, the 1.0-in. diameter steel columns that support the upper piston guide). All grid points are then identified manually and their x- and y-locations (relative to a constant reference point) are exported to a data file for further analysis.

3.4. Two-Stage Resin Impregnation Procedure

At the completion of a test, the microstructure within the sand specimen is preserved using a glue solution and subsequently solidified with a two-stage epoxy resin. This is in contrast to the more common single-stage procedure (e.g., Chen, 2000) or plaster casting followed by single-stage impregnation (Alshibli and Sture, 1999) typically employed by previous researchers. There are two reasons for employing the two-stage impregnation in the current study:

- Single-stage impregnation in triaxial specimens was performed using a modified triaxial cell wherein any components of the cell that come into contact with the resin are sacrificed. Given the geometry of the biaxial device and the fact that the large axial load cell is affixed to the upper platen, it was not possible to configure the device to allow all resin-contacting components to be disposed.
- In the plaster-casting followed by impregnation procedure, the specimen is removed from the biaxial device prior to impregnation. In this manner, resin-contacting components no longer have to be sacrificed, but a vacuum has to be applied to the specimen so that the confining stress can be

released and the biaxial device disassembled. As implemented previously, this results in a doubling of the confining stress (15 kPa vacuum + 15 kPa cell pressure) at the completion of the test prior to disassembly of the device. It is possible that the void structure in the loosest parts of the specimen (i.e., the shear band) could be altered by this sudden doubling of the confining stress. Furthermore, once the plaster of Paris sets, the vacuum must be removed from the specimen prior to impregnation. Thus, if volume change has occurred in the plaster, there could be additional changes in soil microstructure due to soil particle rearrangement.

Two-stage impregnation was first implemented by Yang (2002) to prevent volume change in very loose triaxial sand specimens that could possibly be caused by resin impregnation alone. A dilute (5% by weight) glue solution was used to lightly cement loose sand specimens in a modified triaxial cell. Yang found that by using the two stage process, axial shrinkage due to resin impregnation was reduced from 2% to 1.1%. Yang also used a two-stage process to preserve the contents of a "sandblow tank" used in his research. After impregnation and curing of the glue in the sandblow tank, the sand mass was stable enough that small cuboidal (approximately two inches to a side) specimens could be successfully carved from the global mass. Additional details of the sandblow tank and associated impregnation procedure can be found in Yang (2002).

In the present study, the first stage of the two-stage impregnation process begins by flushing the soil specimen with a dilute solution (7% by weight) of Elmer's Carpenter Glue under a small vacuum (~10-15 kPa). A more concentrated solution than that used

by Yang (2002) was required because of the high void ratios in the shear band, as discussed subsequently. The solution is drawn through the specimen from bottom to top and into a waste reservoir outside of the biaxial device. Once the waste reservoir contains approximately one-half to one pore volume of solution, the vacuum is released and excess glue solution is allowed to drain from the pores. After excess glue solution has drained from the specimen pores, the vacuum is reactivated, but instead of drawing glue solution through the specimen, desiccated air is flushed through the pores. The relative humidity of the air leaving the top of the specimen is monitored. Schematics of the glue impregnation (Figure 3.12) and desiccation (Figure 3.13) processes are shown below.

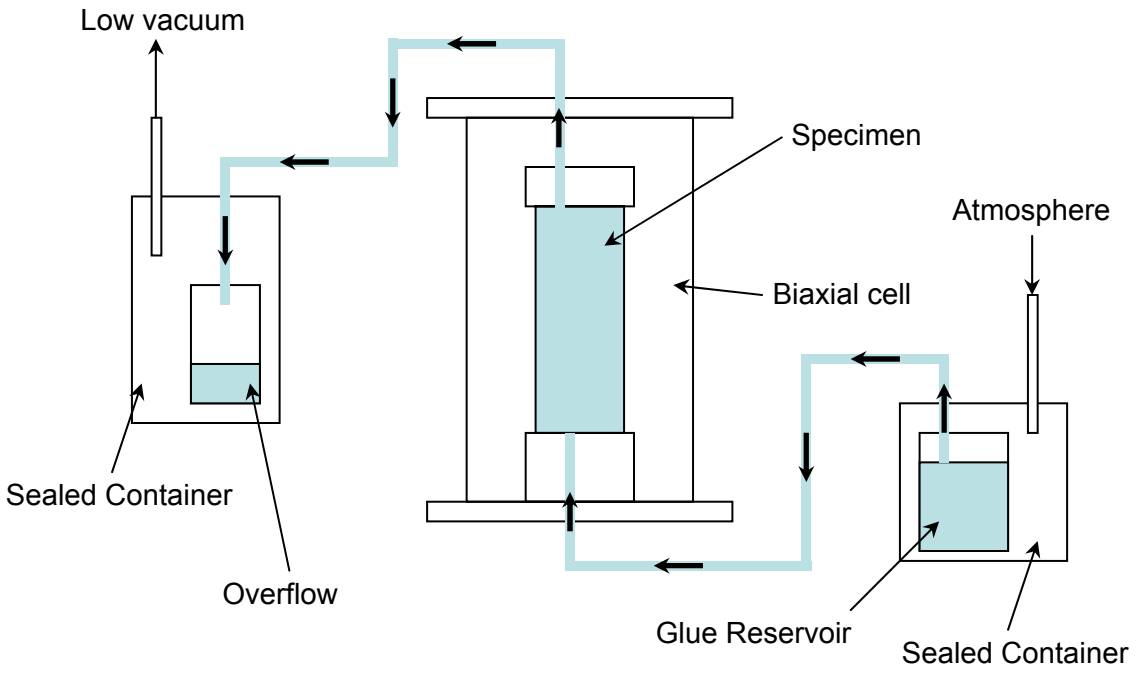

Figure 3.12: Schematic of glue impregnation processes

Once the relative humidity of the air leaving the specimen is below 40% (usually after 5-7 days), the glue has cured and the specimen may be disassembled. A vacuum is applied to the top and bottom platens and the confining stress is released form the cell. The device is disassembled and a collar is placed around the loading piston to prevent small movements once the vacuum is released. Finally, the vacuum is released, the membrane is carefully pulled back from the specimen, and the cemented specimen is carved from between the platens. Only the portion of the specimen containing the shear band is extracted from the device (Figure 3.14).

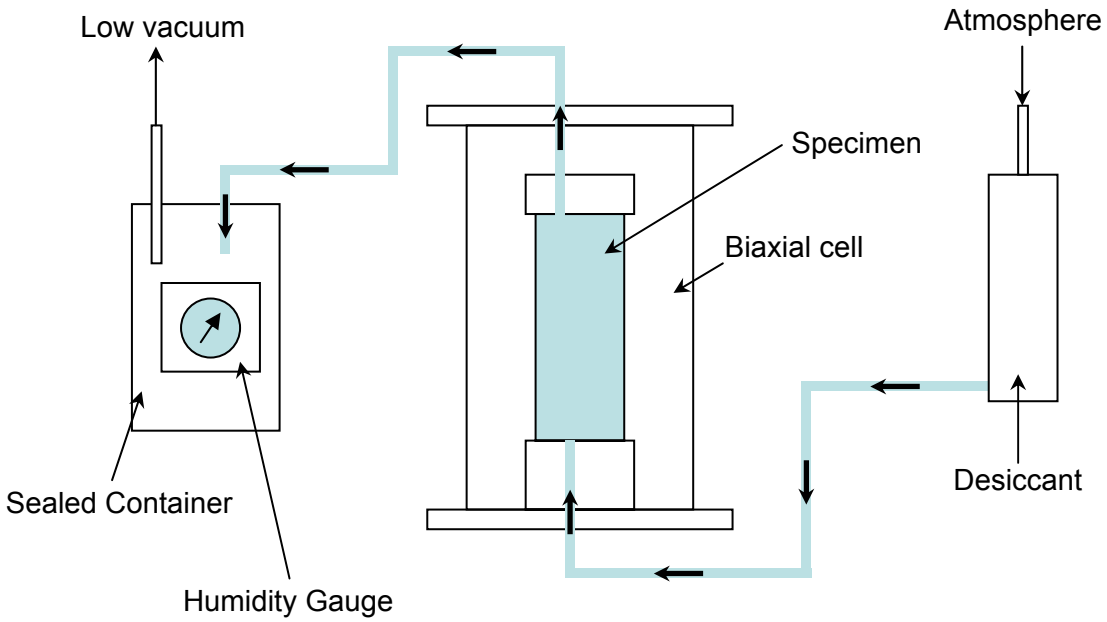

Figure 3.13: Schematic of desiccation processes

The lightly cemented specimen is then impregnated with an epoxy resin to allow for sectioning and polishing. Epo-Tek 301 epoxy resin from Epoxy Technology is used for the second impregnation because it is low viscosity, optically clear, and undergoes

very little volume change during curing. Properties of Epo-Tek 301 are listed in Table 3.2. The extracted sand specimen is placed on a Plexiglas sheet that is

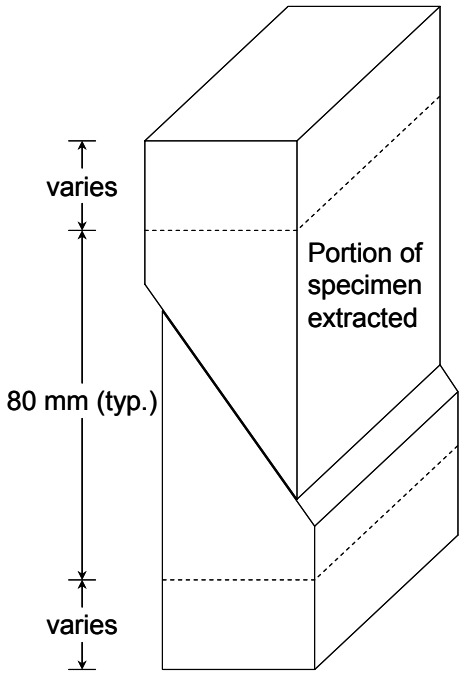

Figure 3.14: Portion of the sample extracted after testing for resin impregnation and sectioning

nominally 80 mm x 80 mm x 3.2 mm (3.15 in x 3.15 in x 0.125 in) to provide support and rigidity during the resin impregnation. A "bowl" of aluminum foil is then formed around the specimen to contain the resin during the impregnation. Aluminum foil was selected because it may be readily formed to the size and shape of the specimen, which reduces the amount of resin required. This is significant because the epoxy resin is expensive (~$300/gal) and the reaction between the base and the hardener is exothermic, with greater resin volumes generating greater heat. Epoxy resin is mixed in 75-g batches (60 g base and 15 g hardener), deaired under vacuum for five minutes, and added very slowly

to the aluminum foil bowl using a disposable funnel to fill from the bottom up. The impregnated specimen is then allowed to cure for 24 hours, at which stage it can be dissected into coupons on which imaging can be conducted.

Table 3.2: Properties of Epo-Tek 301

Property	**Value**
Mixing Ratio	4:1 base to hardener
Color	clear
Viscosity	100-200 cPs
Specific Gravity	Part A: 1.15, Part B: 0.87
Shore D Hardness	81
Index of Refraction	1.539

Several issues needed to be addressed before the two-stage impregnation procedure was considered a viable method for specimen solidification. The first issue is similar to the problem described by Oda and Kazama (1998) wherein they found that they were unable to impregnate the upper portion of the specimen. In the current study, it was found that forcing the glue solution into the portion of the specimen above the shear band was difficult without using high vacuum or driving pressures. It is postulated that the cause of this is the high void ratio of the shear band relative to the remainder of the specimen. This high void ratio results in a capillary barrier effect (Stormont and Anderson, 1999) that is more often associated with fine-over-coarse soil layers. From a thermodynamic standpoint, however, this capillary barrier effect will occur any time a

water attempts to move from a region with relatively small pore space to a region with relatively large pore space. Flow from small to large pores is impeded because water will not enter the large pores until the negative matric potential (i.e., the "suction") in the pore water increases to the water entry potential associated with the area of the larger pores. This water entry potential is typically associated with water content values very near saturation in the region of small pores (e.g., -3 to -5 kPa). On the pore scale, Hillel (1980) refers to this phenomenon as the "ink bottle effect". This difficulty was overcome by slightly increasing the vacuum used for impregnation and by ensuring that the membrane was very tightly sealed at the top and bottom platens using silicone grease and multiple O-rings. However, in some tests, it was still not possible to impregnate the entire specimen.

The second major issue in the two-stage impregnation process arises when disassembling the device and extracting the specimen after the glue has cured. Due to the high void ratios within the shear band, there are relatively fewer particle contacts compared to the remainder of the specimen. Thus, the shear band represents a weak zone in the cemented specimen. As such, it is very easy to fracture the specimen along the shear band when extracting it from the test device. A fractured specimen is shown in Figure 3.15. Unfortunately, it is not possible to prevent the shear band from becoming a weak zone due to the inherent mechanics of the system. Several cemented specimens were destroyed when attempting to remove them from the device.

Figure 3.15: Sample that fractured along the shear band during extraction from the biaxial device

3.5. Coupon Surface Preparation and Mosaic Generation

The solidified specimens were cut to a manageable size and then sliced into sections that were then planed, ground, and polished. The initial rough cuts were made with a Buehler slab saw (Figure 3.16) with an 18-in. diamond blade. The purpose of the initial rough cuts was to remove any excess aluminum foil from the specimen and to finish with a parallelepiped that measured nominally 40 mm x 40 mm x 80 mm (1.6 in. x 1.6 in. x 3.2 in.), as shown in Figure 3.17. The resulting block fits into a modified mount for the Buehler Isomet 1000 precision saw (Figure 3.18). The block is sliced into five slabs of approximately equal thickness using a Buehler Series 15 Low Concentration (LC) Diamond wafering blade (see Figure 3.19). Four surfaces from approximately the $^1/_5$ points in the block are used for analysis. These surfaces are identified as -20, -40, -60, and -80 to designate their locations as a percentage of total sample width. All efforts are made to produce four slices of identical thickness with perfectly parallel faces using the

Isomet 1000 Precision Saw, but this isn't possible in practice because the specimen must be removed from the saw and remounted after the first two cuts. Thus, the surfaces must be planed and ground before they can be polished for imaging.

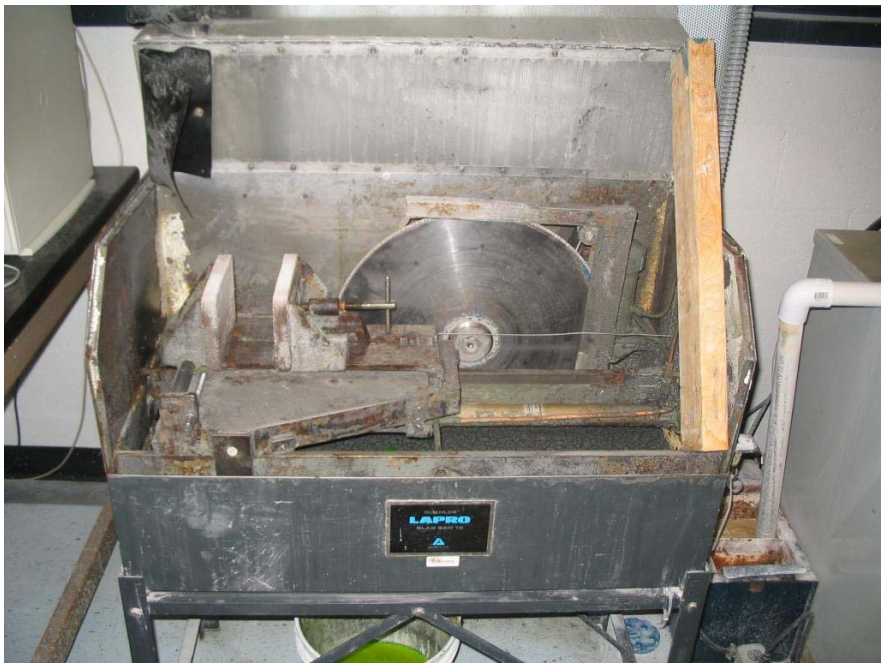

Figure 3.16: Buehler Lapro slab saw

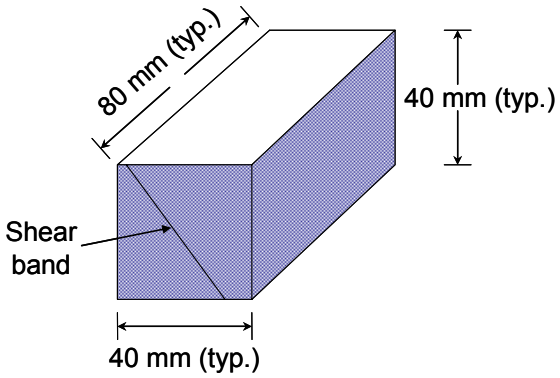

Figure 3.17: Specimen dimensions after trimming with the slab saw

Figure 3.18: Isomet 1000 precision saw

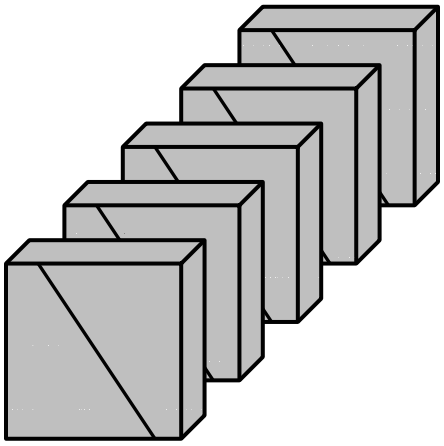

Figure 3.19: Specimen sectioned for planing, grinding, and polishing

Planing is accomplished by means of a surface planer manufactured by Structural Behavior Engineering Laboratories (SBEL). This device consists of a 0.25-in. (6.35 mm) wide grinding wheel that can be moved up and down with 0.0001-in. (2.54-μm) precision that is mounted above a two-degree-of-freedom table whose movement is controlled hydraulically (see Figure 3.20). The table moves from side to side and moves from back to front automatically at the completion of each pass. For the present work, front-to-back movement was set at 0.1 in. (2.54 mm) per pass during coarse planing and 0.05 in. (1.27 mm) per pass during fine planing. Thus, the number of passes required to fully cover a 40-mm (1.57-in.) deep section would be 16 for coarse planing and 32 for fine planing.

Figure 3.20: SBEL surface planer

After sectioning, the four blocks to be used for analysis are mounted onto 2.8-in. diameter epoxy discs using a cyanoacrylate adhesive. The bonded slice-disc couples are then mounted onto a 2-in. wide steel bar using the same adhesive and the steel bar is then placed on the table of the SBEL surface planer. The bar is held in place by means of a permanent magnet on the table of the planer. The purpose of the surface planer is to remove quantities of material from the sections that it would be unreasonable to remove using the grinding procedure described below. The surface planer is used to take the rough cut sections and create four sections of identical thickness whose surfaces are parallel to the back sides of the mounting discs. Material is first removed from the surfaces at a rate of 0.01 in. (0.254 mm) per pass. Once the wheel is in contact with all four surfaces, the material removal depth is reduced in stages from 0.005 in. (0.127 mm) to 0.0001 in. (2.54 μm). Material must be removed gradually to minimize the "plucking" of grains from the epoxy matrix. At the completion of this process, all sections should be of the same thickness. The steel bar is removed from the permanent magnet and the mounting discs are removed from the steel bar.

Both the grinding and polishing phase required the use of a Buehler Metaserv polishing table with an Autopol II attachment (Figure 3.21) to hold the sections. The grinding phase is required prior to polishing to compensate for moving from the surface planer to the polishing table. As the sections sit in the Autopol II attachment, there may be some slight misalignment present that could potentially result in the surfaces not being completely parallel to the polishing wheel. By grinding the surfaces first, better alignment is achieved during the polishing phase. The methodology used in the grinding and polishing stages is evolved from that presented by Yang (2002) and is outlined in

Table 3.3. The primary differences between the current grinding and polishing procedure and previous work (e.g., Yang, 2002) are that the overburden stress applied to the surfaces is higher than in previous studies and polishing time is increased.

Figure 3.21: Buehler Metaserv polishing table with Autopol II attachment

Table 3.3: Parameters used for polishing and grinding

Parameter	**Grinding Phase**	**Polishing Phase**
Wheel Surface	cast iron	Texmet 1000 cloth on aluminum
Abrasive	600-grit SiC powder	1000-grit SiC powder
Mixing	50 g/250 ml Metadi Fluid	50 g / 250 ml water
Wheel Speed	120 rpm	120 rpm
Overburden Stress	29 kPa (typ.)	23 kPa (typ.)
Duration	until flat, 30-60 min	10-13 min

Once the surfaces have been polished, images of the surfaces are captured using a Leica DM4000 M microscope interfaced to a Pentium IV personal computer running Leica Qwin v2.8 image capture and analysis software. The microscope is capable of automatically scanning a surface and collecting a series of subimages that can later be stitched together to form a large image of the entire surface. Each subimage is 640 x 480 pixels and each pixel is 7.83 μm square. The software was originally configured to capture images with an overlap of 20% to aid alignment during the stitching process. However, as shown in Figure 3.22, using a 20% overlap resulted in shadowing in the stitched image, which is a product of the fact that incident light during imaging is focused to the center of the surface where the image is taken. To overcome this effect, overlap was increased to 50% in both the vertical and horizontal directions. With a 50% overlap and the given size of individual subimages, a grid of 460 images (23 columns and 20 rows) was sufficient to capture a nominal 40 mm (1.6 in.) square surface. All images are captured with camera settings of 70% contrast, 59% brightness, and a lamp intensity of 11.37%.

PanaVue ImageAssembler software is used to stitch the subimages into a mosaic. The software looks for common patterns in adjacent subimages and then overlays the subimages to create a single image of the entire surface. Several parameters can be adjusted in the stitching process, but the same parameters are used for each stitching operation. The parameters selected in the current study are described in Table 3.4. Once the mosaic has been created, it is saved as a bitmap to prevent loss of information. Because of limitations in the Qwin image analysis software, the mosaic must be trimmed to a smaller size before the image is usable. The Qwin v2.8 software has an

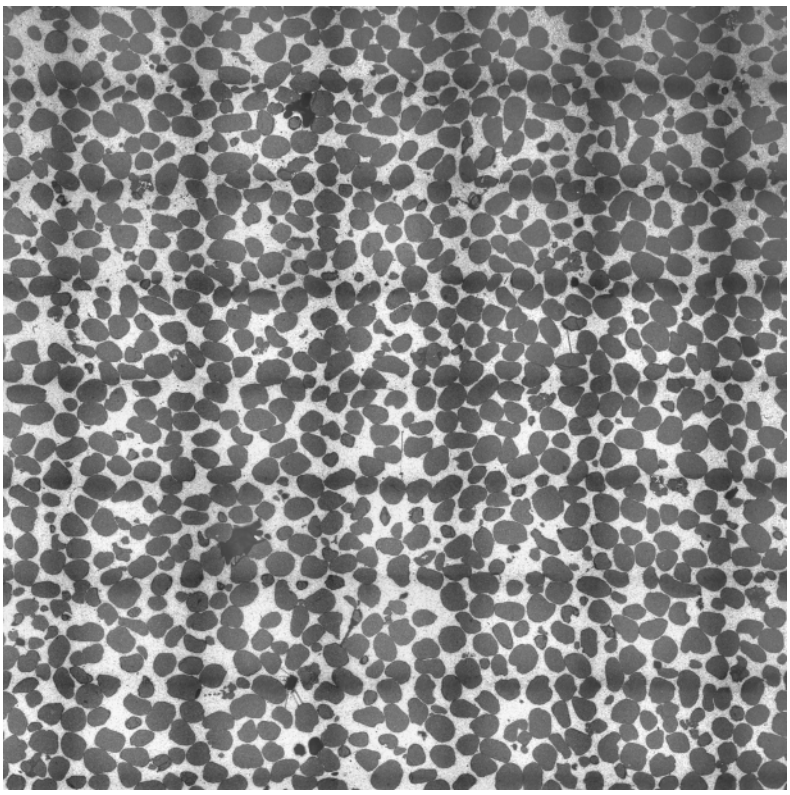

Figure 3.22: Mosaic stitched with 20% overlap (note shadow effects)

undocumented maximum image size of 4096 x 4096 pixels (Bunn, 2005) and larger images cause the software to incorrectly map image pixels to the screen, creating a distorted image. Through trial and error, however, it was determined that the largest image that would not cause these adverse effects was 4400 x 4400 pixels, so all mosaics were cropped down to this size. The cropping window in each case was selected manually to center the shear band in the image to the greatest extent possible, while leaving the window near the center of the overall mosaic. Staying near the center of the mosaic is important because image quality can degrade near the surface edges due to the relative unevenness of the surface (which is to be expected on surfaces of this size).

Table 3.4: Parameters used for mosaic stitching operation

Parameter	Value	Description
Anti-aliasing	on	Anti-aliasing is an averaging scheme used to smooth the edges of pixilated objects. PanaVue uses a bicubic algorithm.
Image blending	40%	A weighted average used to adjust colors in overlapping portions of images. The suggested value is between 20% and 60%.
Force first row/column	on	Forces the first row and first column of the mosaic to fall in a straight line.

4. MATERIAL AND MODEL PROPERTIES

4.1. Material Properties

The sand tested in the current study is Ottawa 20-30 sand from the U.S. Silica Company in Ottawa, Illinois. Ottawa 20-30 sand is a poorly graded subrounded sand composed primarily (99.8%) of silicon dioxide (quartz) (U.S. Silica Company, 1997). An image of Ottawa 20-30 grains is presented as Figure 4.1, a grain size distribution chart is shown as Figure 4.2, and significant properties of the sand are presented in Table 4.1. The grain size distribution curve was fit to data obtained by a sieve analysis performed in accordance with ASTM D422 (ASTM, 2002) using the mathematical form suggested by Fredlund, et al. (2000). This allows for very precise and accurate determination of grain size parameters (e.g., d_{10}, d_{50}, etc.).

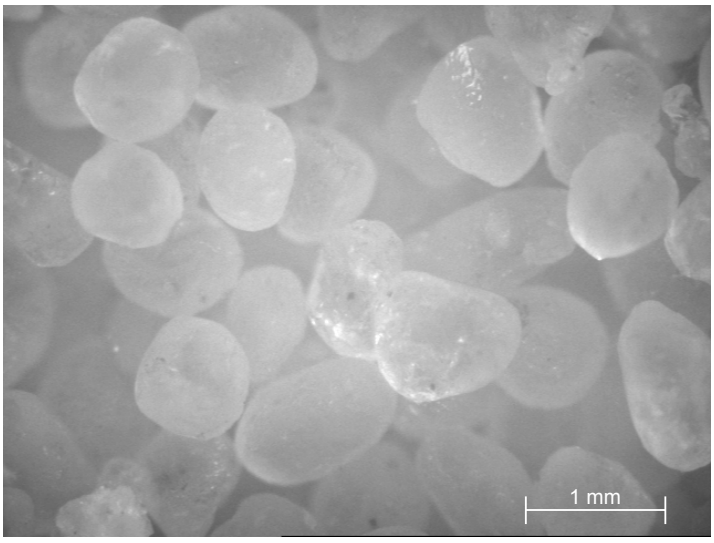

Figure 4.1: Microscopic image of Ottawa 20-30 sand

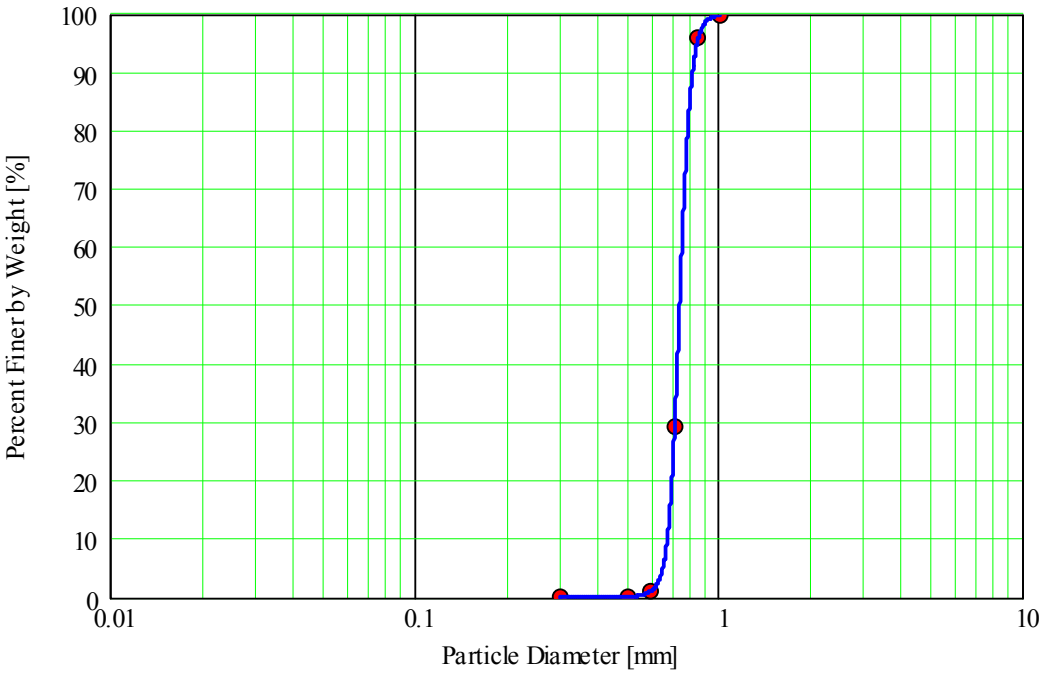

Figure 4.2: Grain size distribution for Ottawa 20-30 sand

Table 4.1: Physical characteristics of Ottawa 20-30 sand

Parameter	Value	Reference
d_{10}	0.67 mm	ASTM D422
d_{30}	0.71 mm	ASTM D422
d_{50}	0.74 mm	ASTM D422
d_{60}	0.76 mm	ASTM D422
C_c	1.00	ASTM D422
C_u	1.12	ASTM D422
e_{max}	0.742	(Cho, 2001)
e_{min}	0.502	(Cho, 2001)
G_s	2.65	(Cho, 2001)
ϕ_{cs}	27°	(Santamarina and Cho, 2001)

4.2. Model Properties

4.2.1. Introduction

The discrete element method (DEM) was used for the numerical studies conducted as part of the current work. The specific implementation of the DEM used herein is *PFC2D: Particle Flow Code in Two Dimensions v3.00* (Itasca, 2003). This implementation of the DEM was selected for its well-verified performance, excellent documentation, flexibility, and ease of use. While other implementations of the method are available free of charge (e.g., Kuhn, 2003) the documentation is often not as comprehensive and support is typically not provided. Two types of objects may be simulated in PFC2D, "balls" and "walls". Balls may either be spheres whose centroids lie in a plane or disks of a specified thickness. Walls are straight and rigid and interact only with balls, but not with each other.

4.2.2. Mathematical Formulation of the Discrete Element Method

The DEM is based upon the solution of Newton's equations of motion for each particle in an assembly. The mathematics of the problem are, thus, not very complex. However, some important assumptions are necessary for solution of these equations using the DEM (after Itasca, 2003):

- Particles may be represented as rigid disks or balls;
- Contacts (ball-ball and ball-wall) occur at a point; and
- Particle overlap is allowed at contacts (soft-contact approach) but these overlaps are small relative to particle size.

Given these assumptions, the calculation cycle begins with determining the unit normals of the contacts in the assembly (the following derivation is after Itasca, 2003, but is included here for completeness):

$$n_i = \frac{x_i^{\langle B \rangle} - x_i^{\langle A \rangle}}{d} \tag{4.1}$$

where n_i is the normal vector, $x_i^{<A>}$ and $x_i^{<B>}$ are the locations of particle centers for particles A and B, respectively, and d is the distance between particle centers. For ball-wall contacts, the normal is taken along the shortest path from the particle center to the wall. The overlap at contacts, U^n, may then be calculated as:

$$U^n = \begin{cases} R^{\langle A \rangle} + R^{\langle B \rangle} - d, (ball - ball) \\ R^{\langle B \rangle} - d, (ball - wall) \end{cases} \tag{4.2}$$

where $R^{<\Phi>}$ is the radius of ball Φ. The location of the contact point, $x_i^{<C>}$, may then be calculated and used to determine the relative distance between particles:

$$x_i^{\langle C \rangle} = \begin{cases} x_i^{\langle A \rangle} + \left(R^{\langle A \rangle} - \frac{1}{2} U^n \right) n_i, (ball - ball) \\ x_i^{\langle b \rangle} + \left(R^{\langle b \rangle} - \frac{1}{2} \cdot U^n \right) \cdot n_i, (ball - wall) \end{cases} \tag{4.3}$$

Now that the contact location is known, it is straightforward to calculate velocities and invoke the constitutive relation for contact theory (linear or Hertz-Mindlin) to calculate normal and shear forces on each particle. First, particle forces are resolved into normal and shear components:

$$F_i = F_i^n + F_i^s \tag{4.4}$$

where F_i is total contact force vector and F_i^n and F_i^s are the normal and shear components, respectively. Force in the normal direction is then calculated as:

$$F^n = K^n \cdot U^n \tag{4.4}$$

where K^n is contact normal stiffness (secant modulus). To calculate shear forces, first the shear contact velocity, V^s, must be determined:

$$V^s = \left(\frac{d}{dt} x_i^{\langle \Phi 2 \rangle} - \frac{d}{dt} x_i^{\langle \Phi 1 \rangle} \right) t_i - \omega_3^{\langle \Phi 2 \rangle} \cdot \left| x_k^{\langle C \rangle} - x_k^{\langle \Phi 2 \rangle} \right| - \omega_3^{\langle \Phi 1 \rangle} \cdot \left| x_k^{\langle C \rangle} - x_k^{\langle \Phi 1 \rangle} \right| \tag{4.5}$$

where ω_3 is rotational velocity and $<\Phi^j>$ is used to denote either a wall or ball at the given contact as follows:

$$\left(\Phi^1, \Phi^2 \right) = \begin{vmatrix} (A, B), (ball - ball) \\ (b, w), (ball - wall) \end{vmatrix} \tag{4.6}$$

The incremental shear force (ΔF^s) over a time increment (Δt) is then calculated as:

$$\Delta F^s = -k^s V^s \Delta t \tag{4.7}$$

where k^s is the tangent shear stiffness for the contact. Forces and moments for the particles are then updated as follows:

$$\begin{aligned} F^s &\leftarrow F^s + \Delta F^s \le \mu \cdot F^n \\ F_i &= F^n \cdot n_i + F^s \cdot t_i \\ F_i^{\langle \Phi 1 \rangle} &\leftarrow F_i^{\langle \Phi 1 \rangle} - F_i \\ F_i^{\langle \Phi 2 \rangle} &\leftarrow F_i^{\langle \Phi 2 \rangle} + F_i \\ M_3^{\langle \Phi 1 \rangle} &\leftarrow M_3^{\langle \Phi 1 \rangle} - e_{3jk} \cdot \left(x_j^{\langle C \rangle} - x_j^{\langle \Phi 1 \rangle} \right) \cdot F_k \\ M_3^{\langle \Phi 2 \rangle} &\leftarrow M_3^{\langle \Phi 2 \rangle} + e_{3jk} \cdot \left(x_j^{\langle C \rangle} - x_j^{\langle \Phi 2 \rangle} \right) \cdot F_k \end{aligned} \tag{4.8}$$

where μ is the friction coefficient at the contact, M_3 is moment, and e_{3jk} is the permutation operator. Note that there is only one rotational degree of freedom in two dimensions. The new particle forces and moments are used to calculate the new acceleration and angular momentum using the following relationships:

$$F_i = m\cdot\left(\frac{d^2}{dt^2}x_i - g_i\right)$$
$$M_3 = \beta\cdot m\cdot R^2\cdot\frac{d}{dt}\omega_3 \tag{4.9}$$

where m is particle mass, g is acceleration due to gravity, and β is 0.4 for spheres and 0.5 for disks. The equations of motion (4.9) are discretized and solved using central finite differences:

$$\frac{d^2}{dt^2}x_i^{\langle t\rangle} = \frac{1}{\Delta t}\left(\frac{d}{dt}x_i^{\langle t+0.5\Delta t\rangle} - \frac{d}{dt}x_i^{\langle t-0.5\Delta t\rangle}\right)$$
$$\frac{d}{dt}\omega_3^{\langle t\rangle} = \frac{1}{\Delta t}\left(\omega_3^{\langle t+0.5\Delta t\rangle} - \omega_3^{\langle t-0.5\Delta t\rangle}\right)$$
$$\frac{d}{dt}x_i^{\langle t+0.5\Delta t\rangle} = \frac{d}{dt}x_i^{\langle t-0.5\Delta t\rangle} + \left(\frac{F_i^{\langle t\rangle}}{m} + g_i\right)\cdot\Delta t \tag{4.10}$$
$$\omega_3^{\langle t+0.5\Delta t\rangle} = \omega_3^{\langle t-0.5\Delta t\rangle} + \frac{M_3^{\langle t\rangle}}{\beta\cdot m\cdot R^2}\cdot\Delta t$$
$$x_i^{\langle t+\Delta t\rangle} = x_i^{\langle t\rangle} + \left(\frac{d}{dt}x_i^{\langle t+0.5\Delta t\rangle}\right)\cdot\Delta t$$

where all terms are as previously defined.

The critical value of the time step (Δt) for a stable solution to a DEM problem depends on the minimum eigenperiod of the entire system. Calculating this value is computationally expensive, so PFC-2D uses a simplified spring and mass logic to calculate the time step and then applies a safety factor. A complete discussion of critical time step calculations is provided in Itasca (2003).

4.2.3. DEM Modeling of Biaxial Compression Tests

A significant advantage of using PFC-2D for simulation of particulate assemblies is the flexibility afforded by the built-in programming language FISH. FISH allows for the generation of complex models and for precise control of most simulation parameters. Essentially, PFC-2D provides the mathematical foundation (as discussed in the previous section) on which many types of models can be built. The model developed in the current study was for the simulation of biaxial compression tests and is discussed below.

Because of the difficulty of capturing an inherently nonlinear, inhomogeneous phenomenon (i.e., shearing of soil) in a computer simulation, many numerical steps must be included in the simulation that are not explicitly present in experimental work. However, these steps are implemented in an attempt to most closely mimic experimental work without undue numerical effects. A description of the steps implemented in the current model is as follows:

1. Particles are generated one at a time in a random location within a model space that is twice as large as the desired final specimen size. Prior to the generation of a given particle, the random centroid location is checked against the centroid location list of all previously generated particles to

ensure that a particle does not already exist in that exact location (while particles are allowed to overlap, if two particles were exactly on top of each other, the normal contact vector vanishes and there is no way to determine how the particles will interact). After each particle is generated, the following inequality is checked:

$$n_{desired} > 1 - \frac{\sum_{i} A_{p_i}}{A_{total}} \tag{4.11}$$

where $n_{desired}$ is the desired sample porosity, A_{pi} is the area of the i^{th} particle, and A_{total} is the desired total area of the specimen prior to shearing. As long as equation 4.11 remains true, a new particle is created. All particles are generated with zero shear stiffness and a zero friction coefficient to prevent locked-in shear stresses during consolidation.

2. Once all particles have been generated, four rigid walls are placed at the oversized specimen boundaries. The walls are initially stationary.
3. Because the particle overlaps that occur during sample generation can be quite high, resulting in very high normal forces, an energy dissipation algorithm is applied after all particles have been created. In this algorithm, velocities within the specimen are zeroed after every fifth time step through a series of several thousand steps. The oversized specimen is then allowed to cycle to equilibrium normally.
4. Once the specimen has equilibrated, the top and bottom walls (loading platens) are accelerated towards each other to reduce specimen size. The left and right walls remain stationary.

5. After the loading platens reach their final pre-consolidation locations, the energy dissipation algorithm discussed in step 3 is reapplied and the specimen is then re-equilibrated.
6. The specimen is consolidated to the desired consolidation stress using a numerical servo algorithm to control wall movement in both the x- and y-directions.
7. When the specimen has achieved the desired state of stress, the simulation is paused and the left and right walls are replaced with a flexible membrane comprised of particle chains (discussed in detail in Chapter 6). The specimen is then re-equilibrated to compensate for minor stress rearrangements that occur during this operation.
8. The state of stress is checked and, if necessary, readjusted to the desired consolidated state.
9. The loading platens are accelerated to a constant velocity to provide strain-controlled loading conditions. Confining stress is maintained through a numerical servo algorithm applied to the membranes.

Over the course of the simulation, time series of deviatoric stress, confining stress, axial strain, and volumetric strain are maintained for later analysis. At the consolidated state and at each one percent of global strain thereafter, the model state is preserved to allow for subsequent recreation of the microstructure.

4.2.4. Model Characteristics

A certain amount of scaling is required relative to laboratory testing when simulating particulate assemblies with the discrete element method. The two main reasons for this are purely practical and relate to the amount of time required to perform a simulation. The first reason relates to the order of the solution time for the system. Generally speaking, the time required to converge to a solution varies as the square of the number of particles in the system. Thus, doubling the number of particles in a simulation magnifies the solution time four-fold.

The second reason relates to the minimum stable time step for solution of the system and overall numerical stability of the solution. Using simplified spring and mass logic, the stable time step is inversely related to the maximum normal stiffness at any contact in the system. Force at a contact is directly proportional to the normal stiffness, as shown in Equation 4.4. If normal stiffnesses are very high, then time steps must be very small to prevent unreasonable displacements over a given timestep. Furthermore, there are no inherent units within PFC-2D. The only requirement with regards to units is that they be consistent, and this is the responsibility of the user. In order to achieve reasonable property values, it is advisable to either consistently use meters, kilograms, and seconds or centimeters, grams, and seconds. While it would be possible to use a unit system comprised of, say, centimeters, kilograms, and seconds, this may lead to unreasonable property values and is not advisable. Examples of typical parameter values in different unit systems are presented in Table 4.2. It should also be noted that numerical roundoff errors increase as the number of particles increase, so increased numbers of particles do not necessarily lead to "better" simulation results.

Table 4.2: Examples of typical model properties under different unit systems

Parameter	m-kg-s System	cm-g-s System	Mixed System
Particle Density	2650 kg/m^3	2.65 g/cm^3	0.00265 kg/cm^3
Particle Diameter	0.05 m	0.05 cm	0.05 cm
Specimen Width	6 m	6 cm	6 cm
Normal Stiffness	10^8 kg/s^2	10^{11} g/s^2	10^8 kg/s^2

Given the global constraints discussed above, the following general parameters were used for the simulations performed in this study (and discussed further in Chapter 6):

- specimen height: 12 m
- specimen width: 6 m
- mean ball diameter: 0.05 m

For the specimen and particle dimensions shown above, approximately 10,000 balls were required for a given simulation. However, it has been noted (Bardet, 1994; Oda and Iwashita, 2000) that discrete element method simulations on circular particles tend to overestimate the magnitude of particle rotations, leading to unrealistic material response. In the past, this has typically been addressed by bonding primal particles (i.e., disks or spheres) together to create more complex geometries (e.g., Powrie et al., 2005) or by artificially restraining particle rotations through an empirical modification to the underlying mathematics of the problem (Oda and Iwashita, 2000). In the present study, the inherent "clump logic" in PFC-2D is used to form complex-shape particles. Clump logic allows any number of primal particles to be joined together in clumps that are then treated as static bodies for the remainder of the simulation. The advantage of this method over a bonding method is that it is not necessary to consider the reactions between

particles in a clump, greatly speeding up processing time. The clumps used in the current study were comprised of two identically-sized balls overlapping by 50% (by diameter). Thus, the simulations discussed herein were nominally comprised of 5,000 clumps generated from 10,000 balls. Specimen width to particle size ratios for both numerical and experimental tests in this study are summarized in Table 4.3.

Table 4.3: Specimen-to-particle size ratios

Property	**Experimental**	**Numerical**
Specimen height	140 mm	12 m
Specimen width	40 mm	6 m
Mean particle size (long axis)	0.74 mm	0.075 m
Mean particle size (short axis)	n/a	0.05 m
Height-to-diameter ratio (long axis)	189	160
Height-to-diameter ratio (short axis)	n/a	240
Width-to-diameter ratio (long axis)	54	80
Width-to-diameter ratio (short axis)	n/a	120

5. EXPERIMENTAL PROGRAM

5.1. Introduction

The experimental portion of the current study was performed using a biaxial shear device based on the design described in Drescher, et al. (1990) and configured as described in Chapter 3. A total of twenty tests on Ottawa 20-30 sand and fifteen tests on ASTM graded sand were performed. A number of the tests were performed for device testing, calibration, and validation purposes while others were conducted to assess the global response behavior of the test soils subjected to various loading states. Many of the tests involved both shearing and subsequent glue impregnation to lock the microstructure as a precursor to resin impregnation and image analysis studies reported hereinafter. A number of the tests that were successfully sheared and glue impregnated failed during the specimen extraction phase (see Figure 3.15) prior to resin impregnation as this two-phase process was being developed for use with the biaxial device.

Two of the sheared specimens of Ottawa 20-30 sand were impregnated, solidified, sliced, and polished (as described in Sections 3.4 and 3.5) and two additional specimens were impregnated, solidified, sliced, and polished prior to shearing to allow for comparison of sheared and unsheared specimens. Test parameters for these four specimens are presented in Table 5.1. Note that hereinafter the specimens will be categorized as either “slightly dilatant” or “highly dilatant” and either “sheared” or “unsheared” for clarity.

Table 5.1: Test parameters for four impregnated specimens

Test ID	Initial Void Ratio	Confining Stress	State
BT-2030-13	0.60	20 psi	Slightly dilatant-sheared
BT-2030-16	0.56	10 psi	Highly dilatant -sheared
BT-2030-UN	0.57	10 psi	Highly dilatant -unsheared
BT-2030-U2	0.60	20 psi	Slightly dilatant -unsheared

5.2. Biaxial Compression Tests

5.2.1. Stress-Strain Response of Ottawa 20-30 Sand Specimens

The global stress-strain response of several specimens of Ottawa 20-30 sand are presented in this section. Table 5.2 lists test parameters for each of the specimens of interest.

Table 5.2: Test parameters for Ottawa 20-30 sand specimens

Test ID	Confining Stress [psi]	Initial Void Ratio	Initial Relative Density [%]	Impregnated? (Y/N)
BT-2030-03	20	0.55	80	N
BT-2030-04	20	0.57	74	N
BT-2030-05	20	0.56	76	N
BT-2030-07	10	0.65	39	N
BT-2030-09	20	0.60	60	N
BT-2030-10	20	0.59	64	N
BT-2030-11	20.5	0.59	63	N
BT-2030-12	20	0.60	59	N
BT-2030-13	20	0.60	61	Y
BT-2030-14	30	0.56	77	N
BT-2030-16	10	0.56	77	Y

Data from the tests were generally analyzed using the procedures proposed by Drescher, et al. (1990). A sample Mathcad worksheet used for reduction of the biaxial compression test data is presented as Appendix A.1. Normalized load, displacement, and

volume change are presented in Figures 5.1 and 5.2 (the normalized parameters are equivalent to axial stress, axial strain, and volumetric strain prior to the onset of localization – see below). For clarity, these data are delineated at a void ratio of 0.58, with looser specimens presented in Figure 5.1 and denser specimens presented in Figure 5.2. It should be noted that once localization occurs (near the peak stress) the constitutive relations shown do not necessarily apply because the specimen is no longer deforming homogenously. However, plots are presented for the entire test, consistent with prior convention (e.g., Han and Drescher, 1993). Note that after the onset of localization, the data curves are shown as dotted lines to indicate that the typical constitutive relations no longer apply. The volume change data for test BT-2030-11 presented in Figure 5.1 should be treated with skepticism because the shear band daylighted at the point where one of the LVDT's contacted the specimen, thus invalidating that measurement.

Because both void ratio and confining stress are being varied over the test program, it is also beneficial to consider the test results in terms of mean stress and shear stress. Mean and shear stresses are given by (Finno and Rechenmacher, 2003):

$$p = \frac{1}{3}\left(\sigma_1 + \sigma_2 + \sigma_3\right) \tag{5.1}$$

$$q = \frac{1}{\sqrt{2}} \cdot \left[\left(\sigma_1 - \sigma_2\right)^2 + \left(\sigma_1 - \sigma_3\right)^2 + \left(\sigma_2 - \sigma_3\right)^2 \right]^{\frac{1}{2}} \tag{5.2}$$

where p and q are mean and shear stresses, respectively, and σ_1, σ_2, and σ_3 are major, intermediate, and minor principal stresses, respectively. Note that because all specimens were tested in the dry state, total and effective stresses are equivalent.

In p-q space, it is also possible to plot failure lines corresponding to different global states within the specimen: peak, critical state, and residual. At critical state in triaxial compression, the slope of these lines, M, is a function of the critical state friction angle, ϕ_{cs}, and is given by:

$$M = \frac{6 \cdot \sin(\phi_{cs})}{3 - \sin(\phi_{cs})} \tag{5.3}$$

The above formulation for M neglects the effects of the intermediate effective stress (it is derived from a Mohr-Coulomb failure criteria) and thus, may not be directly applicable to plane strain tests. Furthermore, at states other than the critical state, stress-induced dilation (in the form of plastic strain increments) will affect the value of M (Mooney et al., 1998). Data plotted in p-q space with corresponding best-fit failure lines are presented in Figure 5.3.

In Figure 5.3, it may be seen that the M-values at critical state are very similar for all specimens (i.e., the critical state line provides a good fit to the end points of the stress paths). This is consistent with the idea that the effective stress ratio at critical state is "typically assumed to be a material constant for a given loading path" (Mooney et al., 1998). However, biaxial and triaxial critical state lines are not necessarily equal (as seen in Figure 5.3 The "peak" line does not necessarily provide a good fit to the data because peak strength will change as a function of initial void ratio (which varies across tests) but is provided as a reference line.

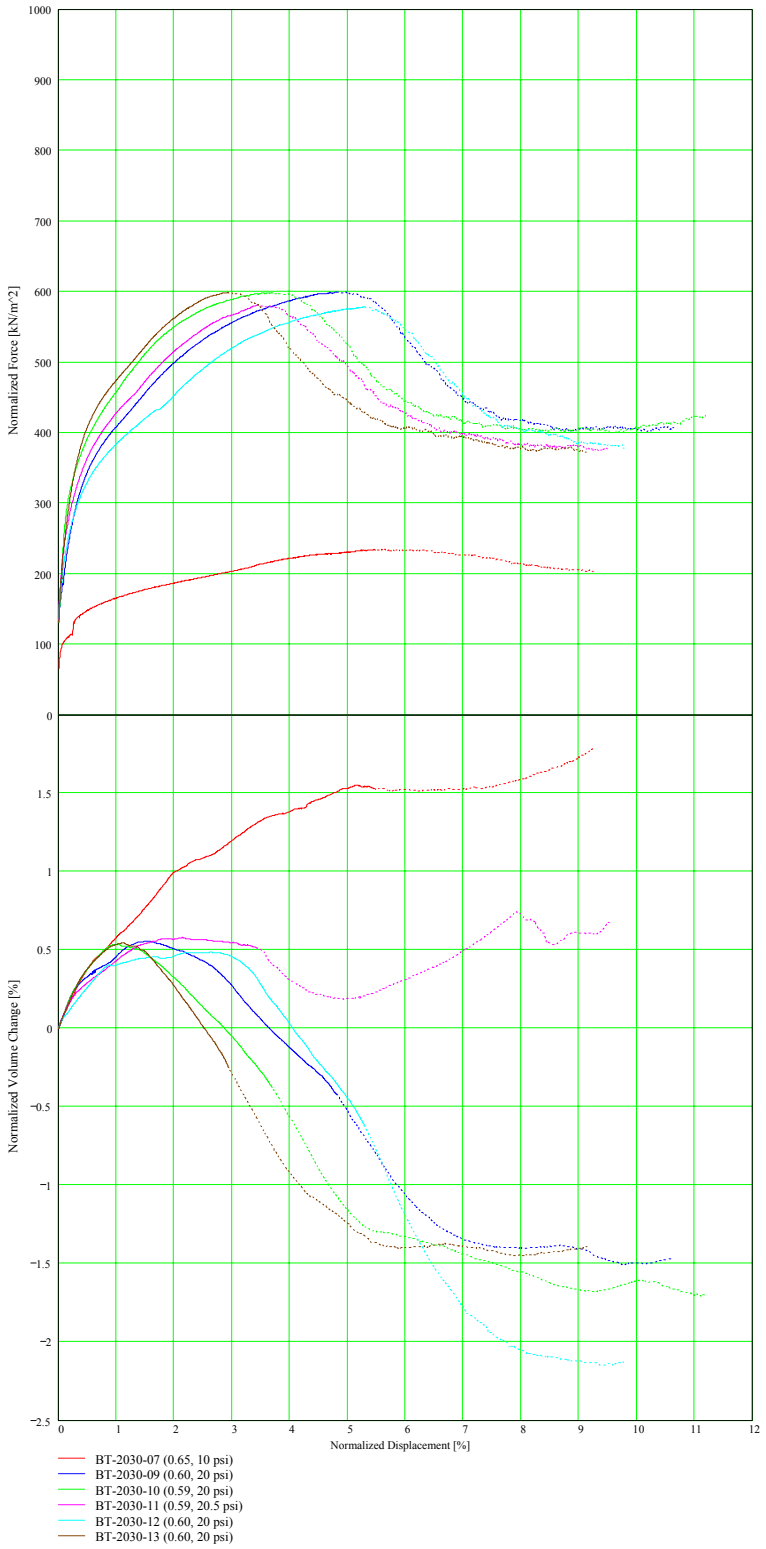

Figure 5.1: Stress-strain and volume change plots for specimens with $e_0 > 0.58$ (the numbers in parentheses in the legend indicate initial void ratio and confining stress)

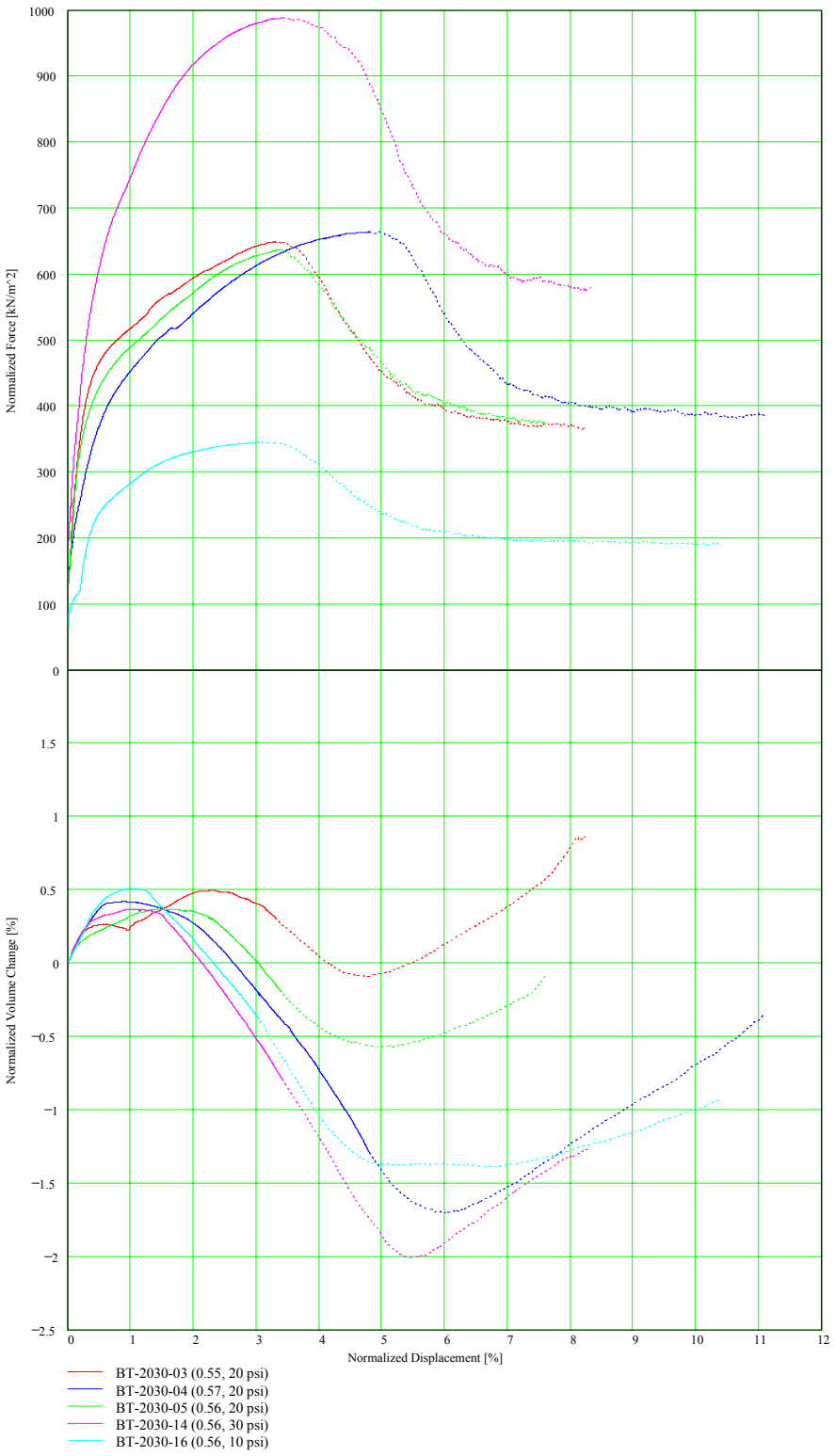

Figure 5.2: Stress-strain and volume change plots for specimens with $e_0 < 0.58$ (the numbers in parentheses in the legend indicate initial void ratio and confining stress)

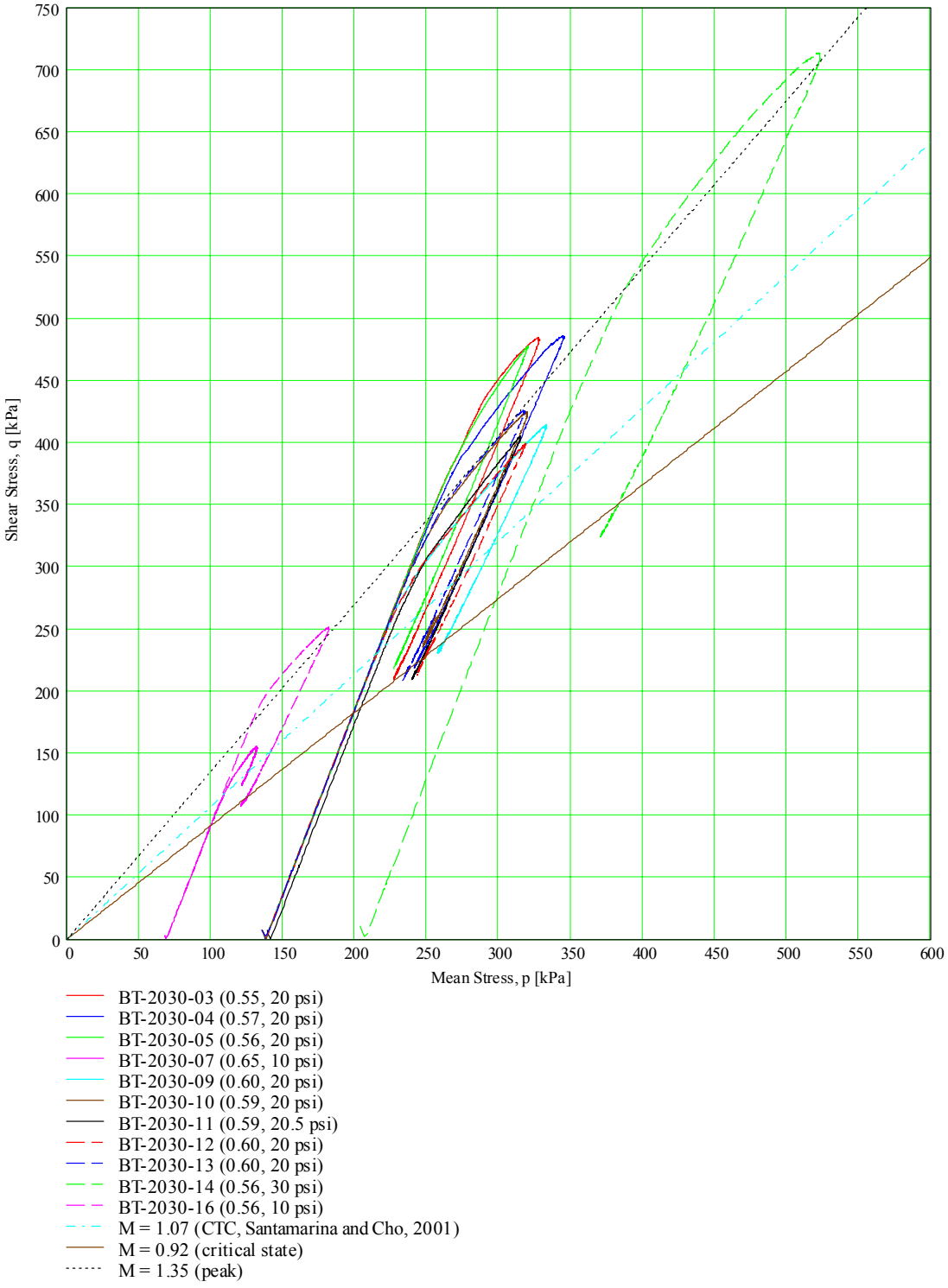

Figure 5.3: p-q plots for biaxial specimens (e_0, σ_3)

5.2.2. Detailed Analysis of Global Response in Impregnated Specimens

Section 5.2.1 presents global stress-strain-strength response for several of the Ottawa 20-30 sand specimens tested in this study. Because the biaxial shear device is highly internally instrumented, it is also possible to analyze other aspects of specimen behavior beyond the typical analyses presented previously. In this section, a more detailed analysis of specimen response for the two successfully impregnated specimens is presented.

Because the constitutive relationships (e.g., Mohr-Coulomb) that are typically applied to laboratory data assume that the specimen is deforming homogenously, it is necessary to be able to accurately identify the onset of localization within the specimen. In this manner, it is possible to delineate two distinct test phases: the constitutive phase and the localized phase. The four primary indicators of the transition from the constitutive phase to the localized phase are: peak stress, sled movement, specimen thickness, and visual observation. Plots of stress and specimen thickness as functions of global axial strain are presented in Figures 5.4 through 5.7. The vertical line in each plot is indicative of the onset of localization for that individual measure. In the stress-strain plots, this is the point of maximum major principal stress. The onset of localization in the specimen thickness plots is indicated by the marked change of slope in both measures of specimen thickness (i.e., both lines in the plot are essentially bilinear in the region of localization, with the onset of localization indicated by the transition from one portion of the bilinear line to the next). Note that in specimen thickness measurements there is some small divergence at very low strain levels. This is due to slight misalignment of the

specimen on the sled (Drescher et al., 1990) which causes minor sled translation during specimen "seating" prior to the onset of localization.

From Figures 5.4 through 5.7, it may be seen that the indications of localization are similar from both stress-strain and specimen thickness plots. An additional indicator (possibly the most reliable) is sled movement. If the specimen is perfectly aligned on the platen and the platen is perfectly aligned on the sled and if the specimen deforms completely homogenously, then no sled movement should be observed prior to the onset of localization. It is very difficult (if not impossible) to meet these requirements, but sled movement is nonetheless a strong indicator of localization because sled movement increases drastically once the shear band forms. Previously, most researchers (e.g., Drescher et al., 1990; Finno et al., 1996) have relied on plots of total sled movement to identify the onset of localization. However, as can be seen below, incremental sled movement provides for identification of the onset of localization with much greater accuracy. Figures 5.8 through 5.11 provide plots to total and incremental sled movement.

The onset of localization is much more apparent from the plots of sled movement than from the other two indicators shown above. In the slightly dilatant specimen, the onset of localization as indicated by sled movement is between the values indicated by peak stress and specimen thickness, pointing to the fact that localization occurs very near peak stress, prior to strain softening. For the highly dilatant specimen, however, sled movement begins well after the peak stress is achieved, indicating that localization occurs in the strain softening regime. The final measure of localization is visual observation of the boundary of the specimen. Shear banding was first visually observed at 3.5% global axial strain in the slightly dilatant specimen and at 3.4% global axial strain in the highly

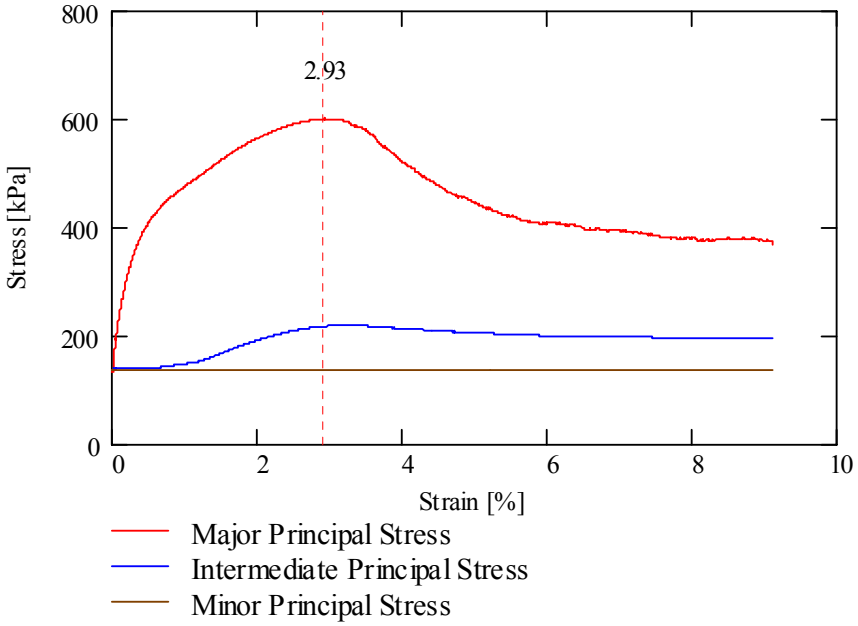

Figure 5.4: Stress-strain plot for slightly dilatant specimen

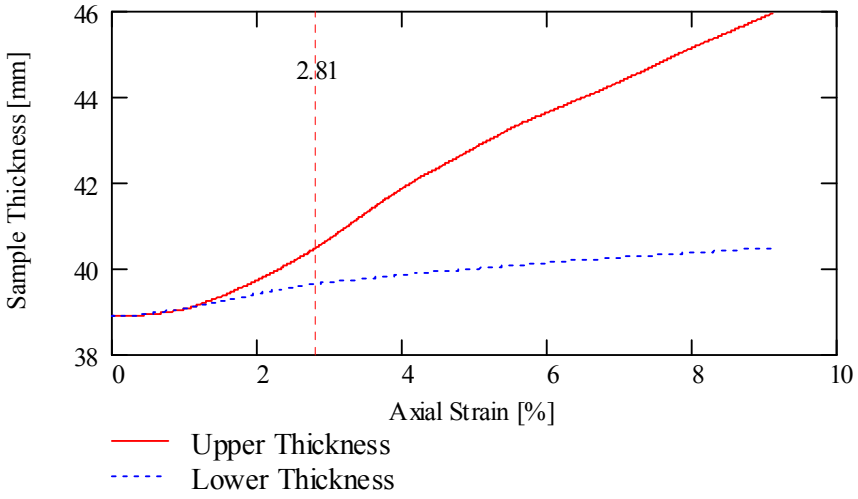

Figure 5.5: Specimen thickness plot for slightly dilatant specimen

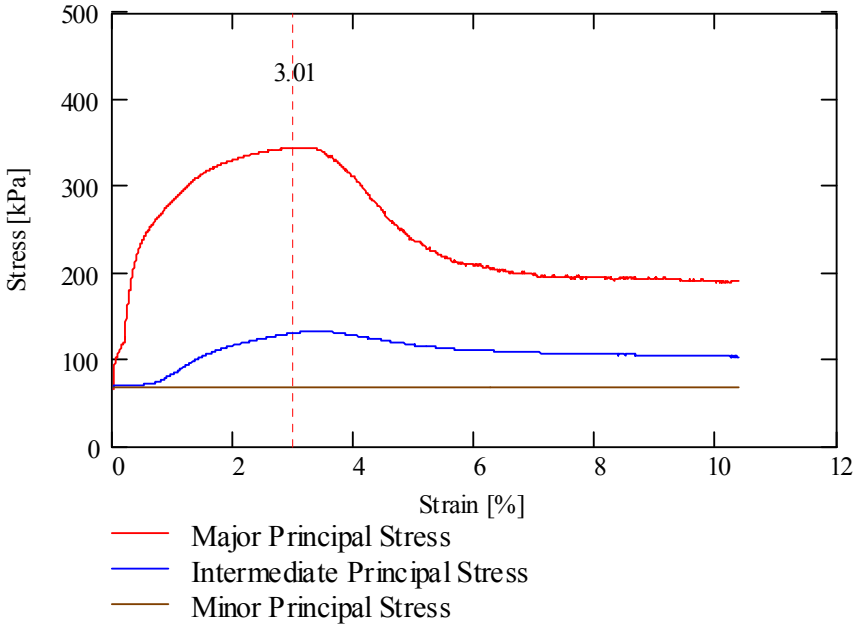

Figure 5.6: Stress-strain plot for highly dilatant specimen

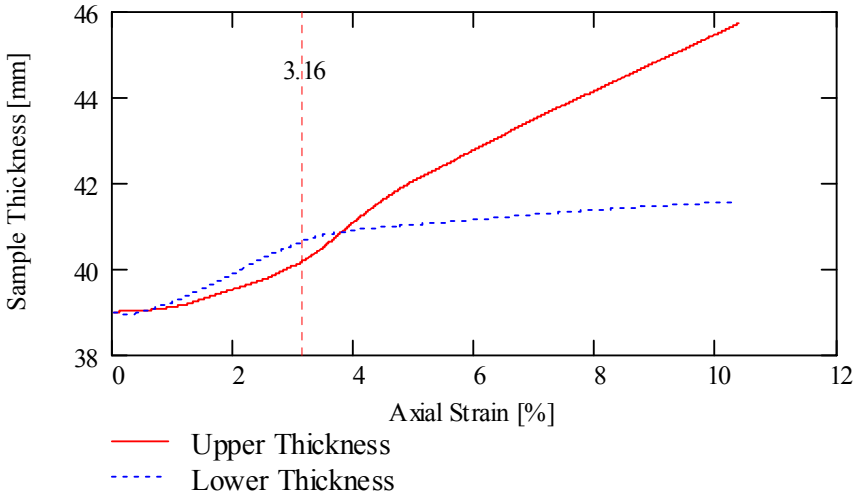

Figure 5.7: Specimen thickness plot for highly dilatant specimen

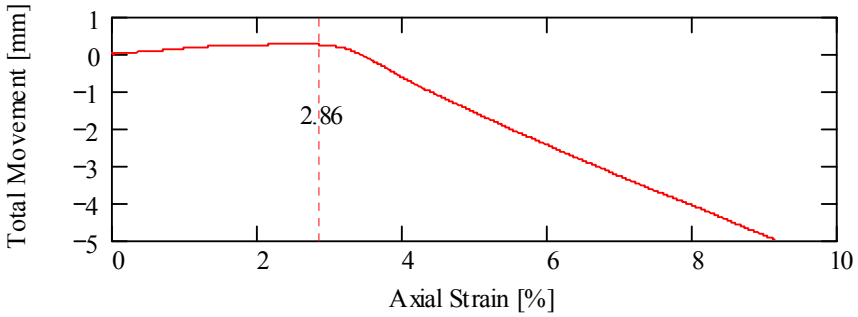

Figure 5.8: Total sled movement for slightly dilatant specimen

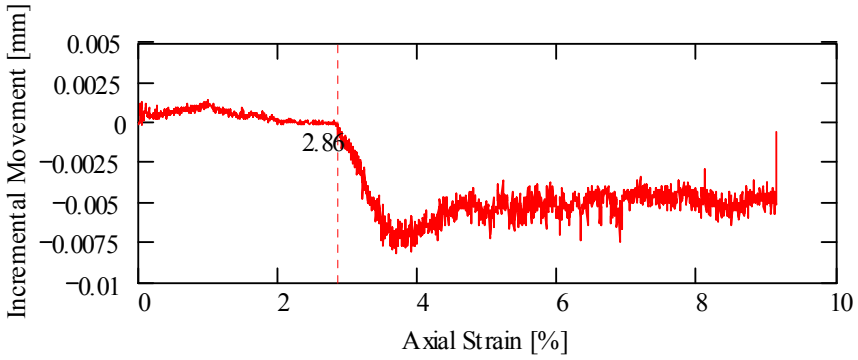

Figure 5.9: Incremental sled movement for slightly dilatant specimen

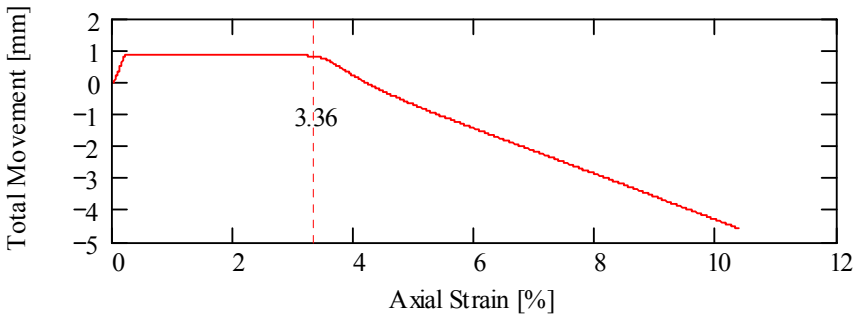

Figure 5.10: Total sled movement for highly dilatant specimen

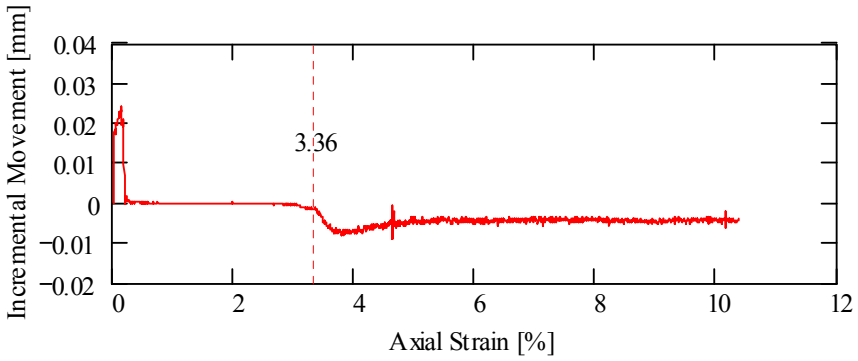

Figure 5.11: Incremental sled movement for highly dilatant specimen

dilatant specimen. Thus, localization occurs prior to visual observation of the shear band and the lag between localization and observation is greater in the slightly dilatant specimen than in highly dilatant specimen.

Additional calculations may be performed to assess dilation angle, mobilized friction, and stresses on the shear plane, but knowledge of shear band inclination is required. Shear band inclination is measured on images taken during shearing and was found to be essentially constant (i.e., within the accuracy of the qualitative measurement). Shear band inclinations at the end of shearing are presented in Figures 5.12 and 5.13.

Once the angle of inclination of the shear band is known, the dilation angle within the shear band may be calculated as (Drescher et al., 1990):

$$\psi_s = \theta_e - \text{atan}\left(\frac{\Delta u_a}{\Delta u_h}\right) \tag{5.4}$$

where ψ_s is the angle of dilation in the shear band, θ_e is the experimentally measured inclination of the shear band, Δu_a is incremental axial displacement, and Δu_h is incremental sled displacement. High frequency calculations (i.e., every time step) of the

angle of dilation are quite noisy (Figure 5.14) because of the resolution of the LVDT's and the fact that measurements are not taken simultaneously but sequentially. Therefore, a moving average kernel is convolved onto the calculated dilation angle series to yield a more stable result. Mathematically, this convolution may be expressed as:

$$\Delta u_{av_y} = \sum_{q=0}^{Q-1} \kappa_q \cdot \Delta u_{y+q} \tag{5.5}$$

where Δu_{av} is the averaged incremental displacement, Q is the length of the moving average kernel, κ_q is the q^{th} element of the moving average kernel (all values are equal and sum to one), Δu is the original incremental displacement, and y is the counting index

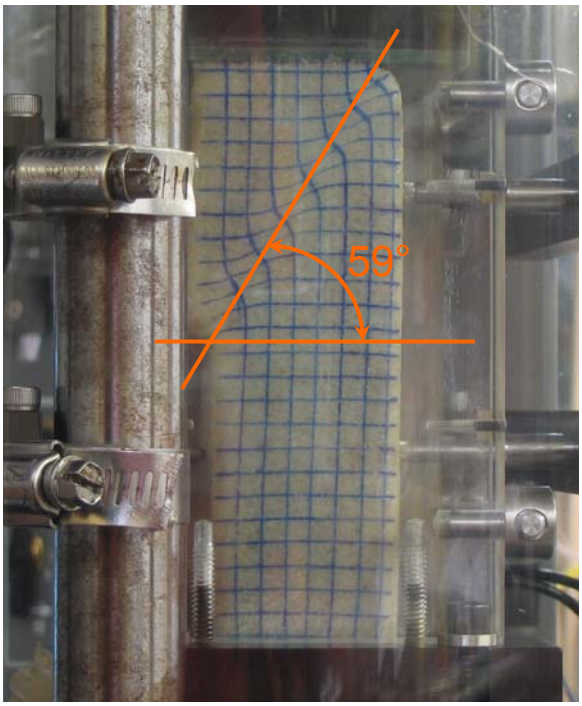

Figure 5.12: Shear band inclination for slightly dilatant specimen

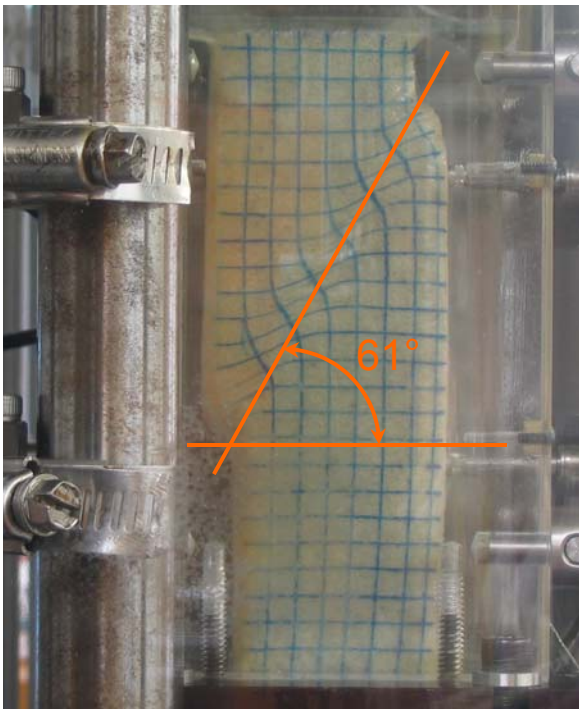

Figure 5.13: Shear band inclination for highly dilatant specimen

for the measured incremental displacements (see Appendix A.1 for a complete description of the calculations). Figure 5.14 shows calculated dilation angles both before and after averaging. Figures 5.15 and 5.16 show the averaged displacement angles for slightly dilatant and highly dilatant specimens, respectively. The plots indicate that the shear band in the highly dilatant specimen is initially more dilatant than that in the slightly dilatant specimen, but that the dilation angle eventually settles to a value near zero for both specimens.

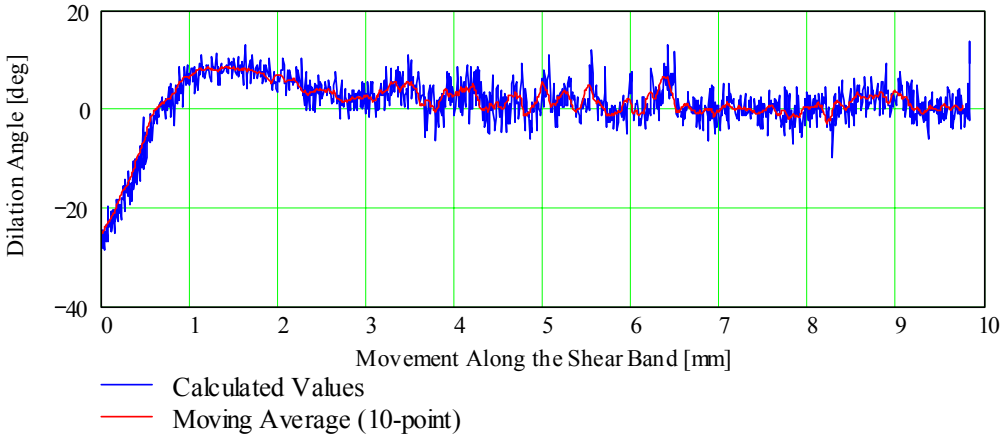

Figure 5.14: Calculated and averaged dilation angles

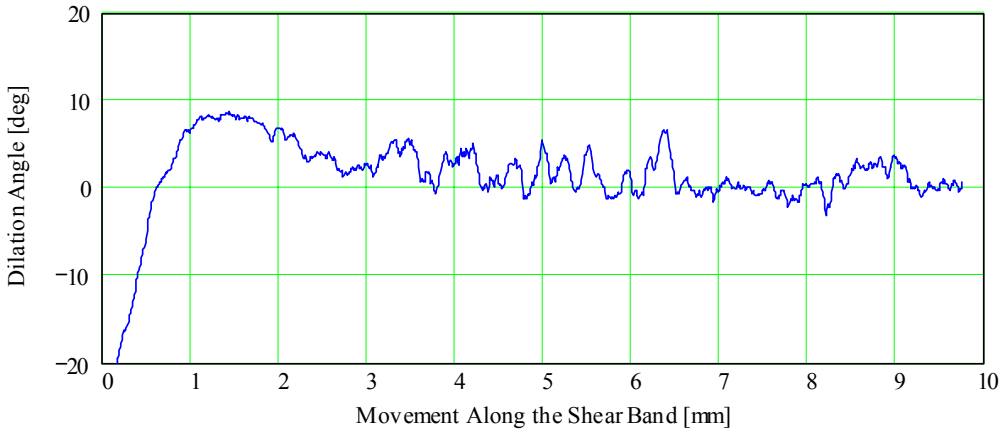

Figure 5.15: Averaged dilation angle for slightly dilatant specimen

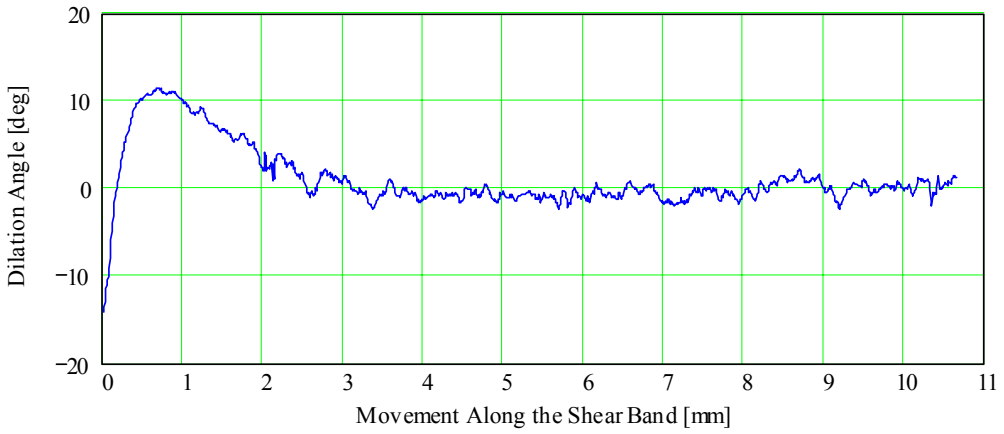

Figure 5.16: Averaged dilation angle for highly dilatant specimen

It is also possible to calculate the mobilized (global) friction angle, the normal and shear stresses on the failure plane, and the friction angle on the failure plane from the measured data. The mobilized friction angle for the specimen is calculated using the major and minor principal stresses as follows:

$$\sin\left(\phi_m\right) = \frac{\sigma_1 - \sigma_3}{\sigma_1 + \sigma_3} \tag{5.6}$$

where ϕ_m is the mobilized angle of internal friction. The normal and shear stresses on the failure plane are then calculated as:

$$\sigma_n = \sigma_1 \cdot \cos\left(\theta_e\right)^2 + \sigma_3 \cdot \sin\left(\theta_e\right)^2 \tag{5.7}$$

$$\sigma_s = \left(\sigma_1 - \sigma_3\right) \cdot \cos\left(\theta_e\right) \cdot \sin\left(\theta_e\right) \tag{5.8}$$

where σ_n and σ_s are the normal and shear stresses, respectively. Finally, the friction angle on the shear plane is calculated by assuming that the system may be approximated by rigid block sliding:

$$\tan\left(\phi_s\right) = \frac{\sigma_s}{\sigma_n} \tag{5.9}$$

where ϕ_s is the friction angle on the failure plane. Friction angles are plotted in Figures 5.17 and 5.18 and normal and shear stresses in Figures 5.19 and 5.20. It is evident that the two values for friction angle converge to the same value shortly after peak, indicating that friction along the shear plane is the sole resistance to shear after localization.

Theoretical inclinations for a shear bands have been predicted by Coulomb (1773), Roscoe (1970), and Arthur, et al. (1977), as discussed in Chapter 2. Given the results plotted in Figures 5.17 and 5.18, which indicate that, after localization, the

measured global mobilized friction angle is very close to the calculated friction angle on the failure plane, it is possible to consider an additional derivation of shear band inclination. Assuming that the two friction angles are equal ($\phi_m = \phi_s$), Equations 5.6 through 5.9 may be combined as follows:

$$\tan\left(\operatorname{asin}\left(\frac{\sigma_1 - \sigma_3}{\sigma_1 + \sigma_3}\right)\right) = \frac{\left(\sigma_1 - \sigma_3\right)\cdot\cos\left(\theta_e\right)\cdot\sin\left(\theta_e\right)}{\sigma_1\cdot\cos\left(\theta_e\right)^2 + \sigma_3\cdot\sin\left(\theta_e\right)^2} \tag{5.10}$$

Using trigonometric identities, Equation 5.10 simplifies to:

$$\frac{1}{2}\cdot\left(\sigma_1\cdot\sigma_3\right)^{-\frac{1}{2}} = \frac{\sin\left(\theta_e\right)\cdot\cos\left(\theta_e\right)}{\sigma_1\cdot\cos\left(\theta_e\right)^2 + \sigma_3\cdot\sin\left(\theta_e\right)^2} \tag{5.11}$$

Which can be solved for θ_e:

$$\theta_e = \operatorname{atan}\left(\sqrt{\frac{\sigma_1}{\sigma_3}}\right) \tag{5.12}$$

Equation 5.12 indicates that the shear band inclination angle may be determined without explicit knowledge of the mobilized friction angle. However, noting that σ_1/σ_3 is a function of the mobilized angle of internal friction and using further trigonometric identities, it may be shown that Equation 5.12 is exactly equal to the Coulomb prediction for shear band inclination. Thus, the Coulomb prediction implicitly requires that the mobilized angle of internal friction is equal to the sliding friction on the failure plane. Theoretical predictions and measured values for the two tests discussed in this chapter are summarized in Table 5.3. The symbols are as previously defined.

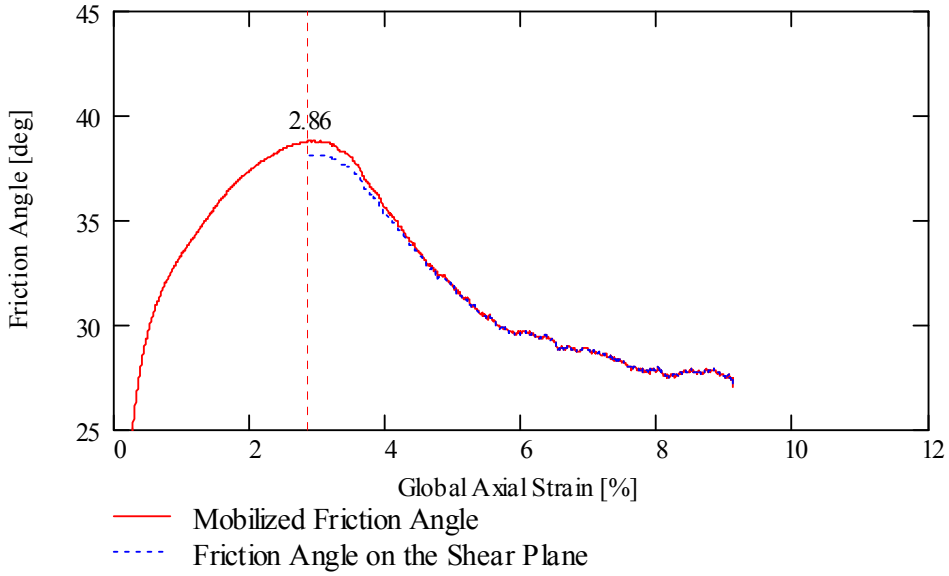

Figure 5.17: Friction angles for slightly dilatant specimen

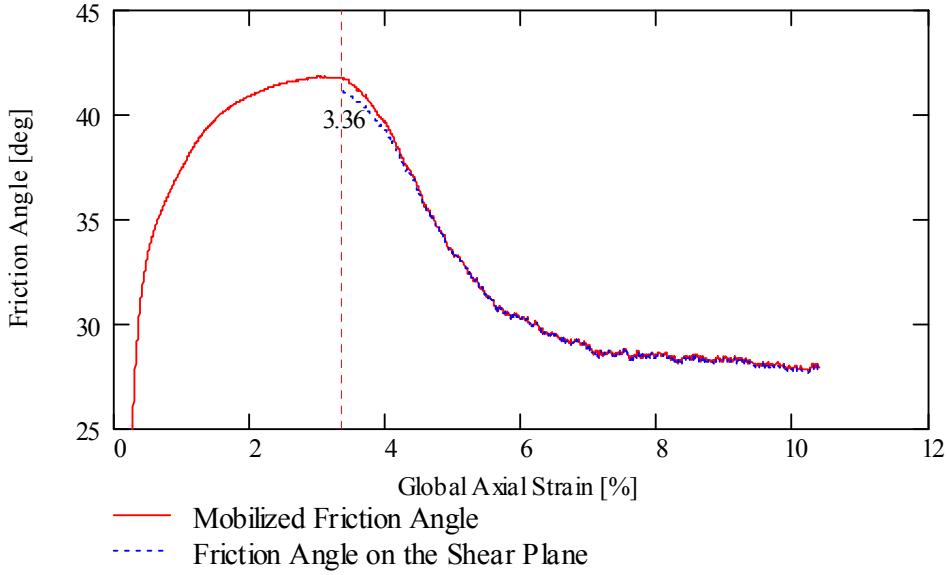

Figure 5.18: Friction angles for highly dilatant specimen

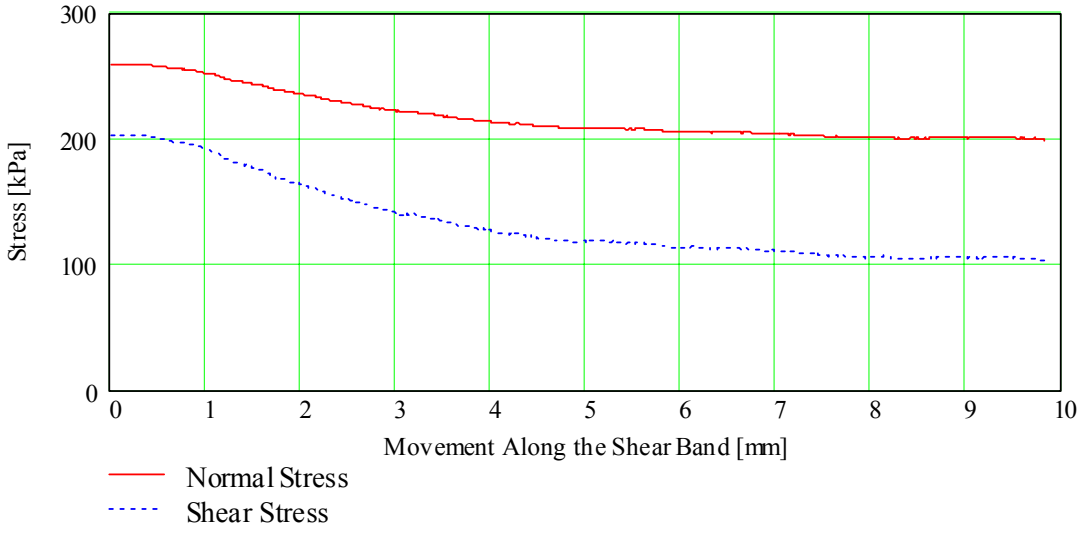

Figure 5.19: Normal and shear stresses on the failure plane for slightly dilatant specimen

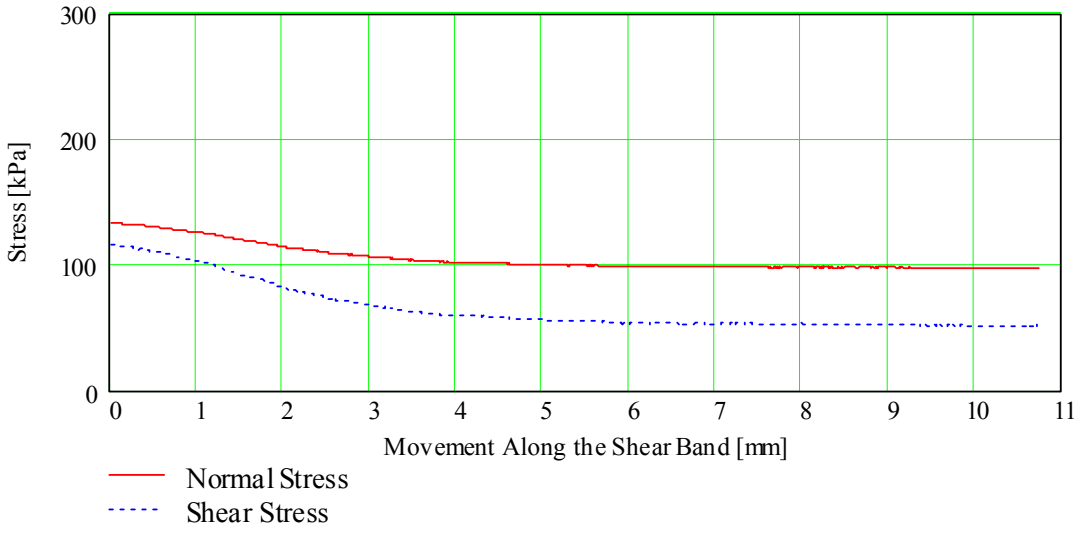

Figure 5.20: Normal and shear stresses on the failure plane for highly dilatant specimen

Table 5.3: Summary of friction, dilation, and shear band inclination angles

Test Designation	ϕ_p	ψ_p	ϕ_{cs}	ϕ_s	ψ_{cs}	θ_e	θ_C	θ_R	θ_A
Slightly dilatant	38.8°	8.8°	27.7°	27.7°	1.0°	59°	64°	49°	57°
Highly dilatant	41.8°	11.5°	27.9°	27.9°	0.2°	61°	66°	51°	58°

Examination of Table 5.3 shows that the measured shear band inclination is most closely approximated by the Arthur, et al. (1977) prediction (which is also the approximate solution to the bifurcation problem (Vardoulakis, 1980)). This is consistent with the findings of other researchers (e.g., Arthur et al., 1977; Drescher et al., 1990; Han and Drescher, 1993) who have tested sands in plane strain compression. The measured values are also relatively close to the Coulomb approximations, which is not surprising given the similarity between the global mobilized friction angle and the shear stress across the failure plane.

5.3. Membrane Deformation Analyses

5.3.1. Introduction

As discussed in Chapter 2, the effects of the confining membrane on specimen deformation and stress measurements during laboratory testing can be significant. However, the majority of previous work (e.g., Henkel and Gilbert, 1952; La Rochelle, 1967) has focused on conventional triaxial compression tests. The relatively small body of knowledge (e.g., Duncan and Seed, 1967) for plane strain tests focuses on corrections to measured lateral and axial strain and does not consider shear banding. Vermeer (1990) has shown that the confining membrane can have significant effects on shear band

formation and behavior, particularly as particle size becomes large and out-of-balance forces at the membrane edges increase. A new method for studying membrane deformation effects in plane strain specimens is presented in this section and the corrections are applied to the biaxial compression test data presented in Section 5.2.2.

5.3.2. Collection of Membrane Deformation Data

As discussed in Section 3.3, a grid with nominal point spacings of four to five millimeters was drawn on the side of each membrane prior to testing. In fourteen of the biaxial tests, photographs of the membrane were taken at one to two minute intervals over the course of a test (Figure 3.11). The times that the photographs were taken were referenced to the beginning of the test and recorded to the nearest second. For six of the specimens, these pictures were then imported into AutoCAD and scaled by the known diameter of the cylindrical supporting column in the biaxial device. The x- and y-coordinates of each grid point were identified by zooming in on the image and the collected grid points for each image were then exported as a text file.

Using the exported data, relative displacements of grid points were calculated as a function of global axial strain. Considering these displacements as elevations above a plane defined by the x- and y-coordinates of the grid points, displacement surfaces were calculated to qualitatively assess grid point movement inside and outside of the shear band. From these data it was determined that after the onset of localization very little displacement occurs outside of the shear band. This finding was used as the basis for the calculations presented in Section 5.3.3. Plots showing typical membrane displacement

contours from a typical biaxial test are shown in Figure 5.21. Localization occurred in this particular test at an axial strain of approximately 5%, as evident from the contours.

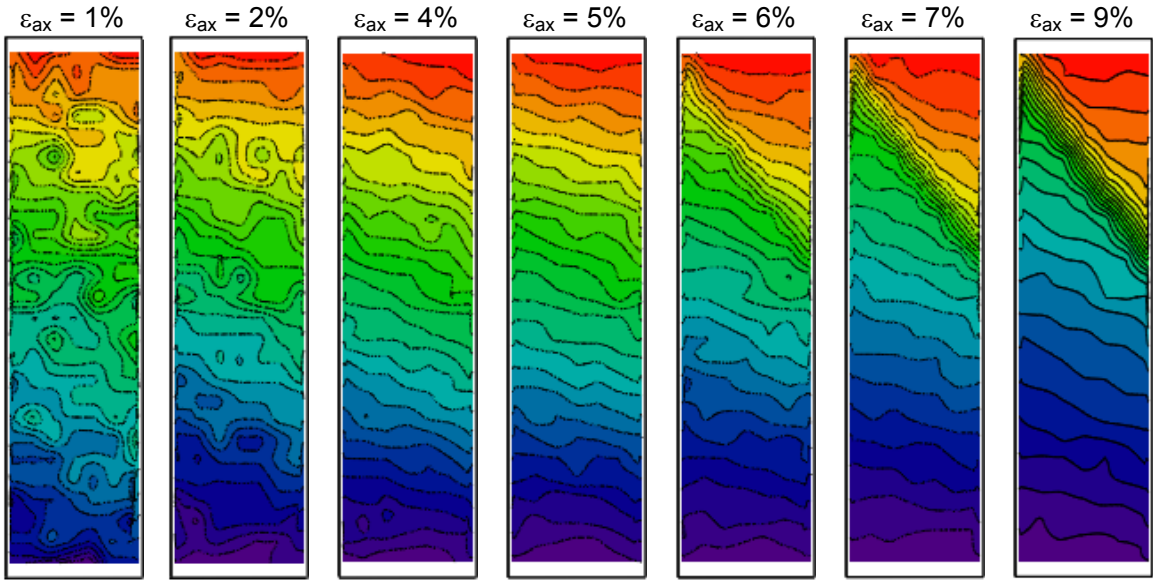

Figure 5.21: Membrane deformation contours for a biaxial specimen

5.3.3. Analysis of Membrane Deformation Data

Because grid points on the membrane outside of the shear band are essentially stationary after the onset of localization, it is possible to calculate local strains in the membrane across the shear band. First, stationary grid point locations from just prior to the observation of localization were plotted on the same set of axes as grid point locations at the end of testing. This allowed for selection of control grid points immediately above, but outside of, the shear band. A set of moving grid points was then selected such that, to the greatest extent possible, a line drawn between a moving grid point and its control grid point was normal to the orientation of the shear band. It was not possible to select points

that created lines absolutely orthogonal to the shear band due to the coarse discretization of the grid. The grid point locations for the highly dilatant specimen are presented in Figure 5.22.

Once the necessary grid points were identified, the relative displacements between control points and corresponding moving grid points were calculated as a function of global axial strain (detailed examples of all calculations in this section are presented in Appendix A.2). Displacements were then used to calculate strain tensors as follows:

$$\varepsilon_k = \begin{bmatrix} \dfrac{\Delta x_k}{X_0} & \dfrac{1}{2}\left(\dfrac{\Delta x_k}{Y_0} + \dfrac{\Delta y_k}{X_0}\right) \\ \dfrac{1}{2}\left(\dfrac{\Delta x_k}{Y_0} + \dfrac{\Delta y_k}{X_0}\right) & \dfrac{\Delta y_k}{Y_0} \end{bmatrix} \tag{5.13}$$

where ε_k is the local strain tensor at the k^{th} global axial strain level, Δx_k and Δy_k are x- and y-displacements at the k^{th} global axial strain level, and X_0 and Y_0 are the initial x- and y-separations between control and moving grid points. Assuming plane stress and using known elastic constants for the membrane, the stress tensor was calculated:

$$\begin{pmatrix} \sigma_x \\ \sigma_y \\ \sigma_{xy} \end{pmatrix} = \frac{E}{1-\nu^2} \cdot \begin{pmatrix} 1 & \nu & 0 \\ \nu & 1 & 0 \\ 0 & 0 & \dfrac{1-\nu}{2} \end{pmatrix} \cdot \begin{pmatrix} \varepsilon_x \\ \varepsilon_y \\ 2\varepsilon_{xy} \end{pmatrix} \tag{5.14}$$

where σ_x, σ_y, and σ_{xy} are x-, y-, and shear stresses, E is the Young's modulus for the membrane (1300 kPa), ν is the Poisson's ratio (0.5) and ε_x, ε_y, and ε_{xy} are x-, y-, and shear strains within the membrane. The local shear strains were then converted to tractions, which were then used to calculate normal and shear stress in the membrane, referenced to the orientation of the shear band:

$$\sigma_{ns} = T \cdot s \tag{5.15}$$

where T is the traction vector, s is a unit vector parallel to the shear band (i.e., orthogonal to the unit normal) and referenced to the upper interface of the shear band, and σ_{ns} is the shear stress in the membrane along the shear band. Using the known cross-sectional area of the membrane and the sand specimen at a given global axial strain, the shear stress imposed on the specimen by the membrane was calculated.

It was also possible to convert the La Rochelle (1967) membrane correction for conventional triaxial specimens to predict membrane effects in plane strain specimens. The original La Rochelle correction was given as equation 2.16:

$$\Delta\left(\sigma_1 - \sigma_3\right) = \frac{p}{a_c} \cdot \sqrt{\frac{k \cdot f \cdot h \cdot \delta}{\cos(\alpha) \cdot \sin(\alpha)^2}} \tag{2.16}$$

where $\Delta(\sigma_1-\sigma_3)$ is the deviator stress carried by the membrane, p is the perimeter of the specimen, a_c is the corrected cross-sectional area of the specimen, f is the friction coefficient between the soil and the membrane, δ is the strain due to shearing along the plane, k is the modulus of elongation of the membrane, h is specimen height, and α is the inclination of the shear plane. The perimeter and corrected cross-sectional area from the plane strain specimens was used and substitution for the membrane stiffness and friction were made, yielding:

$$q_{corr} = \frac{P}{A} \cdot \sqrt{\frac{E \cdot t_m \cdot \sigma_3 \cdot \tan(\phi) \cdot h_s \cdot \delta}{\cos(\theta) \cdot \sin(\theta)^2}} \tag{5.16}$$

where t_m is the membrane thickness, q_{corr} is the deviator stress correction, and the more conventional θ has been used for the inclination of the shear band.

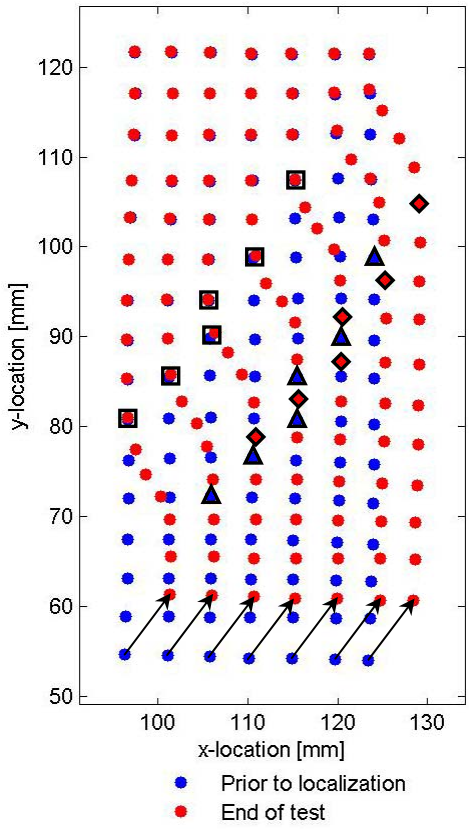

Figure 5.22: Membrane grid point locations before localization and at the end of the highly dilatant test. Squares (□) indicate control points, triangles (△) indicate moving points before localization, and diamonds (◇) indicate moving points after localization.

The deviator stress correction can be converted to a correction in the direction of the shear plane as follows:

$$\sigma_s = q_{corr} \cdot \cos(\theta) \cdot \sin(\theta) \tag{5.17}$$

Finally, a rigid block model was developed to allow for theoretical comparison with measured values. The rigid block model makes the following assumptions:

- the membrane does not slip against the soil specimen;

- the gauge length for calculating strains across the shear band is equal to the average gauge length for the experimental measurements; and
- the strains are calculated along a line that is orthogonal to the shear band inclination.

The rigid block model was developed by considering the geometry shown in Figure 5.23. By considering two points, A and B, prior to the onset of localization and two points, A and B′, after the onset of localization (note that B and B′ are actually the same point, but offset by a distance δ due to movement along the shear band) it was possible to calculate the local strains in the membrane as a function of global axial strain using the procedures outlined above. These calculations are presented in detail in Appendix A.2 and results are presented in Figures 5.24 and 5.25.

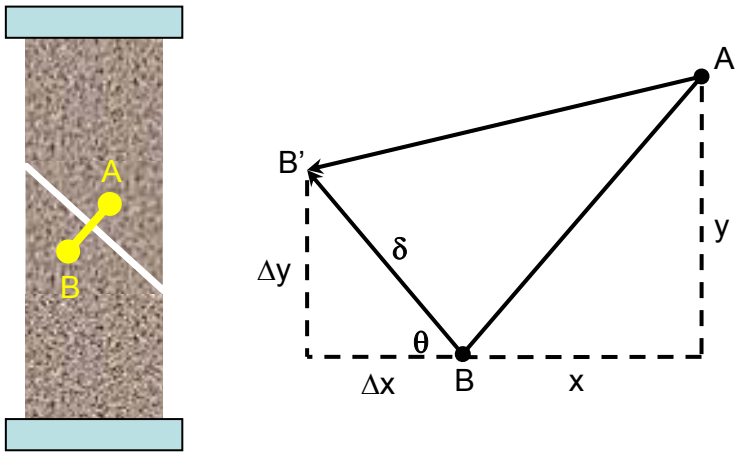

Figure 5.23: Geometry used for the rigid block model

The differences between the proposed correction and that of La Rochelle arise primarily from the fact that La Rochelle makes some simplifying assumptions regarding

linear deformation of the membrane whereas the proposed correction employs the two-by-two strain tensor. Because the measured correction agrees closely with the rigid block model, it was possible to use the rigid block model to correct the measured shear stress on the failure plane, as discussed in the next section.

Using the procedure outlined above, it is also possible to calculate a correction for the normal force component on the shear band due to the membrane. In this case however, the rigid block model does not adequately describe the measured membrane effects. This is due to the fact that the rigid block model assumes that relative movement between the two blocks occurs parallel to the shear plane. In reality however, the dilation angle in the shear band for both specimens is positive, so the true movement involves sliding along a plane that is slightly flatter than the shear band. This results in two rigid blocks that are not only sliding against each other but also separating. When the dilation

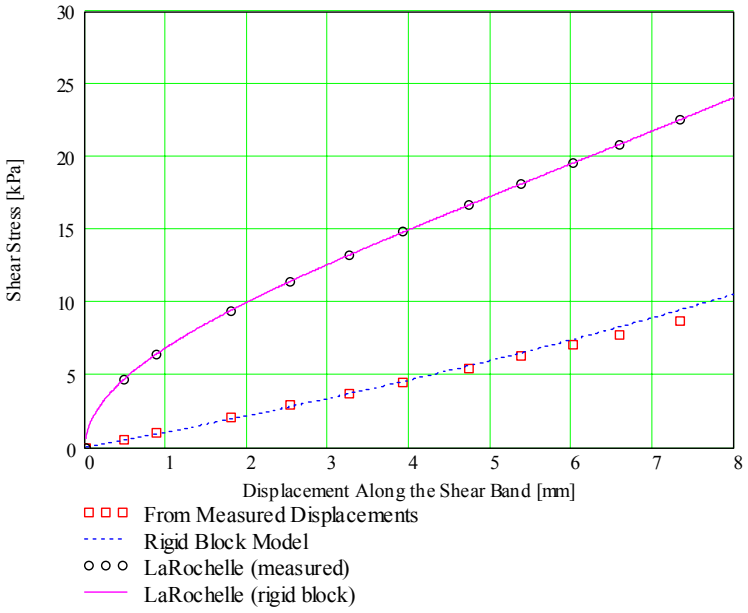

Figure 5.24: Membrane correction for slightly dilatant specimen

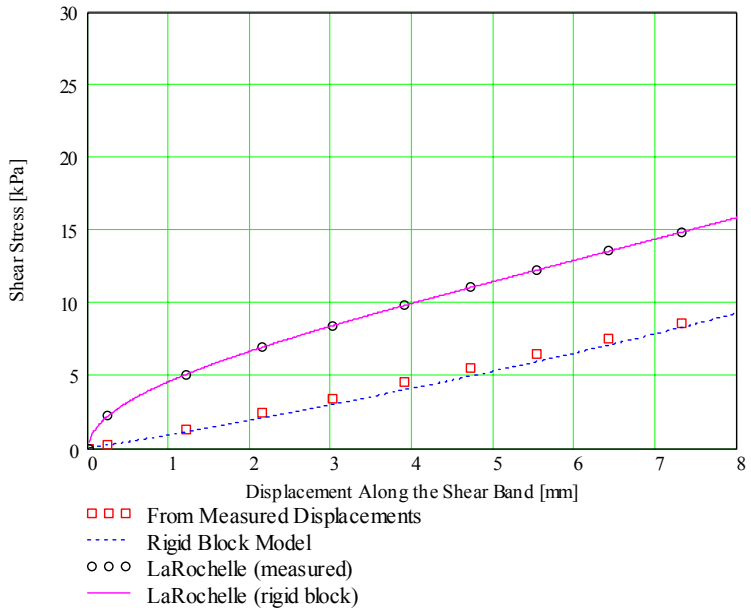

Figure 5.25: Membrane correction for highly dilatant specimen

angle is neglected, the rigid block model produces a correction that indicates negative (i.e., compressive) stresses in the membrane normal to the shear band. Normal stresses calculated from measured data, however, produce small positive values. These results are presented in Figures 5.26 and 5.27.

5.3.4. Correction of In-Plane Shear Stress after Localization

The rigid block approximation was used to correct the measured shear stress in the plane of localization. The imposed shear stress calculated by the rigid block model (as a function of movement along the shear band) was subtracted from the calculated shear stress on the plane. The results are presented in Figures 5.28 and 5.29. At very high strain levels, the membrane begins to slip adjacent to the specimen in the measured

membrane data. To account for this, the correction is assumed to be a constant above the final measured value. The normal stress on the shear plane was also corrected, but the rigid block model could not be used, as described in Section 5.3.3. Based on the results presented in Figures 5.26 and 5.27, it was determined that the overall normal stress

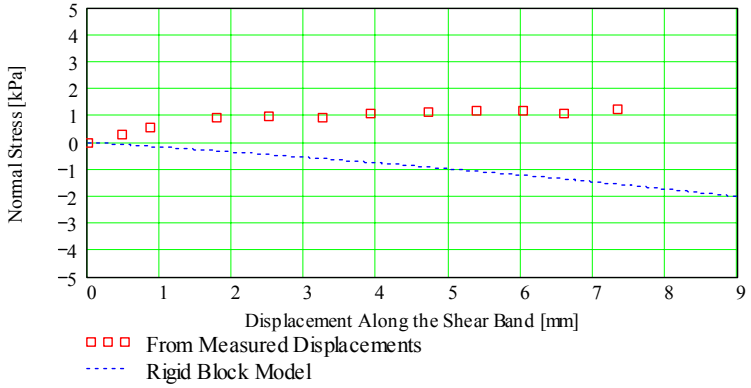

Figure 5.26: Membrane normal stress correction for slightly dilatant specimen

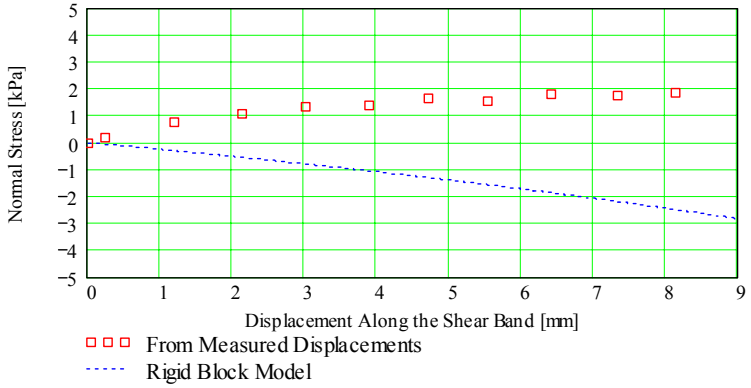

Figure 5.27: Membrane normal stress correction for highly dilatant specimen

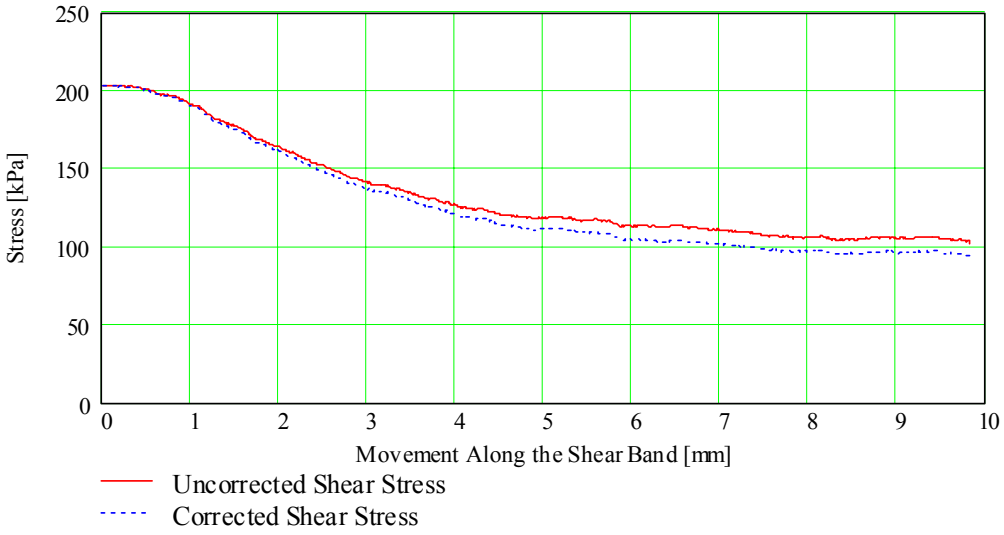

Figure 5.28: Corrected shear stress on the failure plane for slightly dilatant specimen

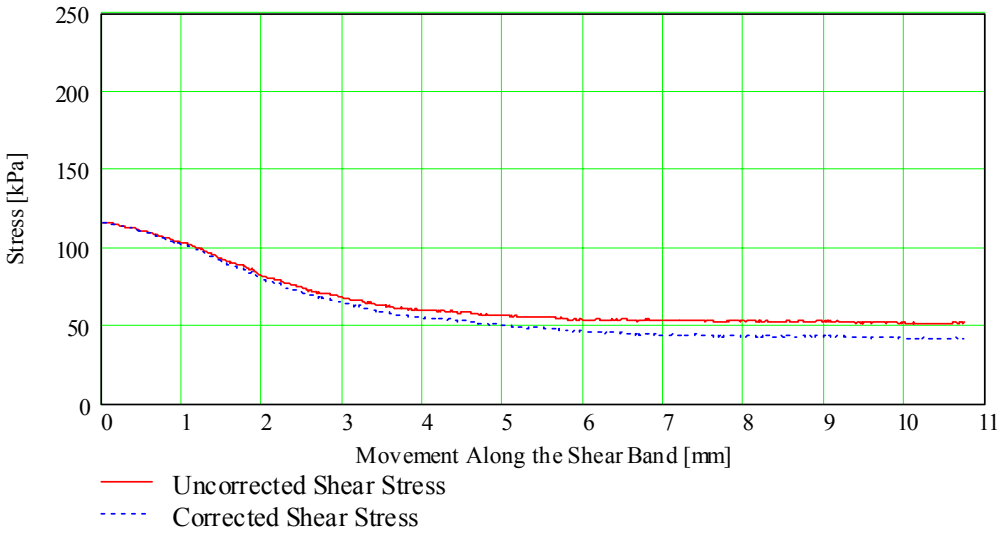

Figure 5.29: Corrected shear stress on the failure plane for highly dilatant specimen

correction should be on the order of 1 kPa for the entire length of displacement along the shear band. This amounts to an average correction of approximately 0.5% in the slightly dilatant specimen and approximately 1% in the highly dilatant specimen.

It is apparent from Figures 5.28 and 5.29 that membrane effects on the shearing stress are significant. At large displacements, this correction amounts to approximately 9% of the total shear stress in the slightly dilatant specimen and approximately 18% of the total shear stress in the highly dilatant specimen. When this effect is considered (in conjunction with the small correction to normal stress), the friction angle on the failure plane becomes 25.7° in the slightly dilatant specimen and 23.6° in the highly dilatant specimen. These values can be considered to be pseudo-residual friction angles and they depend on the confining stress applied. This is because the membrane correction is seen to be largely independent of the confining stress (i.e., the absolute correction for both tests is similar), so the correction as a percentage of the total shear stress along the plane increases with decreasing deviator stress.

5.3.5. Analysis of Membrane Data for a Kaolinite Specimen

This section presents an example of the application of the membrane correction outlined above on previously published data. Peric and Hwang (2002) present the results of biaxial compression tests on a soft, normally consolidated kaolinite. It was demonstrated above that the deviator stress at critical state has little impact on the magnitude of the membrane correction, which is dependent on membrane deformation in the direction of the shear band. Thus, it stands to reason that for soft soils failing at low deviator stresses, this correction will have a major impact on the interpreted strength results from biaxial compression tests.

Peric (2003) provided membrane deformation data and images for one of the tests (PS139-S) presented in Peric and Hwang (2002). Sample images from the biaxial

compression test on kaolinite are presented in Figure 5.30. Using the data supplied by Peric (i.e., grid point locations), it was possible to calculate the membrane correction for the kaolinite specimen. The shear stress and normal stress corrections are presented in Figure 5.31. The "bunching up" of data points in the shear stress plot (and the scatter in the normal stress plot) may be attributed to slippage of the membrane against the kaolinite. Membrane slippage can be visualized by considering a transect placed across the shear band on the membrane displacement contours of the specimen. Contour elevation may then be plotted as distance along a transect. If there is no membrane slippage, the contour elevations should consistently increase with increasing strain levels. If there is slippage, however, this will not be the case. This is illustrated in Figure 5.32, which shows membrane contour elevation steadily increasing from a global axial strain of 2% to a global axial strain of 8%. When significant slippage begins to occur, the contour elevations decrease, as seen from 8% global axial strain to 9% global axial strain. An

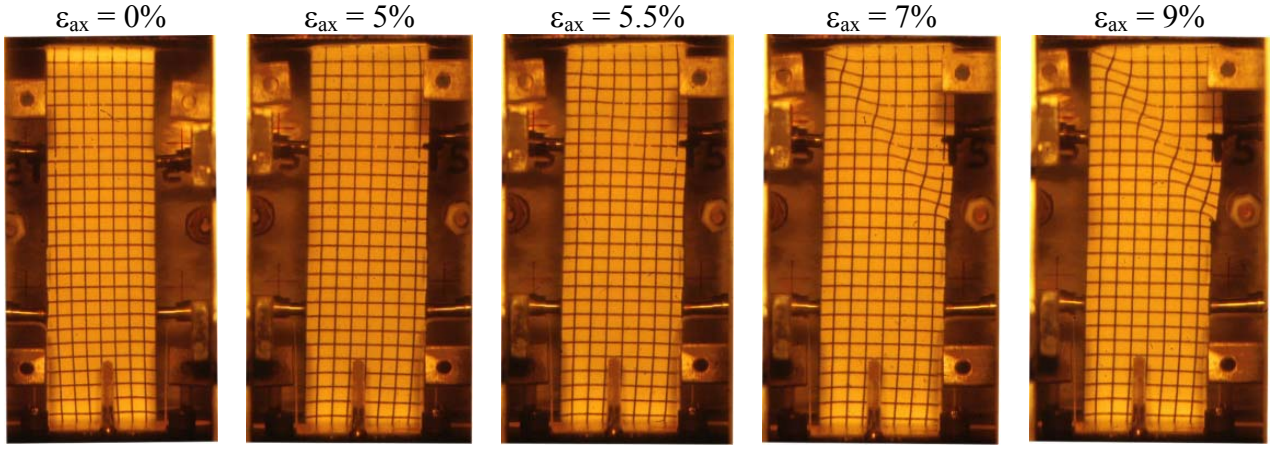

Figure 5.30: Sample images for biaxial test on kaolinite (Peric, 2003)

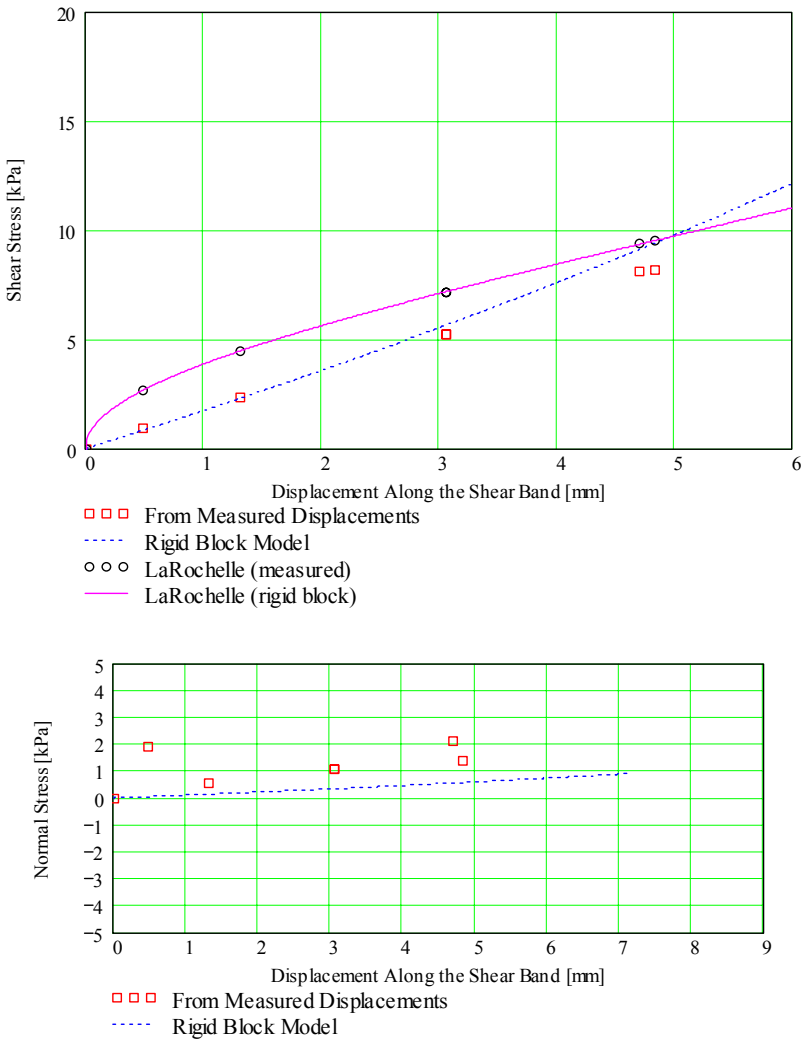

Figure 5.31: Membrane shear stress (upper plot) and normal stress (lower plot) corrections for kaolinite specimen

interesting artifact of Figure 5.32 is that the transect plots switch from generally concave upward (indicating homogenous deformation) to generally concave downward (indicating localized deformation) between 5% global axial strain and 5.5% global axial strain, which is the strain regime where localization is first observed.

Based on the results presented in Peric and Hwang (2002), it is also possible to

calculate the corrected shear and normal stresses (and thus, friction angle) on the shear plane due to the membrane effects. Peric and Hwang report that the deviator stress at critical state is 27.7 kPa with an effective confining stress of 158 kPa, which result in normal and shear stresses on the plane of 166 kPa and 13 kPa, respectively. The normal stress correction at critical state is again assumed to be 1 kPa (0.6%) and the shear stress correction is taken to be the measured correction at maximum strain, 8 kPa (64%). The uncorrected friction angle on the plane at critical state is 4.4° and the corrected friction angle is 1.6°.

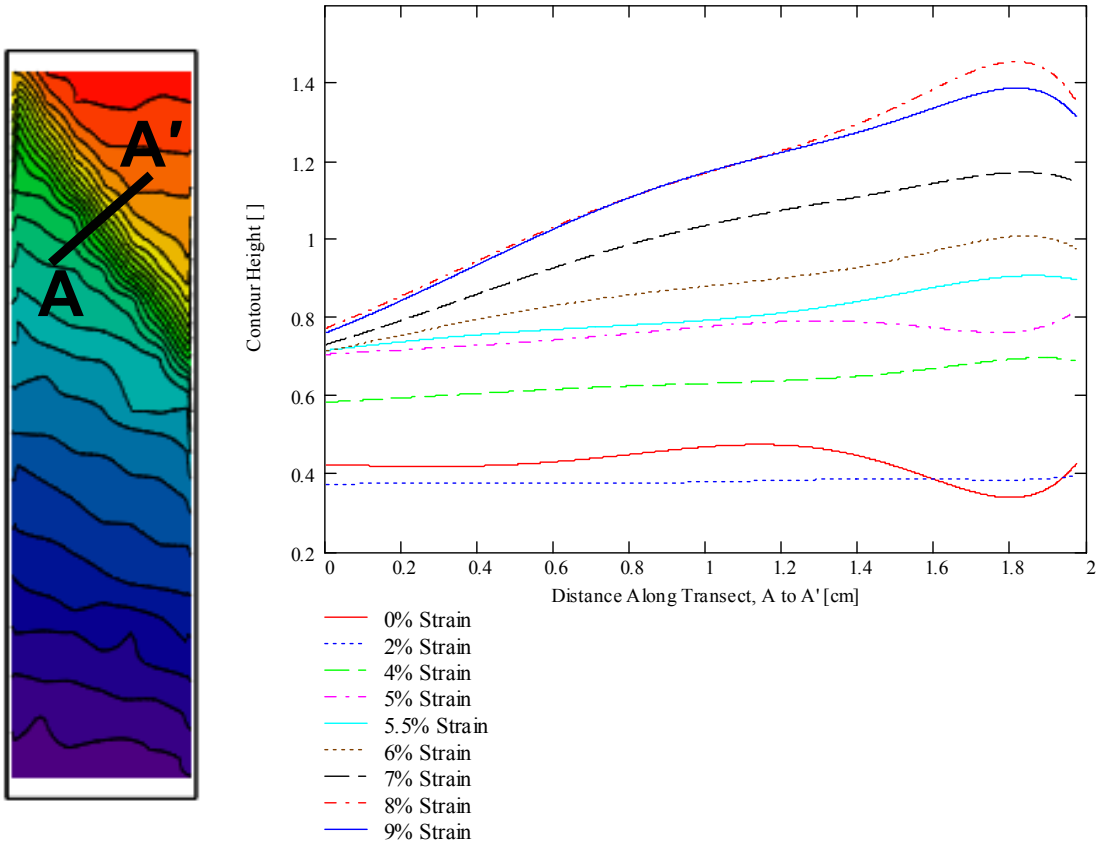

Figure 5.32: Transect plots of membrane displacement contours for kaolinite specimen

5.4. Microstructure Analyses

5.4.1. Introduction

Digital image analysis techniques were used to analyze the mosaic images that were created as described in Section 3.5. The original mosaics were nominally 6500 pixels wide by 5500 pixels high. As discussed in Section 3.5, these images were cropped to 4400 × 4400 pixels (34.5 mm square) to avoid use of portions of the composite image affected by image capture and stitching operations. Using Leica Qwin image analysis software, the images were binarized prior to analysis (Figure 5.33).

Once binarized, the images were analyzed to assess local void ratios, mesoscale void ratios and mean free paths, and the roughness of virtual surfaces inside and outside of the shear bands. As previously discussed, four specimens were successfully impregnated and four surfaces were generated from each specimen. The surfaces were approximately evenly spaced through the width of the specimen, and thus were taken at locations that represent 20%, 40%, 60%, and 80% of the specimen width. The surfaces

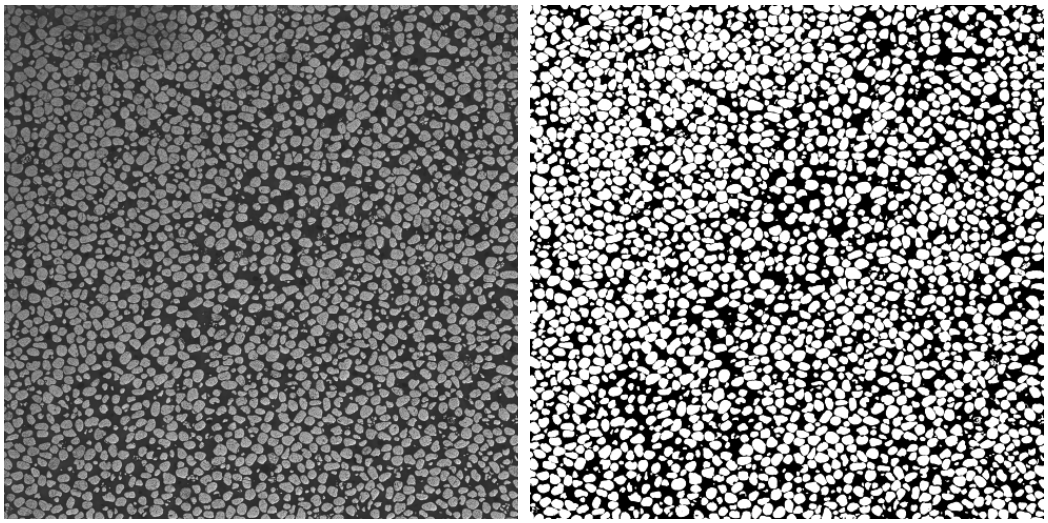

Figure 5.33: Sample image before and after binarization

described hereinafter will be designated using their location in conjunction with an "SD" for slightly dilatant, an "HD" for highly dilatant, an "S" for sheared, and a "U" for unsheared. For example, the surface taken at 20% thickness from the slightly dilatant sheared specimen would be designated SDS-20.

5.4.2. Local Void Ratio Distributions

There are two predominant methods available for assessing local void ratio distributions in binary images, but both are based on the original work of Oda (1976). The first method is morphological and was outlined by Kuo and Frost (1995). The second approach involved Voronoi tessellation and has been described by Alshibli and El-Saidany (2001). The two methods should produce similar results and differ only in the steps taken to generate the polygon network used for local void ratio calculations (see Figure 5.34). The morphological approach is well-documented and has been used

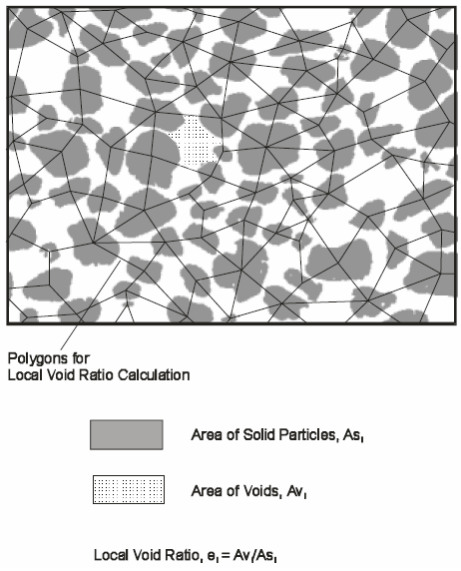

Figure 5.34: Polygon network for local void ratio calculations (after Jang, 1997)

successfully in many studies to quantify local void ratios in triaxial specimens (e.g., Kuo, 1994; Park, 1999; Chen, 2000; Yang, 2002). This is the procedure that was selected for the current study. Details of this procedure may be found in any of the above references and are not repeated here.

Once the polygon network was established, the local void ratio distributions within the images were quantified. Rather than considering local void ratios directly, analyses were conducted on solid area averaged local void ratios as discussed in Section 2.3.2. The equations to calculate the pertinent surface area averaged statistical parameters may be summarized as follows:

Mean:
$$\mu = \frac{\sum_{i=1}^{N} A_{S_i} \cdot e_i}{\sum_{i=1}^{N} A_{S_i}} \tag{5.18}$$

Standard Deviation:
$$\sigma = \sqrt{\frac{\sum_{i=1}^{N} A_{S_i} \cdot (e_i - \mu)^2}{\sum_{i=1}^{N} A_{S_i} \cdot e_i}} \tag{5.19}$$

Skewness:
$$\beta_1 = \frac{\sum_{i=1}^{N} A_{S_i} \cdot \frac{(e_i - \mu)^3}{\sigma^3}}{\sum_{i=1}^{N} A_{S_i}} \tag{5.20}$$

Kurtosis:
$$\beta_2 = \frac{\sum_{i=1}^{N} A_{S_i} \cdot \frac{(e_i - \mu)^4}{\sigma^4}}{\sum_{i=1}^{N} A_{S_i}} \tag{5.21}$$

where all terms are as previously defined. Each image contained between 4600 and 5100 polygons, with the variation attributable to variations in microstructure within the image. To visualize the data, it is useful to plot histograms of surface area averaged local void ratios. By way of illustration, the histogram for surface HDS-80 is presented in Figure 5.35, with complete histograms for all surfaces presented in Appendix B.

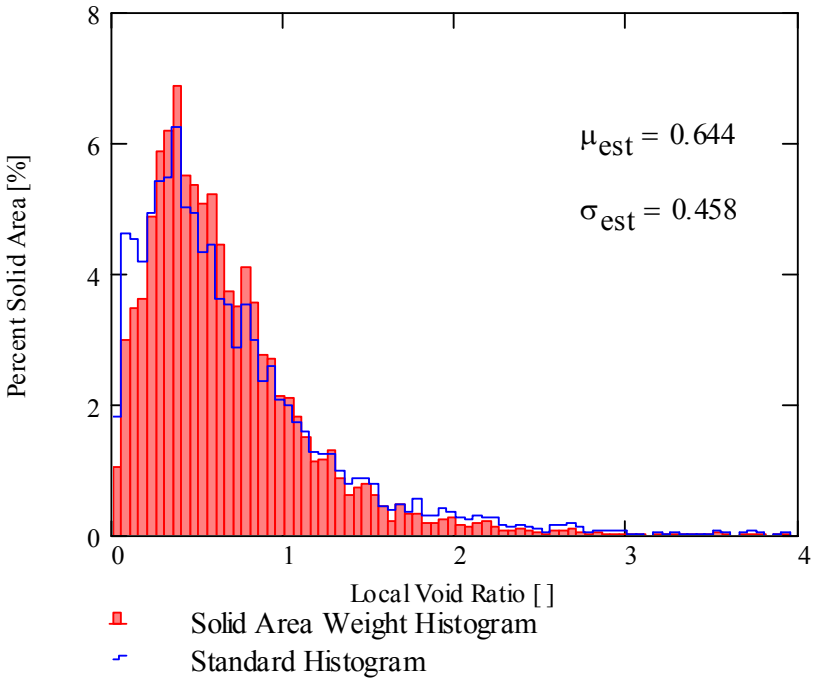

Figure 5.35: Solid area weighted histogram for surface HDS-80

In order to observe the effects of shearing on local void ratio distribution, total histograms for each specimen (i.e., the histograms for all polygons on all four surfaces from a specimen) were generated (Figures 5.36 and 5.37). Note that in contrast to Figure 5.35, where solid and linear histograms represented solid area weighted and standard values, the solid and linear histograms in Figures 5.36 and 5.37 represent solid area weighted histograms for unsheared and sheared specimens, respectively. These histograms show that shearing tends to shift the histogram to the right and flatten it noticeably. This is indicative of dilation within the specimen and an increase in the heterogeneity of the local void ratios. These effects are also evident from the statistical parameters for the histograms, with mean void ratio and standard deviation increasing with shearing.

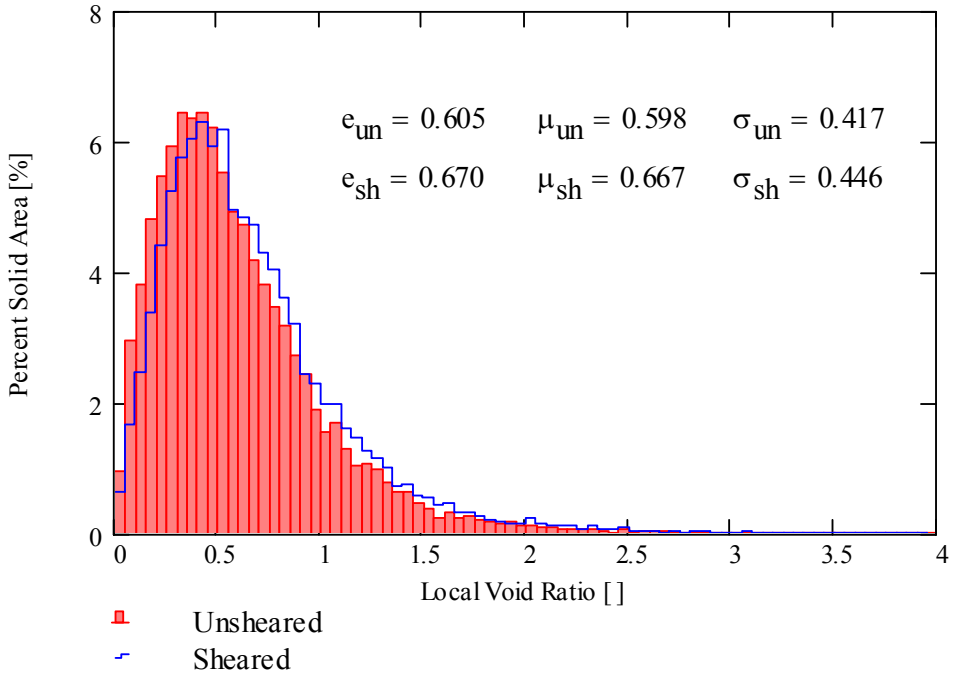

Figure 5.36: Total histograms for slightly dilatant specimens (e_{un} and e_{sh} indicate global image void ratios before and after shearing, respectively)

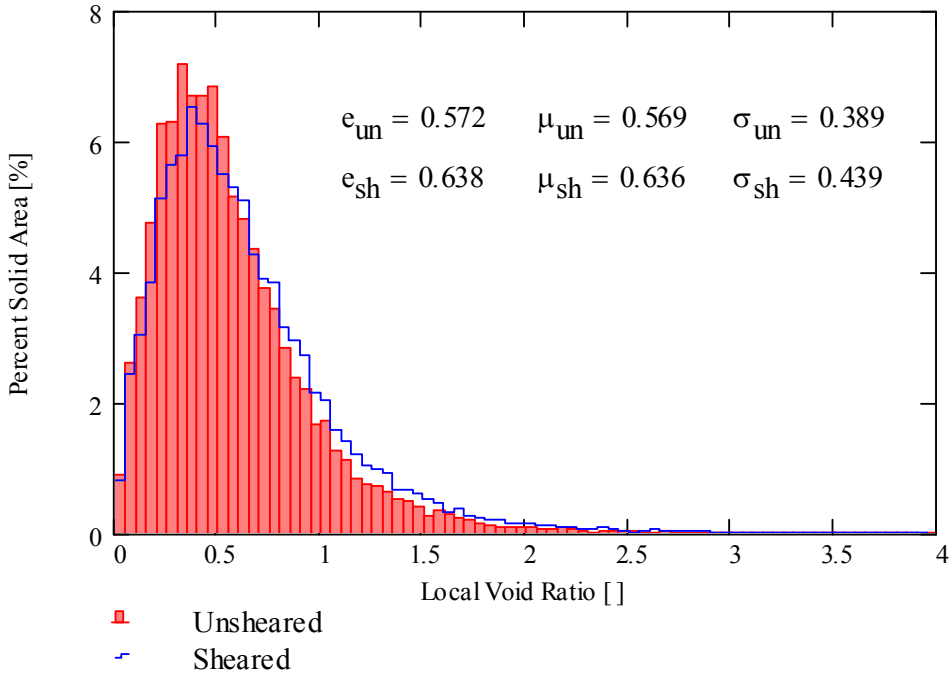

Figure 5.37: Total histograms for highly dilatant specimens (e_{un} and e_{sh} indicate global image void ratios before and after shearing, respectively)

To further characterize the local void ratio distributions, statistical distributions were fit to the data. Three main steps were used in fitting the statistical distributions:

- selection of a distribution function;
- selection of a fitting method; and
- characterization of the ability of the distribution to describe the data.

For selection of a distribution function, the Pearson probability chart was used, as suggested by Harr (1987). The Pearson chart divides kurtosis-squared skewness space into well delineated regions. The locations of the given datasets in Pearson space were determined, and appropriate distributions were selected. A plot of Pearson probability space, along with the locations of the local void ratio sets, is shown in Figure 5.38. The

two main features of Figure 5.38 are that the data points for unsheared surfaces tend to be more clustered than those for the sheared surfaces (indicative of higher nonuniformity on the sheared surfaces) and that the points plot in the regions of the gamma and lognormal distributions. In addition to the gamma and lognormal distributions, the Weibull distribution was selected for comparison to the given histograms. Details concerning these distributions and their parameters may be found in Appendix A.3.

Each of the three distributions was fit to the data using three methods: the maximum likelihood estimate, fitting of the probability distribution function to the histogram, and fitting of a cumulative distribution function to the sorted dataset (note that, when sorted in ascending order with respect to solid area weighted void ratio and normalized to the total area of solids, the data become a type of cumulative distribution function). Figures 5.39 through 5.41 show each of the three distribution functions fitted with each of the three fitting methods.

The final step was determining the quality of the fits for each of the three distributions and each of the three methods. Previous studies (e.g., Chen, 2000) have used an ad-hoc implementation of the Kolmogorov-Smirnov goodness-of-fit test. However, the Kolmogorov-Smirnov test is not applicable to the case when the mean and standard deviation of the distribution are estimated from the measured data (Lilliefors, 1967). In this case, an alternate "Kolmogorov-Smirnov-type" test, such as those presented by Lilliefors (1967) or Finkelstein and Schafer (1971), should be used. Furthermore, computed values for the critical statistic as a function of dataset size and significance level are not widely available for a large number of distributions (normal, lognormal, and exponential are most common). Given the above information, the

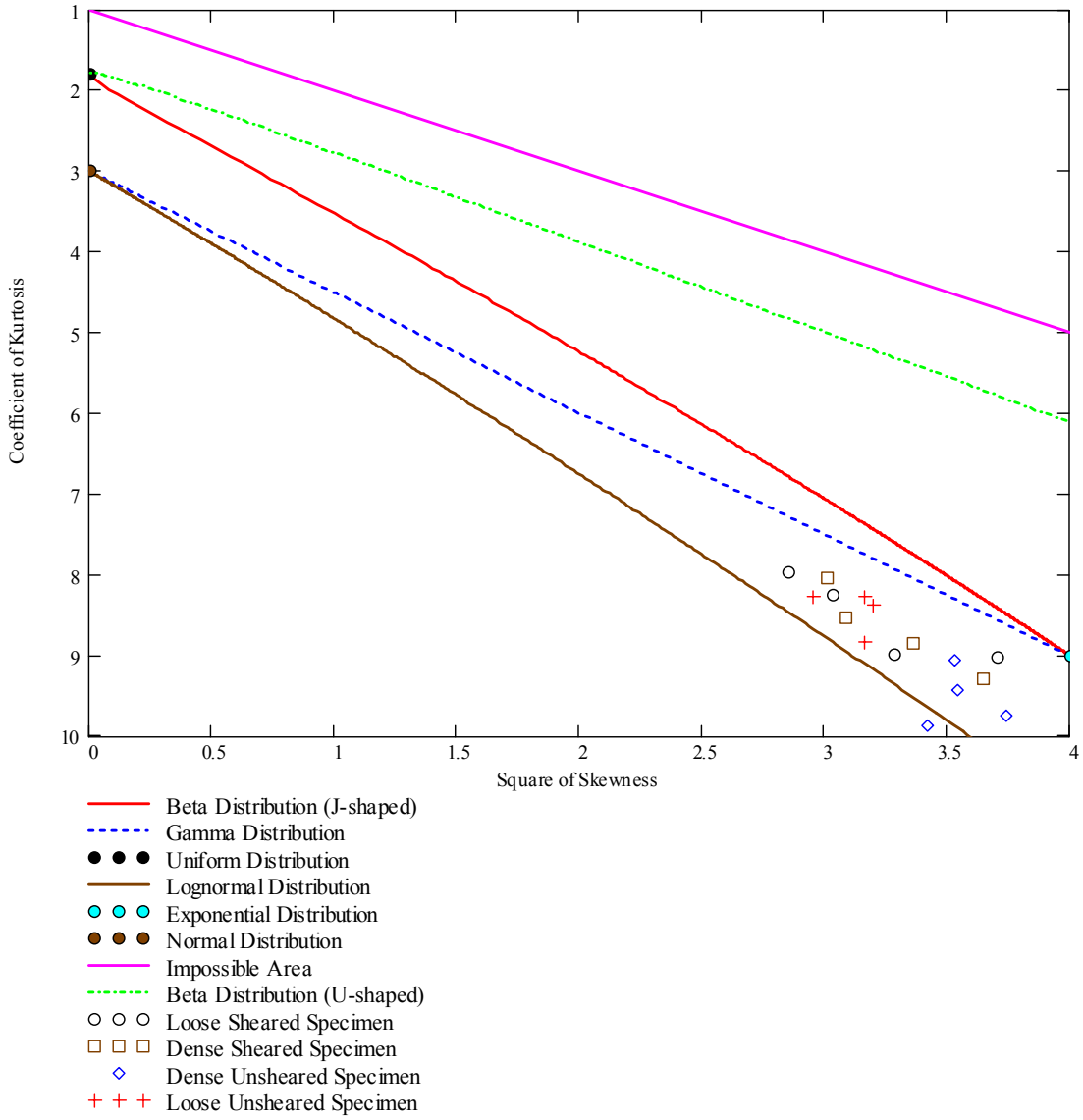

Figure 5.38: Pearson probability space

Kolmogorov-Smirnov test as previously implemented for local void ratio distribution significance level are not widely available for a large number of distributions (normal, lognormal, and exponential are most common). Given the above information, the Kolmogorov-Smirnov test as previously implemented for local void ratio distribution data reduces to an assessment of the L_∞ norm (Santamarina and Fratta, 1998), which is the maximum absolute difference between the measured and predicted value at any point in the series. This is the implementation used herein. Additionally, the sum of squares of

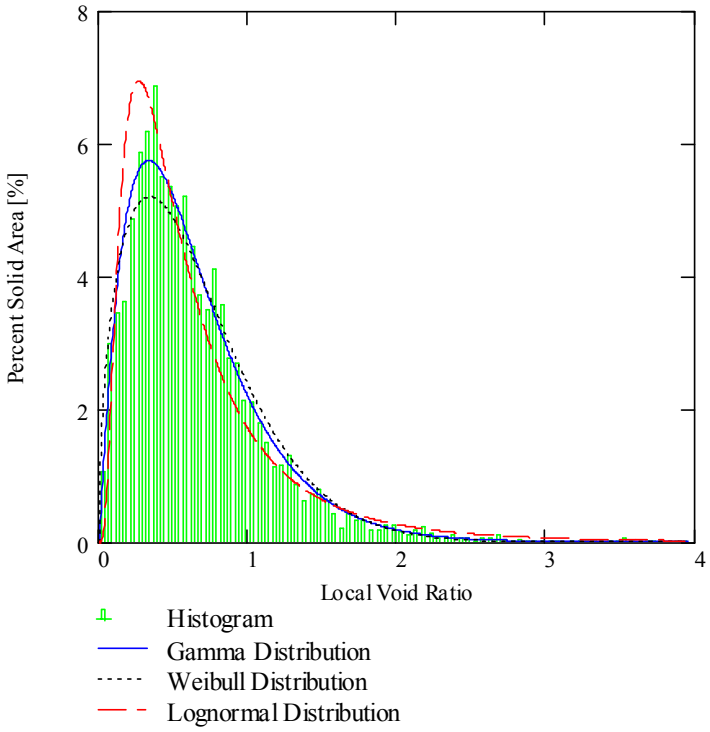

Figure 5.39: Maximum likelihood fitting to the histogram from surface HDS-80

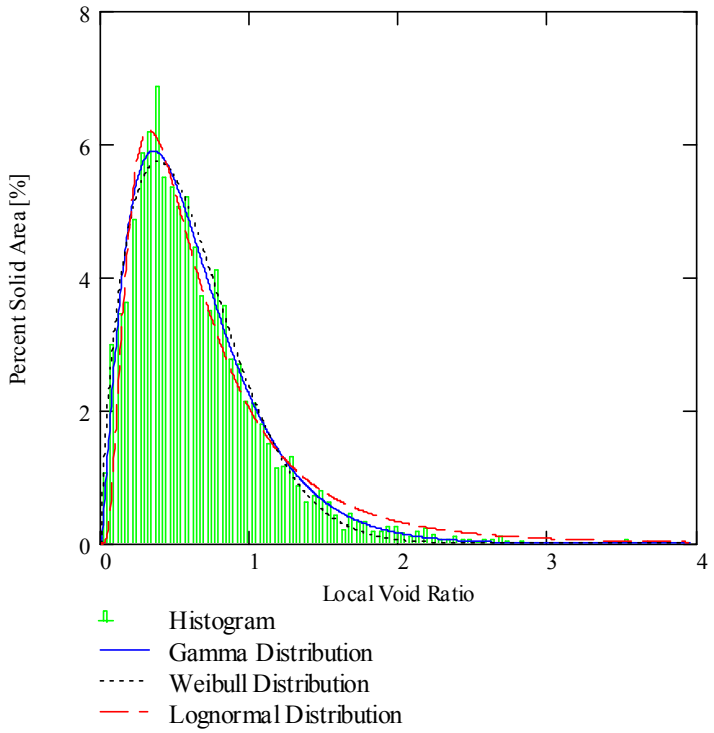

Figure 5.40: Probability distribution fitting to the histogram from surface HDS-80

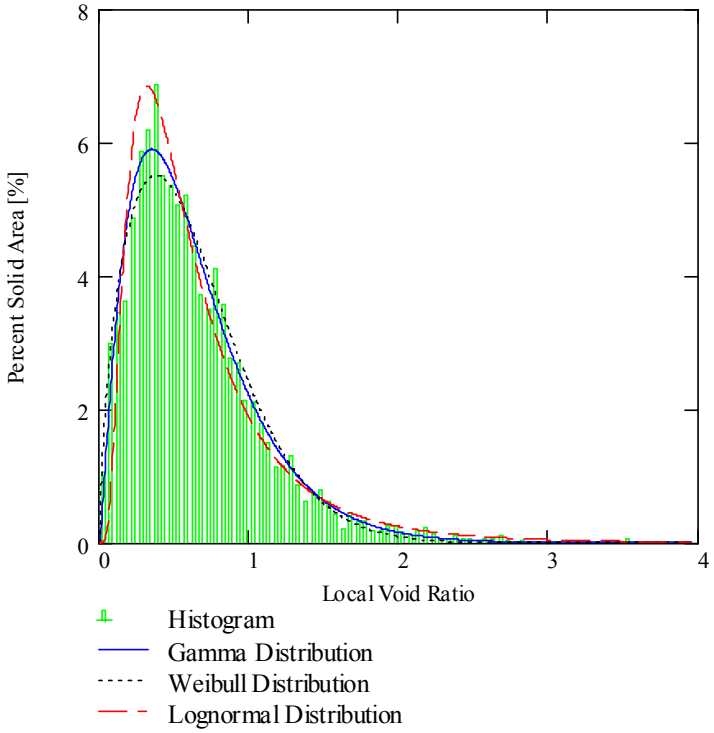

Figure 5.41: Cumulative distribution fitting to the histogram from surface HDS-80

the errors (the L_2 norm) and the correlation coefficients were calculated for each fit. Sample calculations are presented in Appendix A.3.

Based on the results of the above analyses, it was determined that the gamma distribution provided the best fit to the histograms of local void ratios. The gamma distribution consistently provided better goodness-of-fit statistics across all 16 surfaces and for all fitting methods. The cumulative distribution function fitting method consistently provided the best goodness-of-fit statistics across all 16 surfaces and all distributions. However, due to the large sample size, the maximum likelihood estimates of fitting parameters were selected for each surface. The goodness-of-fit statistics for maximum likelihood estimates were very close to those for the cumulative distribution function method. The maximum likelihood estimates are less affected by outlying data points than the other methods and in the limit, the maximum likelihood parameters will asymptotically approach the true values for the histogram (NIST, 2005). It is not expected that the maximum likelihood method will produce goodness-of-fit statistics that are as good as the other methods because less emphasis is placed on the tails of the distribution. Gamma distributions for each surface are presented in Figures 5.42 and 5.43 and parameters are summarized in Table 5.4.

In previous studies (e.g., Jang, 1997) it was found that the best distribution to describe the local void ratio histograms was the lognormal distribution. The previous studies, however, were based on sands with a smaller grain size than the Ottawa 20-30 used in the current study. This suggests that the correct distribution depends on the particle size of the soil being studied and may be explained as follows: Because two-dimensional images are used for these studies, the range in particle area in an image will

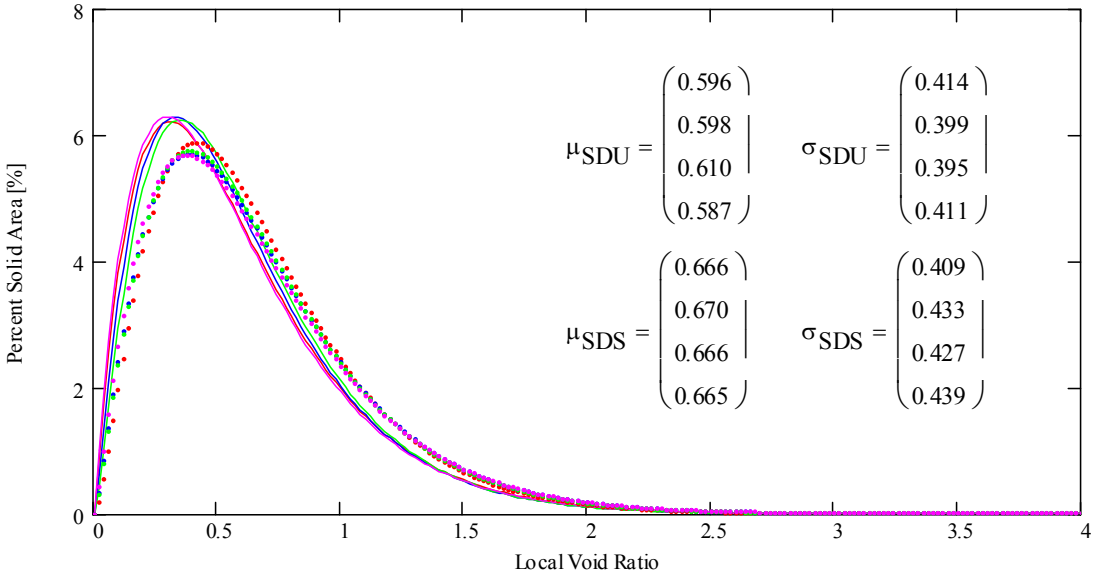

Figure 5.42: Gamma distributions for slightly dilatant specimens (solid lines correspond to unsheared surfaces and dotted lines correspond to sheared surfaces).

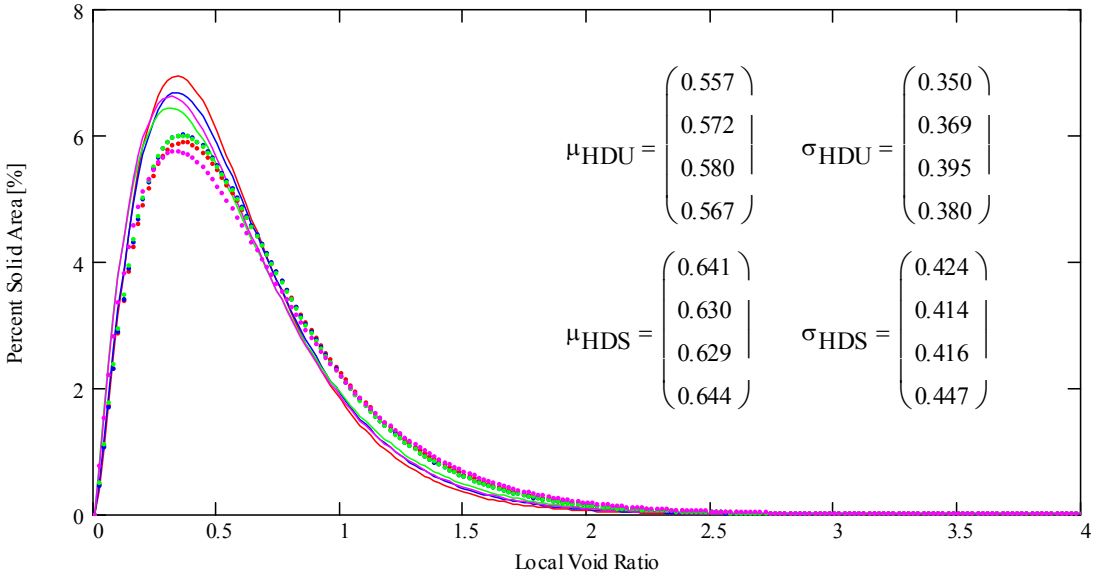

Figure 5.43: Gamma distributions for highly dilatant specimens (solid lines correspond to unsheared surfaces and dotted lines correspond to sheared surfaces).

Table 5.4: Void ratios and standard deviations for each surface

Surface	$e_{as\ prepared}$	e_{image}	μ	σ	μ_{gamma}	σ_{gamma}
SDU-20	0.60	0.601	0.596	0.428	0.596	0.414
SDU-40	0.60	0.607	0.598	0.410	0.598	0.399
SDU-60	0.60	0.616	0.610	0.407	0.610	0.395
SDU-80	0.60	0.596	0.587	0.424	0.587	0.411
SDS-20	0.60	0.669	0.666	0.427	0.666	0.409
SDS-40	0.60	0.672	0.670	0.460	0.670	0.433
SDS-60	0.60	0.667	0.666	0.441	0.666	0.427
SDS-80	0.60	0.671	0.665	0.446	0.665	0.439
HDU-20	0.57	0.560	0.557	0.363	0.557	0.350
HDU-40	0.57	0.579	0.572	0.383	0.572	0.369
HDU-60	0.57	0.583	0.580	0.412	0.580	0.395
HDU-80	0.57	0.565	0.567	0.398	0.567	0.380
HDS-20	0.56	0.647	0.641	0.441	0.641	0.424
HDS-40	0.56	0.632	0.630	0.429	0.630	0.414
HDS-60	0.56	0.627	0.629	0.429	0.629	0.416
HDS-80	0.56	0.645	0.644	0.458	0.644	0.447

depend only on the maximum particle size in the specimen (i.e., the minimum particle size remains constant). The rates of the erosion and dilation processes used in creating the polygon network are independent of particle size. Thus, when very large particle areas are adjacent to very small particle areas, the generated polygons may lie almost entirely within the large particle. This leads to very low (i.e., <0.10) local void ratio values, which tend to skew the histogram to the left. This skewing is what makes the lognormal distribution inappropriate in the current study.

5.4.3. Subregional Analyses

Of particular interest in the current study were the structural differences inside and outside of the shear band. These differences were quantified using three methods:

subregional void ratios, subregional mean free paths, and predetermined inclined strips. In the subregional calculations, each 4400 × 4400 pixel image was divided into a grid of 484 subimages, each 200 pixels square (see Figure 5.44). The void ratio and mean free path were calculated for each subimage. To calculate the mean free path, a series of test lines was overlain on each subimage and the number of intersections of test lines with particle perimeters per unit length of test line was calculated (Underwood, 1970). The mean free path for each subimage was then calculated as follows:

$$\lambda = 4 \cdot \frac{\left(1 - V_V\right)}{2 \cdot P_L} \tag{5.22}$$

where λ is the mean free path, V_V is the volume fraction of solids in the subregion (mathematically equal to the area fraction of solids), and P_L is the number of intersections of test lines with particle perimeters per unit length of test line. Calculated in this manner, this is the completely general three-dimensional mean free path. The solution is mathematically general and exact (Underwood, 1970), although there are statistical sampling errors involved. Complete calculations are provided in Appendix A.4.

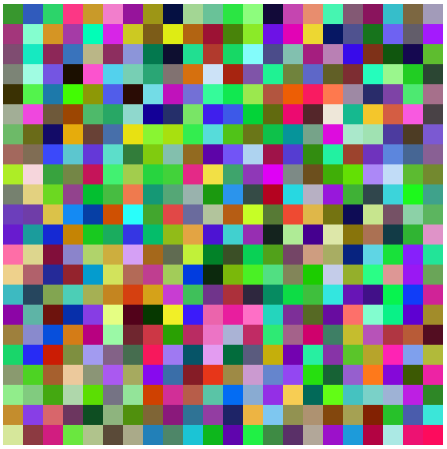

Figure 5.44: Schematic of 22 × 22 grid for subregional calculations

Once the subregional void ratios and mean free paths were calculated, contour plots were generated to allow for observation of the variation of these properties over the surface. These plots are presented in Figures 5.45 to 5.52. It is apparent from these plots that void ratio and mean free path do not vary greatly across the surfaces from the unsheared specimens. After shearing, however, it may be seen that void ratio and mean free path increase markedly within the region of localized shear, allowing for identification of the shear band from calculated values. This type of analysis provides an advantage over the local void ratio analyses because parameters are calculated over regions that are approximately two mean particle diameters square (i.e., 1.57 mm square) which tends to smooth out some of the large local variations that are evident even in unsheared specimens.

A beneficial side effect of the subregional calculations is that the values may be used to calculate measures of grain size within the system very simply (Underwood, 1970). Because grain size should not vary greatly from image to image, regardless of void ratio and state of shear, these calculations can be used as a qualitative assessment of the uniformity and quality of the images, serving as a check on image processing procedures. The two measures of grain size implemented in this study were the mean intercept grain size and the surface area averaged grain size. These values were calculated as follows:

$$l_S = \frac{1}{P_L} \tag{5.23}$$

$$d_S = \frac{3 \cdot V_V}{P_L} \tag{5.24}$$

where l_s is mean intercept grain size and d_s is surface area averaged grain size, and other terms are as previously defined. It is not expected that these two values will agree exactly with each other or with the mean grain size as determined by mechanical sieving (0.74 mm in this case) because the methods for determining the values are inherently different. However, as with the mean free path calculations, these are three-dimensional, exact measures of grain size that make no assumptions with respect to particle shape, other than the fact that particles must be convex. Calculated mean grain sizes are presented in Table 5.5.

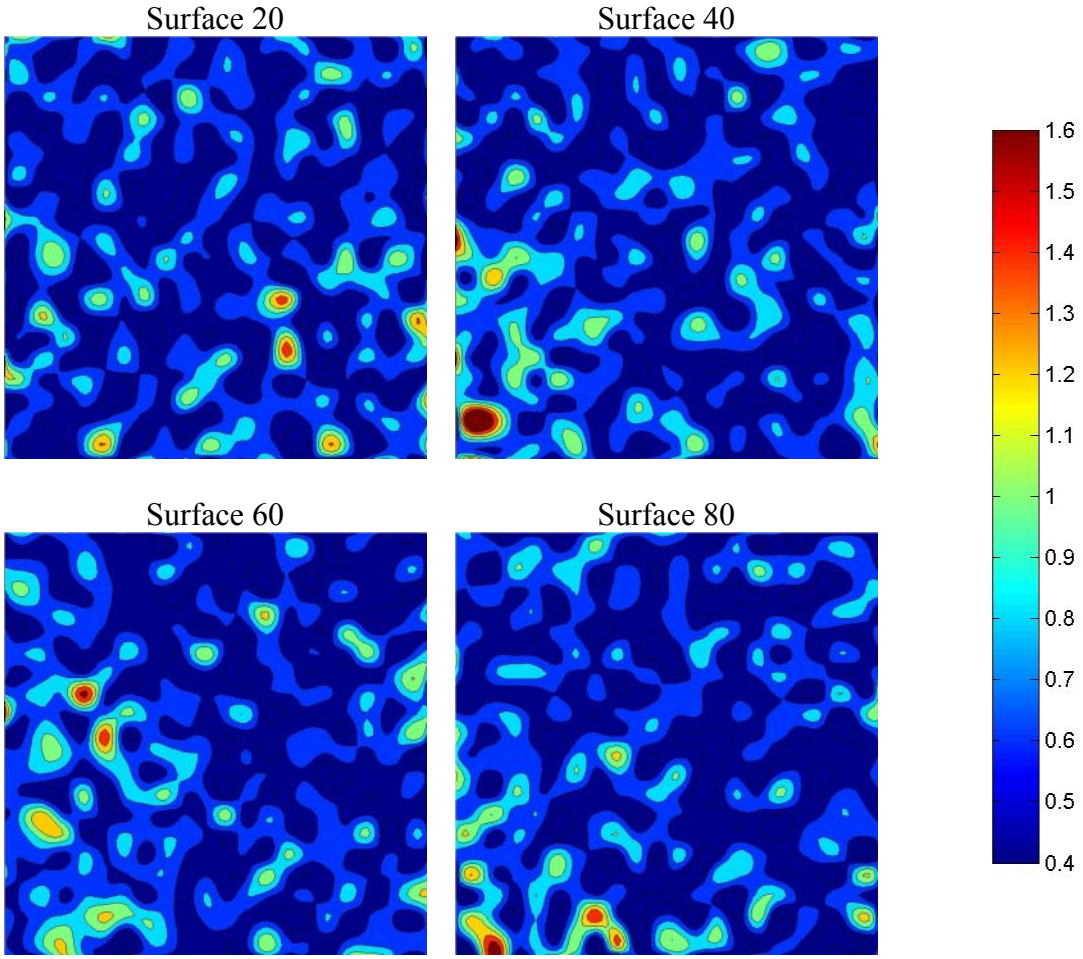

Figure 5.45: Void ratio contours for slightly dilatant unsheared specimen

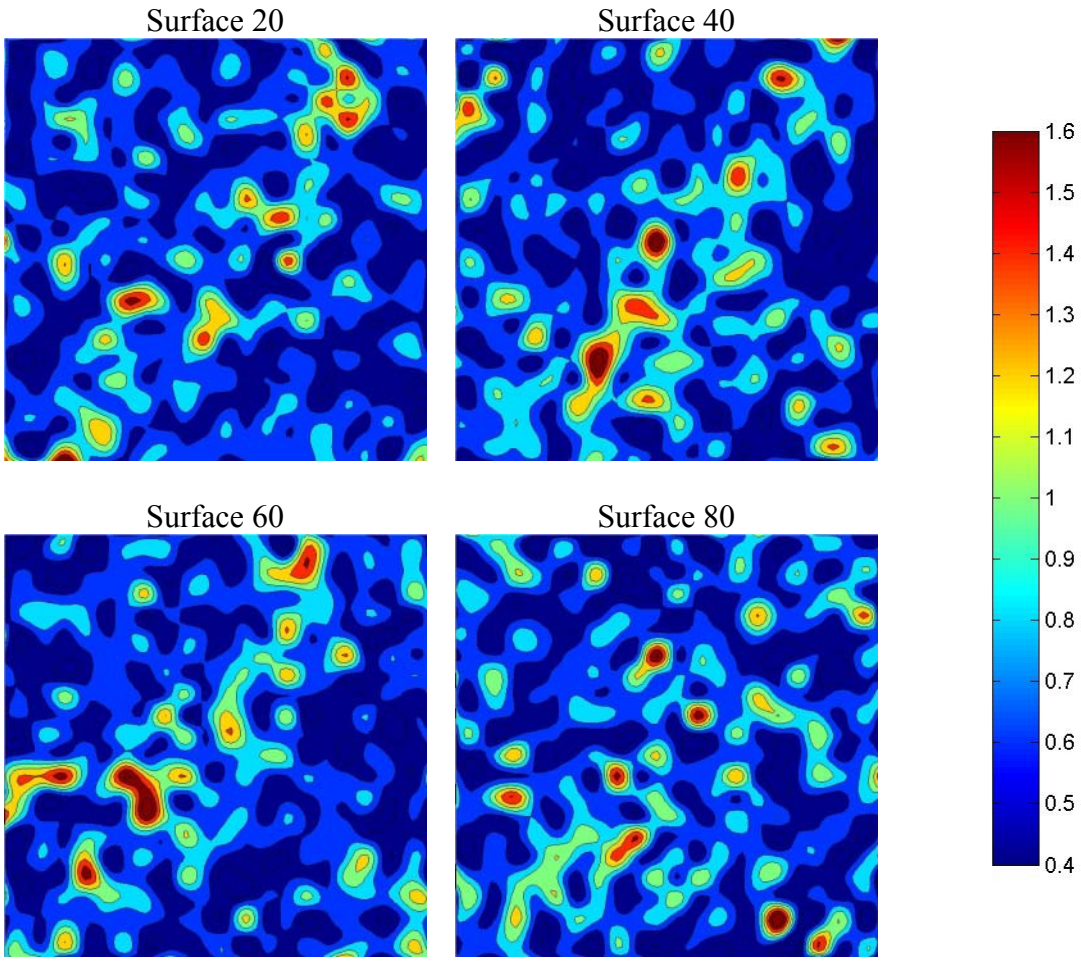

Figure 5.46: Void ratio contours for slightly dilatant sheared specimen

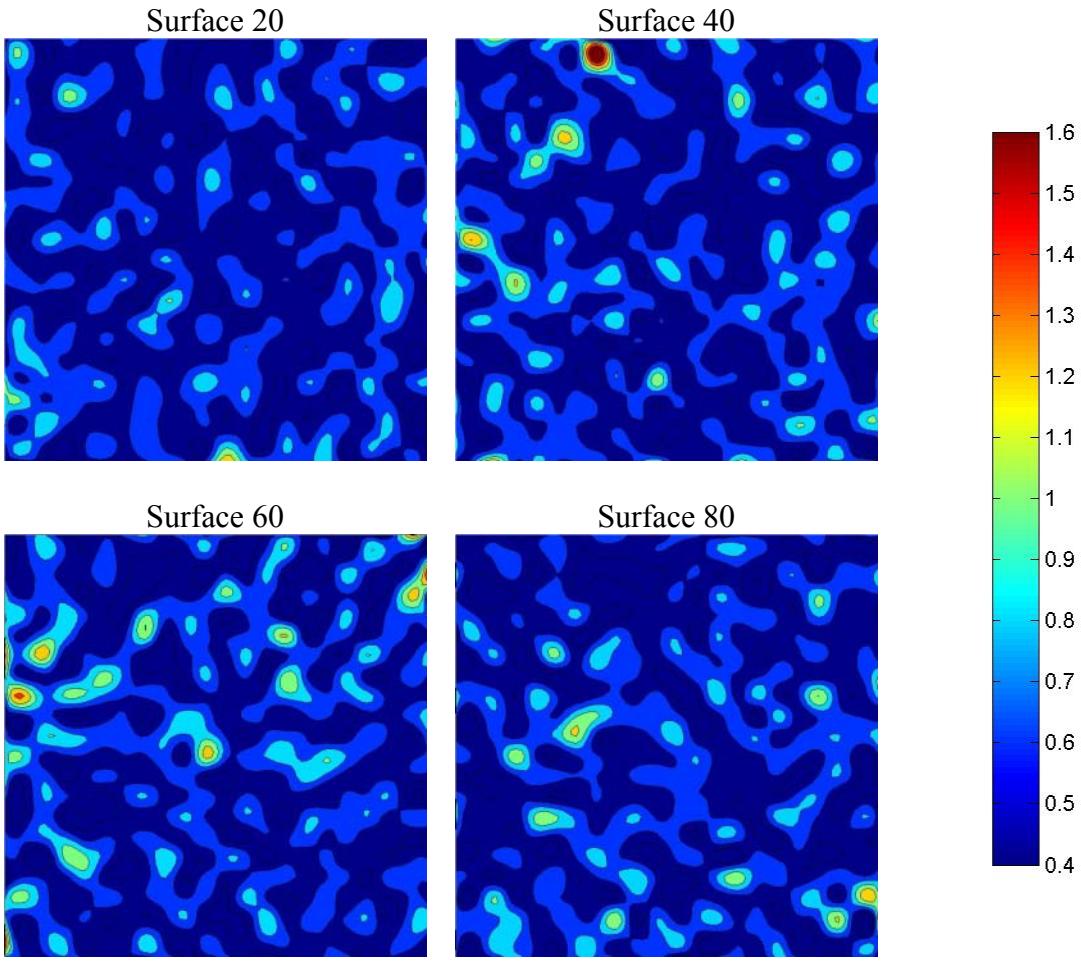

Figure 5.47: Void ratio contours for highly dilatant unsheared specimen

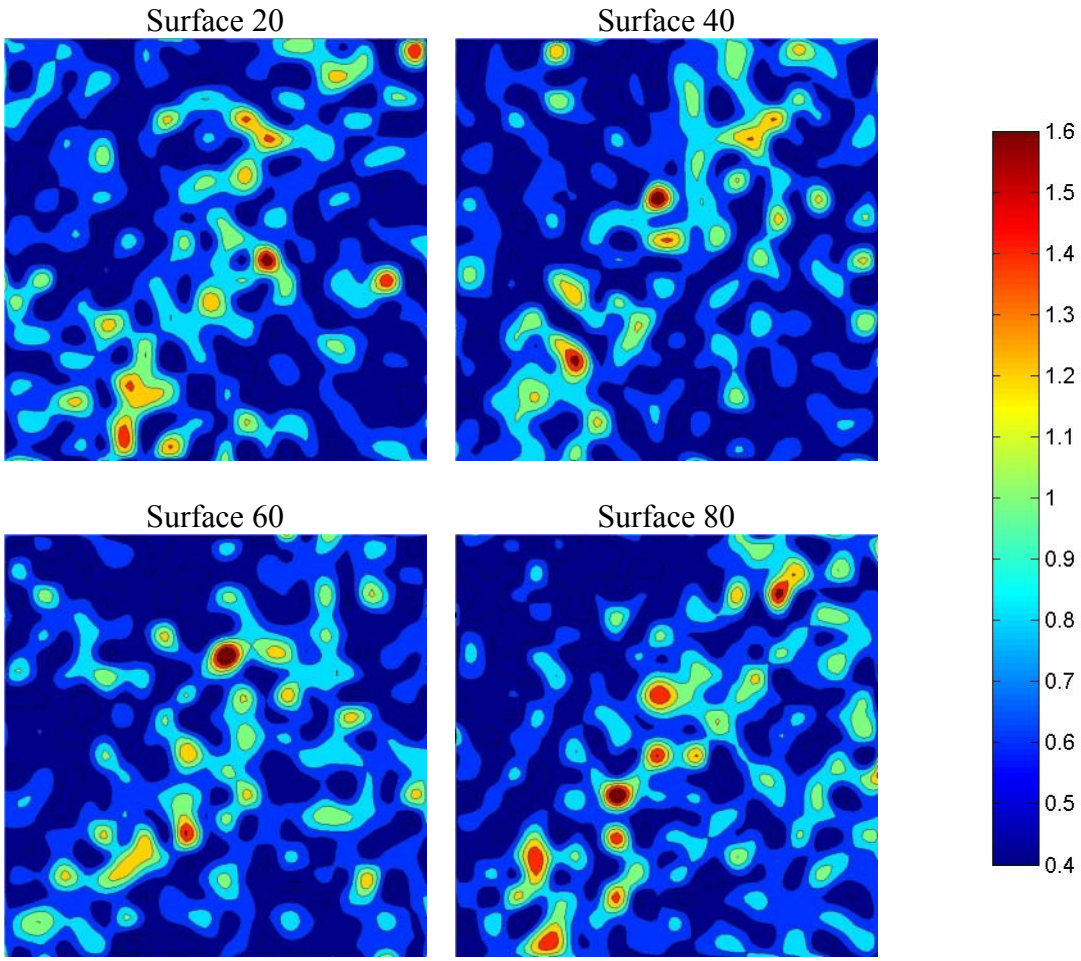

Figure 5.48: Void ratio contours for highly dilatant sheared specimen

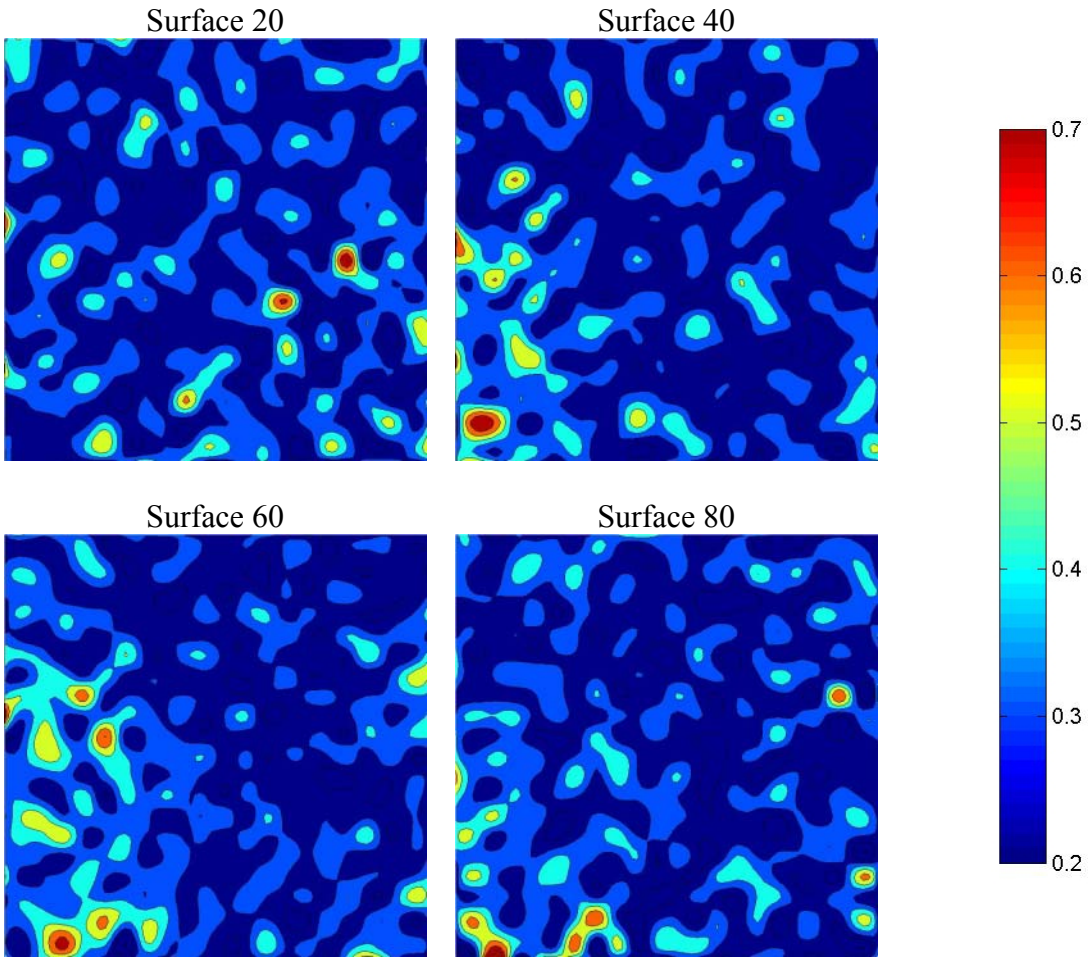

Figure 5.49: Mean free path contours for slightly dilatant unsheared specimen

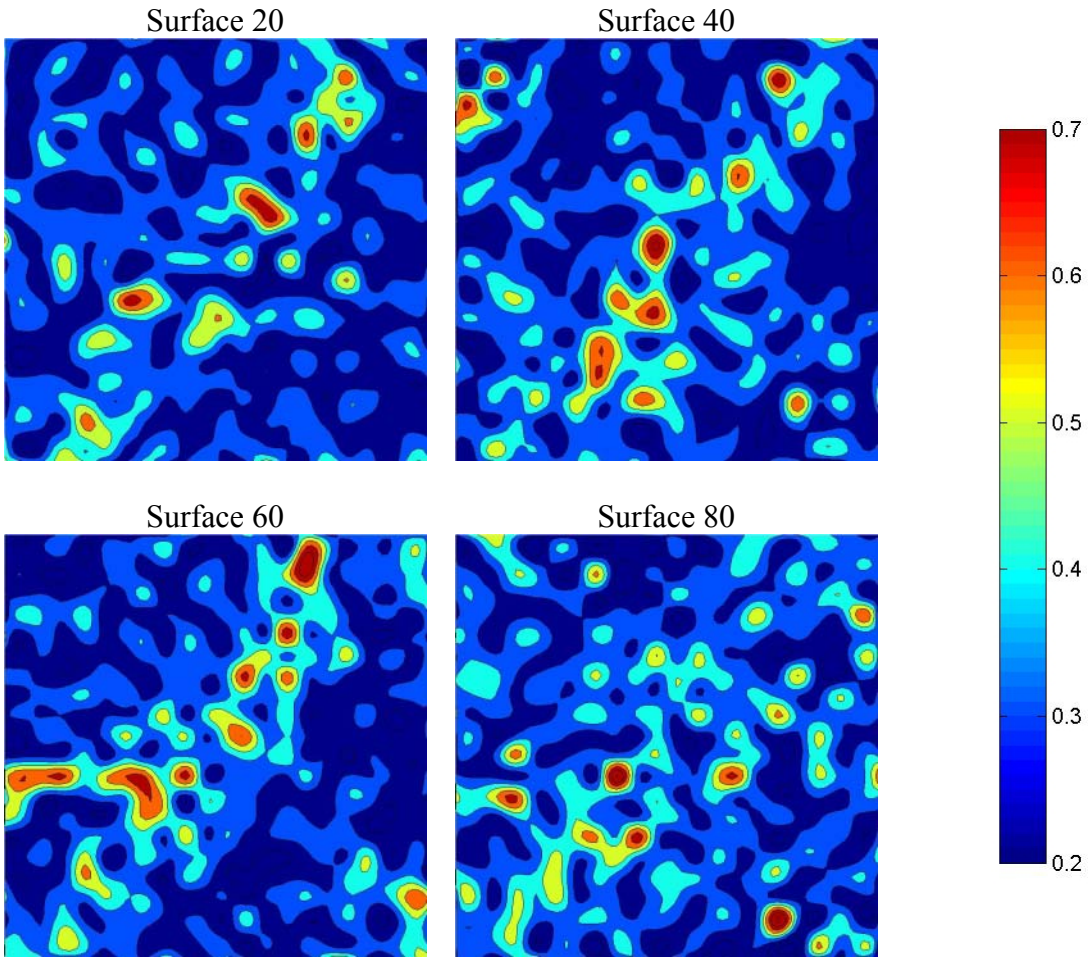

Figure 5.50: Mean free path contours for slightly dilatant sheared specimen

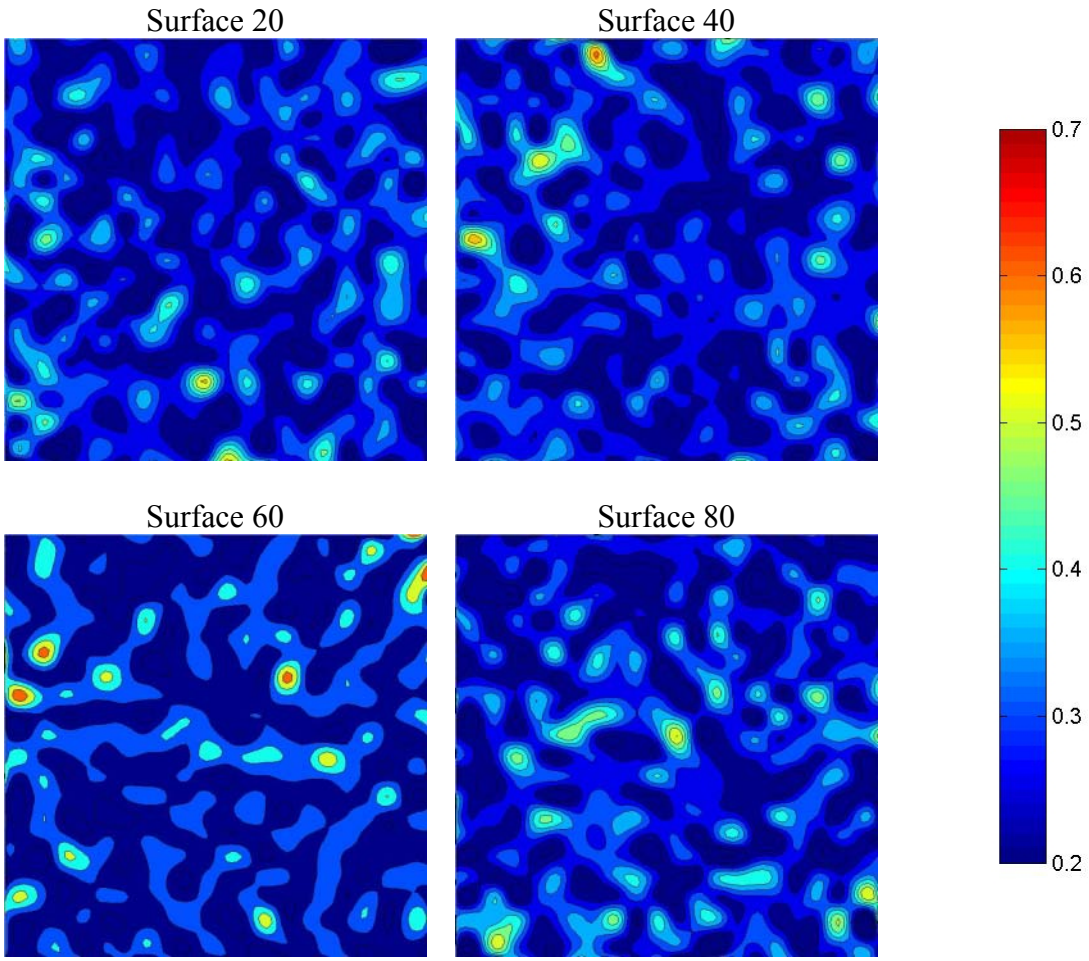

Figure 5.51: Mean free path contours for highly dilatant unsheared specimen

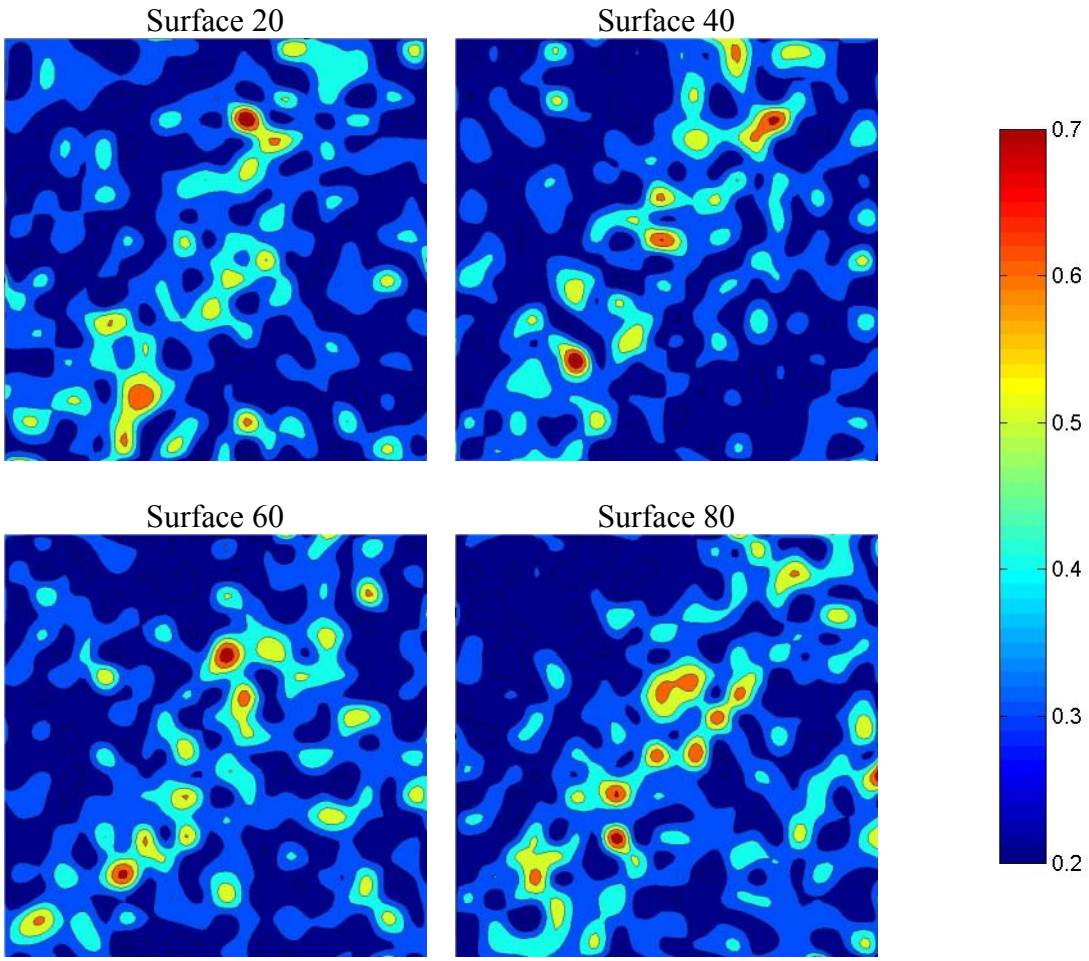

Figure 5.52: Mean free path contours for highly dilatant sheared specimen

Table 5.5: Calculated mean grain sizes

Specimen	Surface 20		Surface 40		Surface 60		Surface 80	
	l_s (mm)	d_s (mm)	l_s (mm)	d_s (mm)	l_s (mm)	d_s (mm)	l_s (mm)	d_s (mm)
SDU	0.401	0.747	0.393	0.729	0.404	0.745	0.398	0.742
SDS	0.403	0.719	0.411	0.731	0.415	0.739	0.426	0.759
HDU	0.382	0.732	0.380	0.721	0.392	0.737	0.384	0.733
HDS	0.409	0.740	0.403	0.736	0.410	0.749	0.412	0.745

5.4.4. Spatial Averaging Along Pre-Determined Inclined Strips

In the spatial averaging calculations, each image was divided into 200-pixel (1.57-mm, approximately $2 \times d_{50}$) wide strips that were oriented along the shear band. This allowed for direct calculation of microstructural parameters both inside and outside of the shear band. A schematic of this strip-wise segregation is presented in Figure 5.53.

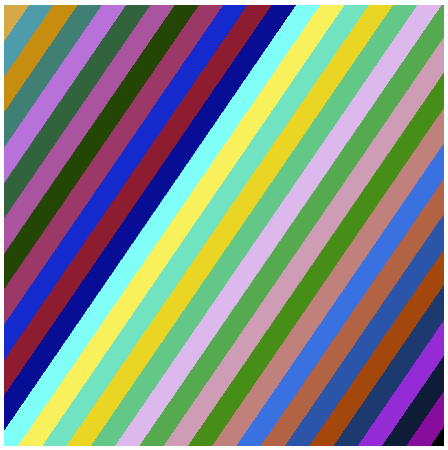

Figure 5.53: Schematic of oriented strips for calculation of void ratios

Once the void ratio within each strip was calculated, void ratios were plotted as a function of distance along a transect that is normal to the shear band, by traversing the

transect from the corner of the surface below the shear band to the corner of the surface above the shear band. In unsheared specimens, spatial averaging strips were inclined at the same angle as in the corresponding (i.e., slightly dilatant or highly dilatant) sheared specimens. The demarcation lines for shear band extents were determined by plotting accumulated area void ratios from the left and the right on the same axes as the incremental void ratio data (see Figure 5.54). Accumulated area void ratios were calculated using the following formula:

$$e_k = \frac{\sum_{i=0}^{k} A_{V_i}}{\sum_{i=0}^{k} A_{S_i}} \tag{5.22}$$

where e_k is the k^{th} accumulated area void ratio (incremented either from right-to-left or left-to-right), A_{vi} is the area of voids in the i^{th} pre-determined inclined strip, and A_{si} is the area of solids in the i^{th} pre-determined inclined strip.

In this manner, it is apparent that as the accumulated void ratio curves begin to encompass more and more area, they asymptote to a constant value as the transect approaches the location of the shear band. As the transect enters the shear band, the slope of the line of accumulated void ratios changes. The point between two strips that is closest to the location of change in the slope of the accumulated void ratio line was selected as a shear band extent. To check this calculation, the ultimate values of the accumulation lines on either side of the shear band (and inside the shear band) were plotted on the same axes as the incremental void ratio values (Figure 5.55). Examination of Figure 5.55 indicates that the first point inside the shear band represents the first

significant deviation from the ultimate value lines, which indicates a reasonable selection of the shear band extents. Note that Figure 5.55 cannot be constructed without *a priori* knowledge of the shear band location. It should also be noted that there appears to be a transitional area when moving from a rigid block portion of the specimen into the fully formed shear band, but no efforts were made to further quantify the extents of this region. While other manners of determining shear band extents (e.g., monitoring deviation from the mean) may provide slightly different (yet, internally consistent) results, this method was selected as being straightforward to implement, intuitive, robust, and readily checked using the plot shown in Figure 5.55. Sample plots of these data are presented in Figures 5.56 through 5.59. Full plots for all surfaces are presented in Appendix C.

It is apparent from Figures 5.56 through 5.59 and Appendix C that the void ratio transects clearly indicate the presence of a localization within the sheared specimens and that void ratios are relatively constant in the unsheared specimens. Furthermore, the location and size of the shear band appears to shift slightly from surface to surface as one moves through the specimen. The slight location change arises from the cropping operations used to develop useable images, as discussed in Section 3.5. The change in thickness is due to nonuniformity of the shear band, which arises from local variations in microstructure during shearing.

5.4.5. Histograms from Pre-Determined Inclined Strips

The pre-determined inclined strips (and subsequent delineation of shear band location) were used to develop local void ratio distribution histograms for regions inside and outside of the shear band on each surface from the sheared specimens. Because the

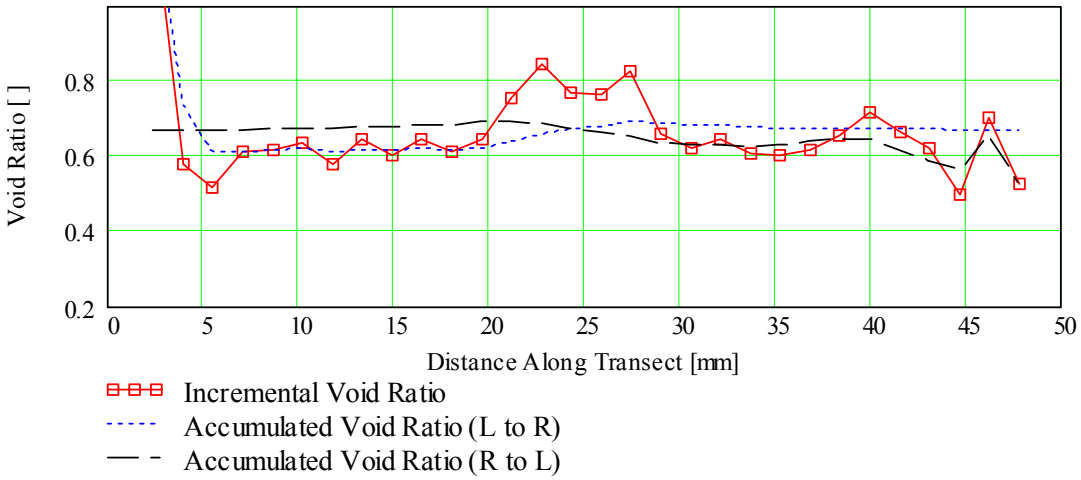

Figure 5.54: Incremental and accumulated void ratios for surface SDS-20

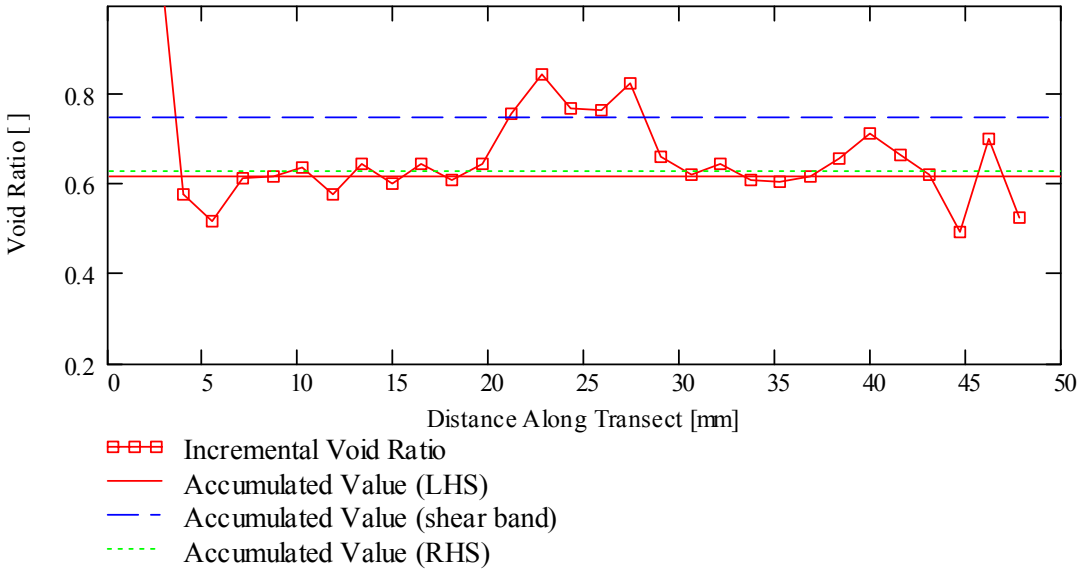

Figure 5.55: Incremental and ultimate void ratios for surface SDS-20

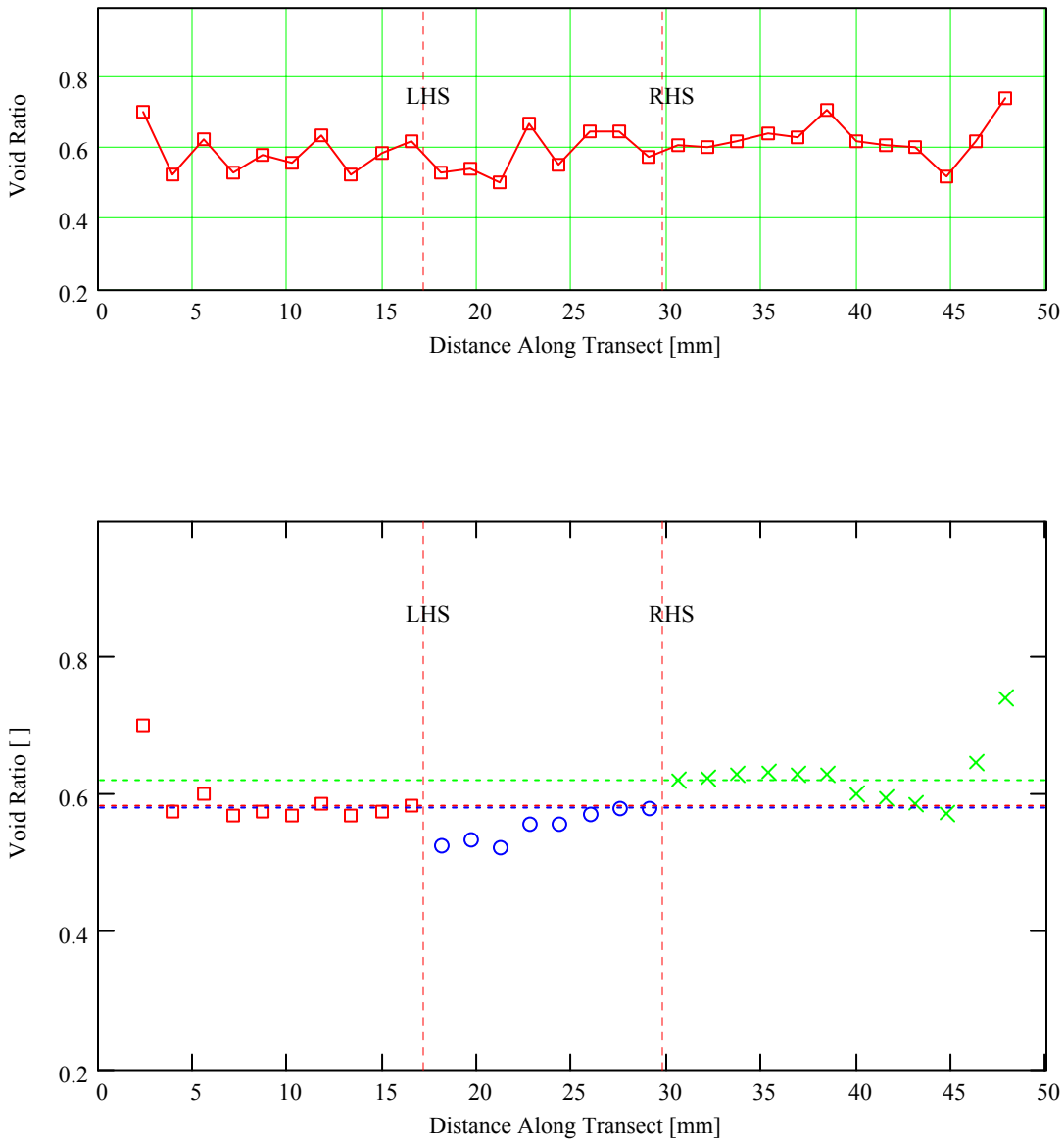

Figure 5.56: Incremental (top) and accumulated (bottom) void ratio transects for surface SDU-80 (LHS and RHS indicated inferred shear band extents; horizontal lines in accumulated void ratio plots indicate asymptotic values for each region)

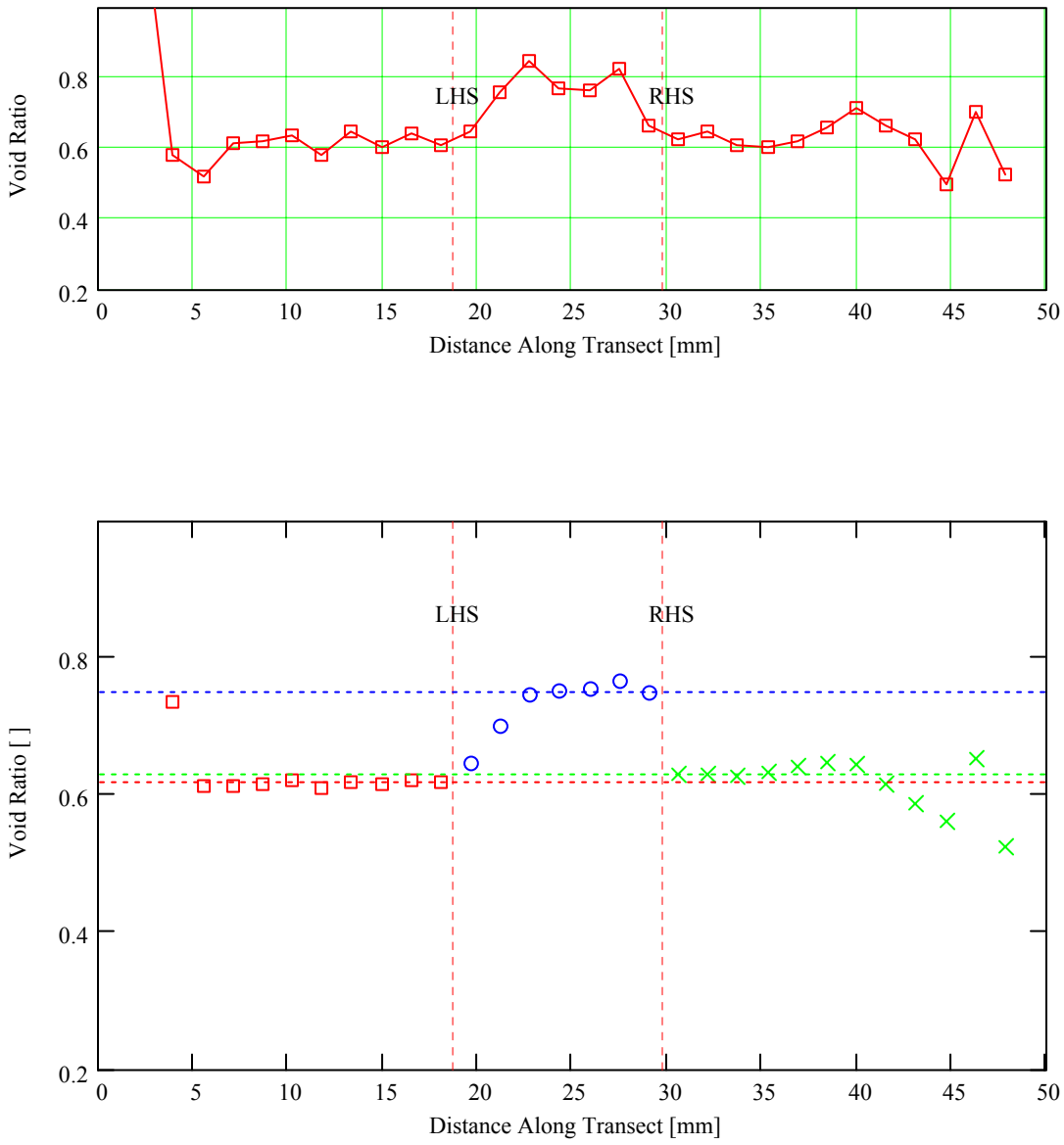

Figure 5.57: Incremental (top) and accumulated (bottom) void ratio transects for surface SDS-20 (LHS and RHS indicated inferred shear band extents; horizontal lines in accumulated void ratio plots indicate asymptotic values for each region)

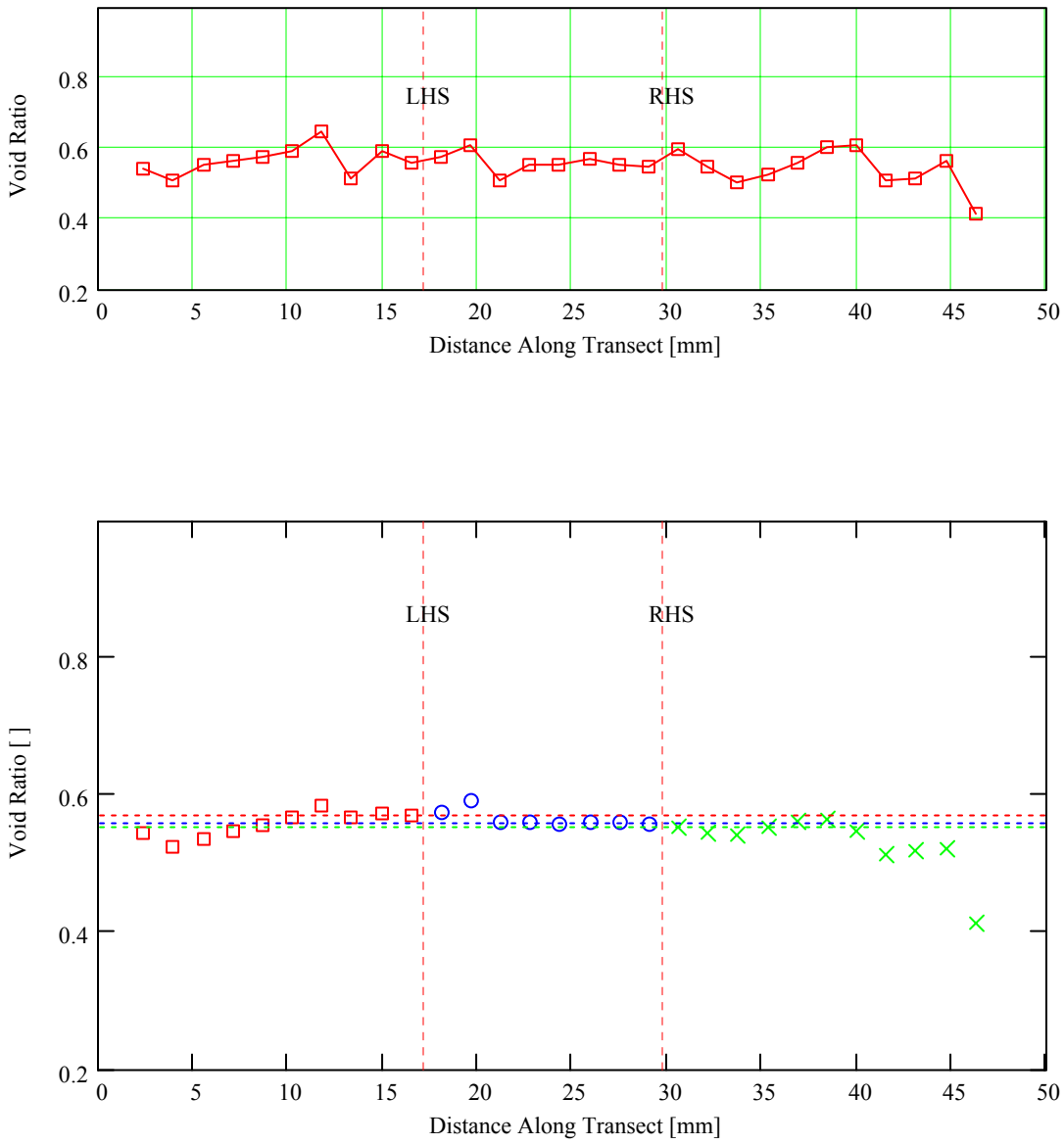

Figure 5.58: Incremental (top) and accumulated (bottom) void ratio transects for surface HDU-20 (LHS and RHS indicated inferred shear band extents; horizontal lines in accumulated void ratio plots indicate asymptotic values for each region)

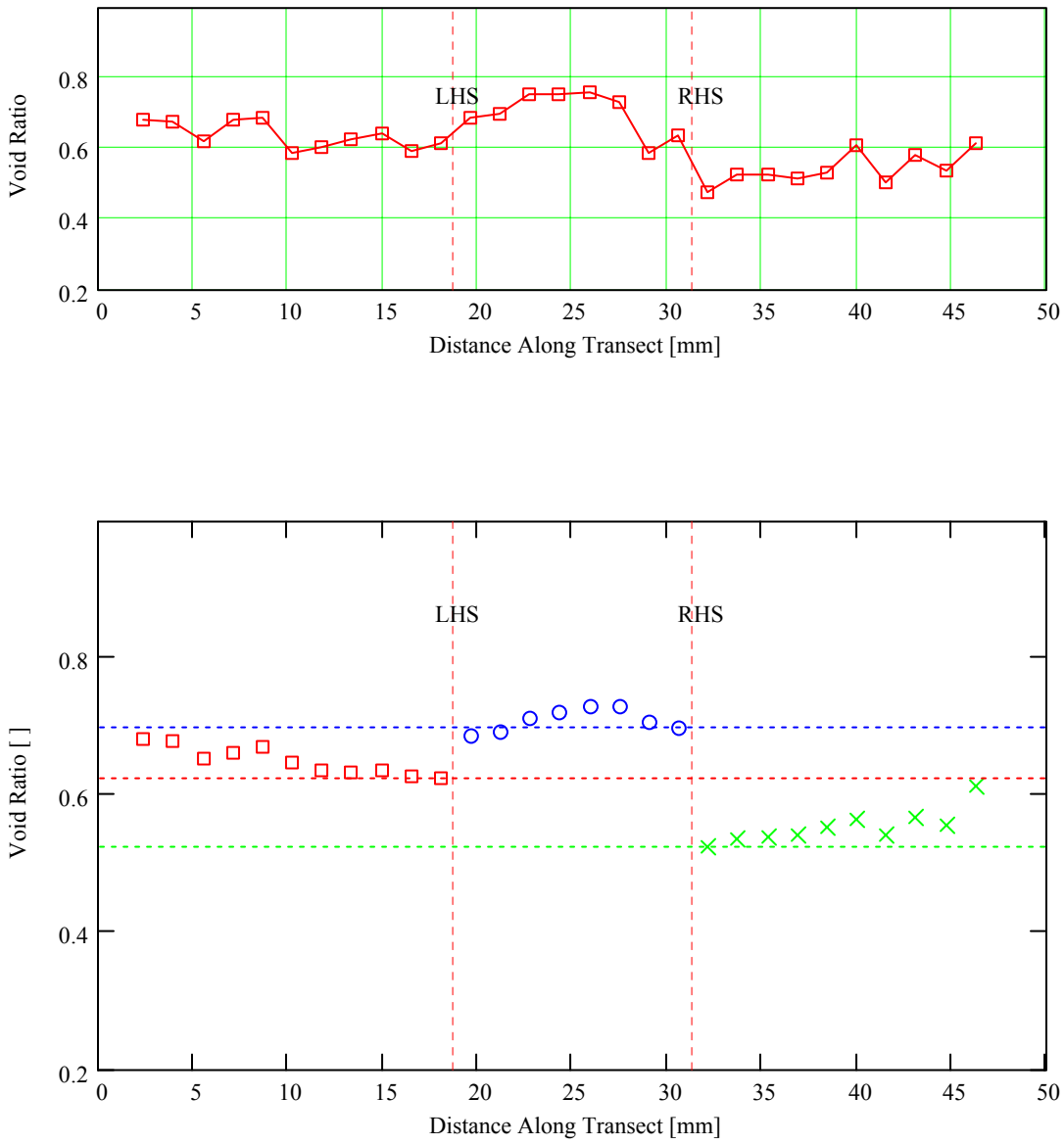

Figure 5.59: Incremental (top) and accumulated (bottom) void ratio transects for surface HDS-60 (LHS and RHS are inferred approximations from sheared specimens; horizontal lines in accumulated void ratio plots indicate asymptotic values for each region)

boundaries of the polygons used for local void ratio calculations are irregular, their inclusion in a given strip was based on the centroid of a given polygon. Thus, if a polygon centroid was within the delineation of a given strip, it was included, even if the majority of the polygon was outside of the strip boundaries (although it would be unlikely for this to occur). Once the local void ratio distribution histograms were calculated both inside and outside of the shear band, the means and standard deviations of those histograms were calculated for comparison to the overall mean and standard deviation for the entire surface. Local void ratio histograms for inside and outside of the shear bands in the two sheared specimens are presented in Figures 5.60 and 5.61. Detailed calculations for spatial averaging analysis of inclined strips are presented in Appendix A.5.

The internal and external local void ratio histograms indicate that local void ratios within the shear band increase dramatically relative to the local void ratios outside of the shear bands. As with the sheared versus unsheared specimens, the mean and standard deviation tend to increase within zones of localized shear, flattening the histogram and shifting it to the right.

5.4.6. Virtual Surface Analysis

As discussed in Section 2.3.4, in the case of a continuum-particulate interface, the roughness of the continuum surface has been shown to have a significant effect on the microscale behavior of the particulate material at the interface. From a localization standpoint, it has been shown that there are significant microscale similarities between continuum-particulate shear zones and free-forming shear bands within a particulate mass

(Frost et al., 2004). If a sand specimen is considered at a static instant (e.g., an image

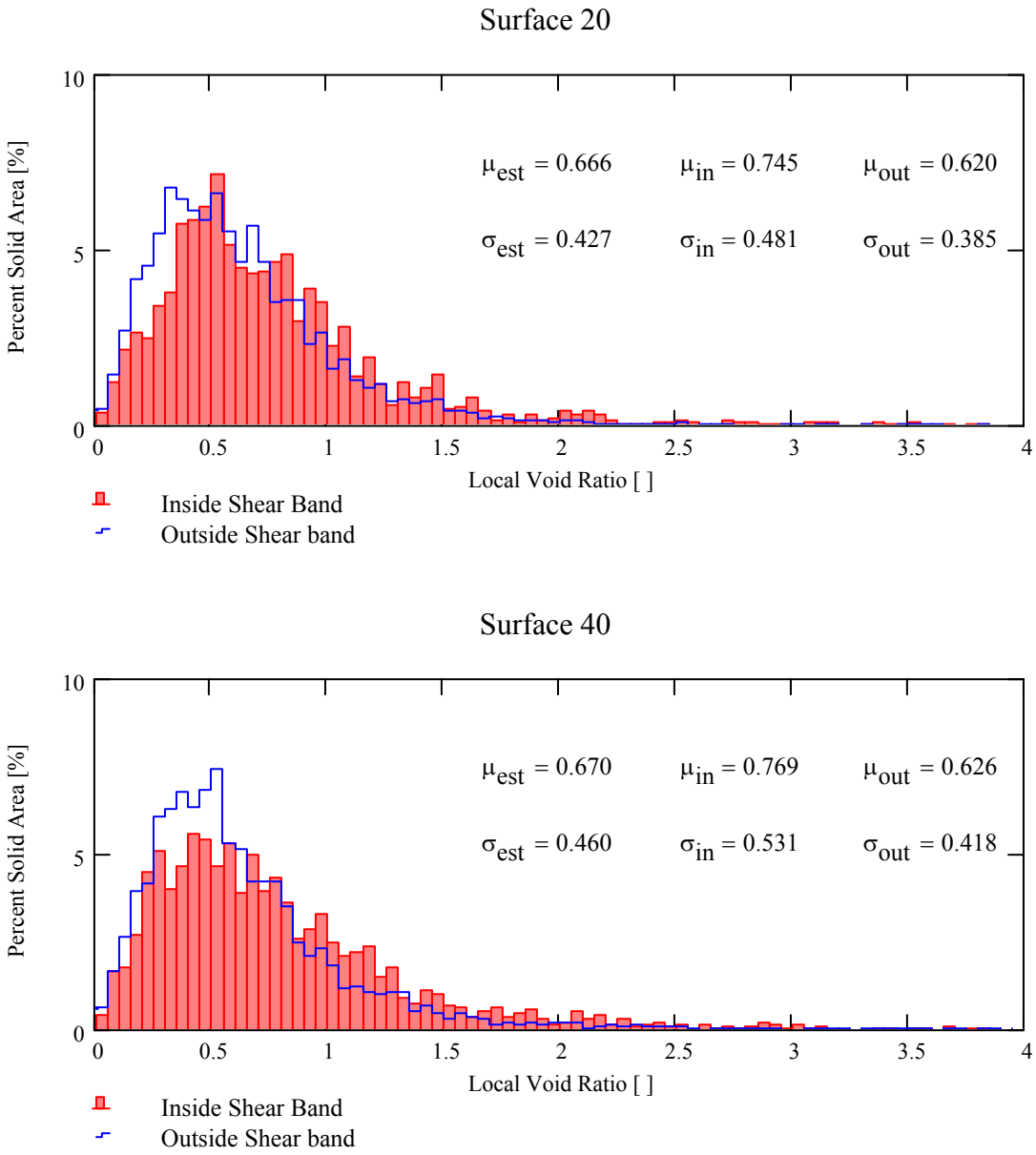

Figure 5.60: Internal and external void ratio histograms for the slightly dilatant specimen

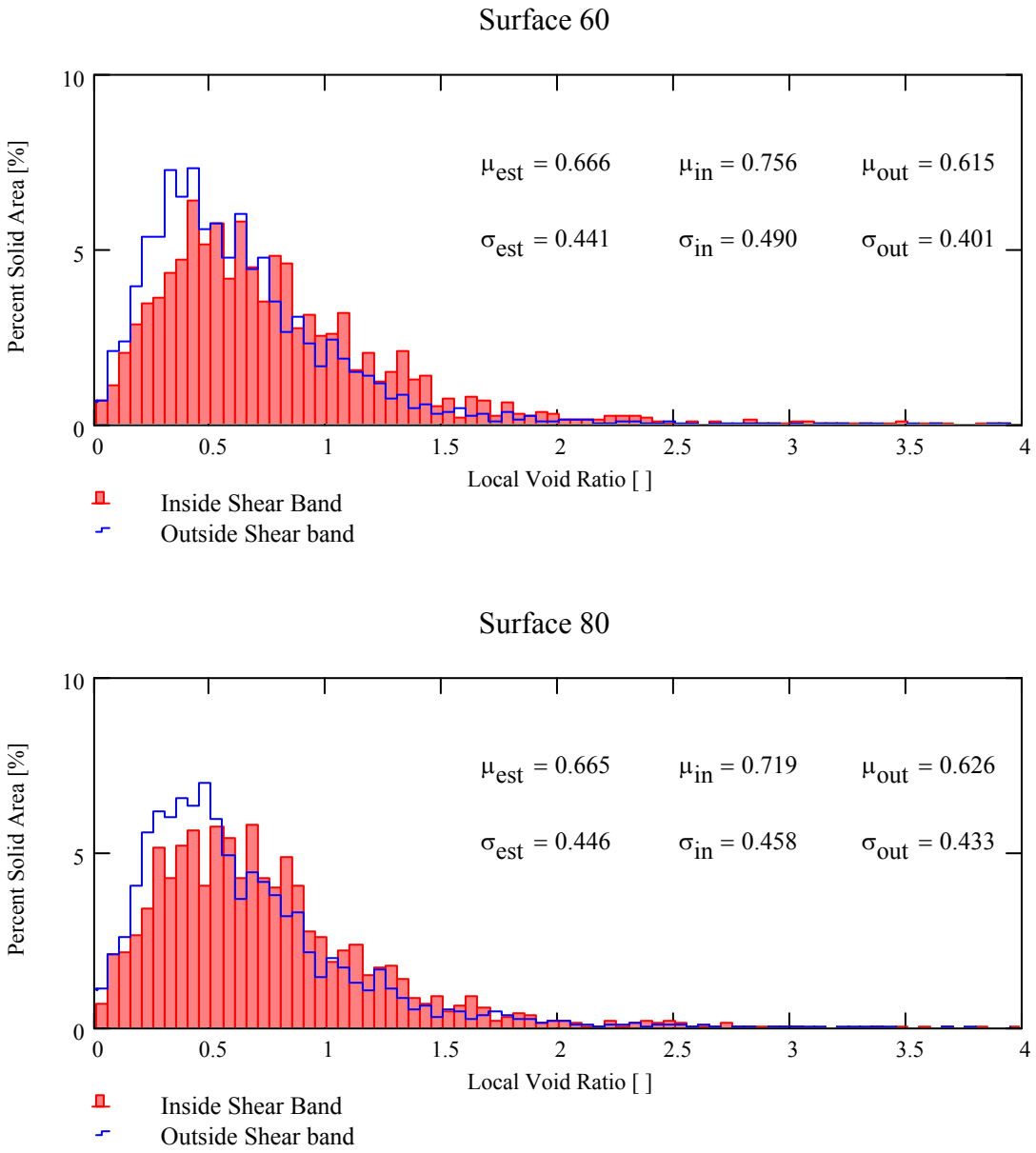

Figure 5.60 (cont.): Internal and external void ratio histograms for the slightly dilatant specimen

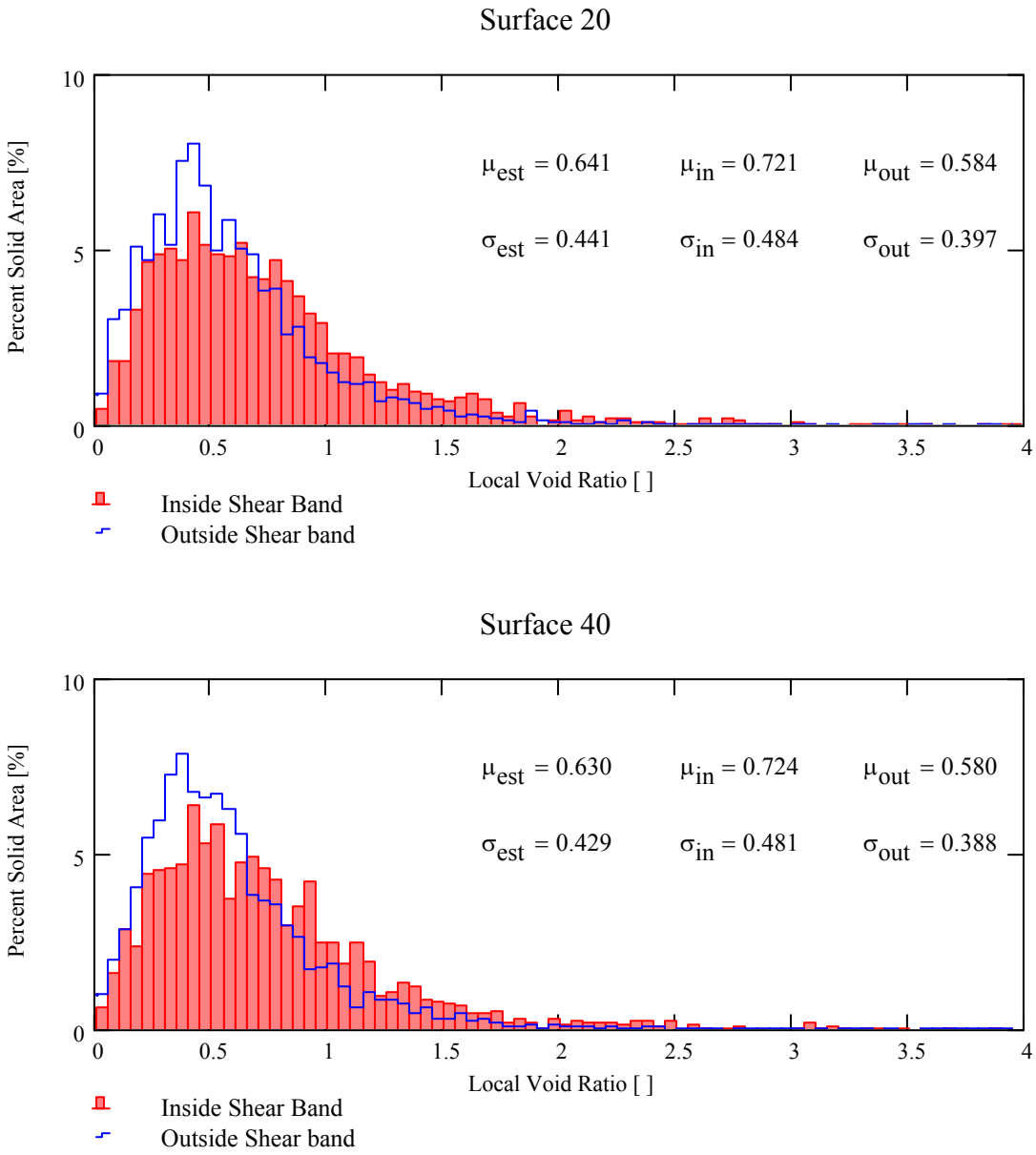

Figure 5.61: Internal and external void ratio histograms for the highly dilatant specimen

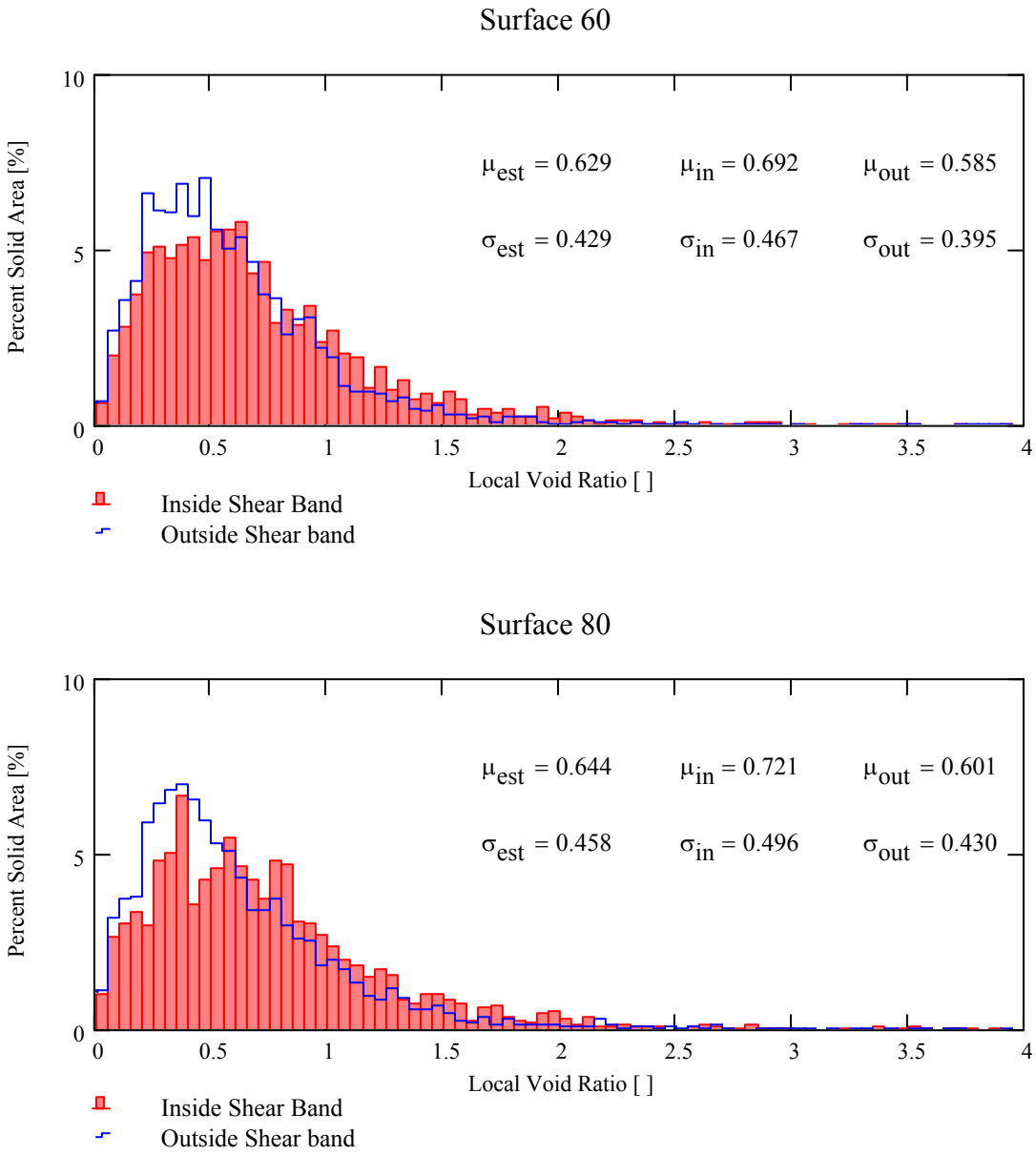

Figure 5.61 (cont.): Internal and external void ratio histograms for the highly dilatant specimen

taken from a solidified specimen), mathematical means can be used to construct "virtual surfaces" within the specimen. Given the effects of counterface surfaces on shear zone behavior, it is possible that the roughness parameters associated with these virtual surfaces could provide insight into the shearing characteristics of the specimen both inside and outside of the shear band.

Eleven virtual surfaces were generated for each surface of the four solidified specimens using a multistep approach. Surfaces were generated using the following steps:

- the binary image was rotated such that the shear band was horizontal;
- the image was re-binarized to eliminate the effects of the anti-aliasing that occurs during rotation (the binarization threshold was selected such that the global void ratio of the image before and after rotation were equal);
- eleven horizontal lines (each of one-pixel width) were laid across the image, with the center line approximating the center of the shear band;
- a burning algorithm, typically used for analysis of percolation (Garboczi, 2002), was used to identify all particles in contact with a given line (a burning algorithm identifies all pixels of the same color that are contiguous with a given pixel);
- the line and touching particles are exported to a separate image, which is then "cleaned up" to remove any secondary particles (i.e., particles that were touching a particle that was touching the line) (Figure 5.62);
- a "rubber sheeting" algorithm was developed to retain only the uppermost and lowermost pixels in any given column (this will prevent the

breakdown of some surface characterization algorithms that fail at concave surfaces and is physically realistic) (Figure 5.63);

- cubic splines are fit to the upper and lower surface of the rubber sheeted sand grains;
- the splines are traversed sequentially from left to right and their lengths are measured whenever they deviate from one another (i.e., when they diverge from the horizontal line) (Figure 5.64); and
- all shortest-path spline segments are retained to create a minimum energy path along the horizontal line and around the particles.

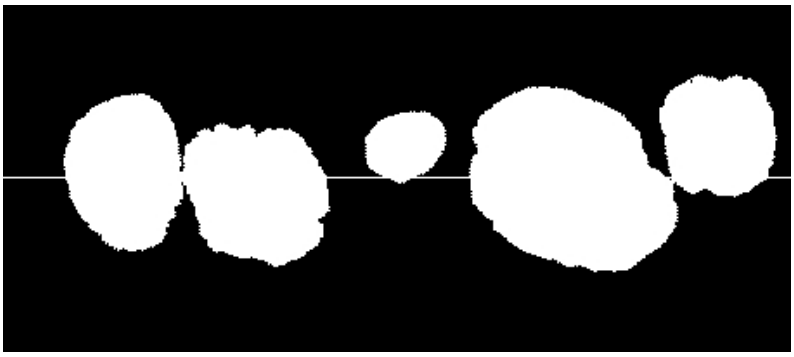

Figure 5.62: Initial particles and horizontal line used to form a virtual surface

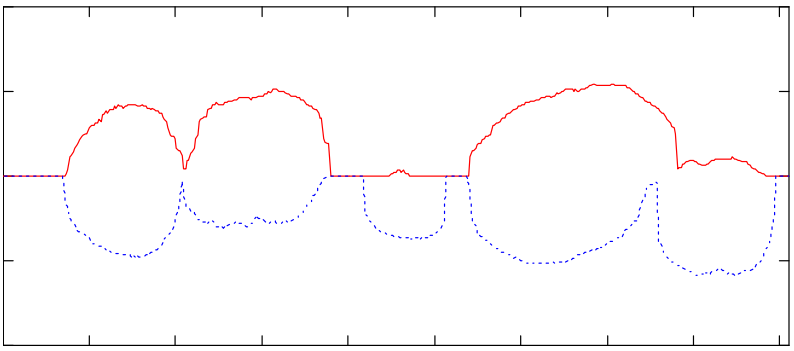

Figure 5.63: After the rubber sheeting algorithm is applied to the segment of the surface in Figure 5.62

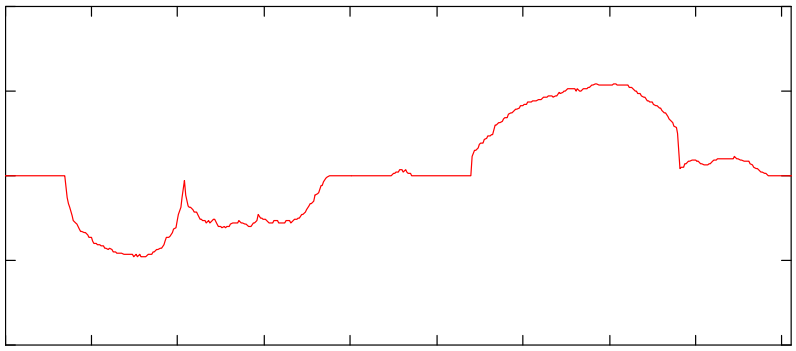

Figure 5.64: The minimum energy surface developed from the rubber sheets shown in Figure 5.63

Once the surfaces hade been generated, they were trimmed such that the length of all surfaces for a given specimen was equal. The trimming process was automated and consisted of removing an equal number of data points from the beginning and end of each profile. The surfaces were then characterized using six roughness parameters:

Average roughness:
$$R_a = \frac{1}{L} \cdot \int_0^L |z(x)| \, dx \tag{5.25}$$

Root mean square roughness:
$$R_q = \left(\frac{1}{L} \cdot \int_0^L z(x)^2 \, dx \right)^{\frac{1}{2}} \tag{5.26}$$

Profile roughness parameter:
$$R_L = \frac{L_0}{L} \tag{5.27}$$

Average slope:
$$\Delta_a = \frac{1}{L} \cdot \int_0^L \left| \frac{dz}{dx} \right| dx \tag{5.28}$$

Normalized roughness:
$$R_n = \frac{R_{max}}{d_{50}} \tag{5.29}$$

Total input energy: $$E = \frac{1}{2} \cdot \sum_{i} \left| z(x_i) - z(x_{i-1}) \right| \tag{5.30}$$

where L is the profile length, z(x) is profile elevation as a function of horizontal location, L_0 is actual profile length, and R_{max} is the largest peak-to-valley height over a length of d_{50} (mean particle diameter). Detailed descriptions of each of these parameters may be found in DeJong (2001). After calculating roughness parameters for all profiles in all surfaces, the parameters were averaged across surfaces (i.e., profile-1 for surfaces 20, 40, 60, and 80) to remove noise.

Roughness parameters were then plotted as a function of transect distance normal to the shear band. These plots are presented as Figures 5.65 and 5.66. The symbols "LHS" and "RHS" indicate shear band extents as determined from roughness parameter analysis. This was accomplished by identifying surfaces on either side of the shear band that had significantly different roughness values and placing a demarcation line between them. Figures 5.65 and 5.66 indicate that there is a significant decrease in virtual surface roughness inside of the shear band. This is likely due to an alignment of the long axis of particles along the shear plane at very high strains.

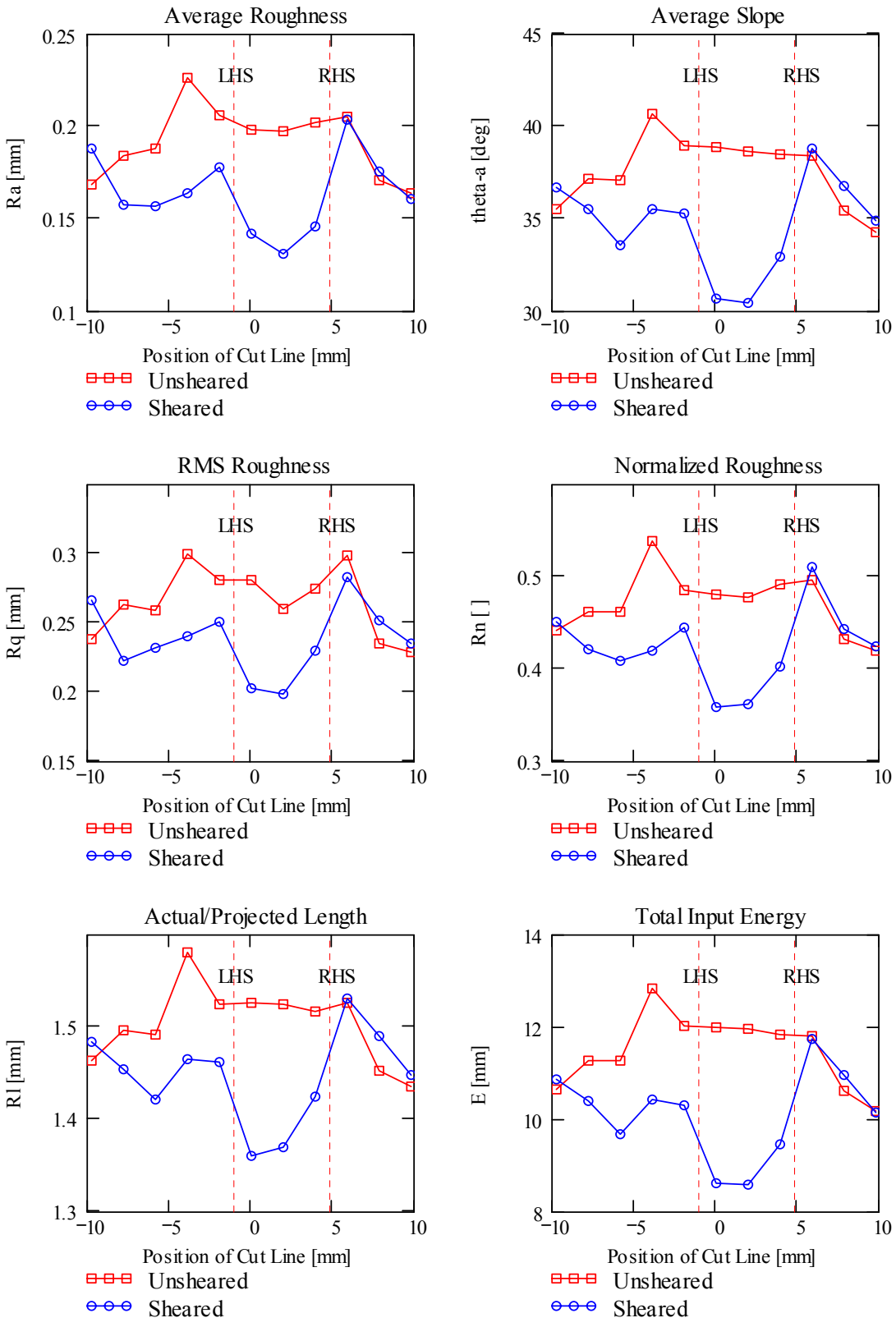

Figure 5.65: Roughness parameters for slightly dilatant specimens

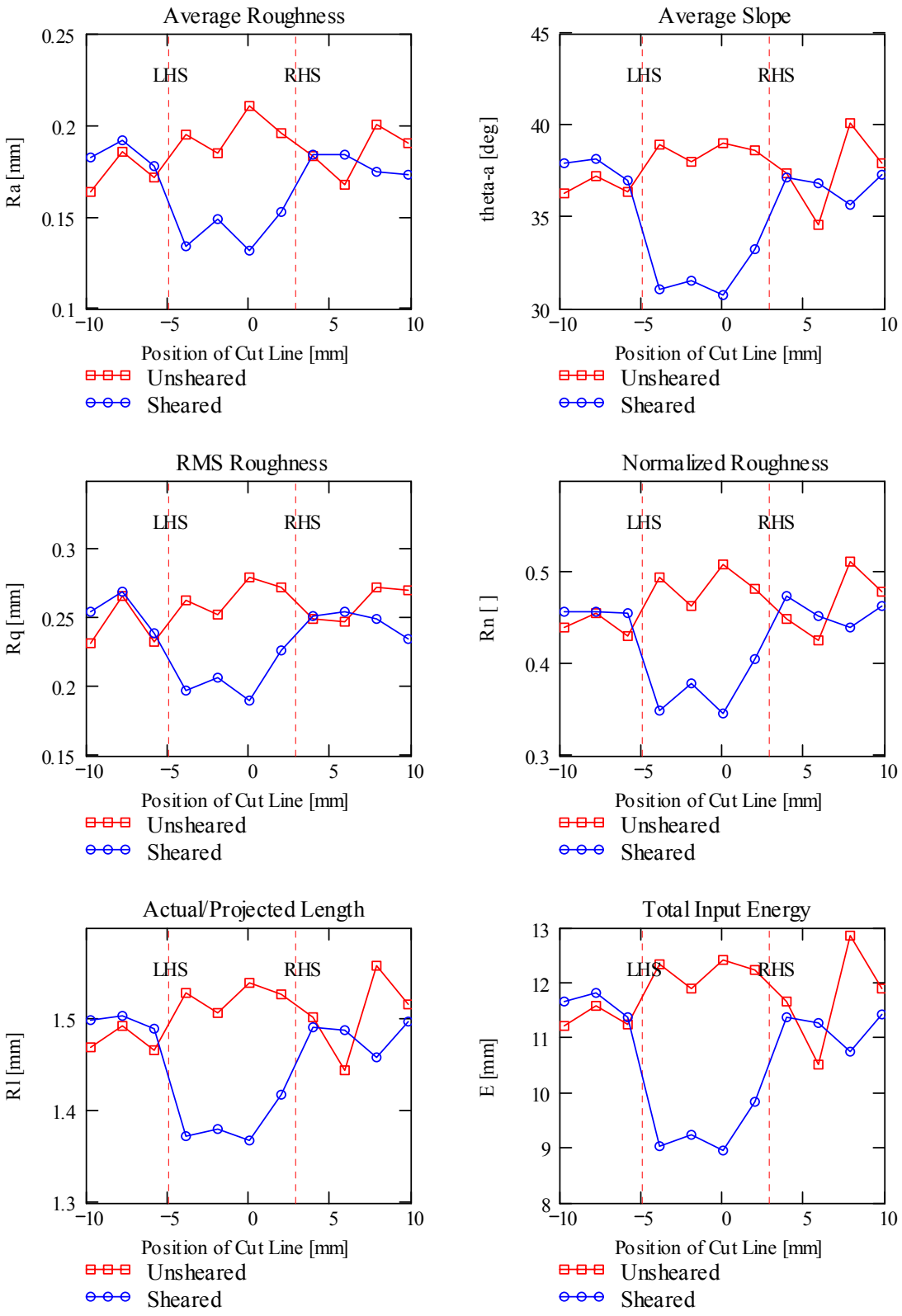

Figure 5.66: Roughness parameters for highly dilatant specimens

6. NUMERICAL MODELING PROGRAM

6.1. Discrete Element Method Modeling of Biaxial Compression

6.1.1. Introduction

The discrete element method program PFC-2D (Itasca, 2003) was used to model the micromechanical deformation response of particulate assemblies in two dimensions. A disadvantage of using laboratory experiments for the study of the micromechanics of soils is that detailed information about a specimen's microstructure is typically only available at one state in a test sequence due to the destructive nature of the forensic process. So, while it is possible to quantify microstructure at a state, it is difficult to quantify the evolution of microstructure in a given specimen. In the past, microstructure has been characterized on replicate specimens tested to various global axial strain levels (e.g., Frost and Jang, 2000), but this procedure presents practical and theoretical problems. From a practical standpoint, the testing and impregnation phase for the current experimental program can last for seven to nine days for a single specimen, so a series of replicate tests to different strain levels could easily take two months. The second drawback is that analyses are being performed on "identical" specimens, the microstructures in replicate specimens may be statistically similar, but the correlation is by no means exact. Thus, the numerical program undertaken as part of the current study is used to gain further insight into the microscale response of sand specimens without the need for laboratory testing of replicate specimens. The underlying assumption is that if a model is reasonably predicting the macroscale shearing response of a laboratory

specimen under one set of boundary conditions, then it is also reasonably predicting the microscale response of the specimen under those boundary conditions. The remainder of this chapter will focus on the description and analysis of the discrete element simulations conducted as part of the current study.

6.1.2. Membrane Confinement Algorithm

An overview of the algorithm sequence for the current numerical experiments was presented in Chapter 4. This overview discussed the need for several intermediate steps that are required numerically but not explicitly present in laboratory studies. One item of note was the need to remove the vertical walls which confine the specimen laterally and replace them with a chain of particles which represent the confining membrane. This section discusses why the membrane confinement is necessary and how it is implemented in this study.

As mentioned previously, PFC2D is capable of simulating two types of objects: balls and walls. Because walls are rigid, difficulty arises when attempting to model flexible confinement similar to that from a confining membrane. This is of particular concern when the particular phenomenon of concern is the development of strain localization. Cundall (1989) has shown that localizations occur naturally in discrete systems tested with periodic boundary conditions and subjected to direct shear. However, periodic boundary conditions are not appropriate for the simulation of biaxial compression and, thus, an alternative lateral boundary condition must be employed. Because large out-of-balance forces exist at the tips of shear bands (Vermeer, 1990), the boundary conditions at shear band daylights are of particular importance. Most previous

simulations using the discrete element method have used rigid walls (e.g., Rothenburg and Bathurst, 1992; Kuhn, 1999; Claquin et al., 2003), direct applied force to boundary particles (e.g., Bardet and Proubet, 1991; Bardet, 1994), or direct applied force to a string of membrane particles (Tannant and Wang, 2002) to provide lateral restraint to the assembly. Rigid wall boundaries, may prevent the full formation of shear bands by failing to conform with respect to the forces at shear band tips. Force controlled boundaries likewise pose difficulties because small particle reorientations can result in large changes in force, making equilibrium difficult to maintain. This problem increases in magnitude as deformations become large. In the current study, rigid walls are used to model the axial loading platens and strings of servo velocity-controlled bonded particles are used to simulate membrane confinement. An assembled specimen is shown in Figure 6.1.

Figure 6.1: Assembled DEM specimen prior to consolidation

Two types of particle bonding are possible in PFC2D: contact bonding and parallel bonding. In contact bonding, only separation of particles is inhibited while in parallel bonding, both separation and rotation of the two particles with respect to each other are inhibited. To allow the membrane to deform around the particle assembly, contact bonding only was used to assemble the membrane particle chains. Figure 6.2 shows a magnified view of a particle membrane conforming to particles in a biaxial assembly.

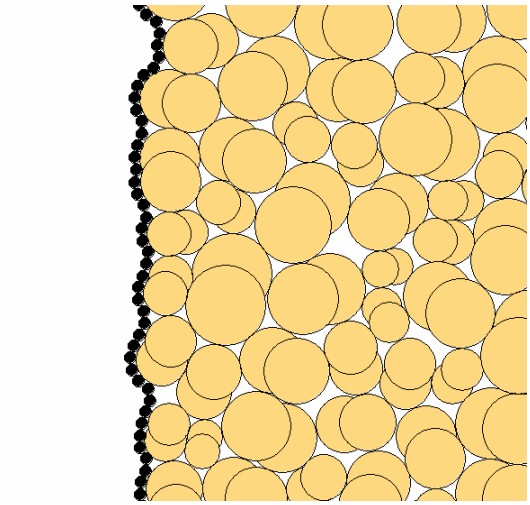

Figure 6.2: Magnified view of particle membrane conforming to particle assembly

The complexity associated with using a chain of particles to simulate a membrane arises from the fact that the membrane will need to change length (i.e., "stretch") over the course of a simulation. To overcome this problem, membrane endpoints (top and bottom) are closely monitored throughout the simulation. Once loading begins, the endpoint locations relative to the positions of the loading platens is checked at every time

step. If a membrane end particle is more than 1.5 particle diameters away from the platen (measured normal to the platen), then a new ball is added to the end of the membrane to decrease the gap between the membrane and the platen. Similarly, if a membrane endpoint is less than 0.5 particle diameter away from a platen (measured normal to the platen) then a ball is removed from the membrane end. In this manner, the membrane length is constantly adjusted to prevent particles from escaping the assembly and to prevent "bunching" of the membrane adjacent to a platen.

Membrane motion is velocity controlled using a numerical servo algorithm that constantly adjusts the velocity of the membrane particles based on a gain parameter that is calculated based on the number of contacts at the membrane, the stiffness of those contacts, and the value of the current time step. This is similar to a procedure outlined by Itasca (2003) for servo controlled motion of walls. The gain parameter is multiplied by the difference between the average stress on the membrane and the desired confining stress for the simulation to determine the magnitude and direction of the required velocity for the membrane. The membrane on each side of the specimen is monitored separately.

6.1.3. Parametric Analysis of Constitutive Parameters

As stated previously, the goal of the modeling effort presented herein was to provide additional insight into the micromechanics of shear bands in conjunction with laboratory tests. In order to do this it is first necessary to develop a set of material constitutive parameters that result in model behavior that closely mimics laboratory results on a global scale. To this end, a series of parametric analyses were performed to qualitatively assess the effects of changing microscale constitutive properties on

macroscale specimen response. These sets of parametric analyses were not intended to provide any quantitative insight into specimen response and were not performed using the material properties outlined below for comparison with laboratory experiments. Rather, the simulations were performed using a generic model setup for biaxial simulations and were intended to provide general insight into material response. Thus, the results presented for the parametric analyses are not necessarily directly comparable to the modeling results presented below for comparison with laboratory experiments.

The first series of parametric simulations were performed to investigate the effects of particle normal stiffness on material response. As discussed in Chapter 4, the normal force at particle contacts is proportional to the contact normal stiffness:

$$F^n = K^n \cdot U^n \tag{4.4}$$

where F^n is normal force at the contact, K^n is contact normal stiffness, and U^n is particle overlap at the contact. Three simulations were performed using three different contact normal stiffnesses: low, medium, and high. All other parameters were kept constant. Results from these simulations are presented in Figure 6.3.

It is apparent from Figure 6.3 that increasing particle stiffness results in increased initial tangent modulus, increased strength, a greater degree of post-peak softening, and greater dilation during shear. Intuitively, these results are expected given the dependence of the stiffness of the assembly on the stiffness of the contacts and the fact that particles with higher contact stiffnesses can be considered to be more "repulsive" than those with lower normal stiffnesses.

A second set of parametric analyses was performed to assess the effects of particle friction coefficients. Again, three different particle coefficients were used: low,

medium, and high. Results of these simulations are presented in Figure 6.4 and indicate that peak strength, dilation, and degree of softening all increase with increasing particle friction coefficients. The large strain strengths are comparable. The final series of parametric simulations on constitutive properties was performed to assess the influence of contact shear stiffness on model behavior. These results are presented in Figure 6.5. The effect of shear stiffness is quite pronounced and manifests itself in terms of model instabilities with respect to stress-strain behavior. At high shear stiffness, there is a large displacement once slip occurs at a contact, leading to large rearrangements on particles. With low shear stiffness, there is very little movement after slip, which can lead to stick-slip behavior as particle movement is frustrated. Varying shear stiffness has very little effect on calculated dilation.

A final set of parametric simulations was performed to assess the effects of initial particle locations on specimen behavior. As discussed previously, specimens are generated one particle at a time in random locations. These random locations are affected by the seed value given to the random number generator at the beginning of each simulation (this allows simulations to be repeated exactly even though particle locations are random). These results are presented in Figure 6.6. These results indicate that the model is relatively stable for different initial particle locations.

6.1.4. Comparison with Macroscale Laboratory Results

In order to draw comparisons between laboratory and numerical micromechanics, the macroscale response of the specimens should be similar. It is difficult to simulate laboratory response exactly for several reasons, including the dimensionality of the model

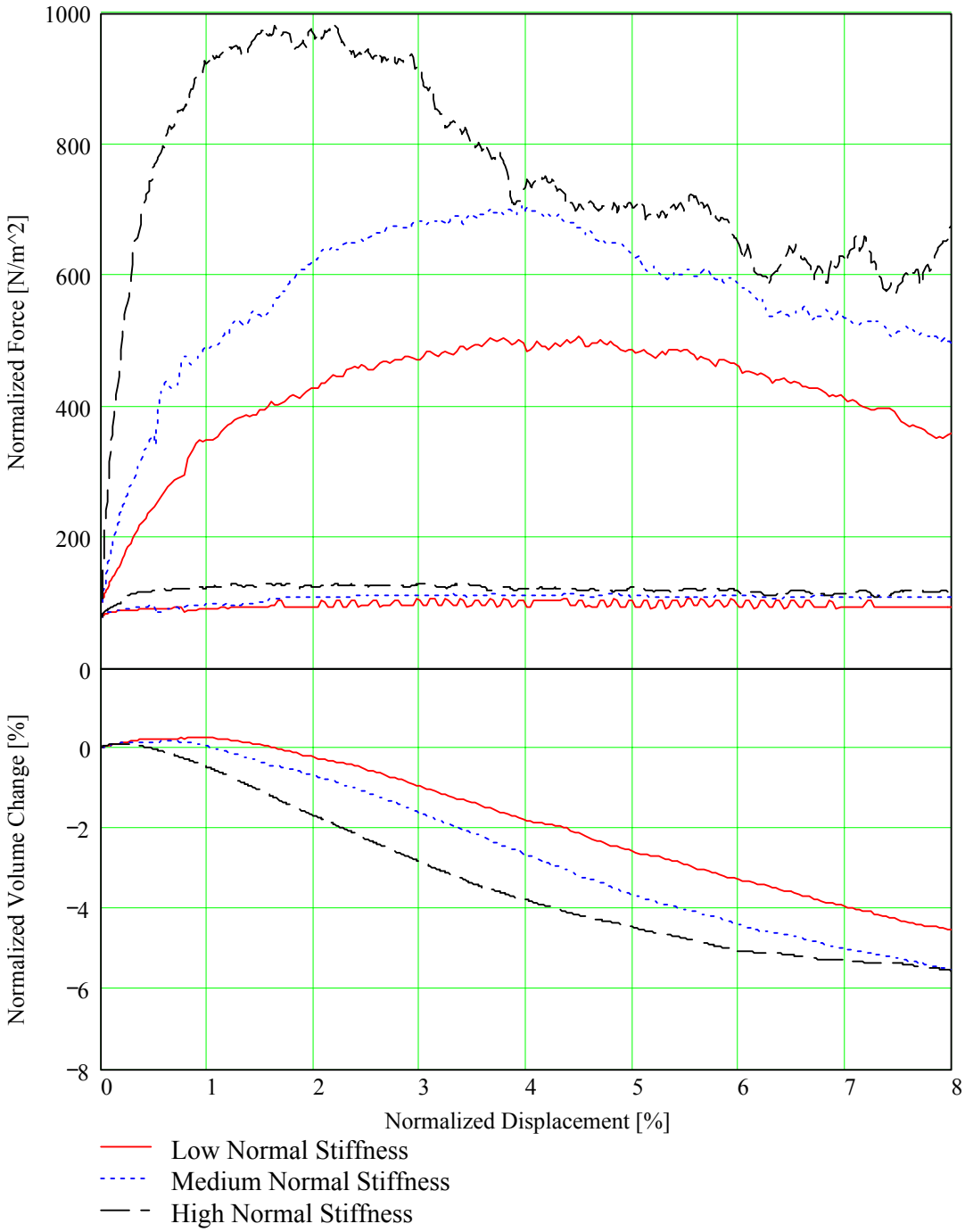

Figure 6.3: Normalized axial and confining force (upper plot) and normalized volume change (lower plot) for parametric analyses on the effects of contact normal stiffness

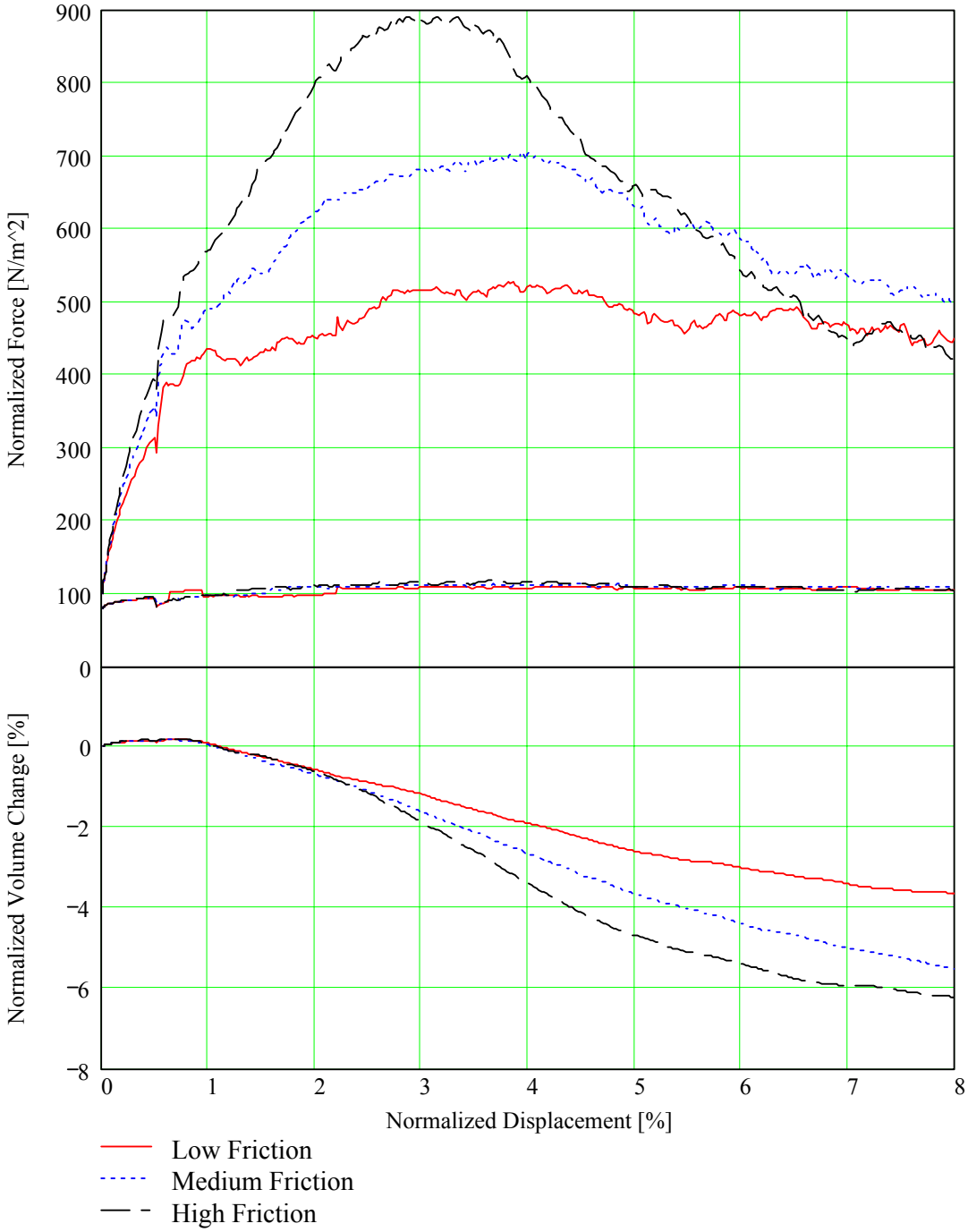

Figure 6.4: Normalized axial and confining force (upper plot) and normalized volume change (lower plot) for parametric analyses on the effects of contact friction coefficient

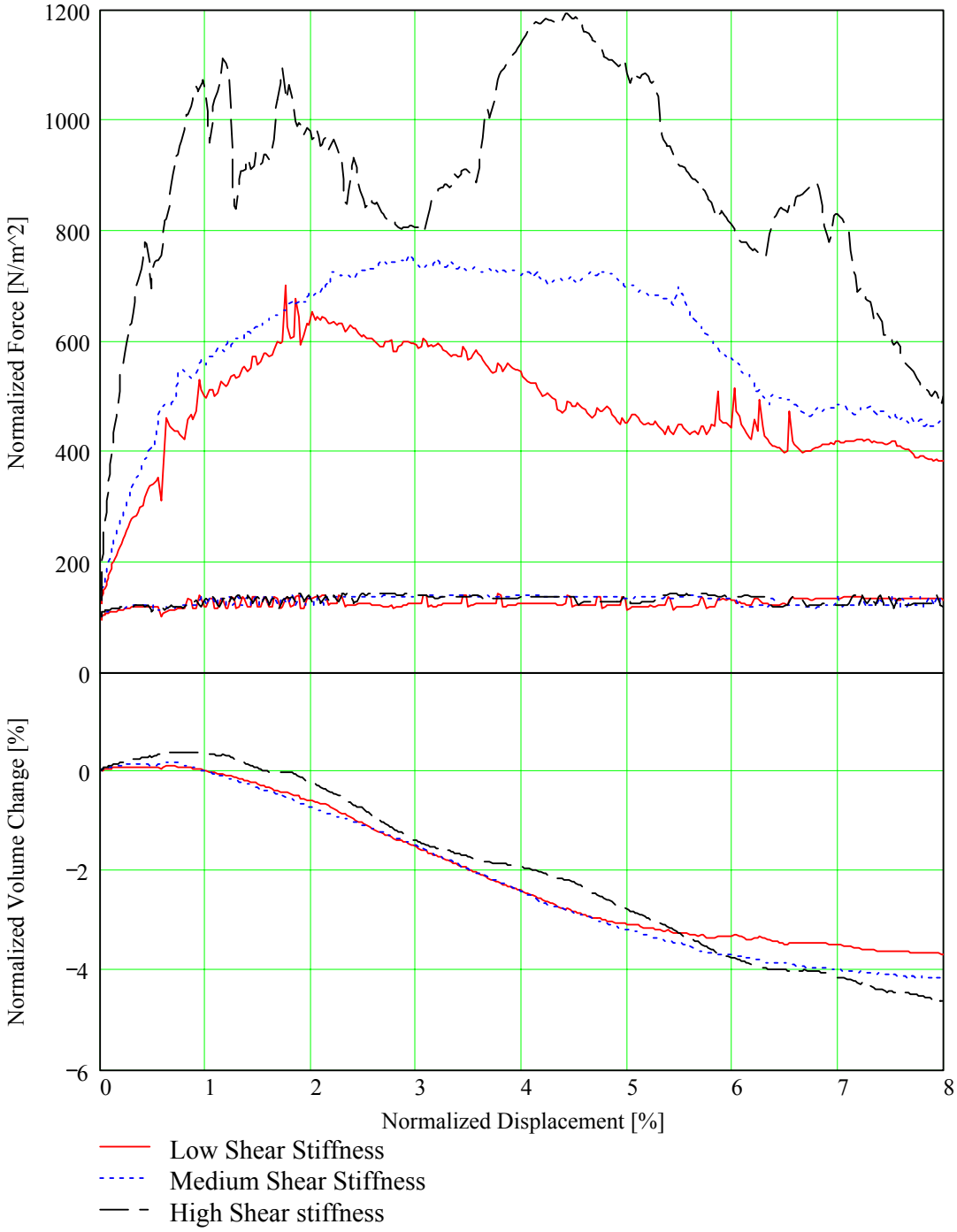

Figure 6.5: Normalized axial and confining force (upper plot) and normalized volume change (lower plot) for parametric analyses on the effects of contact shear stiffness

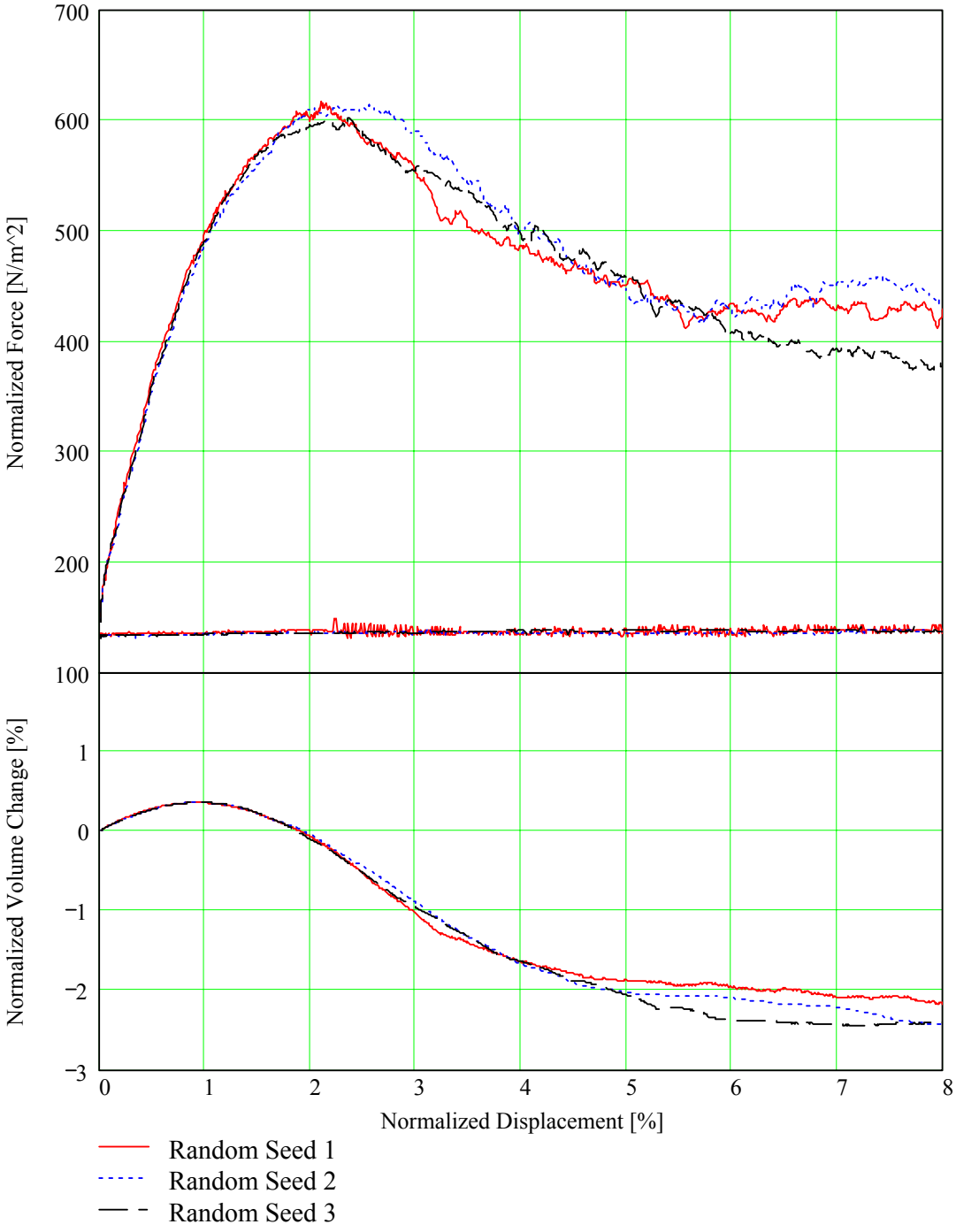

Figure 6.6: Normalized axial and confining force (upper plot) and normalized volume change (lower plot) for parametric analyses on the effects of seed values in the random number generator

(2D vs. 3D), irregular shape of soil grains, variations of grain packing in experimental specimens, and numerical error. However, given a fundamentally correct model and a knowledge of the effects of various microscale parameters on macroscale response, it is possible to generate a model that reasonably simulates the macroscale response of laboratory specimens. The material parameters employed in the current study are presented in Table 6.1. In Table 6.1, "n/a" indicates that reference values were not readily available. The reference friction value is based on results from experiments wherein a quartz sand grain was sheared against a polished quartz plane in a dry state.

Table 6.1: Material properties for PFC-2D simulations

Parameter	Numerical Simulations	Physical Comparison	Reference
Particle normal stiffness	10^8 N/m	4×10^6 N/m	(Santamarina et al., 2001)
Particle shear stiffness	10^7 N/m	n/a	n/a
Particle friction coefficient	0.31	0.31	(Proctor and Barton, 1974)
Particle specific gravity	2.65	2.65	(Yang, 2002)
Platen stiffness	10^8 N/m	n/a	n/a
Membrane stiffness	10^7 N/m	500 N/m	(Frost, 1989)
Platen/membrane friction coefficient	0.31	n/a	n/a
Membrane specific gravity	1.50	1.10	(MatWeb, 2005)

The reference normal stiffness value was calculated assuming a Hertzian contact using the following equation (Santamarina et al., 2001):

$$\delta = \frac{1}{2 \cdot R^{\frac{1}{3}}} \cdot \left[\frac{3 \cdot \left(1 - \nu_g\right)}{G_g} \cdot N \right]^{\frac{2}{3}} \tag{6.1}$$

where δ is displacement, R is particle radius (0.05 m), ν_g is the Poisson's ratio for a single grain (0.31), G_g is the shear modulus for a single grain (29 GPa), and N is applied normal force. Because PFC-2D uses the initial tangent modulus in calculating normal displacements at contacts, the slope of this function at a load of 1 N is presented in Table 6.1. It should be noted that because bonded particles (i.e., the membranes) are used in the simulation, a linear contact algorithm was required (PFC-2D only supports Hertzian contacts in simulations with unbonded particles). Thus, there is some error associated with using this method for determination of particle normal stiffness. In cases where the values used for numerical simulation deviate from the reference values, this was either to provide numerical stability (membrane properties) or to more closely model system response in the laboratory (particle properties). Comparisons of laboratory and numerical results are presented in Figures 6.7 and 6.8. The stress-strain plots agree quite well, but the numerical simulation tends to overpredict dilation in both cases. This is due to the two-dimensional nature of the numerical model. As a real soil specimen is sheared, each particle has six degrees of freedom whereas a particle in a two-dimensional DEM simulation has only three degrees of freedom. It is therefore more difficult for particles to rearrange themselves in two dimensions, leading to greater dilatancy in shear. This is further evidenced by the values of friction and dilation angles presented in Table 6.2, which indicate that there is better agreement between experimental and numerical results with respect to friction angles than dilation angles. However, as with

the experimental results, the Arthur, et al. (1977) prediction of shear band inclination (which includes the angle of dilatancy at peak) provides the best agreement with the measured inclination of the shear band.

Consistent with Chapter 5, two numerical specimens were simulated corresponding to a slightly dilatant and highly dilatant state at different confining stresses: 20 psi (138 kPa) and 10 psi (69 kPa), respectively. This was done to encourage greater dilation in the denser specimen. An attempt was made to recreate these conditions in the two-dimensional numerical specimens. However, because particles must percolate in two dimensions (for stability), there is only a very narrow (unique?) range of stable initial porosities for a given combination of confining stress, particle shape, and particle size distribution. For the slightly dilatant numerical specimen, an initial porosity of 0.14 was used, but this value had decreased to 0.1394 immediately prior to the initiation of deviatoric loading. Similarly, an initial porosity of 0.13 was used for the highly dilatant specimen, but this value had increased to 0.1416 immediately prior to the initiation of deviatoric loading. Thus, while initial confining stress variations were carried over from the experimental to the numerical specimens (see Figures 6.7 and 6.8), the initial densities of the two specimens relative to each other did not vary. Nonetheless, the numerical simulations will be referred to as "slightly dilatant" and "highly dilatant", depending on the laboratory specimen to which they are referenced throughout the remainder of this document (Figures 6.7 and 6.8 and Table 6.2 also indicate that the "highly dilatant" numerical specimen is more dilatant than the "slightly dilatant" numerical specimen). It is apparent that initial specimen porosity is largely a function of confining stress in DEM simulations.

It can be seen from Figures 6.7 and 6.8 that both numerical specimens reach peak strength at approximately 2% global axial strain. The sensitivities of the two specimens (between peak and 10% global axial strain) are 1.6 and 2.0 for the slightly dilatant and highly dilatant specimens, respectively.

Table 6.2: Summary of friction, dilation, and shear band inclination angles for slightly dilatant and highly dilatant experimental (E) and numerical (N) specimens

Test Designation	ϕ_p	ψ_p	ϕ_{cs}	ϕ_s	ψ_{cs}	θ_e	θ_C	θ_R	θ_A
SD (E)	38.8°	8.8°	27.7°	27.7°	1.0°	59°	64°	49°	57°
SD (N)	39.5°	16.7°	28.3°	28.2°	3.0°	57°	65°	53°	59°
HD (E)	41.8°	11.5°	27.9°	27.9°	0.2°	61°	66°	51°	58°
HD (N)	42.8°	9.5°	27.8°	27.8°	3.8°	58°	66°	50°	58°

6.2. Microstructure Analyses

6.2.1. Introduction

The microstructures of the DEM specimens were analyzed using the methods outlined in Chapter 5 for laboratory specimens. Performing microstructure analyses on numerical specimens has the added advantage of allowing for the observation of evolving patterns in the microstructure as a function of induced shear. The microstructure of the DEM specimen was captured at 0%, 2%, 4%, 6%, 8%, and 10% global axial strain and used for the subsequent analyses. Images at each of these strain levels are presented in Figures 6.9 and 6.10 for the slightly dilatant and highly dilatant specimens, respectively. It is apparent from these images that localization initiates prior to 4% of global axial strain (and possibly as early as 2%, near the peak stress) and that the localization becomes more diffuse at increasing axial strain, with families of shear bands forming.

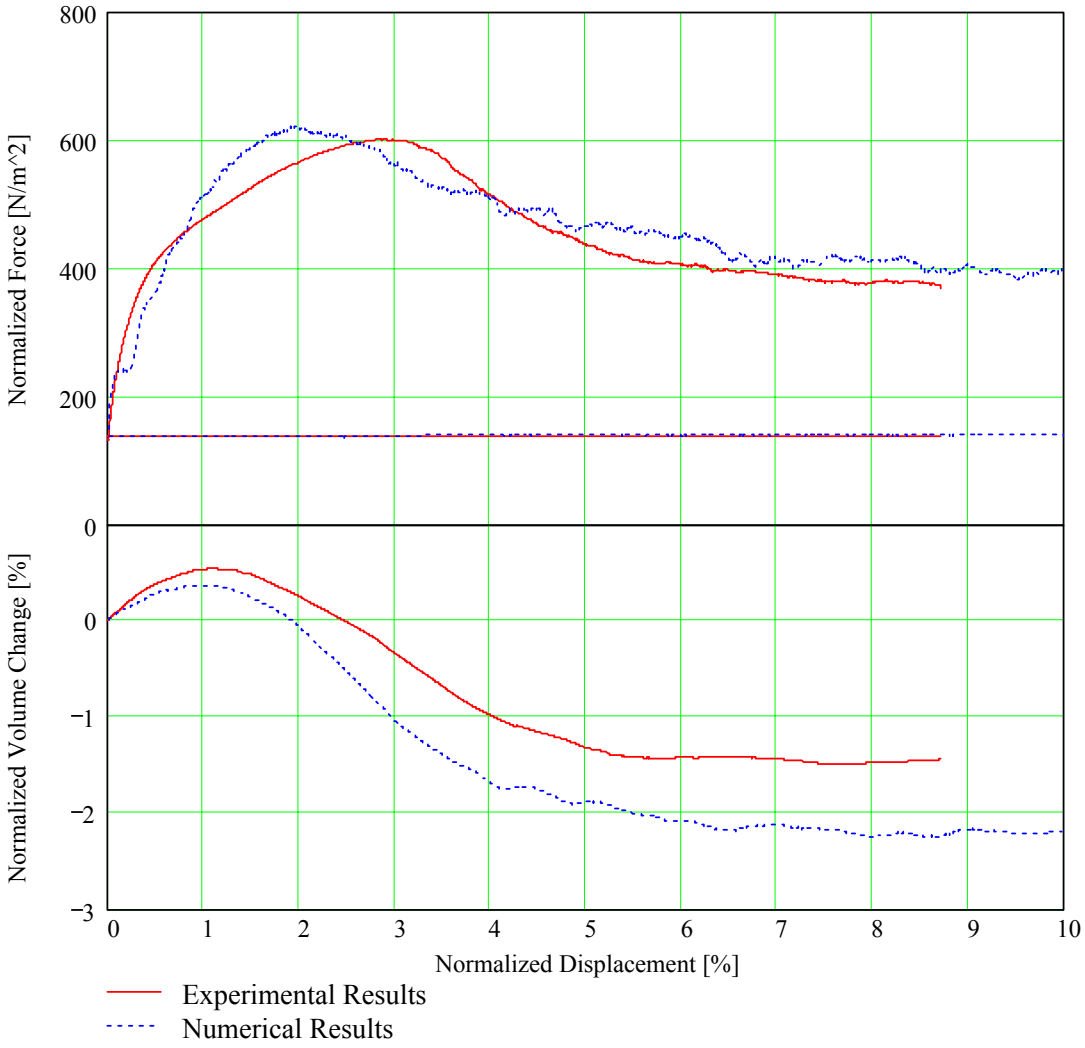

Figure 6.7: Normalized axial and confining force (upper plot) and normalized volume change (lower plot) for slightly dilatant specimen and corresponding numerical simulation

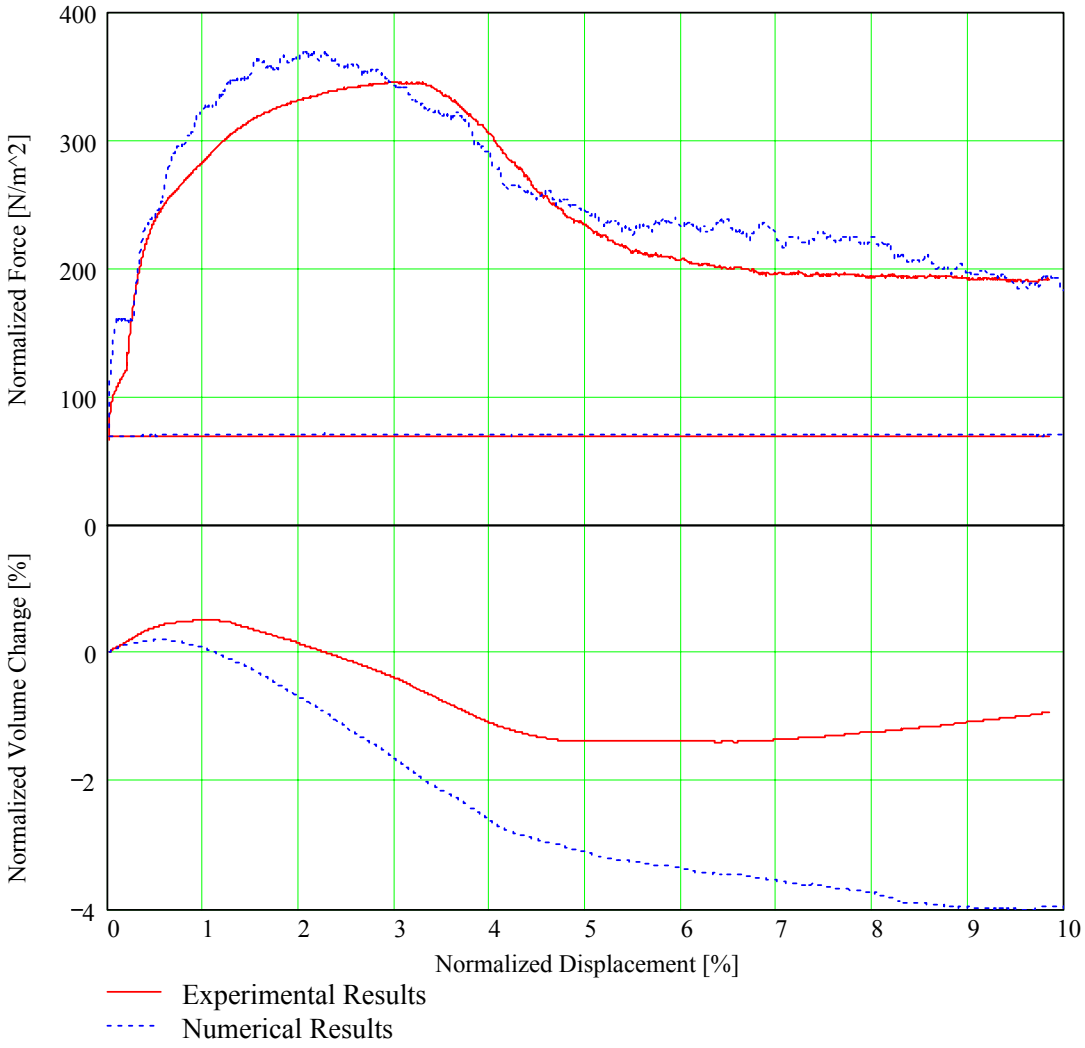

Figure 6.8: Normalized axial and confining force (upper plot) and normalized volume change (lower plot) for highly dilatant specimen and corresponding numerical simulation

The following sections will discuss results of local void ratio analyses, subregional void ratio analyses, subregional mean free path analyses, and inclined strip analyses. The calculation procedures are identical to those presented in Chapter 5, except as noted.

6.2.2. Subregional Void Ratio and Mean Free Path Analyses

The images of model microstructure were cropped to an area of 3200 pixels wide by 1600 pixels tall, which represents 10.4 m by 5.2 m in model space (recall from Chapter 4 that initial specimen dimensions were 12 m by 6 m). Cropping eliminates the white space in the image around the specimen and allows for analysis of equal size images at each strain level. A window 160 pixels square was used to calculate void ratio and mean free path on a 10 by 20 grid within the cropped images. Contour plots of these results, where the void ratio and mean free path values are plotted at the center of each window, are presented in Figures 6.11 through 6.14.

These figures indicate an initial dominant shear band initiates prior to 4% global axial strain and propagates from the lower right corner of the specimen to the upper left corner of the specimen in both cases. This initial major shear band is soon followed by other diffuse localizations, as also evidenced in Figures 6.9 and 6.10. The inclined strip and local void ratio analyses that follow consider the initial dominant shear band to be "the shear band" in the specimen for purposes of identifying the location of the major localizations and the orientation of inclined strips.

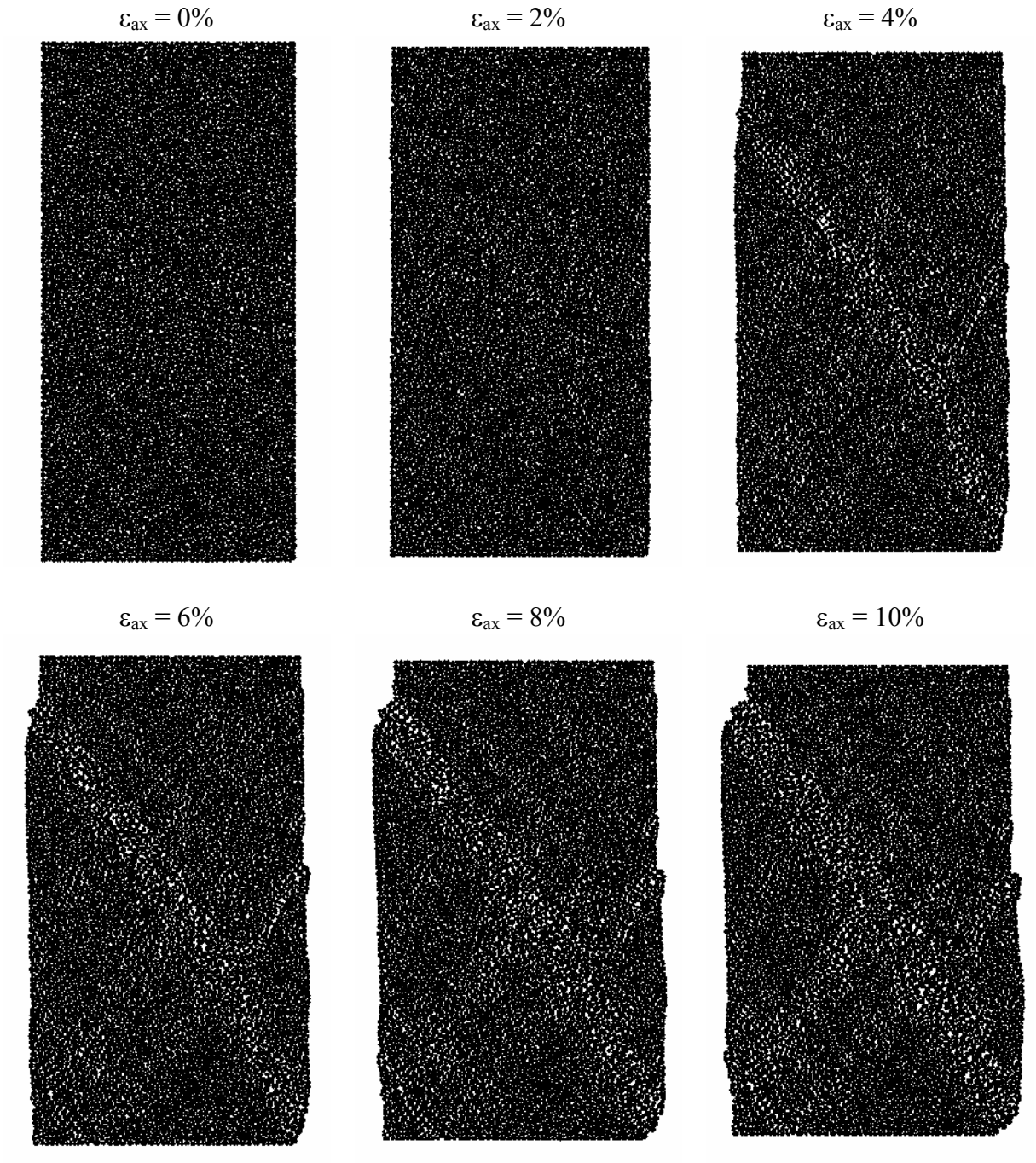

Figure 6.9: Slightly dilatant specimen images at various levels of global axial strain

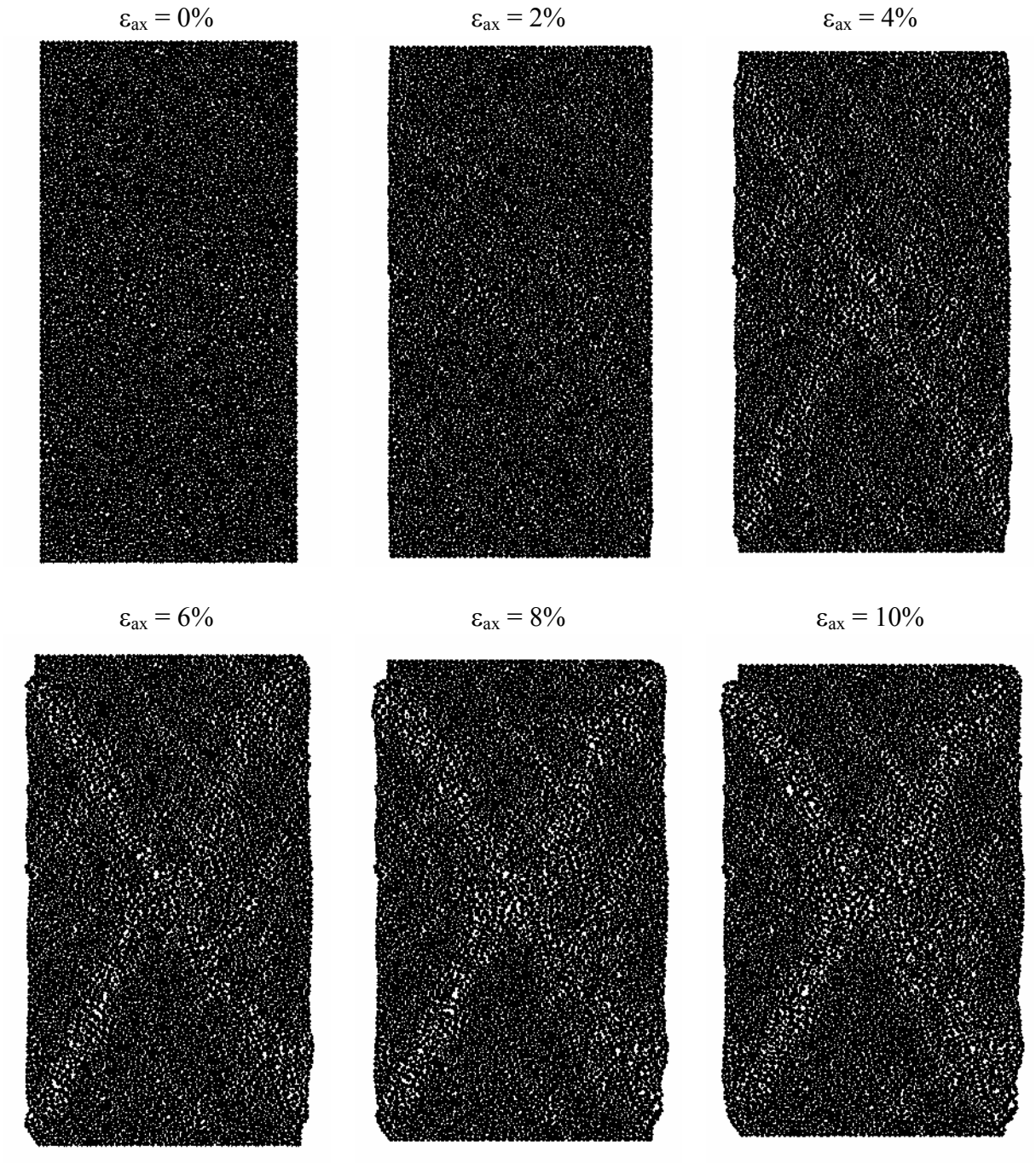

Figure 6.10: Highly dilatant specimen images at various levels of global axial strain

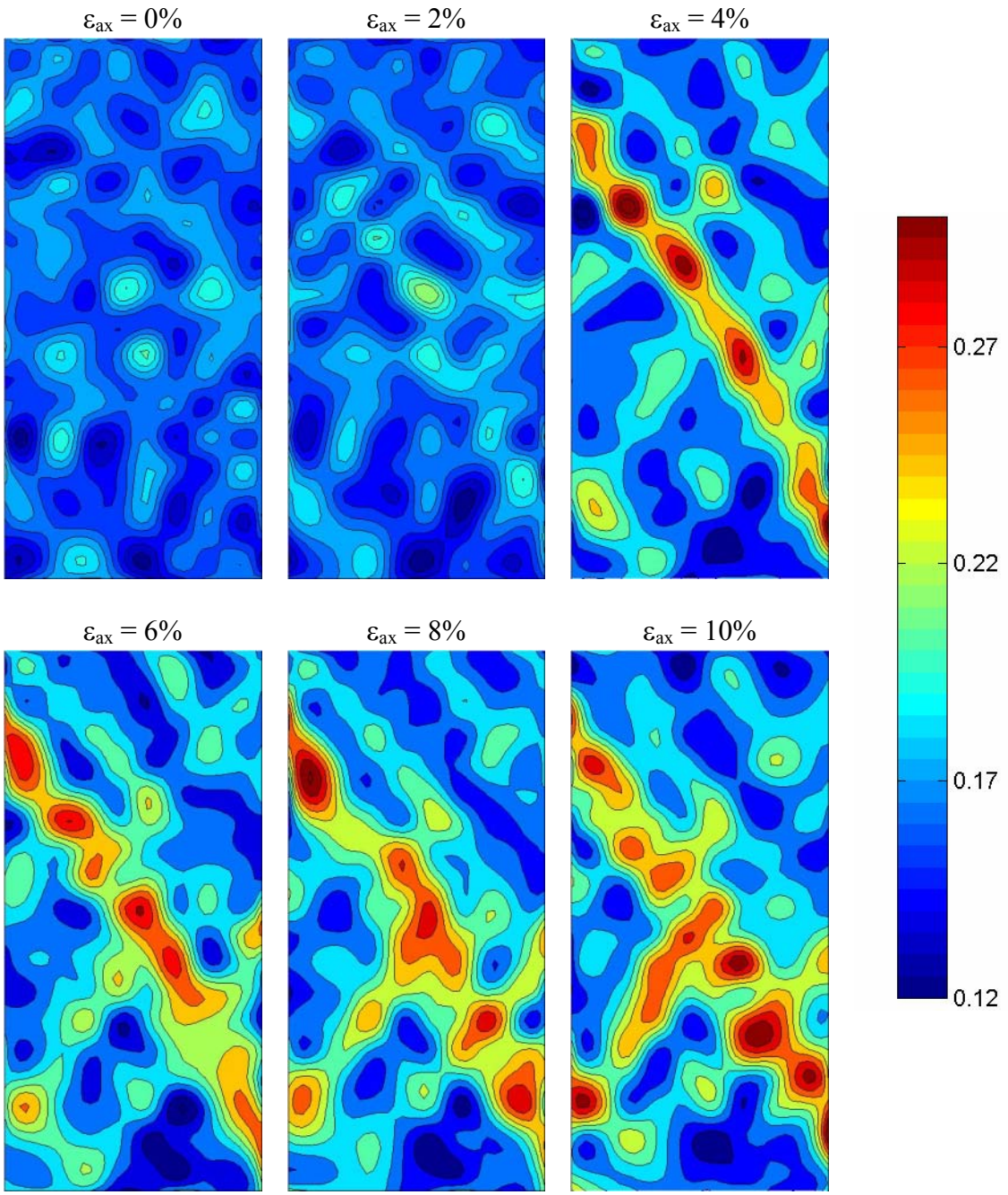

Figure 6.11: Subregional void ratio contours for the slightly dilatant specimen

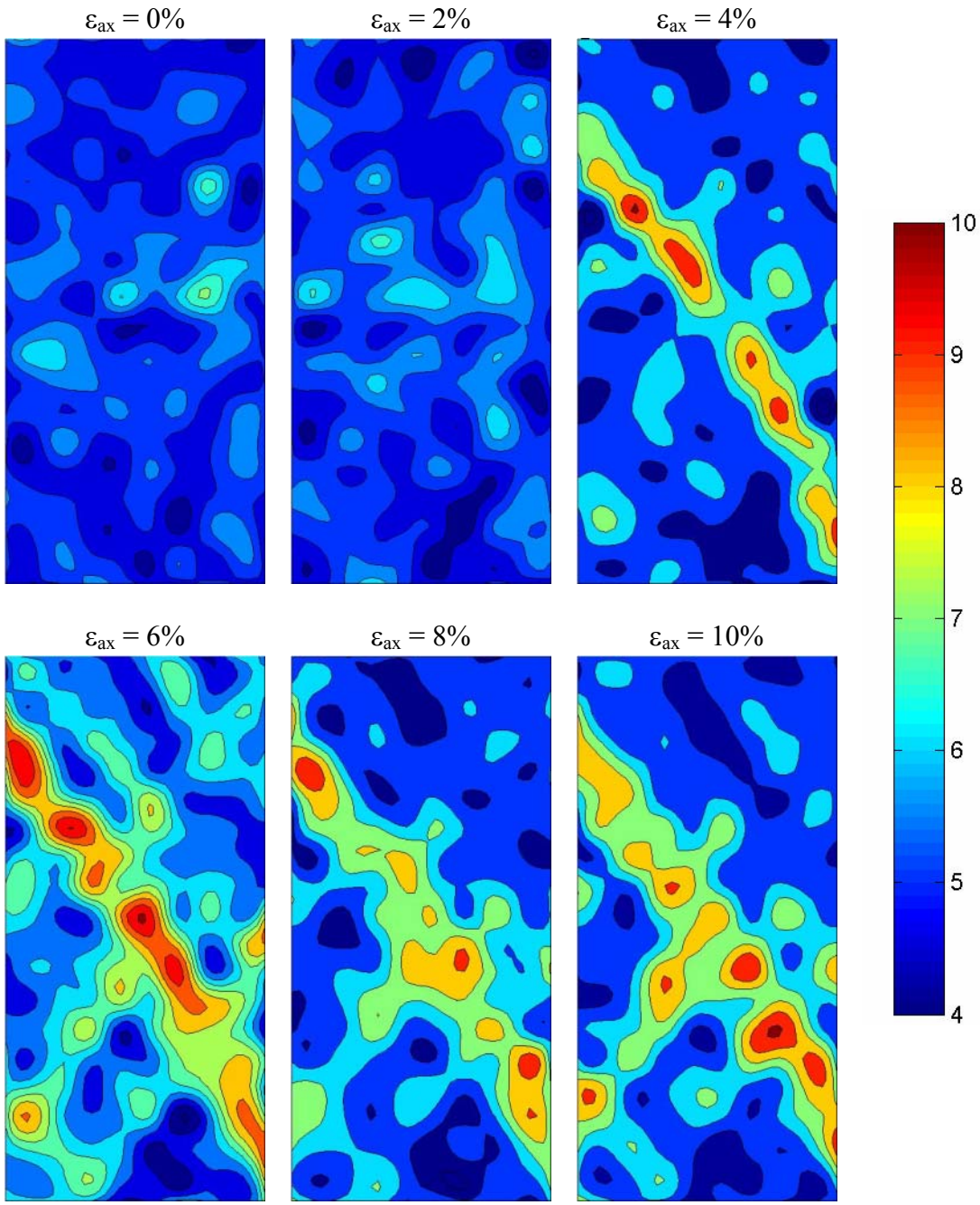

Figure 6.12: Subregional mean free path contours for the slightly dilatant specimen

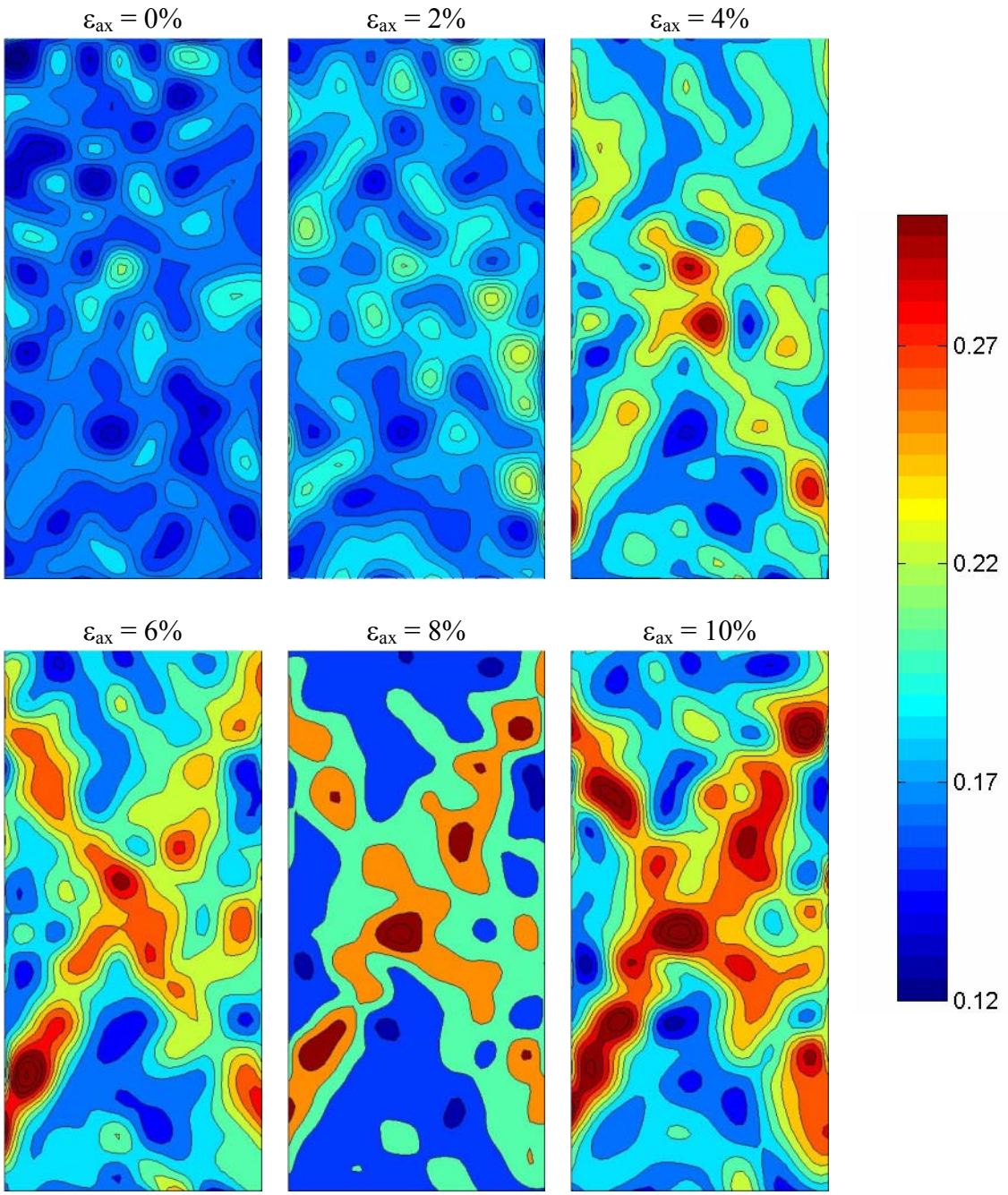

Figure 6.13: Subregional void ratio contours for the highly dilatant specimen

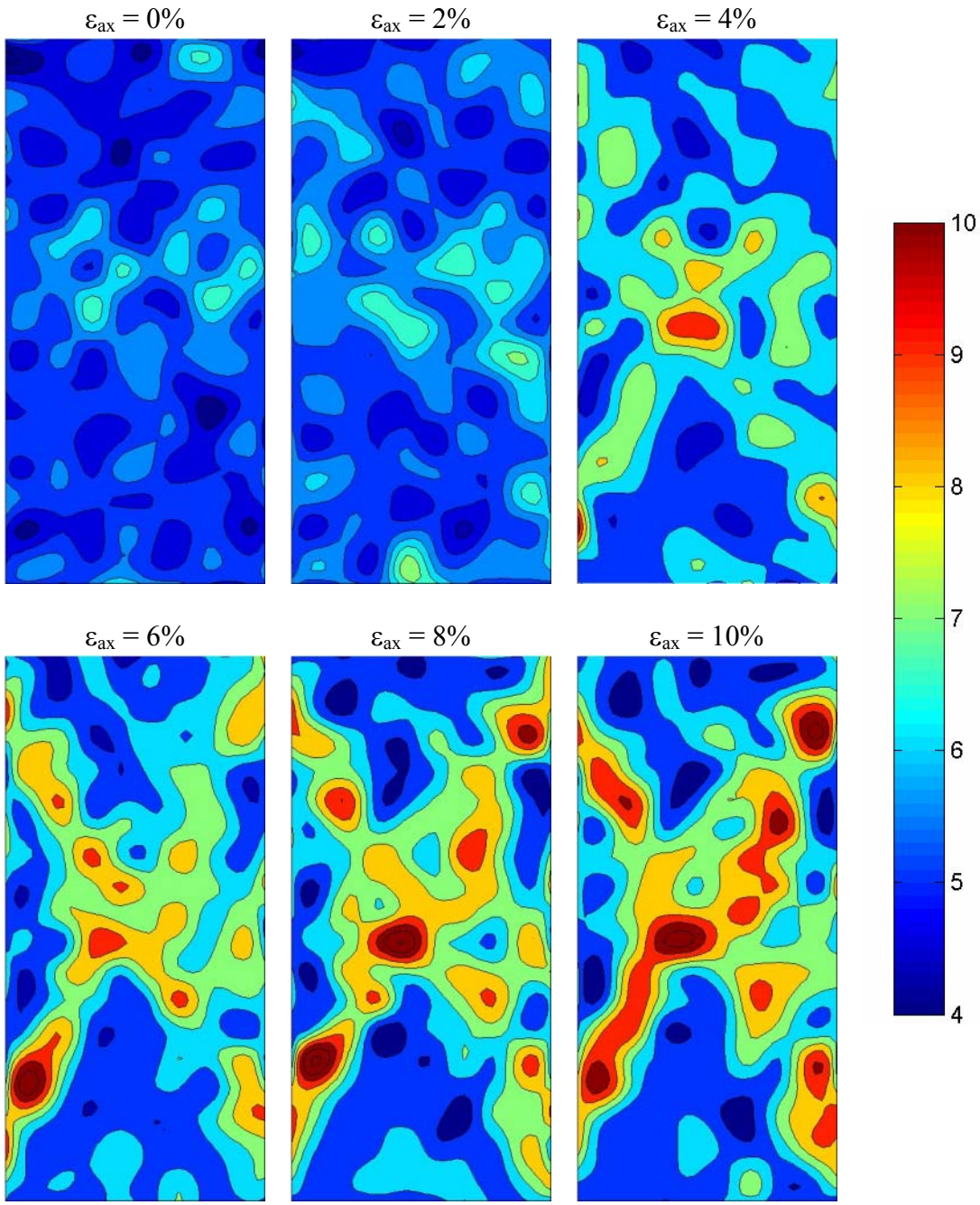

Figure 6.14: Subregional mean free path contours for the highly dilatant specimen

6.2.3. Local Void Ratio Distributions and Inclined Spatial Averaging

As described in Chapter 5 for laboratory test images, local void ratios were calculated from a polygon network and gamma distributions were used to model the histograms of local void ratio within the complete specimen as well as separately inside and outside of the shear band. The calculated mean void ratios, image void ratios, and fitted void ratios are presented in Table 6.3, which shows that image void ratio, mean void ratio, and the standard deviation of the void ratio all increase dramatically from 2% to 4% strain. Figures 6.15 and 6.16 present the gamma distributions for the two simulations at the different global axial strain levels. It can be seen that the distributions for 0% and 2% global axial strain (recall that peak stress is near 2% global axial strain) are comparable and that changes occur predominantly between 2% and 4% global axial strain.

Using areal strips within the image aligned parallel to the shear band, the means and standard deviations of local void ratios and total void ratio (within a given strip) may be calculated for regions both inside and outside of the shear band, as discussed in Chapter 5. Shear band extents are delineated using the same procedure outlined for surfaces taken from laboratory tests: lines of accumulated void ratio in both directions are plotted on the same axes as incremental void ratios and shear band extents are selected as the points when an increase in accumulated void ratio is evident (Figure 6.17). Once the extents are selected, they are compared with cumulative void ratios on either side of the shear band to assess the viability of the selection (Figure 6.18). Results of strip calculations are presented in Figures 6.19 through 6.30 for the slightly dilatant and highly dilatant specimens at different strain levels. This family of figures indicates a

significantly higher void ratio and standard deviation within the shear band and a relatively more constant void ratio outside the shear band after the onset of localization. It is also evident that the void ratio is relatively constant in both regions prior to the onset of localization and that the local void ratio histograms do not begin to deviate from each other significantly until a global axial strain of 4%.

Table 6.3: Void ratios for specimens by different measures

Specimen	e_{image}	μ	σ	μ_{gamma}	σ_{gamma}
SD – 0%	0.162	0.159	0.050	0.159	0.049
SD – 2%	0.164	0.162	0.050	0.162	0.049
SD – 4%	0.185	0.184	0.069	0.184	0.065
SD – 6%	0.191	0.190	0.074	0.190	0.069
SD – 8%	0.193	0.192	0.075	0.192	0.070
SD – 10%	0.196	0.195	0.078	0.195	0.073
HD – 0%	0.165	0.162	0.051	0.162	0.049
HD – 2%	0.174	0.171	0.053	0.171	0.052
HD – 4%	0.199	0.196	0.070	0.196	0.067
HD – 6%	0.209	0.208	0.083	0.208	0.078
HD – 8%	0.214	0.215	0.090	0.215	0.083
HD – 10%	0.217	0.219	0.093	0.219	0.086

To summarize some of the data presented in Figures 6.19 through 6.30 (and also Table 6.3) , it is beneficial to consider plots of void ratios versus global axial strain level. Figures 6.31 and 6.32 show variation of image void ratio, mean of local void ratios for the entire image, and means of local void ratios inside and outside of the shear band as a function of global axial strain for both specimens.

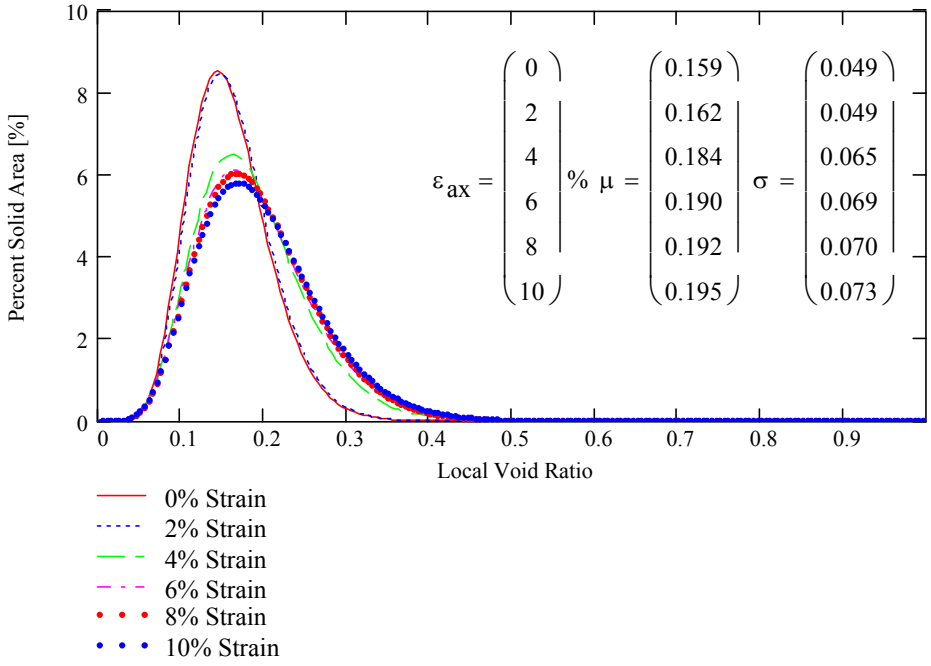

Figure 6.15: Gamma distributions for local void ratios in the slightly dilatant specimen

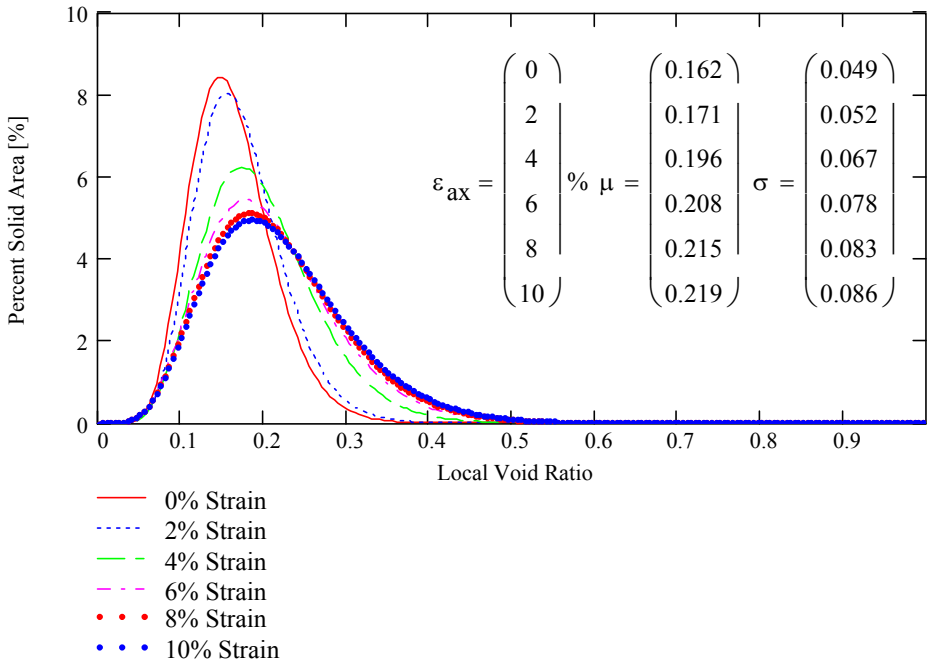

Figure 6.16: Gamma distributions for local void ratios in the highly dilatant specimen

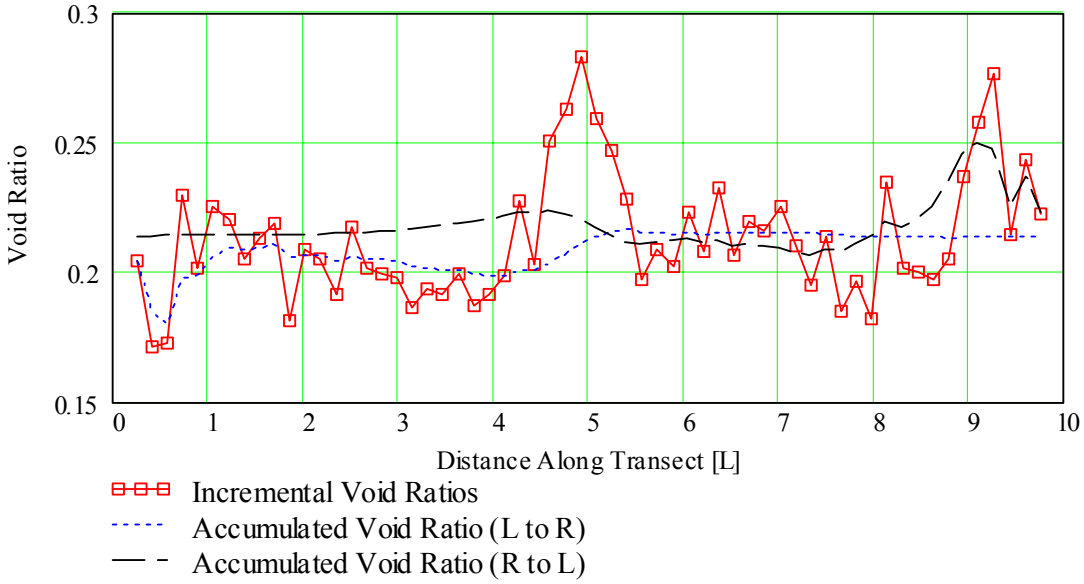

Figure 6.17: Incremental and accumulated void ratios for the HD specimen at 8% strain

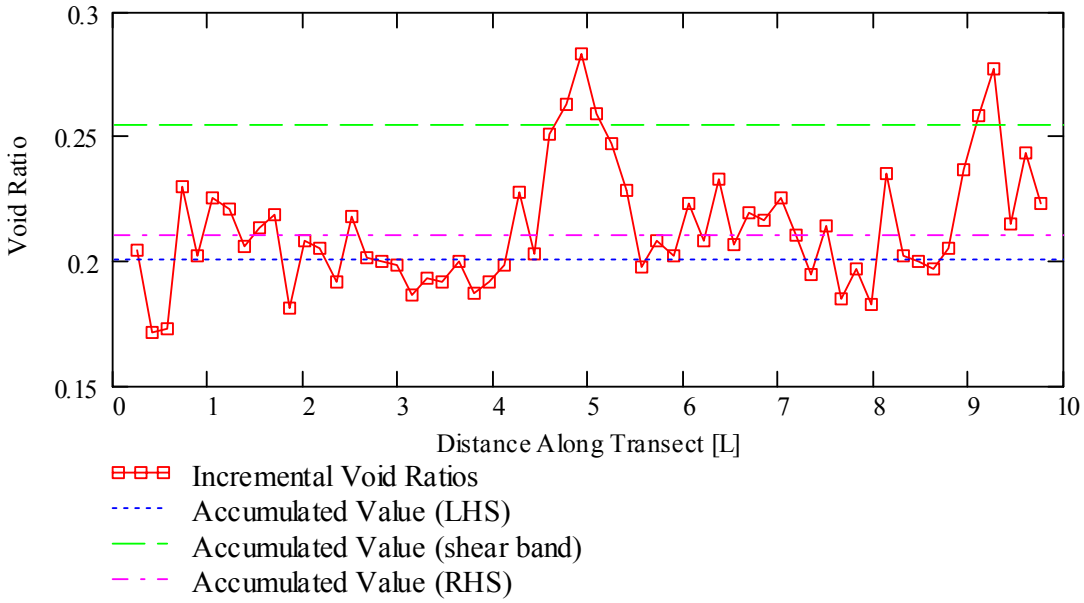

Figure 6.18: Incremental and asymptotic void ratios inside and outside of the shear band for the HD specimen at 8% strain

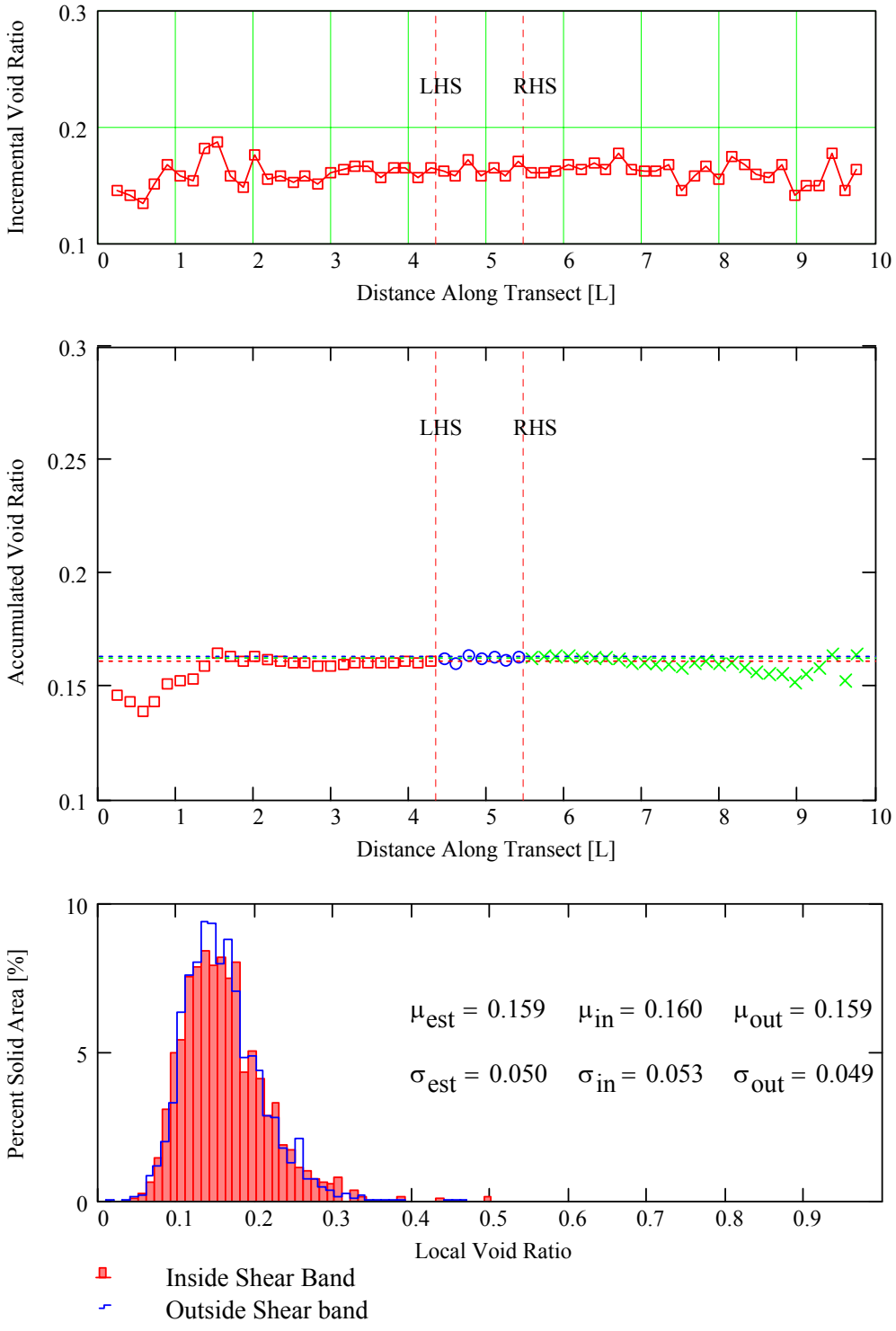

Figure 6.19: Incremental (upper) and accumulated (middle) void ratios of strips parallel to the shear band and a histogram (lower) of local void ratio distributions for regions inside and outside of the shear band, slightly dilatant specimen at 0% global axial strain

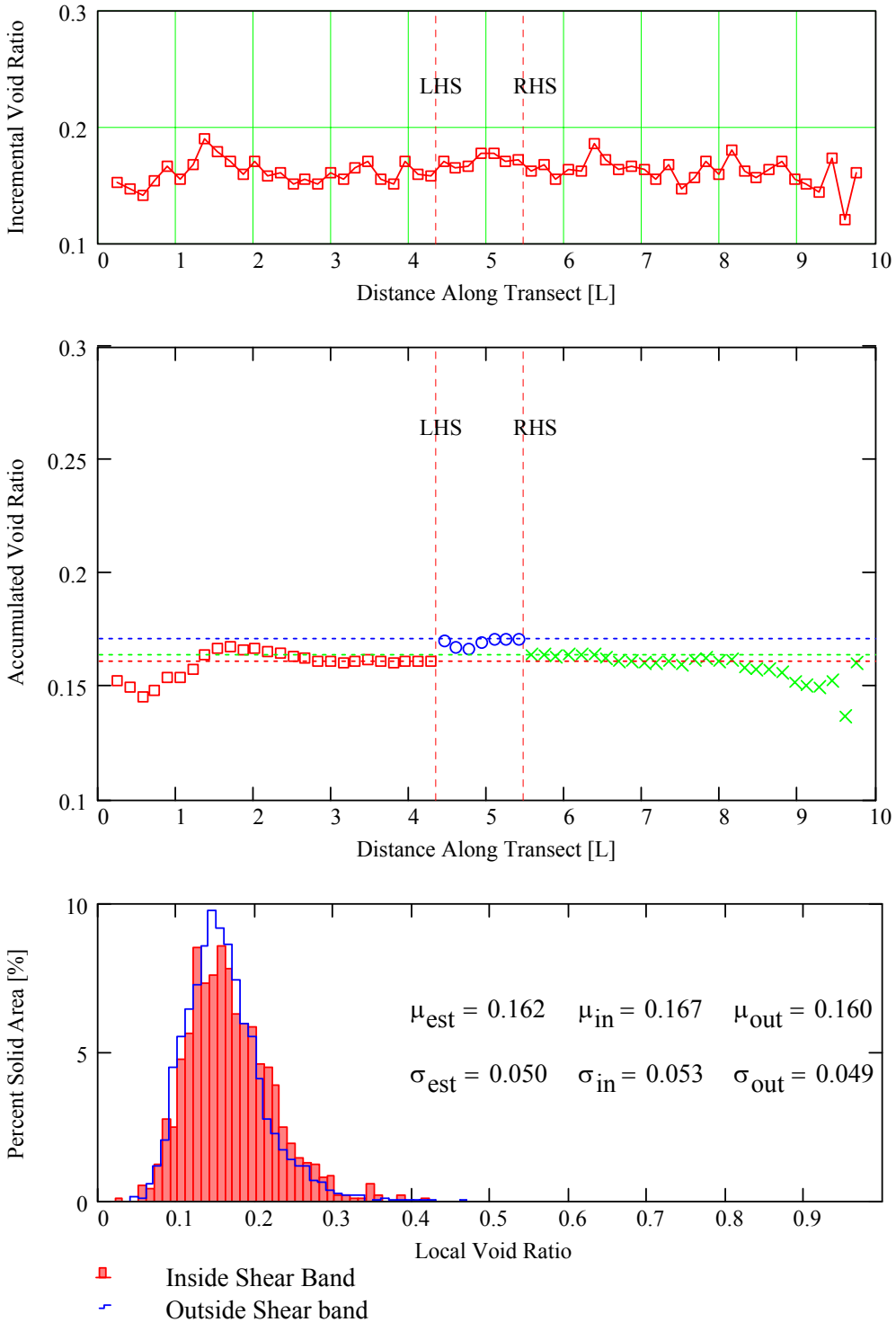

Figure 6.20: Incremental (upper) and accumulated (middle) void ratios of strips parallel to the shear band and a histogram (lower) of local void ratio distributions for regions inside and outside of the shear band, slightly dilatant specimen at 2% global axial strain

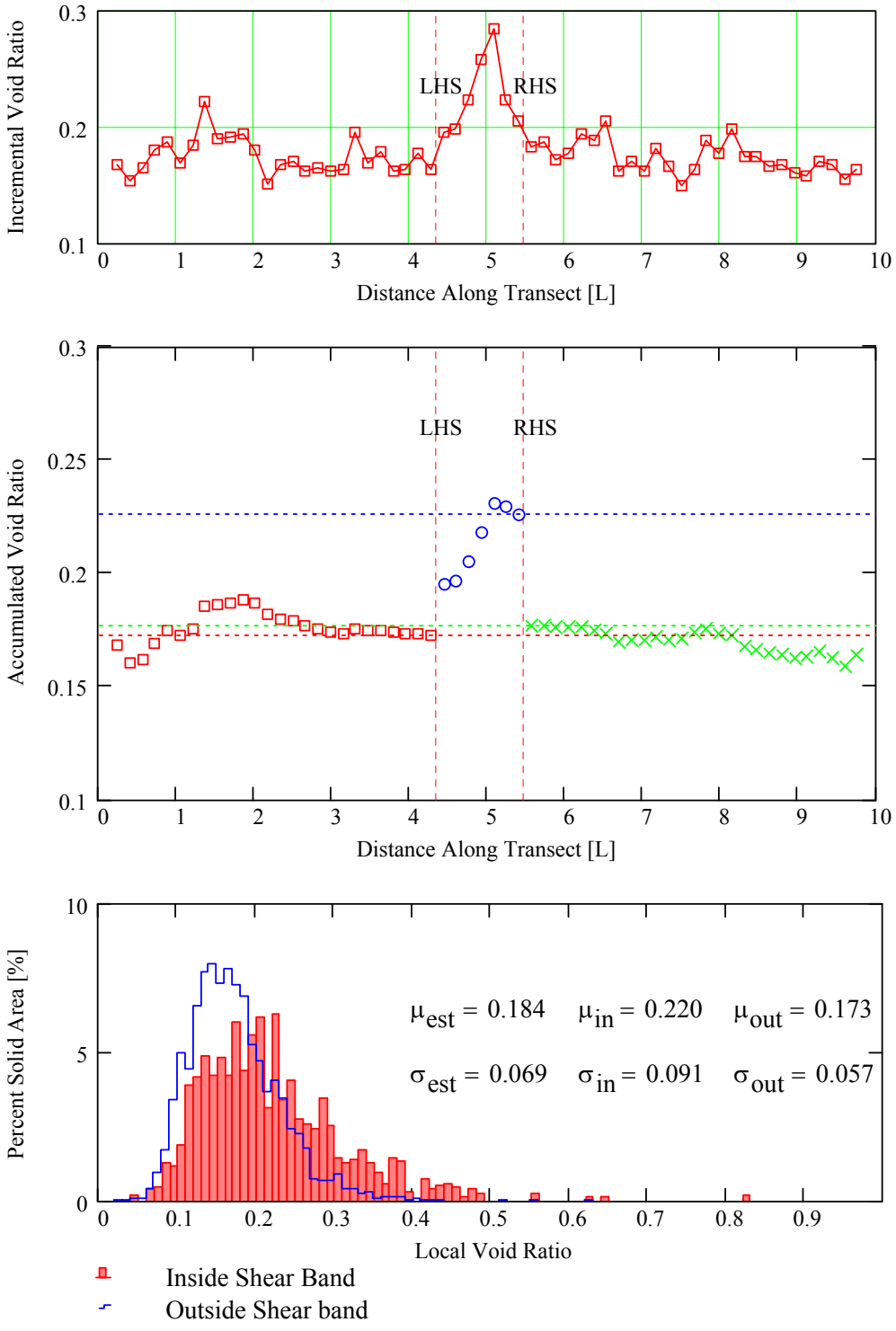

Figure 6.21: Incremental (upper) and accumulated (middle) void ratios of strips parallel to the shear band and a histogram (lower) of local void ratio distributions for regions inside and outside of the shear band, slightly dilatant specimen at 4% global axial strain

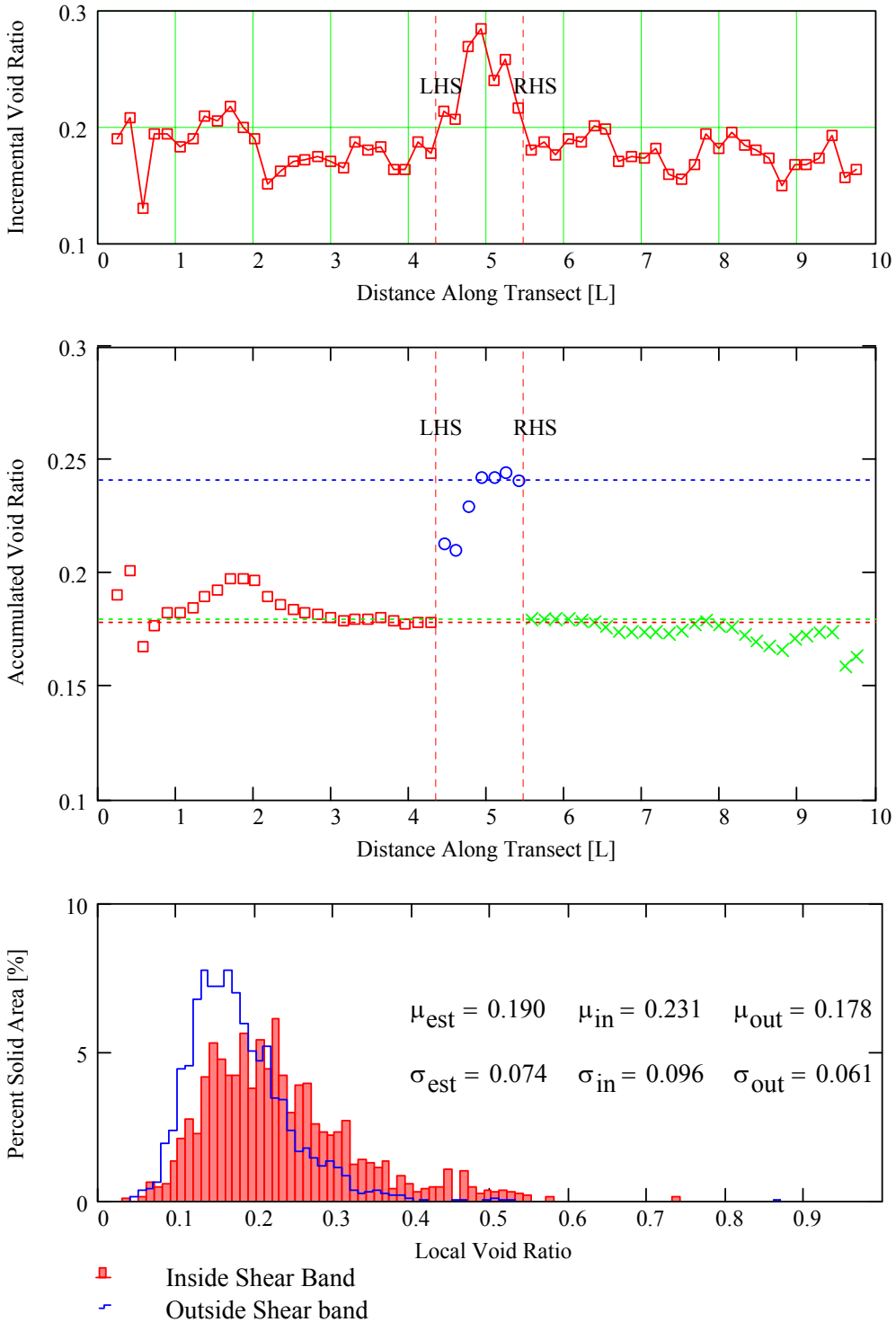

Figure 6.22: Incremental (upper) and accumulated (middle) void ratios of strips parallel to the shear band and a histogram (lower) of local void ratio distributions for regions inside and outside of the shear band, slightly dilatant specimen at 6% global axial strain

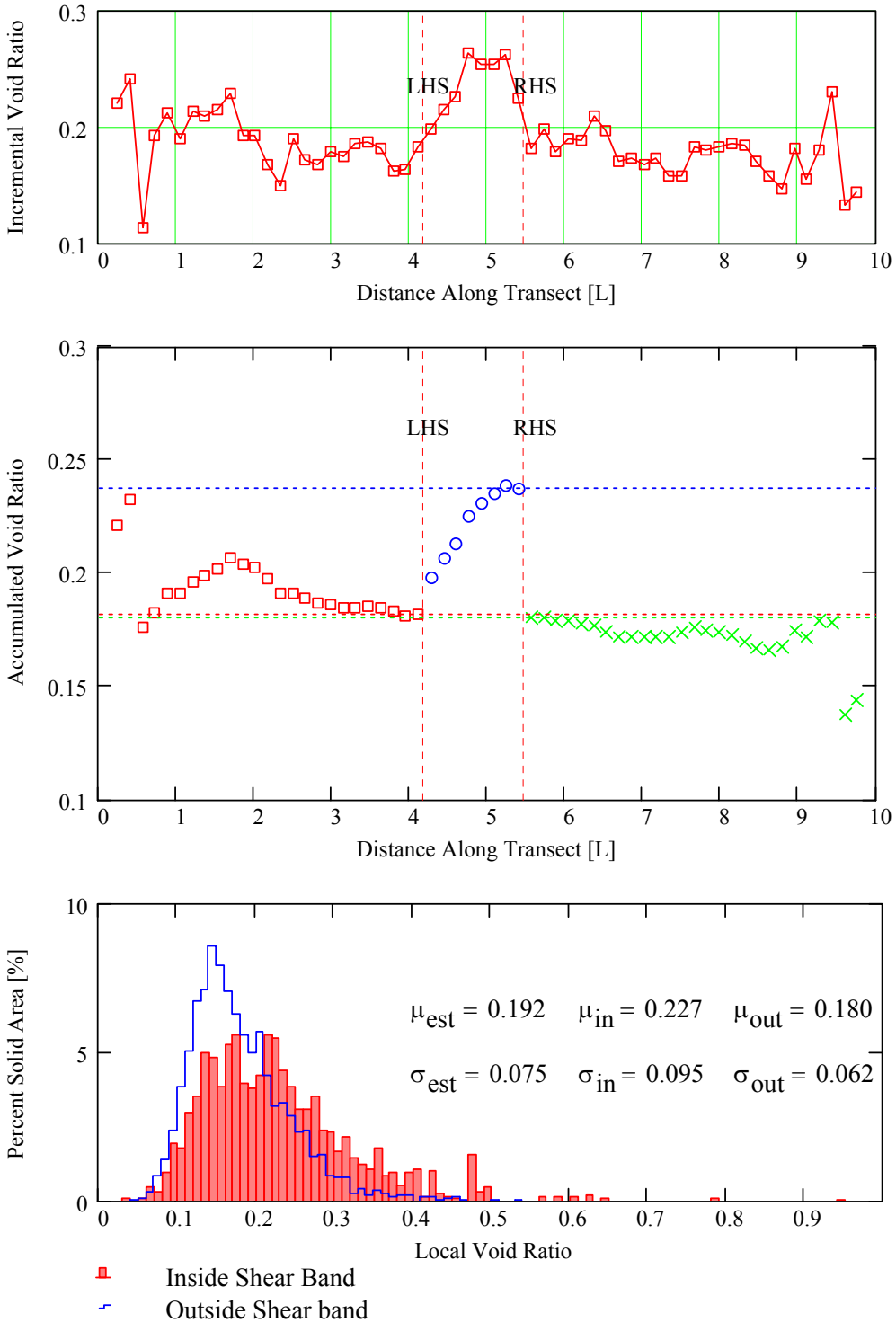

Figure 6.23: Incremental (upper) and accumulated (middle) void ratios of strips parallel to the shear band and a histogram (lower) of local void ratio distributions for regions inside and outside of the shear band, slightly dilatant specimen at 8% global axial strain

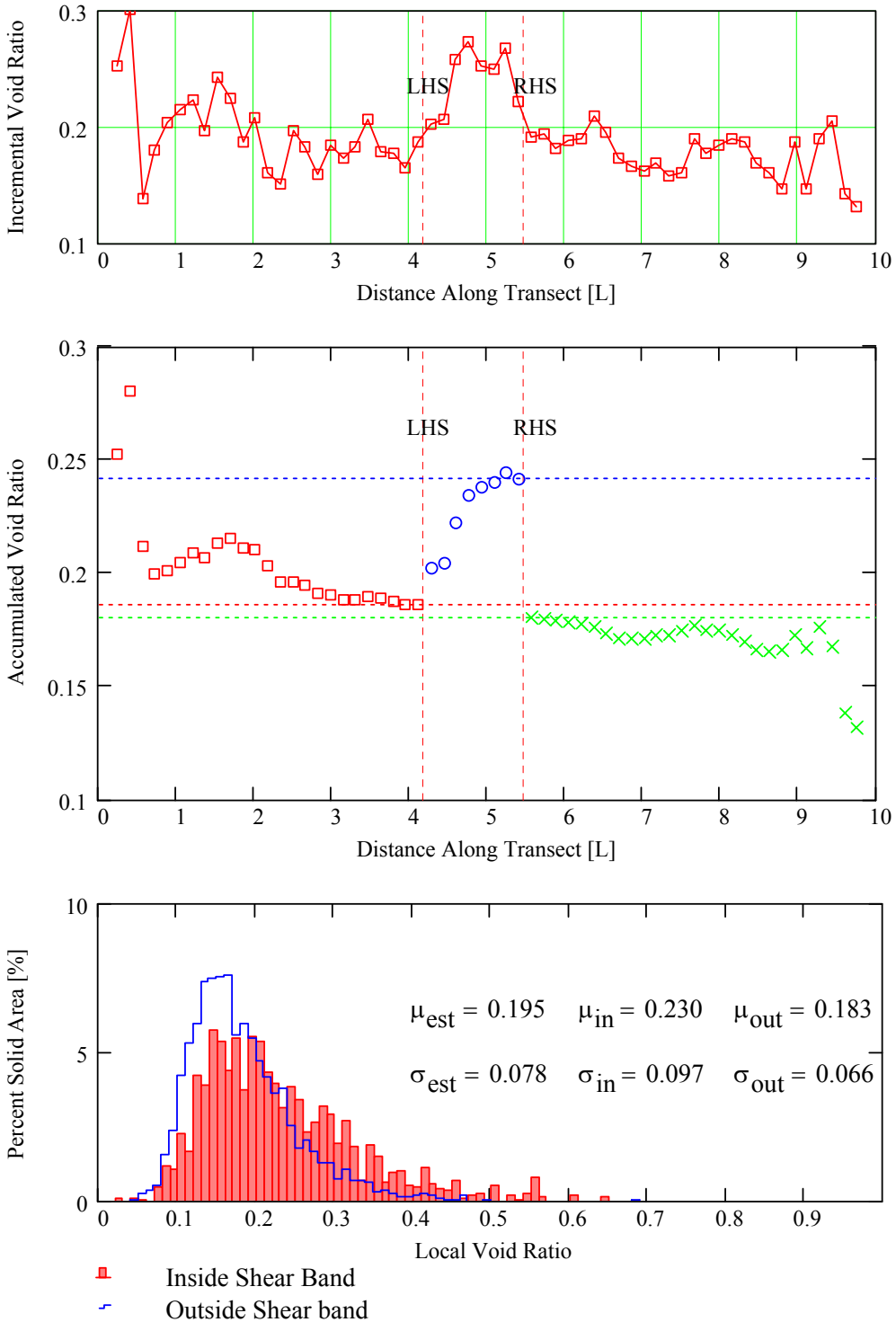

Figure 6.24: Incremental (upper) and accumulated (middle) void ratios of strips parallel to the shear band and a histogram (lower) of local void ratio distributions for regions inside and outside of the shear band, slightly dilatant specimen at 10% global axial strain

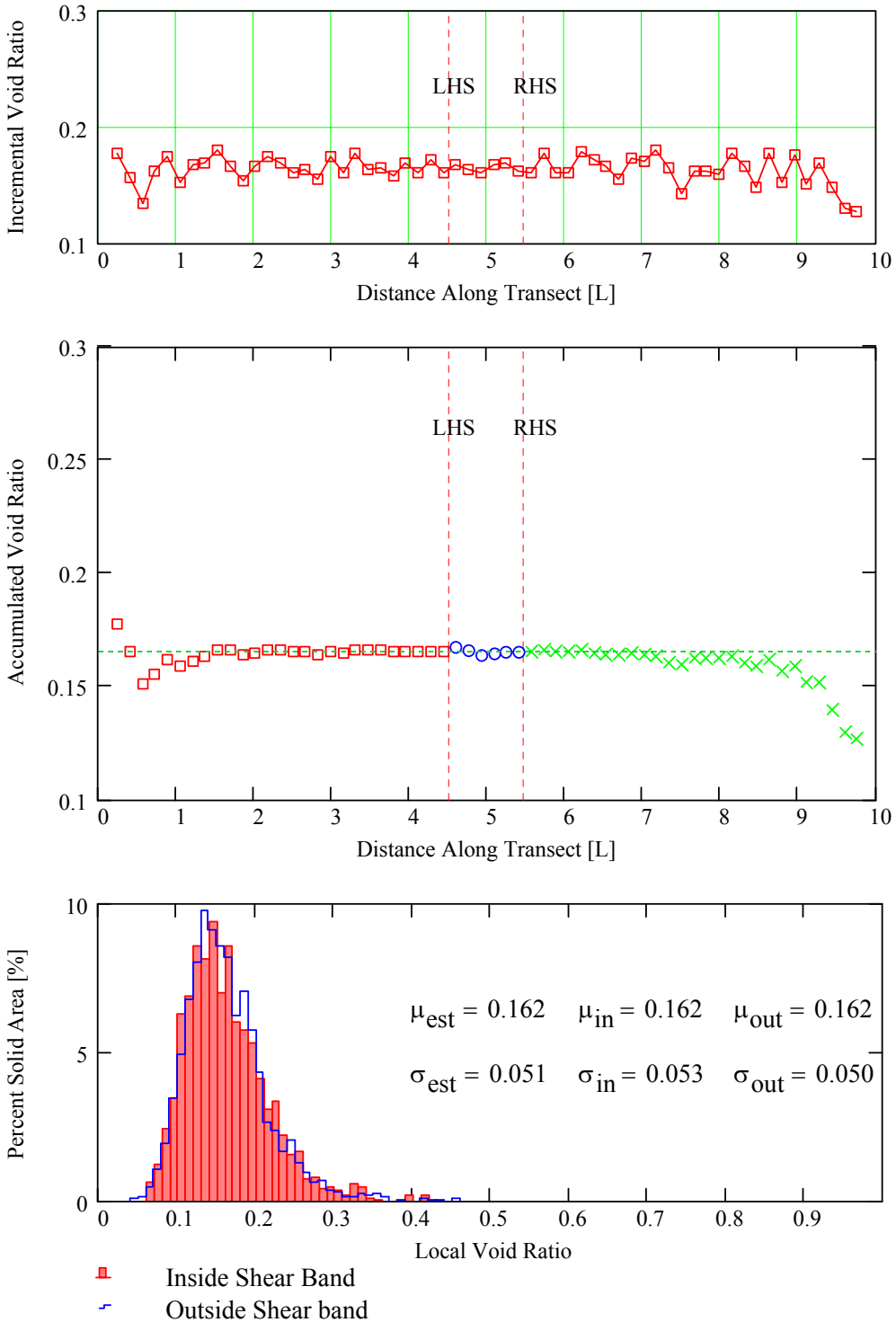

Figure 6.25: Incremental (upper) and accumulated (middle) void ratios of strips parallel to the shear band and a histogram (lower) of local void ratio distributions for regions inside and outside of the shear band, highly dilatant specimen at 0% global axial strain

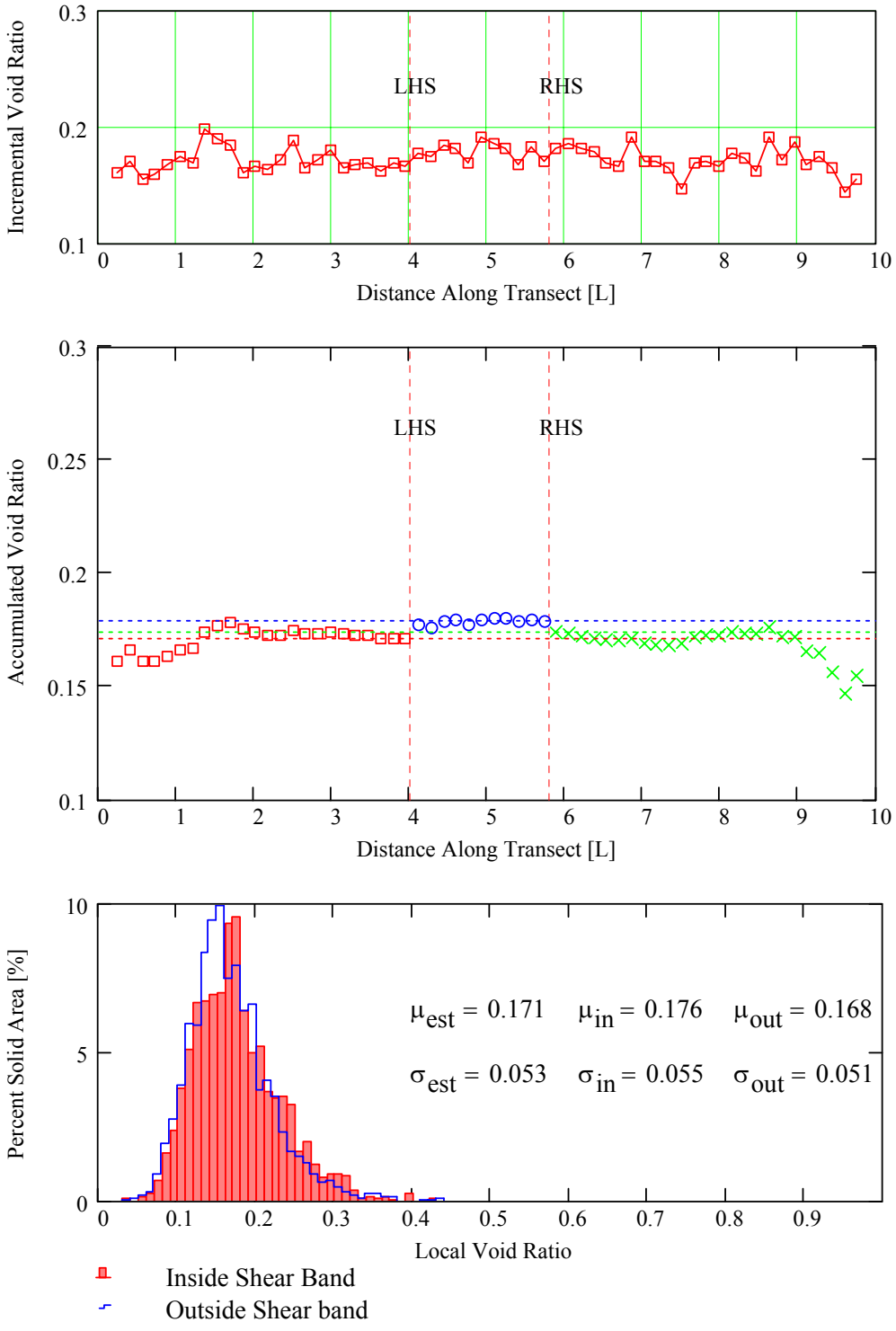

Figure 6.26: Incremental (upper) and accumulated (middle) void ratios of strips parallel to the shear band and a histogram (lower) of local void ratio distributions for regions inside and outside of the shear band, highly dilatant specimen at 2% global axial strain

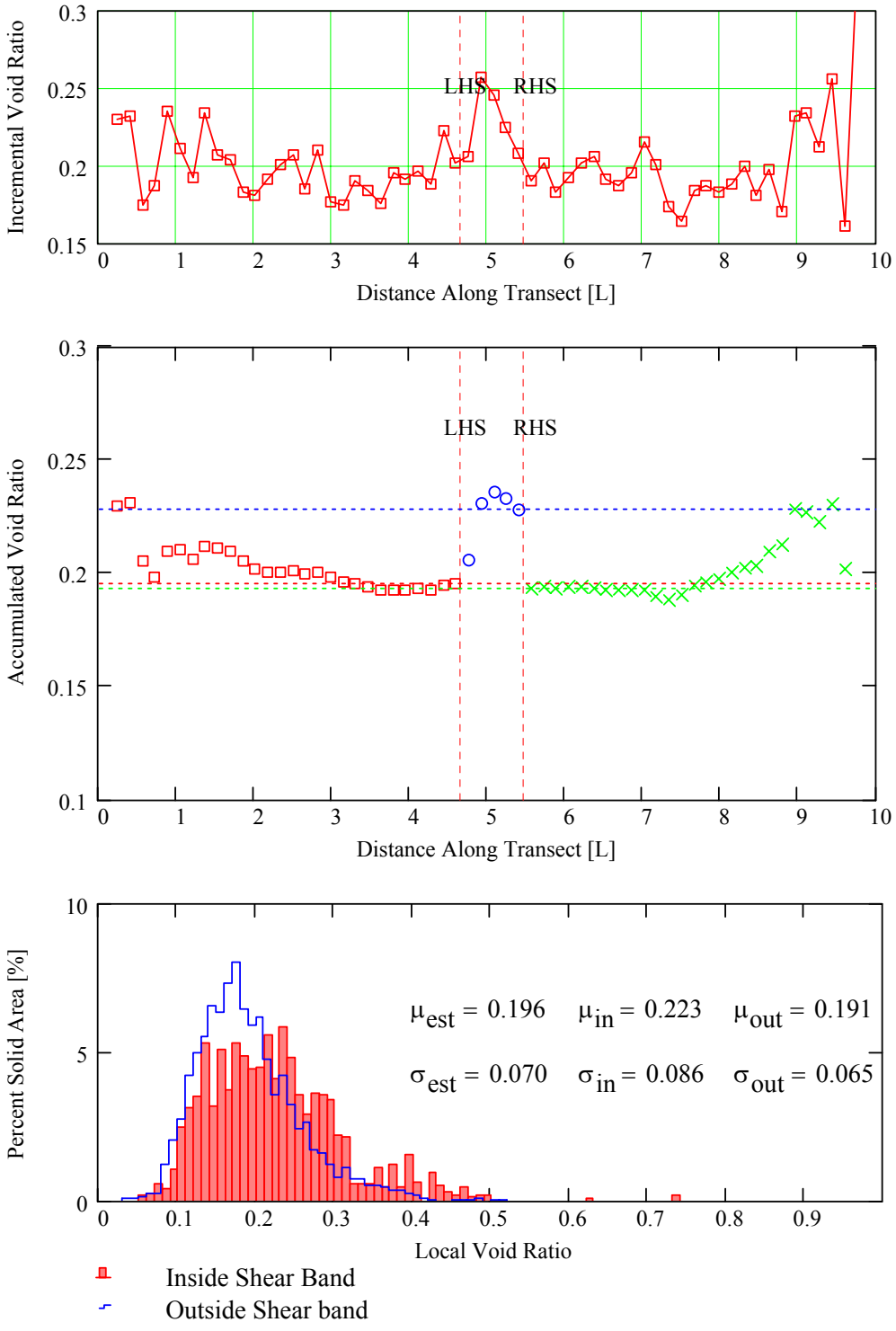

Figure 6.27: Incremental (upper) and accumulated (middle) void ratios of strips parallel to the shear band and a histogram (lower) of local void ratio distributions for regions inside and outside of the shear band, highly dilatant specimen at 4% global axial strain

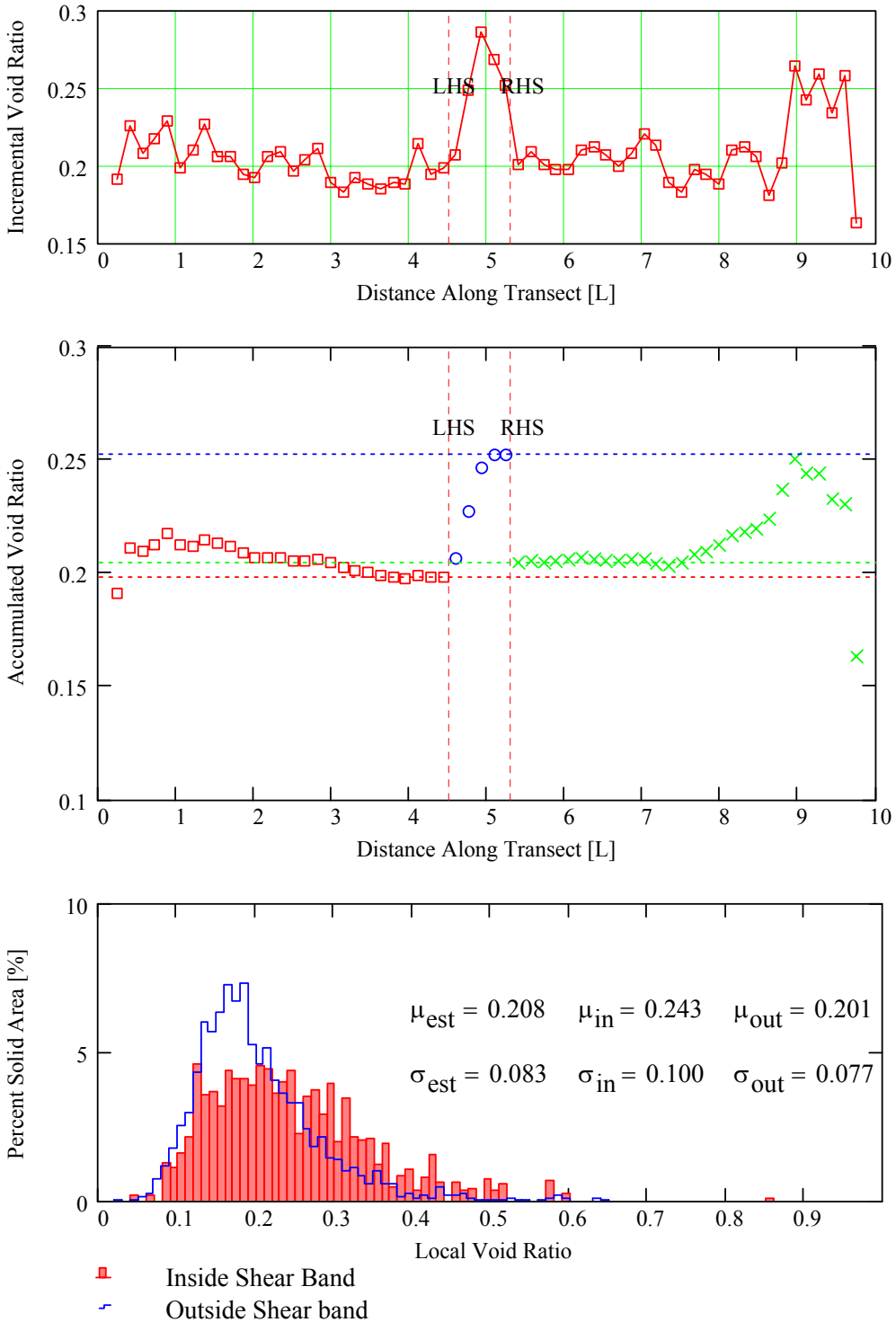

Figure 6.28: Incremental (upper) and accumulated (middle) void ratios of strips parallel to the shear band and a histogram (lower) of local void ratio distributions for regions inside and outside of the shear band, highly dilatant specimen at 6% global axial strain

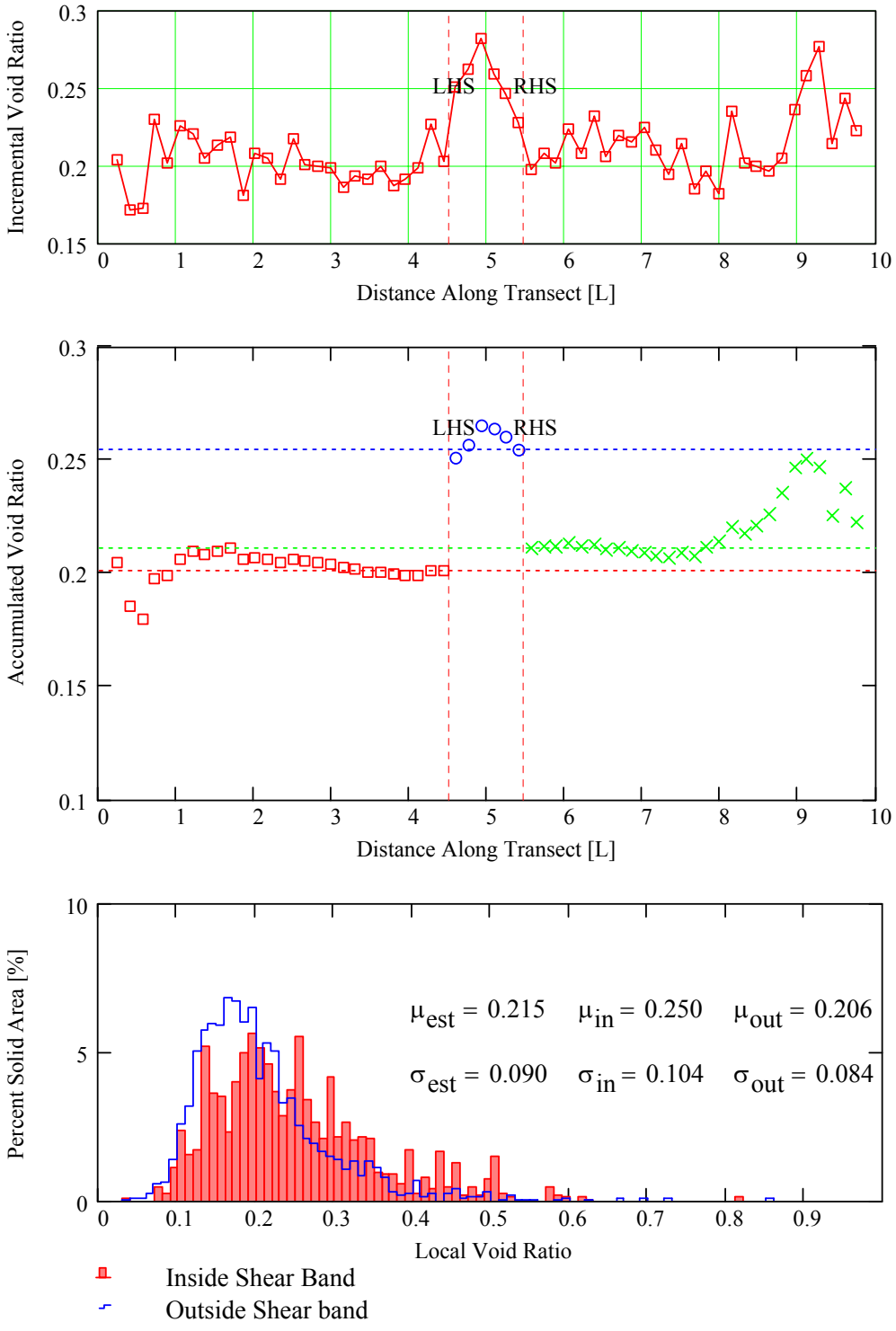

Figure 6.29: Incremental (upper) and accumulated (middle) void ratios of strips parallel to the shear band and a histogram (lower) of local void ratio distributions for regions inside and outside of the shear band, highly dilatant specimen at 8% global axial strain

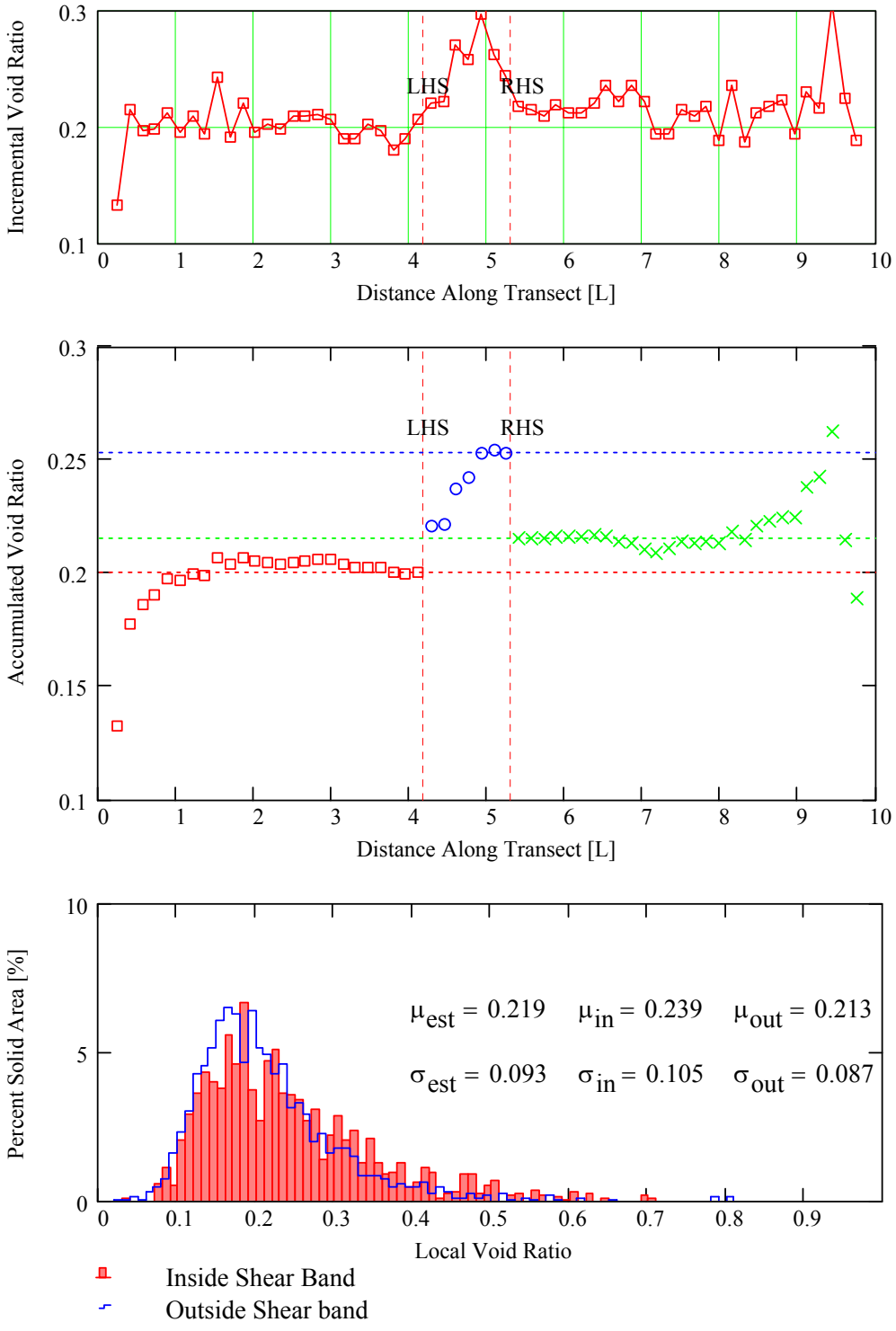

Figure 6.30: Incremental (upper) and accumulated (middle) void ratios of strips parallel to the shear band and a histogram (lower) of local void ratio distributions for regions inside and outside of the shear band, highly dilatant specimen at 10% global axial strain

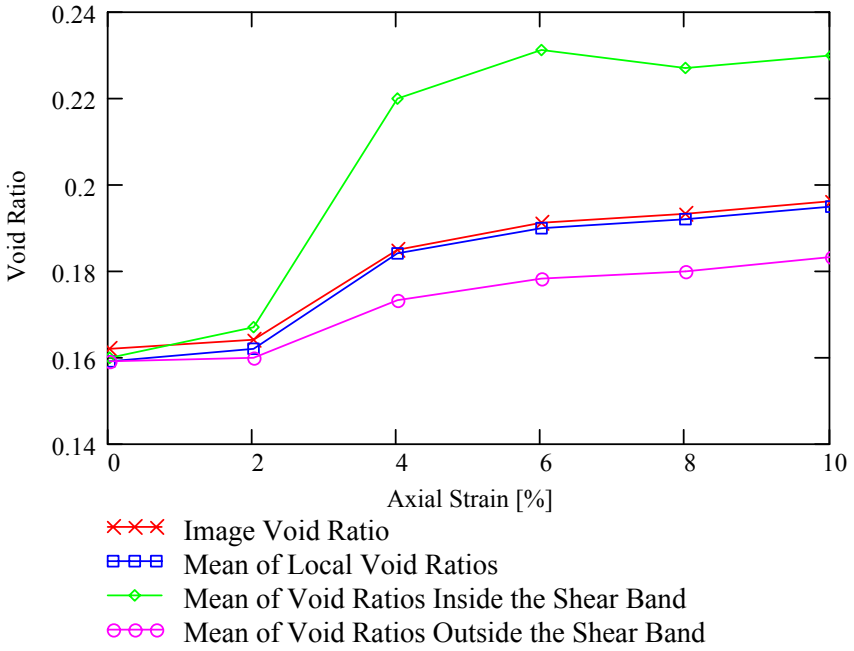

Figure 6.31: Evolving void ratios in the slightly dilatant specimen

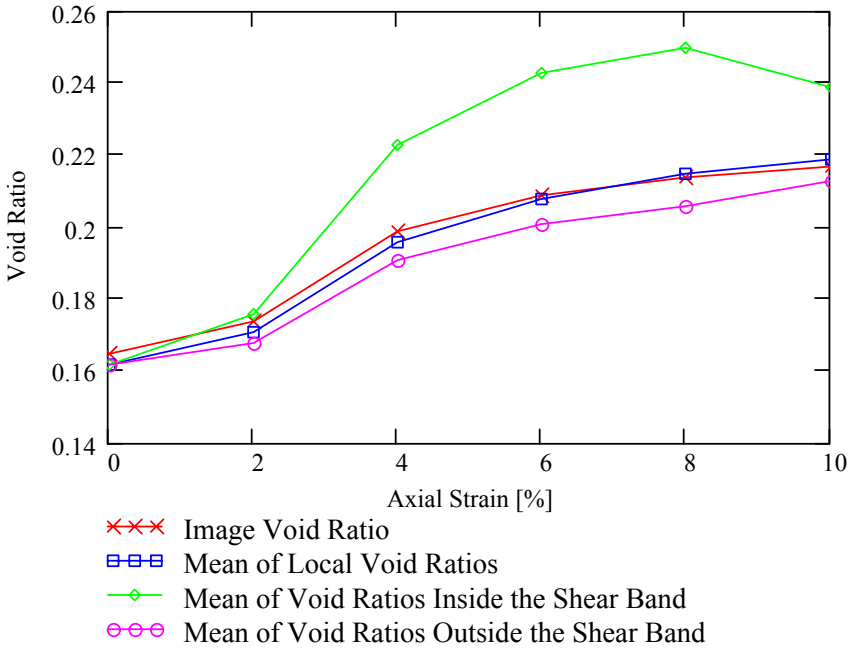

Figure 6.32: Evolving void ratios in the highly dilatant specimen

6.3. Virtual Surface Analyses

The procedures outlined in Chapter 5 for analyzing the roughness of virtual surfaces within images of laboratory specimens was employed for the numerical specimens as well. A total of 44 surfaces were developed, each inclined parallel to the shear band. The horizontal distance between any two subsequent surfaces was 0.15 length units (~2-3 mean particle diameters). Roughness values were calculated for every surface and plotted as a distance along a transect oriented orthogonal to the shear band inclination. Roughness parameter transects are plotted for both specimens at 0% and 10% global axial strain and are presented in Figures 6.33 and 6.34. In previous analyses (spatial averaging of inclined strips for experimental and numerical specimens and virtual surface analyses for experimental specimens) the left-hand side (LHS) and right-hand side (RHS) of the shear bands was determined through analysis of the given data set. In the present case of virtual surfaces for the numerical specimens, however, the shear band boundaries are not clearly evident. Thus, the LHS and RHS designations are determined based on qualitative analysis of Figures 6.9 and 6.10 at the 10% strain level.

Additionally, it is possible to plot average roughness coefficients for virtual surfaces both inside and outside of the shear band as a function of global axial strain. This method provides insight into the evolving average roughness of virtual surfaces as particles are rearranged during shear. These results are presented as Figures 6.35 and 6.36. Implications of the results presented in Figures 6.33 through 6.36 will be further discussed in Chapter 7.

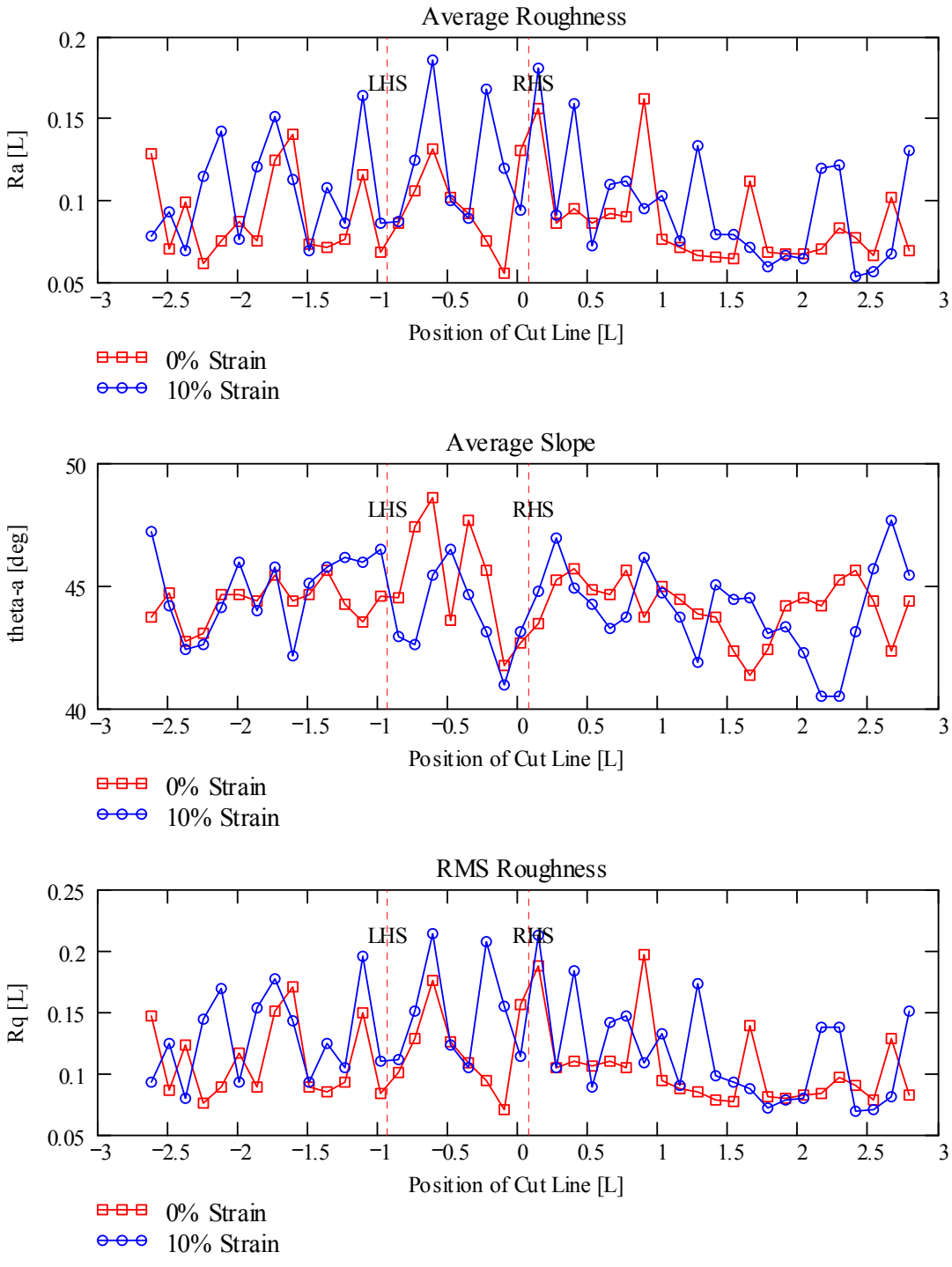

Figure 6.33: Roughness of virtual surfaces in the slightly dilatant specimen

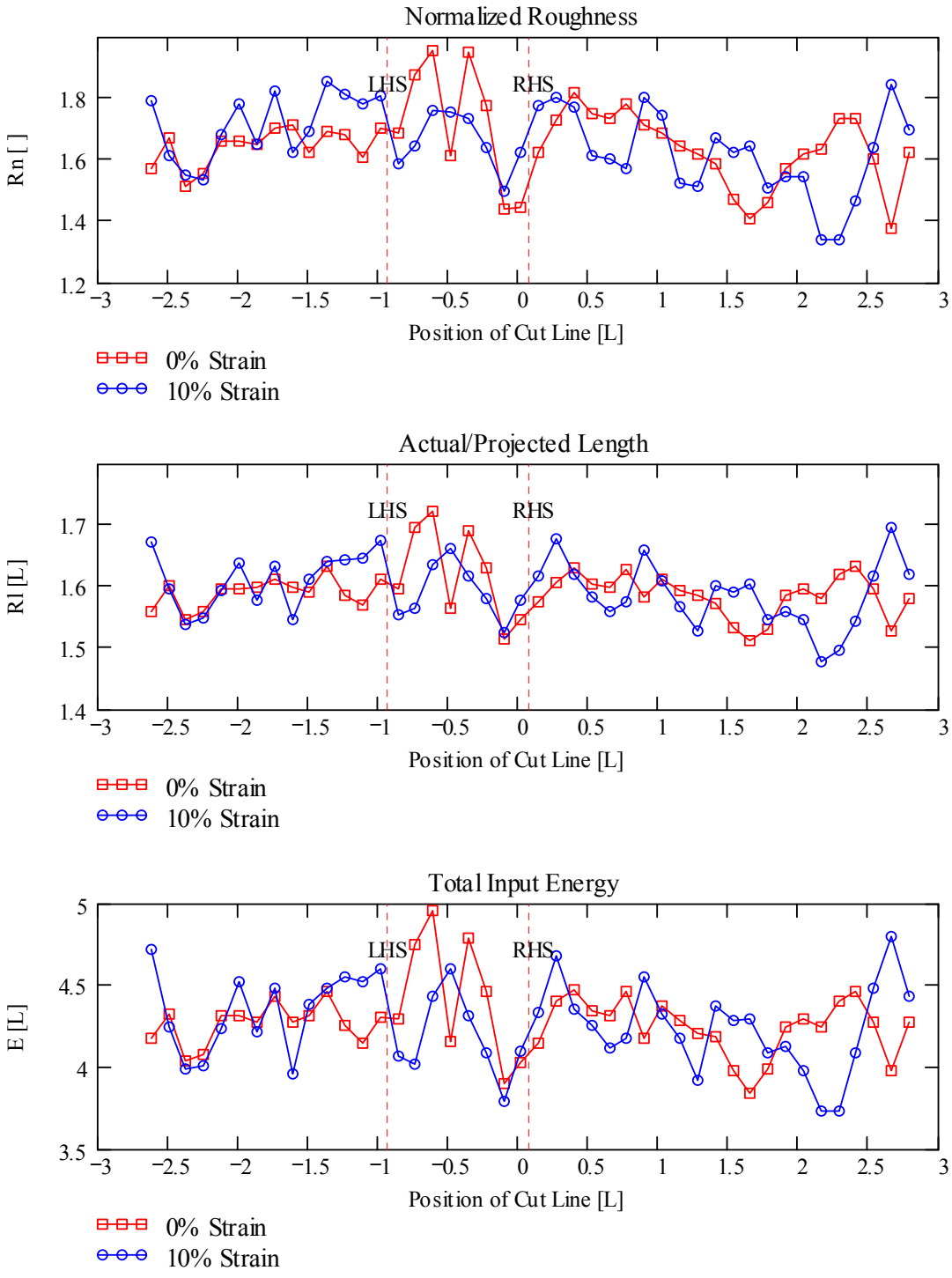

Figure 6.33 (cont.): Roughness of virtual surfaces in the slightly dilatant specimen

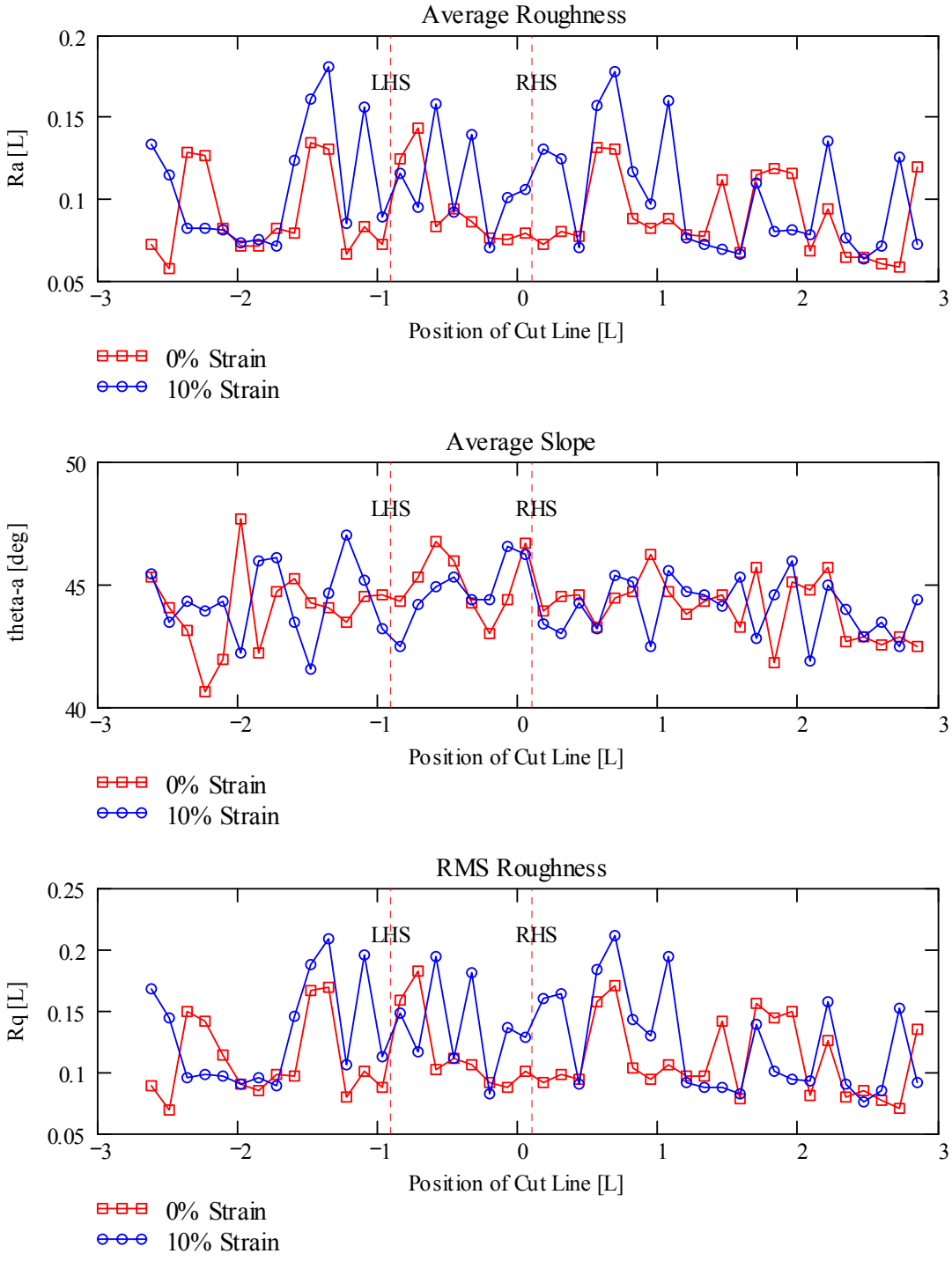

Figure 6.34: Roughness of virtual surfaces in the highly dilatant specimen

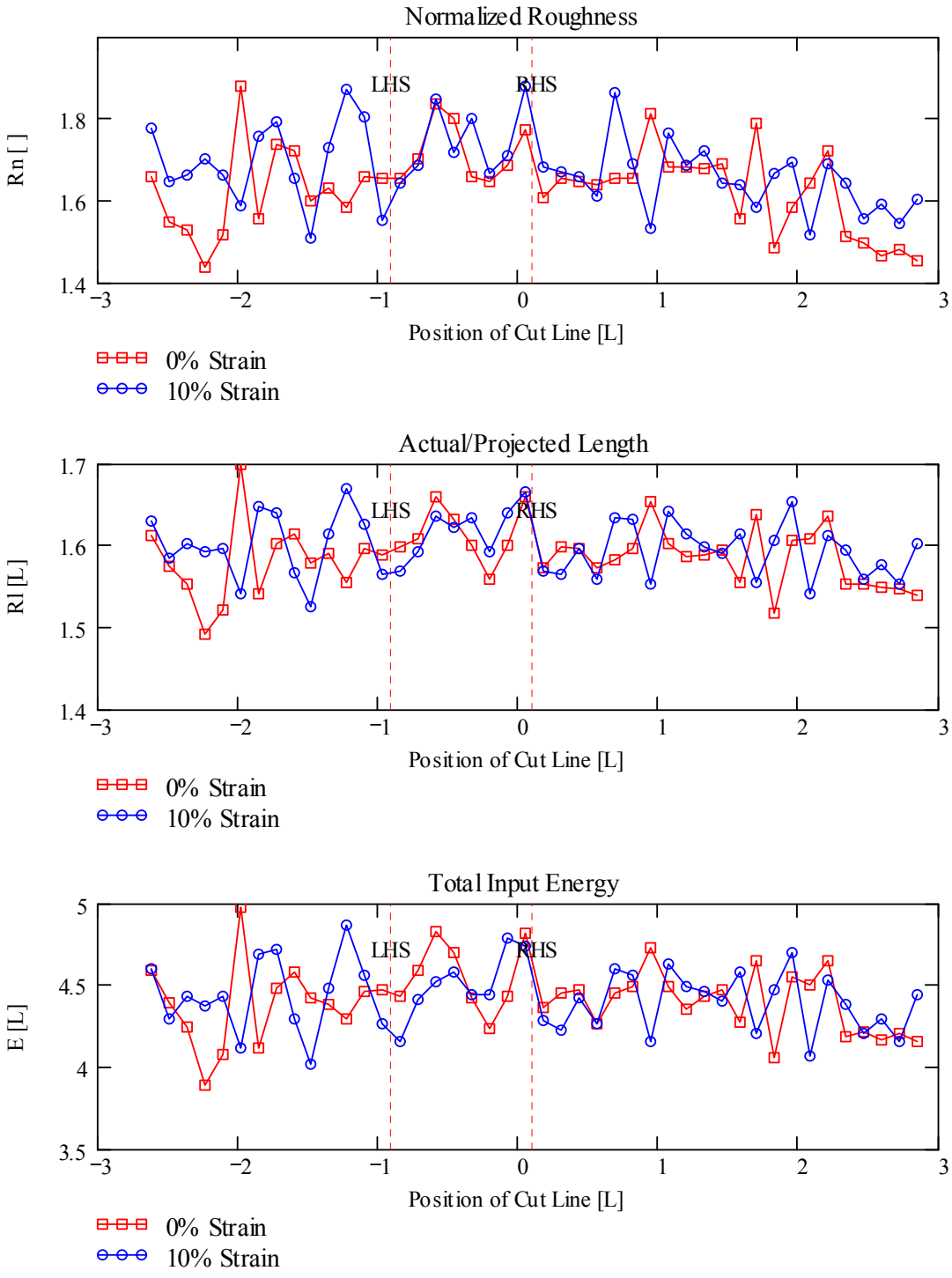

Figure 6.34 (cont.): Roughness of virtual surfaces in the highly dilatant specimen

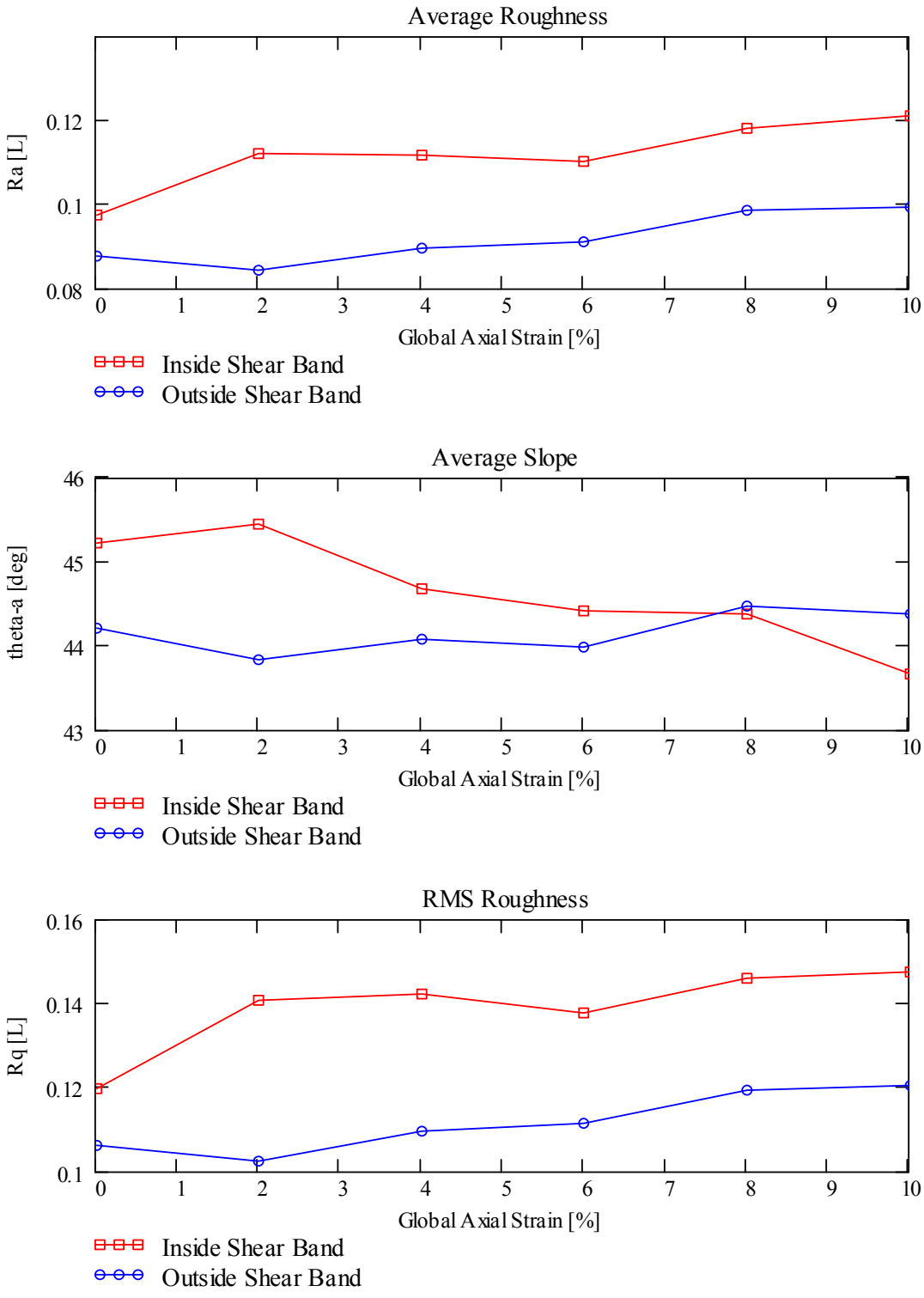

Figure 6.35: Roughness of virtual surfaces inside and outside of the shear band as a function of global axial strain in the slightly dilatant specimen

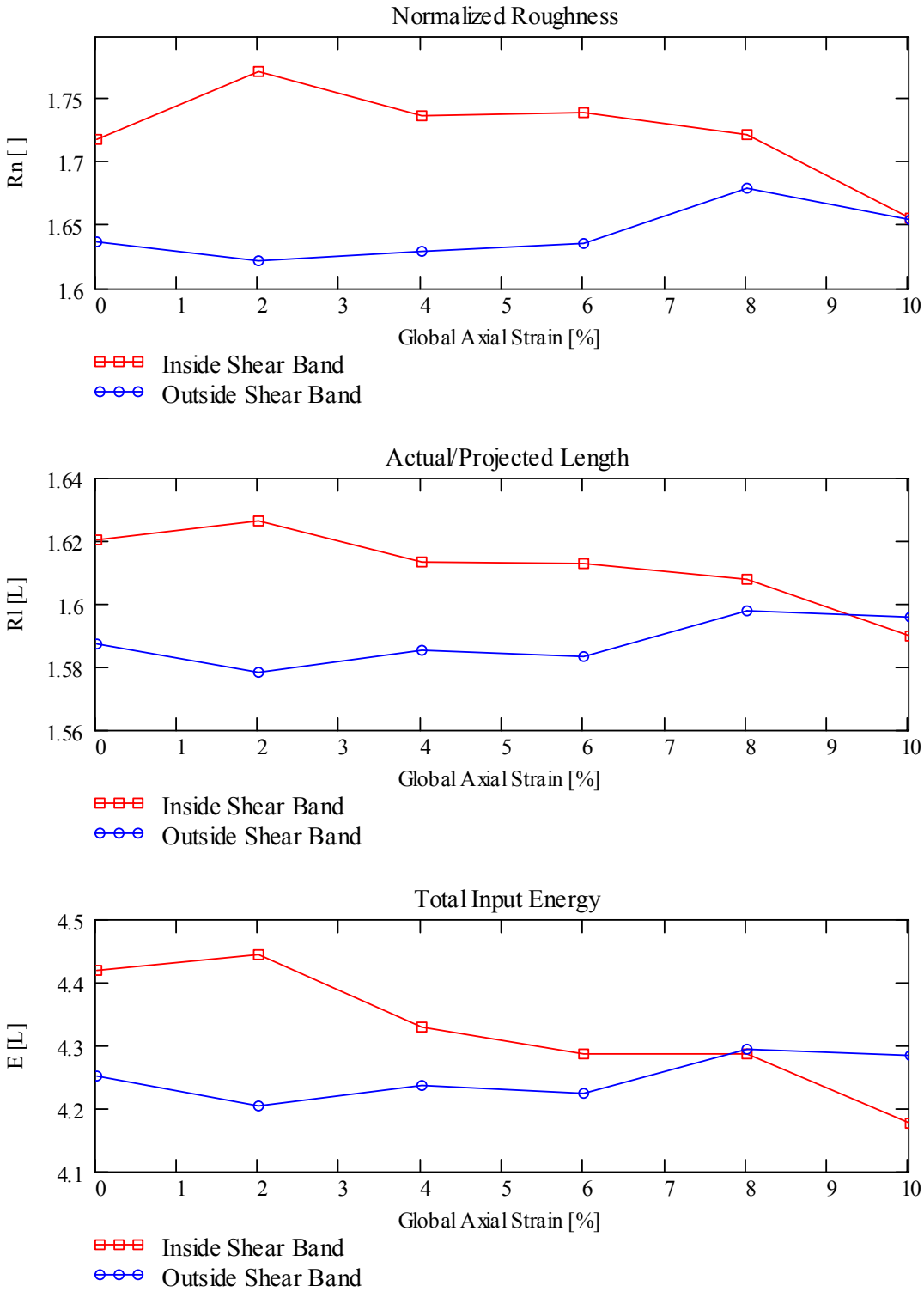

Figure 6.35 (cont.): Roughness of virtual surfaces inside and outside of the shear band as a function of global axial strain in the slightly dilatant specimen

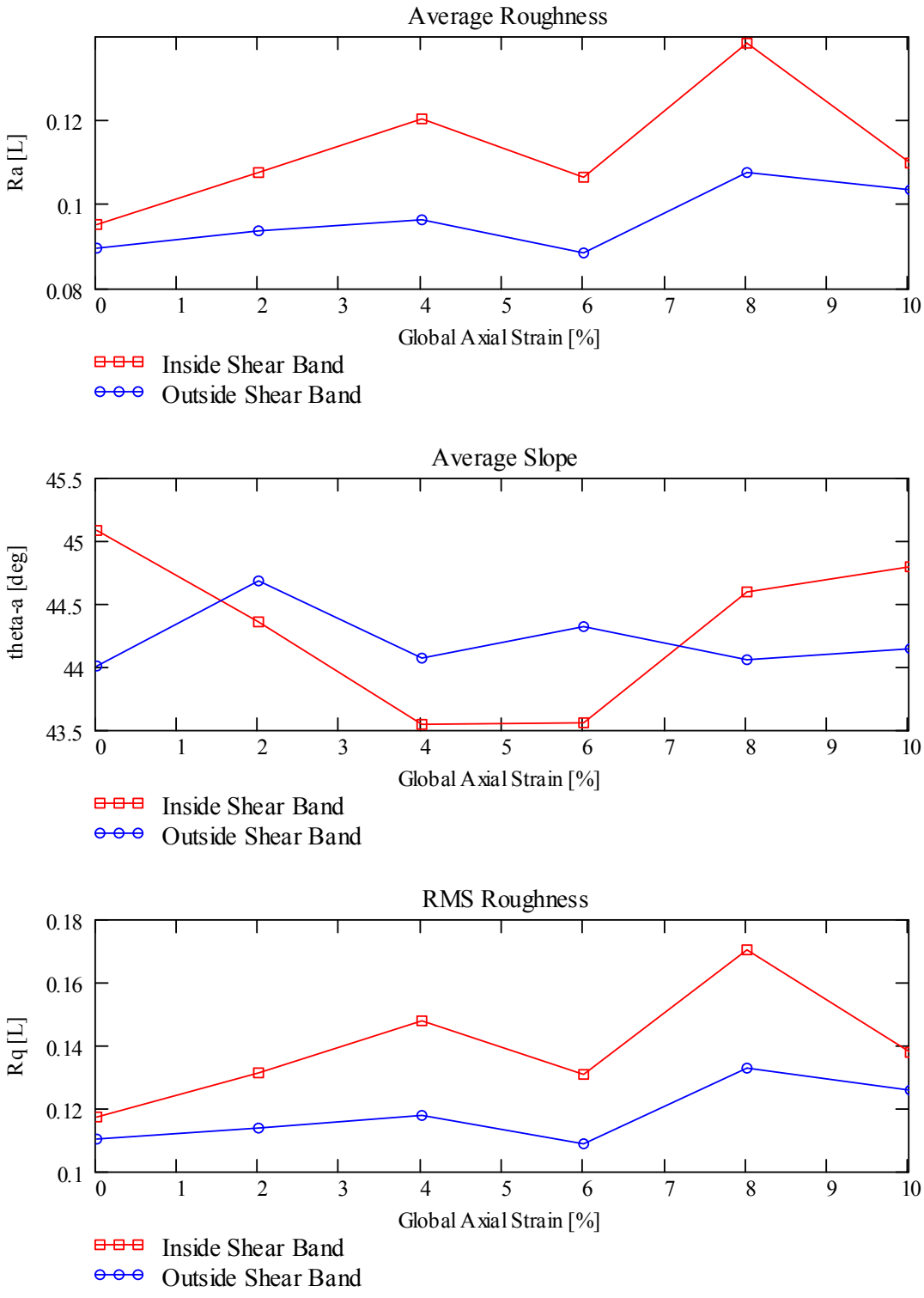

Figure 6.36: Roughness of virtual surfaces inside and outside of the shear band as a function of global axial strain in the highly dilatant specimen

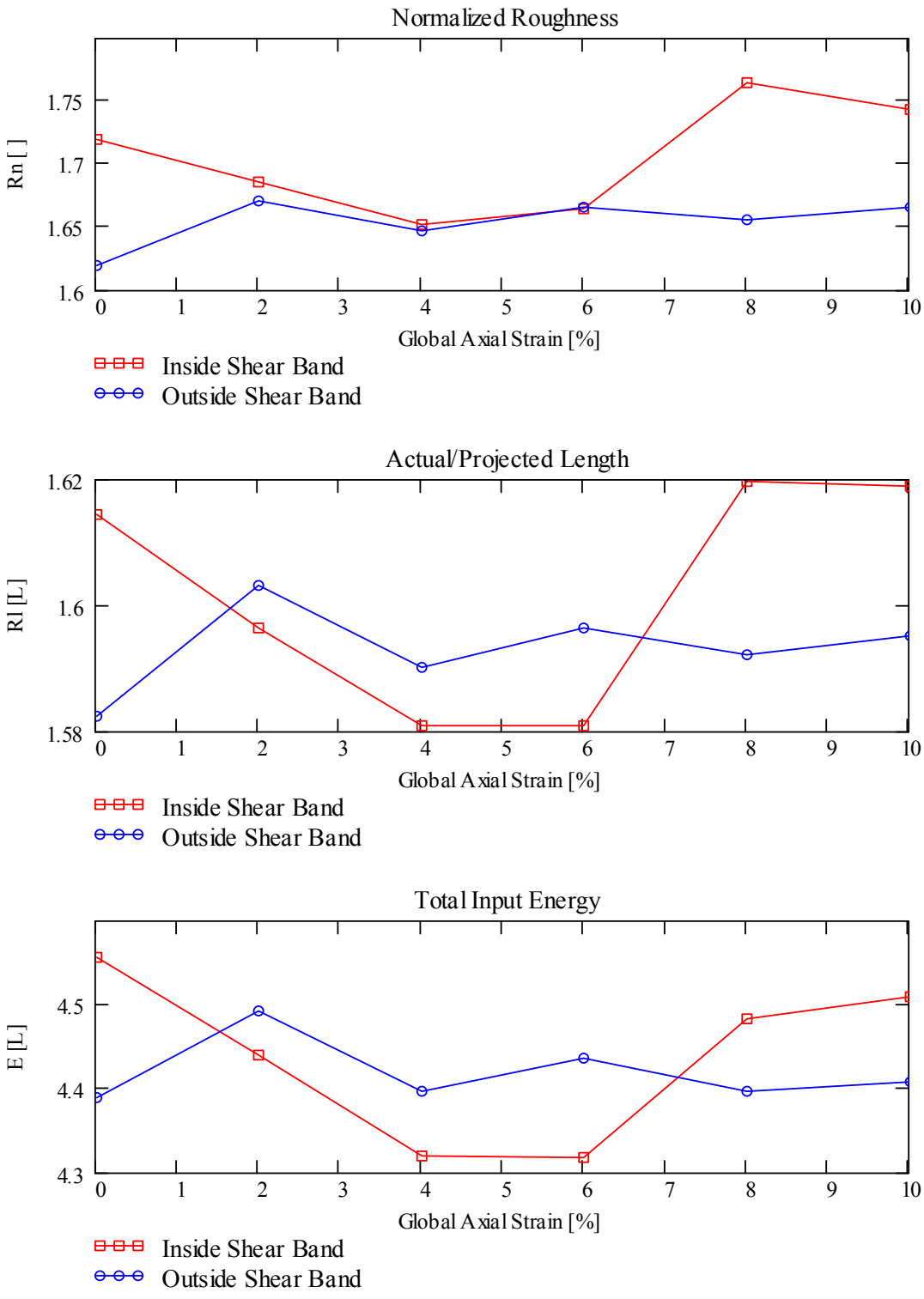

Figure 6.36 (cont.): Roughness of virtual surfaces inside and outside of the shear band as a function of global axial strain in the highly dilatant specimen

7. DISCUSSION AND ANALYSIS OF RESULTS

7.1. Introduction

This chapter presents the analysis and synthesis of the experimental and numerical study results presented in Chapters 5 and 6. A detailed investigation of microstructural results from both phases of the current study is presented. Most previous investigations into plane strain testing of granular materials have focused on macroscale plane strain response (e.g., Vardoulakis and Goldscheider, 1981), constitutive modeling (e.g., Vermeer, 1990), boundary deformation (e.g., Finno et al., 1996), microscale analysis (e.g., Oda and Kazama, 1998), or microstructural modeling (e.g., Bardet, 1994), but few studies have extensively combined several of these measures. Thus, results of the experimental and numerical programs described previously will be integrated hereinafter.

7.2. Analysis of Experimental Results

7.2.1. Local Void Ratio Distributions

Local void ratio distributions were analyzed for four cases: unsheared, sheared, inside the shear band, and outside the shear band. A summary of void ratio means and standard deviations (averaged across all slices for a given specimen) is presented in Table 7.1. The values in Table 7.1 indicate that shearing increases the mean and standard deviation of the local void ratios, inside and outside of the shear band. The increases in void ratios inside the shear bands (relative to the as prepared void ratios) are comparable to values reported by Alshibli and Sture (1999) who observed increases of up to 30%.

Note, too, that the global volumetric strains at localization were 0.2% and 0.6% in the slightly dilatant and highly dilatant specimens, respectively. Based on measurements of boundary deformations and assuming right orthorhombic specimen deformation, the global void ratios as calculated from global volumetric strains in the SD and HD specimens at the onset of localization are 0.603 and 0.570, respectively. These values differ significantly from values outside the shear band presented for both specimens in Table 7.1. Thus, given the increases in void ratio outside of the shear band shown in Table 7.1, deformation is not due to pure rigid block sliding after the onset of localization, but continued macroscopically homogenous deformation is still occurring outside of the zone of localized shear.

The means of local void ratios inside and outside of the shear band showed a larger increase in the highly dilatant specimen relative to the slightly dilatant specimen. This indicates that there was a greater degree of dilation in the highly dilatant specimen than in the slightly dilatant specimen, even though the slightly dilatant specimen has a higher absolute void ratio inside and outside of the shear band than the highly dilatant specimen. The standard deviations, which are a measure of the scatter in local void ratios, are comparable for both specimens. A plot of standard deviation versus mean for all slices is presented as Figure 7.1.

Another measure of variation in local void ratios is the entropy of the histogram, H_v (Chen, 2000):

$$H_V = -\sum_{i=1}^{n} P_i \cdot \log_n(P_i) \tag{7.1}$$

where n is the number of bins in the histogram and P_i is the probability of the i^{th} bin and

Table 7.1: Estimated means and standard deviations of local void ratios (numbers in parenthesis are percent change from as-prepared void ratio)

	Mean (μ_{est})	Standard Deviation (σ_{est})
Slightly Dilatant Specimen		
Unsheared	0.598	0.417
Sheared	0.667 (11.1%)	0.444
Inside Shear Band	0.747 (24.6%)	0.490
Outside Shear Band	0.622 (3.6%)	0.409
Highly Dilatant Specimen		
Unsheared	0.569	0.389
Sheared	0.636 (13.6%)	0.439
Inside Shear Band	0.715 (27.6%)	0.482
Outside Shear Band	0.588 (4.9%)	0.403

when, if $P_i = 0$ (i.e., logarithm is undefined but multiplied by zero), the entire term is taken to be zero. Entropy is a measure of disorder in a system. If void ratios are equally divided among all bins in a histogram, entropy is maximized ($H_v = 1$) and if all void ratios are in a single bin, entropy is minimized ($H_v = 0$). A plot of entropy versus mean is presented at Figure 7.2.

Figures 7.1 and 7.2 clearly indicate that the scatter in and disorder of local void ratio distributions increases with shearing. This is particularly true in regions of high deformation, such as within the shear band. Within the shear band there is a greater range of void ratios and a greater chaos in their distribution. Thus, void ratios within the shear band do not increase uniformly, but rather, there is a collection of large and small void ratios within the shear band. Indeed, Oda and Kazama (1998) indicate that, based on plane strain experiments of assemblies of photoelastic rods, columnar structures

develop during localized shear wherein the majority of the load is carried across the shear band by relatively few force chains. The presence of these large force chains will require regions of relatively low void ratio to support the applied load across the shear band but will allow for regions of relatively high void ratio to form.

Figures 7.3 through 7.5 present gamma distribution functions for local void ratio distributions inside and outside of the shear band for slightly and highly dilatant

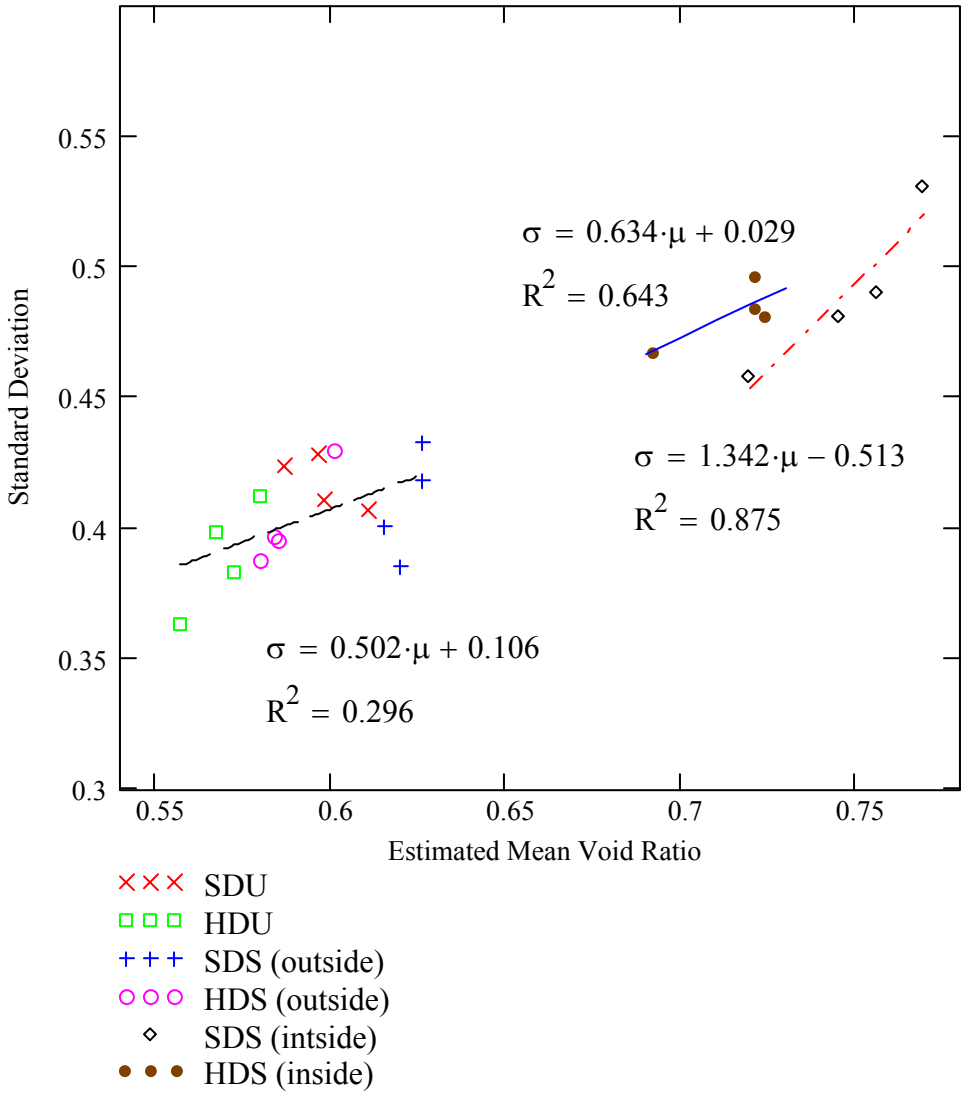

Figure 7.1: Standard deviation of local void ratio distributions as a function of the mean

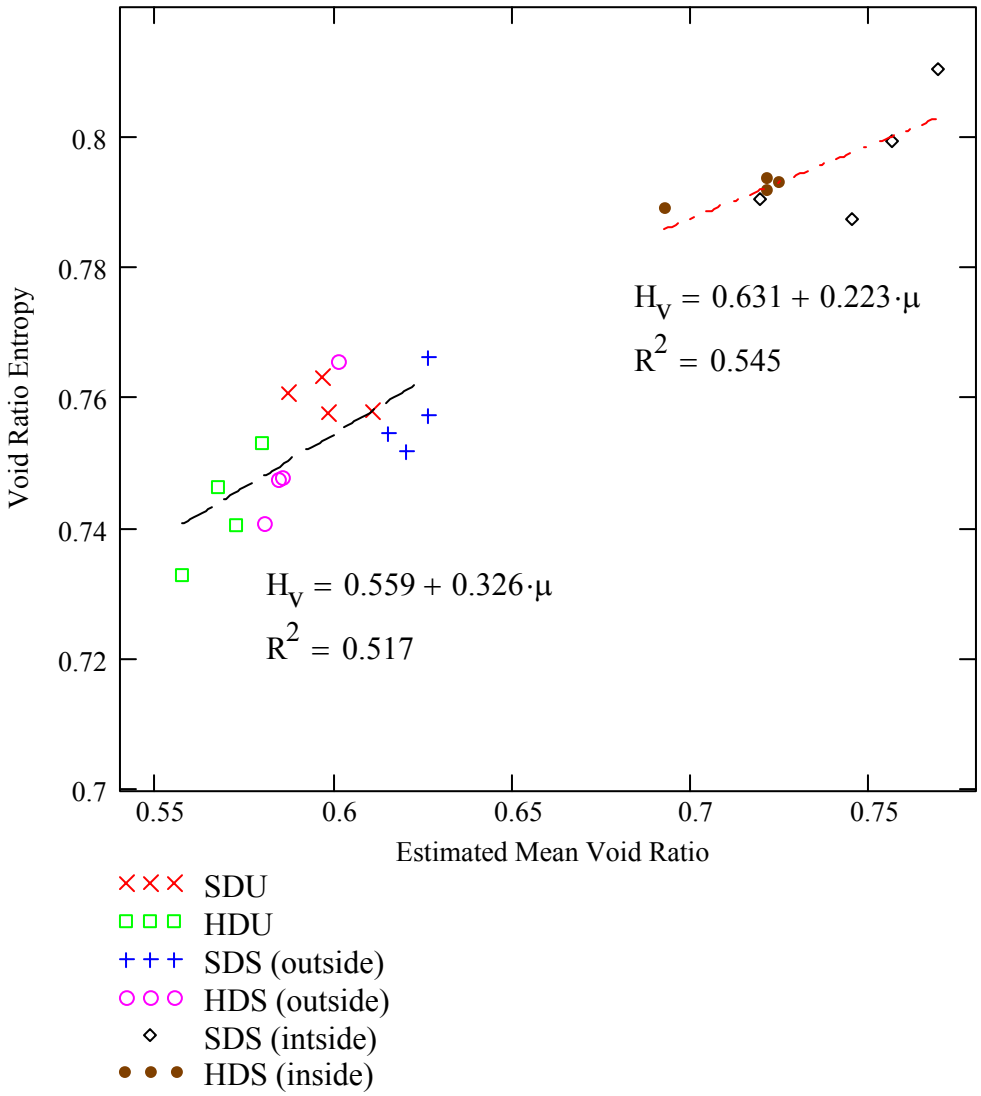

Figure 7.2: Entropy of local void ratio distributions as a function of the mean

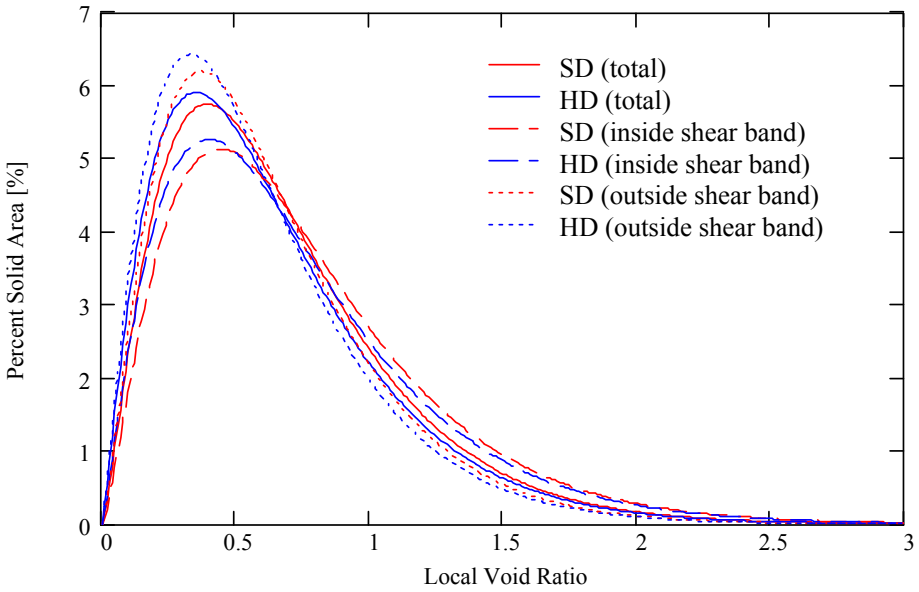

Figure 7.3: Comparison of void ratio distributions inside and outside the shear band for slightly dilatant and highly dilatant specimens

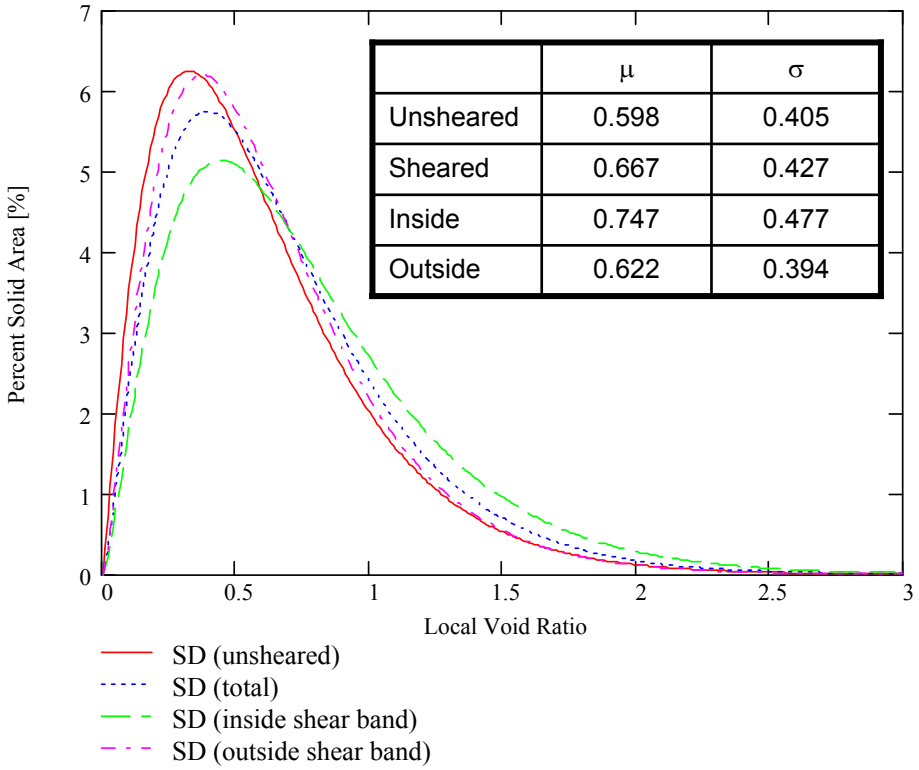

	μ	σ
Unsheared	0.598	0.405
Sheared	0.667	0.427
Inside	0.747	0.477
Outside	0.622	0.394

Figure 7.4: Comparison of void ratio distributions inside and outside the shear band for slightly dilatant specimens in the sheared and unsheared states

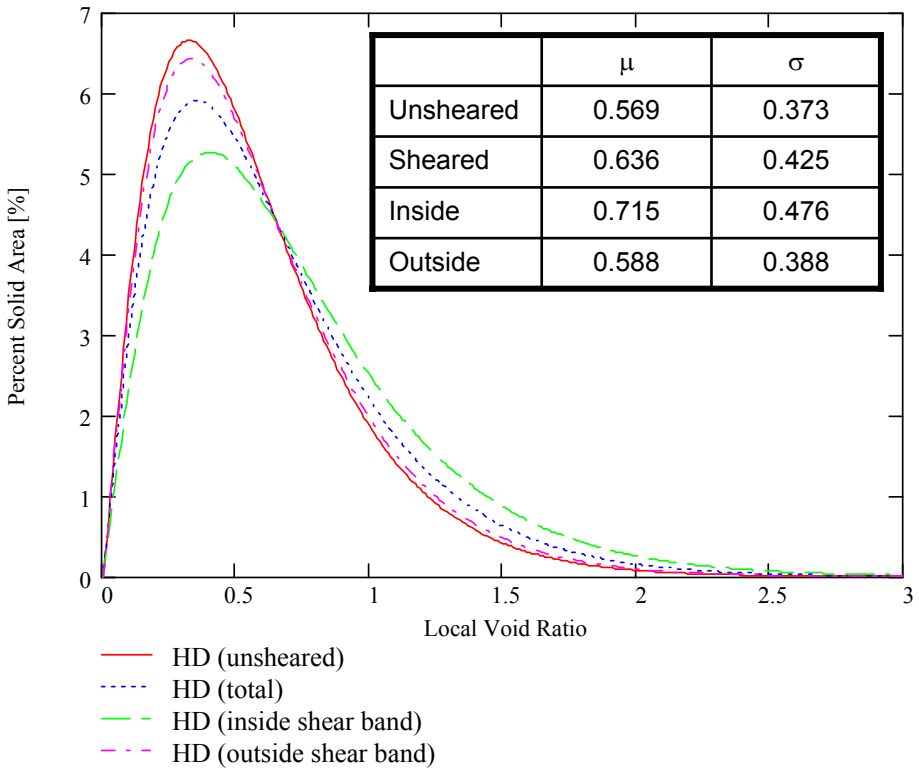

	μ	σ
Unsheared	0.569	0.373
Sheared	0.636	0.425
Inside	0.715	0.476
Outside	0.588	0.388

Figure 7.5: Comparison of void ratio distributions inside and outside the shear band for highly dilatant specimens in the sheared and unsheared states

specimens. Observation of these figures provide a visual understanding of the evolution of void ratios inside and outside of the shear band. The behavior of the slightly dilatant and highly dilatant specimens is similar. These observations tend to reinforce the conclusions drawn from Figures 7.1 and 7.2 in a more qualitative manner, particularly that microstructures evolves much more noticeably inside the shear band than outside the shear band.

7.2.2. Terminal Density Inside the Shear Band

Previous researchers (Mooney et al., 1998) have noted that a unique critical state line in e-log(p′) space does not exist for drained sand specimens that localized under plane strain compression. They note that the slope of the e- p′ line is a material property and indicate that at a given stress state an infinite number of void ratios are possible. Thus, they conclude, the critical state void ratio within the shear band is actually a function of the initial void ratio of the specimen (see also Figure 7.1). Mooney, et al. (1998) further note that for their densest specimen to reach critical state would require a void ratio increase equal to 85% of the range between e_{max} and e_{min} and could not be achieved even if the peak dilatancy angle (23°) was constant throughout the softening regime.

Similar results to those described above were also observed in the current study. The critical state points for the specimens tested in this study fall on an approximately straight line in q-p′ space (see Figure 5.3). However, there is no clearly defined critical state line in e-log(p′) space, as shown in Figure 7.6 (mean effective stress is calculated from σ_n and σ_s on the shear plane and from σ_1, σ_2, and σ_3 for global values and outside of the shear band). Thus, it makes more sense to consider some "terminal density" within the shear band that is a function of external factors and is not a true material property. In fact, the void ratio inside the shear band for the slightly dilatant specimen is above the critical state line and comparable to the maximum void ratio (0.742) for Ottawa 20-30 sand. This phenomenon has been previously reported by Mooney, et al. (1998) who reported points from within shear bands above the critical state line (measured by observing particles of contrasting color adjacent to the membrane) and Oda and Kazama

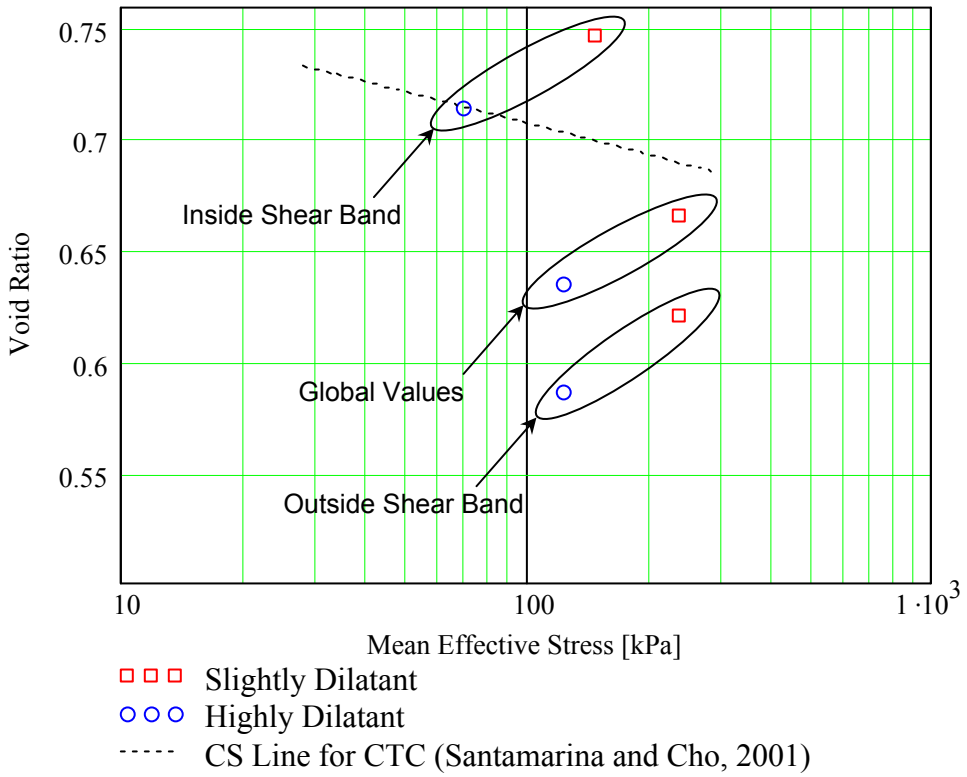

Figure 7.6: e-log(p′) plot for slightly dilatant and highly dilatant specimens

(1998), who reported void ratios in the shear band that were up to 19% greater than the maximum void ratio for their tested sand (as measured by image analysis).

Even though there is not a unique critical state line in e-log(p′) space when considering either global void ratio or void ratio within the shear band, it is likely that the sand within the shear band has reached terminal density and a state of constant deformation, as evidenced by the fact that the dilatancy angles within the shear band are very small (1.0° and 0.2° for the slightly dilatant and highly dilatant specimens, respectively) indicating little or no volume change at high values of global axial strain:

thus, the soil within the shear band is shearing at constant volume. The author hypothesizes that the primary reason that the void ratio in the shear band in the highly dilatant specimen terminates at a lower void ratio than the void ratio in the shear band of the slightly dilatant specimen is that the soil mass surrounding the shear band in the highly dilatant specimen is more prone to dilate itself, in effect "pushing back" on the soil within the shear band. If shear banding resulted in true rigid block sliding (as is often assumed), this would not be the case and it would be expected that the shear band in the highly dilatant specimen would continue to increase to a value closer to that of the slightly dilatant specimen. In reality, a more appropriate model may not be of two rigid blocks interacting, but rather, at large strains the two primary rigid blocks are separated by a secondary shear block and there are transition zones between the various blocks, as shown in Figure 7.7.

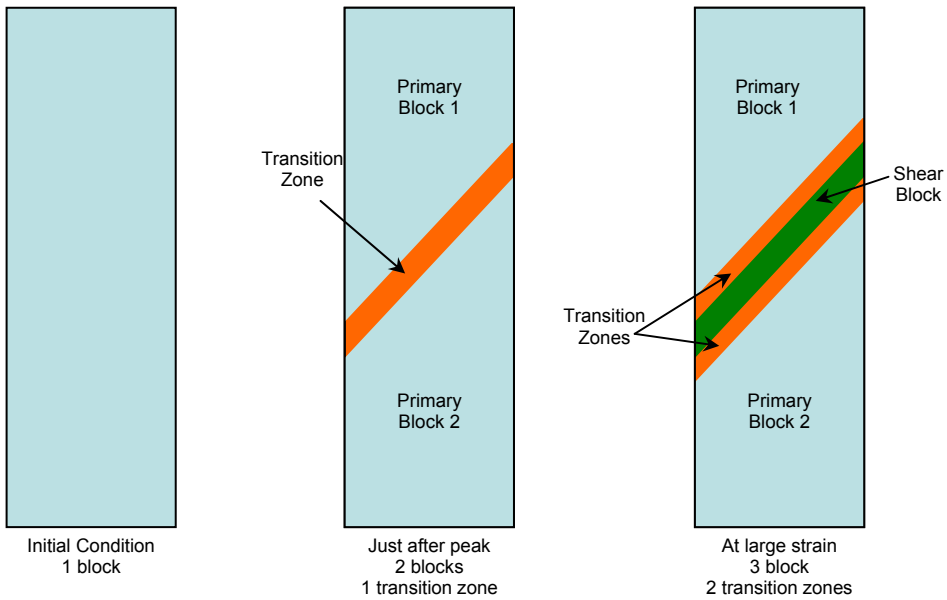

Figure 7.7: Conceptual model of shear banding with transition zones

7.2.3. Void Ratios Above and Below Shear Bands

Yang (2002) determined that in conventional triaxial compression tests that a "dead zone" existed near the loading platens wherein very little deformation occurred. He noted that the dead zone was essentially conical in shape and that lubricating the platen-soil interface served to reduce the size of the dead zone but not eliminate it entirely. Finally, Yang noted that the dead zone appeared to be more severe in specimens that tended to exhibit a greater degree of dilatancy.

It stands to reason that a similar dead zone will exist within biaxial compression tests even though the end platens on the device used in the current study are made of glass to reduce friction. If this dead zone effect does exist, it should be possible to observe it by noting differences in local void ratios above and below the shear band. Observation of the plots presented in Appendix C (developed from inclined strip calculations) indicates that the average void ratios above and below the shear band are similar in the slightly dilatant specimen. In the highly dilatant specimen, void ratios above the shear band are significantly less than below the shear band in three of the four slices. Figures 7.8 and 7.9 show standard deviation and void ratio distribution entropy as a function of the estimated mean of the local void ratios. Each of these plots has three distinct groupings of data points: (i) inside the shear band; (ii) below the shear band for both specimens and above the shear band for the SDS specimen (no dead zone); and (iii) above the shear band for the HDS specimen (dead zone). It is evident from these plots that there is a dead zone above the shear band for the HDS specimen, as evidenced by the

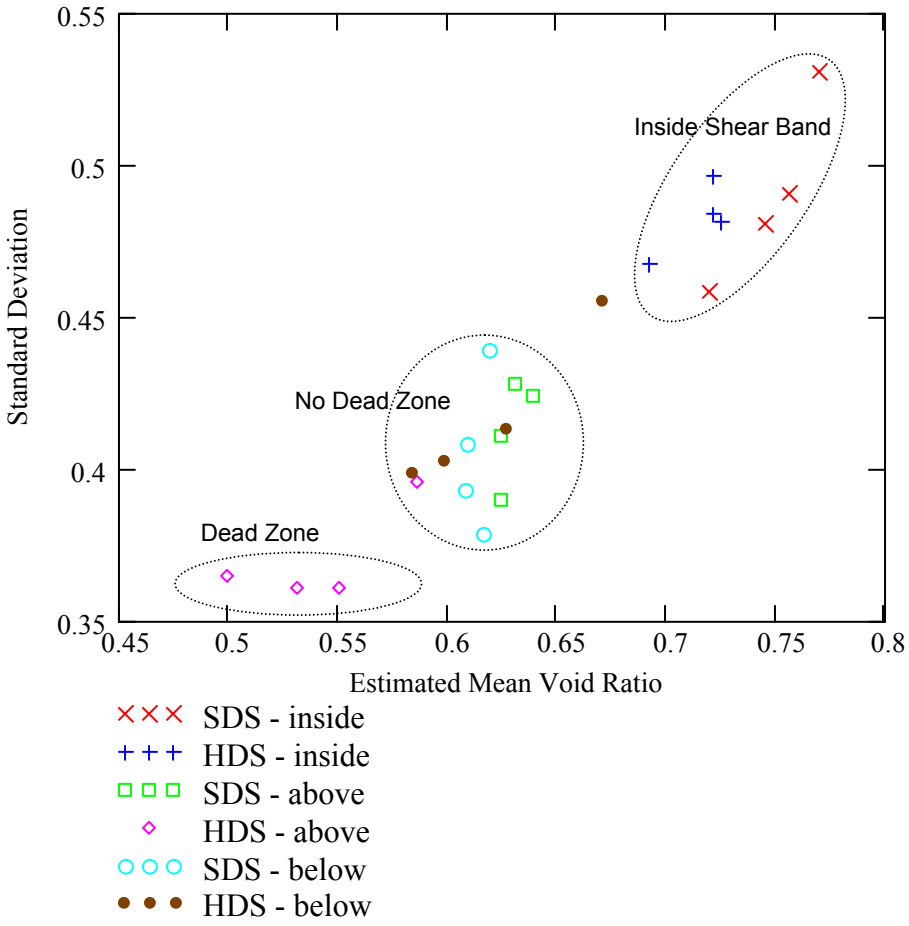

Figure 7.8: Standard deviations of void ratio distributions inside, above, and below the shear band

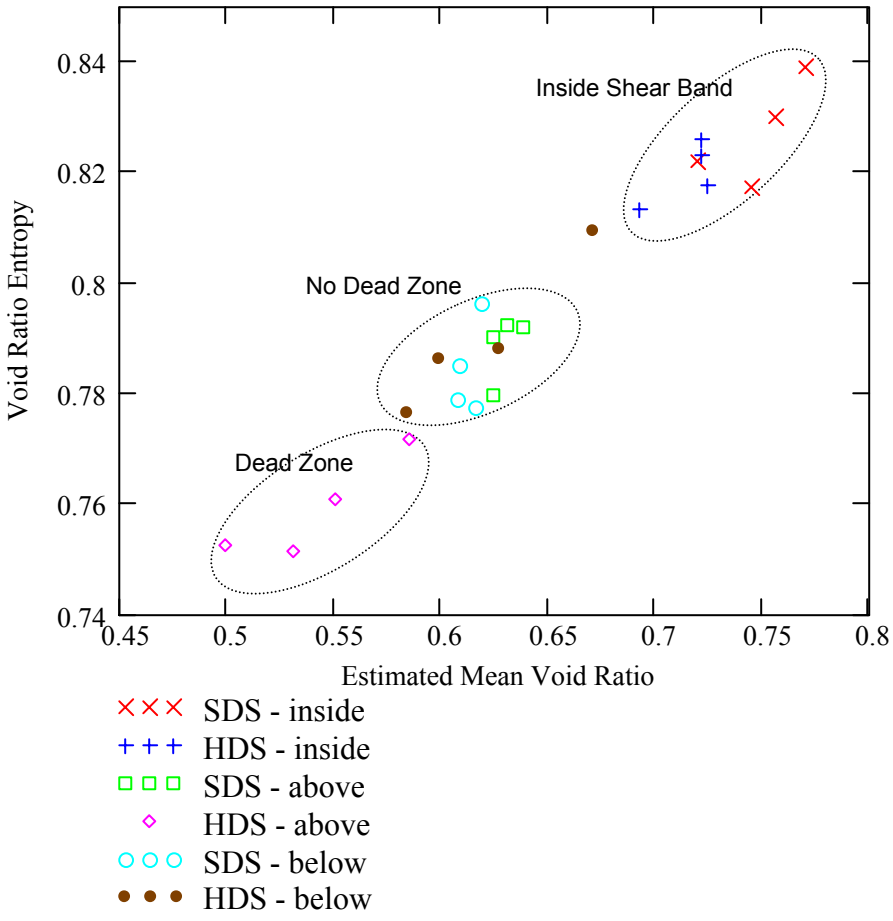

Figure 7.9: Entropies of void ratio distributions inside, above, and below the shear band

lower standard deviation, mean void ratio, and void ratio entropy in this region, all of which are consistent with observations for unsheared specimens. It is unclear how the presence of this dead zone affects shear band formation.

Another item of note in Figures 7.8 and 7.9 is that one of the points that should be in the dead zone (HDS-20) could apparently be grouped with the "no dead zone" region as this point lies approximately midway between the "no dead zone" and "dead zone" regions. A similar argument could be made with regards to surface HDS-80, which lies between the "no dead zone" region and inside the shear band. This is likely an artifact of surface selection. When specimens were sliced to generate surfaces for polishing, each cut creates two potential surfaces, one on either side of the cut. Ultimately, five sections are acquired from a specimen, each comprising approximately 20% of the specimen thickness: 0%-20%, 20%-40%, 40%-60%, 60%-80%, and 80%-100%. Only four of these sections are required for analysis, thus either the 0%-20% section or the 80%-100% section could be discarded. It was decided in the current study that the 80%-100% section would be discarded for each specimen, meaning that surfaces were acquired from the "high side" of each section. Thus, during the grinding phase of surface preparation, as section thickness was decreased, the 20% surface would be moving towards the edge of the specimen while the 80% surface would be moving towards the center of the specimen. Given that the dead zone in a conventional triaxial compression test is conical in nature, it is reasonable to believe that the dead zone in a biaxial compression test would take the form of a four-sided pyramid due to specimen geometry. Given this fact, it is possible that the 20% slice was at least partially outside of the dead zone while the 80% slice was fully inside of it.

7.2.4. Shear Band Thickness

Significant previous work has been done to assess the thickness of shear bands in sand (see Frost et al., 2004 for a review of previous work), but the majority of the work has been theoretical (e.g., Muehlhaus and Vardoulakis, 1987) or based upon external measurements of shear band thickness (e.g., Han and Drescher, 1993), while relatively little work has been based on internal measurements (e.g., Alshibli and Sture, 1999). In the present study, shear band thickness has been quantified by four different measures: (i) spatial averaging along pre-defined inclined strips; (ii) virtual surface measurements; (iii) visual assessment of captured images; and (iv) visual assessment of membrane deformations. In this manner, comparisons can be made between traditional ad hoc measures of shear zone thickness and more rigorous, quantifiable measures.

Shear band thickness from spatial averaging of inclined strips and virtual surfaces was measured as the difference between the "LHS" and "RHS" lines in Figures 5.65 and 5.66 and Appendix C. The method used for selection of these demarcation lines was discussed in Chapter 5. In the captured images, two parallel lines were drawn across each image and the distance between them measured. External measurements were made on photographs taken of the specimen at the end of the test. Grid lines on the membrane were used for guidance in selection of the shear band extents and, again, the distance between two parallel lines was measured. Typical images of the internal and external images are presented in Figures 7.10 and 7.11. A summary of shear band thickness measurements is presented in Table 7.2.

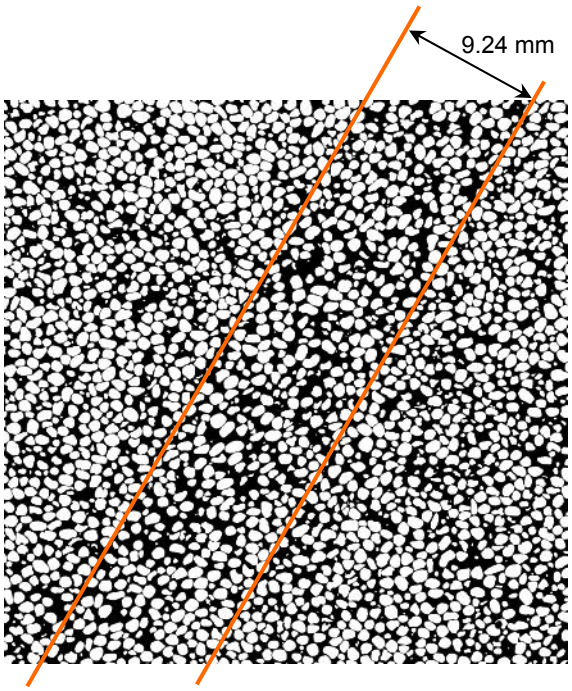

Figure 7.10: Measurement of shear band thickness from an image (HDS-60) captured in a laboratory specimen (measurement shown is in millimeters)

Figure 7.11: Measurement of shear band thickness from membrane deformations on the highly dilatant specimen (measurement shown is in millimeters)

Table 7.2: Summary of shear band thickness measurements (experimental)

	Slightly Dilatant Specimen		**Highly Dilatant Specimen**	
	(mm)	**(d_{50})**	**(mm)**	**(d_{50})**
Spatial Averaging in Inclined Strips				
20	11.0	15	12.5	17
40	9.4	13	11.0	15
60	11.0	15	12.5	17
80	12.5	17	11.0	15
Virtual surfaces	5.9	8	7.8	11
Image measurement				
20	8.7	12	8.4	11
40	8.5	11	9.7	13
60	9.4	13	9.2	12
80	7.6	10	9.7	13
External measurement	8.3	11	9.0	12

Figures 7.10 and 7.11 illustrate the fact that it is difficult to definitively identify the exact shear band extents using visual observation alone. Table 7.2 indicates that thicknesses measured using spatial averaging in inclined strips are the highest while those measured with virtual surfaces are the lowest, with visual observations falling in between. The visual observations are most closely in line with typical values reported in the literature as a function of mean particle diameter (Frost et al., 2004). To understand the differences between measurements, it is helpful to consider where the different quantitative approaches place shear band extents. A schematic of shear band locations for a typical image is presented in Figure 7.12.

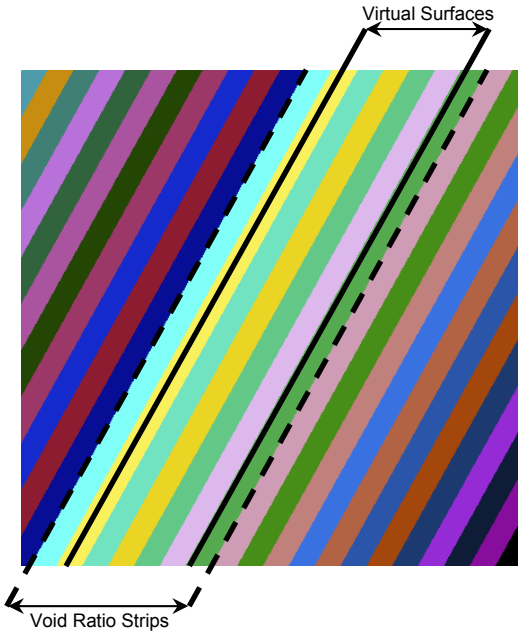

Figure 7.12: Schematic of shear band extents for image HDS-60

Figure 7.12 indicates that the method of virtual surfaces identifies shear band extents that are within the extents identified by the inclined strip method. This result is indicative of a transition zone between the fully formed shear band and the rigid block portion of the specimen. The inclined strip method is a sensitive measurement capable of picking up not only regions of greatly increased void ratio, but also regions of void ratio gradient. The virtual surface method relies on significant particle alignment in the direction of shear to decrease overall roughness parameters in the fully-formed shear zone. However, in the transition region where there has been significant increase in void ratio, there is not sufficient particle alignment for the localization to be detected but the virtual surface method.

Close observation of images previously published by Hebeler (2005) indicate that this phenomenon is also present in systems comprised of granular soils sheared adjacent to a continuum. Figure 7.13 is a typical image of a locked sand microstructure obtained

by displacing a rough continuum surface axisymmetrically through a sand mass (see Hebeler, 2005 for details). This figure indicates that there is clearly a transition zone between the fully-formed shear zone and the undisturbed zone. The three zones are indicated by the three different line slopes that can be drawn between regions of dark and light particles. It is possible that the presence of this transition zone is a product of different degrees of particle rotation versus particle translation in the two regions.

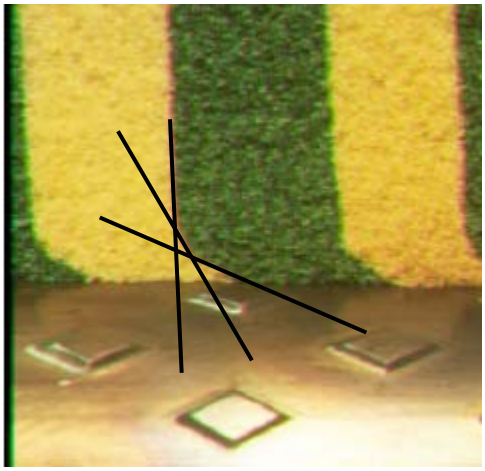

Figure 7.13: Transition zone in interface shear

Measurement of the fully formed shear zone and the transition zone in Figure 7.13 indicates that both regions are approximately seven particle diameters wide. In the slightly dilatant specimen, the difference between the virtual surface measurement and the spatial averaging inclined strip measurement is seven particle diameters (say, 3.5 particle diameters on either side of the shear band) while in the highly dilatant specimen it is five particle diameters (2.5 diameters on either side). The differences between the granular shear zones and the interfacial shear zone could arise from many factors,

including different grain diameters, loading conditions, and the asperity height on the textured continuum. However, this analysis indicates that transition zones do exist in both types of shearing and that the sizes of these zones are of the same magnitude. Similar observations are emerging from particle image velocimetry (PIV) studies being undertaken by others (DeJong, 2005).

As reported by previous researchers (e.g., Drescher et al., 1990) there is also a relationship between shear band thickness and internal void ratio (or density). Drescher, et al. (1990) report that this relationship may be described as follows for a shear band of continuously increasing thickness:

$$\Delta\rho_d = -\rho_d \cdot \frac{u_s}{t} \cdot \tan\left(\psi_s\right) \tag{7.1}$$

where ρ_d is the initial specimen dry density, u_s is movement along the shear band, t is shear band thickness, and ψ_s is the dilation angle. The tests described herein do not have constantly growing shear bands, and so Equation 7.1 does not apply and there is not a comparable theoretical expression for shear bands in steady state. However, Equation 7.1 does provide some guidance as to the magnitudes of the void ratios that are expected within a shear band. A plot of shear band thickness as a function of void ratio is presented in Figure 7.14. For reference, several curves representing Equation 7.1 are also presented. It should be noted that for free-forming shear bands, the true thickness will be a function of kinematic constraints.

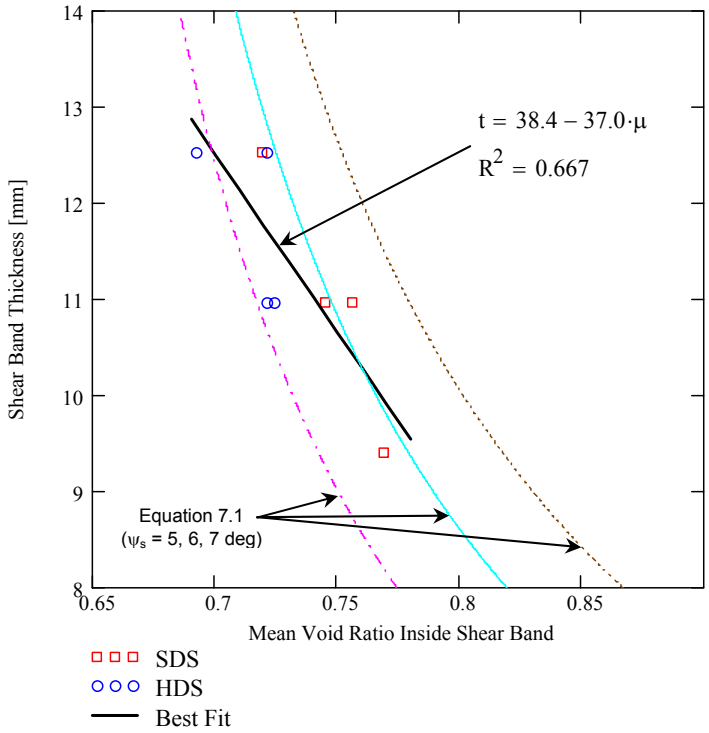

Figure 7.14: Shear band thickness as a function of void ratio

7.3. Analysis of Numerical Results

7.3.1. Local Void Ratio Distributions

Local void ratio distributions were analyzed for numerical specimens in much the same way as for the experimental specimens. Numerical specimens have the added advantage of allowing for the monitoring of the evolution of distribution statistics as a function of strain. Figures 7.15 and 7.16 present the variation of standard deviation and entropy with increasing global axial strain, respectively. These figures indicate that both variation and disorder are increasing as functions of strain, with the most marked increases occurring in the shear band after the onset of localization. Thus, similar to the experimental results, void ratios within the shear band do not necessarily increase

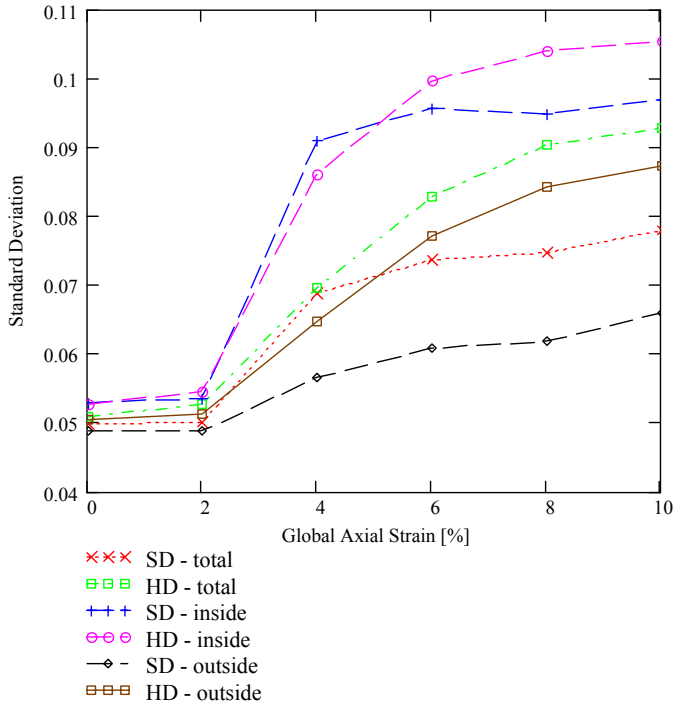

Figure 7.15: Standard deviation of local void ratio distributions as a function of global axial strain

monotonically, but rather, they increase locally in some regions and decrease in others. However, as can be seen in Figures 7.17 and 7.18, there is a nearly unique relationship between mean and standard deviation and between mean and entropy. This is a function of the two-dimensional nature of the model and indicates that there is only a very narrow range of stable packing distributions. This was evidenced during model generation and packing, as discussed in Chapter 6.

7.3.2. Shear Band Thickness

Previous researchers (e.g., Cundall, 1989) have reported shear band thicknesses in DEM models that are on the same order as those reported in plane strain laboratory experiments (i.e., anywhere from 8 to 20 mean particle diameters). This is likely due to the formation of particle chains bridging the shear band, as discussed by Oda and Kazama (1998). There is likely some equilibrium thickness required by the formation of these chains. Above this thickness, the chains become unstable and buckle. Below this

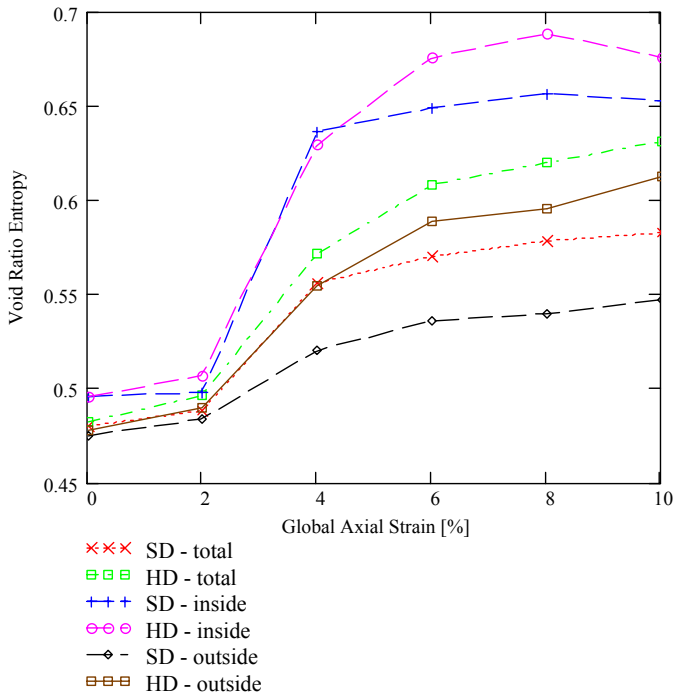

Figure 7.16: Local void ratio distribution entropy as a function of global axial strain

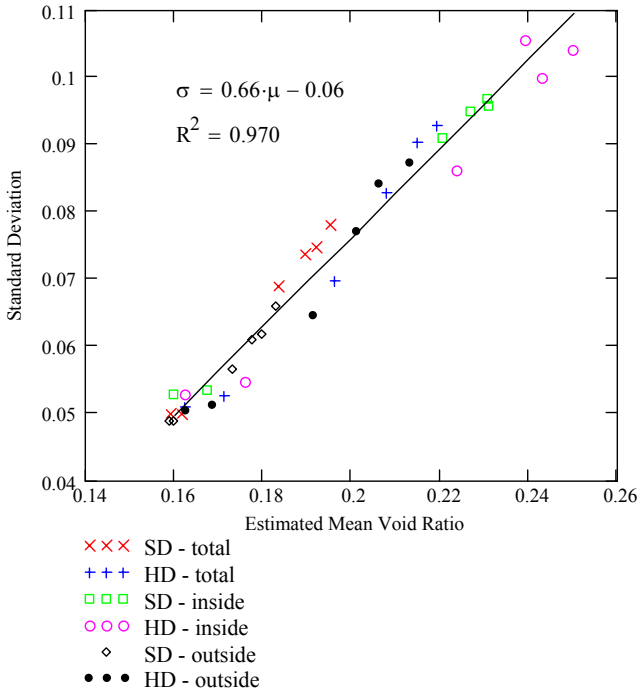

Figure 7.17: Standard deviation of local void ratio distribution as a function of estimated mean void ratios

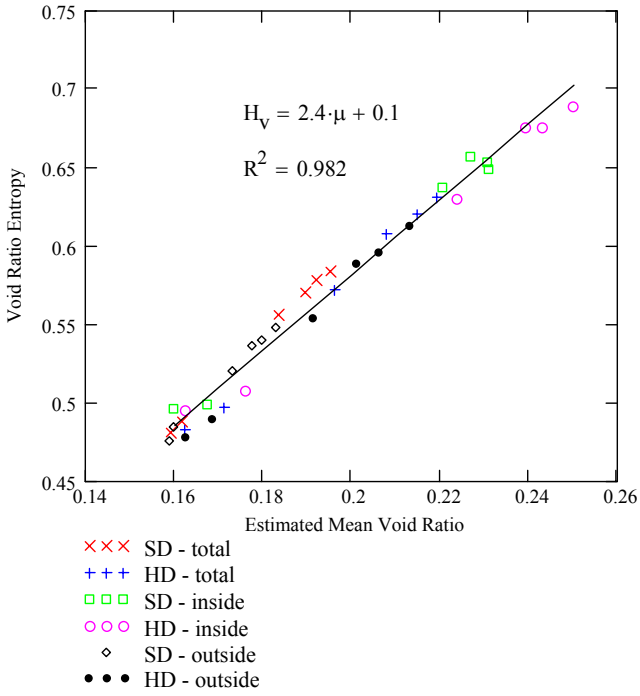

Figure 7.18: Local void ratio distribution entropies as a function of estimated mean void ratios

thickness, there is no true formation of a shear band, with forces being more diffuse along the shearing plane. The evolution of normal contact forces with global axial strain is presented in Figures 7.19 through 7.24 for the slightly dilatant specimen and Figures 7.25 through 7.30 for the highly dilatant specimen.

Observation of Figures 7.19 through 7.30 indicates that specimens initially have dense, uniform arrays of contact forces. However, after the onset of localization, the overall distribution of contact forces becomes less diffuse, with several large force chains dominating the assembly and other areas being relatively devoid of contact forces. As mentioned previously, it is the formation of these chains that facilitates the regions of very high void ratio within the shear band.

It is not possible to measure shear band thickness from plots of contact forces such as those in the above figures. Rather, these figures provide qualitative insight in to the micromechanics of the shear band. Shear band thicknesses were measured from inclined strip transects, as in Section 7.2 above for laboratory specimens. Results of these measurements are presented in Table 7.3, which indicates that there is good general agreement between inclined strip measures and direct measurement of shear band thickness. Overall, measured shear band thickness is slightly greater than, but comparable to, the measured thicknesses for laboratory specimens. This can be attributed to the two-dimensional nature of the PFC model. When particles are constrained to two dimensions, they have only three degrees of freedom instead of six. Thus, because particles are unable to move out of the plane, the dilation of the shear band is greater than that observed in experimental specimens, as was evident in the calculated dilation angles and volumetric strains for the global behavior of the numerical specimens.

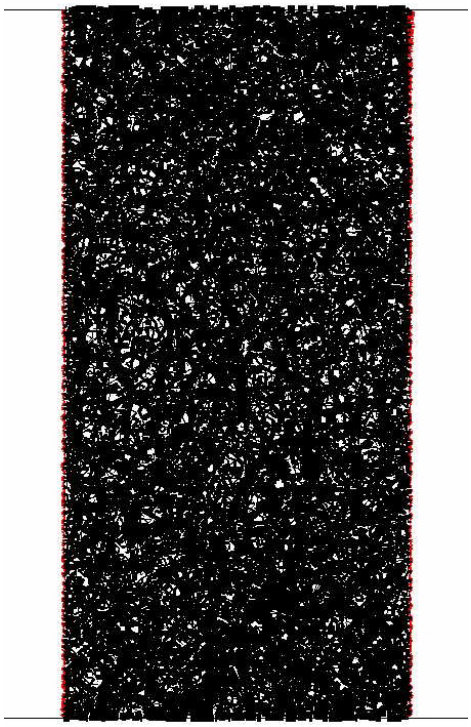

Figure 7.19: Normal contact force chains for slightly dilatant specimen at $\varepsilon_{ax} = 0\%$

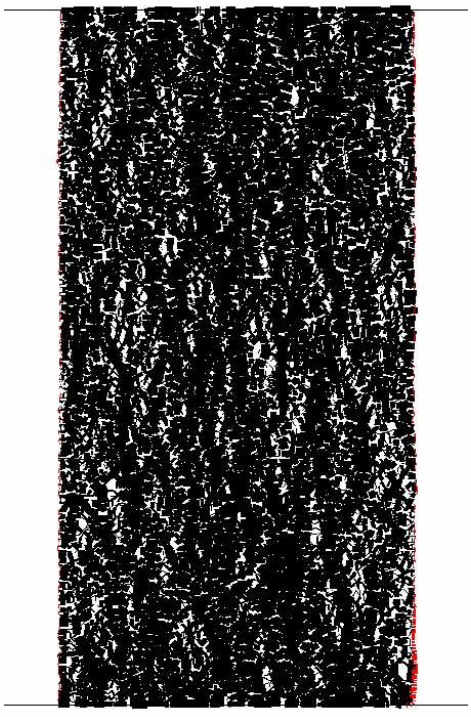

Figure 7.20: Normal contact force chains for slightly dilatant specimen at $\varepsilon_{ax} = 2\%$

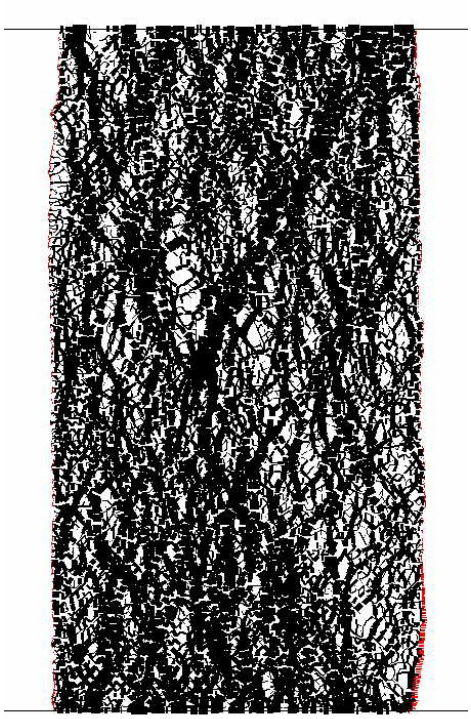

Figure 7.21: Normal contact force chains for slightly dilatant specimen at $\varepsilon_{ax} = 4\%$

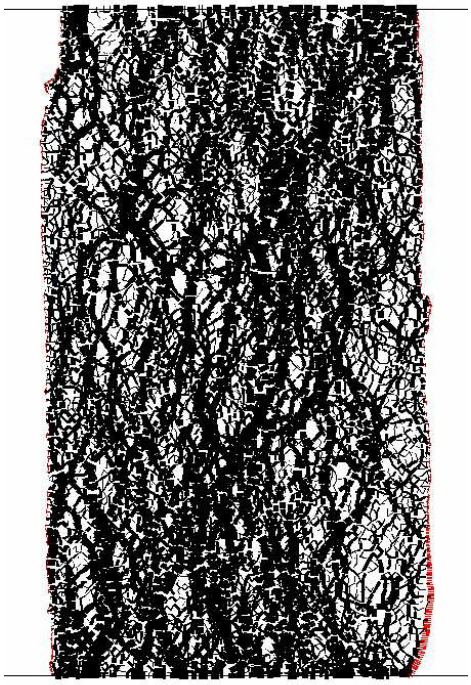

Figure 7.22: Normal contact force chains for slightly dilatant specimen at $\varepsilon_{ax} = 6\%$

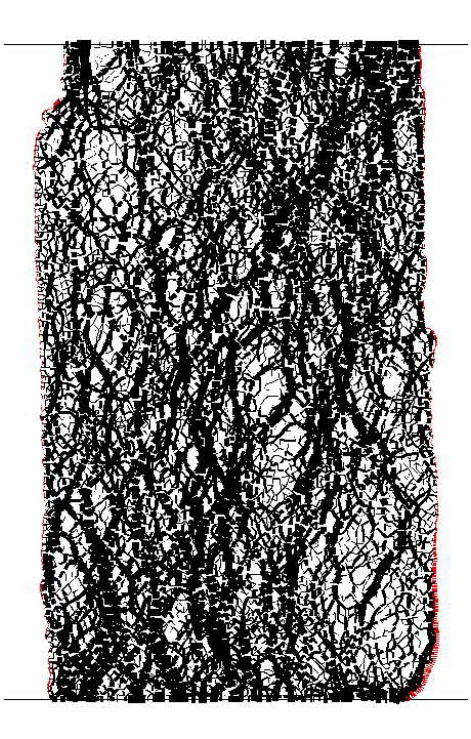

Figure 7.23: Normal contact force chains for slightly dilatant specimen at ε_{ax} = 8%

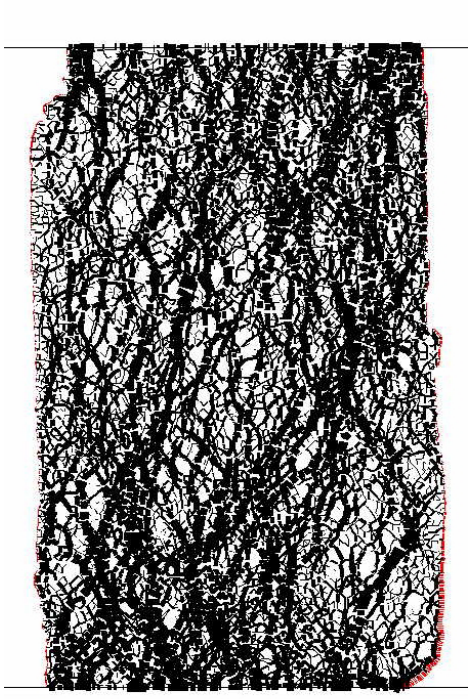

Figure 7.24: Normal contact force chains for slightly dilatant specimen at ε_{ax} = 10%

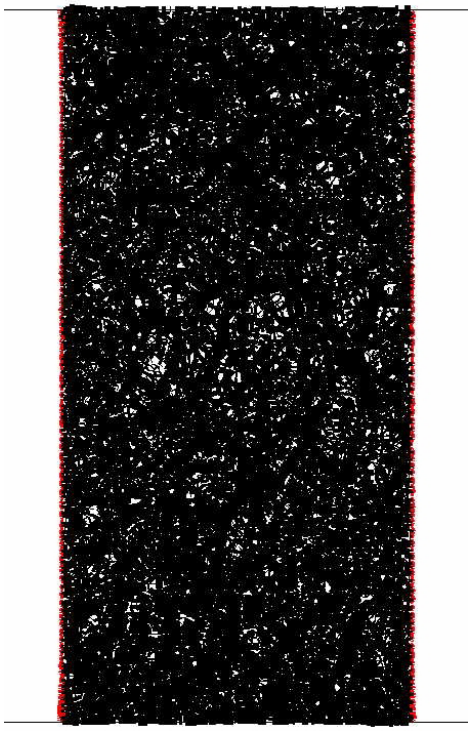

Figure 7.25: Normal contact force chains for highly dilatant specimen at $\varepsilon_{ax} = 0\%$

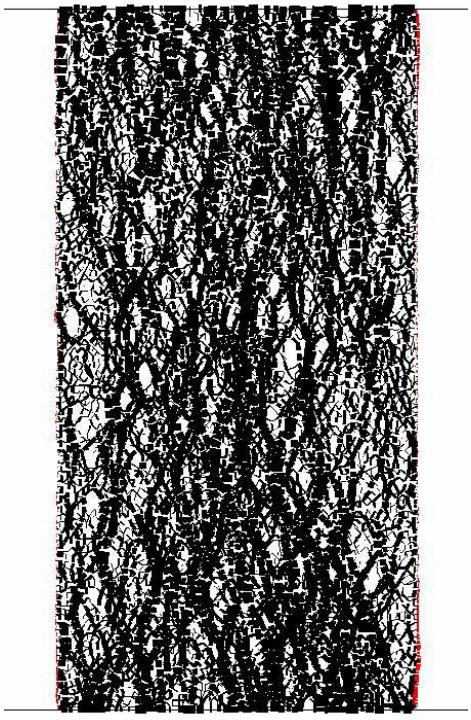

Figure 7.26: Normal contact force chains for highly dilatant specimen at $\varepsilon_{ax} = 2\%$

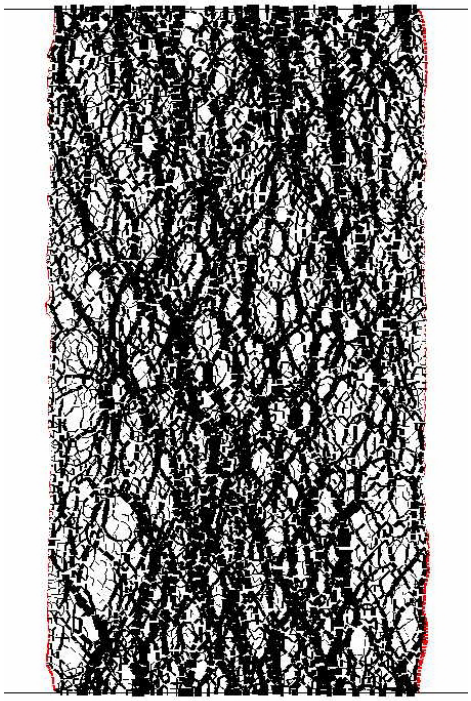

Figure 7.27: Normal contact force chains for highly dilatant specimen at ε_{ax} = 4%

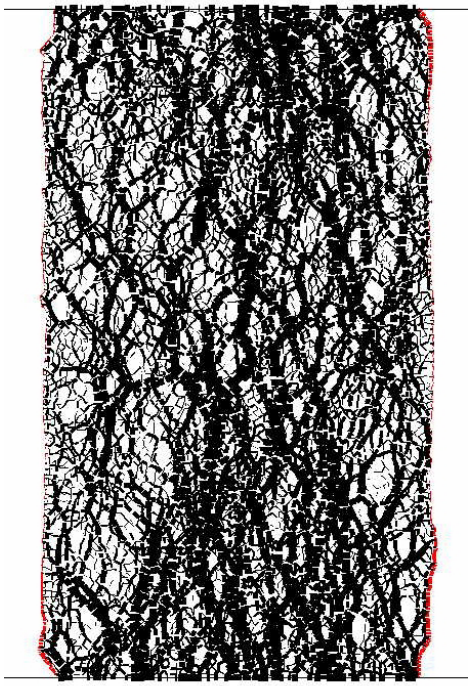

Figure 7.28: Normal contact force chains for highly dilatant specimen at ε_{ax} = 6%

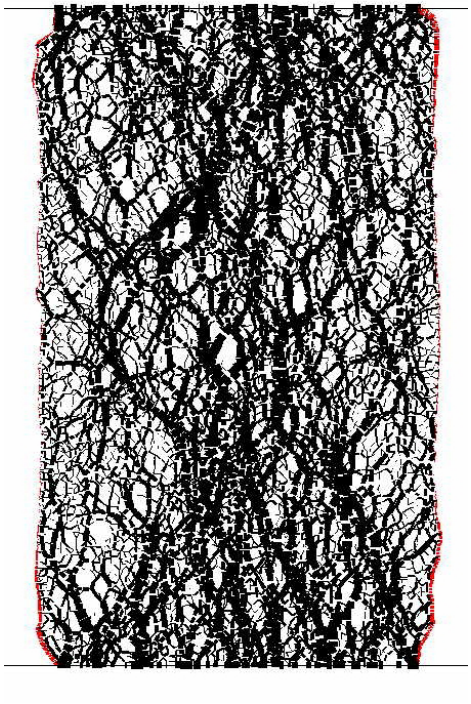

Figure 7.29: Normal contact force chains for highly dilatant specimen at ε_{ax} = 8%

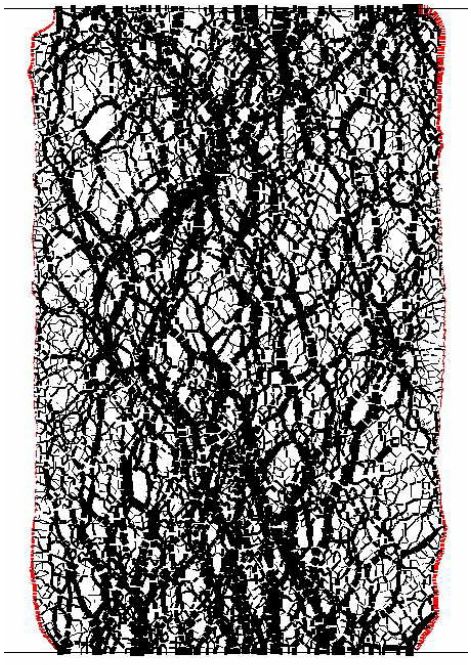

Figure 7.30: Normal contact force chains for highly dilatant specimen at ε_{ax} = 10%

Table 7.3: Summary of shear band thickness measurements (numerical)

	Inclined Strips		Direct Measurement	
	(L)	**(d_{50})**	**(L)**	**(d_{50})**
Slightly Dilatant Specimen				
ε_{ax} = 4%	0.97	15	0.91	15
ε_{ax} = 6%	0.97	15	0.97	15
ε_{ax} = 8%	1.1	18	1.1	18
ε_{ax} = 10%	1.1	18	1.3	21
Highly Dilatant Specimen				
ε_{ax} = 4%	0.65	10	0.99	16
ε_{ax} = 6%	0.65	10	0.99	16
ε_{ax} = 8%	0.81	12	1.1	18
ε_{ax} = 10%	0.97	15	1.2	19

7.3.3. Additional Notes on Numerical Simulations

Two primary items preclude the full analysis of microstructures in numerical specimens relative to the experimental specimens: two-dimensionality and multiple shear bands. The effects of the two-dimensionality of the model have been discussed previously, but also have significant effects on virtual surface analysis of microstructure. The plots of varying virtual surface roughness with increasing strain that were presented in Figures 6.35 and 6.36 indicate only weak trends with respect roughness evolution. If any conclusion can be drawn from these plots, it is that roughness of virtual surfaces within the shear band increase slightly with increasing shear, which is divergent from the observation of decreasing roughness in experimental specimens. In experimental specimens, particles are free to move in and out of a plane, as a minimum energy solution requires. However, in two dimensions, this is not the case, so a highly misaligned particle (e.g., a particle with its long axis perpendicular to the direction of shear) will remain in the shear band. As particle alignments become increasingly chaotic with

developing movement along the shear band, virtual surface roughness will tend to increase. Additionally, because families of shear bands exist within the model, virtual surfaces aligned parallel to the major shear band will still pass though minor shear bands, which will tend to disturb the roughness calculations. This effect is amplified when surface lengths are trimmed to a constant value because then the minor shear bands occupy an increasingly significant portion of the entire surface.

With respect to void ratios above and below the shear band, similar difficulties arise. It was noted in the discussion of the highly dilatant experimental specimen that distribution statistics above and below the shear band are different from each other. This is attributed to the presence of a dead zone near the top loading platen. Similar effects may exist in numerical specimens (see Yang, 2002), but it is difficult to them in a manner similar to that used for experimental specimens. Indeed, void ratio above the shear band in the highly dilatant specimen is constantly increasing relative to void ratio below the shear band after the onset of localization (see figures 6.27 through 6.30). Thus, similar effects are qualitatively observed in the current numerical models, but their rigorous quantification is restricted by the similarity of distribution parameters in two dimensions and by the presence of secondary shear bands.

8. CONCLUSIONS AND RECOMMENDATIONS

8.1. Conclusions

This dissertation presents the results of an integrated experimental and numerical investigation of particulate behavior in the vicinity of shear bands, which are evident in many laboratory and field-scale failures of geotechnical systems, including shallow foundations, retaining walls, and engineered slopes. There currently exists a significant body of work on the use of constitutive models to describe strain localizations and on the effects of different test conditions and materials on shear banding in laboratory specimens. Relatively less information is available regarding the soil structure within and in the vicinity of a fully developed shear band. This study sought to address some of the gaps in existing knowledge by studying soil structure within shear bands at the particulate level.

Developments made in this study may be broadly classified into three categories: experimental, numerical, and analytical. The primary experimental developments included advancements in specimen testing and preservation:

- A low-cost, robust system for biaxial device control and data acquisition was implemented. Most previous devices of this type are controlled and monitored using complex and expensive electronics and peripheral devices. However, these systems are prone to failure and difficult to use. The equipment that was designed and built herein for device control uses a highly stable linear power supply which was wired to provide a common

ground reference for all measurement channels and for all supply channels. The data acquisition system provides for data collection at high scanning rates (15 channels per second) with excellent noise suppression, resulting in data being collected at 22-bit accuracy. The current system is simple to use and maintain, modular, and represents a significant step forward from the systems currently used for controlling highly-instrumented plane strain compression devices. It is estimated that the current setup cost less than one-quarter of what other supply-and-collection systems for plane strain devices cost.

- Previous sample solidification efforts on plane strain specimens have suffered either from incomplete impregnation (Oda and Kazama, 1998) or significant changes in boundary conditions during impregnation (Alshibli and Sture, 1999). Thus, the two-stage glue-resin impregnation procedure suggested by Yang (2002) for loose triaxial specimens was modified for use with the biaxial device. There was still significant difficulty with preventing specimen fracture along the shear band during extraction, but specimens were fully impregnated without significant alteration of boundary conditions, indicating that the current procedure is a step forward from those used previously.
- A modified surface preparation, image capture, and stitching procedure was developed to allow for analysis of large surfaces. Previous studies (e.g., Jang, 1997; Chen, 2000) on triaxial specimens have relied upon capture of representative images from large coupons dissected from

impregnated triaxial specimens. The advantage of this method is that one can compensate for small variations in surface height (i.e., the surface is not entirely planar) by refocusing the microscope optics between images. However, this method does not allow for the comprehensive study of large sections of a specimen and instead relies upon statistical analysis and interpolation to estimate microstructural properties across distances that are large relative to particle size. To address the problem of surface non-planarity and allow for quantification of large surfaces, several improvements were made to the procedures used by others. First, surfaces were originally planed on the SBEL surface grinder to within a few microns (the limits of the system) of truly plane. Surfaces were then ground on the polishing table at high overburden stresses (an increase of 20% to 100% over the values recommended by previous researchers) to maintain intimate contact between the surfaces and the plate. High overburden stresses and an increased duration were also used during the polishing phase of surface preparation to ensure removal of small undulations in the surface over small distances. To further counteract surface elevation imperfections, an overlap of 50% was used in the image capture and stitching operations, which helped to compensate for slight deviations from true focus on certain portions of the image.

The most significant numerical development described herein was the development of the membrane confinement algorithm used in PFC-2D. While chains of particles had been used (although rarely) previously for simulation of membrane

confinement, the most common method of biaxial testing is to use rigid walls for lateral confinement of the particulate assembly. The disadvantage of rigid walls is that they, by definition, do not conform to localized deformations at the specimen boundaries, thus preventing the initiation and propagation of shear bands. Previous implementations of particle chain confinement have relied upon the application of a constant force to each particle in the chain. However, in DEM modeling, small reorganizations of microstructure can result in large changes in boundary forces for a given particle. Thus, stress application of boundary conditions is inherently unstable. The servo-controlled particle chains used in the current study successfully applied a relatively constant (± 2%) confining stress and readily conformed to particles within the assembly in response to localized deformations at specimen boundaries. As a result, "natural" shear band formation was unimpeded and governed only by the contact mechanics of the particles rather than by boundary conditions.

The analytical developments in the current work mostly involve the analysis and quantification of microstructural properties in two-dimensional images (either sections from three-dimensional laboratory tests or two-dimensional numerical models):

- Subregional void ratio and mean free path analyses were developed for the identification of areas of localization within a microstructure.
- Inclined strip spatial averaging analyses were employed for strict delineation of shear band extents. Once shear band limits were defined, a derivative analysis was used to segregate local void ratio polygons into regions of "inside the shear band", "above the shear band", and "below the shear band" for further analyses. This methodology allows for the strict

analysis and interpretation of data from inside and outside of the shear band, as opposed to previous studies, which have been more smeared in nature.

- The concept of virtual surfaces for the analysis of soil microstructure was introduced in this dissertation. Mathematical procedures were used to develop minimum energy surfaces through particle assemblies. These surfaces were then analyzed using tribological procedures to assess roughness both inside and outside of the shear band. While these are not static surfaces (i.e., they are snapshots of dynamic systems), they do provide a competent measure of microstructure in physical specimens.
- An observational/analytical procedure for assessing membrane effects in the direction of shear along the plane of maximum deformation is proposed. This process allows for corrections to calculated normal and shear stresses on the failure plane in an orthorhombic specimen failing via localization in plane strain compression. A companion rigid block model was derived for comparison to values obtained through the observational/analytical approach.

In addition to the experimental, numerical, and analytical developments described above, several observations may be made regarding soil microstructure inside and outside of a shear band:

- Relative to unsheared specimens, the local void ratio distributions in sheared specimens show higher mean values, higher standard deviations, and higher entropy in the distributions. This effect is significantly more

pronounced in the shear band than out of it and is observed in both experimental and numerical specimens. Furthermore, observation of numerical specimens indicates that these parameters increase gradually with increasing shear until the point of localization, at which point they increase dramatically before leveling off again when critical state is achieved. One implication of these observations is that all voids within the specimen (or, even within the shear band) are not increasing in size. Rather, the distribution is becoming flatter (i.e., some voids grow, other shrink), moving to the right (mean is increasing) and disorder is increasing (the probability that a given local void ratio will occupy a given bin is approaching a constant). This is consistent with previous findings which indicate that large force chains bridge the shear band during localization: thus, both very large and very small void spaces will exist within the band.

- The "shapes" of the local void ratio distributions for unsheared specimens and for the region of sheared specimens outside of the shear band are very similar, lending credence to the popularly held notion that after the onset of localization all deformation is due purely to rigid block sliding. Indeed, the purpose of the freely translating base platen in the biaxial device used for the current study is to "ensure" rigid block sliding after the formation of the shear band. However, local measures of void ratio at the end of testing indicate that additional deformation continues to occur in the regions outside of the shear band after the shear band nucleates. This additional dilation in the homogenous region is difficult (impossible?) to

quantify with external measurements (given the current state of biaxial devices used for research). Internal measurements readily quantify this additional deformation. These effects are apparent in both numerical and experimental specimens. It is unclear how this observation will effect existing constitutive relations used to model localized deformation in soils.

- The soil within a shear band reaches a terminal density and shears at constant load and constant volume. While failure points lie in a straight line in q-p′ space, however, there is no unique critical state line in e-log(p′) space, either locally or globally. It is possible that the concepts of traditional critical state soil mechanics do not apply within localized regions of very high void ratio.
- Shear bands are typically considered to have abrupt boundaries. Careful observation of inclined strip and virtual surface analyses indicate that this may not be the case. There appears to be a transition zone wherein a void ratio gradient exists from the homogenous portion of the specimen to the fully formed shear band. Inclined strip spatial averaging analyses identify a void ratio gradient when moving normally to the shear band, but cannot identify the presence of a transition zone explicitly. When coupled with virtual surface analyses, however, the presence of this transition zone becomes apparent. Virtual surfaces are not capable of measuring the difference between the homogenous portion of the specimen and the transition zone, but very distinctly identify the boundary of the fully formed shear band. This is likely due to a lack of significant

rearrangement of particles in the transition zone. Thus, while there is some degree of dilation (as evidenced from spatial averaging of inclined strips), the overall roughness parameters are not significantly different in the transition zone than in the homogenous specimen. The impact of this realization manifests itself primarily in the measurement of shear band thickness.

- The two quantitative measures of shear band thickness differ by approximately seven particle diameters in the slightly dilatant specimen and five particle diameters in the highly dilatant specimen. The fully formed shear zone is approximately eight particle diameters in the slightly dilatant specimen and 11 particle diameters in the highly dilatant specimen. Total thickness of the shear zones is 15 and 16 particle diameters in the slightly dilatant and highly dilatant specimens, respectively. The close agreement between measures of shear band thickness for the two specimens is consistent with the traditional understanding that shear band thickness is dependent only on mean particle diameter. External and internal visual measurements of shear band thickness are also in close agreement with each other for both specimens, but are several particle diameters less than the values obtained using quantitative measures. Two primary conclusions may be drawn form these data: (i) traditional methods of thickness measurement tend to underestimate the true size of the entire shear zone but tend to overestimate the size of the fully formed shear band; and (ii) state

variables (specifically initial void ratio and confining stress) do not appear to have a significant effect on the overall thickness of the shear zone but they do have an effect on the thickness of the fully formed shear band. As discussed previously, these phenomena may be a product of different degrees of particle rotation versus translation in the transition zone versus the fully formed shear zone.

- There is an observed inverse relationship between shear band thickness and void ratio inside a shear band at critical state. This is consistent and on the same order of magnitude as the predicted relationship between void ratio and shear band thickness for a constantly dilating shear band.
- The effects of membrane confinement on shear stress on the failure plane are significant and should be addressed in biaxial testing. The observed and predicted (via the rigid block model) stresses are in good agreement. The correction is driven by membrane deformation and thus is only slightly effected by confining stress (only to the extent to which the membrane slips against the soil), so the correction is much larger (as a percentage of deviatoric load) for specimens tested as low confining stresses.

8.2. Recommendations

In addition to providing insight into the microscale behavior of particles within a shear band, the current work also served to highlight the need for additional work. In this section suggestions for additional numerical and experimental work are proposed. The

experimental procedure outlined herein has been largely refined through trial and error and could be implemented for several additional biaxial tests. The recommendations for additional experimental work are as follows:

- Only a single soil type was tested in the current study. Shear band mechanics are largely considered independent of particle shape and size. However, results from the current study indicate that state variables can have an effect on shear band mechanics when the two have been previously considered to be independent. Additional laboratory tests to asses the effects of particle shape and size on shear banding should be performed. It is expected that virtual surface measures will vary significantly with variations in particle characteristics. Particle characteristics may also have an effect on the size of the transition zone, as evidenced from the comparison of transition zones in particulate-continuum systems and in sand specimens.
- With one exception, all of the tests in the current study were performed on dilatant specimens. Additional tests should be performed on Ottawa 20-30 sand such that global volume change behavior with be contractive rather than dilatant. Given the mechanics and geometry of the current biaxial testing system, contractive specimens will still tend to fail along a single well-defined plane. The mechanics of this plane should be investigated.
- Given the current capability to recreate three-dimensional microstructure from images on closely spaced sliced in a solidified specimen (Yang, 2005) and the fact that this type of three-dimensional reconstruction

provides additional insight into soil microstructure (relative to two-dimensional measures alone), it is recommended that three dimensional recreations of shear band microstructure be generated. Existing slices from the specimens used for the current study could be used as a starting point for these recreations.

- The effects of some of the observations in the current study (specifically, the presence of a transition zone and the continued dilation of the homogenous portion of the specimen after the onset of localization) on existing constitutive models should be assessed. Some of these results could also be used for the further calibration of existing constitutive models.

In addition to the above suggestions for continued experimental work, there are also numerical studies that could be performed to build on the current work:

- The existing numerical model, including the membrane confinement algorithm, should be expanded to three dimensions. Several measures of microstructure characterization that worked well on experimental specimens failed when applied to the two-dimensional model. It is expected that many of the features observed in the experimental specimens could be captured more accurately using a three-dimensional DEM.
- If use of a two-dimensional model is continued, an algorithm should be developed to allow for translation of the base platen after the onset of localization to more closely mimic laboratory tests. This will encourage the formation of only a single shear band and will simplify the subsequent

microstructural analyses. The algorithm could be based on monitoring total shear stress applied to the base platen by the contacting particles. A threshold value would be selected that was less than the force required for slip of all particles in contact with the platen but greater than zero. The author anticipates that an attempt to simulate truly "frictionless" platen translation would result in numerical instabilities.

- In conjunction with the laboratory tests outlined above, studies should be performed on the effects of particle shape on microstructure evolution. This would be particularly relevant for three-dimensional model studies. To that end, given the state of the existing model (i.e., it was developed in such a manner to allow for additional simulations in a relatively straightforward manner), any additional laboratory tests should be accompanied by additional numerical work.

APPENDIX A.1

Reduction of Raw Data from Biaxial Experiments

Reduced Data from Biaxial Tests

GLOBAL DATA

Test Identification: $test\_id := "BT\text{-}2030\text{-}16"$

Soil type: $Soil\_Type := "Ottowa\ 20\text{-}30\ Sand"$

Loading rate: $load\_rate := 0.4 \cdot \frac{mm}{min}$

DAQ integration time: $PLC := 2$

Membrane thickness: $t_m := 0.40mm$

Units: $kPa := 10^3 Pa$ $kN := 10^3 N$

SAMPLE PREPARATION DATA

Water Content (click to expand)

Density

Sample height: $h_0 := 141.28mm$ $h_1 := 141.36mm$

$h_2 := 141.12mm$ $h_3 := 141.07mm$

Sample width: $w_0 := 80.26mm$ $w_1 := 80.33mm$ $w_2 := 80.33mm$

Sample thickness: $t_0 := 39.87mm$ $t_1 := 39.76mm$ $t_2 := 39.71mm$

Total mass: $m_i := 752.05gm$ $m_f := 0.00gm$ $m_t := m_i - m_f$

Specific gravity of soil solids: $G_s := 2.67$

Density of water: $\rho_w := 0.99707 \frac{gm}{cm^3}$

Maximum and minimum void ratios: $e_{max} := 0.742$ $e_{min} := 0.502$

Sample dimensions: $h_s := mean(h) + 2 \cdot t_m$ $h_s = 142.007\ mm$

$w_s := mean(w) - 2 \cdot t_m$ $w_s = 79.507\ mm$

$t_s := mean(t) - 2 \cdot t_m$ $t_s = 38.980\ mm$

Sample volume: $V_{sam} := h_s \cdot w_s \cdot t_s$ $V_{sam} = 4.401 \times 10^5\ mm^3$

Density of soil solids: $\rho_s := G_s \cdot \rho_w$ $\rho_s = 2.662 \frac{gm}{cm^3}$

Mass of soil: $m_t = 752.050\ gm$ $m_s := (1 - w_g) \cdot m_t$ $m_s = 751.227\ gm$

Sample dry density: $\rho_d := \frac{m_s}{V_{sam}}$ $\rho_d = 1.707 \frac{gm}{cm^3}$

Sample void ratio: $e := \frac{\rho_s}{\rho_d} - 1$ $e = 0.560$

Sample relative density: $D_r := \frac{e_{max} - e}{e_{max} - e_{min}}$ $D_r = 75.986\,\%$

INPUT DATA

Note that the data from the Agilent 34770A DMM is output as comma-separated values with three columns each for the fourteen measured channels. Columns for each channel are (in order) time stamp, time (seconds), and reading (VDC).

Filename containing raw data: data := C:\..\BT-2030-16.csv

Number of channels measured: nchan := 14

Remove the last row of the data matrix as it most likely contains some zero measurements:

$$data := submatrix(data, 0, rows(data) - 2, 0, cols(data) - 1)$$

Use visual inspection to determine the number of rows of data to be omitted from the beginning of the test to compensate for seating time.

Number of rows to remove: rem_rows := 14 end_rows := rows(data) − 1

$$data := submatrix(data, rem\_rows, end\_rows, 0, cols(data) - 1)$$

Number of columns (channels x 3): ncols := cols(data) ncols = 42.000

Number of rows (data points): nrows := rows(data) $nrows = 1.830 \times 10^3$

Extract the columns containing time and voltage data from the main matrix (the time stamp data are not used in calculations performed on this sheet):

$i := 0 .. nchan - 1$ $volts^{\langle i \rangle} := data^{\langle 3 \cdot i + 2 \rangle} \cdot V$ $time^{\langle i \rangle} := data^{\langle 3 \cdot i + 1 \rangle} \cdot s$

Subtract baseline readings to normalize data:

$baseline := (volts^T)^{\langle 0 \rangle}$ $volts^{\langle i \rangle} := volts^{\langle i \rangle} - baseline_i$ $time := time - time_{0,0}$

BUOYANT WEIGHT DATA AND CALCULATIONS (click to expand)

CALIBRATION FACTORS FOR EACH CHANNEL (click to expand)

CALCULATE LOAD AND DISPLACEMENT

Index for LVDT channel counting: $j := 1 .. 7$

Index for load cell channel counting: $k := 8 .. 14$

$$disp^{\langle j-1\rangle} := \frac{volts^{\langle j-1\rangle}}{lvdt_j} \qquad force^{\langle k-8\rangle} := \frac{volts^{\langle k-1\rangle}}{load_k}$$

CALCULATION OF GLOBAL STRESS AND STRAIN (based on Drescher, et al., 1990)

Indices: $n := 0 .. nrows - 1$

Confining Stress: $\sigma 3_n := 10psi$

Sample thickness (upper): $t_u := t_s - \left(disp^{\langle 2\rangle} + disp^{\langle 5\rangle}\right)$

Sample thickness (lower): $t_l := t_s - \left(disp^{\langle 1\rangle} + disp^{\langle 6\rangle}\right)$

Sample thickness (average): $d2_n := mean\left(tu_n, tl_n\right)$

Sample axial deformation: $ua_n := mean\left[\left(disp^{\langle 3\rangle}\right)_n, \left(disp^{\langle 4\rangle}\right)_n\right]$

Sample height: $d_1 := h_s - u_a$

Natural strains: $\varepsilon_1 := -\ln\left(1 - \frac{u_a}{h_s}\right) \qquad \varepsilon_2 := -\ln\left(\frac{d_2}{t_s}\right)$

Volumetric and shear strains: $\varepsilon_v := \varepsilon_1 + \varepsilon_2 \qquad \gamma := \varepsilon_1 - \varepsilon_2$

Calculation of average axial load (see *drescher data reduction.mcd*):

Area of loading piston: $d_p := \begin{pmatrix} 25.40 \\ 25.38 \\ 25.37 \end{pmatrix} mm \qquad A_p := \frac{1}{4}\pi \cdot mean\left(d_p\right)^2$

Initial loads: $P_{10} := \sigma_3 \cdot A_p \qquad P_{20} := \left(force^{\langle 0\rangle}\right)_0$

$P_{30} := \left(force^{\langle 1\rangle}\right)_0 \qquad P_{40} := \left(force^{\langle 2\rangle}\right)_0$

$$P_{50} := \left(force^{\langle 3 \rangle}\right)_0 \qquad P_{60} := \left(force^{\langle 4 \rangle}\right)_0$$

$$P_{70} := \left(force^{\langle 5 \rangle}\right)_0$$

Load on base platen: $P_L := force^{\langle 0 \rangle} + force^{\langle 1 \rangle} + force^{\langle 2 \rangle} - P_{20} - P_{30} - P_{40}$

Load on upper platen: $P_u := force^{\langle 6 \rangle} - P_{10}$

Load on side wall: $P_s := \left(force^{\langle 4 \rangle} + force^{\langle 5 \rangle}\right) \cdot 1.5 - \left(P_{60} - P_{70}\right) \cdot 1.5$

Average axial load: $P := P_L + \dfrac{\left(P_u - P_L + W_{top} - 2 \cdot W_{bot} - \dfrac{W_{sam}}{2}\right)}{3}$

Major principal stress: $\sigma_1 := \left(\overrightarrow{\dfrac{P}{w_s \cdot d_2}}\right) + \sigma_3$

Intermediate principal stress: $\sigma_2 := \sigma_3 + \dfrac{\overrightarrow{P_s}}{d_1 \cdot d_2}$

Stress at base platen: $\sigma_b := \sigma_3 + \dfrac{\overrightarrow{P_L}}{w_s \cdot d_2}$

System friction: $f1_n := \left|\dfrac{P_{u_n} - P_{L_n}}{P_n}\right|$ **Method 1**

$f2_n := \left|\dfrac{P_{u_n} - P_{L_n}}{mean\left(P_{u_n}, P_{L_n}\right)}\right|$ **Method 2**

$f_n := \dfrac{f1_n - f2_n}{mean\left(f1_n, f2_n\right)}$ **Difference**

Mobilized friction angle: $\phi_m := asin\left(\overrightarrow{\dfrac{\sigma_1 - \sigma_3}{\sigma_1 + \sigma_3}}\right)$

Calculation and output file:

$\varepsilon_{ax} := \dfrac{u_a}{h_s}$ $\quad output := augment\left(\dfrac{\sigma_1}{Pa}, \dfrac{\sigma_3}{Pa}, \varepsilon_{ax}, \varepsilon_v\right)$

$WRITEPRN(concat(test\_id, ".out")) := output$

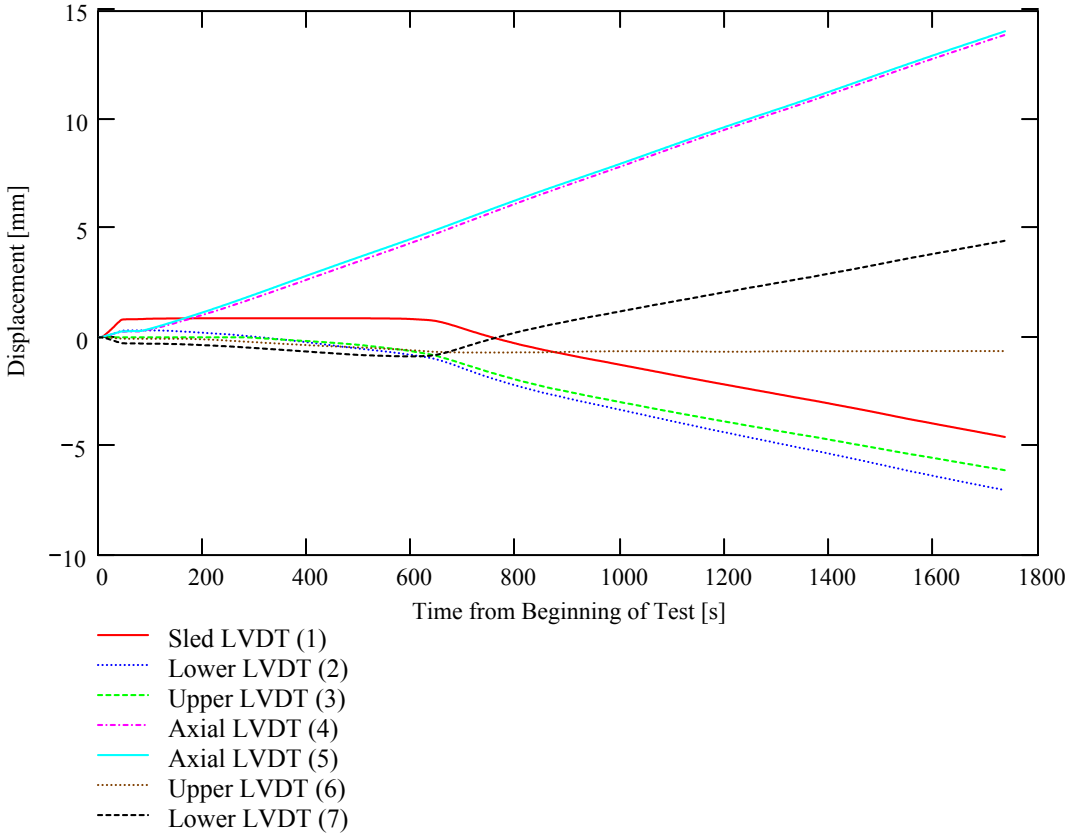
15
10
5
0
−5
−10
Displacement [mm]
0
200
400
600
800
1000
1200
1400
1600
1800
Time from Beginning of Test [s]
Sled LVDT (1)
Lower LVDT (2)
Upper LVDT (3)
Axial LVDT (4)
Axial LVDT (5)
Upper LVDT (6)
Lower LVDT (7)

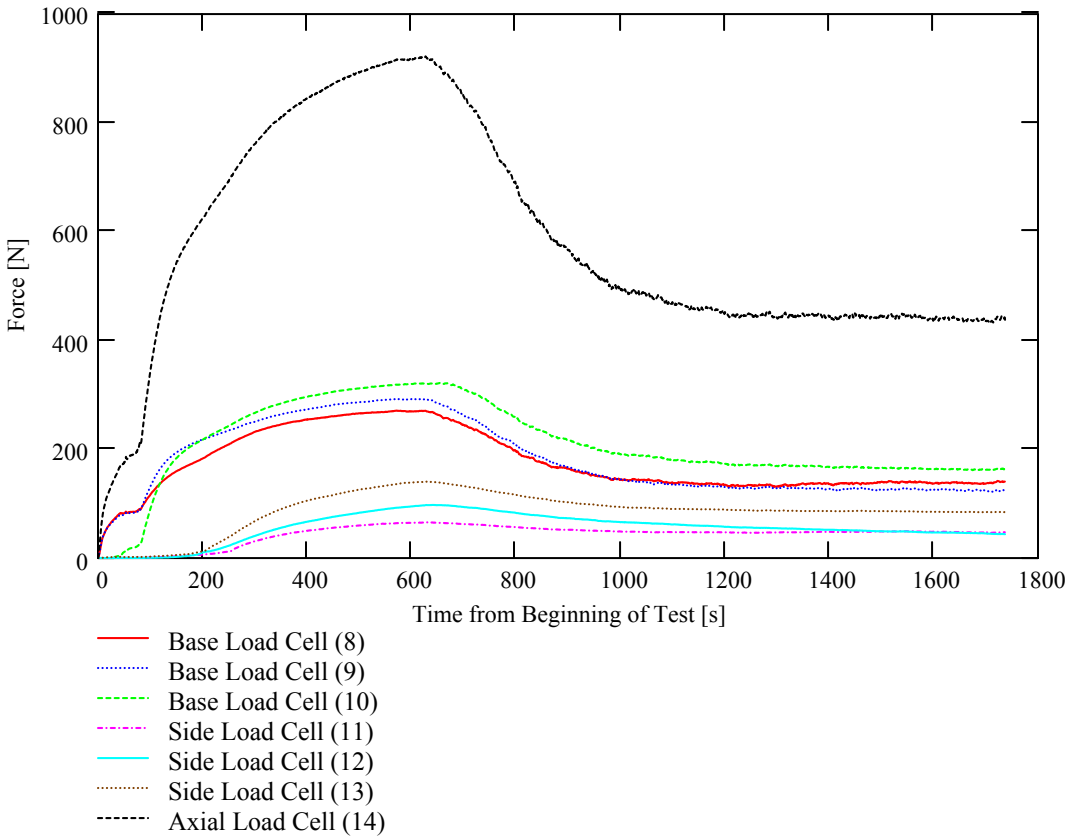
1000
800
600
400
200
0
Force [N]
0
200
400
600
800
1000
1200
1400
1600
1800
Time from Beginning of Test [s]
Base Load Cell (8)
Base Load Cell (9)
Base Load Cell (10)
Side Load Cell (11)
Side Load Cell (12)
Side Load Cell (13)
Axial Load Cell (14)

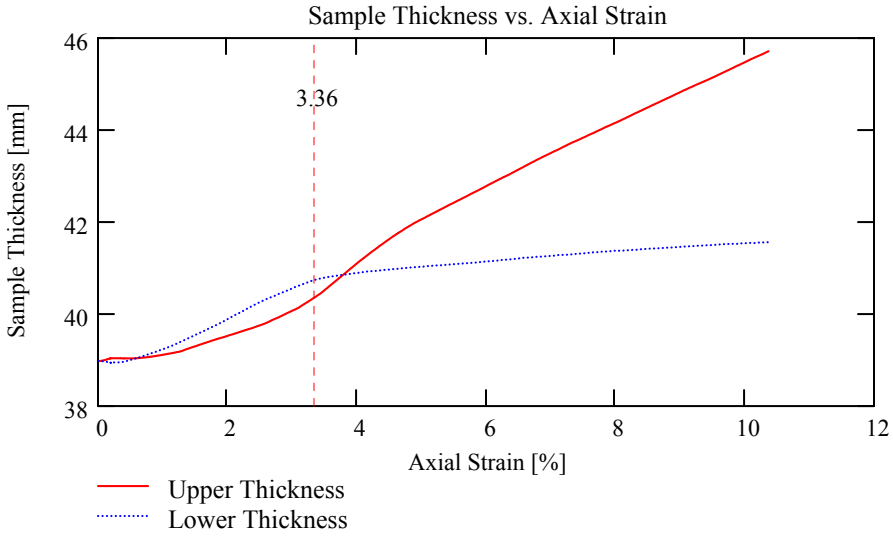
Sample Thickness vs. Axial Strain
Sample Thickness [mm]
46
44
42
40
38
3.36
0
2
4
6
8
10
12
Axial Strain [%]
Upper Thickness
Lower Thickness

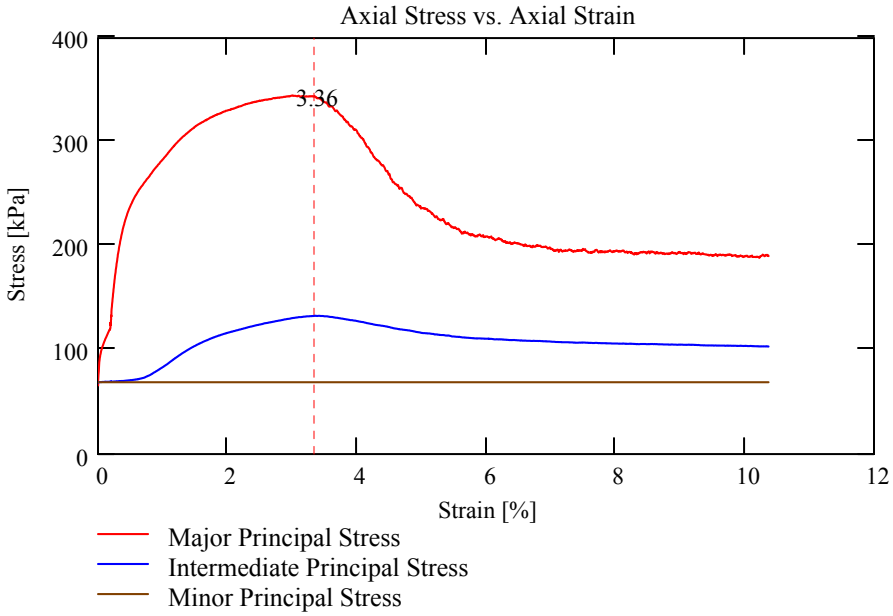
Axial Stress vs. Axial Strain
Stress [kPa]
400
300
200
100
0
3.36
0
2
4
6
8
10
12
Strain [%]
Major Principal Stress
Intermediate Principal Stress
Minor Principal Stress

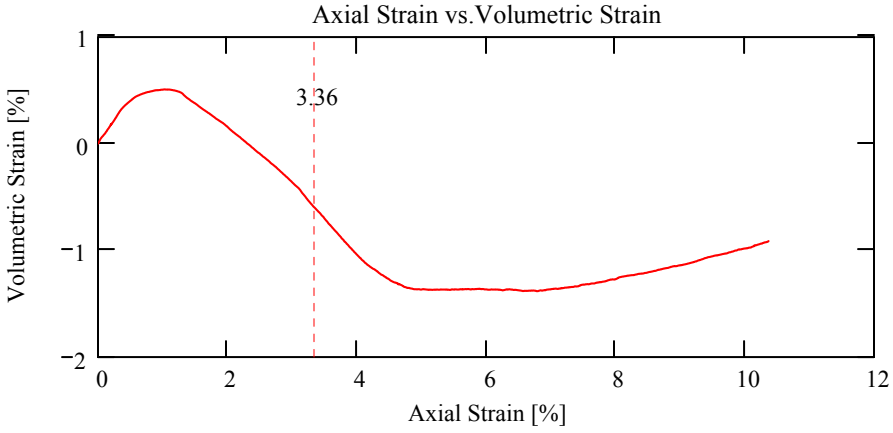
Axial Strain vs.Volumetric Strain
Volumetric Strain [%]
1
0
−1
−2
3.36
0
2
4
6
8
10
12
Axial Strain [%]

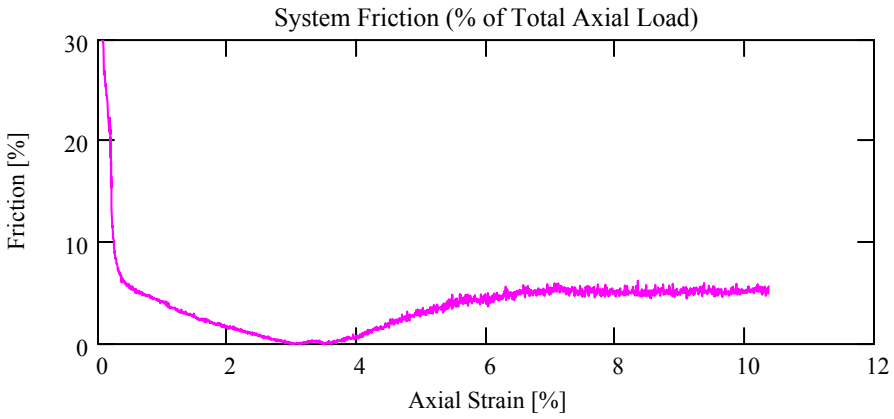
System Friction (% of Total Axial Load)
Friction [%]
30
20
10
0
0
2
4
6
8
10
12
Axial Strain [%]

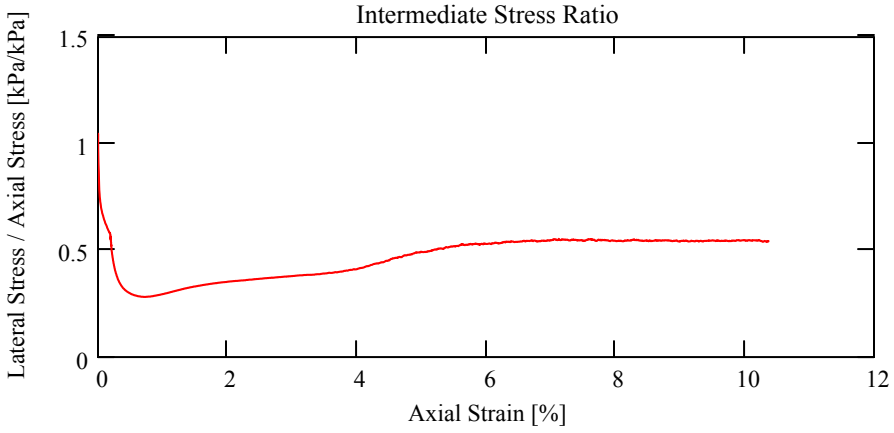
Intermediate Stress Ratio
Lateral Stress / Axial Stress [kPa/kPa]
1.5
1
0.5
0
0
2
4
6
8
10
12
Axial Strain [%]

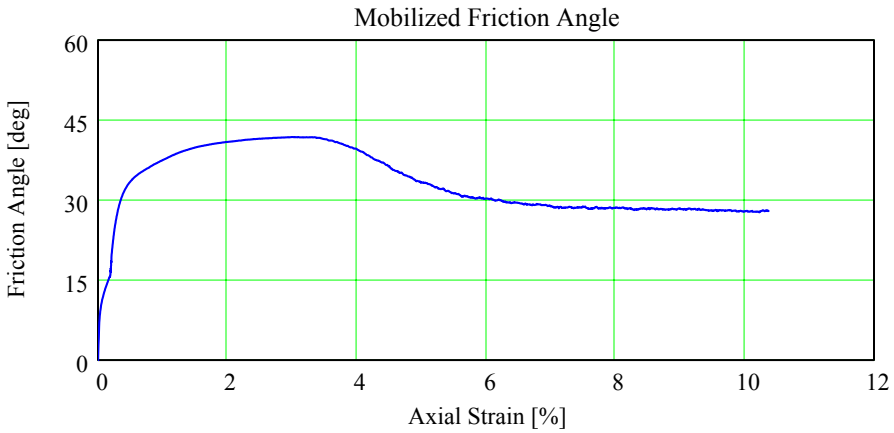
Mobilized Friction Angle
Friction Angle [deg]
60
45
30
15
0
0
2
4
6
8
10
12
Axial Strain [%]

CALCULATION OF STRESS AND STRAIN AFTER THE ONSET OF LOCALIZATION
(based on Drescher, et al., 1990)

Inclination of failure plane: $\theta_e := 61deg$

Global strain at onset of shear banding: $\varepsilon_b := 3.36\%$

Shift data vectors to correspond to the onset of shear banding:

$$\text{Locate}(v,\varepsilon) := \left| \begin{array}{l} i \leftarrow 0 \\ L \leftarrow 0 \\ \text{for } m \in 0 .. \text{last}(v) \\ \quad \text{if } v_m \geq \varepsilon \\ \quad\quad L \leftarrow m \\ \quad\quad \text{return } L \end{array} \right.$$

$new := \text{Locate}(\varepsilon_1, \varepsilon_b)$

$new = 663$ $\quad p := new .. nrows - 1$

$u_h := -disp^{\langle 0 \rangle}$

$uhh_{p-new} := u_{h_p}$ $\quad uaa_{p-new} := u_{a_p}$ $\quad \sigma 11_{p-new} := \sigma 1_p$ $\quad \sigma 33_{p-new} := \sigma 3_p$

Calculate incremental axial and sled displacements:

$i := 0 .. \text{last}(uhh) - 1$ $\quad \Delta u_{h_i} := uhh_{i+1} - uhh_i$ $\quad \Delta u_{a_i} := uaa_{i+1} - uaa_i$

Normal stress on failure plane: $\sigma_n := \sigma_{11} \cdot \cos(\theta_e)^2 + \sigma_{33} \cdot \sin(\theta_e)^2$

Shear stress on failure plane: $\sigma_s := (\sigma_{11} - \sigma_{33}) \cdot \cos(\theta_e) \cdot \sin(\theta_e)$

Friction on the shear band: $\phi_s := \text{atan}\left(\frac{\overrightarrow{\sigma_s}}{\sigma_n}\right)$

Calculate the angle of dilation: $\psi_s := \theta_e - \text{atan}\left(\frac{\overrightarrow{\Delta u_a}}{\Delta u_h}\right)$

Calculate movement along the shear band:

$r := 0 .. \text{last}(\Delta u_h)$ $\quad \Delta u_s := \frac{\overrightarrow{\cos(\psi_s) \cdot \Delta u_a}}{\sin(\theta_e - \psi_s)}$ $\quad u_{s_r} := \sum_{p=0}^{r} \Delta u_{s_p}$

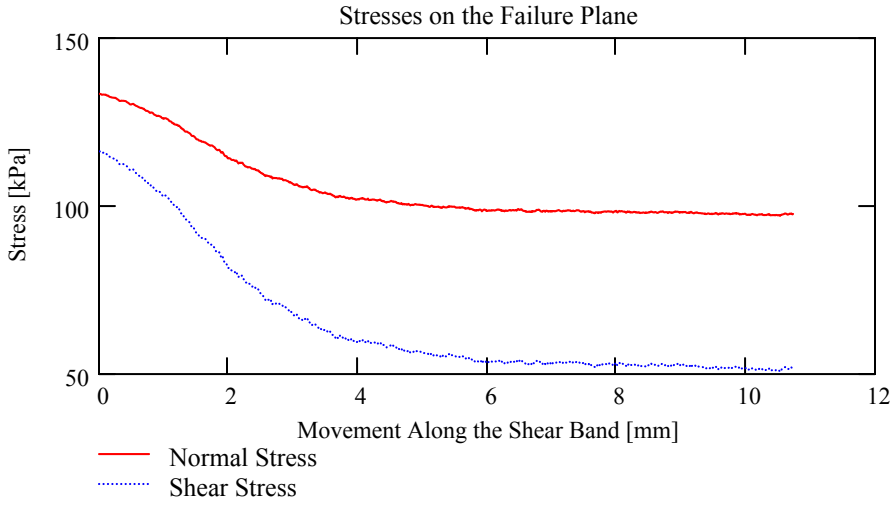
Stresses on the Failure Plane
Stress [kPa]
150
100
50
0
2
4
6
8
10
12
Movement Along the Shear Band [mm]
Normal Stress
Shear Stress

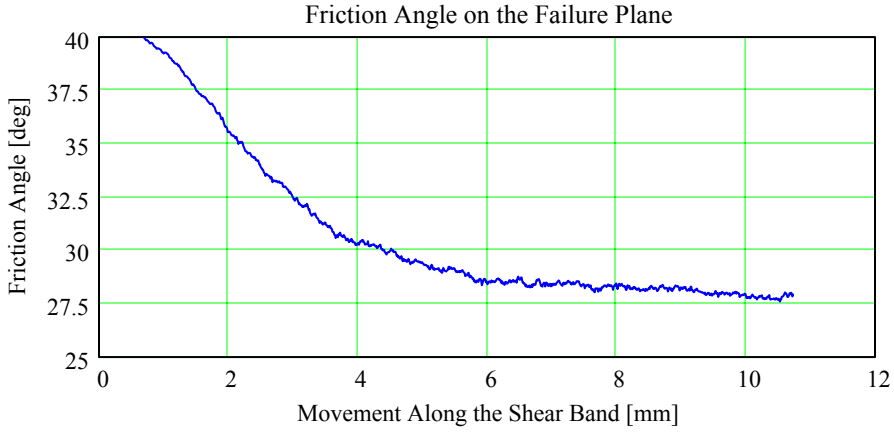
Friction Angle on the Failure Plane
Friction Angle [deg]
40
37.5
35
32.5
30
27.5
25
0
2
4
6
8
10
12
Movement Along the Shear Band [mm]

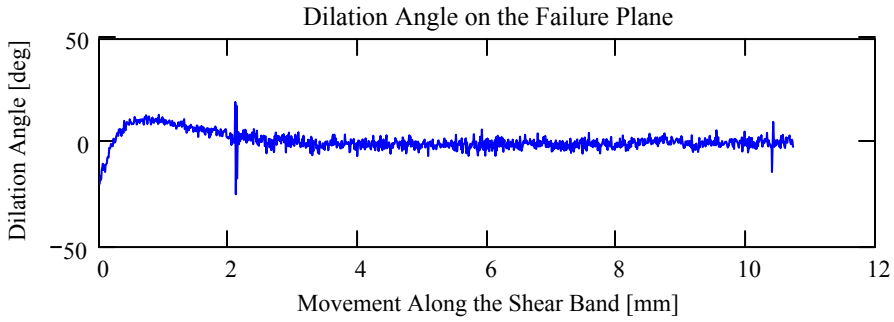
Dilation Angle on the Failure Plane
Dilation Angle [deg]
50
0
−50
0
2
4
6
8
10
12
Movement Along the Shear Band [mm]

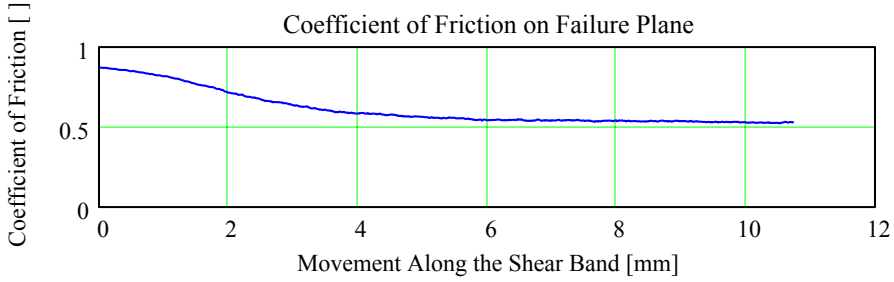
Coefficient of Friction on Failure Plane
Coefficient of Friction [ ]
1
0.5
0
0
2
4
6
8
10
12
Movement Along the Shear Band [mm]

Smooth the measured displacements using a 10-point moving average (to prevent divide-by-zero errors when calculating dilation angle):

$X := \text{last}(\Delta u_a) \qquad x := 0 .. X - 1 \qquad Q := 10 \qquad q := 0 .. Q - 1 \qquad \kappa_q := \frac{1}{Q}$

$Y := X - Q + 1 \qquad y := 0 .. Y - 1 \qquad \Delta u_{h\_av_y} := \sum_q \kappa_q \cdot \Delta u_{h_{y+q}} \qquad \Delta u_{a\_av_y} := \sum_q \kappa_q \cdot \Delta u_{a_{y+q}}$

$$\psi_{s1} := \theta_e - \text{atan}\left(\frac{\overrightarrow{\Delta u_{a\_av}}}{\Delta u_{h\_av}}\right)$$

Calculate a straight average of every 10 points:

$avg := 10 \qquad s := 0 .. \text{floor}\left(\frac{\text{length}(\Delta u_a)}{avg}\right) - 1 \qquad \Delta u_{aa_s} := \sum_{r=0}^{avg-1} \Delta u_{a_{r+avg \cdot s}} \qquad \Delta u_{hh_s} := \sum_{r=0}^{avg-1} \Delta u_{h_{r+avg \cdot s}}$

$$\psi_{s2} := \theta_e - \text{atan}\left(\frac{\overrightarrow{\Delta u_{aa}}}{\Delta u_{hh}}\right) \qquad u_{s2_s} := u_{s_{avg \cdot s}}$$

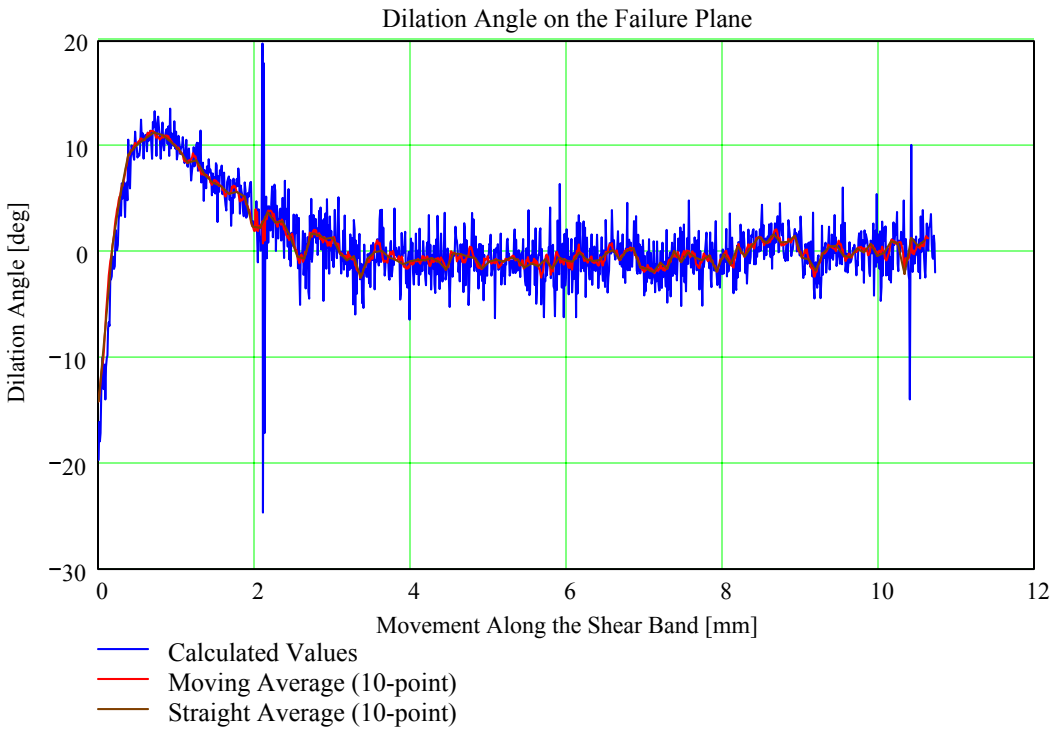

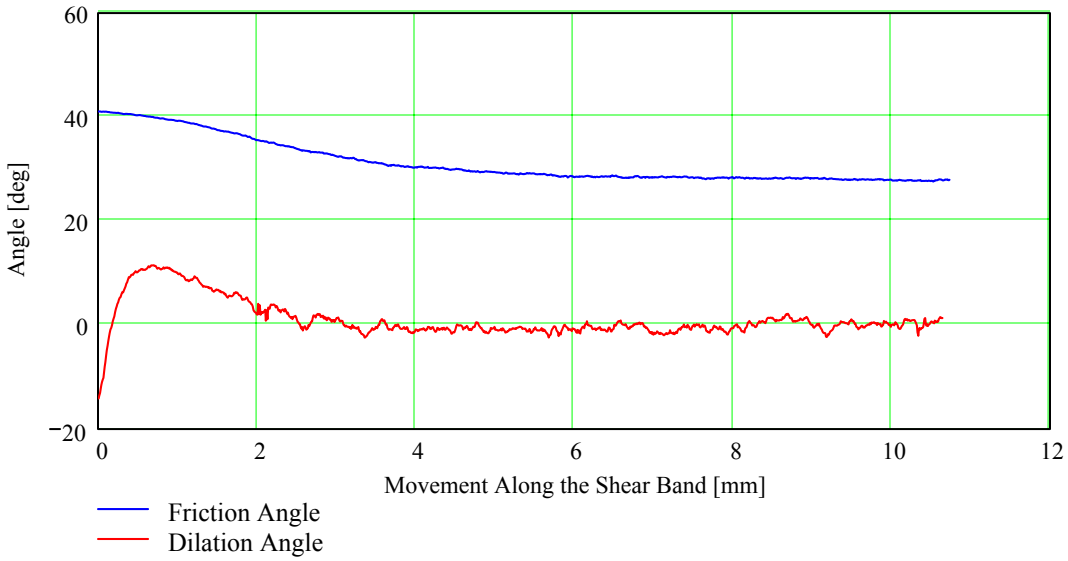
60
40
20
0
−20
Angle [deg]
0
2
4
6
8
10
12
Movement Along the Shear Band [mm]
Friction Angle
Dilation Angle

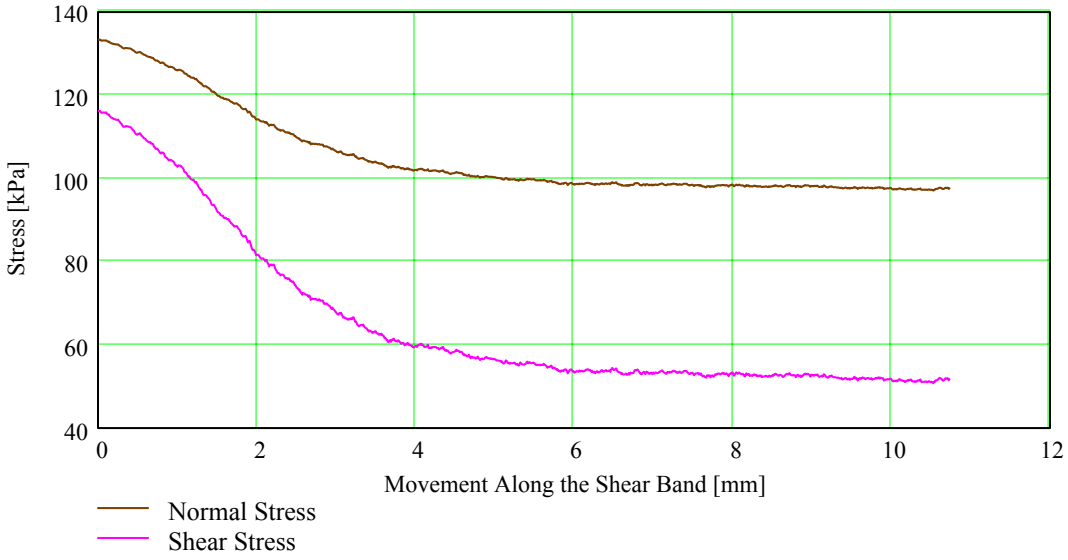
140
120
100
80
60
40
Stress [kPa]
0
2
4
6
8
10
12
Movement Along the Shear Band [mm]
Normal Stress
Shear Stress

APPENDIX A.2

Calculation of Membrane Correction for Biaxial Experiments

Calculation of Stresses Imposed by Membrane During Localization

User-defined units: $kPa := 10^3 Pa$ $kN := 10^3 N$ **Sample ID:** BT-2030-16

Sample dimensions: $h_s := 142.007mm$ $w_s := 79.507mm$ $t_s := 38.980mm$ $t_m := 0.40mm$

Membrane constants: $E := 1300kPa$ $\nu := 0.5$ $G := \frac{E}{2\cdot(1+\nu)}$ $k_m := E\cdot t_m$

Shear band inclination, confining stress and friction angle: $\theta := 61deg$ $\sigma_3 := 10psi$

Elapsed time and image numbers to be read from disk: $\phi := 28deg$

$t_{im} := (632 \quad 664 \quad 777 \quad 900 \quad 1019 \quad 1150 \quad 1260 \quad 1379 \quad 1499 \quad 1622 \quad 1740)^T \cdot s$ $type := ".txt"$

$$image\_num := \begin{pmatrix} "2507" \\ "2508" \\ "2509" \\ "2510" \\ "2511" \\ "2512" \\ "2513" \\ "2514" \\ "2515" \\ "2516" \\ "2517" \end{pmatrix} \quad ii := 0 .. last(image\_num)$$

Modify the following items each time this worksheet is used:
1. header information
2. sample ID
3. inclination of shear band
4. confining stress
5. friction angle
6. time and image number
7. vector of control points
8. separation value

$mem_{ii} := READPRN(concat(CWD, image\_num_{ii}, type))$

$x_{ii} := (mem_{ii})^{\langle 0 \rangle} \cdot in$ $y_{ii} := (mem_{ii})^{\langle 1 \rangle} \cdot in$

Read time series measured data and correlate to images:

$data := READPRN("TS-2030-16.txt")$ $jj := 0 .. rows(data) - 1$

$t_{jj} := mean\left[(data^{\langle 1 \rangle})_{jj}, (data^{\langle 2 \rangle})_{jj}\right] \cdot s$ $dis_{jj} := mean\left[(data^{\langle 4 \rangle})_{jj}, (data^{\langle 5 \rangle})_{jj}\right] \cdot mm$

$Locate(V, U) :=$
for $n \in 0 .. last(V)$
  $\Delta_{n,0} \leftarrow n$
  $\Delta_{n,1} \leftarrow \frac{|V_n - U|}{s}$
$D \leftarrow csort(\Delta, 1)$
$dis_{(D_{0,0})}$

$\varepsilon_{axm_{ii}} := \frac{Locate(t, t_{im_{ii}})}{h_s}$

$\varepsilon_{axm}^T =$

	0	1	2	3	4
0	3.238	3.439	4.157	4.909	5.605

%

Define and execute a function rearrange(v) to rearrange the raw global strain data and create location vectors to be used in the subsequent calculations.

$$\text{rearrange}(v) := \left| \begin{array}{l} \text{out} \leftarrow 0 \\ \text{for } ii \in 0 .. 13 \\ \quad \left| \begin{array}{l} \text{for } jj \in 0 .. 6 \\ \quad temp_{jj} \leftarrow v_{jj+7\cdot ii} \\ \text{out} \leftarrow \text{stack}(\text{out}, \text{temp}) \text{ if } \frac{ii}{2} = \text{floor}\left(\frac{ii}{2}\right) \\ \text{out} \leftarrow \text{stack}(\text{out}, \text{reverse}(\text{temp})) \text{ if } \frac{ii}{2} \neq \text{floor}\left(\frac{ii}{2}\right) \end{array} \right. \\ \text{submatrix}(\text{out}, 1, \text{last}(\text{out}), 0, 0) \end{array} \right. \qquad x_{ii} := \text{rearrange}\left(x_{ii}\right) \qquad y_{ii} := \text{rearrange}\left(y_{ii}\right)$$

Functions DXY*(v,x_a,y_a,diff)* and *disp(v,x_a,x_b,y_a,y_b,diff)* are defined to calculate local deformations across the shear band and local displacements for a vector of control points and vectors of beginning (x_a,y_a) and ending (x_b,y_b) location data.

$$\text{DXY}\left(v, x_a, y_a, \text{diff}\right) := \left| \begin{array}{l} \text{for } ii \in 0 .. \text{last}(v) \\ \quad \left| \begin{array}{l} dis_{ii,0} \leftarrow \left| x_{a\left(v_{ii}-1+\text{diff}\right)} - x_{a\left(v_{ii}-1\right)} \right| \\ dis_{ii,1} \leftarrow \left| y_{a\left(v_{ii}-1+\text{diff}\right)} - y_{a\left(v_{ii}-1\right)} \right| \end{array} \right. \\ \text{dis} \end{array} \right.$$

$$\text{disp}\left(v, x_a, x_b, y_a, y_b, \text{diff}\right) := \left| \begin{array}{l} \text{for } ii \in 0 .. \text{last}(v) \\ \quad \left| \begin{array}{l} dis_{ii,0} \leftarrow \left| x_{b\left(v_{ii}-1+\text{diff}\right)} - x_{a\left(v_{ii}-1+\text{diff}\right)} \right| \\ dis_{ii,1} \leftarrow \left| y_{b\left(v_{ii}-1+\text{diff}\right)} - y_{a\left(v_{ii}-1+\text{diff}\right)} \right| \end{array} \right. \\ \text{dis} \end{array} \right.$$

Manually create a vector of control points (based on observations of shear band location).

$$\text{vec} := (26 \quad 33 \quad 39 \quad 45 \quad 46 \quad 52 \quad 58 \quad 64 \quad 65 \quad 71)^T \qquad \text{sep} := 16$$

Calculate incremental displacements for each strain level:

$$k := 1 .. \text{length}(\text{image\_num}) - 1 \qquad d_{loc_{k-1}} := \text{disp}\left(\text{vec}, x_0, x_k, y_0, y_k, \text{sep}\right)$$

$$D_{x_k} := \text{mean}\left[\left(d_{loc_{k-1}}\right)^{\langle 0 \rangle}\right] \qquad D_{y_k} := \text{mean}\left[\left(d_{loc_{k-1}}\right)^{\langle 1 \rangle}\right] \qquad D := \text{augment}\left(D_x, D_y\right)$$

Extract mean values for x- and y- deformations and calculate their relative changes:

$$\delta_{ii} := \text{DXY}\left(\text{vec}, x_{ii}, y_{ii}, \text{sep}\right) \qquad X_{ii} := \text{mean}\left[\left(\delta_{ii}\right)^{\langle 0 \rangle}\right] \qquad Y_{ii} := \text{mean}\left[\left(\delta_{ii}\right)^{\langle 1 \rangle}\right]$$

$$\Delta x_k := X_k - X_0 \qquad \Delta y_k := Y_k - Y_0 \qquad i := 0 .. \text{last}\left(\Delta x\right)$$

Calculate the local strain tensors based on incremental changes in x- and y-distances between points:

$$\varepsilon_k := \begin{bmatrix} \frac{\Delta x_k}{X_0} & \frac{1}{2}\left(\frac{\Delta x_k}{Y_0} + \frac{\Delta y_k}{X_0}\right) \\ \frac{1}{2}\left(\frac{\Delta x_k}{Y_0} + \frac{\Delta y_k}{X_0}\right) & \frac{\Delta y_k}{Y_0} \end{bmatrix}$$

Using elastic constants and the strain tensor, calculate stresses in the membrane:

$$\sigma_k := \left| \begin{array}{l} sig_{0,0} \leftarrow \frac{E}{1-\nu^2}\left[(\varepsilon_k)_{0,0} + \nu\cdot(\varepsilon_k)_{1,1}\right] \\ sig_{1,1} \leftarrow \frac{E}{1-\nu^2}\left[(\varepsilon_k)_{1,1} + \nu\cdot(\varepsilon_k)_{0,0}\right] \\ sig_{0,1} \leftarrow 2\cdot G\cdot(\varepsilon_k)_{0,1} \\ sig_{1,0} \leftarrow 2\cdot G\cdot(\varepsilon_k)_{1,0} \\ sig \end{array} \right.$$

Vectors defining the normal and shear directions of the shear plane:

$$n := \begin{pmatrix} \sin(\theta) \\ -\cos(\theta) \end{pmatrix} \qquad s := \begin{pmatrix} \cos(\theta) \\ \sin(\theta) \end{pmatrix}$$

Convert stresses into tractions along the shear plane:

$$T_k := \left| \begin{array}{l} \text{for } q \in 0..1 \\ \quad trac_q \leftarrow \sum_{p=0}^{1} (\sigma_k)_{p,q}\cdot n_p \\ trac \end{array} \right.$$

Calculate normal and shear stresses on the shear plane from the tractions:

$$\sigma_{ns_k} := T_k\cdot s \qquad \sigma_{nn_k} := T_k\cdot n$$

$\sigma_{ns}^{T} =$

	0	1	2	3	4	5	6	7
0	0	11.533	64.468	114.659	158.543	204.473	243.195	277.761

kPa

$\sigma_{nn}^{T} =$

	0	1	2	3	4	5	6	7	8
0	0	9.384	35.968	51.185	61.469	63.258	72.494	66.994	76.13

kPa

(scroll tables to the right for additional data)

Calculate normal and shear force in the membrane and apply to the surface of the shear plane:

$$S := \sigma_{ns}\cdot\left[t_m\cdot 2\cdot\left(\frac{t_s}{\cos(\theta)} + w_s\right)\right] \qquad d_{proj_i} := s\cdot\begin{pmatrix} D_{i,0} \\ D_{i,1} \end{pmatrix} \qquad \sigma_{sample_i} := \frac{S_i}{\left[\left(\frac{t_s}{\cos(\theta)} - 2\,d_{proj_i}\right)\cdot w_s\right]}$$

$$N_{sam} := \sigma_{nn}\cdot\left[t_m\cdot 2\cdot\left(\frac{t_s}{\cos(\theta)} + w_s\right)\right] \qquad \sigma_{nsam_i} := \frac{N_{sam_i}}{\left[\left(\frac{t_s}{\cos(\theta)} - 2\,d_{proj_i}\right)\cdot w_s\right]}$$

For the rigid block model, calculate the mean x and y separations for the data points used above and create a tensor of strain values as a function of global axial displacement:

$$\begin{pmatrix} x_{av} \\ y_{av} \end{pmatrix} := \left|\begin{array}{l} \text{for } a \in 0 .. \text{last(vec)} \\ \quad x_{r_a} \leftarrow \left|\left(x_0\right)_{(vec_a - 1)} - \left(x_0\right)_{(vec_a - 1 + sep)}\right| \\ \quad y_{r_a} \leftarrow \left|\left(y_0\right)_{(vec_a - 1)} - \left(y_0\right)_{(vec_a - 1 + sep)}\right| \\ \begin{pmatrix} \text{mean}(x_r) \\ \text{mean}(y_r) \end{pmatrix} \end{array}\right.$$

$x_{av} = 9.335\ \text{mm}$

$y_{av} = 8.838\ \text{mm}$

$\delta y :=$

	0
0	$8.03\cdot10^{-6}$
1	$1.61\cdot10^{-5}$

$q := 0 .. \text{length}(\delta y) - 1 \qquad \delta y := \delta y\cdot m$

$$strain_q := \begin{bmatrix} \frac{\delta y_q\cdot\cot(\theta)}{x_{av}} & \frac{1}{2}\left(\frac{\delta y_q\cdot\cot(\theta)}{y_{av}} + \frac{-\delta y_q}{x_{av}}\right) \\ \frac{1}{2}\left(\frac{\delta y_q\cdot\cot(\theta)}{y_{av}} + \frac{-\delta y_q}{x_{av}}\right) & -\frac{\delta y_q}{y_{av}} \end{bmatrix}$$

Perform stress calculations as above:

$$\sigma_{rb_q} := \left|\begin{array}{l} sig_{0,0} \leftarrow \frac{E}{1-\nu^2}\left[\left(strain_q\right)_{0,0} + \nu\cdot\left(strain_q\right)_{1,1}\right] \\ sig_{1,1} \leftarrow \frac{E}{1-\nu^2}\left[\left(strain_q\right)_{1,1} + \nu\cdot\left(strain_q\right)_{0,0}\right] \\ sig_{0,1} \leftarrow 2\cdot G\cdot\left(strain_q\right)_{0,1} \\ sig_{1,0} \leftarrow 2\cdot G\cdot\left(strain_q\right)_{0,1} \\ sig \end{array}\right. \qquad T_{rb_q} := \left|\begin{array}{l} \text{for } r \in 0 .. 1 \\ \quad trac_r \leftarrow \sum_{p=0}^{1}\left(\sigma_{rb_q}\right)_{p,r}\cdot n_p \\ trac \end{array}\right.$$

$$\sigma_{nn\_rb_q} := T_{rb_q} \cdot n \qquad \sigma_{rbn_q} := \frac{\sigma_{nn\_rb_q} \cdot t_m \cdot 2\left(w_s + \frac{t_s}{\cos(\theta)}\right)}{\left(\frac{t_s}{\cos(\theta)} - 2\frac{\delta y_q}{\sin(\theta)}\right) \cdot w_s}$$

$$\sigma_{ns\_rb_q} := T_{rb_q} \cdot s \qquad \sigma_{rb_q} := \frac{\sigma_{ns\_rb_q} \cdot t_m \cdot 2\left(w_s + \frac{t_s}{\cos(\theta)}\right)}{\left(\frac{t_s}{\cos(\theta)} - 2\frac{\delta y_q}{\sin(\theta)}\right) \cdot w_s}$$

La Rochelle Calculations

Sample perimeter along the shear band:

$$P := 2 \cdot \left(\frac{t_s}{\cos(\theta)} + w_s\right)$$

Cross-sectional areas for measured data and rigid block model:

$$A_i := \left(\frac{t_s}{\cos(\theta)} - 2\,d_{proj_i}\right) \cdot w_s \qquad A_{rb_q} := \left(\frac{t_s}{\cos(\theta)} - 2\frac{\delta y_q}{\sin(\theta)}\right) \cdot w_s$$

Friction between the membrane and the soil:

$$f := \sigma_3 \cdot \tan(\phi) \qquad f = 36.66\,\text{kPa}$$

Global strain due to movement along the shear band for measured data and rigid block model:

$$\delta_L := \frac{d_{proj} \cdot \sin(\theta)}{h_s} \qquad \delta_{rb_q} := \frac{\delta y_q}{h_s}$$

Calculate resisting stress along the shear plane imposed by the membrane:

$$q_{corr_i} := \frac{P}{A_i} \cdot \sqrt{\frac{k_m \cdot f \cdot h_s \cdot \delta_{L_i}}{\cos(\theta) \cdot \sin(\theta)^2}} \qquad q_{corr\_rb_q} := \frac{P}{A_{rb_q}} \cdot \sqrt{\frac{k_m \cdot f \cdot h_s \cdot \delta_{rb_q}}{\cos(\theta) \cdot \sin(\theta)^2}}$$

$$\sigma_{s\_corr} := q_{corr} \cdot \cos(\theta) \cdot \sin(\theta) \qquad \sigma_{s\_corr\_rb} := q_{corr\_rb} \cdot \cos(\theta) \cdot \sin(\theta)$$

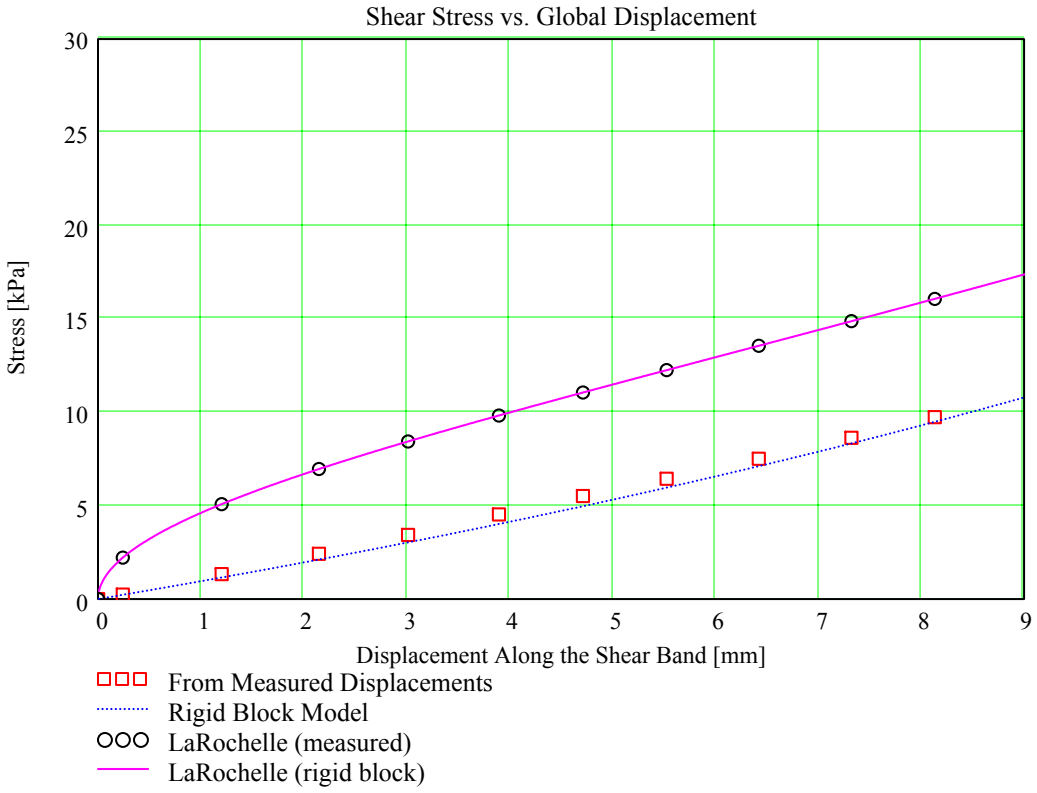
Shear Stress vs. Global Displacement
Stress [kPa]
30
25
20
15
10
5
0
0
1
2
3
4
5
6
7
8
9
Displacement Along the Shear Band [mm]
From Measured Displacements
Rigid Block Model
LaRochelle (measured)
LaRochelle (rigid block)

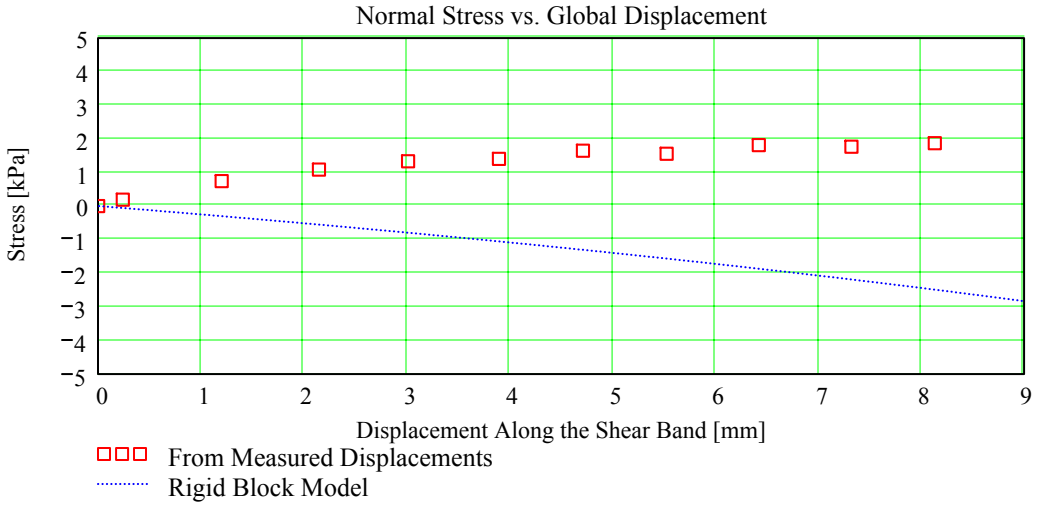
Normal Stress vs. Global Displacement
Stress [kPa]
5
4
3
2
1
0
−1
−2
−3
−4
−5
0
1
2
3
4
5
6
7
8
9
Displacement Along the Shear Band [mm]
From Measured Displacements
Rigid Block Model

APPENDIX A.3

Calculation of Fitting Functions for Local Void Ratio Distributions

Calculation of Local Void Ratio Distributions from Particle Images

Read output file from image analysis software: sample_ID := "BT-2030-16" slice_ID := "-80"

lvrd := C:\..\BT-2030-16-80.dat lvrd := augment(lvrd^⟨0⟩, lvrd^⟨1⟩, lvrd^⟨2⟩, lvrd^⟨3⟩, lvrd^⟨7⟩)

Trim data to remove polygons with void ratios greater than a specified threshold:

```
trimdata(M, Loc, lo, hi) :=
  M ← M^T
  v ← 0
  for k ∈ 0 .. cols(M) − 1
    if lo < (M^⟨k⟩)_Loc < hi
      MM^⟨v⟩ ← M^⟨k⟩
      v ← v + 1
  MM^T
```

lo := 0

hi := 4

Loc := cols(lvrd) − 1

$lvrd_t := trimdata(lvrd, Loc, lo, hi)$ $\frac{rows(lvrd_t)}{rows(lvrd)} = 99.397\,\%$

$\max(lvrd_t^{\langle 4\rangle}) = 3.947$ $\min(lvrd_t^{\langle 4\rangle}) = 1 \times 10^{-3}$

Assign position and local void ratio data to vectors for manipulation and plotting:

$A_s := lvrd_t^{\langle 0\rangle}$ $A_v := lvrd_t^{\langle 1\rangle}$ $x := lvrd_t^{\langle 2\rangle}$ $y := lvrd_t^{\langle 3\rangle}$ $e_{local} := \frac{\overrightarrow{A_v}}{A_s}$

Read binary image and calculate void ratio for the entire image:

image := READ_IMAGE(concat(sample_ID, slice_ID, ".bmp")) rc := rows(image)·cols(image)

$A_{solid} := mean\left(\frac{image}{255}\right)\cdot rc$ $A_{void} := rc - A_{solid}$ $e_{tot} := \frac{A_{void}}{A_{solid}}$ $e_{tot} = 0.645$

Calculate solid area weighted mean and standard deviation of local void ratios:

$\mu(A_s, e_{local}) := \frac{1}{\sum A_s}\cdot\sum\overrightarrow{(A_s\cdot e_{local})}$ $\sigma(A_s, e_{local}, \mu) := \sqrt{\frac{1}{\sum A_s}\cdot\sum\overrightarrow{\left[A_s\cdot(e_{local}-\mu)^2\right]}}$

$\mu_{est} := \mu(A_s, e_{local})$ $\sigma_{est} := \sigma(A_s, e_{local}, \mu_{est})$

Program to calculate solid area weighted histogram:

$$\text{weighted\_histogram}(\text{binsize}, \text{min}, \text{max}, \text{vr}, A_s) :=$$

$$\text{numbins} \leftarrow \frac{\text{max} - \text{min}}{\text{binsize}}$$

$$\text{hist}_{\text{numbins}-1} \leftarrow 0$$

$$\text{solids}_{\text{numbins}-1} \leftarrow 0$$

for $ii \in 0 .. \text{numbins} - 1$

$$\text{bin\_mid}_{ii} \leftarrow (ii + 1)\cdot\text{binsize} - \frac{\text{binsize}}{2}$$

for $jj \in 0 .. \text{last}(\text{vr})$

if $ii\cdot\text{binsize} \le \text{vr}_{jj} < (ii + 1)\cdot\text{binsize}$

$$\text{hist}_{ii} \leftarrow \text{hist}_{ii} + 1$$

$$\text{solids}_{ii} \leftarrow \text{solids}_{ii} + A_{s_{jj}}$$

$$\text{augment}\left(\text{bin\_mid}, \frac{\text{hist}}{\text{last}(\text{vr})}, \frac{\text{solids}}{\sum A_s}\right)$$

$\text{binsize} := 0.05$ $\quad f := \text{weighted\_histogram}(\text{binsize}, \text{lo}, \text{hi}, e_{\text{local}}, A_s)$ $\quad \text{NN} := \text{length}(e_{\text{local}})$

Plot solid area weighted histogram:

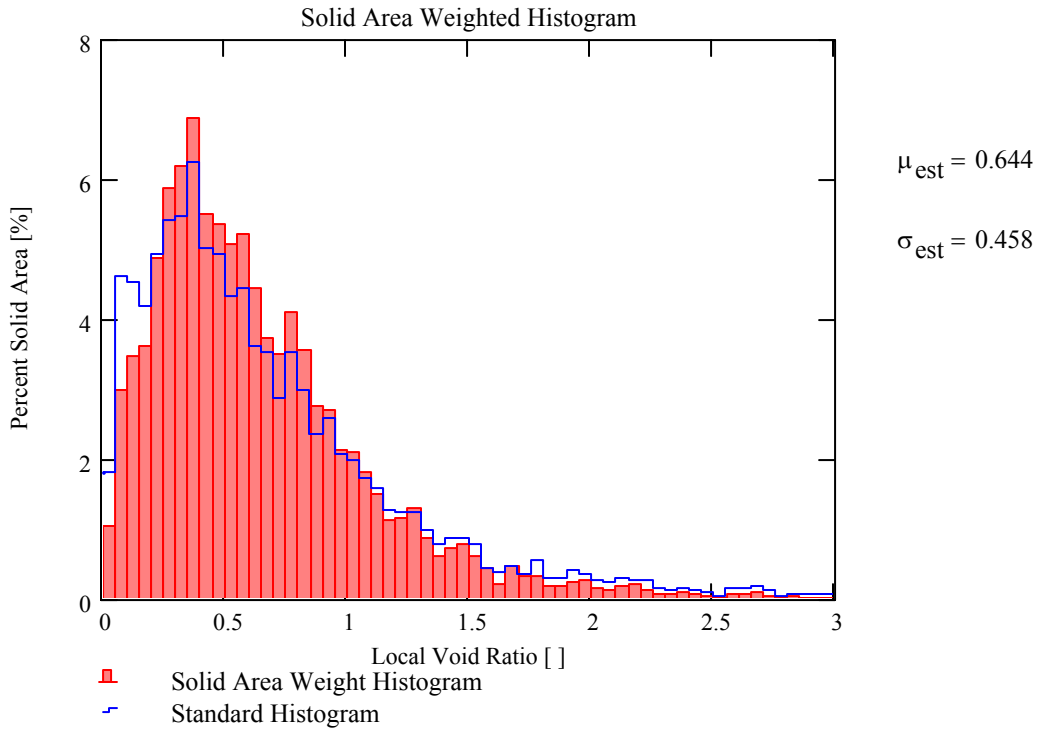

For fitting of cumulative distribution functions and the Kolmogorov-Smirnov test, a well-defined cumulative distribution is required. Generate a CDF from A_s and e_{local} data:

$$e_{sort} := csort(augment(e_{local}, A_s), 0) \qquad jj := 0 .. NN - 1$$

$$F_0 := e_{sort_{0,1}} \qquad j := 1 .. NN - 1 \qquad F_j := F_{j-1} + e_{sort_{j,1}} \qquad F := \frac{F}{\sum A_s}$$

Define the distribution functions to be tested:

Gamma distribution:

$$P(x,\lambda,k) = \begin{cases} \left[\frac{\lambda}{\Gamma(k)} \cdot (\lambda \cdot x)^{k-1} \cdot e^{-\lambda \cdot x}\right] & \text{if } x > 0 \\ 0 & \text{otherwise} \end{cases} \qquad D(x,\lambda,k) = \int_0^x gamma(u,\lambda,k)\, du$$

Weibull distribution:

$$P(x,b,c) = c \cdot b^{-c} \cdot x^{c-1} \cdot \exp\left[\left(-\frac{x}{b}\right)^c\right] \qquad D(x,b,c) = 1 - \exp\left[\left(-\frac{x}{b}\right)^c\right]$$

Lognormal distribution:

$$P(x,m,s) = \frac{1}{s \cdot x \cdot \sqrt{2 \cdot \pi}} \exp\left[-\frac{1}{2 \cdot s^2} \cdot (\ln(x) - m)^2\right] \qquad D(x,m,s) = \int_0^x lnorm(x,m,s)\, du$$

Maximum-likelihood estimates (MLEs) of lognormal distribution parameters:

$$gammaL1(\lambda,k) := \frac{NN}{\sum A_s} \cdot \sum \overrightarrow{\left(A_s \cdot \ln\left(\lambda \cdot dgamma(\lambda \cdot e_{local}, k)\right)\right)} \qquad \begin{pmatrix} \lambda \\ k \end{pmatrix} := \begin{pmatrix} 1 \\ 1 \end{pmatrix}$$

$$weibL1(b,c) := \frac{NN}{\sum A_s} \cdot \sum \overrightarrow{\left(A_s \cdot \ln\left(\frac{dweibull\left(\frac{e_{local}}{b}, c\right)}{b}\right)\right)} \qquad \begin{pmatrix} b \\ c \end{pmatrix} := \begin{pmatrix} 1 \\ 1 \end{pmatrix}$$

$$lnormL1(m,s) := \frac{NN}{\sum A_s} \cdot \sum \overrightarrow{\left(A_s \cdot \ln\left(dlnorm(e_{local}, m, s)\right)\right)} \qquad \begin{pmatrix} m \\ s \end{pmatrix} := \begin{pmatrix} -1 \\ 1 \end{pmatrix}$$

$$\begin{pmatrix} \lambda_{MLE} \\ k_{MLE} \end{pmatrix} := Maximize(gammaL1, \lambda, k) \qquad \begin{pmatrix} \lambda_{MLE} \\ k_{MLE} \end{pmatrix} = \begin{pmatrix} 3.219 \\ 2.073 \end{pmatrix}$$

$$\begin{pmatrix} b_{MLE} \\ c_{MLE} \end{pmatrix} := \text{Maximize}(weibL1, b, c) \qquad \begin{pmatrix} b_{MLE} \\ c_{MLE} \end{pmatrix} = \begin{pmatrix} 0.715 \\ 1.492 \end{pmatrix}$$

$$\begin{pmatrix} m_{MLE} \\ s_{MLE} \end{pmatrix} := \text{Maximize}(lnormL1, m, s) \qquad \begin{pmatrix} m_{MLE} \\ s_{MLE} \end{pmatrix} = \begin{pmatrix} -0.7 \\ 0.79 \end{pmatrix}$$

$$\mu_{MLE} := \begin{pmatrix} \dfrac{k_{MLE}}{\lambda_{MLE}} \\ \dfrac{b_{MLE}}{c_{MLE}} \cdot \Gamma\left(\dfrac{1}{c_{MLE}}\right) \\ \exp\left(m_{MLE} + \dfrac{s_{MLE}^2}{2}\right) \end{pmatrix} \qquad \mu_{MLE} = \begin{pmatrix} 0.644 \\ 0.646 \\ 0.678 \end{pmatrix}$$

$$\sigma_{MLE} := \begin{bmatrix} \sqrt{\dfrac{k_{MLE}}{\lambda_{MLE}^2}} \\ \sqrt{\dfrac{b_{MLE}^2}{c_{MLE}} \cdot \left[2 \cdot \Gamma\left(\dfrac{2}{c_{MLE}}\right) - \dfrac{1}{c_{MLE}}\left(\Gamma\left(\dfrac{1}{c_{MLE}}\right)^2\right)\right]} \\ \sqrt{\exp\left(s_{MLE}^2 + 2m_{MLE}\right) \cdot \left(\exp\left(s_{MLE}^2\right) - 1\right)} \end{bmatrix} \qquad \sigma_{MLE} = \begin{pmatrix} 0.447 \\ 0.441 \\ 0.631 \end{pmatrix}$$

Plot results from maximum likelihood analysis:

$$N := 1000 \qquad i := 0 .. N \qquad n_i := \frac{i}{N} \cdot \max\left(e_{local}\right)$$

$$c_{g_i} := \lambda_{MLE} \, dgamma\left(\lambda_{MLE} \cdot n_i, k_{MLE}\right) \cdot \left(f_{1,0} - f_{0,0}\right)$$

$$c_{w_i} := \frac{dweibull\left(\dfrac{n_i}{b_{MLE}}, c_{MLE}\right)}{b_{MLE}} \cdot \left(f_{1,0} - f_{0,0}\right)$$

$$c_{l_i} := dlnorm\left(n_i, m_{MLE}, s_{MLE}\right) \cdot \left(f_{1,0} - f_{0,0}\right)$$

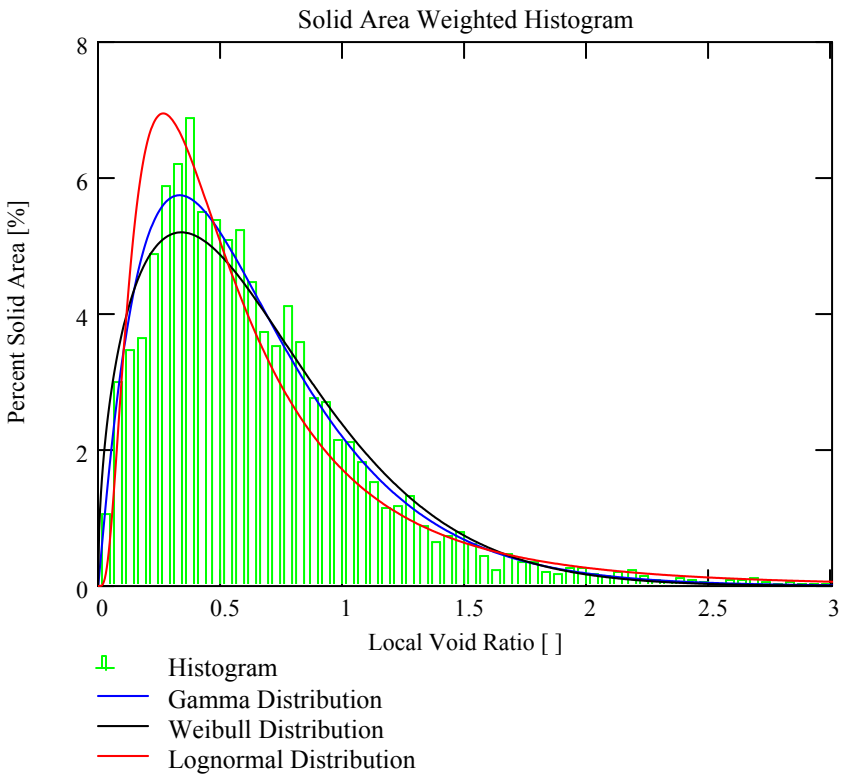

Estimates of distribution parameters from curve fitting of PDF's to histograms:

Given

$$\overrightarrow{\left(\lambda \cdot \mathrm{dgamma}\left(\lambda \cdot f^{\langle 0 \rangle}, k\right)\right)} = \frac{f^{\langle 2 \rangle}}{\left(f_{1,0} - f_{0,0}\right)} \qquad \begin{pmatrix} \lambda_{PDF} \\ k_{PDF} \end{pmatrix} := \mathrm{Minerr}(\lambda, k) \qquad \begin{pmatrix} \lambda_{PDF} \\ k_{PDF} \end{pmatrix} = \begin{pmatrix} 3.5168 \\ 2.2397 \end{pmatrix}$$

$$p_{g_i} := \lambda_{PDF}\, \mathrm{dgamma}\left(\lambda_{PDF} \cdot n_i, k_{PDF}\right) \cdot \left(f_{1,0} - f_{0,0}\right)$$

Given

$$\overrightarrow{\left(\frac{\mathrm{dweibull}\left(\frac{f^{\langle 0 \rangle}}{b}, c\right)}{b}\right)} = \frac{f^{\langle 2 \rangle}}{\left(f_{1,0} - f_{0,0}\right)} \qquad \begin{pmatrix} b_{PDF} \\ c_{PDF} \end{pmatrix} := \mathrm{Minerr}(b, c) \qquad \begin{pmatrix} b_{PDF} \\ c_{PDF} \end{pmatrix} = \begin{pmatrix} 0.6715 \\ 1.6499 \end{pmatrix}$$

$$p_{w_i} := \frac{\mathrm{dweibull}\left(\frac{n_i}{b_{PDF}}, c_{PDF}\right)}{b_{PDF}} \cdot \left(f_{1,0} - f_{0,0}\right)$$

Given

$$\overrightarrow{\left(\mathrm{dlnorm}\left(f^{\langle 0 \rangle}, m, s\right)\right)} = \frac{f^{\langle 2 \rangle}}{\left(f_{1,0} - f_{0,0}\right)} \qquad \begin{pmatrix} m_{PDF} \\ s_{PDF} \end{pmatrix} := \mathrm{Minerr}(m, s) \qquad \begin{pmatrix} m_{PDF} \\ s_{PDF} \end{pmatrix} = \begin{pmatrix} -0.5637 \\ 0.7478 \end{pmatrix}$$

$$p_{l_i} := \mathrm{dlnorm}\left(n_i, m_{PDF}, s_{PDF}\right)\cdot\left(f_{1,0} - f_{0,0}\right)$$

$$\mu_{PDF} := \begin{pmatrix} \dfrac{k_{PDF}}{\lambda_{PDF}} \\ \dfrac{b_{PDF}}{c_{PDF}}\cdot\Gamma\left(\dfrac{1}{c_{PDF}}\right) \\ \exp\left(m_{PDF} + \dfrac{s_{PDF}^{\,2}}{2}\right) \end{pmatrix} \qquad \mu_{PDF} = \begin{pmatrix} 0.637 \\ 0.600 \\ 0.753 \end{pmatrix}$$

$$\sigma_{PDF} := \begin{bmatrix} \sqrt{\dfrac{k_{PDF}}{\lambda_{PDF}^{\,2}}} \\ \sqrt{\dfrac{b_{PDF}^{\,2}}{c_{PDF}}\cdot\left[2\cdot\Gamma\left(\dfrac{2}{c_{PDF}}\right) - \dfrac{1}{c_{PDF}}\left(\Gamma\left(\dfrac{1}{c_{PDF}}\right)^2\right)\right]} \\ \sqrt{\exp\left(s_{PDF}^{\,2} + 2m_{PDF}\right)\cdot\left(\exp\left(s_{PDF}^{\,2}\right) - 1\right)} \end{bmatrix} \qquad \sigma_{PDF} = \begin{pmatrix} 0.426 \\ 0.374 \\ 0.651 \end{pmatrix}$$

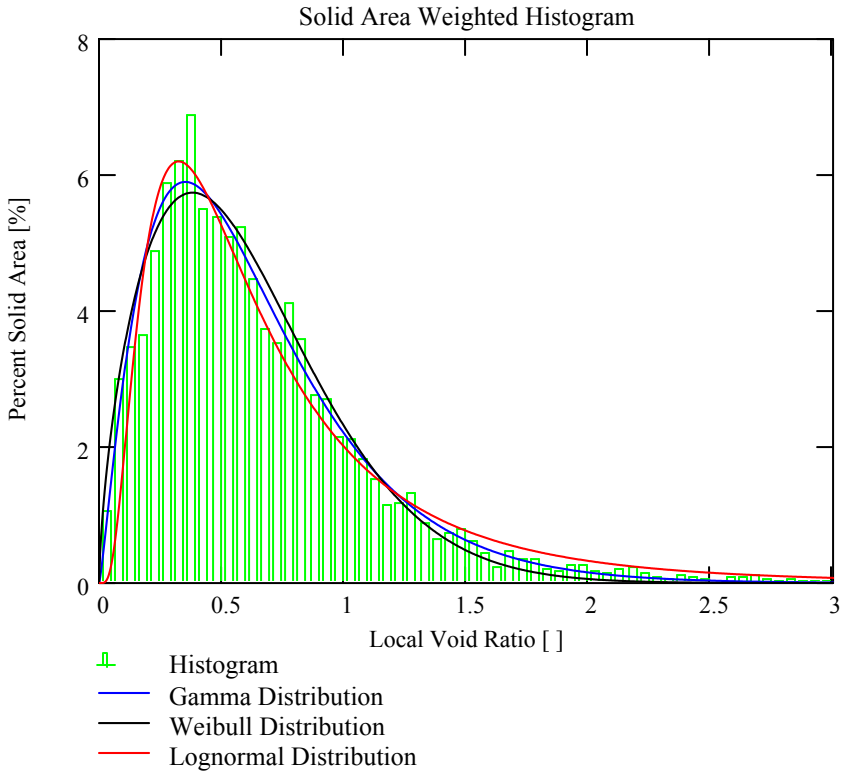

Estimates of distribution parameters from curve fitting of CDF's to entire dataset:

Given

$$\overrightarrow{\left(\text{pgamma}\left(\lambda \cdot e_{\text{sort}}^{\langle 0 \rangle}, k\right)\right)} = F \qquad \begin{pmatrix} \lambda_{CDF} \\ k_{CDF} \end{pmatrix} := \text{Minerr}(\lambda, k) \qquad \begin{pmatrix} \lambda_{CDF} \\ k_{CDF} \end{pmatrix} = \begin{pmatrix} 3.489 \\ 2.2153 \end{pmatrix}$$

$$q_{g_i} := \lambda_{CDF} \cdot \text{dgamma}\left(\lambda_{CDF} \cdot n_i, k_{CDF}\right) \cdot \left(f_{1,0} - f_{0,0}\right) \qquad Q_{g_i} := \text{pgamma}\left(\lambda_{CDF} \cdot n_i, k_{CDF}\right)$$

Given

$$\overrightarrow{\left(\text{pweibull}\left(\frac{e_{\text{sort}}^{\langle 0 \rangle}}{b}, c\right)\right)} = F \qquad \begin{pmatrix} b_{CDF} \\ c_{CDF} \end{pmatrix} := \text{Minerr}(b, c) \qquad \begin{pmatrix} b_{CDF} \\ c_{CDF} \end{pmatrix} = \begin{pmatrix} 0.6918 \\ 1.6034 \end{pmatrix}$$

$$q_{w_i} := \frac{\text{dweibull}\left(\frac{n_i}{b_{CDF}}, c_{CDF}\right)}{b_{CDF}} \cdot \left(f_{1,0} - f_{0,0}\right) \qquad Q_{w_i} := \text{pweibull}\left(\frac{n_i}{b_{CDF}}, c_{CDF}\right)$$

Given

$$\overrightarrow{\left(\text{plnorm}\left(e_{\text{sort}}^{\langle 0 \rangle}, m, s\right)\right)} = F \qquad \begin{pmatrix} m_{CDF} \\ s_{CDF} \end{pmatrix} := \text{Minerr}(m, s) \qquad \begin{pmatrix} m_{CDF} \\ s_{CDF} \end{pmatrix} = \begin{pmatrix} -0.6404 \\ 0.7131 \end{pmatrix}$$

$$q_{l_i} := \text{dlnorm}\left(n_i, m_{CDF}, s_{CDF}\right) \cdot \left(f_{1,0} - f_{0,0}\right) \qquad Q_{l_i} := \text{plnorm}\left(n_i, m_{CDF}, s_{CDF}\right)$$

$$\mu_{CDF} := \begin{pmatrix} \frac{k_{CDF}}{\lambda_{CDF}} \\ \frac{b_{CDF}}{c_{CDF}} \cdot \Gamma\left(\frac{1}{c_{CDF}}\right) \\ \exp\left(m_{CDF} + \frac{s_{CDF}^{2}}{2}\right) \end{pmatrix} \qquad \mu_{CDF} = \begin{pmatrix} 0.635 \\ 0.620 \\ 0.680 \end{pmatrix}$$

$$\sigma_{CDF} := \begin{bmatrix} \sqrt{\frac{k_{CDF}}{\lambda_{CDF}^{2}}} \\ \sqrt{\frac{b_{CDF}^{2}}{c_{CDF}} \cdot \left[2 \cdot \Gamma\left(\frac{2}{c_{CDF}}\right) - \frac{1}{c_{CDF}}\left(\Gamma\left(\frac{1}{c_{CDF}}\right)^{2}\right)\right]} \\ \sqrt{\exp\left(s_{CDF}^{2} + 2m_{CDF}\right) \cdot \left(\exp\left(s_{CDF}^{2}\right) - 1\right)} \end{bmatrix} \qquad \sigma_{CDF} = \begin{pmatrix} 0.427 \\ 0.396 \\ 0.553 \end{pmatrix}$$

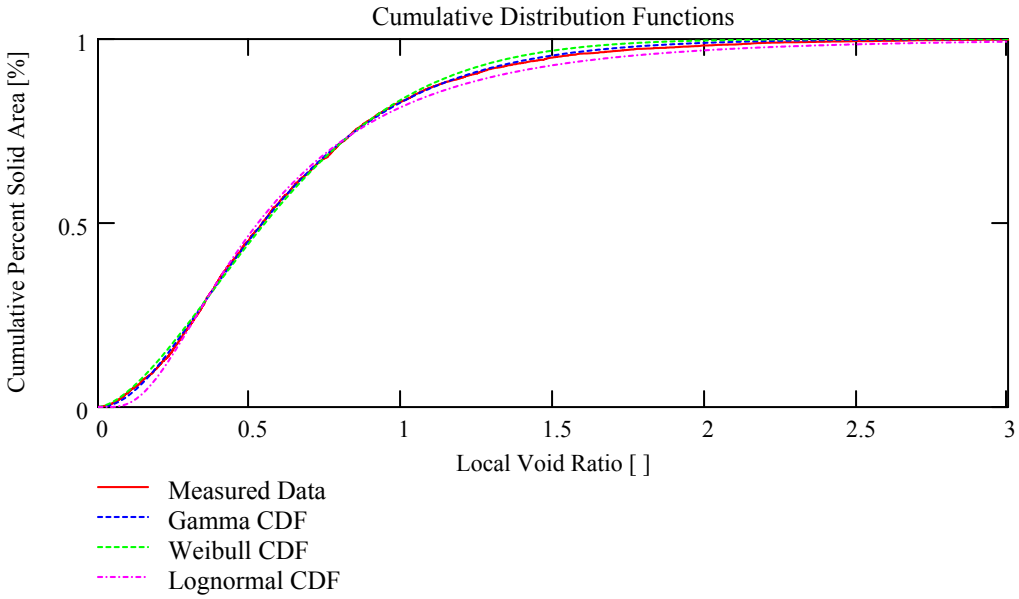
Cumulative Distribution Functions
Cumulative Percent Solid Area [%]
1
0.5
0
0
0.5
1
1.5
2
2.5
3
Local Void Ratio [ ]
Measured Data
Gamma CDF
Weibull CDF
Lognormal CDF

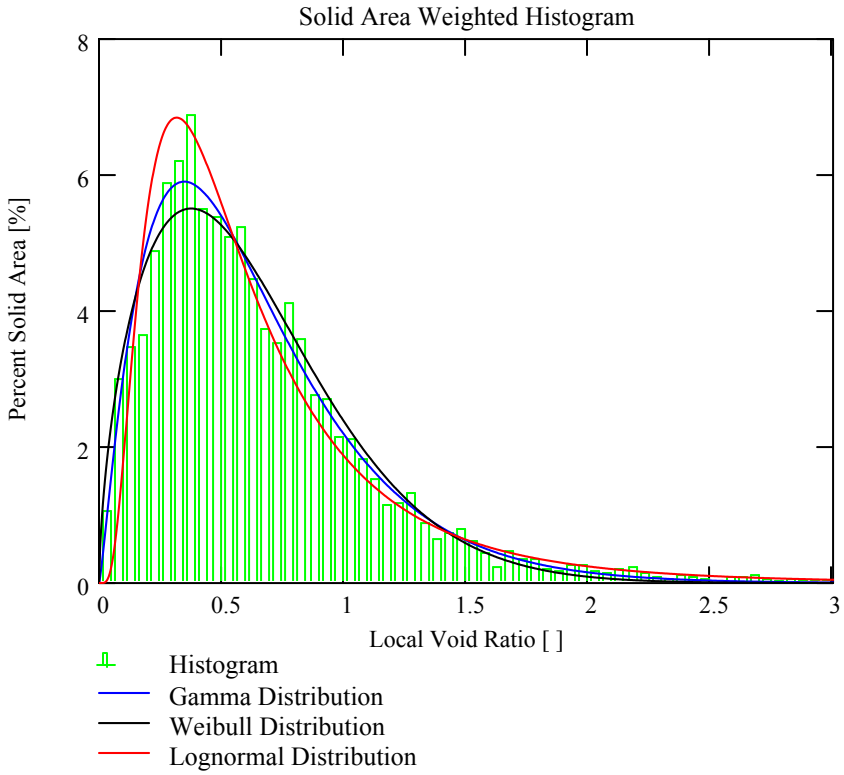
Solid Area Weighted Histogram
Percent Solid Area [%]
8
6
4
2
0
0
0.5
1
1.5
2
2.5
3
Local Void Ratio [ ]
Histogram
Gamma Distribution
Weibull Distribution
Lognormal Distribution

Perform a Kolmogorov-Smirnov test to assess goodness of fit across models and fitting methodologies:

Gamma distribution:

$ii := 0 .. 2$

$\lambda := \text{stack}(\lambda_{MLE}, \lambda_{PDF}, \lambda_{CDF})$ $k := \text{stack}(k_{MLE}, k_{PDF}, k_{CDF})$

$Dg_{jj,ii} := \left| F_{jj} - \text{pgamma}\left[\lambda_{ii} \cdot \left(e_{sort}^{\langle 0 \rangle}\right)_{jj}, k_{ii}\right]\right|$ $Dgmax_{ii} := \max\left(Dg^{\langle ii \rangle}\right)$

Weibull distribution:

$b := \text{stack}(b_{MLE}, b_{PDF}, b_{CDF})$ $c := \text{stack}(c_{MLE}, c_{PDF}, c_{CDF})$

$Dw_{jj,ii} := \left| F_{jj} - \text{pweibull}\left[\frac{\left(e_{sort}^{\langle 0 \rangle}\right)_{jj}}{b_{ii}}, c_{ii}\right]\right|$ $Dwmax_{ii} := \max\left(Dw^{\langle ii \rangle}\right)$

Lognormal distribution:

$m := \text{stack}(m_{MLE}, m_{PDF}, m_{CDF})$ $s := \text{stack}(s_{MLE}, s_{PDF}, s_{CDF})$

$Dl_{jj,ii} := \left| F_{jj} - \text{plnorm}\left[\left(e_{sort}^{\langle 0 \rangle}\right)_{jj}, m_{ii}, s_{ii}\right]\right|$ $Dlmax_{ii} := \max\left(Dl^{\langle ii \rangle}\right)$

Examine correlation coefficients and sums of squares of errors:

Gamma distribution:

$gamma_{jj,ii} := \text{pgamma}\left[\lambda_{ii} \cdot \left(e_{sort}^{\langle 0 \rangle}\right), k_{ii}\right]$ $R2g_{ii} := \text{corr}\left(F, gamma_{jj,ii}\right)^2$

$$SSEg_{ii} := \sum_{jj}\left[F_{jj} - \left(gamma_{jj,ii}\right)_{jj}\right]^2$$

Weibull distribution:

$weibull_{jj,ii} := \text{pweibull}\left(\frac{e_{sort}^{\langle 0 \rangle}}{b_{ii}}, c_{ii}\right)$ $R2w_{ii} := \text{corr}\left(F, weibull_{jj,ii}\right)^2$

$$SSEw_{ii} := \sum_{jj}\left[F_{jj} - \left(weibull_{jj,ii}\right)_{jj}\right]^2$$

Lognormal distribution:

$lognorm_{jj,ii} := \text{plnorm}\left(e_{sort}^{\langle 0 \rangle}, m_{ii}, s_{ii}\right)$ $R2l_{ii} := \text{corr}\left(F, lognorm_{jj,ii}\right)^2$

$$SSE_{l_{ii}} := \sum_{jj} \left[F_{jj} - \left(lognorm_{ii}\right)_{jj} \right]^2$$

$$D_{gmax} = \begin{pmatrix} 0.019 \\ 0.012 \\ 0.011 \end{pmatrix} \qquad R2_g = \begin{pmatrix} 0.9995 \\ 0.9998 \\ 0.9998 \end{pmatrix} \qquad SSE_g = \begin{pmatrix} 0.319 \\ 0.132 \\ 0.11 \end{pmatrix}$$

$$D_{wmax} = \begin{pmatrix} 0.032 \\ 0.032 \\ 0.022 \end{pmatrix} \qquad R2_w = \begin{pmatrix} 0.9978 \\ 0.9994 \\ 0.9990 \end{pmatrix} \qquad SSE_w = \begin{pmatrix} 1.625 \\ 1.183 \\ 0.534 \end{pmatrix}$$

$$D_{lmax} = \begin{pmatrix} 0.05 \\ 0.059 \\ 0.037 \end{pmatrix} \qquad R2_l = \begin{pmatrix} 0.9929 \\ 0.9991 \\ 0.9979 \end{pmatrix} \qquad SSE_l = \begin{pmatrix} 4.65 \\ 6.118 \\ 1.174 \end{pmatrix}$$

Show mean and standard deviation values for all calculations:

$$\mu_{sum} := augment\left(\mu_{MLE}, \mu_{PDF}, \mu_{CDF}\right) \qquad \sigma_{sum} := augment\left(\sigma_{MLE}, \sigma_{PDF}, \sigma_{CDF}\right)$$

$$\mu_{sum} = \begin{pmatrix} 0.644 & 0.637 & 0.635 \\ 0.646 & 0.600 & 0.620 \\ 0.678 & 0.753 & 0.680 \end{pmatrix} \qquad \sigma_{sum} = \begin{pmatrix} 0.447 & 0.426 & 0.427 \\ 0.441 & 0.374 & 0.396 \\ 0.631 & 0.651 & 0.553 \end{pmatrix}$$

APPENDIX A.4

Subregional Calculations for Image Void Ratio Data

Subregional Analyses of Images (e_{av}, λ, d_s, and l_s)

Inputs for calculations include size of the subreagion, spacing of the test lines (in pixels), test designations, and slice designations:

$size := 200$ $space := 10$ $test := \begin{pmatrix} "13" \\ "16" \\ "UN" \\ "U2" \end{pmatrix}$ $slice := \begin{pmatrix} "-20" \\ "-40" \\ "-60" \\ "-80" \end{pmatrix}$ $prefix := "BT-2030-"$

The following program performs all calculations and writes output files with void ratio and mean free path data. The program returns arrays with particle size measures.

$x(size, space, test, slice) :=$

$\mu m \leftarrow 10^{-6} m$

$calib \leftarrow 7.83 \mu m$

$testlines_{size-1,\, size-1} \leftarrow 0$

for $a \in 1 .. \frac{size - 1}{space}$

  for $b \in 0 .. size - 1$

    $testlines_{space \cdot a,\, b} \leftarrow 255$

$L_t \leftarrow size \cdot \sum testlines^{\langle 0 \rangle}$

for $ii \in 0 .. last(slice)$

  for $jj \in 0 .. last(test)$

    $image \leftarrow READ\_IMAGE\left(concat\left(prefix, test_{jj}, slice_{ii}, ".bmp"\right)\right)$

    for $R \in 0 .. \frac{rows(image)}{size} - 1$

      for $C \in 0 .. \frac{cols(image)}{size} - 1$

        $top \leftarrow R \cdot size$

        $bot \leftarrow (R + 1) \cdot size - 1$

        $left \leftarrow C \cdot size$

        $right \leftarrow (C + 1) \cdot size - 1$

        $subimage_{R,C} \leftarrow submatrix(image, top, bot, left, right)$

        $A_{s_{R,C}} \leftarrow \frac{1}{255} \cdot \sum_{rr=0}^{size-1} \sum_{cc=0}^{size-1} \left(subimage_{R,C}\right)_{rr,cc}$

        $A_{V_{R,C}} \leftarrow size^2 - A_{s_{R,C}}$

        $V_{V_{R,C}} \leftarrow \frac{1}{size^2} \cdot A_{s_{R,C}}$

$$e_{av_{R,C}} \leftarrow \frac{\overrightarrow{A_{v_{R,C}}}}{A_{s_{R,C}}}$$

$$point_{R,C} \leftarrow colgrad\left(and\left(testlines, subimage_{R,C}\right)\right)$$

$$point_{R,C} \leftarrow \overrightarrow{\left|point_{R,C}\right|}$$

$$P_{L_{R,C}} \leftarrow \frac{\sum_{rr=0}^{size-1}\sum_{cc=0}^{size-1}\left(point_{R,C}\right)_{rr,cc}}{L_t}\cdot\frac{1}{calib}$$

$$S_v \leftarrow 2\cdot P_L$$

$$\lambda_{R,C} \leftarrow \frac{4\cdot\left(1 - V_{v_{R,C}}\right)}{S_{v_{R,C}}}\cdot\frac{1}{mm}$$

$$l_{s_{R,C}} \leftarrow \frac{\overrightarrow{2}}{S_{v_{R,C}}}$$

$$d_{s_{R,C}} \leftarrow \frac{\overrightarrow{6\cdot V_{v_{R,C}}}}{S_{v_{R,C}}}$$

$$output_{ii,jj} \leftarrow stack\left(e_{av}, \lambda\right)$$

$$WRITEPRN\left(concat\left(prefix, test_{jj}, slice_{ii}, ".txt"\right), output_{ii,jj}\right)$$

$$part\_size_{ii,jj} \leftarrow stack\left(mean\left(l_s\right), mean\left(d_s\right)\right)$$

part_size

Return values of particle size measurements:

$$t := x(size, space, test, slice)$$

$$i := 0..3 \qquad j := 0..3 \qquad l_{s_{i,j}} := \left(t_{i,j}\right)_0 \qquad d_{s_{i,j}} := \left(t_{i,j}\right)_1$$

$$l_s = \begin{pmatrix} 0.403 & 0.409 & 0.382 & 0.401 \\ 0.411 & 0.403 & 0.38 & 0.393 \\ 0.415 & 0.41 & 0.392 & 0.404 \\ 0.426 & 0.412 & 0.384 & 0.398 \end{pmatrix} mm \qquad d_s = \begin{pmatrix} 0.719 & 0.74 & 0.732 & 0.747 \\ 0.731 & 0.736 & 0.721 & 0.729 \\ 0.739 & 0.749 & 0.737 & 0.745 \\ 0.759 & 0.745 & 0.733 & 0.742 \end{pmatrix} mm$$

```
% M-file to create contour plots of
% subregional void ratio and mean-free path data

% Data is read as a space-delimited matrix of void ratios
% with each matrix element corresponding to the void ratio
% of the subregion with the same location as the matrix
% element

clear all;

prefix = 'BT-2030-';
test = {'13' '16' 'UN' 'U2'};
slice = {'-20' '-40' '-60' '-80'};

scaled_colormap = 1;

for jj = 1:length(test)
    for ii = 1:length(slice)
        file = textread([prefix char(test(jj))
char(slice(ii)) '.txt']);
        e_av = file(1:22,:);
        mfp = file(23:44,:);
        g = contourf(interp2(e_av,2,'spline'));
        if scaled_colormap == 1;

mycontourcmap([0.4:0.01:1.6],'jet','colorbar','on');
        else
            colorbar;
        end
        %title(['Subregional Void Ratio Contours, ' prefix
char(test(jj)) char(slice(ii))]);
        axis equal;
        axis tight;
        axis ij;
        axis off;
        saveas(gcf,['e_av-' char(test(jj)) char(slice(ii))
'.jpg'],'jpg');
        h = contourf(interp2(mfp,2,'spline'));
        if scaled_colormap == 1;

mycontourcmap([0.2:0.01:0.7],'jet','colorbar','on');
        else
            colorbar;
        end
        %title(['Mean Free Path Contours, ' prefix
char(test(jj)) char(slice(ii))]);
        axis equal;
```

```
        axis tight;
        axis ij;
        axis off;
        saveas(gcf,['mfp-' char(test(jj)) char(slice(ii))
'.jpg'],'jpg');
        ['File ' prefix char(test(jj)) char(slice(ii)) '
has been processed']
    end
end
```

APPENDIX A.5

Spatial Averaging of Inclined Strip Calculations

Void Ratio Strip Calculations from Particle Images

Read output file from image analysis software: sample_ID := "BT-2030-16" slice_ID := "-80"

lvrd :=
...\BT-2030-16-80.dat

lvrd := augment(lvrd⟨0⟩, lvrd⟨1⟩, lvrd⟨2⟩, lvrd⟨3⟩, lvrd⟨7⟩)

Trim data to remove polygons with void ratios greater than a specified threshold:

trimdata(M, Loc, lo, hi) :=
- M ← M^T
- v ← 0
- for k ∈ 0 .. cols(M) − 1
  - if lo < $(M^{\langle k \rangle})_{Loc}$ < hi
    - $MM^{\langle v \rangle}$ ← $M^{\langle k \rangle}$
    - v ← v + 1
- MM^T

lo := 0

hi := 4

Loc := cols(lvrd) − 1

$lvrd_t$:= trimdata(lvrd, Loc, lo, hi)

$\frac{rows(lvrd_t)}{rows(lvrd)} = 99.397\,\%$

$max(lvrd_t^{\langle 4 \rangle}) = 3.947$ $min(lvrd_t^{\langle 4 \rangle}) = 1 \times 10^{-3}$

Assign position and local void ratio data to vectors for manipulation and plotting:

$A_s := lvrd_t^{\langle 0 \rangle}$ $A_v := lvrd_t^{\langle 1 \rangle}$ $x := lvrd_t^{\langle 2 \rangle}$ $y := lvrd_t^{\langle 3 \rangle}$ $e_{local} := \frac{\overrightarrow{A_v}}{A_s}$

Read binary image and calculate void ratio for the entire image:

image := READ_IMAGE(concat(sample_ID, slice_ID, ".bmp")) rc := rows(image)·cols(image)

$A_{solid} := mean\left(\frac{image}{255}\right) \cdot rc$ $A_{void} := rc - A_{solid}$ $e_{tot} := \frac{A_{void}}{A_{solid}}$ $e_{tot} = 0.645$

Calculate solid area weighted mean and standard deviation of local void ratios:

$\mu(A_s, e_{local}) := \frac{1}{\sum A_s} \cdot \sum \overrightarrow{(A_s \cdot e_{local})}$

$\sigma(A_s, e_{local}, \mu) := \sqrt{\frac{1}{\sum A_s} \cdot \sum \overrightarrow{\left[A_s \cdot (e_{local} - \mu)^2\right]}}$

$\mu_{est} := \mu(A_s, e_{local})$ $\sigma_{est} := \sigma(A_s, e_{local}, \mu_{est})$

Program to calculate solid area weighted histogram:

$$\text{weighted\_histogram}(\text{binsize}, \text{min}, \text{max}, \text{vr}, A_s) :=$$

$$\text{numbins} \leftarrow \frac{\text{max} - \text{min}}{\text{binsize}}$$

$$\text{hist}_{\text{numbins}-1} \leftarrow 0$$

$$\text{solids}_{\text{numbins}-1} \leftarrow 0$$

for $ii \in 0 .. \text{numbins} - 1$

$$\text{bin\_mid}_{ii} \leftarrow (ii + 1)\cdot\text{binsize} - \frac{\text{binsize}}{2}$$

for $jj \in 0 .. \text{last}(\text{vr})$

if $ii\cdot\text{binsize} \le \text{vr}_{jj} < (ii + 1)\cdot\text{binsize}$

$$\text{hist}_{ii} \leftarrow \text{hist}_{ii} + 1$$

$$\text{solids}_{ii} \leftarrow \text{solids}_{ii} + A_{s_{jj}}$$

$$\text{augment}\left(\text{bin\_mid}, \frac{\text{hist}}{\text{last}(\text{vr})}, \frac{\text{solids}}{\sum A_s}\right)$$

$\text{binsize} := 0.05$ $\quad f := \text{weighted\_histogram}(\text{binsize}, \text{lo}, \text{hi}, e_{\text{local}}, A_s)$ $\quad \text{NN} := \text{length}(e_{\text{local}})$

Plot solid area weighted histogram:

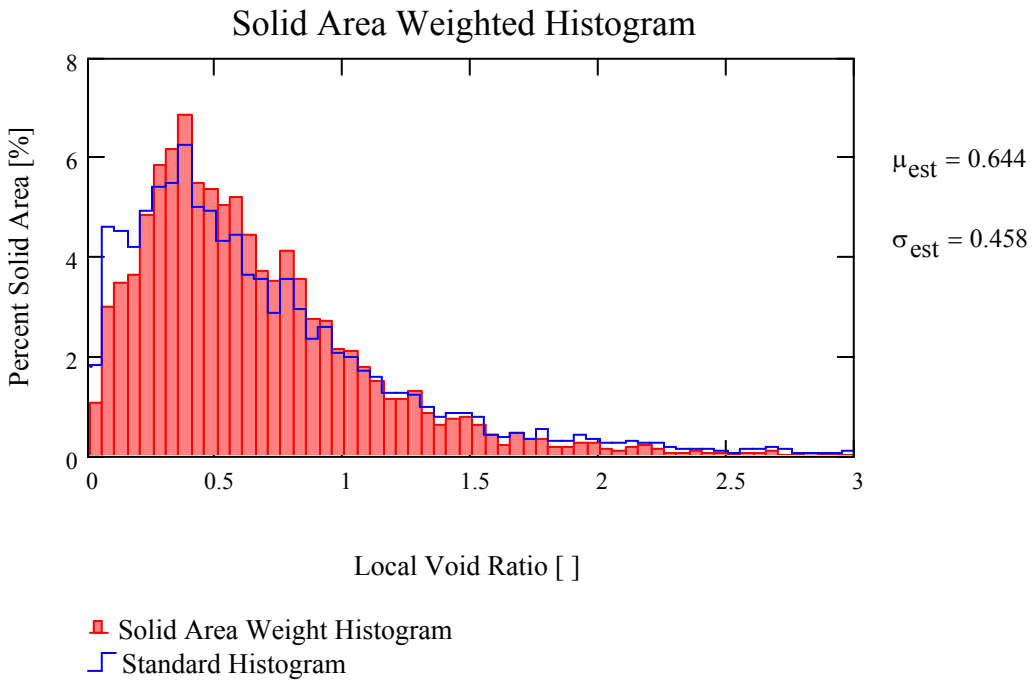

The following program counts the "solid" pixels and the "void" pixels in areas that are bounded by the image edges, inclined at an angle q, and have a width of "offset":

$$\text{v\_count}(M, \text{offset}, \theta) := \left| \begin{array}{l} c \leftarrow \cos(\theta) \\ s \leftarrow \sin(\theta) \\ m \leftarrow \text{ceil}\left[\frac{(\text{cols}(M)-1)\cdot s}{\text{offset}}\right] \\ \text{Min} \leftarrow \text{if}\left[\theta > \frac{\pi}{2}, \text{floor}\left[\frac{(\text{rows}(M)-1)\cdot c - (\text{cols}(M)-1)\cdot s}{\text{offset}}\right] + m, 0\right] \\ n \leftarrow \text{if}\left[\theta > \frac{\pi}{2}, m - \text{Min}, \text{floor}\left[\frac{(\text{rows}(M)-1)\cdot c}{\text{offset}}\right] + m\right] \\ V_n \leftarrow 0 \\ C_n \leftarrow 0 \\ M \leftarrow \frac{M}{255} \\ \text{for } i \in 0..\text{rows}(M)-1 \\ \quad \text{for } j \in 0..\text{cols}(M)-1 \\ \quad\quad \left| \begin{array}{l} k \leftarrow \text{floor}\left(\frac{i\cdot c - j\cdot s}{\text{offset}}\right) + m - \text{Min} \\ V_k \leftarrow V_k + M_{i,j} \\ C_k \leftarrow C_k + 1 \\ \text{region}_{i,j} \leftarrow k \end{array} \right. \\ \begin{pmatrix} \text{augment}(V, C) \\ \text{region} \end{pmatrix} \end{array} \right.$$

$\text{offset} := 200$ $\quad \theta := (180 - 61)\text{deg}$ $\quad \text{calib} := 7.83 \times 10^{-6}\text{m}$

$V := \text{v\_count}(\text{image}, \text{offset}, \theta)$ $\quad v_r := \text{if}\left(\theta < \frac{\pi}{2}, \text{reverse}(V_0), V_0\right)$

Combine the first and last strips with their adjacent strips because of the small number of pixels in the corners and calculate transect distances:

$$v_r := \left| \begin{array}{l} E \leftarrow \text{submatrix}(v_r, 1, \text{rows}(v_r)-2, 0, 1) \\ (L \leftarrow \text{rows}(E) - 1 \quad r \leftarrow \text{rows}(v_r) - 1) \\ \left(E_{0,0} \leftarrow E_{0,0} + v_{r_{0,0}} \quad E_{0,1} \leftarrow E_{0,1} + v_{r_{0,1}}\right) \\ \left(E_{L,0} \leftarrow E_{L,0} + v_{r_{r,0}} \quad E_{L,1} \leftarrow E_{L,1} + v_{r_{r,1}}\right) \\ E \end{array} \right.$$

$$t := \left| \begin{array}{l} \text{for } u \in 0..\text{rows}(v_r)-1 \\ \quad T_u \leftarrow \text{calib}\cdot\left(u + \frac{3}{2}\right)\cdot\text{offset} \\ T \end{array} \right.$$

Calculate void ratios in each of the strips:

$A_{sol} := v_r^{\langle 0 \rangle}$ $A_{tot} := v_r^{\langle 1 \rangle}$ $A_{void} := A_{tot} - A_{sol}$ $i := 0 .. last(A_{sol})$ $\overrightarrow{e_{im} := \frac{A_{void}}{A_{sol}}}$

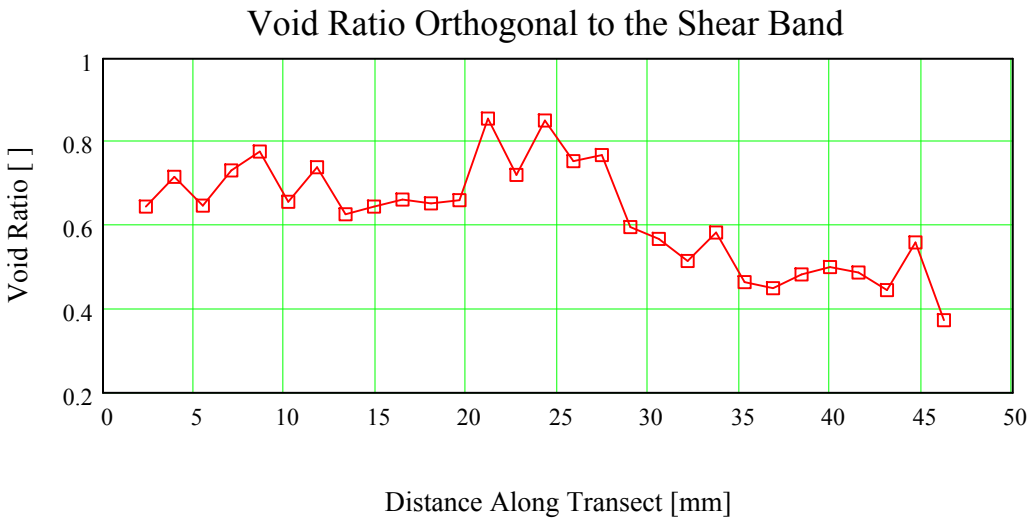

Calculate cumulative void ratios moving from left to right and from right to left:

$A_{sc_i} := \sum_{j=0}^{i} A_{sol_j}$ $A_{vc_i} := \sum_{j=0}^{i} A_{void_j}$ $e_{c_i} := \frac{A_{vc_i}}{A_{sc_i}}$

$A_{scr_i} := \sum_{j=0}^{i} reverse(A_{sol})_j$ $A_{vcr_i} := \sum_{j=0}^{i} reverse(A_{void})_j$ $e_{cr_i} := \frac{A_{vcr_i}}{A_{scr_i}}$

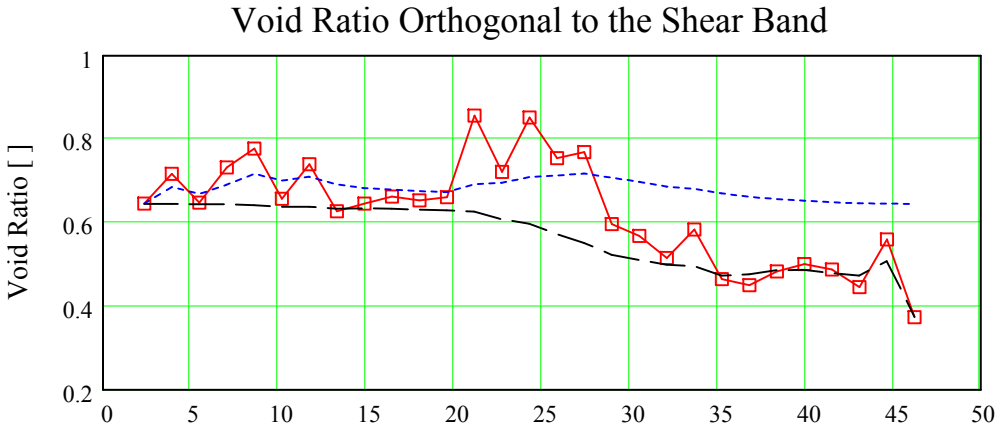

Based on analysis of the above plots, define a vector delineating the beginning and end of the shear band:

$$b := \begin{pmatrix} 0 & 11 & 12 & 18 & 19 & \text{last}(A_{sol}) \end{pmatrix}^T \qquad k := b_0 .. b_1 \qquad u := b_2 .. b_3 \qquad v := b_5 .. b_4$$

$$LHS := \text{mean}\left(t_{b_1}, t_{b_2}\right) \cdot \frac{1}{mm} \qquad RHS := \text{mean}\left(t_{b_3}, t_{b_4}\right) \cdot \frac{1}{mm}$$

Calculate accumulated void ratios moving from either end of the transect towards the shear band. The accumulated void ratio within the shear band is calculated from left to right.

$$A_{s1_k} := \sum_{j=b_0}^{k} A_{sol_j} \qquad A_{v1_k} := \sum_{j=b_0}^{k} A_{void_j} \qquad e_{c1_k} := \frac{A_{v1_k}}{A_{s1_k}}$$

$$A_{s2_u} := \sum_{j=b_2}^{u} A_{sol_j} \qquad A_{v2_u} := \sum_{j=b_2}^{u} A_{void_j} \qquad e_{c2_u} := \frac{A_{v2_u}}{A_{s2_u}}$$

$$A_{s3_v} := \sum_{j=b_5}^{v} A_{sol_j} \qquad A_{v3_v} := \sum_{j=b_5}^{v} A_{void_j} \qquad e_{c3_v} := \frac{A_{v3_v}}{A_{s3_v}}$$

$$plotlim := \begin{pmatrix} 0 \\ 50 \end{pmatrix} \qquad e_{as1} := \begin{pmatrix} e_{c1_{b_1}} \\ e_{c1_{b_1}} \end{pmatrix} \qquad e_{as2} := \begin{pmatrix} e_{c2_{b_3}} \\ e_{c2_{b_3}} \end{pmatrix} \qquad e_{as3} := \begin{pmatrix} e_{c3_{b_4}} \\ e_{c3_{b_4}} \end{pmatrix}$$

Compare accumulated void ratios (horizontal lines) with individual strip void ratios to qualitatively assess the "goodness" of the shear band extents selection:

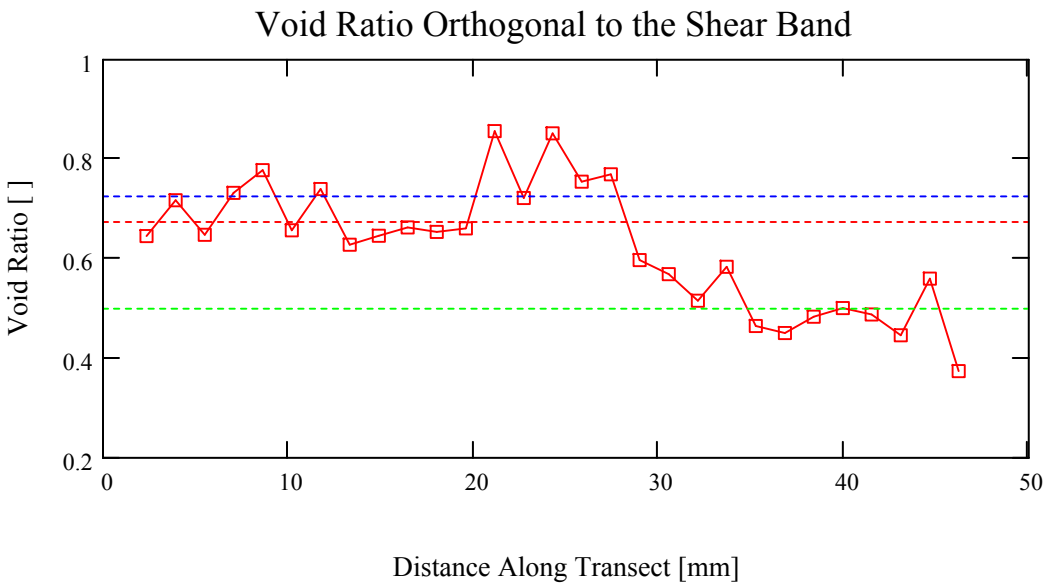

Based on x- and y- centroid locations for the local void ratio polygons, asign each polygon to either inside or outside of the shear band:

$$c := \cos(\theta) \qquad s := \sin(\theta) \qquad a := \text{ceil}\left[\frac{(\text{cols}(\text{image}) - 1)\cdot s}{\text{offset}}\right]$$

$$\text{Min} := \text{if}\left[\theta > \frac{\pi}{2}, \text{floor}\left[\frac{(\text{rows}(\text{image}) - 1)\cdot c - (\text{cols}(\text{image}) - 1)\cdot s}{\text{offset}}\right] + a, 0\right]$$

$$h(x,y) := \text{floor}\left(\frac{y\cdot c - x\cdot s}{\text{offset}}\right) + a - \text{Min} \qquad p := \text{augment}\left(h(x,y), A_s, e_{\text{local}}\right) \qquad \text{lim} := \begin{pmatrix} b_2 + 1 \\ b_3 + 1 \end{pmatrix}$$

$$\begin{aligned}
&\text{segregate}(p, \text{lim}) := \\
&\quad N \leftarrow \text{rows}(p) \\
&\quad j \leftarrow 0 \\
&\quad k \leftarrow 0 \\
&\quad p \leftarrow p^{T} \\
&\quad \text{for } i \in 0..N-1 \\
&\quad\quad \text{if } \text{lim}_0 \le p_{0,i} \le \text{lim}_1 \\
&\quad\quad\quad \text{inside}^{\langle j \rangle} \leftarrow p^{\langle i \rangle} \\
&\quad\quad\quad j \leftarrow j + 1 \\
&\quad\quad \text{otherwise} \\
&\quad\quad\quad \text{outside}^{\langle k \rangle} \leftarrow p^{\langle i \rangle} \\
&\quad\quad\quad k \leftarrow k + 1 \\
&\quad \begin{pmatrix} \text{inside}^{T} \\ \text{outside}^{T} \end{pmatrix}
\end{aligned}$$

$$P := \text{segregate}(p, \text{lim})$$

$$\text{inside} := P_0$$

$$\text{outside} := P_1$$

Calculate histograms for both inside and outside of the shear band and write results to a text file:

$$f_{in} := \text{weighted\_histogram}\left(\text{binsize}, \text{lo}, \text{hi}, \text{inside}^{\langle 2 \rangle}, \text{inside}^{\langle 1 \rangle}\right)$$

$$f_{out} := \text{weighted\_histogram}\left(\text{binsize}, \text{lo}, \text{hi}, \text{outside}^{\langle 2 \rangle}, \text{outside}^{\langle 1 \rangle}\right)$$

$$\text{WRITEPRN}(\text{concat}(\text{sample\_ID}, \text{slice\_ID}, ".\text{his}")) := \text{augment}\left(f_{in}, f_{out}, f\right)$$

Plot results:

$$\mu_{in} := \mu\left(\text{inside}^{\langle 1 \rangle}, \text{inside}^{\langle 2 \rangle}\right) \qquad \mu_{out} := \mu\left(\text{outside}^{\langle 1 \rangle}, \text{outside}^{\langle 2 \rangle}\right)$$

$$\sigma_{in} := \sigma\left(\text{inside}^{\langle 1 \rangle}, \text{inside}^{\langle 2 \rangle}, \mu_{in}\right) \qquad \sigma_{out} := \sigma\left(\text{outside}^{\langle 1 \rangle}, \text{outside}^{\langle 2 \rangle}, \mu_{out}\right)$$

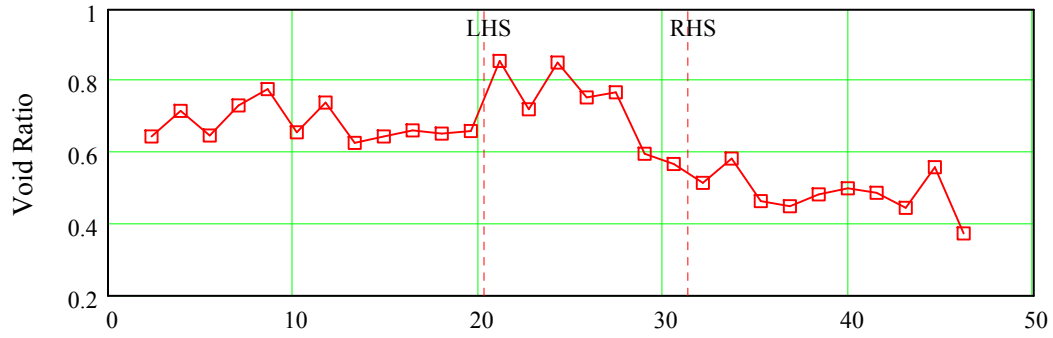

Distance Along Transect [mm]

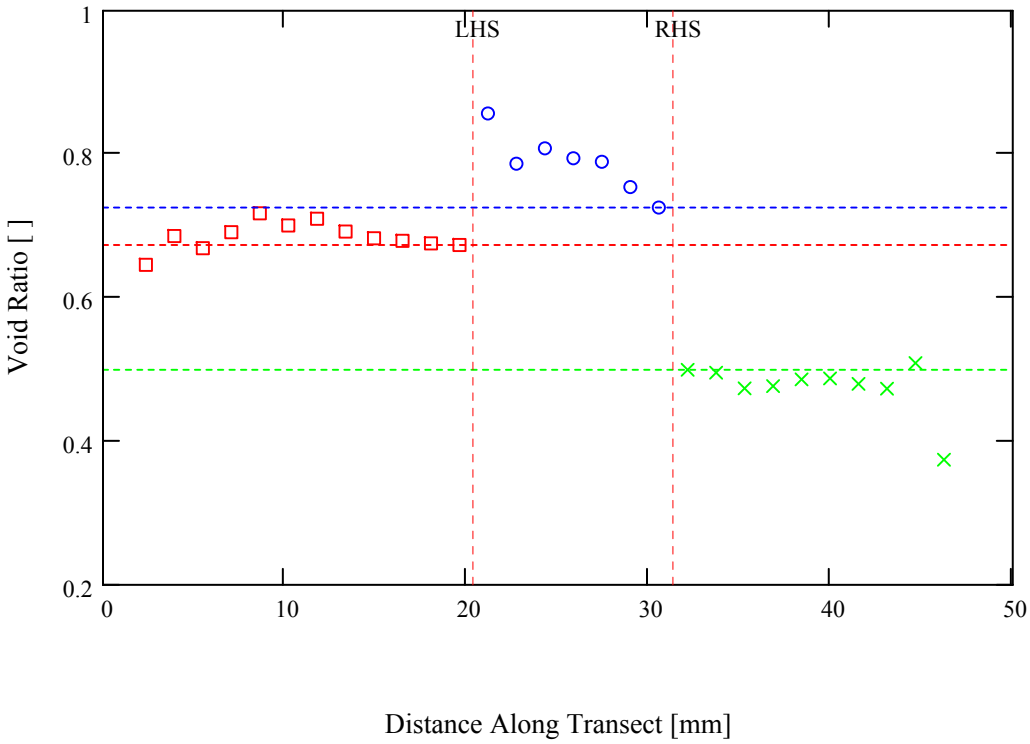
LHS
RHS
1
0.8
0.6
0.4
0.2
Void Ratio [ ]
0
10
20
30
40
50
Distance Along Transect [mm]

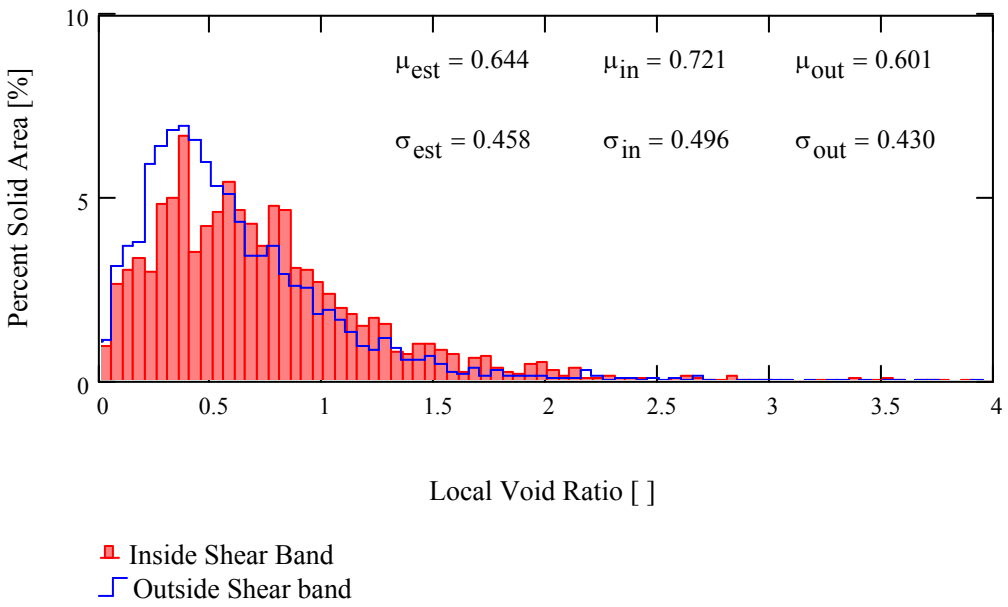
10
5
0
Percent Solid Area [%]
μest = 0.644
μin = 0.721
μout = 0.601
σest = 0.458
σin = 0.496
σout = 0.430
0
0.5
1
1.5
2
2.5
3
3.5
4
Local Void Ratio [ ]
Inside Shear Band
Outside Shear band

APPENDIX B

Local Void Ratio Histograms for All Images from Experimental Studies

SDU-20

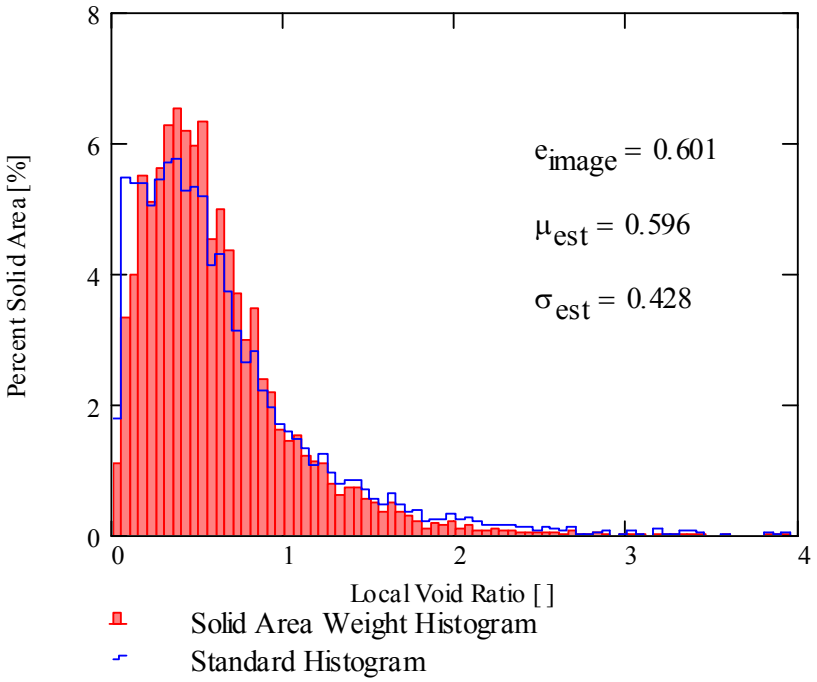
Percent Solid Area [%]
Local Void Ratio [ ]
e_{image} = 0.601
μ_{est} = 0.596
σ_{est} = 0.428
Solid Area Weight Histogram
Standard Histogram

SDU-40

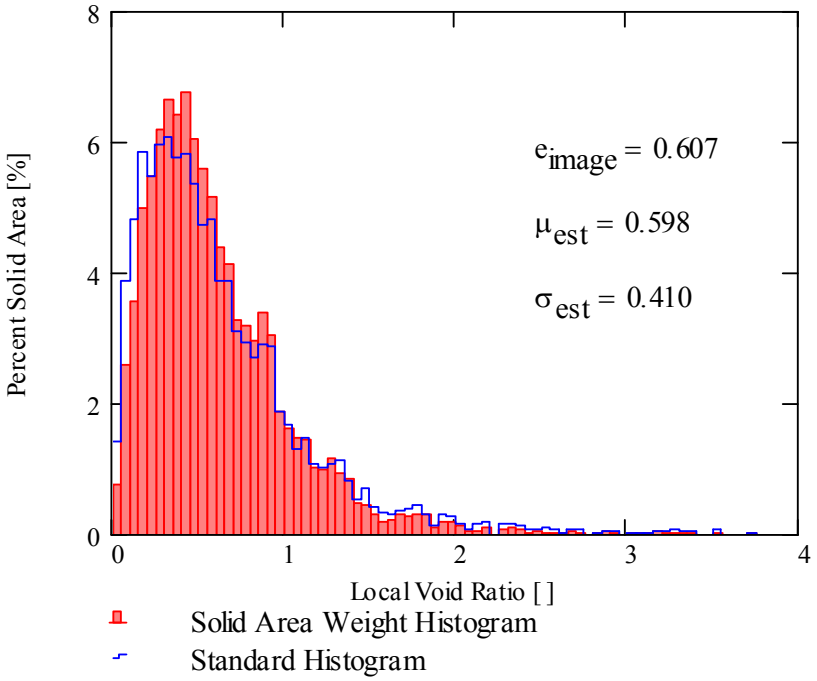
Percent Solid Area [%]
Local Void Ratio [ ]
e_{image} = 0.607
μ_{est} = 0.598
σ_{est} = 0.410
Solid Area Weight Histogram
Standard Histogram

SDU-60

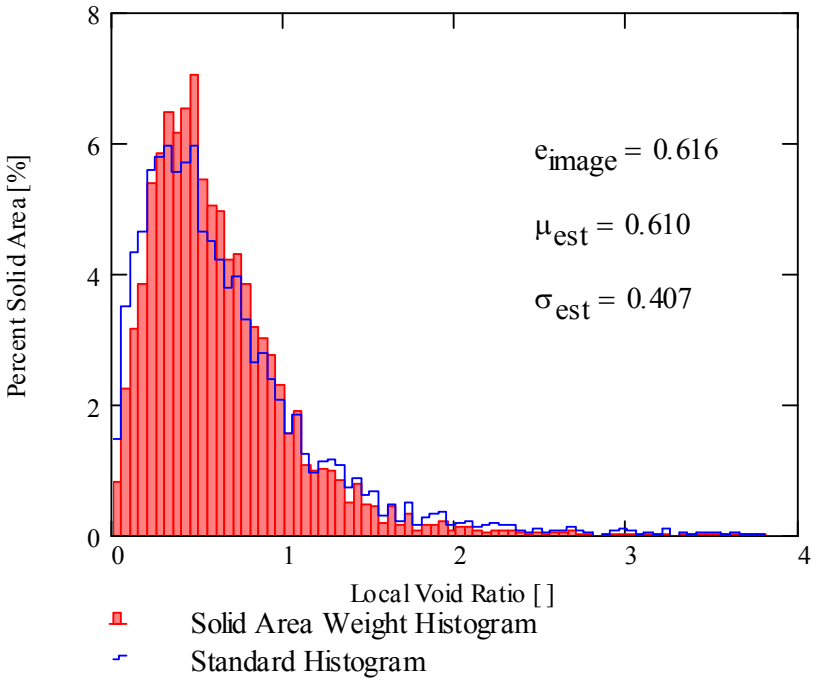
Percent Solid Area [%]
Local Void Ratio [ ]
e_{image} = 0.616
μ_{est} = 0.610
σ_{est} = 0.407
Solid Area Weight Histogram
Standard Histogram

SDU-80

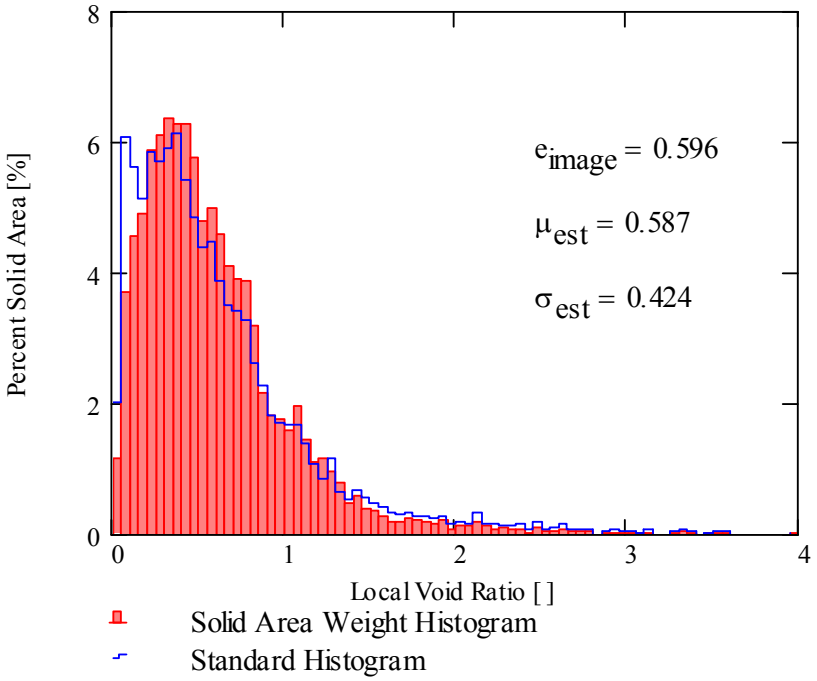
Percent Solid Area [%]
Local Void Ratio [ ]
e_{image} = 0.596
μ_{est} = 0.587
σ_{est} = 0.424
Solid Area Weight Histogram
Standard Histogram

SDS-20

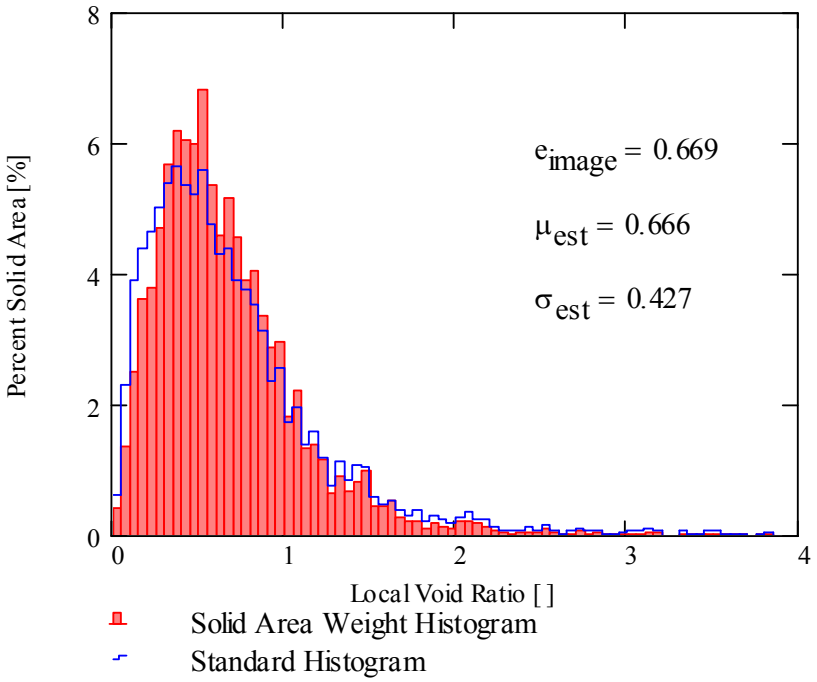
Percent Solid Area [%]
Local Void Ratio [ ]
e_{image} = 0.669
μ_{est} = 0.666
σ_{est} = 0.427
Solid Area Weight Histogram
Standard Histogram

SDS-40

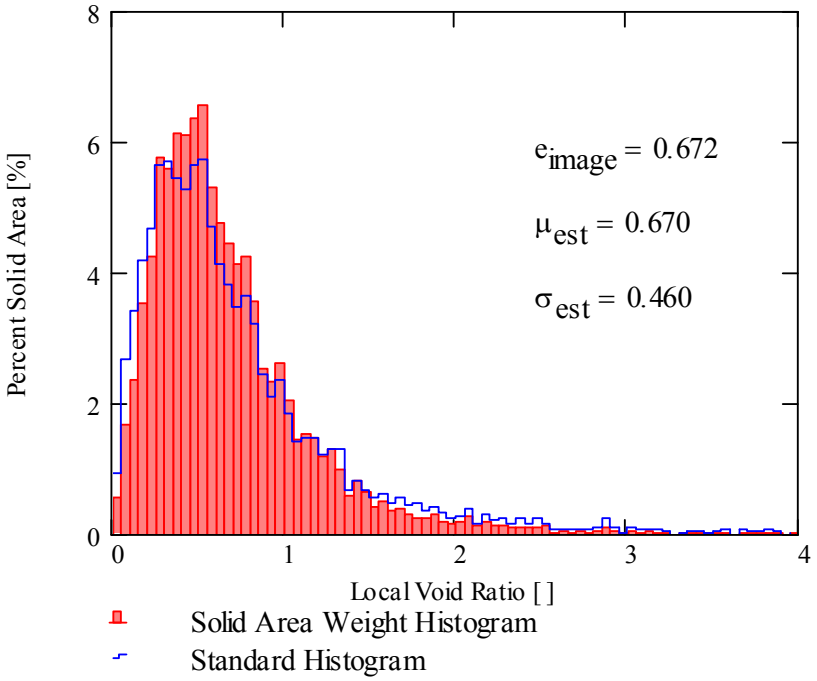
Percent Solid Area [%]
Local Void Ratio [ ]
e_{image} = 0.672
μ_{est} = 0.670
σ_{est} = 0.460
Solid Area Weight Histogram
Standard Histogram

SDS-60

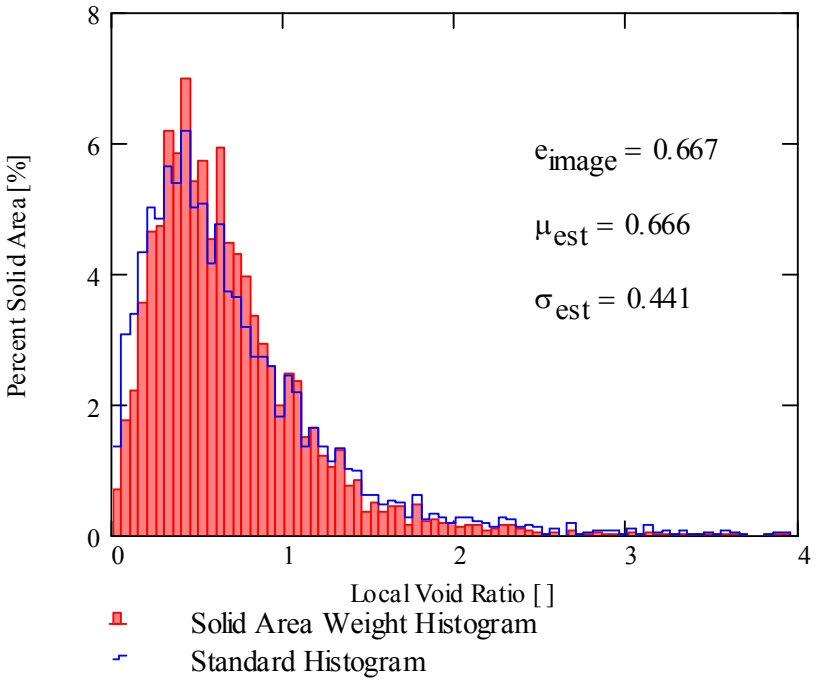
Percent Solid Area [%]
Local Void Ratio [ ]
e_{image} = 0.667
μ_{est} = 0.666
σ_{est} = 0.441
Solid Area Weight Histogram
Standard Histogram

SDS-80

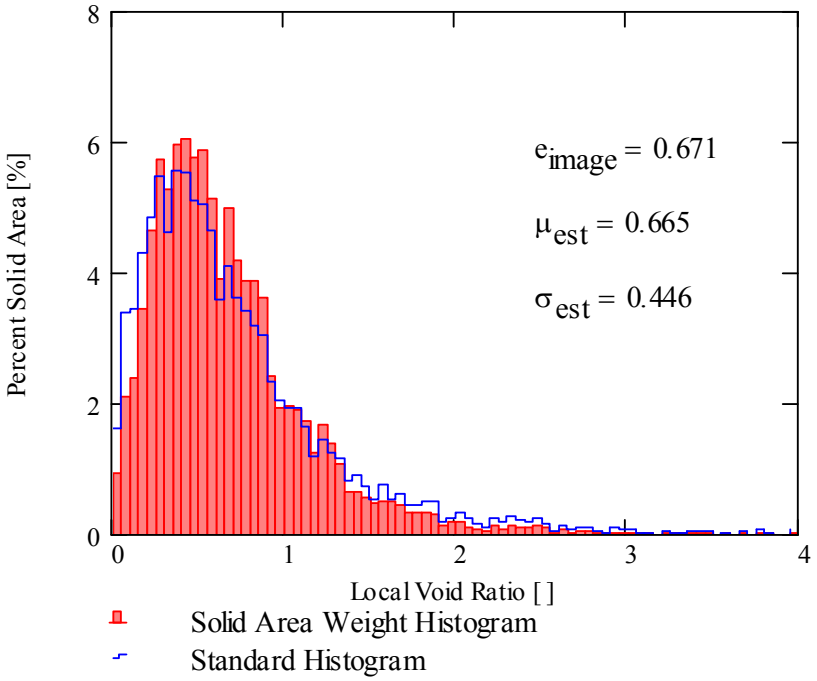
Percent Solid Area [%]
Local Void Ratio [ ]
e_{image} = 0.671
μ_{est} = 0.665
σ_{est} = 0.446
Solid Area Weight Histogram
Standard Histogram

HDU-20

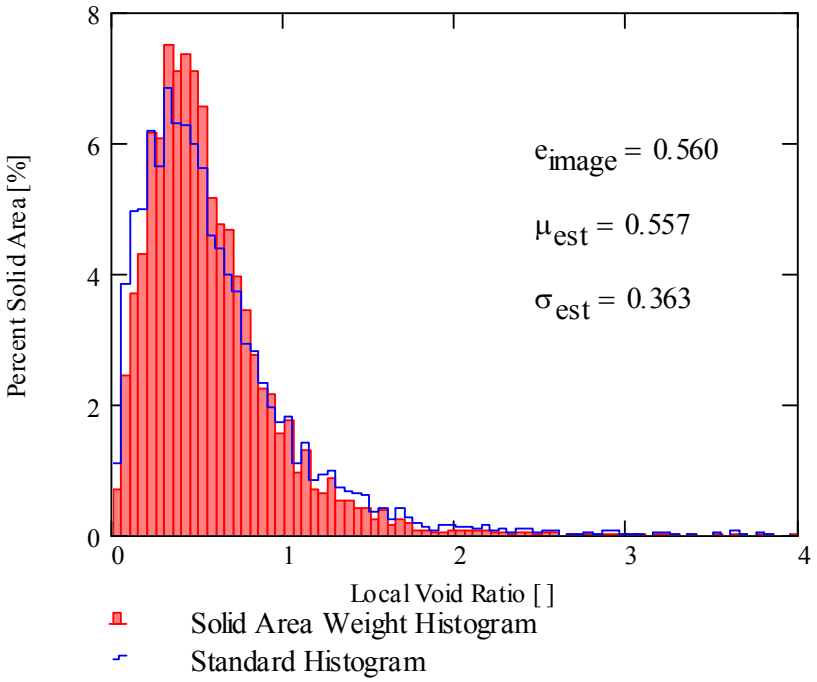
Percent Solid Area [%]
Local Void Ratio [ ]
e_{image} = 0.560
μ_{est} = 0.557
σ_{est} = 0.363
Solid Area Weight Histogram
Standard Histogram

HDU-40

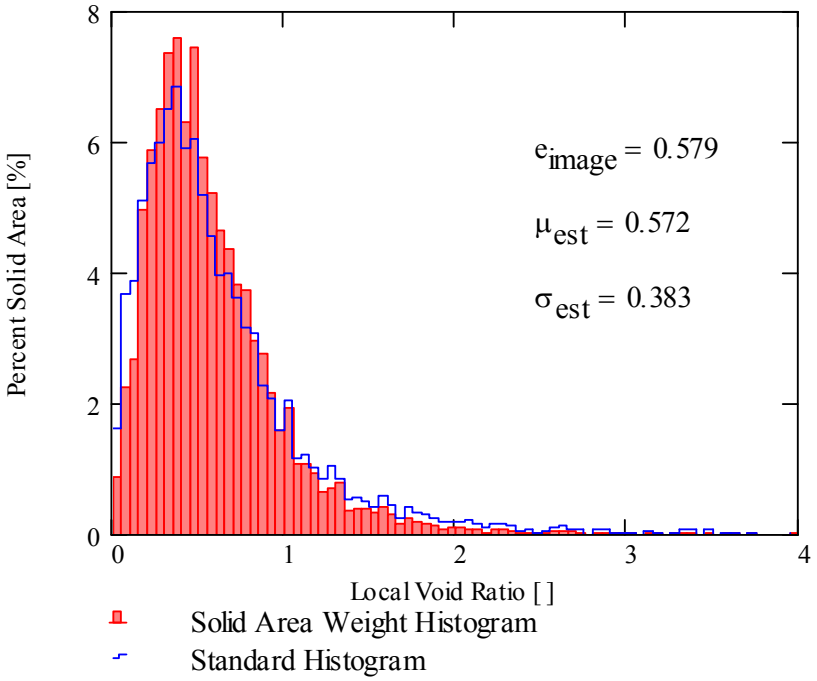
Percent Solid Area [%]
Local Void Ratio [ ]
e_{image} = 0.579
μ_{est} = 0.572
σ_{est} = 0.383
Solid Area Weight Histogram
Standard Histogram

HDU-60

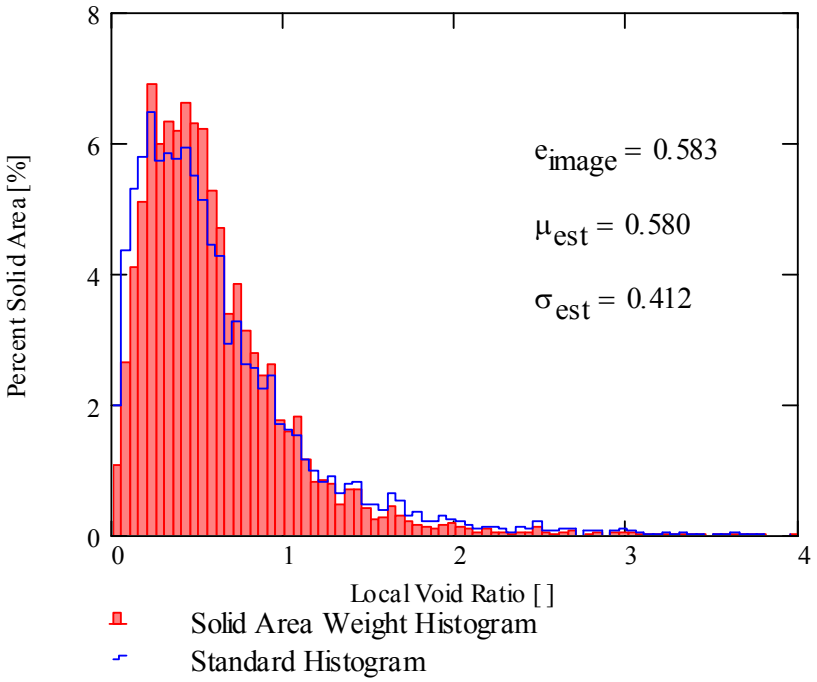
Percent Solid Area [%]
Local Void Ratio [ ]
e_{image} = 0.583
μ_{est} = 0.580
σ_{est} = 0.412
Solid Area Weight Histogram
Standard Histogram

HDU-80

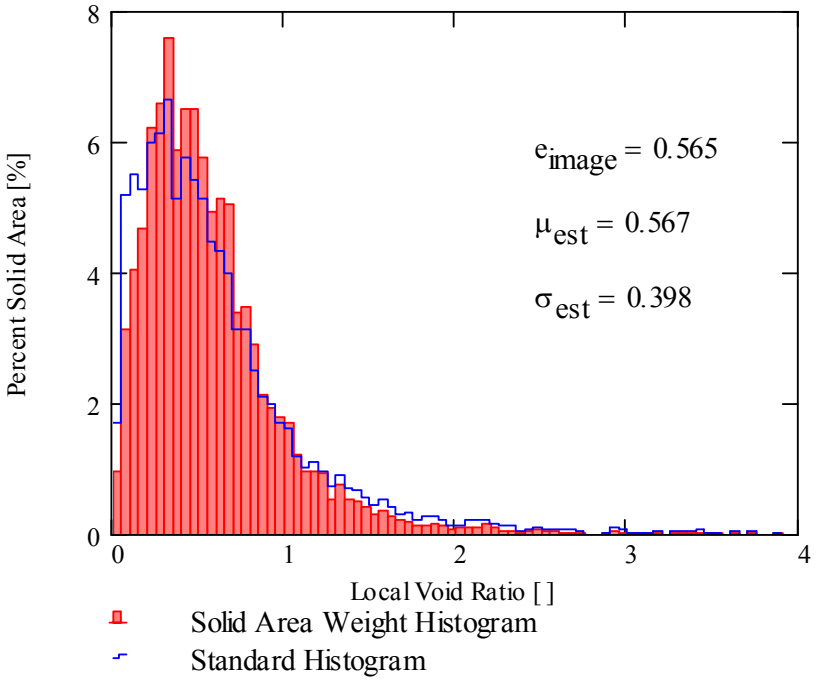
Percent Solid Area [%]
Local Void Ratio [ ]
e_{image} = 0.565
μ_{est} = 0.567
σ_{est} = 0.398
Solid Area Weight Histogram
Standard Histogram

HDS-20

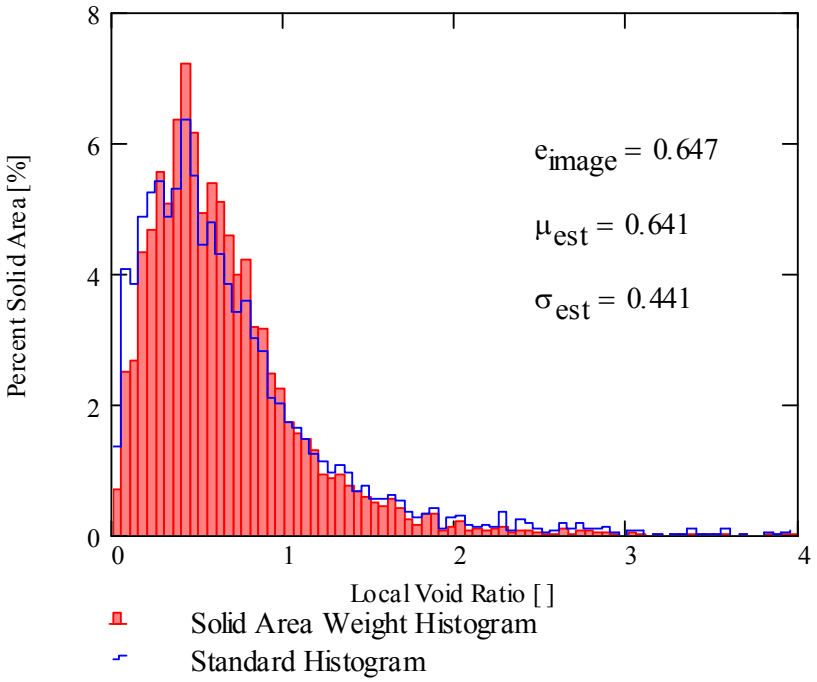
Percent Solid Area [%]
Local Void Ratio [ ]
e_{image} = 0.647
μ_{est} = 0.641
σ_{est} = 0.441
Solid Area Weight Histogram
Standard Histogram

HDS-40

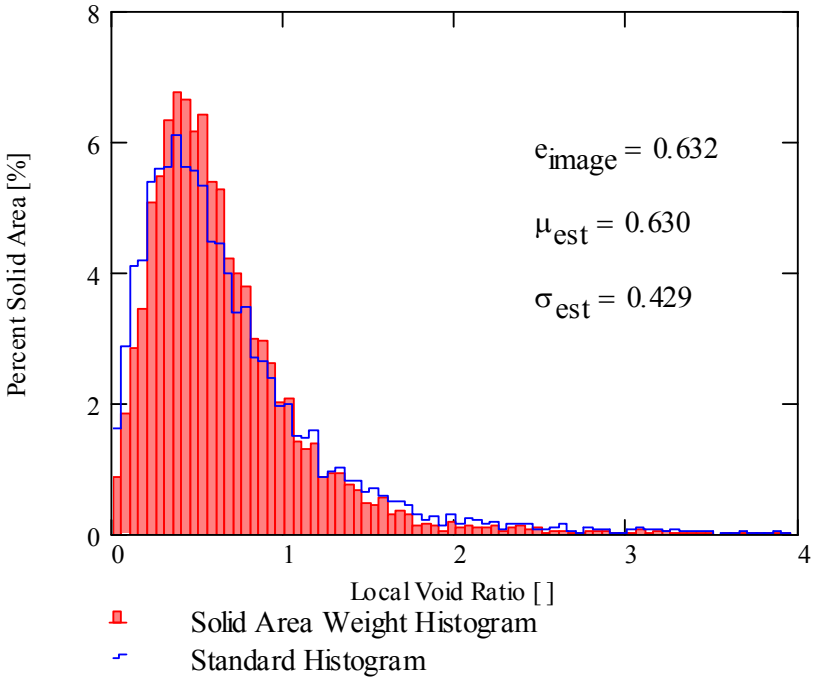
Percent Solid Area [%]
Local Void Ratio [ ]
e_{image} = 0.632
μ_{est} = 0.630
σ_{est} = 0.429
Solid Area Weight Histogram
Standard Histogram

HDS-60

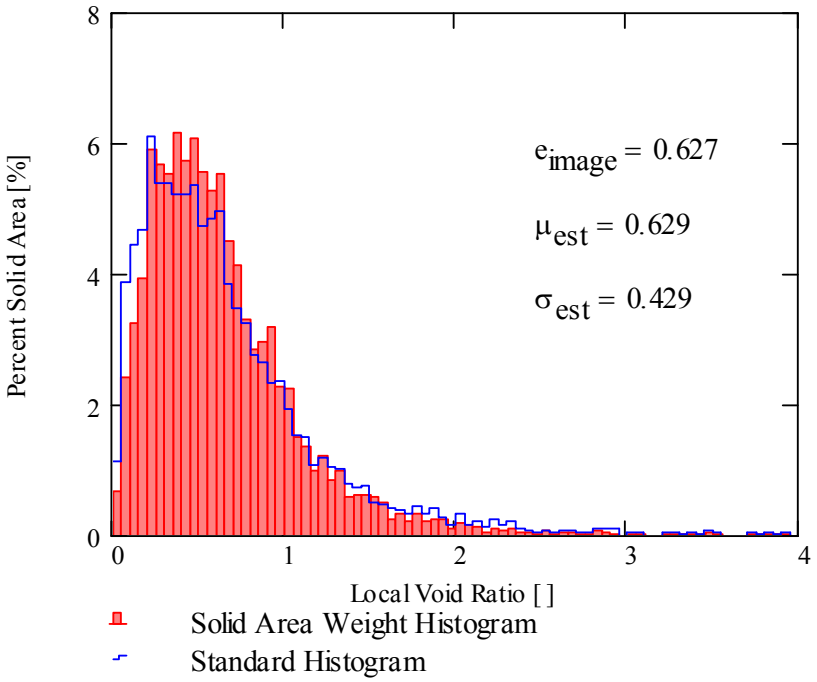
Percent Solid Area [%]
Local Void Ratio [ ]
e_{image} = 0.627
μ_{est} = 0.629
σ_{est} = 0.429
Solid Area Weight Histogram
Standard Histogram

HDS-80

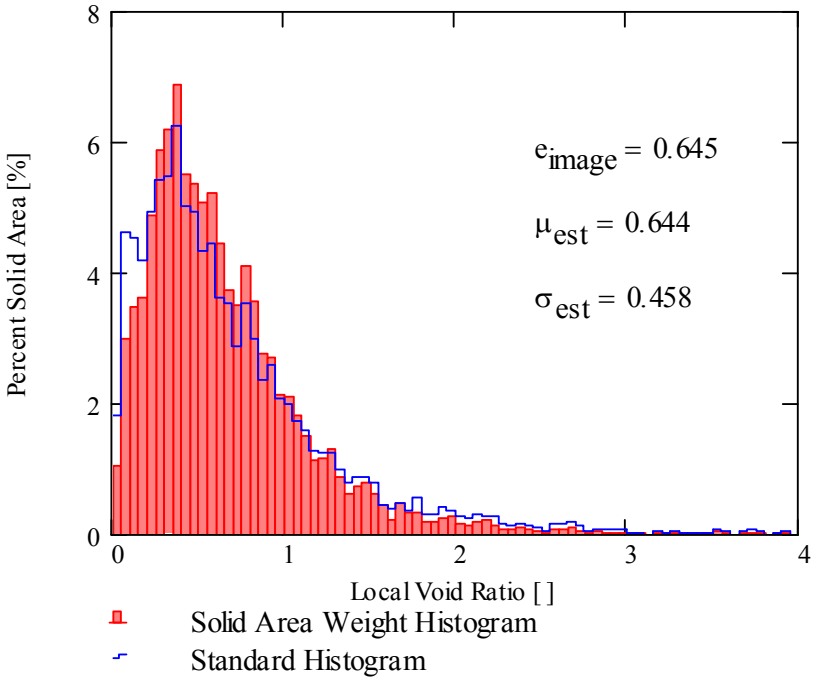
Percent Solid Area [%]
Local Void Ratio [ ]
e_{image} = 0.645
μ_{est} = 0.644
σ_{est} = 0.458
Solid Area Weight Histogram
Standard Histogram

APPENDIX C

Void Ratio Transects for All Images from Experimental Studies

SDU-20

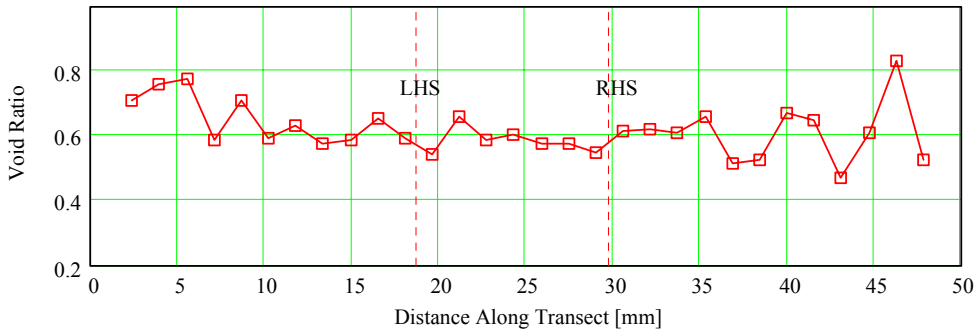
Void Ratio
0.8
0.6
0.4
0.2
LHS
RHS
0
5
10
15
20
25
30
35
40
45
50
Distance Along Transect [mm]

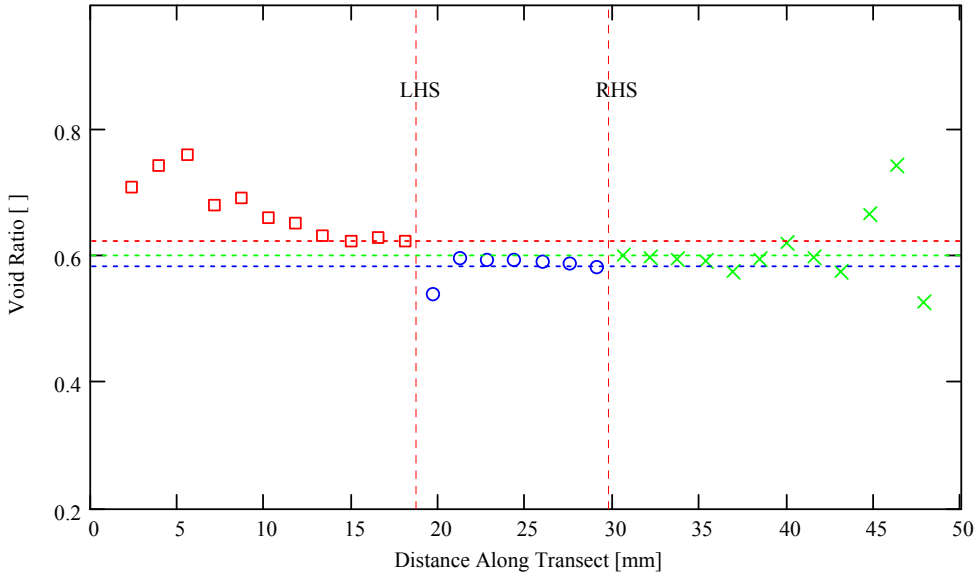
Void Ratio [ ]
0.8
0.6
0.4
0.2
LHS
RHS
0
5
10
15
20
25
30
35
40
45
50
Distance Along Transect [mm]

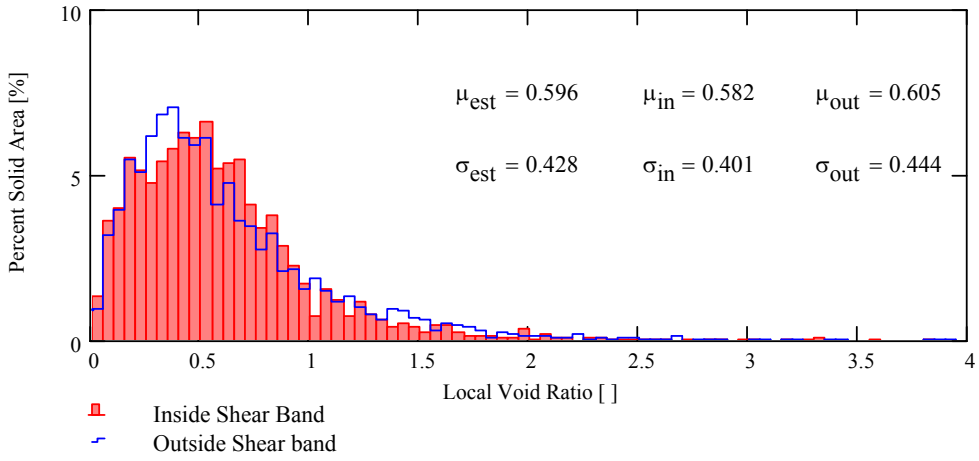
Percent Solid Area [%]
10
5
0
μest = 0.596
μin = 0.582
μout = 0.605
σest = 0.428
σin = 0.401
σout = 0.444
0
0.5
1
1.5
2
2.5
3
3.5
4
Local Void Ratio [ ]
Inside Shear Band
Outside Shear band

SDU-40

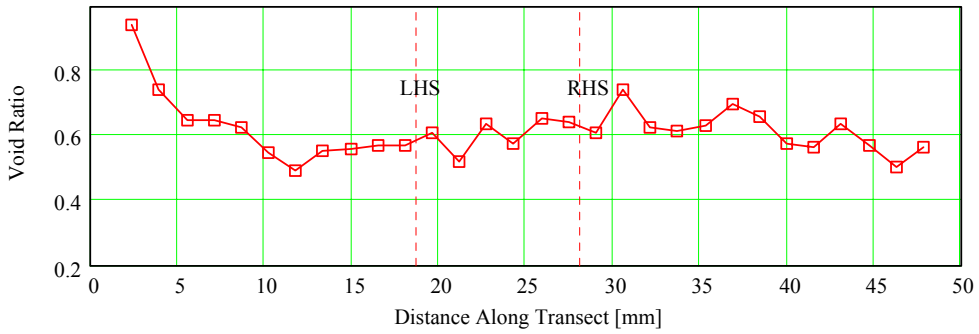
Void Ratio
0.8
0.6
0.4
0.2
LHS
RHS
0
5
10
15
20
25
30
35
40
45
50
Distance Along Transect [mm]

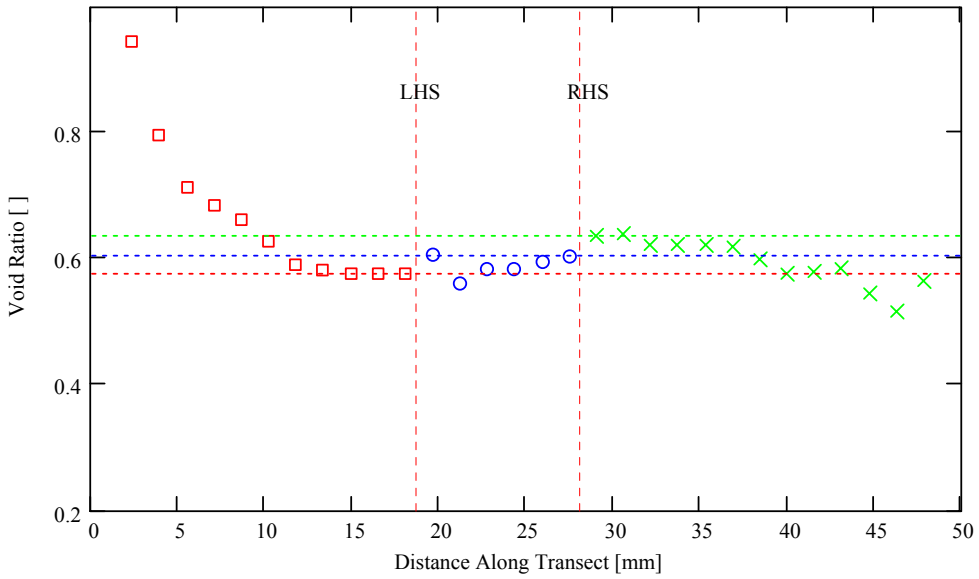
Void Ratio [ ]
0.8
0.6
0.4
0.2
LHS
RHS
0
5
10
15
20
25
30
35
40
45
50
Distance Along Transect [mm]

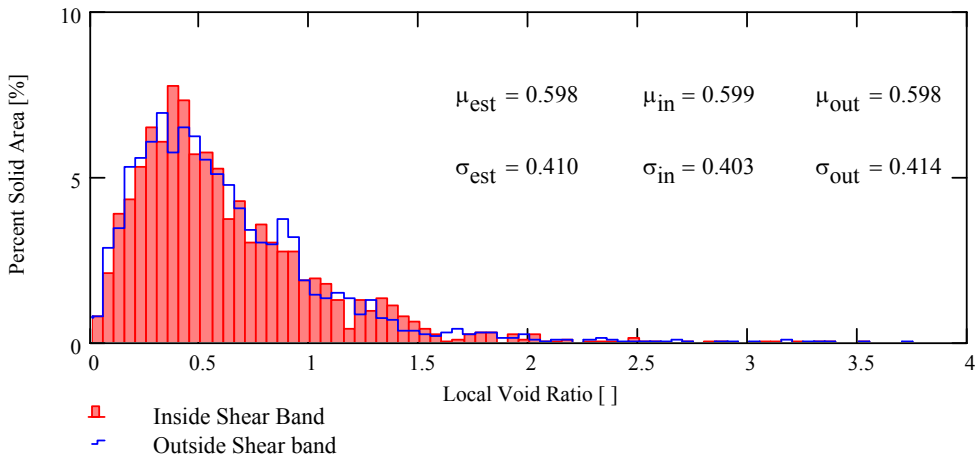
Percent Solid Area [%]
10
5
0
μest = 0.598
μin = 0.599
μout = 0.598
σest = 0.410
σin = 0.403
σout = 0.414
0
0.5
1
1.5
2
2.5
3
3.5
4
Local Void Ratio [ ]
Inside Shear Band
Outside Shear band

SDU-60

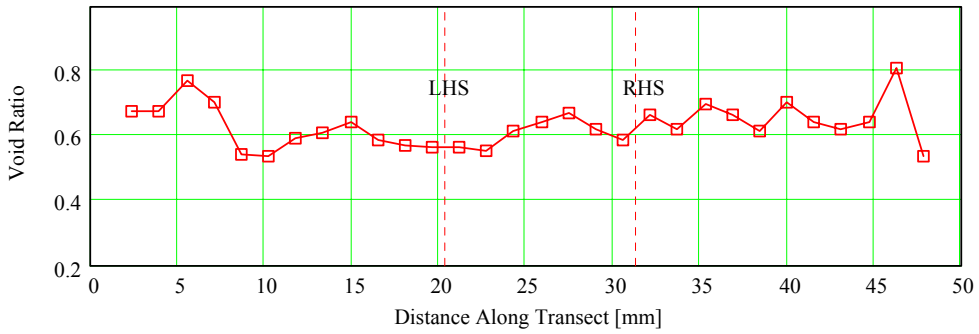
Void Ratio
0.8
0.6
0.4
0.2
LHS
RHS
0
5
10
15
20
25
30
35
40
45
50
Distance Along Transect [mm]

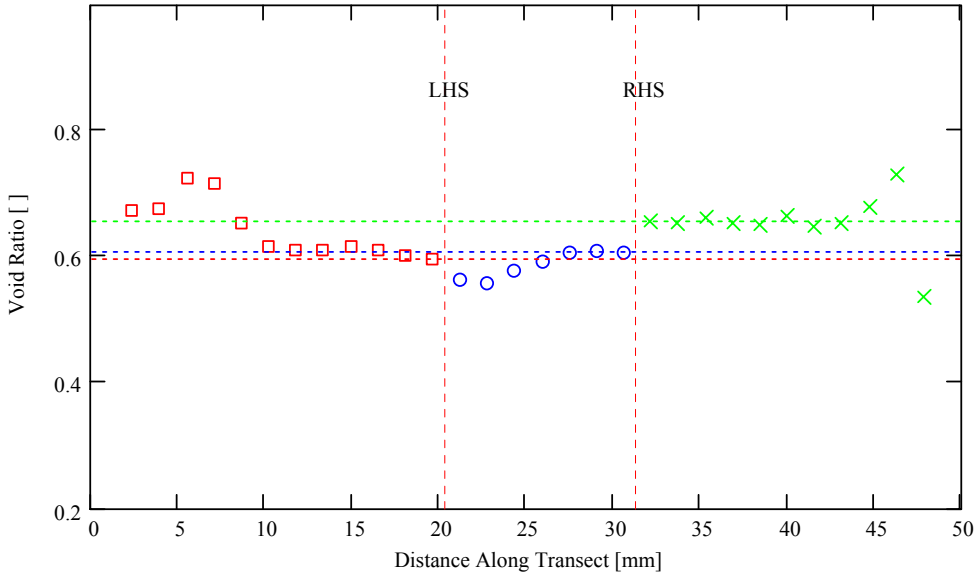
Void Ratio [ ]
0.8
0.6
0.4
0.2
LHS
RHS
0
5
10
15
20
25
30
35
40
45
50
Distance Along Transect [mm]

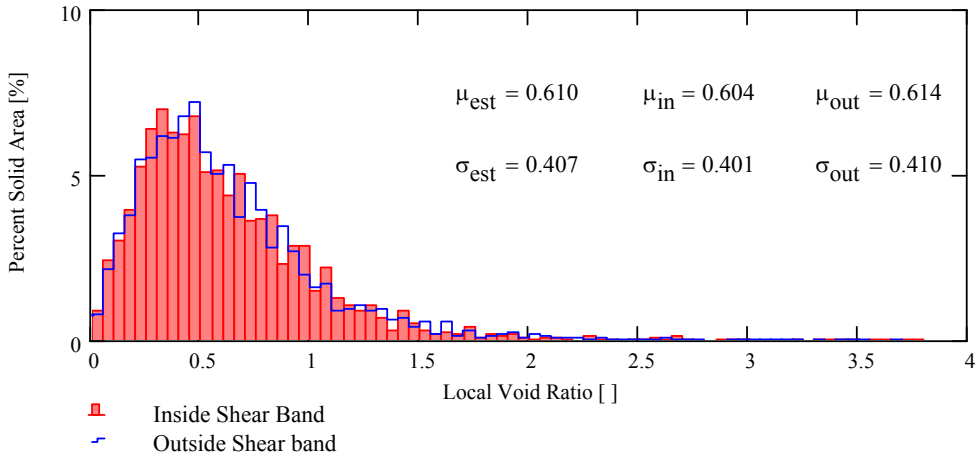
Percent Solid Area [%]
10
5
0
μest = 0.610
μin = 0.604
μout = 0.614
σest = 0.407
σin = 0.401
σout = 0.410
0
0.5
1
1.5
2
2.5
3
3.5
4
Local Void Ratio [ ]
Inside Shear Band
Outside Shear band

SDU-80

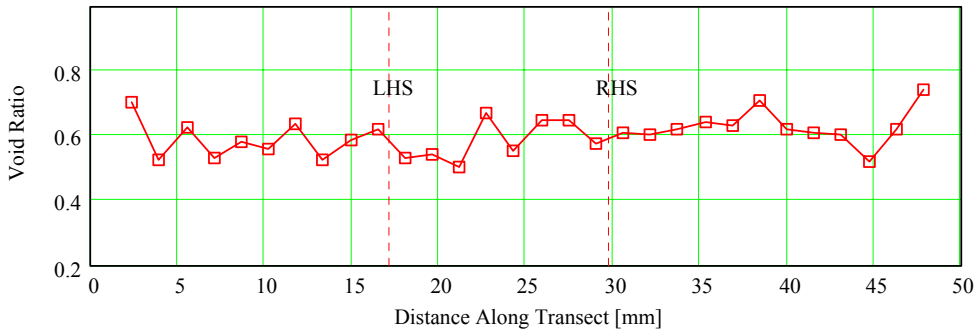
Void Ratio
0.8
0.6
0.4
0.2
LHS
RHS
0
5
10
15
20
25
30
35
40
45
50
Distance Along Transect [mm]

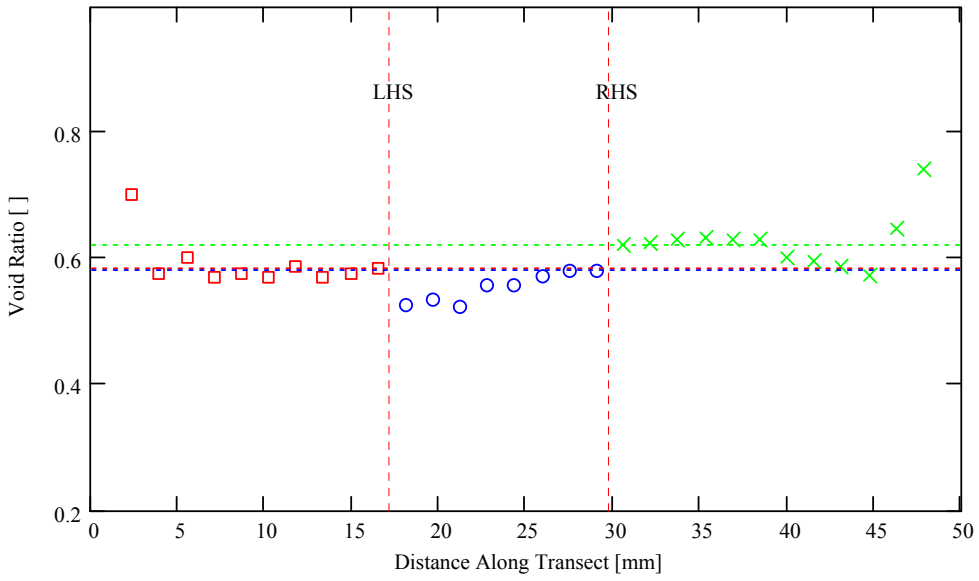
Void Ratio [ ]
0.8
0.6
0.4
0.2
LHS
RHS
0
5
10
15
20
25
30
35
40
45
50
Distance Along Transect [mm]

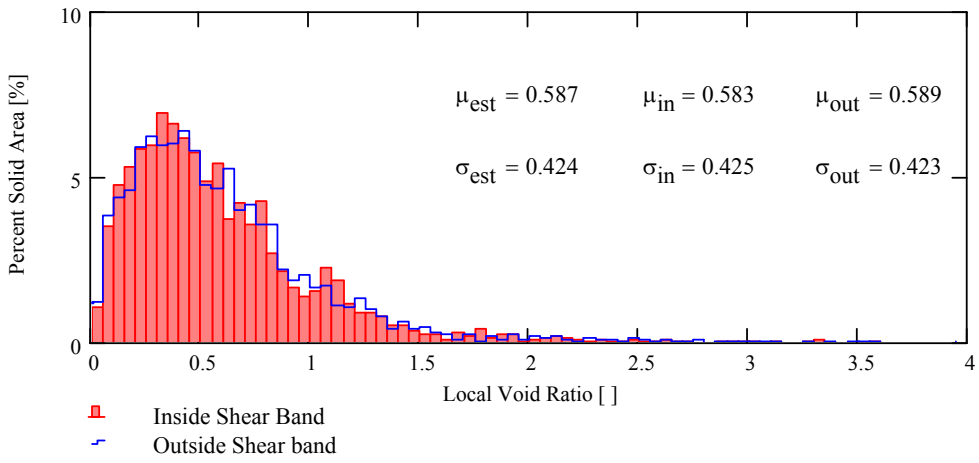
Percent Solid Area [%]
10
5
0
μest = 0.587
μin = 0.583
μout = 0.589
σest = 0.424
σin = 0.425
σout = 0.423
0
0.5
1
1.5
2
2.5
3
3.5
4
Local Void Ratio [ ]
Inside Shear Band
Outside Shear band

SDS-20

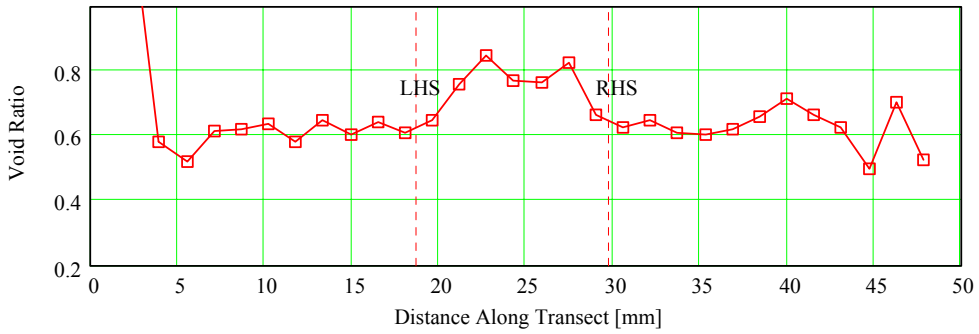
Void Ratio
0.8
0.6
0.4
0.2
LHS
RHS
0
5
10
15
20
25
30
35
40
45
50
Distance Along Transect [mm]

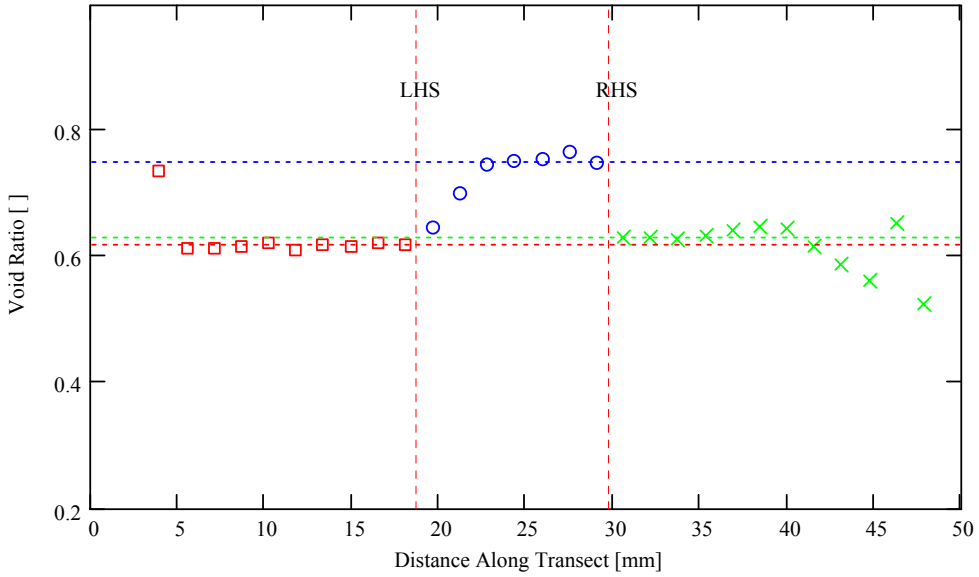
Void Ratio [ ]
0.8
0.6
0.4
0.2
LHS
RHS
0
5
10
15
20
25
30
35
40
45
50
Distance Along Transect [mm]

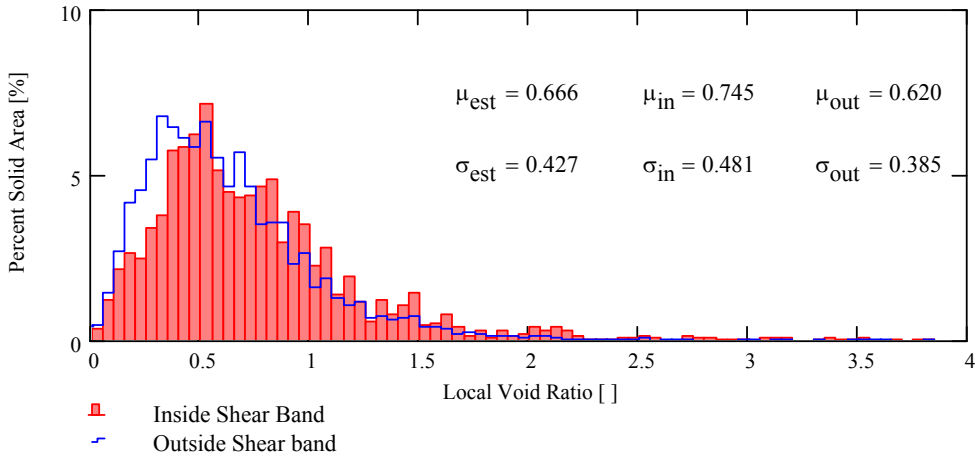
Percent Solid Area [%]
10
5
0
μest = 0.666
μin = 0.745
μout = 0.620
σest = 0.427
σin = 0.481
σout = 0.385
0
0.5
1
1.5
2
2.5
3
3.5
4
Local Void Ratio [ ]
Inside Shear Band
Outside Shear band

SDS-40

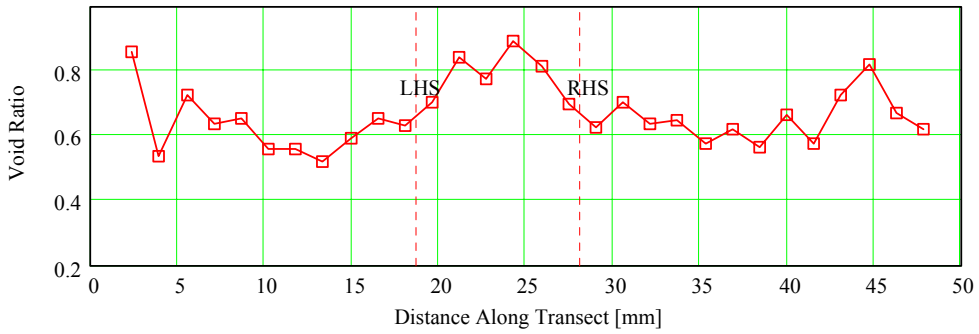
Void Ratio
0.8
0.6
0.4
0.2
LHS
RHS
0
5
10
15
20
25
30
35
40
45
50
Distance Along Transect [mm]

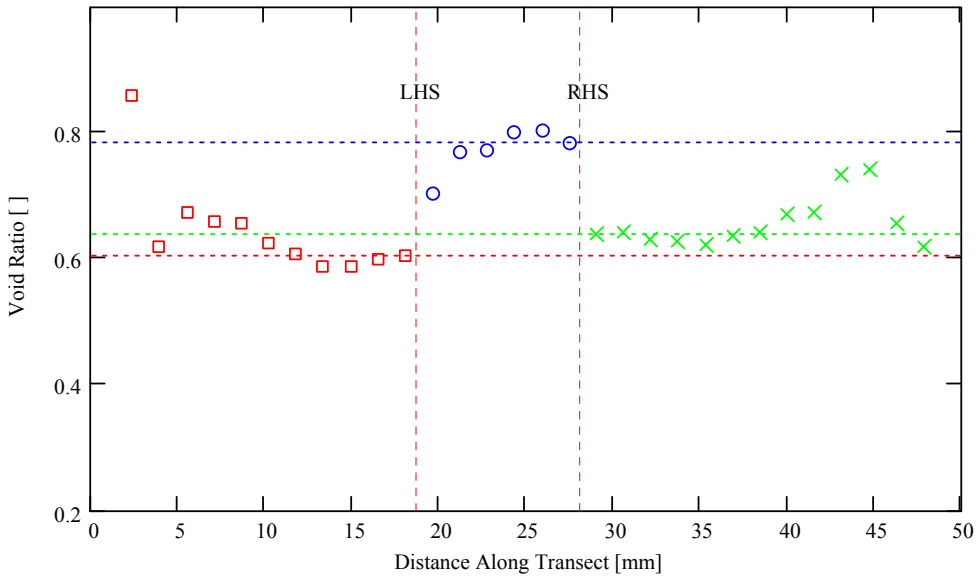
Void Ratio [ ]
0.8
0.6
0.4
0.2
LHS
RHS
0
5
10
15
20
25
30
35
40
45
50
Distance Along Transect [mm]

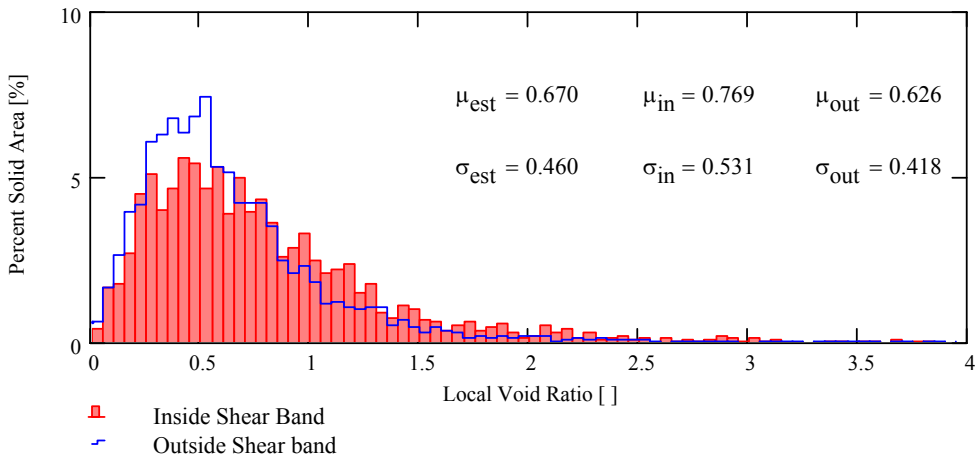
Percent Solid Area [%]
10
5
0
μest = 0.670
μin = 0.769
μout = 0.626
σest = 0.460
σin = 0.531
σout = 0.418
0
0.5
1
1.5
2
2.5
3
3.5
4
Local Void Ratio [ ]
Inside Shear Band
Outside Shear band

SDS-60

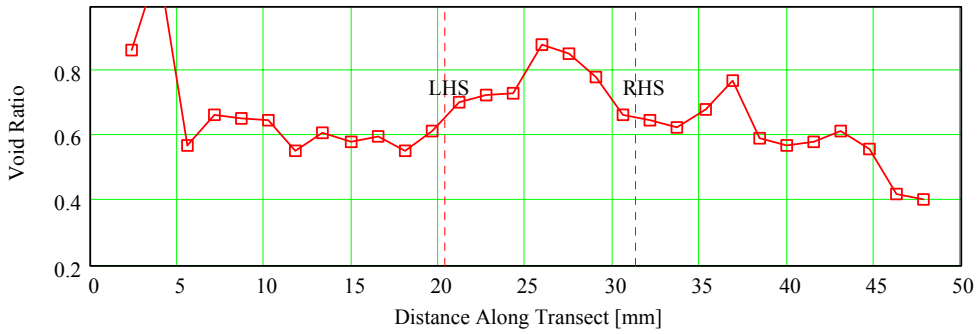
Void Ratio
0.8
0.6
0.4
0.2
LHS
RHS
0
5
10
15
20
25
30
35
40
45
50
Distance Along Transect [mm]

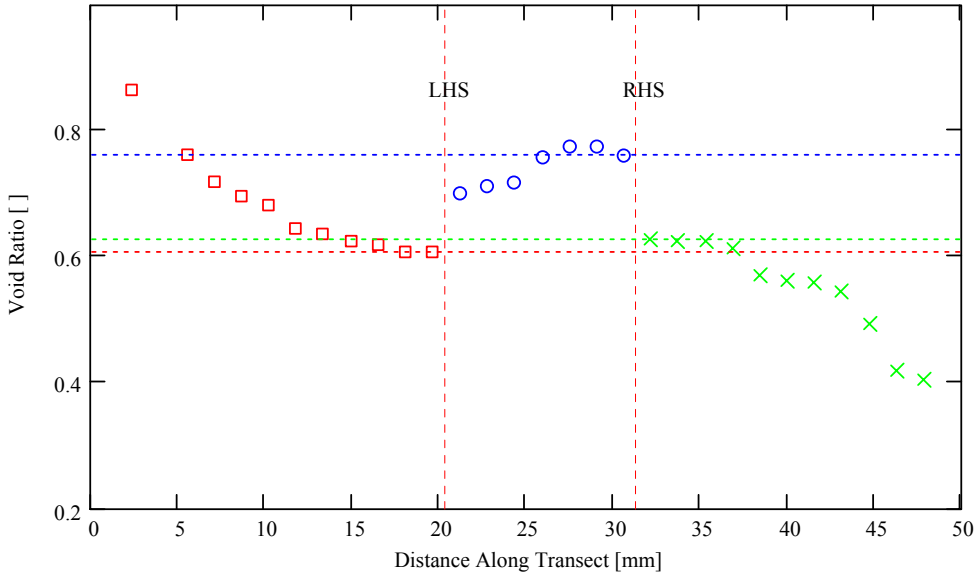
Void Ratio [ ]
0.8
0.6
0.4
0.2
LHS
RHS
0
5
10
15
20
25
30
35
40
45
50
Distance Along Transect [mm]

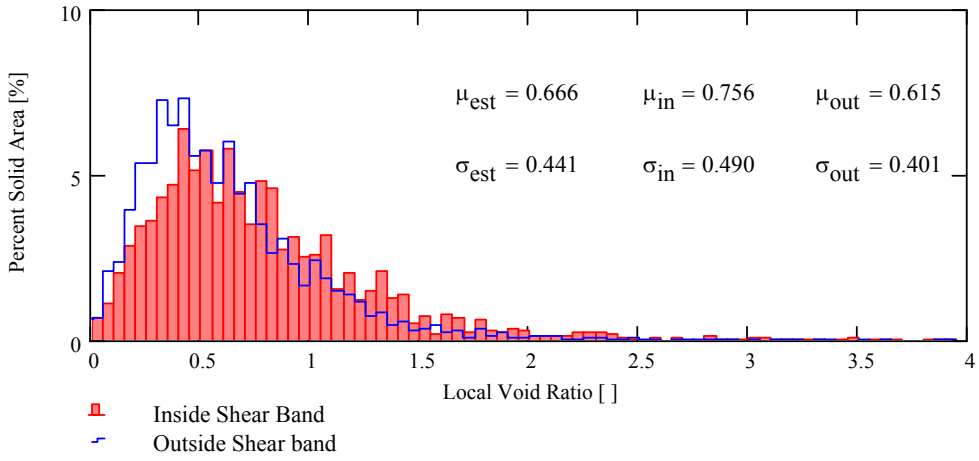
Percent Solid Area [%]
10
5
0
μest = 0.666
μin = 0.756
μout = 0.615
σest = 0.441
σin = 0.490
σout = 0.401
0
0.5
1
1.5
2
2.5
3
3.5
4
Local Void Ratio [ ]
Inside Shear Band
Outside Shear band

SDS-80

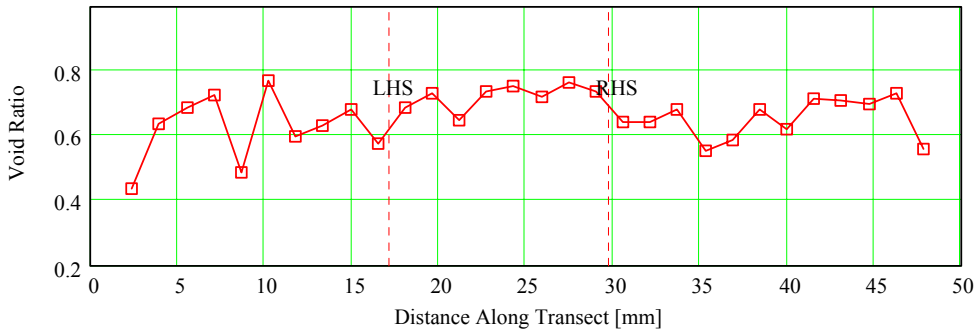
Void Ratio
0.8
0.6
0.4
0.2
LHS
RHS
0
5
10
15
20
25
30
35
40
45
50
Distance Along Transect [mm]

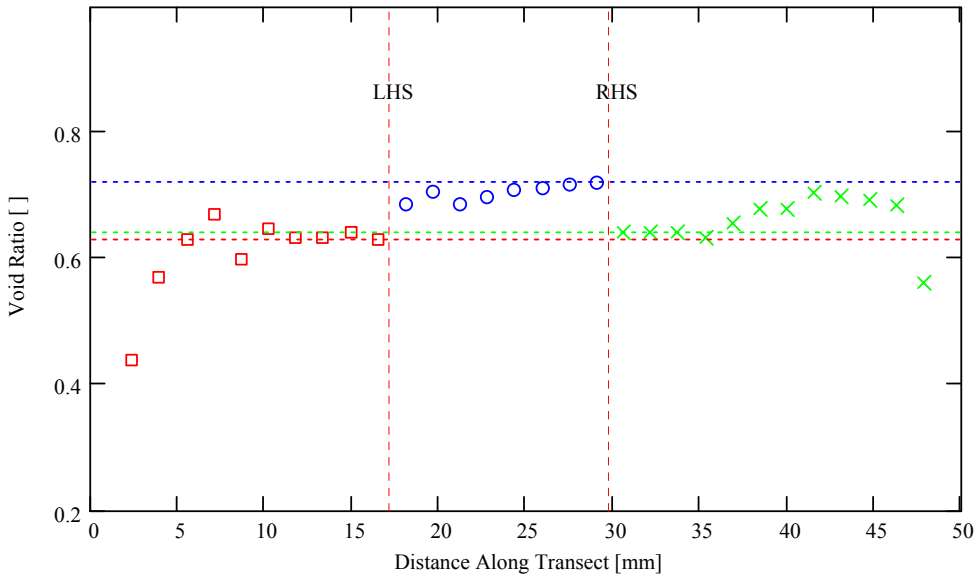
Void Ratio [ ]
0.8
0.6
0.4
0.2
LHS
RHS
0
5
10
15
20
25
30
35
40
45
50
Distance Along Transect [mm]

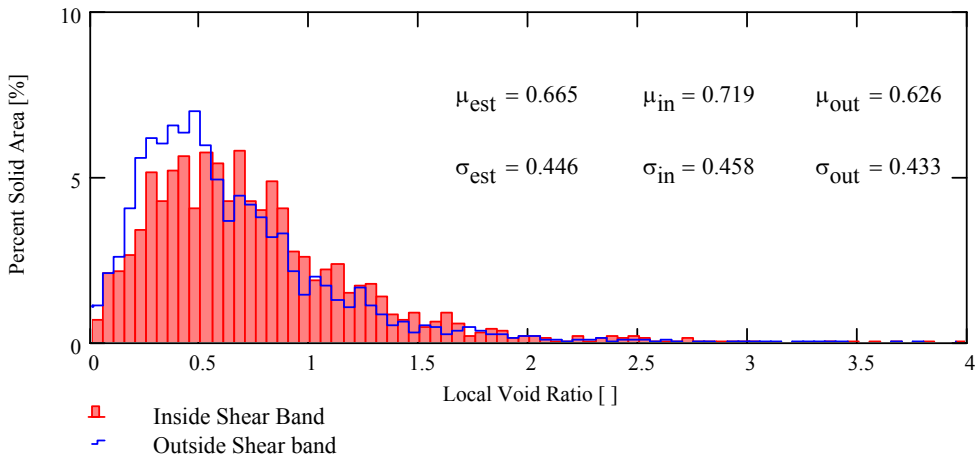
Percent Solid Area [%]
10
5
0
μest = 0.665
μin = 0.719
μout = 0.626
σest = 0.446
σin = 0.458
σout = 0.433
0
0.5
1
1.5
2
2.5
3
3.5
4
Local Void Ratio [ ]
Inside Shear Band
Outside Shear band

HDU-20

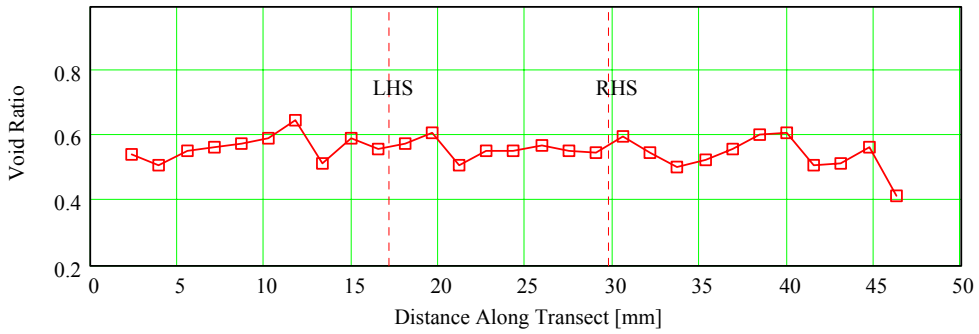
Void Ratio
0.8
0.6
0.4
0.2
LHS
RHS
0
5
10
15
20
25
30
35
40
45
50
Distance Along Transect [mm]

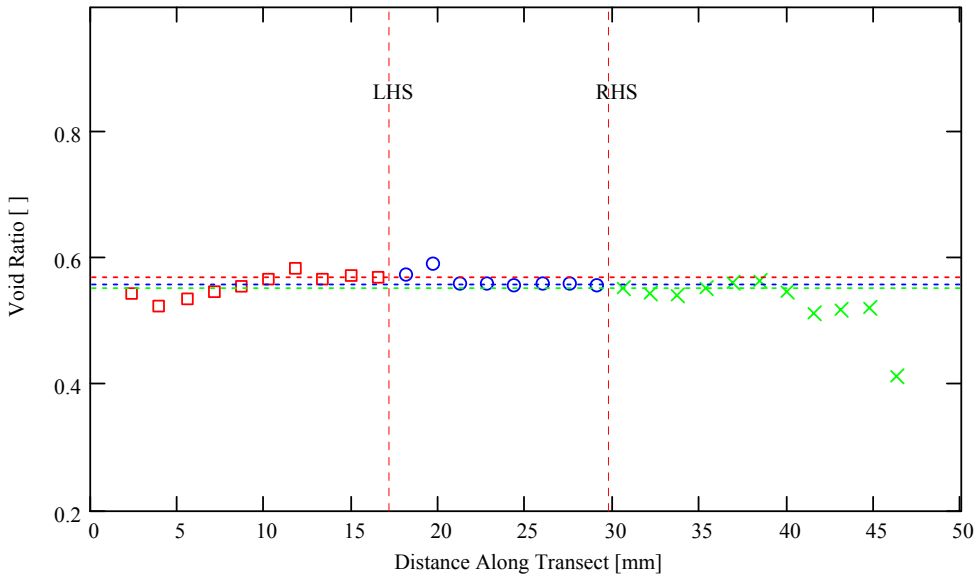
Void Ratio [ ]
0.8
0.6
0.4
0.2
LHS
RHS
0
5
10
15
20
25
30
35
40
45
50
Distance Along Transect [mm]

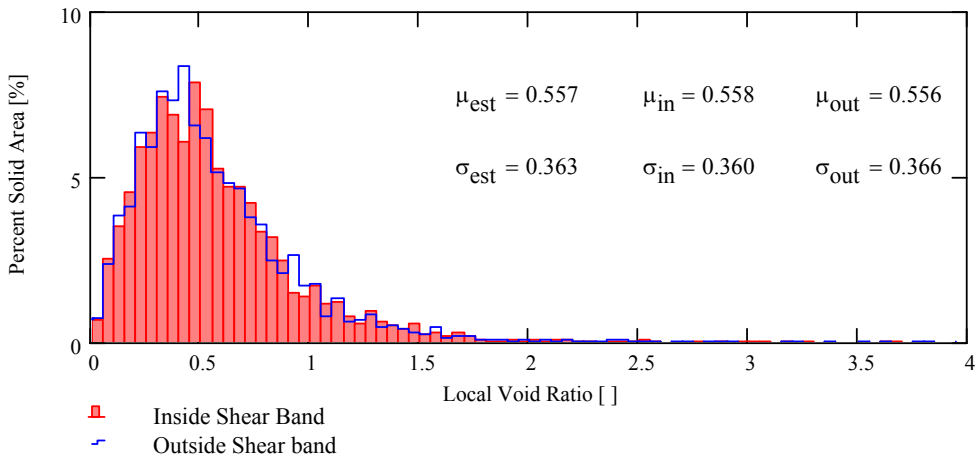
Percent Solid Area [%]
10
5
0
μest = 0.557
μin = 0.558
μout = 0.556
σest = 0.363
σin = 0.360
σout = 0.366
0
0.5
1
1.5
2
2.5
3
3.5
4
Local Void Ratio [ ]
Inside Shear Band
Outside Shear band

HDU-40

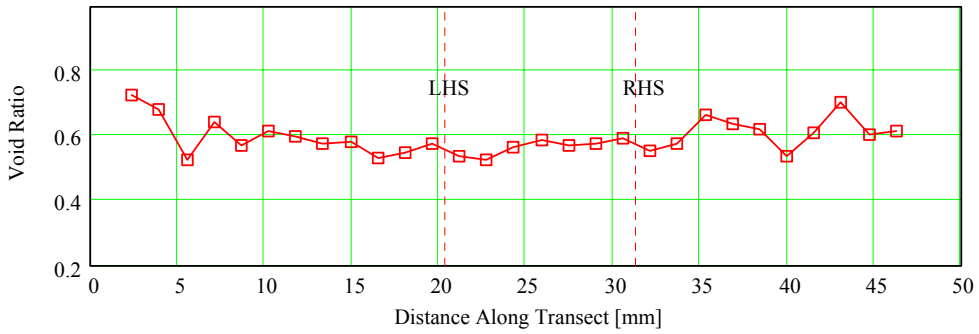
Void Ratio
0.8
0.6
0.4
0.2
LHS
RHS
0
5
10
15
20
25
30
35
40
45
50
Distance Along Transect [mm]

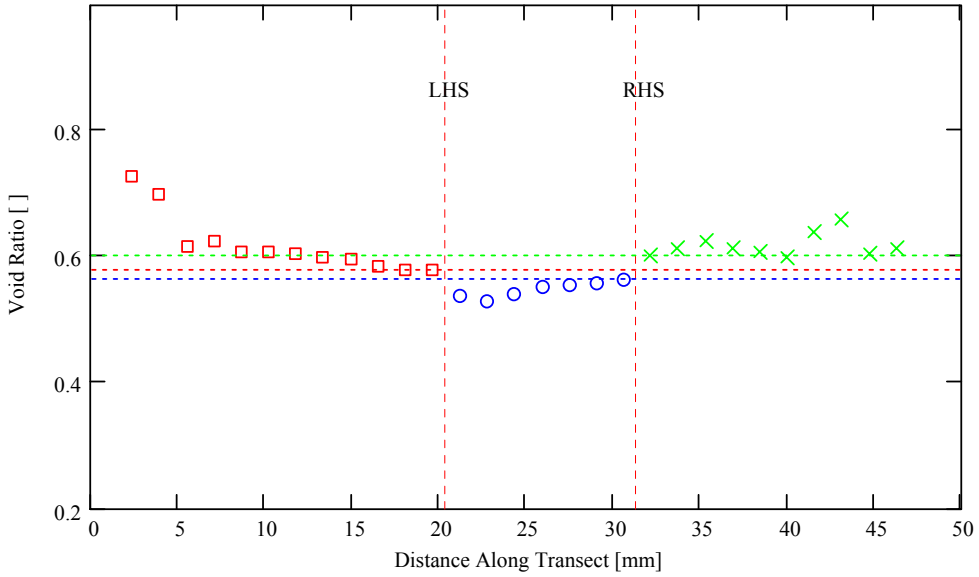
Void Ratio [ ]
0.8
0.6
0.4
0.2
LHS
RHS
0
5
10
15
20
25
30
35
40
45
50
Distance Along Transect [mm]

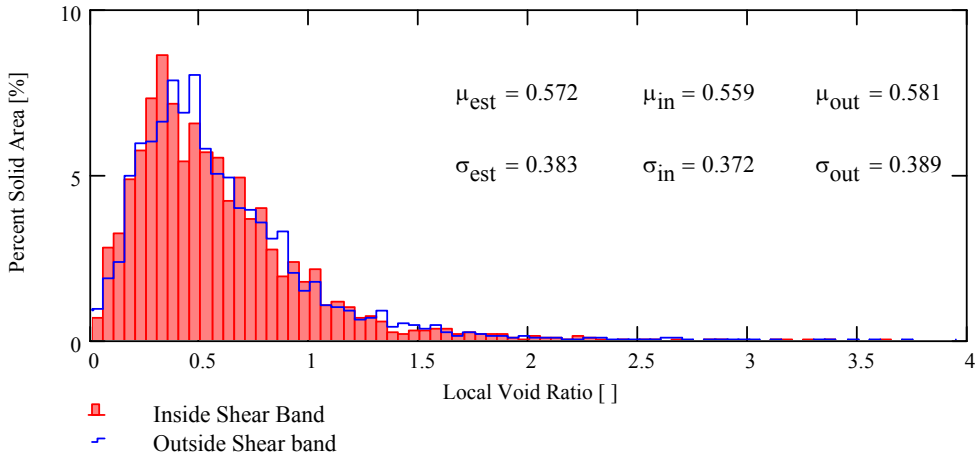
Percent Solid Area [%]
10
5
0
μest = 0.572
μin = 0.559
μout = 0.581
σest = 0.383
σin = 0.372
σout = 0.389
0
0.5
1
1.5
2
2.5
3
3.5
4
Local Void Ratio [ ]
Inside Shear Band
Outside Shear band

HDU-60

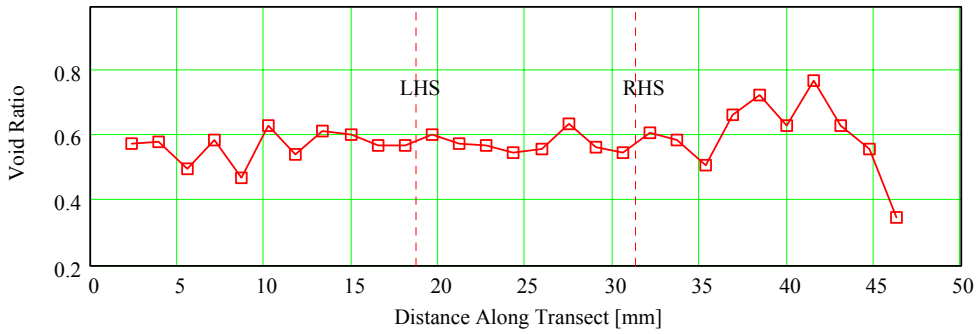
Void Ratio
0.8
0.6
0.4
0.2
LHS
RHS
0
5
10
15
20
25
30
35
40
45
50
Distance Along Transect [mm]

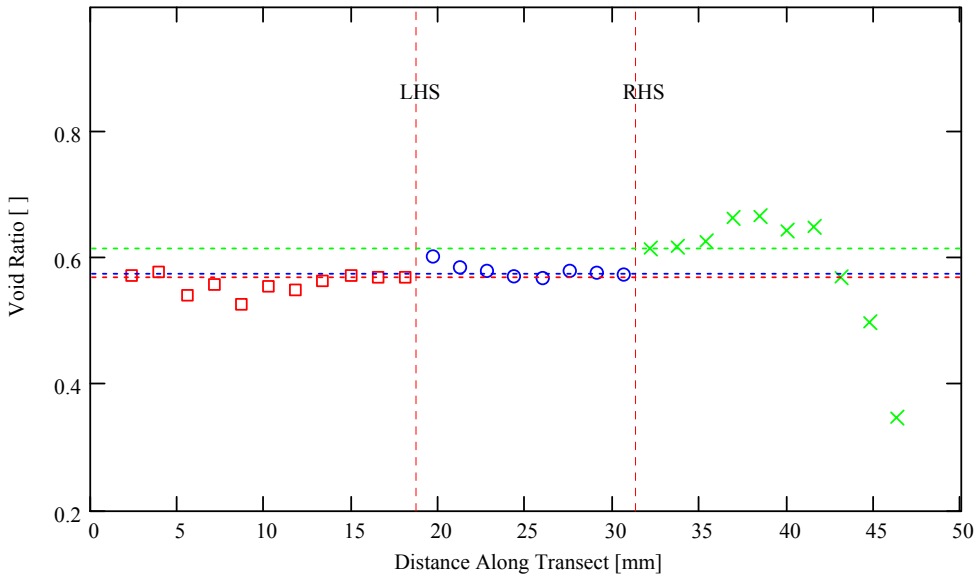
Void Ratio [ ]
0.8
0.6
0.4
0.2
LHS
RHS
0
5
10
15
20
25
30
35
40
45
50
Distance Along Transect [mm]

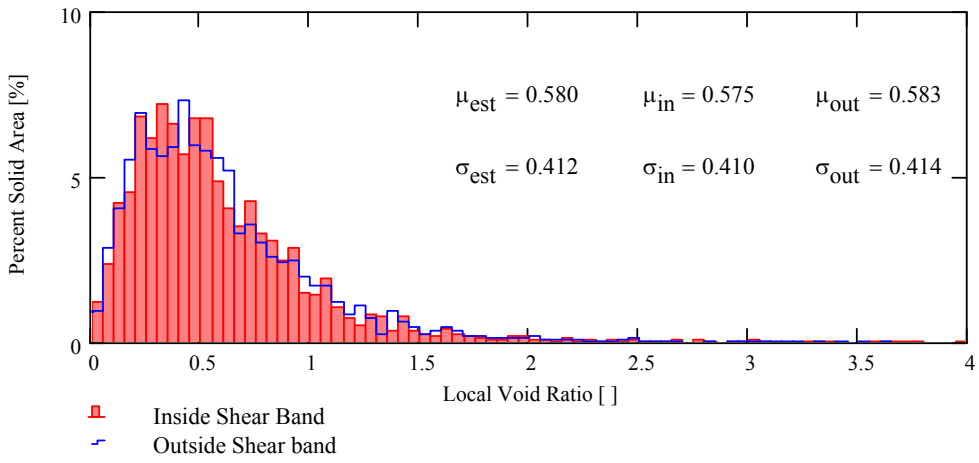
Percent Solid Area [%]
10
5
0
μest = 0.580
μin = 0.575
μout = 0.583
σest = 0.412
σin = 0.410
σout = 0.414
0
0.5
1
1.5
2
2.5
3
3.5
4
Local Void Ratio [ ]
Inside Shear Band
Outside Shear band

HDU-80

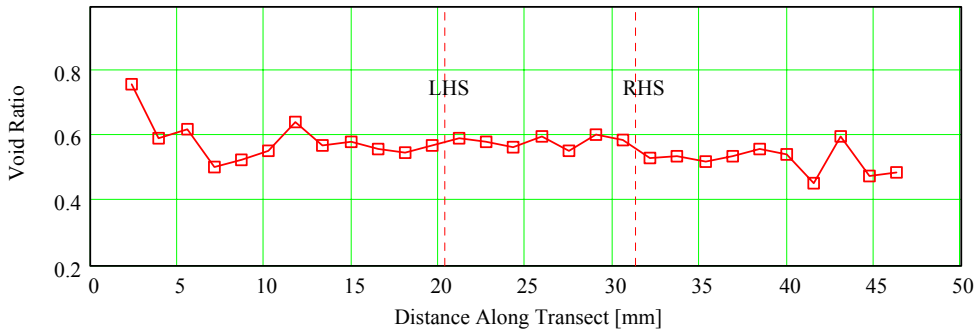
Void Ratio
0.8
0.6
0.4
0.2
LHS
RHS
0
5
10
15
20
25
30
35
40
45
50
Distance Along Transect [mm]

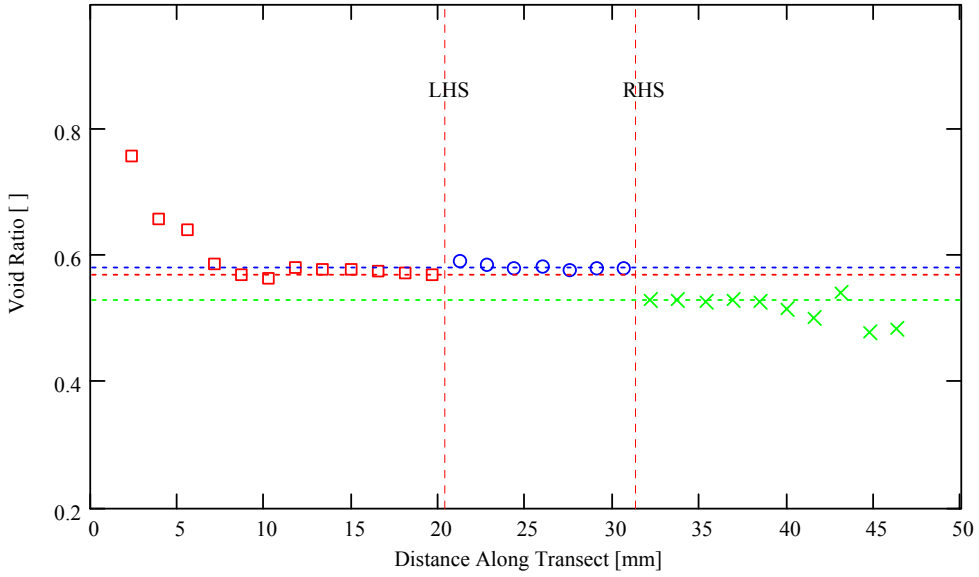
Void Ratio [ ]
0.8
0.6
0.4
0.2
LHS
RHS
0
5
10
15
20
25
30
35
40
45
50
Distance Along Transect [mm]

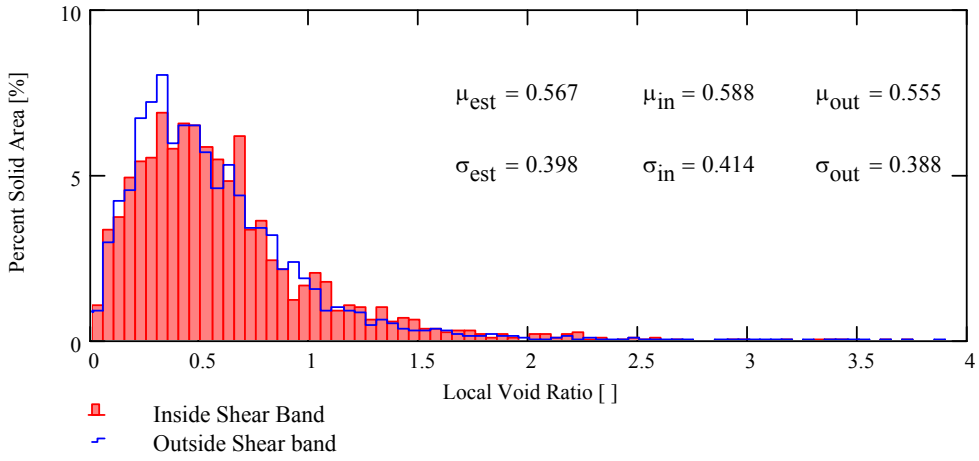
Percent Solid Area [%]
10
5
0
μest = 0.567
μin = 0.588
μout = 0.555
σest = 0.398
σin = 0.414
σout = 0.388
0
0.5
1
1.5
2
2.5
3
3.5
4
Local Void Ratio [ ]
Inside Shear Band
Outside Shear band

HDS-20

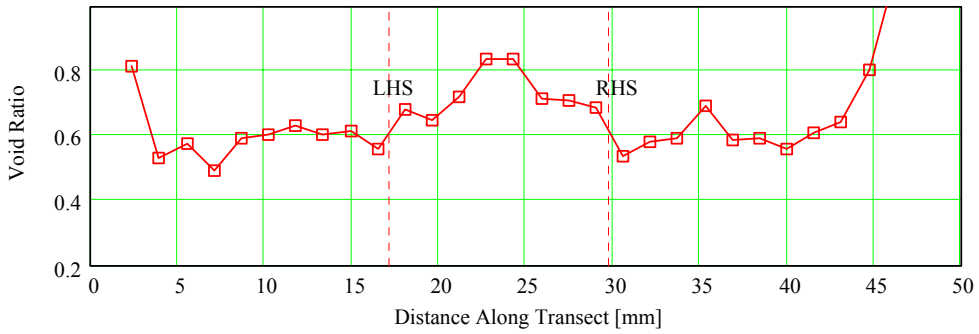
Void Ratio
0.8
0.6
0.4
0.2
LHS
RHS
0
5
10
15
20
25
30
35
40
45
50
Distance Along Transect [mm]

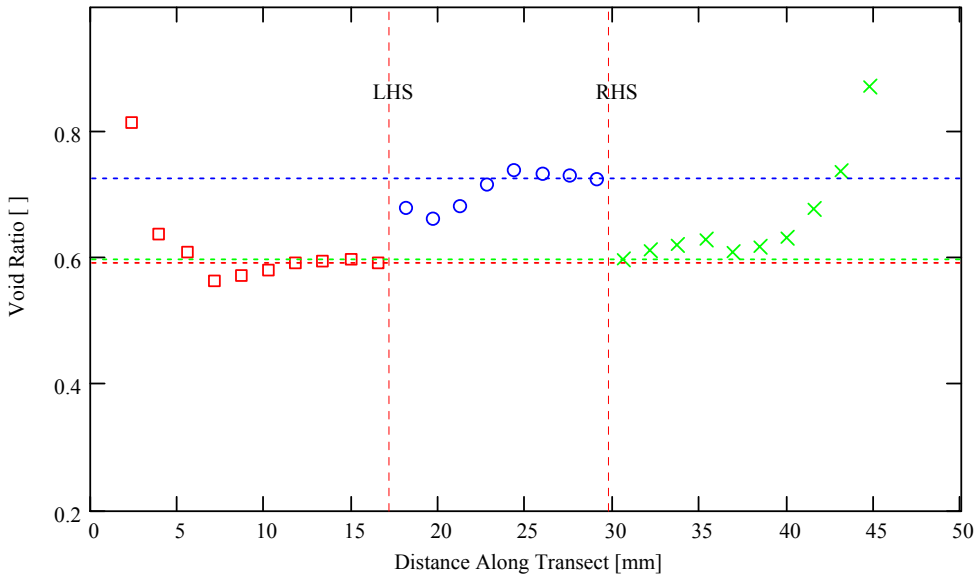
Void Ratio [ ]
0.8
0.6
0.4
0.2
LHS
RHS
0
5
10
15
20
25
30
35
40
45
50
Distance Along Transect [mm]

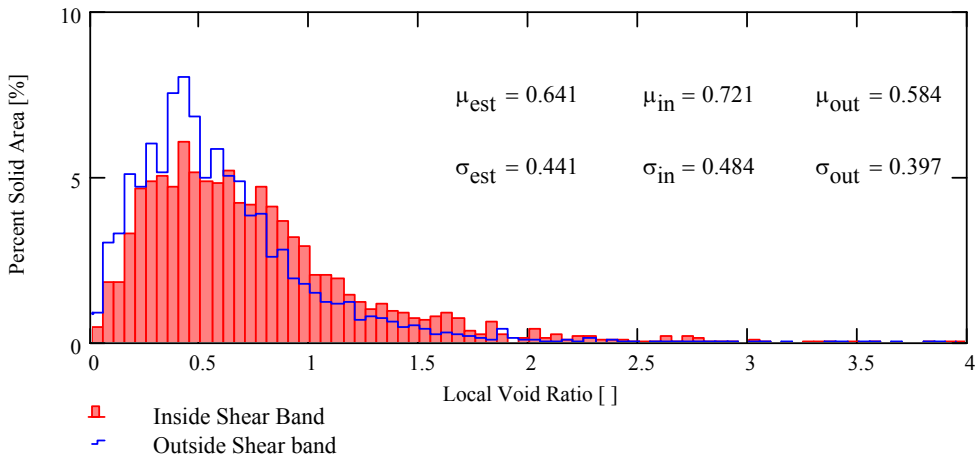
Percent Solid Area [%]
10
5
0
μest = 0.641
μin = 0.721
μout = 0.584
σest = 0.441
σin = 0.484
σout = 0.397
0
0.5
1
1.5
2
2.5
3
3.5
4
Local Void Ratio [ ]
Inside Shear Band
Outside Shear band

HDS-40

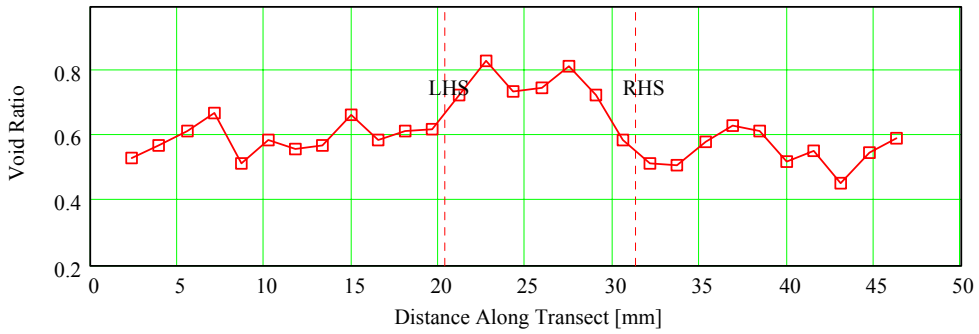
Void Ratio
0.8
0.6
0.4
0.2
LHS
RHS
0
5
10
15
20
25
30
35
40
45
50
Distance Along Transect [mm]

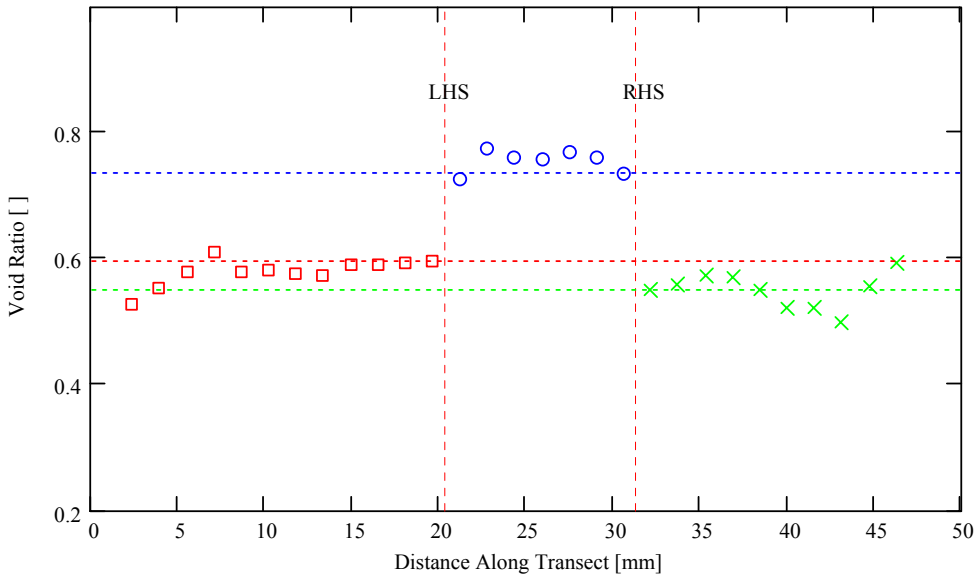
Void Ratio [ ]
LHS
RHS
0.8
0.6
0.4
0.2
0
5
10
15
20
25
30
35
40
45
50
Distance Along Transect [mm]

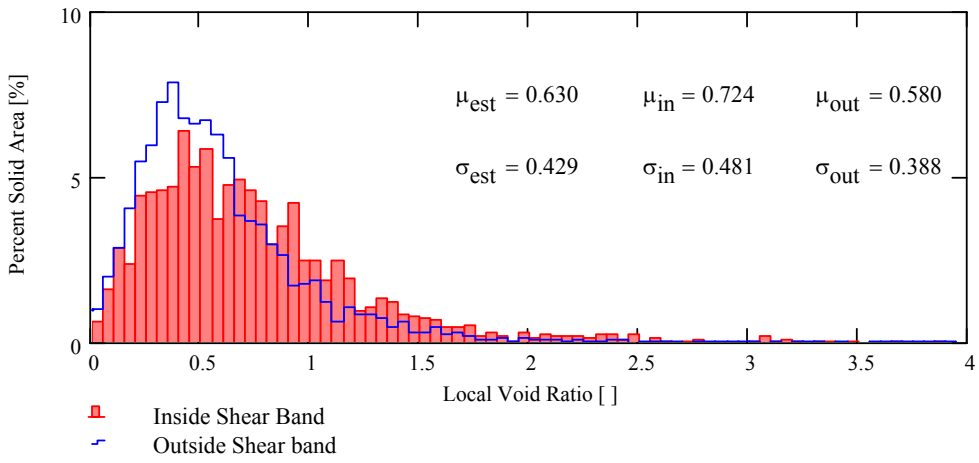
Percent Solid Area [%]
10
5
0
μest = 0.630
μin = 0.724
μout = 0.580
σest = 0.429
σin = 0.481
σout = 0.388
0
0.5
1
1.5
2
2.5
3
3.5
4
Local Void Ratio [ ]
Inside Shear Band
Outside Shear band

HDS-60

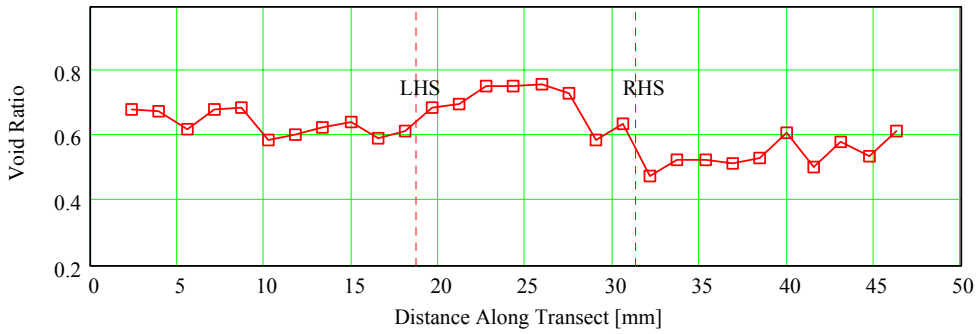
Void Ratio
0.8
0.6
0.4
0.2
LHS
RHS
0
5
10
15
20
25
30
35
40
45
50
Distance Along Transect [mm]

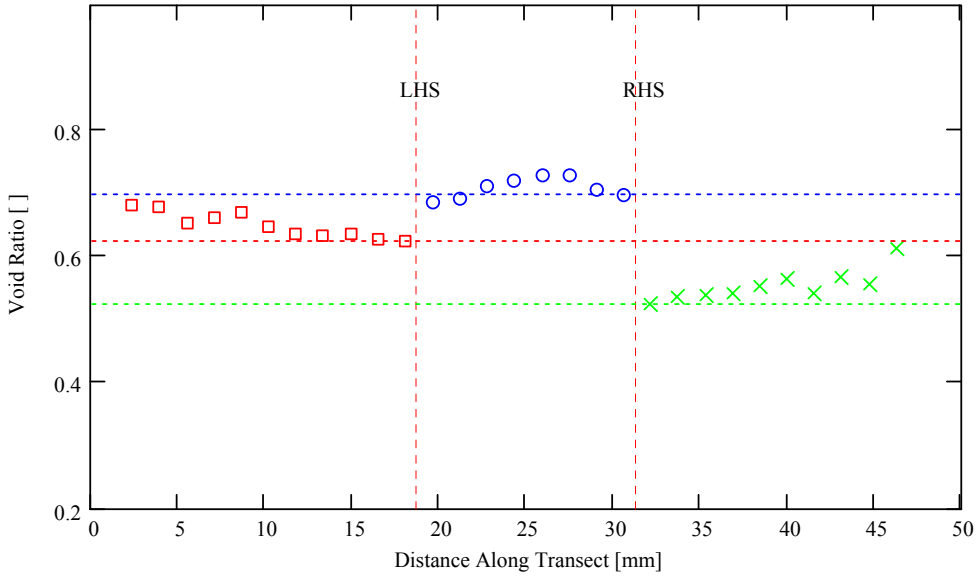
Void Ratio [ ]
0.8
0.6
0.4
0.2
LHS
RHS
0
5
10
15
20
25
30
35
40
45
50
Distance Along Transect [mm]

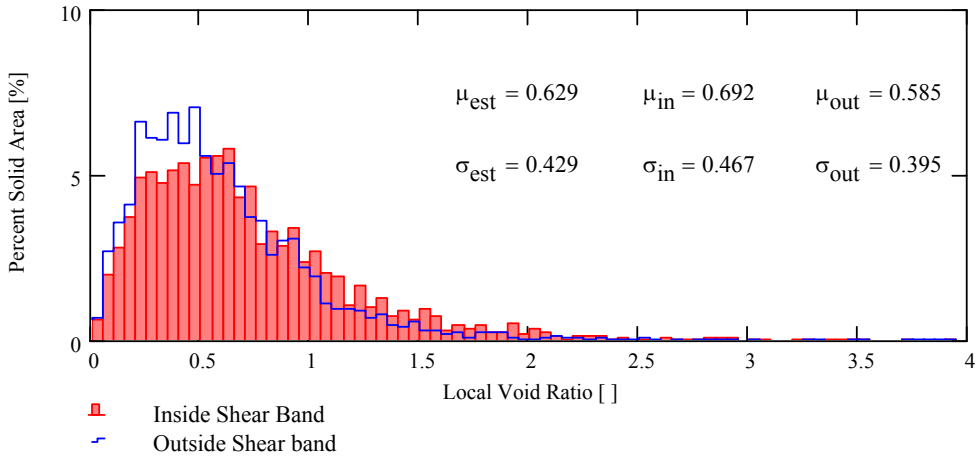
Percent Solid Area [%]
10
5
0
μest = 0.629
μin = 0.692
μout = 0.585
σest = 0.429
σin = 0.467
σout = 0.395
0
0.5
1
1.5
2
2.5
3
3.5
4
Local Void Ratio [ ]
Inside Shear Band
Outside Shear band

HDS-80

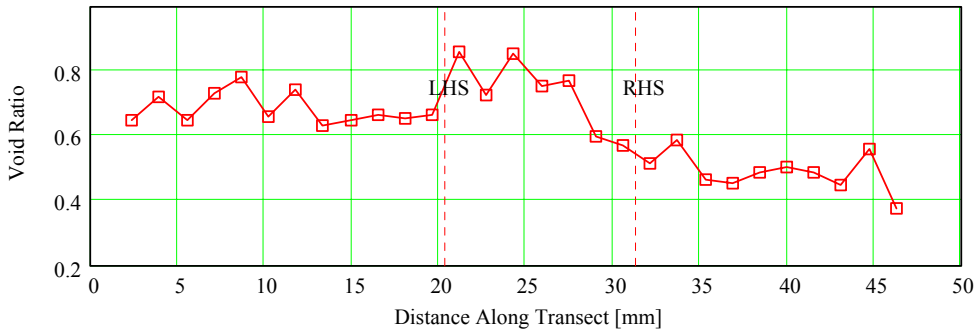
Void Ratio
0.8
0.6
0.4
0.2
LHS
RHS
0
5
10
15
20
25
30
35
40
45
50
Distance Along Transect [mm]

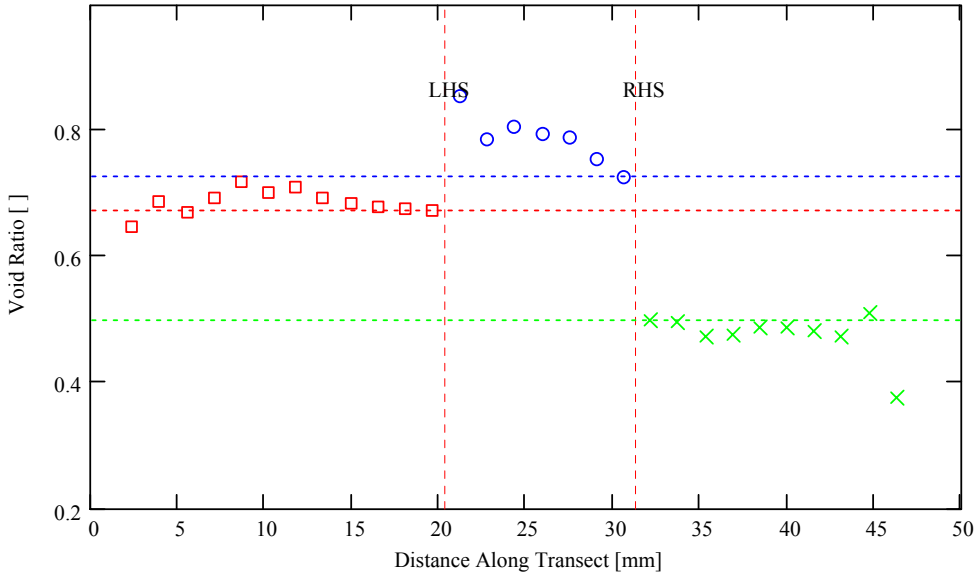
Void Ratio [ ]
0.8
0.6
0.4
0.2
LHS
RHS
0
5
10
15
20
25
30
35
40
45
50
Distance Along Transect [mm]

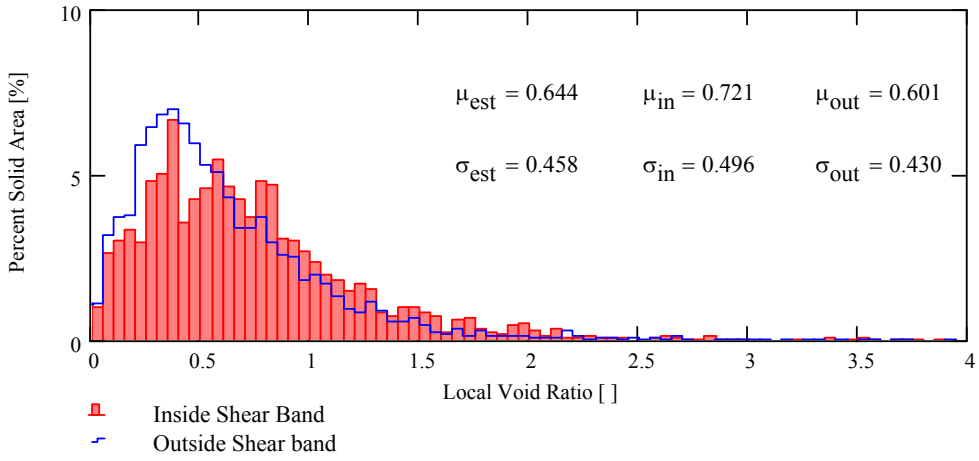
Percent Solid Area [%]
10
5
0
μest = 0.644
μin = 0.721
μout = 0.601
σest = 0.458
σin = 0.496
σout = 0.430
0
0.5
1
1.5
2
2.5
3
3.5
4
Local Void Ratio [ ]
Inside Shear Band
Outside Shear band

REFERENCES

Aloufi, M., and Santamarina, J. C. (1995). "Low and high strain macrobehavior of grain masses - the effect of particle eccentricity." *Transactions of the ASAE*, 38(3), 877-887.

Alshibli, K. A., and El-Saidany, H. A. (2001). "Quantifying void ratio in granular materials using Voronoi tessellation." *Journal of Computing in Civil Engineering*, 15(3), 232-238.

Alshibli, K. A., and Sture, S. (1999). "Sand shear band thickness measurements by digital imaging techniques." *Journal of Computing in Civil Engineering*, 13(2), 103-109.

Alshibli, K. A., and Sture, S. (2000). "Shear band formation in plane strain experiments of sand." *Journal of Geotechnical and Geoenvironmental Engineering*, 126(6), 495-503.

Alshibli, K. A., Sture, S., Costes, N. C., Frank, M. L., Lankton, M. R., Batiste, S. N., and Swanson, R. A. (2000). "Assessment of Localized Deformations in Sand Using X-Ray Computed Tomography." *Geotechnical Testing Journal*, 23(3), 274-299.

Arthur, J. R. F., Dunstan, T., Al-Ani, Q. A. J. L., and Assadi, A. (1977). "Plastic deformation and failure in granular media." *Geotechnique*, 27(1), 53-74.

ASTM. (2002). "Standard Test Method for Particle-Size Analysis of Soils, D422." American Society for Testing and Materials, West Conshohoken, PA.

Bardet, J. P. (1994). "Observations on the effects of particle rotations on the failure of idealized granular materials." *Mechanics of Materials*, 18(2), 159-182.

Bardet, J. P., and Proubet, J. (1991). "Numerical investigation of the structure of persistent shear bands in granular media." *Geotechnique*, 41(4), 599-613.

Baxter, D. Y. (2000). "Mechanical Behavior of Soil Bentonite Cutoff Walls," Ph.D. Thesis, Civil and Environmental Engineering, Virginia Polytechnic Institute and State University, Blacksburg.

Bhatia, S. K., and Soliman, A. F. (1990). "Frequency distribution of void ratio of granular materials determined by an image analyzer." *Soils and Foundations*, 30(1), 1-16.

Bishop, A. W., and Henkel, D. J. (1962). *The Measurement of Soil Properties in the Triaxial Test*, Edward Arnold Limited, London.

Blight, G. E. (1967). "Observations on shear testing of indurated fissured clays." *Proceedings, Geotechnical Conference, Shear Strength Properties of Natural Soils and Rocks*, Oslo, Norway, 97-102.

Bolton, M. D. (1986). "Strength and dilatancy of sands." *Geotechnique*, 36(1), 65-78.

Borja, R.I., and Aydin, A. (2004), "Computational modeling of deformation bands in granular media. I. geological and mathematical framework," *Computer Methods in Applied Mechanics and Engineering*, Vol. 193, pp. 2667-2698.

Bunn, R. (2005). *Personal communication*. Vashaw Scientific, Norcross, GA.

Butterfield, R., Harkness, R. M., and Andrawes, K. Z. (1970). "A stereo-photogrammetric method for measuring displacement fields." *Geotechnique*, 20(3), 308-314.

Chandler, R. J. (1966). "The measurement of residual strength in triaxial compression." *Geotechnique*, 16(3), 181-186.

Chantawarangul, K. (1993). "Numerical simulations of three-dimensional granular assemblies," Ph.D. Thesis, Civil Engineering, University of Waterloo, Waterloo.

Chen, C.-C. (2000). "Shear induced evolution of structure in water-deposited sand specimens," Ph.D. Thesis, Civil and Environmental Engineering, Georgia Institute of Technology, Atlanta.

Cho, G. C. (2001). "Unsaturated Soil Stiffness and Post-Liquefaction Shear Strength," Ph.D. Thesis, Civil and Environmental Engineering, Georgia Institute of Technology, Atlanta.

Claquin, C., Emeriault, F., and Nouguier-Lehon, C. (2003). "Influence of particles shape on the macroscopic behavior of granular material." *Proceedings of the 3rd International Symposium on the Deformation Characteristics of Geomaterials*, Lyon, 1175-1182.

Cooper, R. (2003). *Personal Communication*. Cooper Instruments, Warrenton, VA.

Cornforth, D. H. (1964). "Some experiments on influence of strain conditions on strength of sand." *Geotechnique*, 14(2), 143-167.

Coulomb, C. A. (1773). "On an application of the rules of maximum and minimum to some statistical problems, relevant to architecture." *Mémoires de Mathématique & de Physique, présentés a l'Académie Royale des Sciences par divers Savans, &lus dans ses Assemblées*, Paris, 343-382.

Cundall, P. A. (1989). "Numerical experiments on localization in frictional materials." *Ingenieur-Archiv*, 59, 148-159.

DeJong, J. T. (2001). "Investigation of Particulate-Continuum Interface Mechanisms and Their Assessment Through a Multi-Friction Sleeve Penetrometer Attachment," Ph.D. Thesis, Civil and Environmental Engineering, Georgia Institute of Technology, Atlanta, GA.

DeJong, J. T. (2005). *Personal communication*. University of Massachusetts at Amherst, Amherst, MA.

Desrues, J., Chambon, R., Mokni, M., and Mazerolle, F. (1996). "Void ratio evolution inside shear bands in triaxial sand specimens studied by computed tomography." *Geotechnique*, 46(3), 529-546.

Dodds, J. (2003). "Particle Shape and Stiffness - Effects on Soil Behavior," M.S. Thesis, Georgia Institute of Technology, Atlanta.

Drescher, A., Vardoulakis, I., and Han, C. (1990). "A Biaxial Apparatus for Testing Soils." *Geotechnical Testing Journal*, 13(3), 226-234.

Duncan, J. M., and Seed, H. B. (1967). "Corrections for strength test data." *American Society of Civil Engineers Proceedings, Journal of the Soil Mechanics and Foundation Division*, 93(SM5), 121-137.

Edwards, S. F., and Grinev, D. V. (1999). "Compactivity and transmission of stress in granular materials." *Chaos*, 9(3), 551-558.

Finkelstein, J. M., and Schafer, R. E. (1971). "Improved goodness-of-fit tests." *Biometrika*, 58(3), 641-645.

Finno, R. J., and Rechenmacher, A. L. (2003). "Effects of consolidation history on critical state of sand." *Journal of Geotechnical and Geoenvironmental Engineering*, 129(4), 350-360.

Finno, R. J., Harris, W. W., Mooney, M. A., and Viggiani, C. (1996). "Strain localization and undrained steady state of sand." *Journal of Geotechnical Engineering*, 122(6), 462-473.

Finno, R. J., Harris, W. W., Mooney, M. A., and Viggiani, G. (1997). "Shear bands in plane strain compression of loose sand." *Geotechnique*, 47(1), 149-165.

Fredlund, M. D., Fredlund, D. G., and Wilson, G. W. (2000). "Equation to represent grain-size distribution." *Canadian Geotechnical Journal*, 37(4), 817-827.

Frost, J. D. (1989). "Studies on the Monotonic and Cyclic Behavior of Sands," Ph.D. Thesis, Purdue University, West Lafayette.

Frost, J. D., and Jang, D.-J. (2000). "Evolution of sand microstructure during shear." *Journal of Geotechnical and Geoenvironmental Engineering*, 126(2), 116-130.

Frost, J. D., and Kuo, C.-Y. (1996). "Automated determination of the distribution of local void ratio from digital images." *Geotechnical Testing Journal*, 19(2), 107-117.

Frost, J. D., and Park, J. Y. (2003). "A critical assessment of the moist tamping technique." *Geotechnical Testing Journal*, 26(1), 57-70.

Frost, J. D., Hebeler, G. L., Evans, T. M., and DeJong, J. T. (2004). "Interface behavior of granular soils." *Engineering Construction and Operations in Challenging Environments Earth and Space 2004: Proceedings of the Ninth Biennial ASCE Aerospace Division International Conference*, League City/Houston, TX, United States, 65.

Garboczi, E. (2002). "Materials and Methods." *13th ACBM/NIST Computer Modeling Workshop*, Gaithersburg, MD.

Gilbert, P. A., and Marcuson, W. F., III. (1988). "Density variations in specimens subjected to cyclic and monotonic loads." *Journal of Geotechnical Engineering*, 114(1), 1-20.

Gudehus, G., and Nubel, K. (2004). "Evolution of shear bands in sand." *Geotechnique*, 54(3), 187.

Han, C., and Drescher, A. (1993). "Shear bands in biaxial tests on dry coarse sand." *Soils and Foundations*, 33(1), 118-132.

Han, C., and Vardoulakis, I. G. (1991). "Plane-strain compression experiments on water-saturated fine-grained sand." *Geotechnique*, 41(1), 49-78.

Harr, M. E. (1987). *Reliability-Based Design in Civil Engineering*, Dover Publications, Minneola, New York.

Harris, W. W., Viggiani, G., Mooney, M. A., and Finno, R. J. (1995). "Use of stereophotogrammetry to analyze the development of shear bands in sand." *Geotechnical Testing Journal*, 18(4), 405-420.

Hebeler, G. L. (2005). "Multi-Scale Behavior at Geomaterial Interfaces," Ph.D. Thesis, Georgia Institute of Technology, Atlanta.

Henkel, D. J., and Gilbert, G. D. (1952). "The effect of the rubber membrane on the measured triaxial compression strength of clay samples." *Geotechnique*, 3(1), 20-29.

Henkel, D. J., and Wade, N. H. (1966). "Plane Strain Tests on a Saturated Remolded Clay." *Journal of the Soil Mechanics and Foundations Division, ASCE*, 92(SM6), 67-80.

Hillel, D. (1980). *Fundamentals of Soil Physics*, Academic Press, New York.

Ibrahim, A. A., and Kagawa, T. (1991). "Microscopic measurement of sand fabric from cyclic tests causing liquefaction." *Geotechnical Testing Journal*, 14(4), 371-382.

Itasca. (1996). "FLAC Users Manual", version 3.3, Minneapolis.

Itasca. (2003). "PFC-2D: Particle Flow Code in Two Dimensions", version 3.00, Minneapolis.

Itasca. (2004). "PFC-2D: Particle Flow Code in Two Dimensions", version 3.0, Minneapolis.

Iwashita, K., and Oda, M. (2000). "Micro-deformation mechanism of shear banding process based on modified distinct element method." *Powder Technology*, 109(1), 192.

Jang, D.-J. (1997). "Quantification of sand structure and its evolution during shearing using image analysis," Ph.D. Thesis, Georgia Institute of Technology, Atlanta.

Jang, D.-J., and Frost, J. D. (2000). "Use of image analysis to study the microstructure of a failed sand specimen." *Canadian Geotechnical Journal*, 37(5), 1141-1149.

Jensen, R. P., Bosscher, P. J., Plesha, M. E., and Edil, T. B. (1999). "DEM simulation of granular media-structure interface: Effects of surface roughness and particle shape." *International Journal for Numerical and Analytical Methods in Geomechanics*, 23(6), 531-547.

Kim, H. (2005). "Spatial Variability in Soils: Stiffness and Strength," Ph.D. Thesis, Georgia Institute of Technology, Atlanta.

Kim, M. K., and Lade, P. V. (1988). "Single hardening constitutive model for frictional materials: I. Plastic potential function." *Computers and Geotechnics*, 5(4), 307-324.

Kjellman, W. (1936). "Report on an Apparatus for Consummate Investigation of Mechanical Properties of Soils." *First International Conference on Soil Mechanics and Foundation Engineering*, Vol. 2, Cambridge, MA, 16-20.

Kuhn, M. R. (1999). "Structured deformation in granular materials." *Mechanics of Materials*, 31(6), 407-429.

Kuhn, M. R. (2002). "A torus primitive for particle shapes with the discrete element method." *Discrete Element Methods: Numerical Modeling of Discontinua*, Santa Fe, NM, United States, 42-46.

Kuhn, M. R. (2003). "OVAL", version 0.6.5, Portland, OR.

Kuo, C. Y. (1994). "Quantifying the fabric of granular materials in an image analysis approach," Ph.D. Thesis, Georgia Institute of Technology, Atlanta.

Kuo, C. Y., Frost, J. D., and Chameau, J. L. A. (1998). "Image analysis determination of stereology based fabric tensors." *Geotechnique*, 48(4), 515-525.

Kuo, C., and Frost, J. D. (1995). "Quantifying the Fabric of Granular Materials - An Image Analysis Approach." Research Report No. GIT-CEE/GEO-95-1, School of Civil and Environmental Engineering, Georgia Institute of Technology, Atlanta, 251.

Kuo, C., and Frost, J. D. (1996). "Uniformity evaluation of cohesionless specimens using digital image analysis." *Journal of Geotechnical Engineering*, 122(5), 390-396.

La Rochelle, P. (1967). "Membrane, drain, and area correction in triaxial test on soil samples failing along a single shear plane." *Proceedings of the Third Panamerican Conference on Soil Mechanics and Foundation Engineering*, Vol. 1, Caracas, 273-292.

La Rochelle, P., Leroueil, S., Trak, B., Blais-Leroux, L., and Tavenas, F. (1988). "Observational approach to membrane and area corrections in triaxial tests." Advanced Triaxial Testing of Soil and Rock, ASTM STP 977, R. T. Donaghe, R. C. Chaney, and M. L. Silver, eds., American Society for Testing and Materials, Philadelphia, 715-731.

Lade, P. V., and Kim, M. K. (1988). "Single hardening constitutive model for frictional materials. II. Yield criterion and plastic work contours." *Computers and Geotechnics*, 6(1), 13-29.

Lade, P. V., and Wang, Q. (2001). "Analysis of shear banding in true triaxial tests on sand." *Journal of Engineering Mechanics*, 127(8), 762-768.

Lee, K. L. (1970). "Comparison of Plane Strain and Triaxial Tests on Sand." *Journal of the Soil Mechanics and Foundations Division*, 96(3), 901-923.

Leroueil, S., Tavenas, F., La Rochelle, P., and Tremblay, M. (1988). "Influence of filter paper and leakage on triaxial testing." Advanced Triaxial Testing of Soil and Rock, ASTM STP 977, R. T. Donaghe, R. C. Chaney, and M. L. Silver, eds., American Society for Testing and Materials, Philadelphia, 189-201.

Lilliefors, H. W. (1967). "On the Kolmogorov-Smirnov test for normality with mean and variance unknown." *American Statistical Association Journal*, 62(318), 399-402.

MatWeb. (2005). "DuPont Dow Elastomers Neoprene Latex 671A (Polychloroprene)." Material Property Data, http://www.matweb.com/search/SpecificMaterial.asp?bassnum=PDVE2F.

Mooney, M. A., Finno, R. J., and Viggiani, M. G. (1998). "Unique critical state for sand?" *Journal of Geotechnical and Geoenvironmental Engineering*, 124(11), 1100-1108.

Muehlhaus, H. B., and Vardoulakis, I. (1987). "Thickness of shear bands in granular materials." *Geotechnique*, 37(3), 271-283.

Ng, T. T., and Changming, W. (2001). "Comparison of a 3-D DEM simulation with MRI data." *International Journal for Numerical and Analytical Methods in Geomechanics*, 25(5), 497-507.

Ng, T. T., and Dobry, R. (1992). "Non-linear numerical model for soil mechanics." *International Journal for Numerical and Analytical Methods in Geomechanics*, 16(4), 247-263.

NIST. (2005). "Engineering Statistics Handbook." http://www.itl.nist.gov/, C. Croarkin and P. Tobias, eds., National Institute of Standards and Technology.

Nova, R. (2004). "The role of non-normality in soil mechanics and some of its mathematical consequences." *Computers and Geotechnics*, 31(3), 185-191.

Oda, M. (1976). "Fabrics and Their Effects on the Deformation Behavior of Sand." Special Issue, Department of Foundation Engineering, Faculty of Engineering, Saitama University, Japan.

Oda, M., and Iwashita, K. (2000). "Study on couple stress and shear band development in granular media based on numerical simulation analyses." *International Journal of Engineering Science*, 38(15), 1713-1740.

Oda, M., and Kazama, H. (1998). "Microstructure of shear bands and its relation to the mechanisms of dilatancy and failure of dense granular soils." *Geotechnique*, 48(4), 465-481.

Pachakis, M. D. (1976). "The influence of the membrane restraint on the measured strength of a soil sample failing along a single shear plane in the triaxial test." *Geotechnique*, 26(1), 226-230.

Park, J. Y. (1999). "A critical assessment of moist tamping and its effect on the initial and evolving structure of dilatant triaxial specimens," Ph.D. Thesis, Georgia Institute of Technology, Atlanta.

Peric, D. (2003). *Personal communication*. Kansas State University, Manhattan, KS.

Peric, D., and Hwang, C. (2002). "Experimental investigation of plane strain behavior of Georgia kaolin." *Proceedings of the 8th International Conference on Numerical Methods in Geomechanics -- NUMOG VIII*, Rome, Italy, 93-98.

Peric, D., Runesson, K., and Sture, S. (1992). "Evaluation of plastic bifurcation for plane strain versus axisymmetry." *Journal of Engineering Mechanics*, 118(3), 512-524.

Powrie, W., Ni, Q., Harkness, R. M., and Zhang, X. (2005). "Numerical modeling of plane strain tests on sands using a particulate approach." *Geotechnique*, 55(4), 297-306.

Proctor, D. C., and Barton, R. R. (1974). "Measurements of the angle of interparticle friction." *Geotechnique*, 24(4), 581-604.

Radjai, F., Evesque, P., Bideau, D., and Roux, S. (1995). "Stick-slip dynamics of a one-dimensional array of particles." *Physical Review E. Statistical Physics, Plasmas, Fluids, and Related Interdisciplinary Topics*, 52(5), 5555-5564.

Roscoe, K. H. (1970). "The influence of strains in soil mechanics." *Geotechnique*, 20(2), 129-170.

Rothenburg, L., and Bathurst, R. J. (1991). "Numerical simulation of idealized granular assemblies with plane elliptical particles." *Computers and Geotechnics*, 11(4), 315-329.

Rothenburg, L., and Bathurst, R. J. (1992). "Micromechanical features of granular assemblies with planar elliptical particles." *Geotechnique*, 42(1), 79-95.

Rowe, P. W. (1969). "Relation Between Shear Strength Of Sands In Triaxial Compression Plane Strain And Direct Shear." *Geotechnique*, 19(1), 75-86.

Rudnicki, J. W., and Rice, J. R. (1975). "Conditions for the localization of deformation in pressure-sensitive dilatant materials." *Journal of the Mechanics and Physics of Solids*, 23(6), 371-394.

Santamarina, J. C., and Cho, G. C. (2001). "Determination of Critical State Parameters in Sandy Soils - Simple Procedure." *Geotechnical Testing Journal*, 24(2), 185-192.

Santamarina, J. C., and Cho, G. C. (2003). "The Omnipresence of Localization in Geomaterials." *Proceedings of the 3rd International Symposium on the Deformation Characteristics of Geomaterials*, Lyon, 465-473.

Santamarina, J. C., and Fratta, D. (1998). *Introduction to Discrete Signals and Inverse Problems in Civil Engineering*, ASCE Press, Reston, VA.

Santamarina, J. C., Klein, K. A., and Fam, M. A. (2001). *Soils and Waves*, John Wiley and Sons, West Sussex, England.

Sola/Hevi-Duty. (1999). "Silver Line Series - Single & Multi-Output Linears." http://www.solaheviduty.com/products/powersupplies/silverline.htm, Rosemont, IL.

Stormont, J. C., and Anderson, C. E. (1999). "Capillary barrier effect from underlying coarser soil layer." *Journal of Geotechnical and Geoenvironmental Engineering*, 125(8), 641-648.

Symons, I. F. (1967). "Discussion." *Proceedings, Geotechnical Conference, Shear Strength Properties of Natural Soils and Rocks*, Oslo, Norway, 175-177.

Tannant, D. D., and Wang, C. (2002). "PFC Model of Wedge Penetration into Oil Sands." *Geotechnical Special Publication No. 117: Discrete Element Methods, Numerical Modeling of Discontinua*, Santa Fe, NM, 311-316.

Terzaghi, K. V. (1936). "The shearing resistance of saturated soils." *Proceedings of the First International Conference on Soil Mechanics*, Vol. 1, Cambridge, 54-56.

Thomas, P. A., and Bray, J. D. (1999). "Capturing nonspherical shape of granular media with disk clusters." *Journal of Geotechnical and Geoenvironmental Engineering*, 125(3), 169-178.

Towhata, I., and Lin, C.-E. (2003). "Microscopic observation of shear behavior of granular material." *Proceedings of the 3rd International Symposium on the Deformation Characteristics of Geomaterials*, Lyon, 113-118.

U.S. Silica Company. (1997). "Product Data, ASTM 20/30 Unground Silica." http://www.u-s-silica.com/PDS/Ottawa/OttASTM2030Sand2000.PDF, Berkeley Springs, WV.

Underwood, E. E. (1970). *Quantitative Stereology*, Addison-Wesley Publishing Company, Reading, MA.

Vardoulakis, I. (1980). "Shear band inclination and shear modulus of sand in biaxial tests." *International Journal for Numerical and Analytical Methods in Geomechanics*, 4(2), 103-119.

Vardoulakis, I. (1989). "Shear-banding and liquefaction in granular materials on the basis of a Cosserat continuum theory." *Ingenieur-Archiv*, 59(2), 106-113.

Vardoulakis, I. (1996a). "Deformation of water-saturated sand: I. Uniform undrained deformation and shear banding." *Geotechnique*, 46(3), 441-456.

Vardoulakis, I. (1996b). "Deformation of water-saturated sand: II. Effect of pore water flow and shear banding." *Geotechnique*, 46(3), 457-472.

Vardoulakis, I., and Aifantis, E. C. (1991). "Gradient flow theory of plasticity for granular materials." *Acta Mechanica*, 87(3-4), 197-217.

Vardoulakis, I., and Goldscheider, M. (1981). "Biaxial apparatus for testing shear bands in soils." *Proceedings of the 10th International Conference on Soil Mechanics and Foundation Engineering*, Vol. 1, Stockholm, Sweden, 819-824.

Vardoulakis, I., and Graf, B. (1985). "Calibration of constitutive models for granular materials using data from biaxial experiments." *Geotechnique*, 35(3), 299-317.

Vardoulakis, I., Goldscheider, M., and Gudehus, G. (1978). " Formation of shear bands in sand bodies as a bifurcation problem." *International Journal for Numerical and Analytical Methods in Geomechanics*, 2(2), 99-128.

Vermeer, P. A. (1990). "Orientation of shear bands in biaxial tests." *Geotechnique*, 40(2), 223-236.

Voyiadjis, G. Z., Alsaleh, M. I., and Alshibli, K. A. (2005). "Evolving internal length scales in plastic strain localization for granular materials." *International Journal of Plasticity*, 21(10), 2000-2024.

Voyiadjis, G. Z., and Song, C. R. (2005). "A coupled micro-mechanical based model for saturated soils." *Mechanics Research Communications*, 32(5), 490-503.

Wang, L. B., Frost, J. D., and Lai, J. S. (2004). "Three-dimensional digital representation of granular material microstructure from X-ray Tomography imaging." *Journal of Computing in Civil Engineering*, 18(1), 28-35.

Yang, C.-T. (2002). "Boundary Condition and Inherent Stratigraphic Effects on Microstructure Evolution in Sand Specimens," Ph.D. Thesis, Georgia Institute of Technology, Atlanta.

Yang, X. (2005). "Three-Dimensional Characterization of Inherent and Induced Sand Microstructure," Ph.D. Thesis, Georgia Institute of Technology, Atlanta.

Yoshida, T., and Tatsuoka, F. (1997). "Deformation property of shear band in sand subjected to plane strain compression and its relation to particle characteristics." *Proceedings of the 14th International Conference on Soil Mechanics and Foundation Engineering*, Hamburg, 237-240.

Yoshida, T., Tatsuoka, F., Kamegai, Y., Siddiquee, M. S. A., and Park, C. S. (1994). "Shear banding in sands observed in plane strain compression." *Proceedings of the 3rd International Workshop on Localization and Bifurcation Theory for Soils and Rocks*, Rotterdam, 165-179.